Advanced Materials for Electrochemical Energy Conversion: From Self-Supported Catalytic Electrodes to Atomically Dispersed Catalysts

Zhipeng Yu
Chemistry
Faculty of Sciences
2022

Orientador
Joaquim Luís Bernardes Martins de Faria, Professor Associado com Agregação, FEUP

Coorientador
Lifeng Liu, Staff Researcher, International Nanotechnology Laboratory


U.PORTO
FACULDADE DE CIÊNCIAS
UNIVERSIDADE DO PORTO

Declaração de Honra

Eu, [Zhipeng Yu], natural de [People's Republic of China], residente em [Braga, Portugal] com o telefone [933162879], nacional de [Chinese], portador (a) do Cartão de Passaporte nº [E54586680], inscrito(a) no Programa Doutoral em [Chemistry] da Faculdade de Ciências da Universidade do Porto declaro, nos termos do disposto na alínea a) do artigo 14.º do Código Ético de Conduta Académica da U.Porto, que o conteúdo da presente tese reflete as perspetivas, o trabalho de investigação e as minhas interpretações no momento da sua entrega.

Ao entregar esta tese, declaro, ainda, que a mesma é resultado do meu próprio trabalho de investigação e contém contributos que não foram utilizados previamente noutros trabalhos apresentados a esta ou outra instituição.

Mais declaro que todas as referências a outros autores respeitam escrupulosamente as regras da atribuição, encontrando-se devidamente citadas no corpo do texto e identificadas na secção de referências bibliográficas. Não são divulgados na presente tese quaisquer conteúdos cuja reprodução esteja vedada por direitos de autor.

Tenho consciência de que a prática de plágio e auto-plágio constitui um ilícito académico.

[Nome]

[Local e data]

Acknowledgement

It was already four years since I started my study and research at Faculty of Engineering-University of Porto (FEUP) and International Nanotechnology Laboratory (INL) in 2018. During these four years, I have met many friends and colleagues who have helped me a lot in work and life. Therefore, I have to give a big thanks to all of them.

First of all, I would like to thank my supervisor Prof. Joaquim L. Faria for giving me this opportunity to do a PhD research in his group. Prof. Faria has provided me with huge help in my study and research, facilitating my quick integration into his team and accelerating my research process. During this period, he gave me many good comments and suggestions on my research work, which brought me a new perspective on the problem.

I thank my co-supervisor Dr. Lifeng Liu. He gave me full support in my research topic and provided academic guidance. This thesis was completed under the guidance of Dr. Lifeng Liu. He also shared much valuable information with me, such as experimental skills, academic webinars and literature. Meanwhile, I thank him for offering me financial support for some experimental characterizations and academic conferences, benefiting me greatly. I have learned much in his group and become more confident in scientific research. Thanks again for his support and guidance.

Then, I would like to thank all my colleagues and friends in Portugal. Thanks to the colleagues in my INL group, Junyuan Xu, Zhixin Tai, Isilda Amorim, Ana Araujo, Nan Zhang, Ziyu Lu, Yue Li, Jonathan Ruiz, Haiyan Jin, who help me with patience and kind during my study and research in this group. Morever, I thank the members of LSRE-LCM group in FEUP, Prof. Cláudia G. Silva, Dr. Maria J. Sampaio, André Torres-Pinto. They provided a huge help and gave me good advice when I experimented in FEUP. I am very happy to be colleagues and work with them.

I would like to express my sincere thank to the kind help and support in material characterization and theoretical calculations. Thanks to Dr. Alec P. LaGrow and Dr. Oleksandr Bondarchuk (INL) for the help of transmission electron microscopy and X-ray photoelectron spectroscopy characterization. Thanks to Prof. Yuanyue Liu (University of Texas at Austin, USA), Dr. Yifan Li (Qingdao University of Technology, China), Prof. Bo Li (Institute of Metal Research, China) and his PhD student Chaowei Si for the help of density functional theory calculations. I gratefully acknowledge Dr. Vlad Martin Diaconescu, Dr. Laura Simonelli (ALBA Synchrotron, Spain) and Dr. Wolfgang A.

Caliebe, Dr. Akhil Tayal (Deutsches Elektronen-Synchrotron DESY, Germany) for the help in the X-ray absorption spectroscopy experiments.

I also am grateful for the scholarship for the Ph.D research offered by the China Scholarship Council (Grant no. 201806150015). This work was also financially supported by: LA/P/0045/2020 (ALiCE), UIDB/50020/2020 and UIDP/50020/2020 (LSRE-LCM) funded by national funds through FCT/MCTES (PIDDAC); project PTDC/QUI-QFI/29600/2017 - POCI-01-0145-FEDER-029600 - funded by FEDER funds through COMPETE2020 - Programa Operacional Competitividade e Internacionalização (POCI) and with financial support of FCT/MCTES through national funds (PIDDAC).

Last but not least, I would like to express my greatest gratitude to my family, my parents and my girlfriend. Thanks for their support, understanding, and encouragement.

Resumo

Com o aumento exponencial da demanda por energia e as preocupações com a poluição ambiental causada pelo consumo de energias não renováveis provenientes de fontes de combustíveis fósseis, o desenvolvimento de energias limpas e sustentáveis, assim como a sua disseminação para aplicação em vários sectores industriais, tornou-se uma necessidade essencial para atingir a neutralidade carbónica global. Os dispositivos para conversão eletroquímica de energia, nomeadamente eletrolisadores de água, células de combustível e baterias de metal-ar, têm um papel vital nos sistemas de energias renováveis, e o desempenho destes dispositivos está, em grande parte, dependente do catalisador aplicado, o qual pode reduzir significativamente as barreiras à reação e melhorar a eficiência energética dos dispositivos.

Esta tese é dedicada ao desenvolvimento de novos catalisadores, eficientes, duráveis e de baixo custo, que possam ser usados em várias reações eletroquímicas, tais como reação de evolução do Hidrogénio (HER), reação de evolução do Oxigénio (OER), reação de redução do Oxigénio (ORR) e reação de electro-oxidação (EOR) de moléculas pequenas, e a sua aplicação em eletrolisadores de água, células de combustível e baterias de metal-ar.

O Capítulo 1 apresenta uma introdução generalizada aos desafios a serem superados bem como uma revisão da produção de Hidrogénio (H_2) por via de eletrolisadores de água e baterias de Zinco-ar. Adicionalmente, são também revistos diferentes tipos de catalisadores, incluindo elétrodos auto suportados, *nanoclusters* (NCs) e catalisadores dispersados atomicamente (ADCs), assim como as suas vantagens para uso em conversão eletroquímica de energia.

O Capítulo 2 é dedicado ao desenvolvimento de uma série de materiais baseados em metais de transição (TM) com estruturas eletrónicas e morfologia específicas que promovam a eletrólise de água salgada. Os catalisadores auto suportados são reportados como uma solução eficiente para desenvolver electrocatalisadores com elevadas atividade e estabilidade comparando com os convencionais eletrocatalisadores de revestimento em forma de pó. Neste capítulo, primeiro, nanofios de fósfeto de níquel cobalto depositados em *Carbon Paper* (Co-Ni-P/CP) funcionando como elétrodos catalíticos auto suportados aplicados na eletrólise de água salgada para produção de H_2 acoplada à reação de oxidação da Hidrazina (HzOR) e à HER. Isto prova que adicionar uma molécula pequena como a Hidrazina (N_2H_4) no eletrólito

alcalino-salgado pode efetivamente mover o potencial de oxidação anódico para valores mais negativos e, consequentemente, aumentar a diferença de sobrepotencial entre a formação de hipoclorito e a EOR anódica de moléculas pequenas contendo hidrogénio, o que permite a obtenção de densidades de corrente elevadas que serão aplicadas na HER catódica durante a eletrólise da água salgada, sem formação de hipoclorito que é um composto corrosivo e poluente quando libertado para o meio ambiente. Adicionalmente, uma "espuma" de Níquel e Ferro com maior flexibilidade mecânica foi também desenhada e fabricada por o crescimento *in-situ* de uma matriz de nanotubos com Níquel e Ferro seguida de sulfurização/fosforização a dois passos (NiFeSP). O elétrodo, assim fabricado, combina numerosas qualidades tais como múltiplas componentes metal-não-metal, arquitetura tridimensional, heterointerfaces abundantes e sítios ativos subcoordenados, o que pode resultar numa sinergia para impulsionar a reação de oxidação eletrocatalítica da Ureia (UOR), a OER e a HER. Para evitar a interferência da reação de evolução do Cloro (CER), o autor substituiu a OER pela UOR, o que, ao mesmo tempo, diminui a necessidade de injetar energia na eletrólise de água salgada alcalina. Neste caso, os elétrodos bifuncionais NiFeSP, ativos para HER e UOR, conseguem distribuir elevadas densidades de corrente, com relevância industrial, de 500 $mAcm^{-2}$, a diferenças de potencial baixas e, mais impressionante, sobrevivem em eletrólise contínua a uma corrente tão elevada durante 1000 horas sem degradação notória. Estes trabalhos sugerem uma estratégia eficaz para desenvolvimento e síntese de elétrodos catalíticos de elevadas atividade e estabilidade para eletrólise de água salgada, a qual encontrará aplicações na produção em massa de Hidrogénio renovável a baixo custo.

O Capítulo 3 lida com NCs ultrafinos para melhorar a catálise da oxidação da água com densidades de corrente elevadas em meio ácido. É já sabido que a performance eletroquímica de catalisadores está bastante associada ao número de sítio ativos expostos. Assim, à parte das estruturas tridimensionais auto suportadas que permitem uma rápida transferência carga/massa, reduzir o tamanho das nanopartículas (NPs), *clusters* atómicos ou até a obtenção de átomos isolados é uma estratégia importante para atingir atividades elevadas a baixo custo. Baseado nisto, uma estratégia simples e com custo controlado foi proposta e consistia na deposição de *nanoclusters* de Óxido de Irídio com défice de Oxigénio (IrO_X NCs) ultrafinos (1-2 nm) num coletor corrente de Titânio (H-Ti@IrO_X) com elevada área superficial e estável em meio ácido. Estudos experimentais abrangentes e os cálculos da Teoria da Densidade Funcional (DFT) confirmam que a presença de NCs de tamanho pequeno e a falha de Oxigénio melhora

significativamente a eficiência da OER em meio ácido. H-Ti@IrO_X consegue catalisar continuamente a OER em meio fortemente ácido a 200 mA cm^{-2} durante 130 horas com uma degradação mínima, sustentando o uso promissor para eletrólise da água com membrana de transferência de protões (PEMWE).

No Capítulo 4, uma sucessão de ADCs é investigada em detalhe. A redução do tamanho das partículas metálicas nos catalisadores até átomos isolados pode maximizar a eficiência da utilização de cada átomo metálico e gerar um ambiente com abundantes coordenações insaturadas, o que é expectável que tenha um importante papel na melhoria da atividade catalítica. Aqui, uma série de ADCs foi desenhada e preparada. Em primeira instância, catalisadores com átomos isolados (SACs) de Ródio (Rh) suportados em Carvão Ativado (Rh_1/AC) com prominente performance catalítica para HER foram construídos por via de uma dispersão induzida por reação química de cima para baixo usando Rh NPs como material de partida. Em seguida, ADCs com Ruténio (Ru) (Ru(0.2)-NC) contemdo quantidade de metal adicionado ultra baixa foram aplicados na eletrólise eficiente da água. Os cálculos da DFT provaram que a ligação Ruténio-Azoto (Ru-N) presta um importante papel na redução da barreira energética das reações, impulsionando a atividade da HER e da OER. Além disso, quando assistida por uma membrana bipolar (BPM) ácida-alcalina, onde a HER em solução ácida é favorecida cineticamente e a solução básica favorece cineticamente a OER, esta assimetria ácido-alcalino na eletrólise da água com membrana bipolar (BPMWE) possibilita a operabilidade a baixas diferenças de potencial de célula de apenas 0.89 V para distribuir uma densidade de corrente de 10 mA cm^{-2} e consegue manter a estabilidade mais de 100 horas sem queda de performance significativa devido à assistência da neutralização eletroquímica resultante da passagem de eletrólitos, o que mostra um elevado potencial para produção de Hidrogénio com poupança de energia. Finalmente, Ir/Ru SACs foram introduzidos em nitrato de carbono grafítico mesoporoso (g-CN), os quais exibiram atividades catalíticas elevadas, eletrocatalítica e fotocatalítica, para HER. Além disso, foi demonstrada durabilidade electrocatalítica e fotocatalítica de longo termo excecionais. Os nossos cálculos de DFT revelaram que a quantidade dos átomos isolados de Ir e Ru no g-CN altera a estrutura eletrónica, resultando numa *bandgap* reduzida e facilitando a transferência eletrónica durante o processo catalítico.

No Capítulo 5, foram desenhados centros ativos bimetálicos flexíveis e investigados na catálise do oxigénio. Tem sido bastante reportado que os catalisadores biatómicos (DACs) têm mais chances de ajustar o centro da banda-d através da interação das órbitas eletrónicas e trazer estruturas e propriedades eletrónicas únicas, exibindo

comportamento catalítico melhorado. Aqui, foram desenvolvidos Ir e Fe DACs (IrFe-N-C) e depositados em suporte de Carbono modificado com Nitrogénio por via da estratégia de pirólise com precursor encapsulado. Várias técnicas de caracterização avançada, incluindo microscopia eletrónica de transmissão por varrimento em campo escuro anular de elevado ângulo (HAADF-STEM) e Espectroscopia de absorção de raios-X sincronizada (XAS), confirmaram, inequivocamente, a dispersão atómica do Ir e do Fe e a presença de pares atómicos de IrFe. O IrFe-N-C preparado mostrou performance catalítica substancialmente mais elevada para ORR e OER quando comparado com os homólogos de átomos isolados (i. e., Ir-N-C e Fe-N-C), revelando uma bifuncionalidade favorável e superando muitos dos catalisadores bifuncionais para ORR/OER atualmente reportados na literatura. A excelente bifuncionalidade do IrFe-N-C permite-lhe que funcione como um cátodo de ar de alta performance em baterias de Zinco-ar (ZABs). Além disso, os nossos cálculos de DFT demostraram que a configuração diatómica leva a uma subtil modulação de estrutura eletrónica. O Fe nos sítios diatómicos contribui mais para ORR, enquanto o Ir nos sítios diatómicos presta um papel mais importante para a OER. Ambos os sítios activos trabalham em sinergia e, juntos, promovem a eletrocatálise do Oxigénio.

Esta tese é focada na síntese de electro/foto-catalisadores eficientes com estruturas eletrónicas e morfologia únicas para a conversão de energia. Os estudos experimentais e teóricos deram novas perspetivas acerca dos mecanismos de melhoria da atividade. Os métodos propostos para construir elétrodos auto suportados, Ncs e ADCs podem posteriormente ser aplicados no desenvolvimento de catalisadores heterogéneos de elevado desempenho para sistemas de conversão e armazenamento de energia de baixo custo.

Palavras-chave: Conversão de energia, catálise da água, Baterias Zn-ar, elétrodos auto suportados, catalisadores dispersados atomicamente.

Abstract

With the ever-growing global demand for energy and concerns about environment pollutions caused by the consumption of non-renewable fossil fuels, developing clean and sustainable energy as well as promoting its widespread adoption in various industrial sectors have become a pressing need to achieve global carbon neutrality. Electrochemical energy conversion devices including water electrolyzers, fuel cells, and metal–air batteries play a vital role in the renewable energy systems, and the performance of these devices is largely dependent on the catalysts used, which can significantly lower reaction barriers and improve device's energy efficiency. Therefore, rational design and cost-effective synthesis of high-performance catalysts are of critical importance for widespread deployment of the aforementioned energy conversion devices.

This thesis is dedicated to the development of new efficient, durable and cost-effective catalysts that can be used in a number of electrochemical reactions in water electrolyzes, fuel cells and metal-air batteries, including the hydrogen evolution reaction (HER), the oxygen evolution reaction (OER), the oxygen reduction reaction (ORR), and the electro-oxidation reaction (EOR) of small molecules.

Chapter 1 presents a general introduction to the challenges to be tackled and an overview of the hydrogen (H_2) production *via* water electrolysis and zinc-air batteries. Moreover, different forms of catalysts including self-supported electrodes, nanoclusters (NCs), and atomically dispersed catalysts (ADCs), as well as their advantages for use in electrochemical energy conversion, are briefly reviewed.

Chapter 2 is devoted to designing a series of transition-metal (TM)-based materials with proper electronic structures and morphology towards boosting the saline water electrolysis. The self-supported electrode is regarded as an effective approach to developing highly active electrocatalysts with exceptional stability, compared to the conventional coated powdery-type electrocatalysts. In this chapter, firstly, cobalt nickel phosphide nanowires was coated at carbon paper (Co-Ni-P/CP) as a self-supported bifunctional catalytic electrode for saline water electrolysis to produce H_2 by coupling of hydrazine oxidation reaction (HzOR) and HER. It proves that adding a small-molecule chemical such as hydrazine (N_2H_4) into the alkaline-saline electrolyte can effectively shift the anodic oxidation potential negatively and thereby significantly increase the overpotential gap between the hypochlorite formation and the anodic EOR of small hydrogen-containing molecules, which allows for a large current density to be applied for

the cathodic HER during the saline water electrolysis, without the formation of any environmentally-unfriendly, corrosive hypochlorite species. Furthermore, the nickel/iron foam with more mechanical flexibility was designed and fabricated to *in situ* grow nickel-iron phosphosulfide (NiFeSP) nanotube array through a two-step sulfurization/phosphorization approach. Thus-fabricated electrode combines several merits including multiple metal/non-metal components, 3D hierarchical architecture, and abundant heterointerfaces and under-coordinated active sites, which can work in synergy boosting the electrocatalytic urea oxidation reaction (UOR), OER, and HER activity. To prevent the interfering chlorine evolution reaction (CER) from happening, the author further substituted the OER with UOR, which meanwhile lowers the need for overall energy input in alkaline-saline water electrolysis. In this case, the bifunctional NiFeSP electrode, active for both HER and UOR, can deliver a large industry-relevant current density of 500 mA cm^{-2} under a low cell voltage, and more impressively, survive for continuous electrolysis at such a high current density for 1000 hours without notable degradation. These works provide an effective strategy for the design and synthesis of highly-active and stable catalytic electrodes for saline water electrolysis, which will find applications in massive production of low-cost renewable hydrogen.

Chapter 3 deals with ultrafine NCs for enhancing water oxidation catalysis at high current density in acidic media. It is well known that the electrochemical performance of catalysts is tightly associated with the number of exposed active sites. Hence, apart from the 3-dimensions (3D) self-supported structure enabled rapid charge/mass transfer, reducing the size of particles to nanoparticles (NPs), atomic clusters, or even single atoms is an important strategy to achieve higher activity and lower the cost. Based on this, a simple and cost-effective strategy was proposed to deposit ultrafine oxygen-defective IrO_x NCs (1–2 nm) on a high-surface-area, acid-stable titanium current collector (H-Ti@IrO_x). Comprehensive experimental studies and density functional theory (DFT) calculations confirm that the presence of small size of NCs and oxygen defects significantly improve acidic OER performance. Remarkably, H-Ti@IrO_x can continuously catalyze the OER in strong acidic environment at 200 mA cm^{-2} for 130 hours with minimal degradation, holding substantial promise for use in proton exchange membrane water electrolysis (PEMWE).

In Chapter 4, a succession of ADCs are investigated in detail. Further reducing the size of metal catalysts to isolated atoms can maximize the utilization efficiency of each metal atom and generate an abundance of unsaturated coordination environment, which is expected to play an important role in improving the catalytic performance. Here, a series of ADCs were designed and prepared. Firstly, rhodium (Rh) single-atom catalysts

(SACs) supported on activated carbon (Rh_1/AC) with the outstanding HER performance were constructed *via* a "top-down" chemical reaction induced dispersion process using Rh NPs as the starting materials. Then, the bifunctional ruthenium (Ru) ADCs (Ru (0.2)-NC) with ultralow metal loading was employed for efficient water electrolysis. DFT calculations prove that the ruthenium-nitrogen (Ru-N) bonding plays an important role in lowering the energy barrier of the reactions, boosting the HER and OER activities. Furthermore, assisted by a bipolar membrane (BPM), where HER is accomplished in a kinetically favorable acidic solution and OER in a kinetically favorable basic solution, such asymmetric acid-alkaline bipolar membrane water electrolysis (BPMWE) operates under a low cell voltage of only 0.89 V to deliver a current density of 10 mA cm^{-2} and can sustain over 100 hours without significant performance decay due to the assistance of electrochemical neutralization resulting from the crossover of the electrolytes, which shows a great potential for energy-saving hydrogen production. Finally, the Ir/Ru SACs were anchored on mesoporous graphitic carbon nitride (g-CN), which exhibit superior catalytic activities for both electrocatalytic and photocatalytic HER. Moreover, outstanding long-term electrocatalytic and photocatalytic durability has been demonstrated. Our DFT calculations disclose that loading Ir and Ru single-atoms on g-CN alters the electronic structure, resulting in a reduced bandgap and facilitating electron transfer during the catalytic processes.

In Chapter 5, flexible dual-metal active sites were designed and investigated in the oxygen catalysis. It is well documented that the double-atom catalysts (DACs) have more chances to adjust the d-band center by the interaction of electronic orbits and bring unique structure and electronic properties, thus exhibiting superior catalytic behaviours. Herein, the IrFe DACs (IrFe-N-C) were designed and dispersed on nitrogen-doped carbon *via* a cage-encapsulated precursor pyrolysis strategy. Various advanced characterization techniques including the High-angle annular dark-field scanning transmission electron microscopy (HAADF-STEM) and synchrotron-based X-ray absorption spectroscopy (XAS) unambiguously confirmed the atomic dispersion of Ir and Fe and the presence of IrFe atomic pairs. The as-obtained IrFe-N-C shows substantially higher electrocatalytic performance for both ORR and OER when compared to the single-atom counterparts (*i.e.*, Ir-N-C and Fe-N-C), revealing favorable bifunctionality, and outperform many state-of-the-art bifunctional ORR/OER catalysts reported in the literature. The excellent bifunctionality of IrFe-N-C enables it to serve as a high-performance air cathode in Zinc–air batteries (ZABs). Moreover, our DFT calculations demonstrate that the diatomic configuration leads to subtle electronic structure modulation. Fe in the diatomic sites contributes more to the ORR, while Ir in the diatomic

sites plays a more important role in the OER. The two active sites work in synergy and altogether promote oxygen electrocatalysis.

This thesis focused on the synthesis of efficient electro/photocatalysts with proper electronic structures and morphology for the energy conversion. The experimental and theoretical study gave new insights into the activity enhancement mechanisms. The proposed methods to construct self-supported electrode, NCs, and ADCs can further applied for the design of high-performance heterogeneous catalysts for low-cost energy storage and conversion systems.

Keywords: energy conversion, water catalysis, Zn–air batteries, self-supported electrode, nanocluster, atomically dispersed catalyst.

Contents

List of abbreviatons

Abbreviation	Meanning
AC	Activated carbon
ACL	Alkaline catalyst layer
ADCs	Atomically dispersed catalysts
AEM	Anion exchange membrane or adsorbate evolution mechanism
AEMFC	Anion exchange membrane fuel cell
AEMWE	Anion exchange membrane water electrolysis
AFM	Atomic force microscope
AOR	Ammonia oxidation reaction
AWE	Alkaline water electrolysis
BE	Binding energy
BESS	Battery energy storage systems
BET	Brunauer-Emmett-Teller
BoP	Balance of plant
BPM	Bipolar membranes
BPMWE	Bipolar membranes water electrolysis
CA	Chronoamperometry
CEM	Cation exchange membrane
CER	Chlorine evolution reaction
COHP	Crystal orbital Hamilton populations
CP	Carbon paper or chronopotentiometry
CV	Cyclic voltammetry
DACs	Double-atom catalysts
DFT	Density functional theory
DOS	Calculated density of states
DR UV–vis	Diffuse reflectance ultraviolet-visible
ECSA	Electrochemical active surface area
EDX	Energy-dispersive X-ray spectroscopy
EG	Ethylene glycol
EIS	Electrochemical impedance spectroscopy
ELF	Electron localization function
EOR	Electro-oxidation reaction
ESI-TOF-MS	Electrospray ionization time-of-flight mass spectrometer

EXAFS	Extended X-ray absorption fine structure
FCC	Face-centered cubic
FE	Faradaic efficiency
FFT-ED	Fast Fourier transformation electron diffraction
FT	Fourier transform
FT-IR	Fourier transform infrared spectroscopy
FTO	Fluorine-doped tin oxide
FWHM	Full width at half maximum
GC	Glassy carbon or gas chromatograph
GGA	Generalized gradient approximation
GHG	Greenhouse gases
GW	Gigawatt
g-CN	Graphitic carbon nitride
HAADF-STEM	High-angle annular dark-field scanning transmission electron microscopy
HER	Hydrogen evolution reactions
HSE	Heyd–Scuseria–Ernzerhof
HRTEM	High-resolution transmission electron microscopy
HzOR	Hydrazine oxidation reaction
ICDD	International Centre for Diffraction Data
ICP-OES	Inductively coupled plasma-optical emission spectroscopy
LEDs	Light-emitting diodes
LOM	Lattice oxygen mechanism
LSV	Linear sweep voltammetry
MEA	Membrane Electrode Assemblies
MOFs	Metal organic frameworks
M-S	Mott-Schottky
NC	nitrogen-doped carbon
NCs	Nanoclusters
NPs	Nanoparticles
NRs	Nanorods
NTs	Nanotubes
NWs	Nanowires
OER	Oxygen evolution reaction
ORR	Oxygen reduction reaction

OSWE	Overall saline water electrolysis
OUSWE	Overall urea-mediated saline water electrolysis
PAW	Projected augmented wave
PBE	Perdew-Burke-Ernzerhof
PBS	Phosphate buffered saline
PDOS	Projected density of states
PEM	Proton exchange membrane
PEMFC	Proton exchange membrane fuel cell
PEMWE	Proton exchange membrane water electrolysis
PGMs	Platinum group metals
PHT	$KHTi_4O_9 \cdot 0.5H_2O$
PL	Photoluminescence
RDS	Rate-determining step
RDE	Rotating disk electrode
RHE	Reversible hydrogen electrode
ROS	Reactive oxygen species
RPBE	Revised Perdew-Burke-Ernzerhof
SACs	Single-atom catalysts
SCE	Saturated calomel electrode
SEM	Scanning electron microscopy
SMSIs	Strong metal-support interactions
STEM	Scanning transmission electron microscopy
TACs	Triple-atom catalysts
TEM	Transmission electron microscopy
TMs	Transition-metals
TOF	Turnover frequency
UOR	Urea oxidation reaction
UPS	Ultraviolet photoelectron spectroscopy
VASP	Vienna Ab initio Simulation package
VBM	Valence band maximum
wrBPMWE	Water recombination bipolar membrane water electrolysis
wsBPMWE	Water splitting bipolar membrane water electrolysis
WT	Wavelet transforms
XAFS	X-ray absorption fine spectroscopy
XANES	X-ray absorption near-edge structure

XAS	X-ray absorption spectroscopy
XRD	X-ray diffraction
XPS	X-ray photoelectron spectroscopy
ZABs	Zn–air batteries

List of symbols

Abbreviation	Meaning	Unit
G	Gibbs free energy	eV or KJ mol^{-1}
ΔG	Gibbs free energy changes	eV or KJ mol^{-1}
E	Potential	V
E^{Θ}	Standard electrode potential	V
E_c	conduction band position	eV
E_f	Fermi level	eV
E_g	Band gap	eV
E_v	Valence band position	eV
η	Overpotential	V
R_{ct}	Charge transfer resistance	Ω
R_s	Resistance of electrolyte	Ω
i	Current	A
j	Current density	mA cm^{-2}
T_s	Tafel slope	mV dec^{-1}
C_{dl}	Double-layer capacitance	mF cm^{-2}
A	Area of working electrode	cm^2
F	Faraday constant	96485 C mol^{-1}
V	Voltage	V
n	Number of active sites	mol

1. Introduction

1.1 Problem statement

With rapid development of economy and continuous increase of global population, the demand for energy is increasing rapidly [1, 2]. The U.S. Energy Information Administration predicted that world energy consumption will grow by nearly 50% from 2018 to 2050. At present, conventional fossil fuels, such as coal, oil and natural gas, as the main body of the current energy system, provide more than 80% of the energy consumption for human life and production [3]. Being non-renewable in nature, the over-exploitation and utilization of fossil fuels have caused serious challenges for human health, environmental pollution and energy waste [4, 5]. For example, the emission of carbon dioxide (CO_2) and other greenhouse gases (GHG) makes climate change drastically, consequently leading to extreme weather conditions, rising sea levels, ocean acidification and loss of biodiversity; the emission of sulfur dioxide (SO_2) and other harmful gases from automobiles causes acid rain and other atmospheric pollution, which is a serious threat to human health [4]. Meanwhile, the world's population continues to increase and industrialization expands, which further enlarge energy demand. So the world's energy supply will hardly meet all needs of the entire human society, and the world is facing an increasingly severe energy challenge.

How to realize the transformation and optimization of energy mode, improve the quality of human life, ameliorate the living environment of the earth, and rebuild the ecological balance of the earth is a worldwide challenge. The most effective way to this challenge is to vigorously develop sustainable renewable energy, including solar energy, wind energy, and nuclear energy, etc., to replace traditional fossil fuels [2, 6]. This can only be accomplished by developing corresponding energy conversion and storage technologies, such as water electrolysis (WE), battery energy storage systems (BESS), hydrogen fuel cells and CO_2 capture and conversion [2].

1.2 Hydrogen production *via* water electrolysis

Hydrogen (H_2) has long been proposed to be a very promising carbon-neutral energy carrier due to its high gravimetric energy density (33.6 kWh kg^{-1}) and zero-carbon emission feature [7, 8]. Industrially, about 95% of global hydrogen is produced through methane steam reforming and coal gasification, which heavily rely on non-renewable fossil fuels and emits a great deal of CO_2 [9-11], bringing about a series of environmental

problems [12]. Hydrogen produced by electrolysis of water only accounts for 4% of the total hydrogen production. If renewable electricity is used to power electrolysis of water, thus-produced hydrogen will become “green”, which can decarbonize power and transport sectors as well as hard-to-abate industries (**Figure 1.1**) [13].

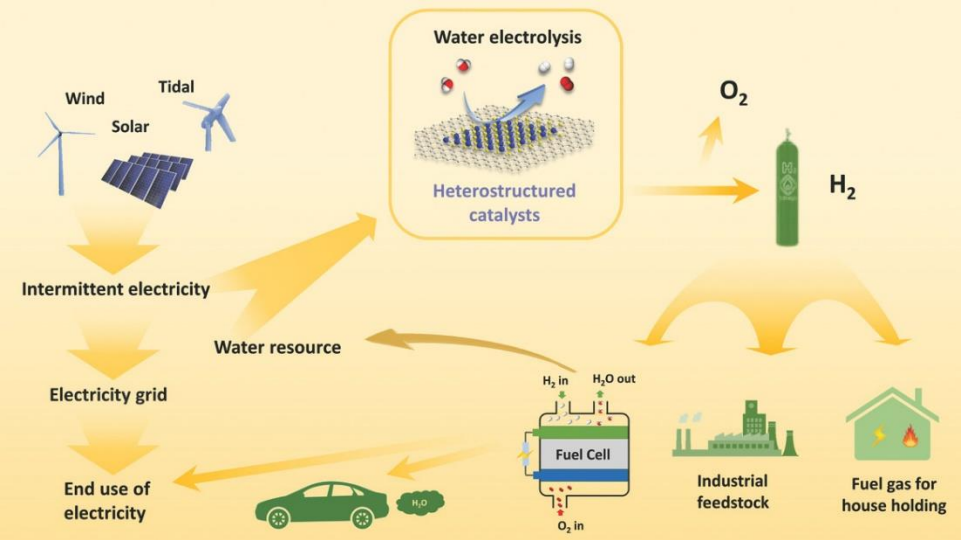

Figure 1.1 A sustainable pathway for the production and utilization of hydrogen energy [13].

Water electrolysis consists of two half-reactions, namely, the hydrogen evolution reaction (HER) at the cathode and the oxygen evolution reaction (OER) at the anode, as illustrated in **Figure 1.2** [14]. Electrolysis is generally carried out in an electrolytic cell, which is separated by either an ion exchange membrane or a porous diaphragm into two compartments where HER and OER take place [15]. It is well known that acids and bases have significantly higher conductivity than pure water, and therefore water electrolysis is typically performed under either acidic or alkaline conditions to avoid large polarization loss [16, 17]. Water electrolysis reactions occurring in acid and alkaline can be described as follows:

Under neutral or alkaline conditions:

$$\text{Cathodic reaction (HER): } 2H_2O + 2e^- \rightarrow H_2\uparrow + 2OH^- \qquad (1\text{-}1)$$

$$\text{Anodic reaction (OER): } 2OH^- \rightarrow H_2O + \tfrac{1}{2}\,O_2\uparrow + 2e^- \qquad (1\text{-}2)$$

Under acidic conditions:

$$\text{Cathodic reaction (HER): } 2H^+ + 2e^- \rightarrow H_2\uparrow \qquad (1\text{-}3)$$

$$\text{Anodic reaction (OER): } H_2O \rightarrow 2H^+ + \tfrac{1}{2}\,O_2\uparrow + 2e^- \qquad (1\text{-}4)$$

The overall reaction: $H_2O \rightarrow H_2 \uparrow + ½\ O_2 \uparrow$ (1-5)

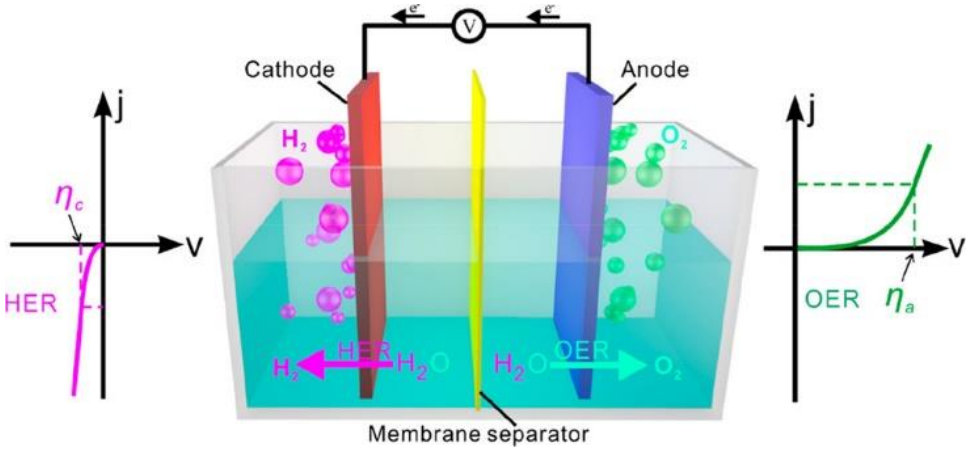

Figure 1.2 Hydrogen evolution reaction and oxygen evolution reaction of electrocatalytic water splitting [18].

When a given voltage is applied to the cell, hydrogen and oxygen gases will evolve from the cathode and anode, respectively. From a thermodynamic point of view, the theoretical minimum voltage required for water electrolysis is 1.23 V [17]. However, both the HER and OER involve multi-step proton-coupled electron transfer processes, and each electron transfer process will introduce a reaction kinetic energy barrier (activation energy). The superposition of these activation energies will lead to an actual water electrolysis voltage much greater than 1.23 V, and this part of the applied voltage is called overvoltage or overpotential (**Figure 1.2**) [18]. The energy loss caused by overvoltage further increases the cost of hydrogen production. Therefore, to diminish energy consumption, the electrolysis voltage should be reduced as much as possible. The hydrogen evolution overpotential and oxygen evolution overpotential can be minimized by employing highly active HER and OER catalysts, thereby increasing the water electrolysis efficiency [14, 19-21].

Membrane-based water electrolysis technologies including proton exchange membrane water electrolysis (PEMWE) and anion exchange membrane water electrolysis (AEMWE), show great promise for mass production of high-purity and pressured hydrogen [22, 23]. Among them, kilowatt- and megawatt-scale PEM electrolyzers have been deployed commercially and showed remarkable advantages, such as higher current densities (0.6 – 2.0 A cm^{-2}), cheap feedstock (pure water), fast response, operational flexibility and high gas purity (**Figure 1.3a**) [24, 25]. However, to enable long-term stability, rare and expensive platinum group metals (PGMs), *e.g.*, platinum (Pt) for cathodic HER and iridium oxides (IrO_2) for anodic OER, must be used, which increases the cost and restrict large-scale commercial application [24, 26]. On the

other hand, alkaline water electrolysis (AWE) is a mature technology and has been widely applied in Europe to produce hydrogen for ammonia synthesis in the early 20th century [27]. AWE allows for the use of earth-abundant transition-metal (TM) catalysts and less-expensive steel in electrolyzer hardware (**Figure 1.3b**) [27-29]. Moreover, the alkaline conditions favors the OER kinetics compared with the acidic environment. However, alkaline electrolyzers can typically only operate at low current densities (0.2 – 0.4 A cm^{-2}), which translate to a low hydrogen production rate [19, 30].

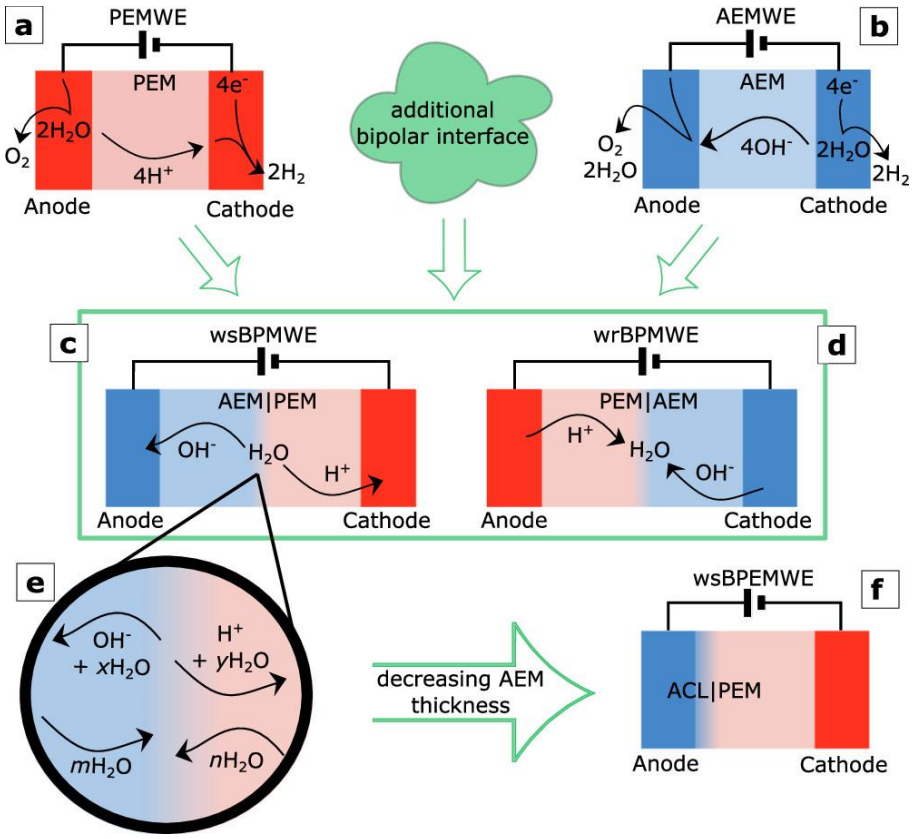

Figure 1.3 Schematic illustrating various membrane based water electrolysis technologies. a) PEMWE, b) AEMWE, c) water splitting bipolar membrane water electrolysis (wsBPMWE), d) water recombination bipolar membrane water electrolysis (wrBPMWE), e) water transport pathways in a bipolar membrane under reverse bias, and f) limiting case of decreasing AEM thickness with respect to PEM in direct contact with the alkaline catalyst layer (ACL), referred to as water splitting bipolar electrode membrane water electrolysis (wsBPEMWE) [31].

So far, the AEMWE and PEMWE systems have been optimized individually. A bipolar membrane (BPM) combines the advantages of AEMWE and PEMWE, and is highly preferable for use in water electrolysis. A BPM consists of a cation exchange membrane (CEM) adjoined with an anion exchange membrane (AEM) and allows for the use of different electrolytes as the anolyte and catholyte in the electrolyzer cell (**Figure 1.3c-f**) [32-35]. Given that the OER is kinetically favorable in alkaline conditions and the HER in acidic media, it would be favorable to accomplish these half reactions simultaneously in different electrolytes separated by the BPM in a single electrolyzer (**Figure 1.3c**) [35, 36].

Besides allowing for separate optimization of catalysts/electrolyte pairing for HER and OER, when bipolar membrane water electrolysis (BPMWE) is performed in the “forward bias” configuration (CEM side facing the cathode and AEM side facing the anode), as shown in **Figure 1.3d**, the external electrical energy needed to drive water electrolysis can be remarkably reduced due to the assistance of electrochemical neutralization energy [31, 37]. The application of the BPMWE could not only break the pH incompatibility of the electrocatalysts but also reduce the electrical energy input, opening up a new avenue toward energy-saving water electrolysis and showing prominent advantages over PEMWE and AWE [38, 39].

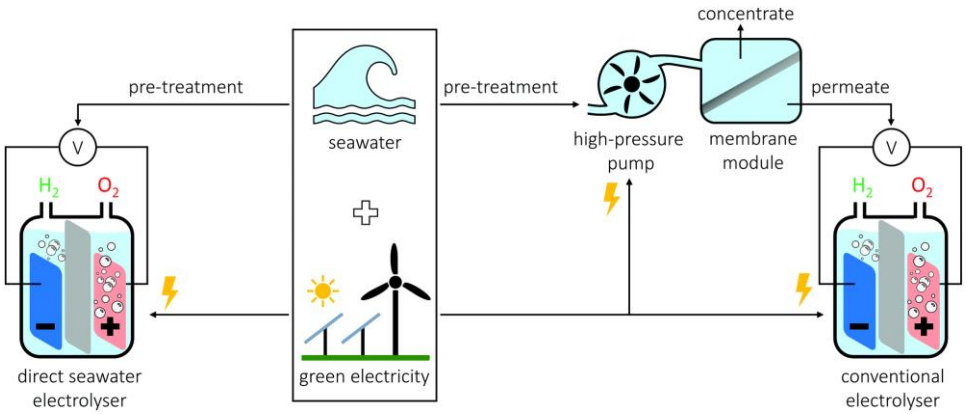

Figure 1.4 Two ways to make hydrogen from seawater and green electricity. The pathway on the left shows direct seawater splitting where only one device is required. In the pathway on the right, the seawater is first desalinated by reverse osmosis and then the water splitting is performed. For this pathway, electricity and a device are required for both desalination and water splitting [40].

Under alkaline conditions: $Cl^- + 2OH^- \rightarrow ClO^- + H_2O + 2e^-$ (1-6)

Under acidic conditions: $2Cl^- \rightarrow Cl_2 + 2e^-$ (1-7)

Water electrolysis requires high-purity water as feedstock, which increases the hydrogen production cost. Recently, direct seawater electrolysis attracted considerable attention and has shown significant potential for offshore green H_2 production, considering that seawater accounts for 96.5% of the world’s water resource and is virtually inexhaustible and that this approach potentially allows for marked reduction of the H_2 fuel price [41]. However, direct electrolysis of seawater faces extra challenges for dealing with the interference of side reactions, ionic poison, and corrosion on cell corrosion due to the presence of chloride ions (Cl^-) in seawater [40]. A notorious problem is the chlorine evolution reaction (CER) which would be competitive with OER on the anode. This reaction releases toxic and corrosive chlorine species (Cl_2 or ClO^- depending on the pH of electrolyte, see equations 1-6 and 1-7), which causes anode dissolution and environmental hazards, substantially reducing the electrolysis efficiency and

operational lifetime of electrolyzers [42, 43]. As a result, ancillary equipment is in most cases needed to desalinate and purify water before it is used for electrolysis. Such desalination/purification units markedly increase the overall cost of the system and thereby the price of H_2 (**Figure 1.4**) [40]. Therefore, it is highly desirable to develop efficient catalytic materials and membranes as well as to design new electrolyzer configurations to enable direct usage of low-grade or saline water for H_2 production [42, 43]. This is particularly favorable for large-scale offshore H_2 production emerged very recently, taking advantage of the largely abundant and free seawater resources and the capability of installing megawatt/gigawatt-scale offshore wind and solar farms, as pointed out by the recent techno-economic analyses [44].

1.2.1 The hydrogen evolution reaction

HER is the reduction process of protons on the cathode, which involves a two-electron transfer step. As shown in **Figure 1.5**, the HER process comprises three elementary reaction steps: Volmer, Heyrovsky or Tafel [18, 45]. Specifically, under acidic media, firstly, the H^+ in the electrolyte couples with electrons from the catalyst surface to generate adsorbed H*, which is called as the Volmer step (equation 1-8). Afterward, the generated H* may undergo two possible pathways: 1) the H* on the surface of the electrode reacts with the second electron and couples another H^+ to evolve H_2, which is called as the Heyrovsky step (equation 1-9); or 2) the Tafel step (equation 1-10): two H* nearby combine to produce H_2. Different from acidic HER, the Volmer step in alkaline electrolyte needs an additional H_2O molecule dissociation barrier to overcome, resulting in a 2−3 orders of magnitude slower rate than in acidic media [45]. In detail, H_2O molecules, act as a proton source, couple with electrons from the catalyst surface to generate adsorbed H* (equation 1-11). Similarly, the following reaction mechanism: either the Heyrovsky step (equation 1-12) or the Tafel step (equation 1-13) is applicable in alkaline conditions.

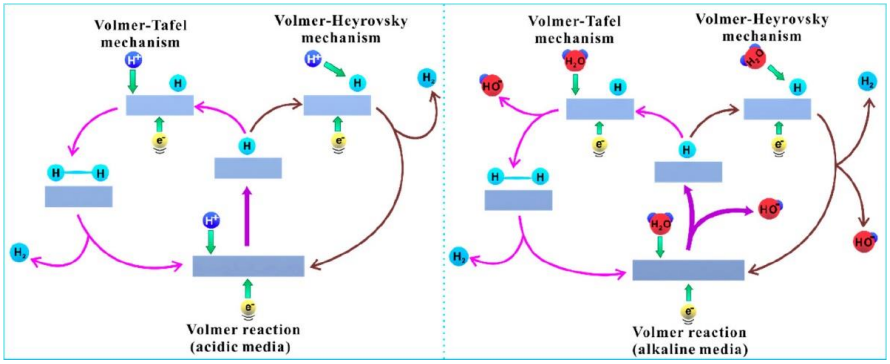

Figure 1.5 Mechanism of hydrogen evolution on the surface of an electrode in acidic (left) and alkaline (right) solutions [18].

In acidic medium:

$H_3O^+ + e^- + * \rightarrow H^* + H_2O$ Volmer (~120 mV dec^{-1}) (1-8)

$H_3O^+ + e^- + H^* \rightarrow H_2 \uparrow + H_2O$ Heyrovsky (~40 mV dec^{-1}) (1-9)

$H^* + H^* \rightarrow H_2 \uparrow$ Tafel (~30 mV dec^{-1}) (1-10)

In alkaline medium:

$H_2O + e^- + * \rightarrow H^* + OH^-$ Volmer (~120 mV dec^{-1}) (1-11)

$H_2O + e^- + H^* \rightarrow H_2 \uparrow + OH^-$ Heyrovsky (~40 mV dec^{-1}) (1-12)

$H^* + H^* \rightarrow H_2 \uparrow$ Tafel (~30 mV dec^{-1}) (1-13)

The Tafel plot represents the dependence of the corresponding current densities on the overpotentials, which provide insights into the reaction mechanism of HER process [46]. The theoretical Tafel slope for the Volmer step in HER is 120 mV dec^{-1}, which means that the discharge reaction (Volmer step) is slow and is regarded as the rate-determining step (RDS) (equations 1-8 and 1-11). When the discharge reaction is fast and the electrochemical desorption (Heyrovsky reaction) is slower, the RDS should be Heyrovsky step with Tafel slope of 40 mV dec^{-1} (equations 1-9 and 1-12). Similarly, the Tafel step (30 mV dec^{-1}) should be the RDS if the chemical desorption reaction is slower (equations 1-10 and 1-13) [18].

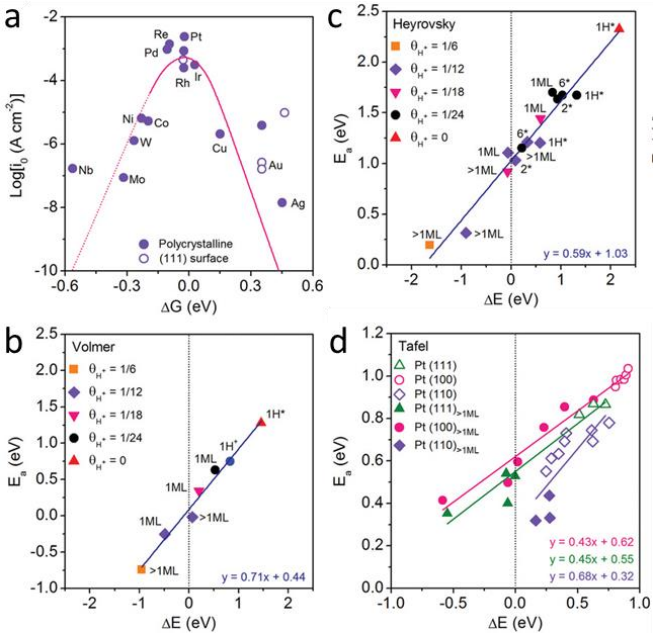

Figure 1.6 a) Hydrogen free binding energy versus activity. Circles represent experimental data, and the curve is from micro kinetic theory. b-d) Scaling relation between hydrogen free binding energy and activation barrier for each elementary HER step [47].

Density functional theory (DFT) calculations allow researchers to gain further insight into the catalytic mechanism of the HER. According to the Sabatier principle, the HER kinetics strongly depends on the interaction between the catalyst and the reactive intermediate (ΔG_{H^*}) [48]. As shown in the **Figure 1.6a**, the closer to zero ΔG_{H^*} is, the higher the HER activity, where the volcano peak is located around iridium (Ir), rhodium (Rh) and Pt that are among the best HER catalysts verified experimentally. The weak interaction will result in few intermediates bound to the catalyst, while the strong interaction will make products dissociation difficult, both causing the poor HER activity [47]. It is further confirmed by the scaling relation between hydrogen free binding energy and activation barrier toward three elementary processes: the Volmer, the Heyrovsky, and the Tafel steps (**Figure 1.6b-d**).

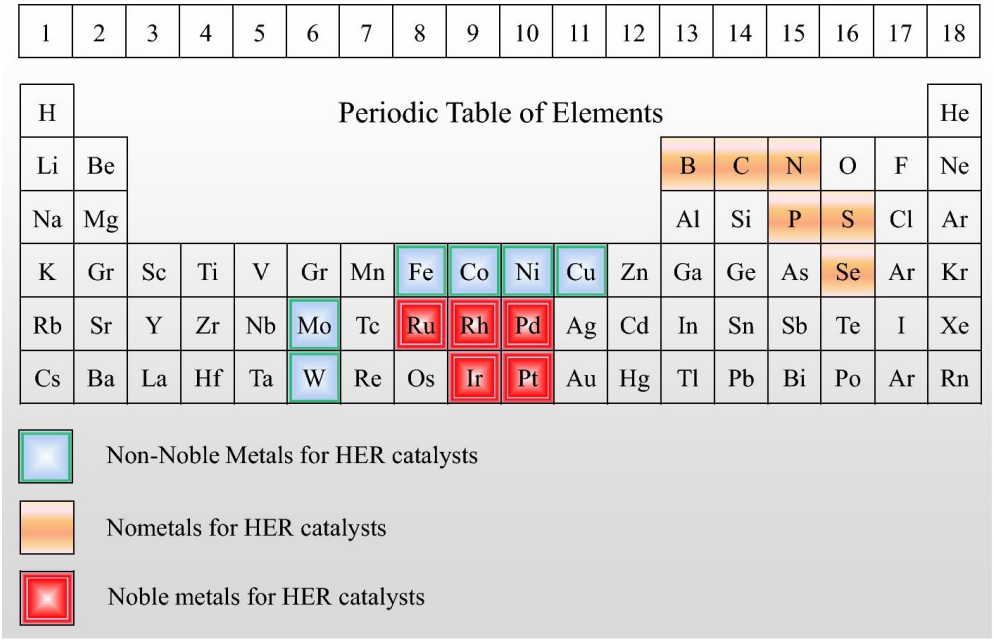

Figure 1.7 Elements that are commonly used for constructing HER electrocatalysts [49].

Thanks to DFT calculations which are useful in validation of experimental results and prediction of novel catalysts, a general guideline for selecting elements to construct efficient HER electrocatalysts has been proposed. As shown in **Figure 1.7**, these elements, according to the general physical and chemical properties, can further be classified into three types as follows: 1) noble metal PGMs including Pt, Rh, Ir, ruthenium (Ru) and palladium (Pd), which locate at the top of the volcano plot, making them highly active as HER electrocatalysts; 2) transition metals (non-noble metals) including mainly iron (Fe), cobalt (Co), nickel (Ni), copper (Cu), molybdenum (Mo), and tungsten (W), which are promising alternatives to noble metal-based electrocatalysts due to their earth-

abundance and potential catalytic activity; 3) non-metals such as boron (B), carbon (C), nitrogen (N), phosphorus (P), sulfur (S), and selenium (Se), which can be used in composites to synthesize HER electrocatalysts [11, 49].

1.2.2 The oxygen evolution reaction

In comparison with the HER, the OER is a sluggish reaction in water electrolysis process, which requires a relatively large thermodynamic potential to generate oxygen through four-electron and four-proton transfer processes [50, 51]. The larger overpoential inevitably impedes the efficiency and increases the cost of water electrolysis, which hinders industrial production of hydrogen via water electrolysis to a certain extent. Many research groups have proposed possible mechanisms for OER. According to the origin of generated oxygen molecules, there are two widely accepted mechanisms, named the conventional adsorbate evolution mechanism (AEM) and the lattice oxygen mechanism (LOM) [26, 52]. According to the AEM, the OER proceeds in four elementary steps with the OH*, O* and OOH* as adsorbed intermediates, which strongly depend on the pH of the reaction medium [53, 54]. As described in **Figure 1.8**, in acidic media, the catalysts initially undergoes a decoupled proton–electron transfer process to form OH* on the active site (equation 1-14). Then, the generated OH* intermediates further deprotonate and couple with electrons transforming into O* (equation 1-15). Subsequently, O* may undergo two different pathways: 1) combining directly two O* to produce oxygen (O_2) (equation 1-16) or 2) converting to OOH* and further to produce O_2 through another two proton coupled electron transfer processes (equations 1-17 and 1-18), as shown by green and black arrows in **Figure 1.8** [54]. However, in alkaline media, the OER involves the oxidation of four hydroxyl ions to form to O_2 and water (equations 1-19 to 1-23, and red arrow in **Figure 1.8**) [52, 55].

In acidic medium:

$$H_2O \rightarrow OH^* + H^+ + e^- \quad (1\text{-}14)$$

$$OH^* \rightarrow O^* + H^+ + e^- \quad (1\text{-}15)$$

$$O^* + O^* \rightarrow O_2 \uparrow \quad (1\text{-}16)$$

$$H_2O + O^* \rightarrow OOH^* + H^+ + e^- \quad (1\text{-}17)$$

$$OOH^* \rightarrow O_2 \uparrow + H^+ + e^- \quad (1\text{-}18)$$

In alkaline medium:

$$OH^- \rightarrow OH^* + e^- \quad (1\text{-}19)$$

$$OH^- + OH^* \rightarrow H_2O + O^* + e^- \quad (1\text{-}20)$$

$$O^* + O^* \rightarrow O_2 \uparrow \quad (1\text{-}21)$$

$$OH^- + O^* \rightarrow OOH^* + e^- \quad (1\text{-}22)$$

$$OH^- + OOH^* \rightarrow O_2 \uparrow + H_2O + e^- \quad (1\text{-}23)$$

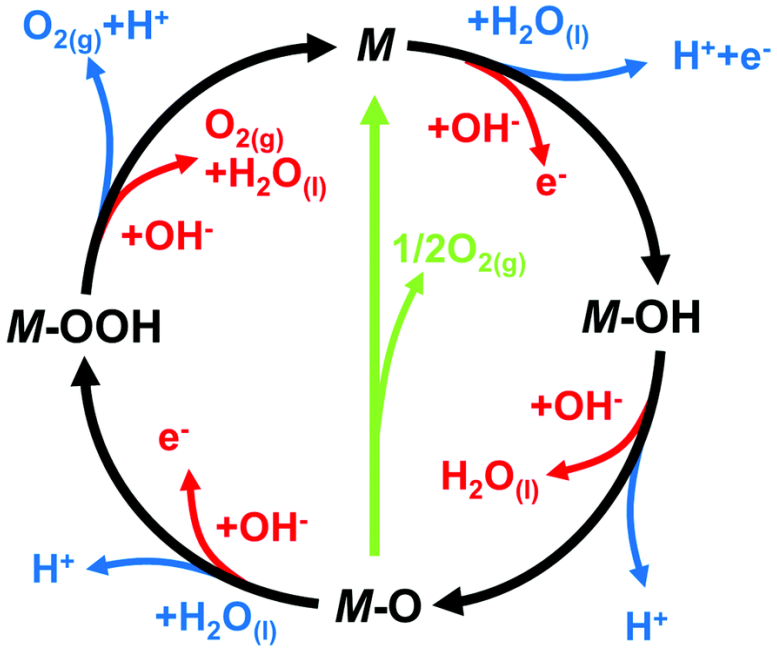

Figure 1.8 The OER mechanism for acid (blue line) and alkaline (red line) conditions. The black line indicates that the oxygen evolution involves the formation of a peroxide (M–OOH) intermediate (black line) while another route for direct reaction of two adjacent oxo (M–O) intermediates (green) to produce oxygen is possible as well [54].

The OER activity of electrocatalysts may be limited by one of the above-mentioned reaction processes. Therefore, it is necessary to theoretically understand the relationships between the active sites and intermediates during the OER process at molecule level. Nørskov and Rossmeisl et al. described the OER reaction pathways for a given electrocatalyst using DFT calculations based on the AEM [56-58]. As shown in **Figure 1.9a**, an ideal OER electrocatalyst exhibits zero overpotential, but the ideal case scenario is almost impossible to realize due to the linear relationships among the binding energies of different intermediates [54, 59]. Previous DFT-based computations have indicated that the binding energies of OH* and OOH* are tightly linked with a constant difference of 3.2 ± 0.2 eV, which is called the scaling relation (**Figure 1.9b**) [51, 58]. In addition, considering that the the second (the formation of O*) or the third (the formation of OOH*) step is often reported as the RDS of the OER process, $\Delta G_{OOH^*} - \Delta G_{OH^*}$ with a

minimum theoretical overpotential of 0.37 V, which is calculated by (3.2 V − 1.23 V × 2)/2, is proposed to be a primary descriptor to evaluate the OER performance [52, 57]. As shown in **Figure 1.9c**, an ideal catalyst with optimal electrocatalytic activity requires intermediate binding strengths, corresponding to the apex of the volcano [60]. According to the Sabatier's principle, either too weak or too strong binding strength of the key intermediates will lead the formation of O* or OOH* to be the RDS, which severely restricts the OER activity [61].

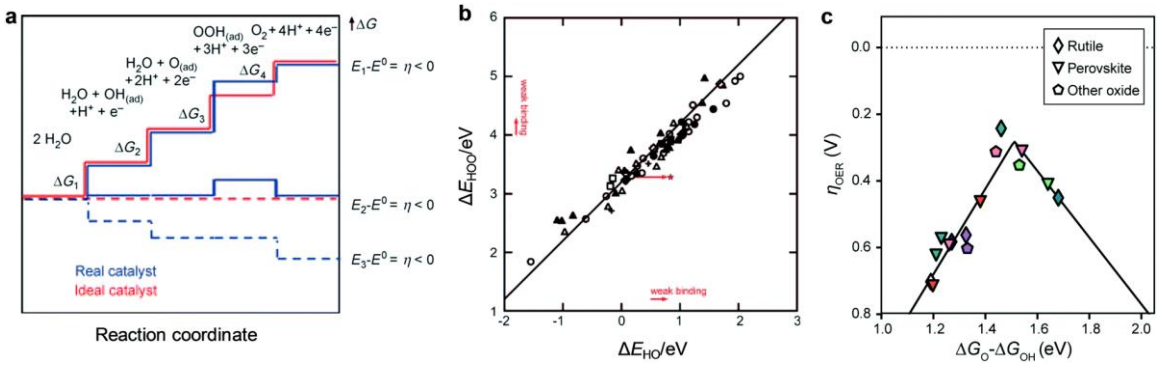

Figure 1.9 a) Gibbs free energies at U = 0 for ideal and actual catalysts. b) Adsorption energy of HOO* plotted against the adsorption energy of HO* on perovskite, rutile, anatase, Mn_xO_y, Co_3O_4, and NiO oxides [58]. c) OER volcano plot for rutile, perovskite, and other oxides [60].

Considering that the oxygen evolution process occurs on metallic surface active sites with the limitation of the scaling relationship, the AEM fails to explain the pH-dependent activity in a series of experimental studies [62-64]. Different from the conventional AEM, LOM breaks the restriction of this scaling relationship by involving the lattice oxygen and nonconcerted proton–electron transfer steps [50, 65]. As shown in **Figure 1.10**, the LOM process involves two neighboring metal sites, which is different with the AEM proceeding on a single metal site [50, 66]. In detail, firstly, the dehydrogenation of two OH* on the metal sites produces two metal–oxo species. And then the direct coupling of two adjacent reactive lattice oxygen species produces the O–O bond instead of involving the formation of OOH*, which can bypass the scaling relation limitation. Finally, O_2 is released and the active sites are subsequently recovered by the replenished OH^-. It is worth noting that in many cases the AEM and LOM occur simultaneously, resulting in a competition between these two mechanisms in the OER process [26]. The significant difference of AEM and LOM is the origin of produced oxygen: AEM assumes that the generated oxygen derives from the electrolyte while LOM postulates that O_2 partially or entirely originates from the lattice oxygen in the catalyst [67, 68].

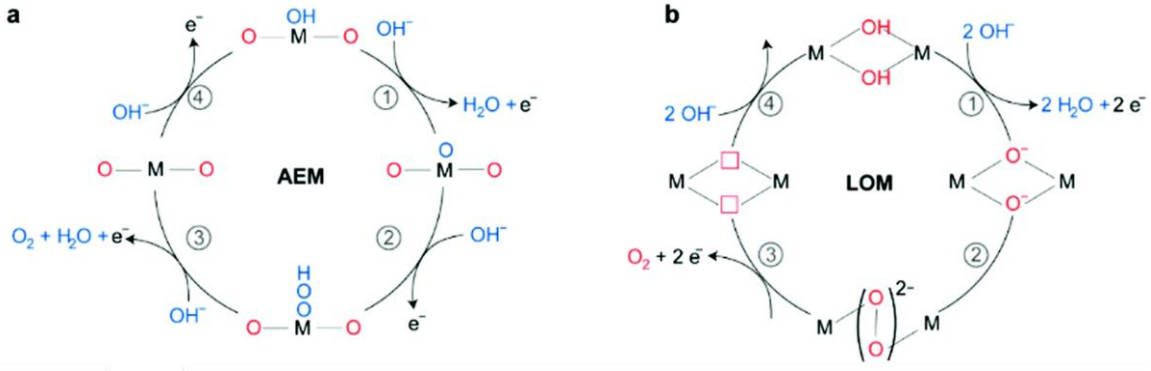

Figure 1.10 Schematic illustration of the OER mechanisms: a) AEM and b) LOM [50].

Electrocatalysts are the core part of a water electrolyzer determining its energy efficiency, so it is vital to develop efficient and stable electrocatalysts to overcome the sluggish reaction kinetics of OER [50, 54]. **Figure 1.11** describes typical elements used for constructing OER catalysts, which can be classified into three groups: PGMs, TMs and non-metal elements [52]. TM-based catalysts have demonstrated outstanding electrocatalytic performance, especially for stable OER in alkaline media. However, they suffer from poor catalytic stability and low activity for acidic OER in PEMWE. In this case, PGMs must be used, though they are expensive and scarce. Therefore, the search for novel catalysts with high efficiency, excellent durability, low cost and large natural abundance is crucially important for realizing large-scale commercialization of water electrolysis technologies.

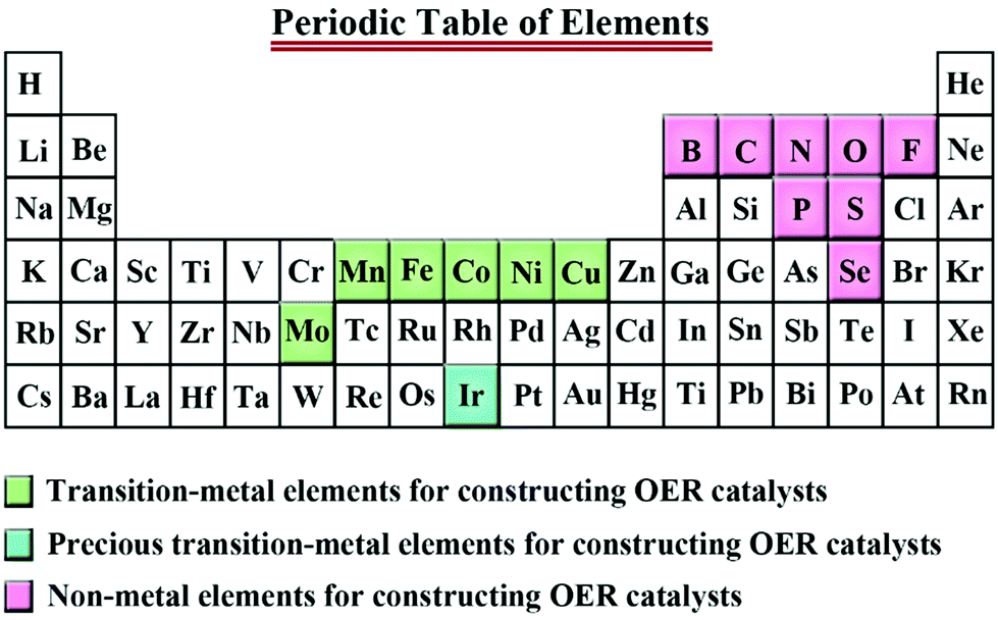

Figure 1.11 Investigated elements for constructing TM-based OER catalysts [52].

1.2.3 Energy-saving hydrogen production assisted by small molecule electro-oxidation

Although numerous excellent OER and HER catalysts have been reported, the overall electrocatalytic reaction rate has been largely restricted due to the sluggish kinetics of anodic OER [50, 54]. Additionally, mass production of H_2 based on technologically mature AWE faces some problems, for example, the generated oxygen and hydrogen gases may crossover the diaphragm causing explosion; moreover, the formation of reactive oxygen species (ROS) may damage the separator [69, 70]. To address these challenges, attempts have been made to replace OER with electro-oxidation reaction (EOR) of small hydrogen-containing molecules that happens at an anodic potential much lower than the thermodynamic onset potential of OER (*i.e.*, 1.23 V vs. reversible hydrogen electrode – RHE), such as hydrazine oxidation reaction (HzOR) [71, 72], urea oxidation reaction (UOR) [73, 74] and ammonia oxidation reaction (AOR) [75, 76]. Besides, the O_2 generated at the anode usually does not bring about added value. Therefore, coupling HER with electro-oxidation of the aforementioned organic molecules into high value-added products has lately attracted considerable attention (alcohols [77, 78], aldehyde [79], and biomass-derived compounds [80, 81]). The selected oxidation reactions with more favorable thermodynamics can not only reduce energy input during the whole electrocatalytic process, resulting in higher energy conversion efficiency, but also markedly pay back the energy investment with the co-production of various value-added products, further reducing the cost of hydrogen production (**Figure 1.12**) [70, 77].

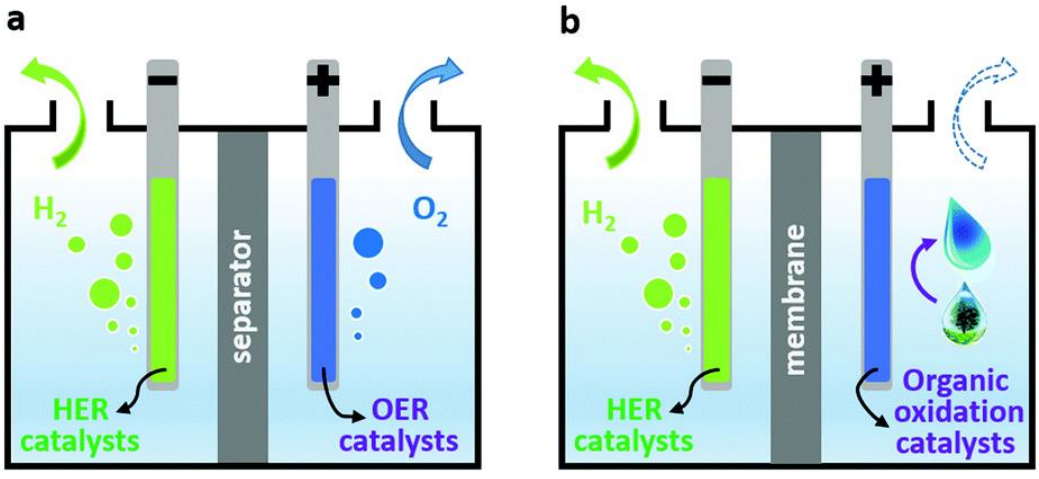

Figure 1.12 Design of a) a conventional water splitting electrolyzer and b) a novel electrolyzer integrating H_2 evolution with organic molecule oxidation [70].

As described above, the electrolysis of seawater is highly intriguing for sustainable energy production, but it also faces formidable technological challenges, in particular the CER happening at the anode, which competes with the OER and generates unfavorable

chlorine and/or hypochlorite that will corrode catalysts, membranes and other components over time and thereby substantially reduce the operational lifetime of the electrolyzer [43, 44]. As shown in the Pourbaix diagram in **Figure 1.13**, the CER can be suppressed by limiting the OER overpotential below 0.48 V under alkaline conditions [44, 82, 83]. However, the OER is a kinetically demanding process involving four proton-coupled electron transfer steps, and within the 480 mV overpotential limit it is unlikely to reach an electrolysis current density that is large enough to enable a high yield of H_2, even the most advanced OER electrocatalysts are employed. Replacing the OER by thermodynamically more favorable EOR not only offers a favorable strategy for energy-saving hydrogen production while enabling the co-production of various valuable products, but also provides an extra benefit in avoiding the notorious problems of chlorine chemistry without limiting the electrolysis current and hydrogen yield [72, 84]. Therefore, coupling EOR with HER in seawater water electrolysis represents a promising approach to sustainable, cost-effective production of hydrogen, which is a research topic of this thesis.

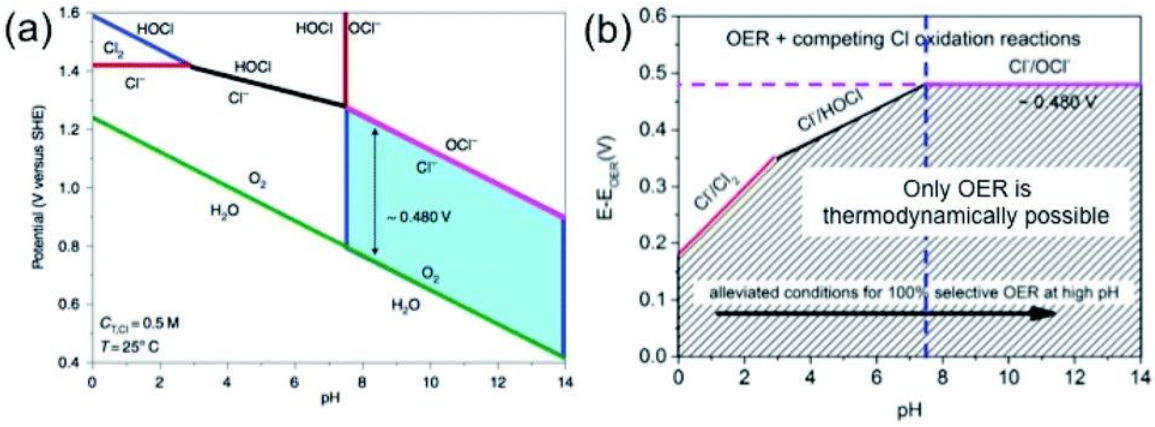

Figure 1.13 a) Pourbaix diagram showing the potential – pH relation of artificial seawater containing 0.5 M NaCl aqueous solution. The green line indicates the thermodynamic equilibrium between H_2O/O_2, and the red line in the alkaline side shows the equilibrium between Cl^-/OCl^- and in acidic side Cl^-/Cl_2. The blue filled area indicates a fixed potential difference of 480 mV at pH > 7. The black and blue lines in the acidic side show the equilibrium of Cl^-/HOCl and Cl_2/HOCl, respectively. b) Representation, derived from the Pourbaix diagram, showing the overpotential ranges for OER and other chlorine evolution reactions at different pH values [83].

1.3 Zinc-air battery

Renewable energy technology has been reshaping the energy consumption landscape of modern society, which would alleviate the relay on traditional fossil fuels and eradicate the environmental pollution issues [85]. Developing effective energy storage technologies and energy conversion devices is of critical importance for widespread deployment of renewable energy technologies [86]. Recently, metal–air batteries,

combining the anode of conventional batteries with the cathode of fuel cells, have received much interest as an alternative battery technology [86]. According to the metal of choice, different types of metal–air batteries including lithium (Li)–air, sodium (Na)–air, magnesium (Mg)–air, aluminum (Al)–air, potassium (K)–air, zinc (Zn)–air and Fe–air, have been developed, and their major characteristics are listed in **Table 1.1** [16, 87].

Table 1.1 Comparison of different metal–air batteries [16].

Battery systems	Li–air	Na–air	Mg–air	Al–air	K–air	Zn–air	Fe–air
Year invented	1996	2012	1966	1962	2013	1878	1968
Metal price (US$ kg^{-1})[a]	20	2.5	2.3	1.9	1.0	2.6	0.5
Cell voltage (V)	2.96	2.27	3.09	2.71	2.48	1.65	1.28
Energy density (Wh kg^{-1})[b]	3458	1106	2840	2796	935	1086	763
Electrolyte	Aprotic	Aprotic	Saline	Alkaline/ Saline	Aprotic	Alkaline	Alkaline

a) Metal prices are obtained from www.infomine.com/investment/metal-prices;
b) Energy densities are calculated including the contribution from O_2.

Although the open structure at the cathode enables continuous oxygen supply from the atmosphere and reduction in the overall battery weight, endowing metal–air batteries with extraordinarily high theoretical energy densities, all alkaline metal-air batteries show some technical drawbacks, such as various safety issues [16, 88, 89]. For example, Li–air batteries might be hardly commercialized on a large scale due to the inherent instability when exposed to O_2 or water and the limited resources of Li [88]. Despite the compatibility with aqueous electrolytes and extraordinary energy densities, the low reduction potentials (*e.g.*, Mg at −2.372 V and Al at −1.662 V) may cause rapid self-discharge and poor coulombic efficiency through HER, which hinder practical applications of Mg–air and Al–air batteries [16, 89]. In contrast, with rich metal abundance, competitive cost, high energy density, environmental friendliness and safety, Zn–air batteries (ZABs) in recent years have become a rechargeable battery technology of choice for stationary energy storage (**Figure 1.14**) [90].

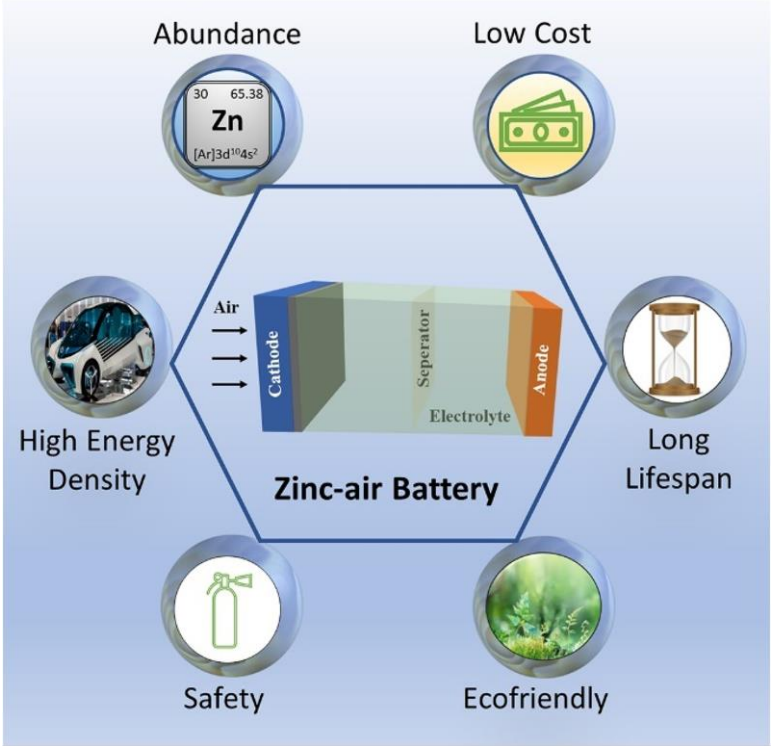

Figure 1.14 Advantages of zinc-air batteries as sustainable energy conversion/storage devices [90].

1.3.1 Principle and working mechanism

In general, ZABs are composed of Zn anode, electrolyte and air cathode [91]. The Zn anode is integrated into the Zn-air assembly as a Zn plate or Zn powders loaded on an electron-conducting support, and alkaline solution is generally used as the electrolyte because of the significant corrosion of Zn in acidic electrolyte [91]. In addition to acting as an ionic conducting medium, the electrolyte may cause unfavorable interfacial reactions on the anode [92, 93] (*e.g.*, zinc corrosion, zinc passivation, dendrite formation, and HER side-reaction) [94], undergo evaporation and poisoning [95], and give rise to electrode corrosion and carbonation on the cathode (**Figure 1.15a**) [93]. As shown in the Pourbaix diagram in **Figure 1.15b**, the electrochemical reaction of zinc and air electrodes critically depends on the pH of the electrolyte [96]. As the concentration of KOH increases (pH > 13), the highly soluble zincate ions (*i.e.*, $Zn(OH)_4^{2-}$) are favored, and 6 M KOH solution is favored for use as an electrolyte in ZABs in most cases because of its compatibility with the Zn anode and air cathode containing active catalysts. Meanwhile, a little amount of zinc chloride or zinc acetate can also be added into the solution to help the reversible re-deposition of Zn on the anode. According to the pH value of the electrolyte, ZABs can be categorized into alkaline-aqueous-electrolyte-based and near-neutral-electrolyte-based ZABs (**Figure 1.15c**).

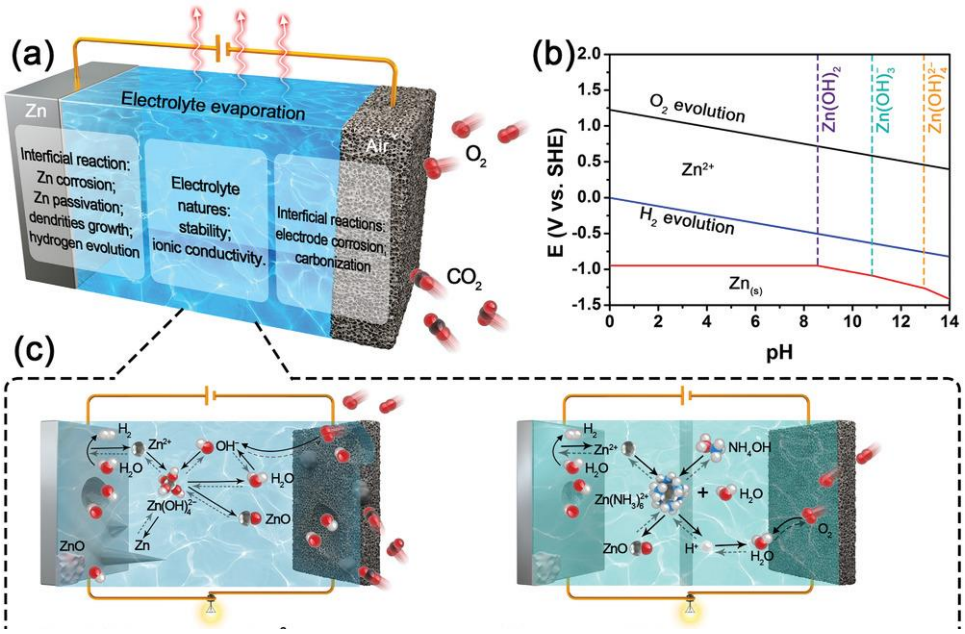

Figure 1.15 a) Potential challenges in ZABs related to electrolytes. b) Pourbaix diagram of zinc and oxygen. c) Schematic illustrating two kinds of ZABs [93].

The active material in the ZABs' cathode is air (oxygen), which is inexhaustible and green. The catalyst in the air cathode is one of the most important components, mainly responsible for reversible oxygen electrochemical reactions, including the oxygen reduction reaction (ORR) and the OER [92, 97]. During the battery charge/discharge process, electrochemical reactions occur at the anode and cathode simultaneously. Firstly, Zn reacts with the electrolyte to release electrons and generate soluble $Zn(OH)_4^{2-}$ (equation 1-24), which is decomposed into insoluble zinc oxide (ZnO) when the concentration increases during discharge process (equation 1-25). Then, the electrons reach the air cathode through the external circuit, where ORR occurs at the air cathode (equation 1-26). Finally, the generated OH^- species migrate from the air cathode to the metallic electrode in electrolyte and complete the overall reaction (equation 1-27) [91]. During recharging, reverse electrochemical reactions take place at anode and cathode, respectively. In this case, the OER occurs at the air electrode, oxidizing OH^- to form O_2. One of the most critical technical challenges in ZABs is that the oxygen reaction kinetics is sluggish, which is largely caused by the high overpotentials of ORR and OER, further resulting in poor charge/discharge performance [91]. For example, the working voltage of a ZAB is much lower than the theoretical value of 1.65 V; a charging voltage of 2 V or even higher is required for rechargeable ZABs when cycling, resulting in a low round-trip efficiency. Hence, developing highly efficient oxygen electrocatalysts toward the OER and ORR are of great importance for the commercialization of ZABs [97].

Anode: $Zn + 4OH^- \rightarrow Zn(OH)_4^{2-} + 2e^-$ (1-24)

$Zn(OH)_4^{2-} \rightarrow ZnO + H_2O + 2OH^-$ (1-25)

Cathode: $O_2 + 4e^- + 2H_2O \rightarrow 4OH^-$ (1-26)

Overall reaction: $2Zn + O_2 \rightarrow 2ZnO$ (1-27)

1.3.2 The oxygen reduction reaction

ORR is the cathodic reaction of almost all fuel cells and metal-air batteries, etc [98]. It is a complex electrochemical process with complicated mechanism, which involves a multi-step transfer of multiple electrons, with a variety of oxygen-containing intermediates generated [99, 100]. Therefore, the cathodic ORR requires a high overpotential, which is accomplished by two pathways: two-electron ($2e^-$) pathway or four-electron ($4e^-$) pathway, leading to the two different end-products, H_2O_2 or H_2O [100]. Currently, the mechanism proposed by Wroblowa in 1976 may be the most commonly accepted explanation for the complex ORR steps (**Figure 1.16**) [101]. In the process of ORR, oxygen molecules in the solution diffuses and are adsorbed on the catalyst surface to form adsorbed active oxygen molecules, which can be electrochemically reduced to either H_2O or H_2O_2. O_2 is directly reduced to H_2O through a direct four-electron pathway with a theoretical potential of 1.23 V (k_1), while O_2 can also be reduced to H_2O_2 through an indirect two-electron pathway with a theoretical potential of 0.70 V (k_2). Alternatively, the adsorbed intermediate H_2O_2 can be electro-reduced to H_2O with a rate constant of k_3, along with reversible decomposition into adsorbed oxygen molecules (k_4) or diffusion to the solution as the final product (k_5) [102].

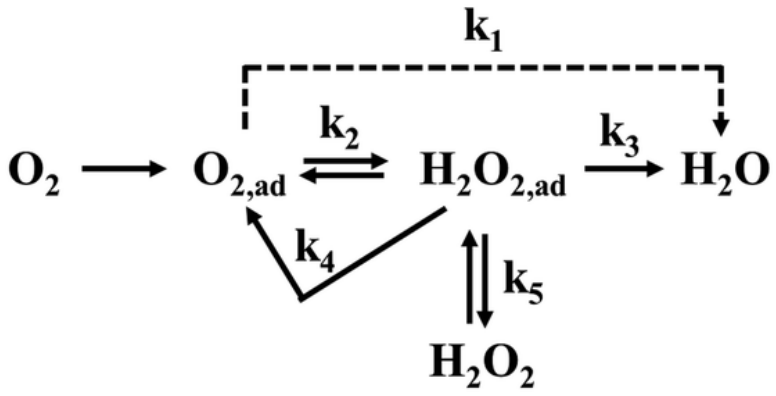

Figure 1.16 Diagram showing the possible pathways during the ORR [102].

The ORR catalytic pathways largely depend on the adsorption configuration of O_2 on the catalyst surface, which mainly consists of three modes (**Figure 1.17**) [56, 103]. In

Griffiths mode, the strong interaction between the oxygen molecule and the d orbital of the central metal atom weakens the O–O bond, which is conducive to the four-electron reaction. In Pauling mode, only one side of the oxygen molecule interacts with the metal atom, which is unfavorable to the breaking of the O–O bond and easily leads to a two-electron reaction. In Bridge mode, the oxygen molecule is activated by two central atoms at the same time in favor of the O–O bond breaking and the occurrence of the four-electron reaction [99].

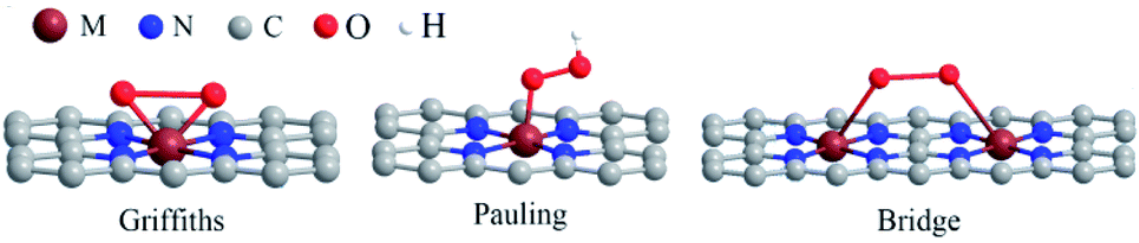

Figure 1.17 Schematic illustration of three different adsorption models of oxygen molecules on the catalyst [99].

In general, the ORR process on the surface of electrocatalysts mainly includes species adsorption, electron transfer, proton transfer, bond breaking and formation and species desorption [104]. The first step is the diffusion and adsorption of oxygen molecule on the catalyst surface of the electrode, giving rise to adsorbed O_2* molecules, followed by a decomposition process [105]. According to whether the O–O bond cleavage can happen before the proton–electron transfer (O–O bond scission), two main possible mechanisms could be involved (**Figure 1.18**) [104, 106]. 1) the oxygen associative mechanism through forming peroxyl (OOH*) radicals: firstly, the adsorbed O_2* molecules combine with H^+ and e^- to form OOH* (equation 1-28), which will dissociate into O* and OH* (equation 1-29). Then, O* will react with H^+ and e^- once again to form OH* (equation 1-30). Finally, OH* continuously combines with H^+ and e^- to form a water molecule (equation 1-31). 2) the oxygen dissociation mechanism by forming dissociated O atoms: the adsorbed O_2* molecules firstly dissociate into two O* due to the low dissociation barrier (equation 1-32), and then the O* further reacts with H^+ and e^- to form OH* (equation 1-33) and further to H_2O* (equation 1-34), which is a relatively simple pathway. The four-electron pathway for ORR is the ideal high-rate reaction pathway without generating extra byproducts. However, there still exists a chance to produce H_2O_2 during the ORR through the two-electron process in the oxygen associative mechanism, in which the adsorbed O_2* molecules successively convert to OOH* and HOOH* (equation 1-35) and then the HOOH* is reduced to OH* (O–O bond

in the HOOH* intermediates is cleaved) (equation 1-36) and further to water (equation 1-37) [102, 107, 108].

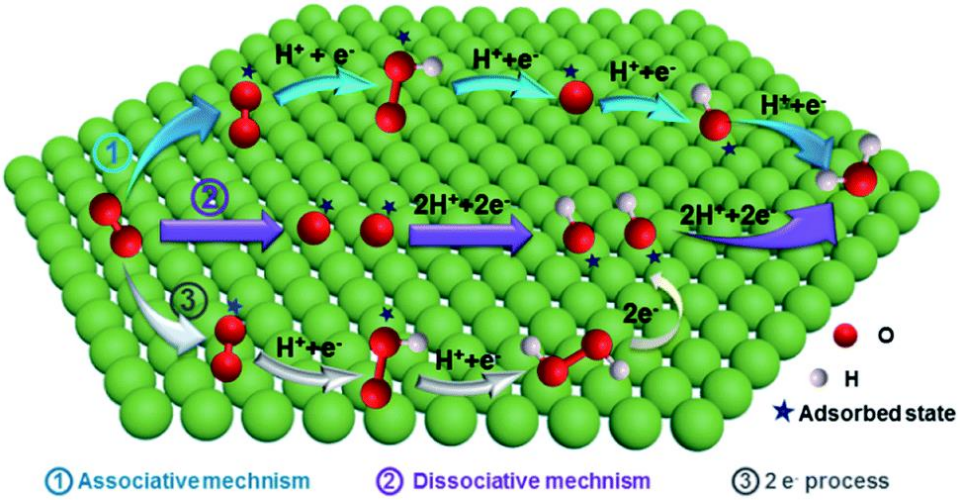

Figure 1.18 Illustration of the reaction pathway of the ORR and the resulting intermediates on the catalyst surface through different mechanisms [106].

Associative pathway:

$$O_2^* + H^+ + e^- \rightarrow OOH^* \quad (1\text{-}28)$$

$$OOH^* \rightarrow O^* + OH^* \quad (1\text{-}29)$$

$$O^* + H^+ + e^- \rightarrow OH^* \quad (1\text{-}30)$$

$$OH^* + H^+ + e^- \rightarrow H_2O^* \quad (1\text{-}31)$$

Dissociation pathway:

$$O_2^* \rightarrow O^* + O^* \quad (1\text{-}32)$$

$$O^* + H^+ + e^- \rightarrow OH^* \quad (1\text{-}33)$$

$$OH^* + H^+ + e^- \rightarrow H_2O^* \quad (1\text{-}34)$$

or 2nd associative (peroxo) pathway:

$$O_2^* + 2H^+ + 2e \rightarrow HOOH^* \quad (1\text{-}35)$$

$$HOOH^* \rightarrow OH^* + OH^* \quad (1\text{-}36)$$

$$OH^* + H^+ + e^- \rightarrow H_2O^* \quad (1\text{-}37)$$

Generally, the four-electron reaction pathway can fully reduce O_2 to H_2O, which produces a higher reduction potential than that of the two-electron reaction and exhibits a higher output voltage [109]. Consequently, the catalysts that favor the four-electron reaction pathway for the ORR are highly preferable for the development of energy conversion devices such as fuel cells and metal-air batteries, etc [110]. If the activity of the catalysts is not very strong, the two-electron reaction pathway or the mixture of two-electron and four-electron pathways would prevail, resulting in some adverse effects,

such as low energy efficiency, the damage of the catalysts and proton exchange membrane by H_2O_2 due to its high oxidizability [111, 112]. On the other hand, the catalysts that promote two-electron ORR to H_2O_2 are preferred for the electrosynthesis of hydrogen peroxide, which is a safer, more environmentally friendly and convenient approach, compared to the traditional synthetic method of H_2O_2 [113, 114]. In addition, reasonable control of the ORR through the two-electron pathway to produce H_2O_2 can find potential application in the treatment of water pollution by free radicals [115].

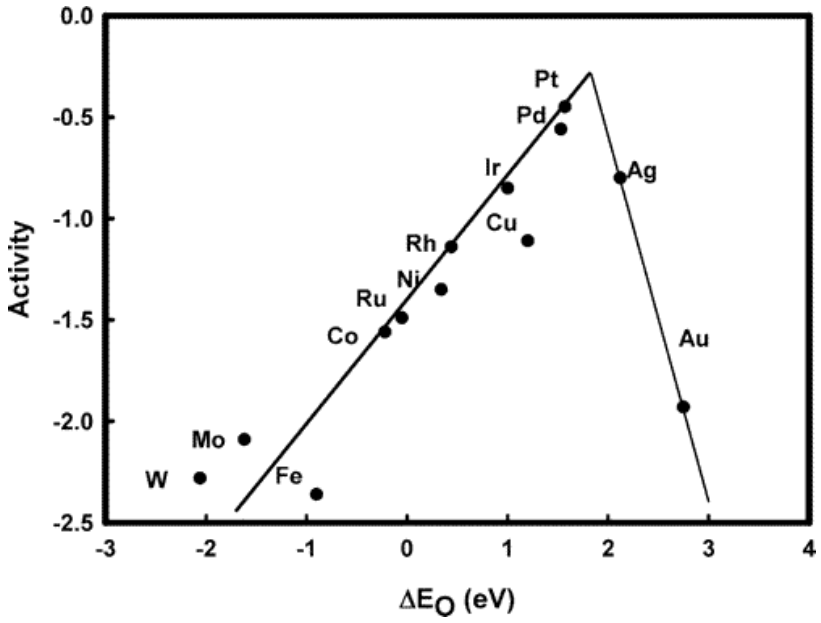

Figure 1.19 Trends in oxygen reduction activity plotted as a function of the oxygen binding energy [56].

The ORR is a reverse process of the OER with four elementary steps, so the adsorption energy of ORR intermediates on the active site of catalysts directly affects the reactivity, the same as the OER process [97]. Based on the Sabatier principle, the adsorption energy should be neither too strong nor too weak. As shown in **Figure 1.19**, Pt and Pd are the best ORR electrocatalysts (the peak of volcano), in good agreement with experiment results [56]. The theoretical investigations have revealed that there is a scaling relation between the binding energies of OH* and OOH* and the catalyst surface [116]. Restricted by this relation, there is little room (minimum theoretical overpotential of 0.37 V) for improvement in ORR activity even for the catalysts at the top of the volcano plot [56, 100]. Thus, how to break this scaling relation has been one of the major focuses on developing highly efficient ORR catalysts [98, 117].

1.4 The commonly used catalysts for electrochemical energy conversion

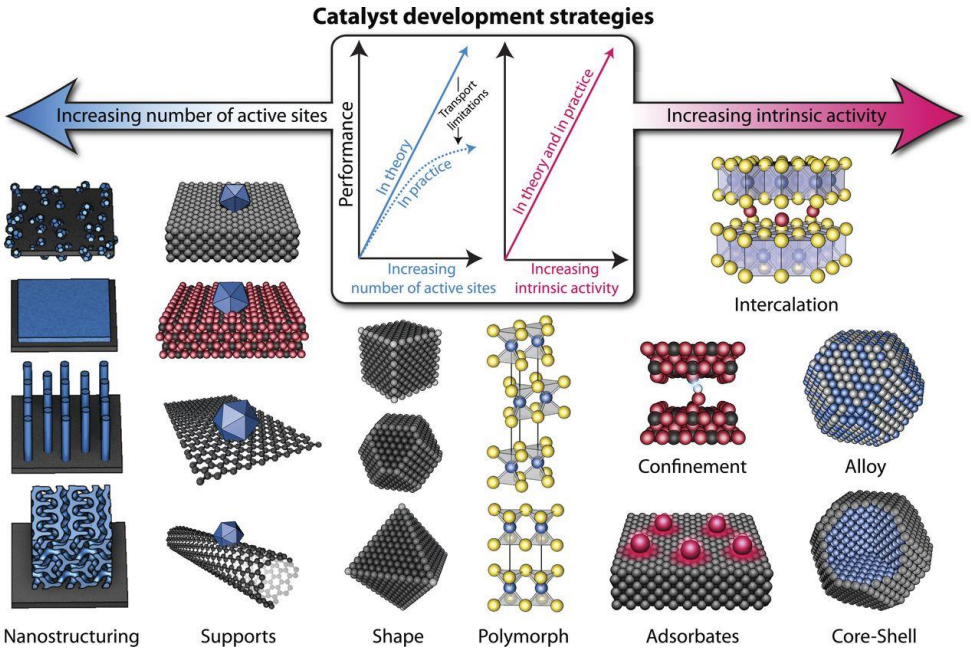

Figure 1.20 Schematic of various catalyst development strategies [116].

As mentioned before, most electrochemical energy conversion processes involve kinetically sluggish reactions, such as HER, OER, ORR and UOR. Therefore, high-performance electrocatalysts with improved activity, selectivity, and durability are critically needed to improve the energy efficiency of these reactions. As shown in **Figure 1.20**, there are generally two strategies to improve the activity of electrocatalysts: increasing the number of active sites over a given electrode surface area and increasing the intrinsic activity of each active site [116]. Following these guidelines, significant experimental and theoretical progress has been made in improving the activity of electrocatalysts by controlling particle size and morphologies, surface ligands, and the interaction of catalysts with supports, and different forms of electrocatalysts have been reported. This thesis work covers mainly three different forms of catalysts, namely, self-supported catalytic electrodes, ultrafine nanoclusters, and atomically dispersed catalysts.

1.4.1 Self-supported nanostructured catalytic electrodes

Nanomaterials have at least one dimension on nanometer scale, typically possessing a large surface-to-volume ratio, a high density of active sites, and unique physicochemical properties, which can result in better catalytic properties and a wider range of applications in electrocatalysis compared to their bulk counterparts [118-120]. In particular, advances in nanotechnology and materials chemistry have greatly boosted the emergence of a range of nanostructured materials for advanced electrocatalysis [120-122]. This is mainly because nanostructure engineering is an effective strategy to

increase the density of active sites within materials [18, 123]. Although most nanostructured catalysts exhibit better electrochemical performance compared to their bulk counterparts, for practical applications in water electrolysis there are several problems facing nanoparticulate catalysts that are yet to be resolved. Firstly, the coating of nanostructured catalysts on a current collector using polymeric binder (*e.g.*, polytetrafluoroethylene or nafion) will inevitably cover parts of active sites, increase contact resistance and impede mass transport (**Figure 1.21a**) [124, 125]. Secondly, the low electrical conductivity of electrocatalysts necessitates the use of conductive additives such as carbon materials, which has proved to easily get dissolved during the anodic process, leading to the deterioration of electrode performance. Thirdly, the loading mass of electrocatalysts and operational current density have been severely restricted by the low physical adhesive force between the catalytically active phase and substrate, where the generated gas bubbles would detach the coated powdery electrocatalysts from the current collector, leading to catalyst loss during long-term or large-current operation. Thus, powdery electrocatalysts consisting of nanomaterials or other forms of nano-objects work well only at small current densities (typically < 100 mA cm^{-2}) for dozens of hours and cannot meet the requirements of practical industrial water electrolysis that operates at a high current density (*e.g.*, > 500 mA cm^{-2}) for many years [125].

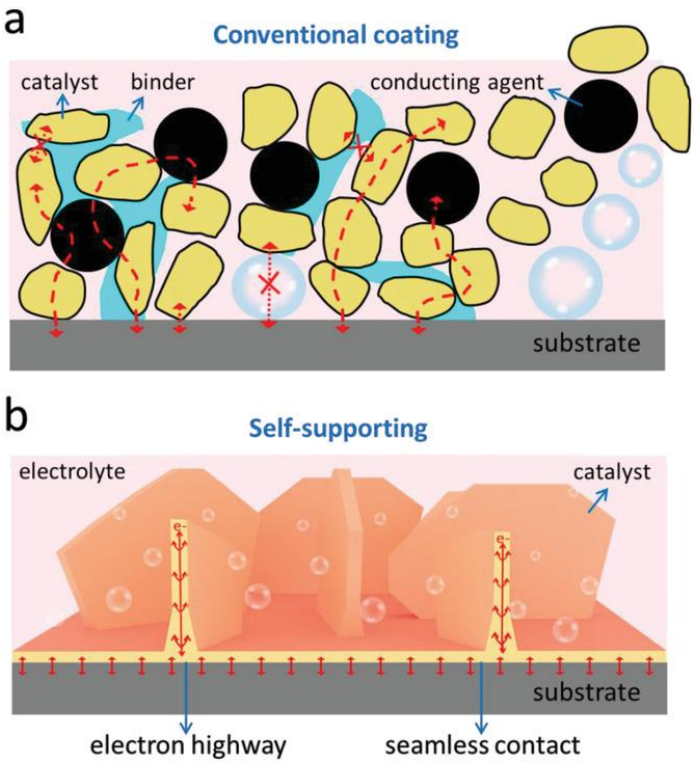

Figure 1.21 Schematic illustration of the structural and electrochemical features of: a) conventional powdery catalysts coated on current collectors with polymer binder and carbon additives, and b) self-supported electrode with *in situ* grown catalysts on the substrates [124].

An effective approach to address these issues is to reasonably design and fabricate self-supported electrodes with catalytically active phase *in situ* grown on the conductive substrates. Compared to the conventional catalyst powder coated electrodes, the self-supported electrodes are more desirable because they are characterized by the following unique merits (**Figure 1.21b**) [124]: on the one hand, the current collectors used (*e.g.*, nickel foam, iron foam, and carbon paper) usually have a 3D interconnected skeleton that can provide a large surface area for active electrocatalysts to grow; moreover, the 3D architecture facilitates mass transport of electrolyte and helps the generated bubbles to release, and the high surface area results in a high areal loading density of catalysts, thus accelerating the electracatalytic process. On the other hand, the nanostructured catalysts are *in situ* grown on current collectors, which can be directly used as a self-supported, binder-free working electrode, markedly reducing the interfacial contact resistance and eliminating the conventional catalyst coating steps. All these advantages render the self-supported electrodes a high catalytic activity and long-term operation stability for practical water electrolysis [125, 126].

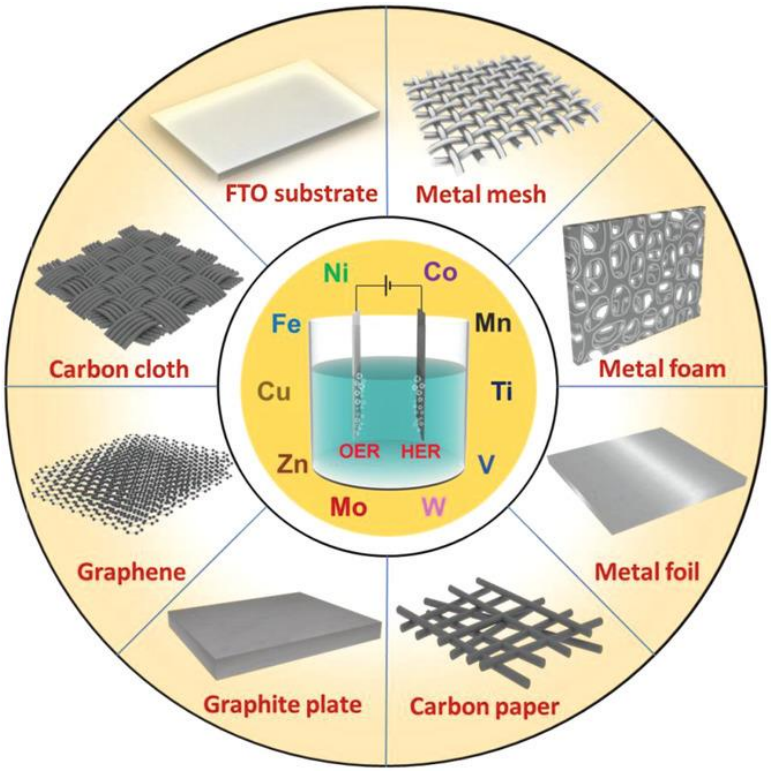

Figure 1.22 Substrate materials and TM elements that are widely used to build self-supported electrodes for electrocatalytic water splitting [124].

At present, the substrates for the construction of self-supporting electrodes have become the most widely studied and expand to most of the TM-based elements such as

Co, Ni, Fe, Cu, Zn, Mo, W, vanadium (V), titanium (Ti) and manganese (Mn). In specific, the various flexible substrates will be introduced in terms of material types, including metallic, carbonaceous, and a few other conductive materials in different forms (**Figure 1.22**) [124]. The metal foil are the most straightforward option for flexible electrode substrate owing to their commercial availability and relatively low-cost property, such as the anode and air electrodes of the metal–air batteries [89]. Compared to the drawbacks of heavy weight and bulk architecture of foil, the metal mesh and foam not only exhibit good mechanical flexibility but also are lighter and porous, which allows for decorating active materials with a high mass loading and are conducive for electrolyte ions diffusion and mass transport, thus prompting the electrochemical performance [127]. The carbon nanomaterials of carbon nanofiber and graphene have excellent mechanical strength, high conductivity, low density, and large specific surface area, which have emerged as promising platforms to prepare binder-free self-supported electrodes. And its commercial carbonized materials, such as carbon cloths, carbon paper and graphite plate are also good substrates to grow active phase owing to their ultrathin diameter, high porosity, and large specific surface area [128]. Comparing with metals and carbons, the fluorine-doped tin oxide (FTO) have the almost stable characteristics in strong acidic environments and enhanced temperatures, which endow it promising application in proton exchange membrane fuel cell (PEMFC) and PEMWE [129].

When used in energy conversion system, including HER, OER, and ORR, these self-supported electrocatalysts exhibited significant potentials for practical application, such as in all-pH electrolysis, seawater splitting, overall water splitting, electrolysis in large current density and long working time, respectively (**Figure 1.23**) [125, 126]. If the electrolysis of water can efficiently be catalyzed in electrolytes with different pH values, the operating process and the cost of water electrolyzers can be significantly simplified and lowed, which will bring practical application foreground for green H_2 production. However, such pH-universal catalysts are hard to obtain due to the complex demands for the catalysts to satisfy different thermodynamic features of water splitting in distinct electrolyte conditions, where most HER electrocatalysts perform the best in acidic electrolyte, while the majority of electrocatalysts for OER possess the highest activity in alkaline medium. Moreover, most OER electrocatalysts is unstable and easy to dissociate in the acidic media. At present, although great progress has been achieved in the development of advanced electrocatalysts for half-reacvistion of water splitting (such as chalcogenides [130], nitrides [131], and phosphides [132] displayed outstanding HER performance, while hydroxides/oxides [133] and perovskites [134] are investigated as

efficient OER catalysts), only a few of them show outstanding bifunctional catalytic performance, capable of catalyzing HER and OER simultaneously at an integrated electrolysis cell (where the catalysts serve as both cathode and anode) in the same media [135, 136]. In this case, self-supported electrocatalysts with a suitable substrate can accelerate ion/electron transfer, promote mass transport and enhance stability, which received increasing interest as a solution to wide-pH electrolyte water-splitting and bifunctional catalysts.

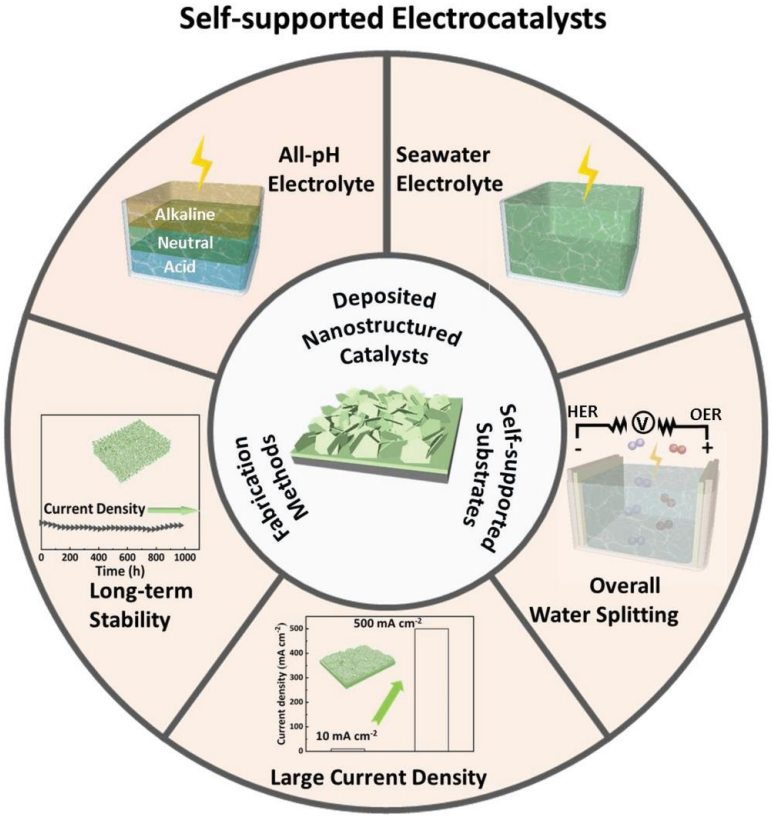

Figure 1.23 Design strategies of self-supported electrocatalysts and their promising practical application potentials [125].

As descripted in the **Chapter 1.2**, the direct seawater electrolysis has shown significant potential for offshore green H_2 production compared to the conventional water electrolysis. However, for the current electrocatalytic seawater splitting technology, several bottlenecks still need to be solved, such as the poison and corrosion of the catalysts from the formation of hypochlorite, the fluctuation of local pH near and existence of dissolved ions such as Na^+, Mg^{2+}, and calcium ion (Ca^{2+}), as well as bacteria/microbes and small particulates in seawater [43, 44, 137]. Benefiting from the easily-tailored electronic structure, enhanced charge conductivity, as well as optimized corrosion resistance and stability, the self-supported electrocatalysts were regarded as promising candidates for practical seawater electrolysis. Driving large current density

efficiently and robustly is vital for industrial application, such as AEMWE (200–400 mA cm^{-2}) and PEMWE (600–2000 mA cm^{-2}) [24]. To construct such an efficient electrocatalyst with satisfactory large-current-density activity and exceedingly robust stability water splitting, rapid electron and mass transfer should be guaranteed. However, conventional powdery electrocatalysts demand polymeric binder to be deposited on the substrates, which would hinder the charge transfer and impede the escape of evolved gas bubbles, further may enable the deposited powder catalysts to be peeled off. On the contrary, the self-supported configuration where the catalysts are chemically bonded with the substrate ensures their tight affinity, beneficial for the transport of charge/mass conductivity, optimization of electrochemically active sites as well as stability under a harsh working environment. Favored with these strong points, several highly efficient self-supported electrodes have been emerged for large-current-density, long-term-durability water splitting and being considered promising candidates for the commercialization and industrialization of H_2 production *via* water electrolysis technology [125, 126]. Meanwhile, motivated by the challenges mentioned above, studies on self-supported electrodes for rechargeable ZABs have received significant achievements in recent years [89, 138, 139].

In the past few years, encouraging progress has been continuously made in the development of self-supported electrocatalysts with outstanding activity and durability for water splitting [126, 140]. Nevertheless, to better exploit advanced self-supported catalysts for practical water electrolysis, some urgent issues as follows should be rationally handled. For example, the majority of currently explored self-supported electrode displayed outstanding performance only for alkaline water electrolysis under the strict conditions of practical application. In other words, in acid or neutral media, such efficient catalysts were rarely reported, especially for full water splitting, at large current density, and within an ultralong working period [124, 125]. The most common substrates for self-supported electrocatalysts are metal foams, which mechanical strength is not able to satisfy the real long-term application at large current density and under high temperature. Lastly but most importantly, most of the self-supported electrode are “pre-catalysts,” which partially or completely transform into real catalytically active structures under different conditions [141, 142]. Paying deeper insight into the real active species, morphological, phase and compositional transformations, *in situ* states for self-supported electrocatalysts can help researchers fully understand the self-supported system and accordingly design the self-supported catalysts which are more in line with expectation.

1.4.2 Nanocluster catalysts

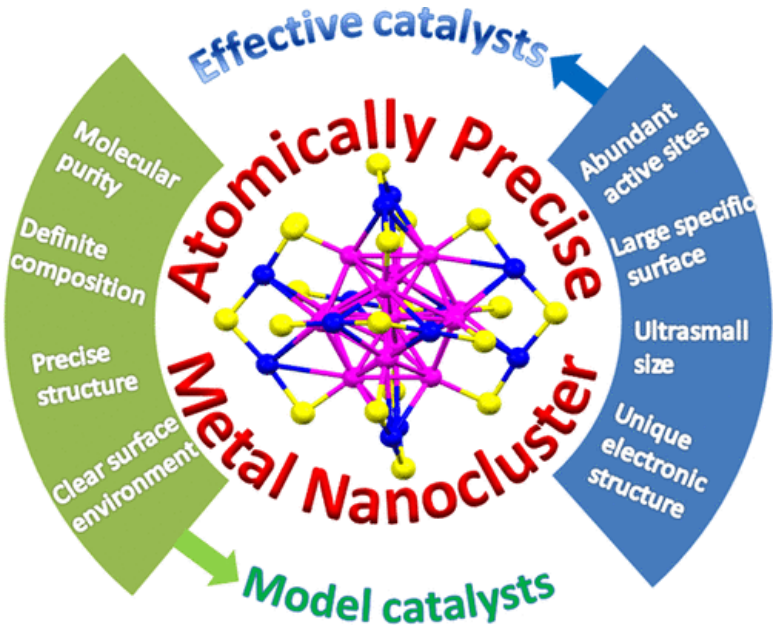

Figure 1.24 Advantages of atomically precise metal NCs as effective model catalysts [143].

During the last decades, metal nanoparticles (NPs) have received much attention as electrocatalysts for water splitting, fuel cells and ZABs [18, 118, 121, 122]. Theoretical and experimental studies have disclosed that the size of NPs has a direct effect on catalytic activity because of the increases in the number of low-coordinated sites on small NPs with decreasing NPs size [144-146]. Remarkable catalytic performance has been observed in a number of heterogeneous reactions upon downsizing particle size [147, 148]. Most recently, nanoclusters (NCs), consisting of several to a few hundred atoms with sizes less than 2 nm, have drawn great attention for use in elerctrocatalysis due to unique physical and chemical properties [144, 149]. As known, the catalytic reactions always occur on the surface of catalysts, thus a significant proportion of atoms in the NPs cannot be effectively utilized in the catalytic process [150, 151]. When materials vary from NPs to NCs, the fraction of under-coordinated surface atoms and the interactions between the deposited cluster and the support has changed dramatically, resulting in the higher the surface-to-volume ratio and more exposure of surface active sites [145, 147]. In addition, the NPs possess the large size and complicated structure, where the reactant would be absorbed on uncertain sites of the surface of the NPs and formed different adsorption structures, resulting in uncertain activity and low catalytic selectivity [152, 153]. But for the NCs, because of their definite composition, precise structure and clear surface environment, they are used as model catalysts to reveal the correlation between catalyst performance and structure at the atomic scale (**Figure 1.24**). Meanwhile, stemming from the unique geometric and electronic structures, the NCs

show excellent catalytic activity and selectivity in many reactions, as a new type of highly efficient catalysts [143-145, 149].

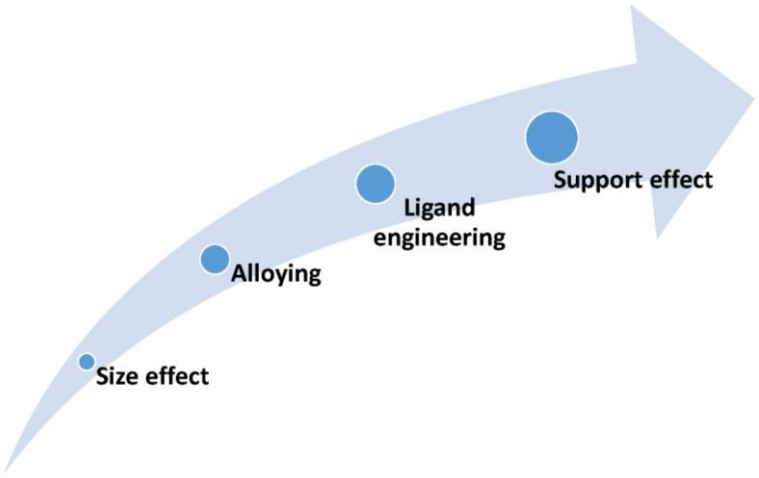

Figure 1.25 The design strategies to construct advanced NC catalysts.

With quick developments in both advanced atomic-resolution characterization technologies and theoretical calculations, the understanding towards the field of NCs is growing, including exact positions, geometry and detailed local coordination environment of the clusters [154]. Therefore, several design strategies have been reported and instructed to construct advanced NC catalysts (**Figure 1.25**) [143, 145, 147]. Firstly, exerting control over the size of a cluster has proven to be a valuable method for increasing activity and tuning the selectivity in a catalytic process. In general, the smaller the size, the larger is the specific surface area, and hence the higher is the catalytic activity and the more efficient the atom-utilization rate [143]. In addition, alloying is also an available way to enhance the catalytic performance, which alters the electronic and chemical properties of metals through intimate interaction and constitutes new forms of architecture, because of their distinct properties from their corresponding monometallic counterparts [145]. One main concern related to NCs is stability. Because of the very small size of NCs, they might aggregate into larger-sized aggregates and, eventually, into larger particles during the catalytic process, causing decreased activity and durability in electrocatalytic tests [155]. There are two ways to address this problem: 1) Ligands stabilization, which can protect the metal cores and play significant roles in the synthesis of precise NCs. However, the exposure of active sites and direct possible contact between the active sites and reactant can be very limited due to the coverage by the ligands, which suppress the overall catalytic activity [152, 153, 156]. 2) Support stabilization, where a desired support is constructed to immobilizes the NCs and keeps

them stable, preventing them from aggregation and loss in electrocatalytic process [152, 155]. Furthermore, in some cases, the ligands and support effects can promote the catalytic efficiency and selectivity, whereby NCs benefit from the ligand steric and electronic effects [149, 155, 157, 158].

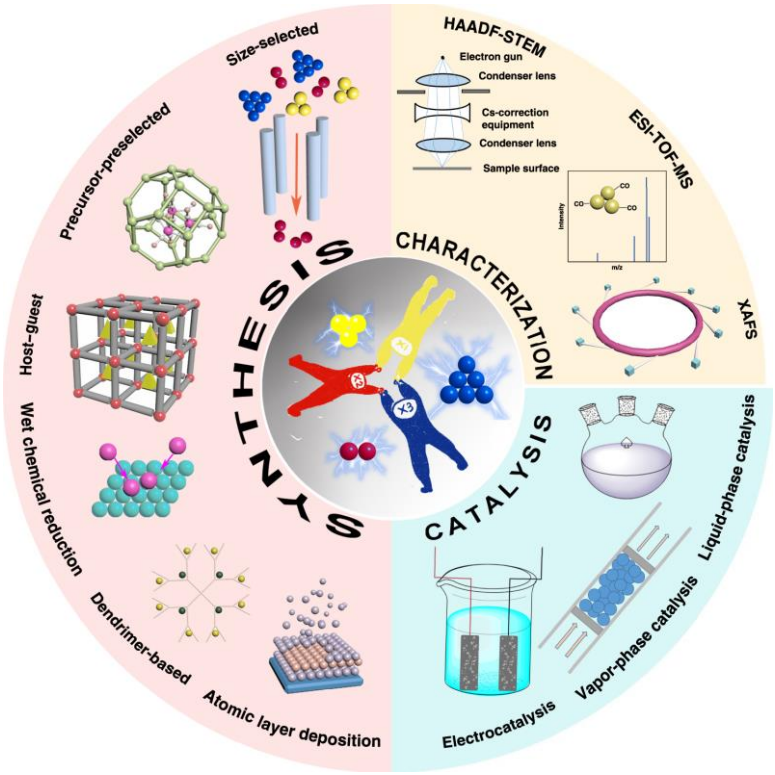

Figure 1.26 Synthesis and catalytic performances of supported atomic clusters [144].

Developing suitable synthetic methods targeted at the above design strategies is important for fabricating uniform and well-defined NCs. As shown in **Figure 1.26**, several synthetic approaches have been proven effective to synthesize the high-quality NCs, including size-selected strategy, precursor-preselected strategy, host-guest strategy, wet chemical reduction, dendrimer-based, and atomic layer deposition method, etc [144, 145]. Among them, the size-selected method and the atomic layer deposition method have a long history and prepared lots of metal NCs with precise numbers of atoms, but the throughput of this method is only enough for laboratory-scale synthesis and far from the requirement of the practical application [144]. As for the large-scale synthesis of metal NCs, the precursor-preselected strategy, host-guest strategy, wet chemical reduction, dendrimer-based method were proposed based on the strong interaction between the metal and support, such as carbon nitride (C_3N_4), metal organic frameworks (MOFs), where the metal atoms can be supported and stabilized *via* ligand protection

from N coordinations [145, 159]. Furthermore, a wide range of advanced atomic-resolution instrument including High-angle annular dark-field scanning transmission electron microscopy (HAADF-STEM), Electrospray Ionization Time-of-Flight Mass Spectrometer (ESI-TOF-MS), and X-ray absorption fine spectrum (XAFS) are three important and typical characterization techniques to characterize obtained NCs, which can be used to gain knowledge of their unique properties and interaction with support materials [143, 144]. Recent synthetic innovations have opened the possibility of well-defined NCs with atomic precision. And much progress has been made toward understanding the relationship between the electronic structure and performance of NCs based on the advanced atomic-resolution characterization technologies. Both of them make NCs with unique physicochemical properties hold great promise in the applications of technological areas such as the electrocatalysis, vapor-, and liquid-phase catalytic performances [143, 144, 146].

1.4.3 Atomically dispersed catalysts

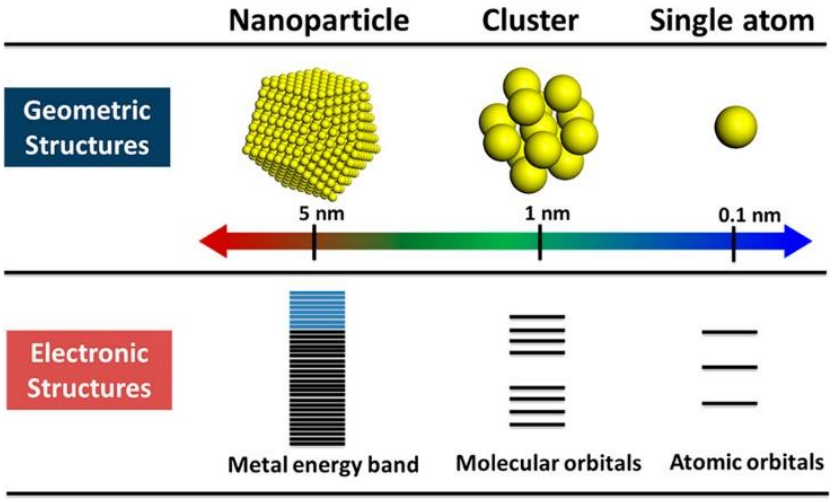

Figure 1.27 Geometric and electronic structures of single atom, clusters, and nanoparticles [160].

With techniques of synthesis and characterization rapidly developing, sub-nano catalysts are emerging as a frontier area in the catalysis community [160-162]. It is well documented that decreasing the dimension and size of nanostructured catalysts can effectively improve their catalytic performance. The ultrafine NCs composed of several atoms would show catalytic properties distinct from bulk metals and metal NPs, due to their discrete electronic structure, unsaturated coordination environments and finite-size effects [160, 163, 164]. Further downsizing of metal NCs can generate atomic level metal distribution on the support surface, the size effects would be more obvious, such as the more unsaturated atoms, the strong metal-support interactions (SMSIs), the distinctive

HOMO–LUMO gap and the discrete energy level distribution (**Figure 1.27**) [160, 161, 165-167]. Such well-defined, atomically distributed metal catalysts have been first proposed and defined by the pioneering work of Zhang in 2011, named as single-atom catalysts (SACs), which brought chemists from the “nano epoch” to the “atomic epoch” step by step [168]. In principal, SACs have all the metal atoms exposed on the surface and thus can achieve 100% efficiency of atomic utilization, performing the perfect approach for constructing cost-effective catalysts, especially those based on precious-metal-based catalysts such as Ir, Ru and Pt (**Figure 1.28**) [169-171].

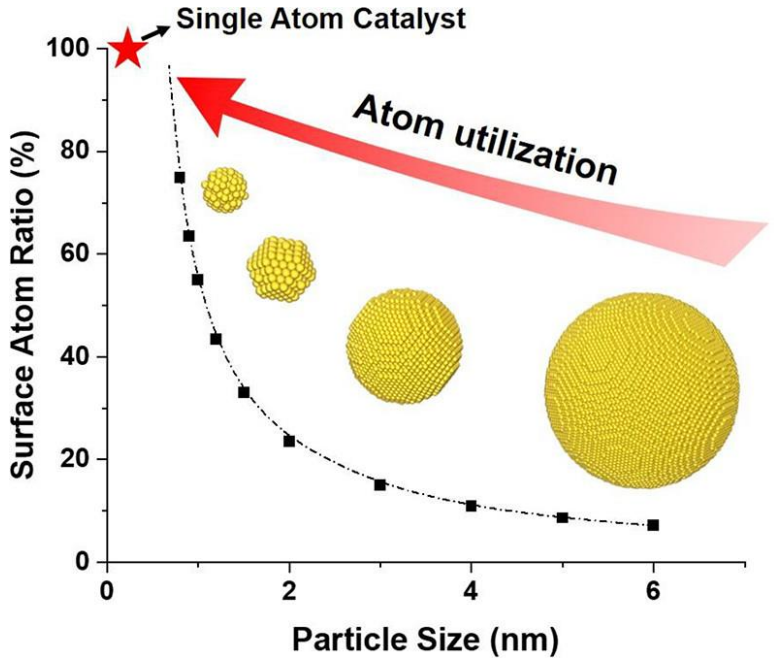

Figure 1.28 Ratio of surface atoms at different particle sizes [169].

The SACs are also featured with the uniformly distributed undercoordinated active sites, providing a model system to bridge the gap between heterogeneous and homogeneous catalysis [170, 172]. The homogeneity in the geometric structures and active sites, similar to their homogeneous catalyst analogues, gives them great potential to enhance the selectivity and catalytic turnover frequency; meanwhile, the heterogeneous catalysts can ensure the robust stability, easy separation and recycle (**Figure 1.29**) [161]. Therefore, the SACs contain homogenized active centers for catalytic reactions, simultaneously combining the merits of heterogeneous and homogeneous catalysts, providing a novel avenue for maximizing the utilization efficiency of each metal atom and improving the catalytic properties in a wide variety of reactions, such as electrocatalysis, photocatalysis and thermal catalysis (**Figure 1.30**) [165, 169, 172, 173].

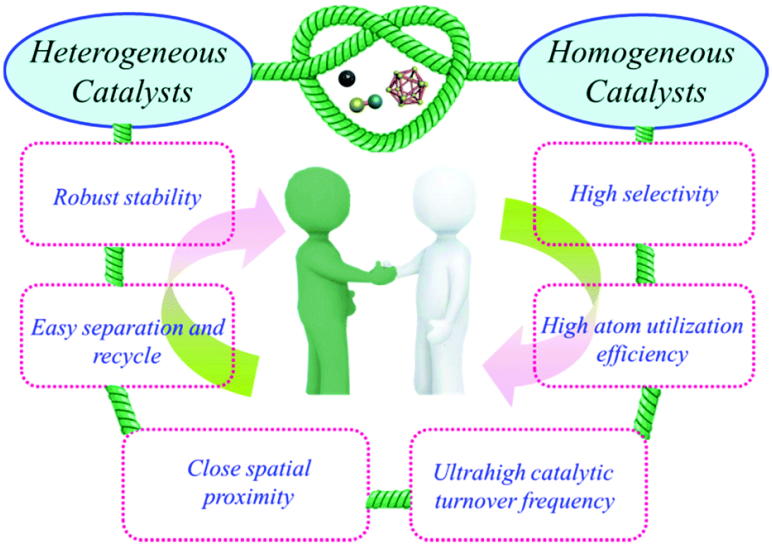

Figure 1.29 Relationships among conventional homogeneous and heterogeneous catalysts and single/dual-atom and cluster catalysts [161].

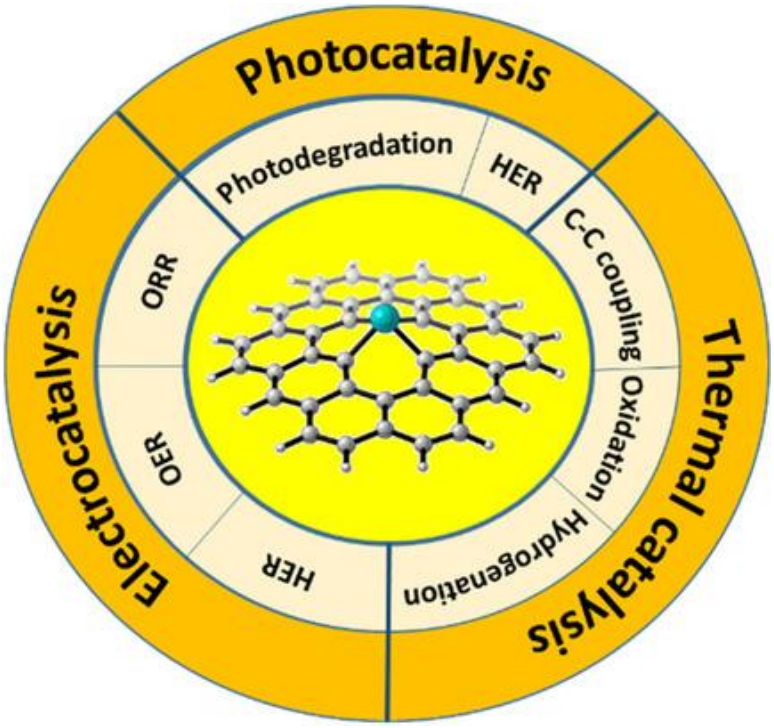

Figure 1.30 Application of the SACs [173].

Although SACs show great prospects in catalysis, there are various restrictions for these kinds of single-atomic structures, which limit their further application [161, 174]. On one hand, subjected to only a single active site in most of SACs, it is tough for SACs to break linear scaling relationships between the adsorption energies of reaction intermediates when it comes to complicated reactions involving multi-intermediates,

leading to a fundamental limitation to the catalytic efficiency [175]. Meanwhile, some reactions need adjacent active sites to catalyze the reaction. For example, the Pt couple with Ru can significantly enhance the electrocatalytic activity for methanol oxidation and improve of CO-poisoning tolerance [176, 177]. On the other hand, in order to avoid the formation of NCs/NPs due to the large surface energy of SACs, the loading amount of metal is often limited to relatively low, resulting in a lower overall activity. Inspired by bimetallic nanocatalysts and SACs, double-atom catalysts (DACs) have recently emerged as a further expansion to the family of SACs in order to further increase the active sites and the metal atom loading [178, 179]. The synergetic effect between the two metal atoms in DACs is also expected to play an important role in improving the catalytic performance. The **Figure 1.31** summarizes the advantages in electrocatalysis of DACs. Comparing to the SACs, the DACs possess the higher loading amount of metal atoms and more accessible active sites, thus promoting the overall catalytic performance [179]. In addition, thanks to the flexible dual-metal active sites in DACs, the adjustment of the geometrical configurations and electronic structures will be more efficient compared with SACs, offering more opportunities to tune the adsorption configuration and break the linear relationship between the adsorption energy of reaction intermediates, further optimizing the catalytic activity and/or selectivity [175, 180].

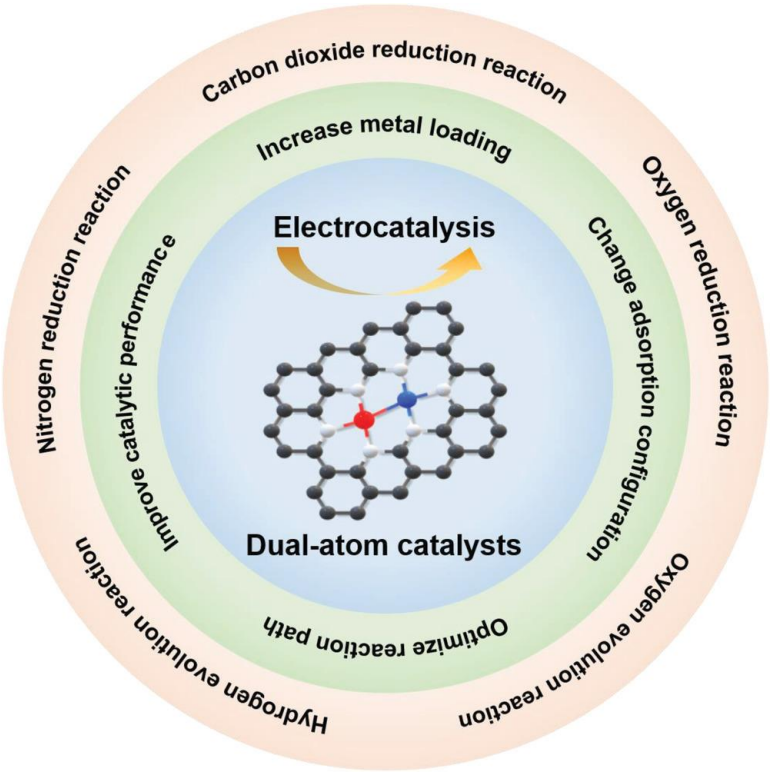

Figure 1.31 Overview of the DACs for energy-related electrocatalysis [175].

Although research on DACs is still in the early stages, the research work reported so far has mainly focused on two aspects: homonuclear and heteronuclear DACs [178]. Currently, the most of these researches are mainly focused on the homonuclear DACs, such as the Fe_2, Pt_2, Co_2 binuclear [181-183]. Just like bimetallic nano-catalysts, the heteronuclear DACs, such as PtFe, NiFe supported on nitrogen-doped carbon [184-186], have more chances to adjust the d-band center by the interaction of electronic orbits and bring unique structure and electronic properties comparing with homonuclear DACs, thus exhibiting superior catalytic behaviours [174, 180]. Finally, there is a large chemical composition space for the design of heteronuclear DACs, due to the vast combination of two different metal atoms [179].

Triple-atom catalysts (TACs), with higher metal atom loading rates and more flexible structure configuration, have attracted a lot of attention recently [187]. Although the preparation of TACs is even harder to precisely regulate and orientate, the TACs also could offer an excellent platform to gain insights into the structure-properties relationship for catalysis at the atomic and electronic level, which meanwhile shown similar and ever better beneficial catalytic properties to DACs [188].

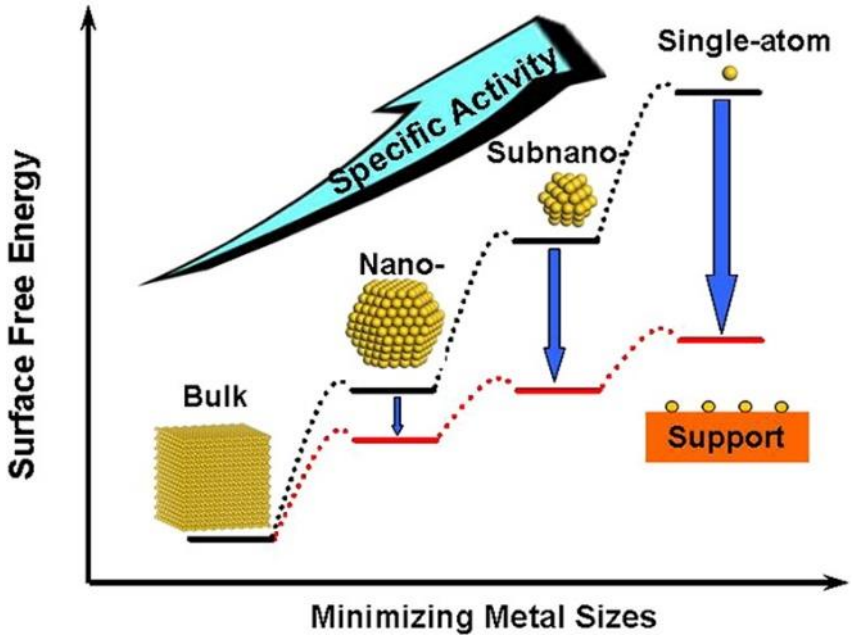

Figure 1.32 Schematic illustrate the changes of surface free energy and specific activity per metal atom with metal particle size and the support effects on stabilizing single atoms [167].

However, the surface energy of atomically dispersed catalysts (ADCs), including SACs, DACs and TACs, is relatively high, and metal atoms tend to agglomerate to form NPs, thereby greatly reducing the catalyst's reactivity (**Figure 1.32**) [167]. Therefore, one

of the first challenges in the development of the ADCs was how to stabilize metal atoms against migrating and agglomerating to give appreciable activity. Through the efforts of numerous research groups, a range of preparation methods have been developed, mainly divided to bottom-up strategy and top-down strategy (**Figure 1.33**) [189-191]. In the bottom-up method, the mononuclear or multinuclear metal precursors are commonly first adsorbed, then reduced and finally confined by the vacancies or defects of the supports [189, 191]. For example, Wet chemical method is currently the most simple and promising approaches to synthesize ADCs [102, 166]. Firstly, the support is immersed in a solution containing a metal precursor, which allows metal atoms to be distributed on the surface or pores of the support. Then, drying and calcination. Finally, reduction or activation. Owing to its good practically and without specialized equipment, it is a widely method for synthesizing ADCs in lab and even in commercial production. As we mentioned above, ADCs possess much higher surface energy than metal NPs, which easily result in the aggregation of ADCs. Therefore, the SMSIs is the key to disperse ADCs on support and to prevent aggregation in the synthetic procedures (**Figure 1.32**) [167, 179].

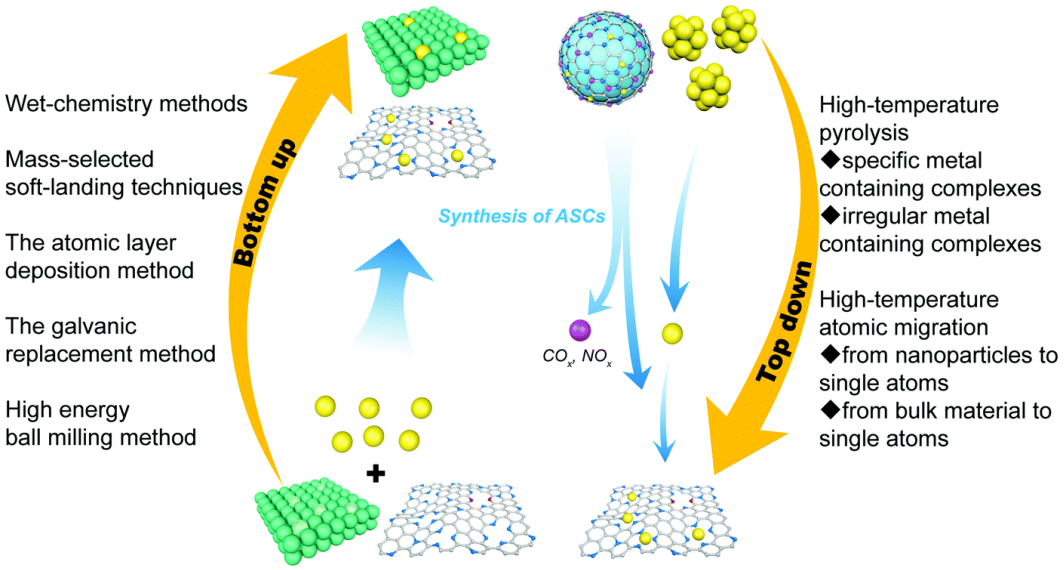

Figure 1.33 Preparation methods for ADCs: bottom-up strategy and top-down strategy [189].

Different from bottom-up strategy to synthesize ADCs, top-down strategy are based on the disbanding of well-organized nanostructures or organic polymer precursors into smaller pieces to give the desired structures [189, 191]. Thus far, extensive research effort has been paid to pursue these goals. Among them, the high-temperature pyrolysis is an effective method in the synthesis of ADCs [98]. Normally, the metal atom-containing precursor is pyrolyzed at appropriate temperatures (*e.g.*, 600-1000 ^{o}C) under the

protection of a controlled atmosphere (*e.g.*, N_2, NH_3, Ar, H_2) [189]. The high-temperature pyrolysis of MOFs is a widely used route to prepare the ADCs [166, 169]. The organic ligand material is firstly used to capture the metal atom, and then the highly dispersed SACs and clusters catalyst is prepared by high temperature pyrolysis. With the aid of the spatial separation effect and coordination with surrounding chelating atoms, the ADCs can be uniformly dispersed in MOF-derived materials [161, 192].

ADCs have recently emerged as a new frontier to bridge the gap between the homogeneous catalysts with well-defined structures and heterogeneous catalysts with structural variety [193, 194]. The atomic dispersion with stable configurations of ADCs heavily relies on the SMSIs between metal atom and support [102, 160]. In turn, the SMSIs in ADCs will afford them a unique electronic and geometric structures, which are directly optimizing the catalytic activity and selectivity [195]. Moreover, the well-defined and uniform structures of ADCs provide a promising platform to reveal the correlation between catalyst performance and structure at the atomic scale, which shed a light on the thorough investigation on the catalytic mechanism, achieving a rational design principle for ADCs [188, 195].

1.5 Outline of the thesis

This PhD thesis focuses on the development of self-supported electrode, NCs and ADCs as efficient electrocatalysts towards to the energy conversion. Nickel/cobalt and nickel/iron-based compounds were employed to boost efficient saline water electrolysis. And the ruthenium, rhodium, iridium and/or iron-based NCs and ADCs were prepared for efficient water electrolysis and ZABs. Experimental and theoretical calculations were combined to investigate the electrochemical process. This thesis consists of six chapters, and the main chapters were published in peer-reviewed journals.

Chapter 1 introduces the research background of the thesis and contains four parts. First, the problems related to the research topic were proposed. Second, the concepts of hydrogen energy from the water electrolysis were introduced, including HER, OER and chemical-assisted electrocatalytic energy-saving hydrogen production. Third, the fundamentals of ZABs were introduced, including the principle and mechanism and ORR. Fourth, an overview of fundamental catalysts for energy conversion relevant to the current development of self-supported electrode, NCs and ADCs were summarized.

Chapter 2 reports a self-supported electrode, *e.g.*, CoNiP and NiFeSP, as an efficient electrocatalyst for the saline water electrolysis. The materials were characterized by XRD,

XPS, SEM, TEM and XAS. With the aid of small hydrogen-containing molecules, *e.g.*, N_2H_4 and urea, the saline water electrolysis not only saved energy but also avoided the notorious problems of chlorine chemistry.

Chapter 3 reports iridium oxide NCs with oxygen defect, which was applied for efficient and durable water oxidation at high current densities in acidic media. Then the DFT calculation confirmed the important role of oxygen defects in the enhanced OER performance.

Chapter 4 reports a series of ADCs towards the hydrogen production. Firstly, the Rh SACs was prepared for electrocatalytic HER. Then the bifunctional Ru ADCs with ultralow metal loading was employed for efficient bipolar membrane water electrolysis. Finally, the Ir/Ru SACs were anchored on graphitic carbon nitride for electrocatalytic/photocatalytic HER.

Chapter 5 continues reports IrFe DACs, derived from MOFs in a facile wet chemical synthesis followed by post-pyrolysis. The HAADF-STEM and XAS characterization confirmed the atomic dispersion of Ir and Fe on the nitrogen-doped carbon support and the presence of atomic pairs. The as-obtained IrFe-N-C showed excellent electrocatalytic performance for both ORR and OER, revealing favorable bifunctionality, which, consequently, was employed at ZABs.

Chapter 6 contains the general conclusions and the outlook for future research.

1.6 References

[1] S. Chu, A. Majumdar, Opportunities and challenges for a sustainable energy future. Nature 488 (2012) 294-303.

[2] A. Hussain, S.M. Arif, M. Aslam, Emerging renewable and sustainable energy technologies: State of the art. Renew. Sust. Energ. Rev. 71 (2017) 12-28.

[3] International Energy Outlook, U.S. Energy Information Administration, Washington, 2019.

[4] S. Pacala, R. Socolow, Stabilization Wedges: Solving the Climate Problem for the Next 50 Years with Current Technologies. Science 305 (2004) 968-972.

[5] P.G. Levi, J.M. Cullen, Mapping Global Flows of Chemicals: From Fossil Fuel Feedstocks to Chemical Products. Environ. Sci. Technol. 52 (2018) 1725-1734.

[6] M.S. Dresselhaus, I.L. Thomas, Alternative energy technologies. Nature 414 (2001) 332-337.

[7] J.A. Turner, Sustainable Hydrogen Production. Science 305 (2004) 972-974.

[8] M. Yue, H. Lambert, E. Pahon, R. Roche, S. Jemei, D. Hissel, Hydrogen energy systems: A critical review of technologies, applications, trends and challenges. Renew. Sust. Energ. Rev. 146 (2021) 111180.

[9] K. Mazloomi, C. Gomes, Hydrogen as an energy carrier: Prospects and challenges. Renew. Sust. Energ. Rev. 16 (2012) 3024-3033.

[10] T. da Silva Veras, T.S. Mozer, D. da Costa Rubim Messeder dos Santos, A. da Silva César, Hydrogen: Trends, production and characterization of the main process worldwide. Int. J. Hydrogen Energy 42 (2017) 2018-2033.

[11] X. Zou, Y. Zhang, Noble metal-free hydrogen evolution catalysts for water splitting. Chem. Soc. Rev. 44 (2015) 5148-5180.

[12] B. Parkinson, P. Balcombe, J.F. Speirs, A.D. Hawkes, K. Hellgardt, Levelized cost of CO_2 mitigation from hydrogen production routes. Energy Environ. Sci. 12 (2019) 19-40.

[13] G. Zhao, K. Rui, S.X. Dou, W. Sun, Heterostructures for Electrochemical Hydrogen Evolution Reaction: A Review. Adv. Funct. Mater. 28 (2018) 1803291.

[14] M.A. Khan, H. Zhao, W. Zou, Z. Chen, W. Cao, J. Fang, J. Xu, L. Zhang, J. Zhang, Recent Progresses in Electrocatalysts for Water Electrolysis. Electrochemical Energy Reviews 1 (2018) 483-530.

[15] X. Li, L. Zhao, J. Yu, X. Liu, X. Zhang, H. Liu, W. Zhou, Water Splitting: From Electrode to Green Energy System. Nano-Micro Letters 12 (2020) 131.

[16] X. Chen, Z. Zhou, H.E. Karahan, Q. Shao, L. Wei, Y. Chen, Recent Advances in Materials and Design of Electrochemically Rechargeable Zinc–Air Batteries. Small 14 (2018) 1801929.

[17] H.J. Kim, H.Y. Kim, J. Joo, S.H. Joo, J.S. Lim, J. Lee, H. Huang, M. Shao, J. Hu, J.Y. Kim, B.J. Min, S.W. Lee, M. Kang, K. Lee, S. Choi, Y. Park, Y. Wang, J. Li, Z. Zhang, J. Ma, S. I. Choi, Recent advances in non-precious group metal-based catalysts for water electrolysis and beyond. J. Mater. Chem. A 10 (2022) 50-88.

[18] J. Zhu, L. Hu, P. Zhao, L.Y.S. Lee, K.Y. Wong, Recent Advances in Electrocatalytic Hydrogen Evolution Using Nanoparticles. Chem. Rev. 120 (2020) 851-918.

[19] D. Xu, M.B. Stevens, M.R. Cosby, S.Z. Oener, A.M. Smith, L.J. Enman, K.E. Ayers, C.B. Capuano, J.N. Renner, N. Danilovic, Y. Li, H. Wang, Q. Zhang, S.W. Boettcher, Earth-Abundant Oxygen Electrocatalysts for Alkaline Anion-Exchange-Membrane Water Electrolysis: Effects of Catalyst Conductivity and Comparison with Performance in Three-Electrode Cells. ACS Catal. 9 (2019) 7-15.

[20] J. Wang, X. Yue, Y. Yang, S. Sirisomboonchai, P. Wang, X. Ma, A. Abudula, G. Guan, Earth-abundant transition-metal-based bifunctional catalysts for overall electrochemical water splitting: A review. J. Alloys Compd. 819 (2020) 153346.

[21] W. J. Jiang, T. Tang, Y. Zhang, J.S. Hu, Synergistic Modulation of Non-Precious-Metal Electrocatalysts for Advanced Water Splitting. Acc. Chem. Res. 53 (2020) 1111-1123.

[22] H. Jin, B. Ruqia, Y. Park, H.J. Kim, H.S. Oh, S.I. Choi, K. Lee, Nanocatalyst Design for Long-Term Operation of Proton/Anion Exchange Membrane Water Electrolysis. Adv. Energy Mater. 11 (2021) 2003188.

[23] G.A. Lindquist, Q. Xu, S.Z. Oener, S.W. Boettcher, Membrane Electrolyzers for Impure-Water Splitting. Joule 4 (2020) 2549-2561.

[24] M. Carmo, D.L. Fritz, J. Mergel, D. Stolten, A comprehensive review on PEM water electrolysis. Int. J. Hydrogen Energy 38 (2013) 4901-4934.

[25] S.A. Grigoriev, V.I. Porembsky, V.N. Fateev, Pure hydrogen production by PEM electrolysis for hydrogen energy. Int. J. Hydrogen Energy 31 (2006) 171-175.

[26] L. An, C. Wei, M. Lu, H. Liu, Y. Chen, G.G. Scherer, A.C. Fisher, P. Xi, Z.J. Xu, C.H. Yan, Recent Development of Oxygen Evolution Electrocatalysts in Acidic Environment. Adv. Mater. 33 (2021) 2006328.

[27] C.C. Pavel, F. Cecconi, C. Emiliani, S. Santiccioli, A. Scaffidi, S. Catanorchi, M. Comotti, Highly Efficient Platinum Group Metal Free Based Membrane-Electrode Assembly for Anion Exchange Membrane Water Electrolysis. Angew. Chem. Int. Ed. 53 (2014) 1378-1381.

[28] H.A. Miller, K. Bouzek, J. Hnat, S. Loos, C.I. Bernäcker, T. Weißgärber, L. Röntzsch, J. Meier-Haack, Green hydrogen from anion exchange membrane water

electrolysis: a review of recent developments in critical materials and operating conditions. Sustain. Energy Fuels 4 (2020) 2114-2133.

[29] Z.Y. Yu, Y. Duan, X.Y. Feng, X. Yu, M.R. Gao, S.H. Yu, Clean and Affordable Hydrogen Fuel from Alkaline Water Splitting: Past, Recent Progress, and Future Prospects. Adv. Mater. 33 (2021) 2007100.

[30] W. Ju, M.V.F. Heinz, L. Pusterla, M. Hofer, B. Fumey, R. Castiglioni, M. Pagani, C. Battaglia, U.F. Vogt, Lab-Scale Alkaline Water Electrolyzer for Bridging Material Fundamentals with Realistic Operation. ACS Sustain. Chem. Eng. 6 (2018) 4829-4837.

[31] B. Mayerhöfer, D. McLaughlin, T. Böhm, M. Hegelheimer, D. Seeberger, S. Thiele, Bipolar Membrane Electrode Assemblies for Water Electrolysis. ACS Appl. Energy Mater. 3 (2020) 9635-9644.

[32] K. Sun, R. Liu, Y. Chen, E. Verlage, N.S. Lewis, C. Xiang, A Stabilized, Intrinsically Safe, 10% Efficient, Solar-Driven Water-Splitting Cell Incorporating Earth-Abundant Electrocatalysts with Steady-State pH Gradients and Product Separation Enabled by a Bipolar Membrane. Adv. Energy Mater. 6 (2016) 1600379.

[33] J. Luo, D.A. Vermaas, D. Bi, A. Hagfeldt, W.A. Smith, M. Grätzel, Bipolar Membrane-Assisted Solar Water Splitting in Optimal pH. Adv. Energy Mater. 6 (2016) 1600100.

[34] J.A. Wrubel, Y. Chen, Z. Ma, T.G. Deutsch, Modeling Water Electrolysis in Bipolar Membranes. J. Electrochem. Soc. 167 (2020) 114502.

[35] J. Xu, I. Amorim, Y. Li, J. Li, Z. Yu, B. Zhang, A. Araujo, N. Zhang, L. Liu, Stable overall water splitting in an asymmetric acid/alkaline electrolyzer comprising a bipolar membrane sandwiched by bifunctional cobalt-nickel phosphide nanowire electrodes. Carbon Energy 2 (2020) 646-655.

[36] I. Amorim, J. Xu, N. Zhang, Z. Yu, A. Araújo, F. Bento, L. Liu, Dual-phase CoP−$CoTe_2$ nanowires as an efficient bifunctional electrocatalyst for bipolar membrane-assisted acid-alkaline water splitting. Chem. Eng. J. 420 (2021) 130454.

[37] Y. Li, J. Chen, P. Cai, Z. Wen, An electrochemically neutralized energy-assisted low-cost acid-alkaline electrolyzer for energy-saving electrolysis hydrogen generation. J. Mater. Chem. A 6 (2018) 4948-4954.

[38] H. Zou, J. Chen, Y. Fang, J. Ding, W. Peng, R. Liu, A dual-electrolyte based air-breathing regenerative microfluidic fuel cell with 1.76V open-circuit-voltage and 0.74V water-splitting voltage. Nano Energy 27 (2016) 619-626.

[39] S.Z. Oener, M.J. Foster, S.W. Boettcher, Accelerating water dissociation in bipolar membranes and for electrocatalysis. Science 369 (2020) 1099-1103.

[40] J.N. Hausmann, R. Schlögl, P.W. Menezes, M. Driess, Is direct seawater splitting economically meaningful? Energy Environ. Sci. 14 (2021) 3679-3685.

[41] C. Wang, H. Shang, L. Jin, H. Xu, Y. Du, Advances in hydrogen production from electrocatalytic seawater splitting. Nanoscale 13 (2021) 7897-7912.

[42] S. Khatun, H. Hirani, P. Roy, Seawater electrocatalysis: activity and selectivity. J. Mater. Chem. A 9 (2021) 74-86.

[43] F. Zhang, L. Yu, L. Wu, D. Luo, Z. Ren, Rational design of oxygen evolution reaction catalysts for seawater electrolysis. Trends Chem. 3 (2021) 485-498.

[44] W. Tong, M. Forster, F. Dionigi, S. Dresp, R. Sadeghi Erami, P. Strasser, A.J. Cowan, P. Farràs, Electrolysis of low-grade and saline surface water. Nat. Energy 5 (2020) 367-377.

[45] J. Wang, T. Liao, Z. Wei, J. Sun, J. Guo, Z. Sun, Heteroatom-Doping of Non-Noble Metal-Based Catalysts for Electrocatalytic Hydrogen Evolution: An Electronic Structure Tuning Strategy. Small Methods 5 (2021) 2000988.

[46] M. Zeng, Y. Li, Recent advances in heterogeneous electrocatalysts for the hydrogen evolution reaction. J. Mater. Chem. A 3 (2015) 14942-14962.

[47] B. You, M.T. Tang, C. Tsai, F. Abild-Pedersen, X. Zheng, H. Li, Enhancing Electrocatalytic Water Splitting by Strain Engineering. Adv. Mater. 31 (2019) 1807001.

[48] E. Skúlason, V. Tripkovic, M.E. Björketun, S. Gudmundsdóttir, G. Karlberg, J. Rossmeisl, T. Bligaard, H. Jónsson, J.K. Nørskov, Modeling the Electrochemical Hydrogen Oxidation and Evolution Reactions on the Basis of Density Functional Theory Calculations. J. Phys. Chem. C 114 (2010) 18182-18197.

[49] H. Wu, C. Feng, L. Zhang, J. Zhang, D.P. Wilkinson, Non-noble Metal Electrocatalysts for the Hydrogen Evolution Reaction in Water Electrolysis. Electrochem. Energy Rev. 4 (2021) 473-507.

[50] J. Song, C. Wei, Z.F. Huang, C. Liu, L. Zeng, X. Wang, Z.J. Xu, A review on fundamentals for designing oxygen evolution electrocatalysts. Chem. Soc. Rev. 49 (2020) 2196-2214.

[51] J. Liu, H. Liu, H. Chen, X. Du, B. Zhang, Z. Hong, S. Sun, W. Wang, Progress and Challenges Toward the Rational Design of Oxygen Electrocatalysts Based on a Descriptor Approach. Adv. Sci. 7 (2020) 1901614.

[52] L. Gao, X. Cui, C.D. Sewell, J. Li, Z. Lin, Recent advances in activating surface reconstruction for the high-efficiency oxygen evolution reaction. Chem. Soc. Rev. 50 (2021) 8428-8469.

[53] J. Shan, Y. Zheng, B. Shi, K. Davey, S.Z. Qiao, Regulating Electrocatalysts via Surface and Interface Engineering for Acidic Water Electrooxidation. ACS Energy Lett. 4 (2019) 2719-2730.

[54] N.T. Suen, S.F. Hung, Q. Quan, N. Zhang, Y.J. Xu, H.M. Chen, Electrocatalysis for the oxygen evolution reaction: recent development and future perspectives. Chem. Soc. Rev. 46 (2017) 337-365.

[55] J. Wang, Y. Gao, H. Kong, J. Kim, S. Choi, F. Ciucci, Y. Hao, S. Yang, Z. Shao, J. Lim, Non-precious-metal catalysts for alkaline water electrolysis: operando characterizations, theoretical calculations, and recent advances. Chem. Soc. Rev. 49 (2020) 9154-9196.

[56] J.K. Nørskov, J. Rossmeisl, A. Logadottir, L. Lindqvist, J.R. Kitchin, T. Bligaard, H. Jónsson, Origin of the Overpotential for Oxygen Reduction at a Fuel-Cell Cathode. J. Phys. Chem. B 108 (2004) 17886-17892.

[57] J. Rossmeisl, Z.W. Qu, H. Zhu, G.J. Kroes, J.K. Nørskov, Electrolysis of water on oxide surfaces. J. Electroanal. Chem. 607 (2007) 83-89.

[58] I.C. Man, H.Y. Su, F. Calle-Vallejo, H.A. Hansen, J.I. Martínez, N.G. Inoglu, J. Kitchin, T.F. Jaramillo, J.K. Nørskov, J. Rossmeisl, Universality in Oxygen Evolution Electrocatalysis on Oxide Surfaces. ChemCatChem 3 (2011) 1159-1165.

[59] H. Dau, C. Limberg, T. Reier, M. Risch, S. Roggan, P. Strasser, The Mechanism of Water Oxidation: From Electrolysis via Homogeneous to Biological Catalysis. ChemCatChem 2 (2010) 724-761.

[60] J.H. Montoya, L.C. Seitz, P. Chakthranont, A. Vojvodic, T.F. Jaramillo, J.K. Nørskov, Materials for solar fuels and chemicals. Nat. Mater. 16 (2017) 70-81.

[61] A.J. Medford, A. Vojvodic, J.S. Hummelshøj, J. Voss, F. Abild-Pedersen, F. Studt, T. Bligaard, A. Nilsson, J.K. Nørskov, From the Sabatier principle to a predictive theory of transition-metal heterogeneous catalysis. J. Catal. 328 (2015) 36-42.

[62] A. Grimaud, A. Demortière, M. Saubanère, W. Dachraoui, M. Duchamp, M.L. Doublet, J.M. Tarascon, Activation of surface oxygen sites on an iridium-based model catalyst for the oxygen evolution reaction. Nat. Energy 2 (2016) 16189.

[63] B. Han, A. Grimaud, L. Giordano, W.T. Hong, O. Diaz-Morales, L. Yueh-Lin, J. Hwang, N. Charles, K.A. Stoerzinger, W. Yang, M.T.M. Koper, Y. Shao-Horn, Iron-Based Perovskites for Catalyzing Oxygen Evolution Reaction. J. Phys. Chem. C 122 (2018) 8445-8454.

[64] Z.F. Huang, J. Song, Y. Du, S. Xi, S. Dou, J.M.V. Nsanzimana, C. Wang, Z.J. Xu, X. Wang, Chemical and structural origin of lattice oxygen oxidation in Co–Zn oxyhydroxide oxygen evolution electrocatalysts. Nat. Energy 4 (2019) 329-338.

[65] X. Rong, J. Parolin, A.M. Kolpak, A Fundamental Relationship between Reaction Mechanism and Stability in Metal Oxide Catalysts for Oxygen Evolution. ACS Catal. 6 (2016) 1153-1158.

[66] A. Grimaud, W.T. Hong, Y. Shao-Horn, J.M. Tarascon, Anionic redox processes for electrochemical devices. Nat. Mater. 15 (2016) 121-126.

[67] Z. Chen, L. Guo, L. Pan, T. Yan, Z. He, Y. Li, C. Shi, Z.F. Huang, X. Zhang, J.J. Zou, Advances in Oxygen Evolution Electrocatalysts for Proton Exchange Membrane Water Electrolyzers. Adv. Energy Mater. 12 2103670.

[68] D.A. Kuznetsov, M.A. Naeem, P.V. Kumar, P.M. Abdala, A. Fedorov, C.R. Müller, Tailoring Lattice Oxygen Binding in Ruthenium Pyrochlores to Enhance Oxygen Evolution Activity. J. Am. Chem. Soc. 142 (2020) 7883-7888.

[69] Y. Li, X. Wei, L. Chen, J. Shi, Electrocatalytic Hydrogen Production Trilogy. Angew. Chem. Int. Ed. 60 (2021) 19550-19571.

[70] B. You, G. Han, Y. Sun, Electrocatalytic and photocatalytic hydrogen evolution integrated with organic oxidation. Chem. Commun. 54 (2018) 5943-5955.

[71] Q. Qian, J. Zhang, J. Li, Y. Li, X. Jin, Y. Zhu, Y. Liu, Z. Li, A. El-Harairy, C. Xiao, G. Zhang, Y. Xie, Artificial Heterointerfaces Achieve Delicate Reaction Kinetics towards Hydrogen Evolution and Hydrazine Oxidation Catalysis. Angew. Chem. Int. Ed. 60 (2021) 5984-5993.

[72] Z. Yu, J. Xu, L. Meng, L. Liu, Efficient hydrogen production by saline water electrolysis at high current densities without the interfering chlorine evolution. J. Mater. Chem. A 9 (2021) 22248-22253.

[73] X. Sun, R. Ding, Recent progress with electrocatalysts for urea electrolysis in alkaline media for energy-saving hydrogen production. Catal. Sci. Technol. 10 (2020) 1567-1581.

[74] M. Zhang, Z. Duan, L. Cui, H. Yu, Z. Wang, Y. Xu, X. Li, L. Wang, H. Wang, A phosphorus modified mesoporous AuRh film as an efficient bifunctional electrocatalyst for urea-assisted energy-saving hydrogen production. J. Mater. Chem. A 10 (2022) 3086-3092.

[75] D.T. Tran, T.H. Nguyen, H. Jeong, P.K.L. Tran, D. Malhotra, K.U. Jeong, N.H. Kim, J.H. Lee, Recent engineering advances in nanocatalysts for NH_3-to-H_2 conversion technologies. Nano Energy 94 (2022) 106929.

[76] Q. Xue, Y. Zhao, J. Zhu, Y. Ding, T. Wang, H. Sun, F. Li, P. Chen, P. Jin, S. Yin, Y. Chen, PtRu nanocubes as bifunctional electrocatalysts for ammonia electrolysis. J. Mater. Chem. A 9 (2021) 8444-8451.

[77] F. Arshad, T.u. Haq, I. Hussain, F. Sher, Recent Advances in Electrocatalysts toward Alcohol-Assisted, Energy-Saving Hydrogen Production. ACS Appl. Energy Mater. 4 (2021) 8685-8701.

[78] Z. Li, Y. Yan, S.M. Xu, H. Zhou, M. Xu, L. Ma, M. Shao, X. Kong, B. Wang, L. Zheng, H. Duan, Alcohols electrooxidation coupled with H_2 production at high current densities promoted by a cooperative catalyst. Nat. Commun. 13 (2022) 147.

[79] T. Wang, L. Tao, X. Zhu, C. Chen, W. Chen, S. Du, Y. Zhou, B. Zhou, D. Wang, C. Xie, P. Long, W. Li, Y. Wang, R. Chen, Y. Zou, X.Z. Fu, Y. Li, X. Duan, S. Wang, Combined anodic and cathodic hydrogen production from aldehyde oxidation and hydrogen evolution reaction. Nat. Catal. 5 (2022) 66-73.

[80] B. You, N. Jiang, X. Liu, Y. Sun, Simultaneous H_2 Generation and Biomass Upgrading in Water by an Efficient Noble-Metal-Free Bifunctional Electrocatalyst. Angew. Chem. Int. Ed. 55 (2016) 9913-9917.

[81] T. Wang, Z. Huang, T. Liu, L. Tao, J. Tian, K. Gu, X. Wei, P. Zhou, L. Gan, S. Du, Y. Zou, R. Chen, Y. Li, X.Z. Fu, S. Wang, Transforming Electrocatalytic Biomass

Upgrading and Hydrogen Production from Electricity Input to Electricity Output. Angew. Chem. Int. Ed. 61 (2022) e202115636.

[82] S. Fukuzumi, Y.M. Lee, W. Nam, Fuel Production from Seawater and Fuel Cells Using Seawater. ChemSusChem 10 (2017) 4264-4276.

[83] F. Dionigi, T. Reier, Z. Pawolek, M. Gliech, P. Strasser, Design Criteria, Operating Conditions, and Nickel–Iron Hydroxide Catalyst Materials for Selective Seawater Electrolysis. ChemSusChem 9 (2016) 962-972.

[84] F. Sun, J. Qin, Z. Wang, M. Yu, X. Wu, X. Sun, J. Qiu, Energy-saving hydrogen production by chlorine-free hybrid seawater splitting coupling hydrazine degradation. Nat. Commun. 12 (2021) 4182.

[85] M. Armand, J.M. Tarascon, Building better batteries. Nature 451 (2008) 652-657.

[86] Y. Li, J. Lu, Metal–Air Batteries: Will They Be the Future Electrochemical Energy Storage Device of Choice? ACS Energy Lett. 2 (2017) 1370-1377.

[87] J. Yi, P. Liang, X. Liu, K. Wu, Y. Liu, Y. Wang, Y. Xia, J. Zhang, Challenges, mitigation strategies and perspectives in development of zinc-electrode materials and fabrication for rechargeable zinc–air batteries. Energy Environ. Sci. 11 (2018) 3075-3095.

[88] J.S. Lee, S. Tai Kim, R. Cao, N.S. Choi, M. Liu, K.T. Lee, J. Cho, Metal–Air Batteries with High Energy Density: Li–Air versus Zn–Air. Adv. Energy Mater. 1 (2011) 34-50.

[89] X. Yan, Y. Ha, R. Wu, Binder-Free Air Electrodes for Rechargeable Zinc-Air Batteries: Recent Progress and Future Perspectives. Small Methods 5 (2021) 2000827.

[90] A.I. Douka, H. Yang, L. Huang, S. Zaman, T. Yue, W. Guo, B. You, B.Y. Xia, Transition metal/carbon hybrids for oxygen electrocatalysis in rechargeable zinc-air batteries. EcoMat 3 (2021) e12067.

[91] P. Gu, M. Zheng, Q. Zhao, X. Xiao, H. Xue, H. Pang, Rechargeable zinc–air batteries: a promising way to green energy. J. Mater. Chem. A 5 (2017) 7651-7666.

[92] Y. Arafat, M.R. Azhar, Y. Zhong, H.R. Abid, M.O. Tadé, Z. Shao, Advances in Zeolite Imidazolate Frameworks (ZIFs) Derived Bifunctional Oxygen Electrocatalysts and Their Application in Zinc–Air Batteries. Adv. Energy Mater. 11 (2021) 2100514.

[93] X. Liu, X. Fan, B. Liu, J. Ding, Y. Deng, X. Han, C. Zhong, W. Hu, Mapping the Design of Electrolyte Materials for Electrically Rechargeable Zinc–Air Batteries. Adv. Mater. 33 (2021) 2006461.

[94] J. Fu, R. Liang, G. Liu, A. Yu, Z. Bai, L. Yang, Z. Chen, Recent Progress in Electrically Rechargeable Zinc–Air Batteries. Adv. Mater. 31 (2019) 1805230.

[95] D. Schröder, U. Krewer, Model based quantification of air-composition impact on secondary zinc air batteries. Electrochim. Acta 117 (2014) 541-553.

[96] P. Delahay, M. Pourbaix, P. Van Rysselberghe, Potential-pH Diagram of Zinc and its Applications to the Study of Zinc Corrosion. J. Electrochem. Soc. 98 (1951) 101.

[97] L. Wei, E.H. Ang, Y. Yang, Y. Qin, Y. Zhang, M. Ye, Q. Liu, C.C. Li, Recent advances of transition metal based bifunctional electrocatalysts for rechargeable zinc-air batteries. J. Power Sources 477 (2020) 228696.

[98] M. Shao, Q. Chang, J.P. Dodelet, R. Chenitz, Recent Advances in Electrocatalysts for Oxygen Reduction Reaction. Chem. Rev. 116 (2016) 3594-3657.

[99] C.W. Ye, L. Xu, Recent advances in the design of a high performance metal–nitrogen–carbon catalyst for the oxygen reduction reaction. J. Mater. Chem. A 9 (2021) 22218-22247.

[100] A. Kulkarni, S. Siahrostami, A. Patel, J.K. Nørskov, Understanding Catalytic Activity Trends in the Oxygen Reduction Reaction. Chem. Rev. 118 (2018) 2302-2312.

[101] H.S. Wroblowa, P. Yen Chi, G. Razumney, Electroreduction of oxygen: A new mechanistic criterion. J. Electroanal. Chem. Interf. Electrochem. 69 (1976) 195-201.

[102] M. Liu, L. Wang, K. Zhao, S. Shi, Q. Shao, L. Zhang, X. Sun, Y. Zhao, J. Zhang, Atomically dispersed metal catalysts for the oxygen reduction reaction: synthesis, characterization, reaction mechanisms and electrochemical energy applications. Energy Environ. Sci. 12 (2019) 2890-2923.

[103] E. Yeager, Electrocatalysts for O_2 reduction. Electrochim. Acta 29 (1984) 1527-1537.

[104] Y. Ji, H. Dong, C. Liu, Y. Li, The progress of metal-free catalysts for the oxygen reduction reaction based on theoretical simulations. J. Mater. Chem. A 6 (2018) 13489-13508.

[105] W. Xia, A. Mahmood, Z. Liang, R. Zou, S. Guo, Earth-Abundant Nanomaterials for Oxygen Reduction. Angew. Chem. Int. Ed. 55 (2016) 2650-2676.

[106] L. Li, J. He, Y. Wang, X. Lv, X. Gu, P. Dai, D. Liu, X. Zhao, Metal–organic frameworks: a promising platform for constructing non-noble electrocatalysts for the oxygen-reduction reaction. J. Mater. Chem. A 7 (2019) 1964-1988.

[107] J.A. Keith, T. Jacob, Theoretical Studies of Potential-Dependent and Competing Mechanisms of the Electrocatalytic Oxygen Reduction Reaction on Pt(111). Angew. Chem. Int. Ed. 49 (2010) 9521-9525.

[108] Y. Wang, J. Li, Z. Wei, Transition-metal-oxide-based catalysts for the oxygen reduction reaction. J. Mater. Chem. A 6 (2018) 8194-8209.

[109] C.R. Raj, A. Samanta, S.H. Noh, S. Mondal, T. Okajima, T. Ohsaka, Emerging new generation electrocatalysts for the oxygen reduction reaction. J. Mater. Chem. A 4 (2016) 11156-11178.

[110] J. Kong, W. Cheng, Recent advances in the rational design of electrocatalysts towards the oxygen reduction reaction. Chin. J. Catal. 38 (2017) 951-969.

[111] V. Goellner, V. Armel, A. Zitolo, E. Fonda, F. Jaouen, Degradation by Hydrogen Peroxide of Metal-Nitrogen-Carbon Catalysts for Oxygen Reduction. J. Electrochem. Soc. 162 (2015) H403-H414.

[112] Y. Pang, H. Xie, Y. Sun, M.M. Titirici, G.L. Chai, Electrochemical oxygen reduction for H_2O_2 production: catalysts, pH effects and mechanisms. J. Mater. Chem. A 8 (2020) 24996-25016.

[113] S.C. Perry, S. Mavrikis, L. Wang, C. Ponce de León, Future perspectives for the advancement of electrochemical hydrogen peroxide production. Curr. Opin. Electrochem. 30 (2021) 100792.

[114] S.C. Perry, D. Pangotra, L. Vieira, L.I. Csepei, V. Sieber, L. Wang, C. Ponce de León, F.C. Walsh, Electrochemical synthesis of hydrogen peroxide from water and oxygen. Nat. Rev. Chem. 3 (2019) 442-458.

[115] X. Zhang, Y. Xia, C. Xia, H. Wang, Insights into Practical-Scale Electrochemical H_2O_2 Synthesis. Trends Chem. 2 (2020) 942-953.

[116] Z.W. Seh, J. Kibsgaard, C.F. Dickens, I. Chorkendorff, J.K. Nørskov, T.F. Jaramillo, Combining theory and experiment in electrocatalysis: Insights into materials design. Science 355 (2017) eaad4998.

[117] Y. Zheng, Y. Jiao, M. Jaroniec, Y. Jin, S.Z. Qiao, Nanostructured Metal-Free Electrochemical Catalysts for Highly Efficient Oxygen Reduction. Small 8 (2012) 3550-3566.

[118] A.S. Aricò, P. Bruce, B. Scrosati, J.M. Tarascon, W. van Schalkwijk, Nanostructured materials for advanced energy conversion and storage devices. Nat. Mater. 4 (2005) 366-377.

[119] F.P. Zamborini, L. Bao, R. Dasari, Nanoparticles in Measurement Science. Anal. Chem. 84 (2012) 541-576.

[120] S.E.F. Kleijn, S.C.S. Lai, M.T.M. Koper, P.R. Unwin, Electrochemistry of Nanoparticles. Angew. Chem. Int. Ed. 53 (2014) 3558-3586.

[121] Y. Bing, H. Liu, L. Zhang, D. Ghosh, J. Zhang, Nanostructured Pt-alloy electrocatalysts for PEM fuel cell oxygen reduction reaction. Chem. Soc. Rev. 39 (2010) 2184-2202.

[122] Q. Zhang, E. Uchaker, S.L. Candelaria, G. Cao, Nanomaterials for energy conversion and storage. Chem. Soc. Rev. 42 (2013) 3127-3171.

[123] H. Mistry, A.S. Varela, S. Kühl, P. Strasser, B.R. Cuenya, Nanostructured electrocatalysts with tunable activity and selectivity. Nature Reviews Materials 1 (2016) 16009.

[124] H. Sun, Z. Yan, F. Liu, W. Xu, F. Cheng, J. Chen, Self-Supported Transition-Metal-Based Electrocatalysts for Hydrogen and Oxygen Evolution. Adv. Mater. 32 (2020) 1806326.

[125] H. Yang, M. Driess, P.W. Menezes, Self-Supported Electrocatalysts for Practical Water Electrolysis. Adv. Energy Mater. 11 (2021) 2102074.

[126] J. Liu, D. Zhu, Y. Zheng, A. Vasileff, S.Z. Qiao, Self-Supported Earth-Abundant Nanoarrays as Efficient and Robust Electrocatalysts for Energy-Related Reactions. ACS Catal. 8 (2018) 6707-6732.

[127] K. Shang, J. Gao, X. Yin, Y. Ding, Z. Wen, An Overview of Flexible Electrode Materials/Substrates for Flexible Electrochemical Energy Storage/Conversion Devices. Eur. J. Inorg. Chem. 2021 (2021) 606-619.

[128] C. Wang, B. Yan, Z. Chen, B. You, T. Liao, Q. Zhang, Y. Lu, S. Jiang, S. He, Recent advances in carbon substrate supported nonprecious nanoarrays for electrocatalytic oxygen evolution. J. Mater. Chem. A 9 (2021) 25773-25795.

[129] D. Schonvogel, J. Hülstede, P. Wagner, A. Dyck, C. Agert, M. Wark, Durability of Electrocatalysts for ORR: Pt on Nanocomposite of Reduced Graphene Oxide with FTO versus Pt/C. J. Electrochem. Soc. 165 (2018) F3373-F3382.

[130] P. Kuang, T. Tong, K. Fan, J. Yu, In Situ Fabrication of Ni–Mo Bimetal Sulfide Hybrid as an Efficient Electrocatalyst for Hydrogen Evolution over a Wide pH Range. ACS Catal. 7 (2017) 6179-6187.

[131] D. Zhang, H. Li, A. Riaz, A. Sharma, W. Liang, Y. Wang, H. Chen, K. Vora, D. Yan, Z. Su, A. Tricoli, C. Zhao, F.J. Beck, K. Reuter, K. Catchpole, S. Karuturi, Unconventional direct synthesis of Ni_3N/Ni with N-vacancies for efficient and stable hydrogen evolution. Energy Environ. Sci. 15 (2022) 185-195.

[132] Z. Pu, J. Zhao, I.S. Amiinu, W. Li, M. Wang, D. He, S. Mu, A universal synthesis strategy for P-rich noble metal diphosphide-based electrocatalysts for the hydrogen evolution reaction. Energy Environ. Sci. 12 (2019) 952-957.

[133] Z. Yan, H. Sun, X. Chen, H. Liu, Y. Zhao, H. Li, W. Xie, F. Cheng, J. Chen, Anion insertion enhanced electrodeposition of robust metal hydroxide/oxide electrodes for oxygen evolution. Nat. Commun. 9 (2018) 2373.

[134] Y. Pan, X. Xu, Y. Zhong, L. Ge, Y. Chen, J.P.M. Veder, D. Guan, R. O'Hayre, M. Li, G. Wang, H. Wang, W. Zhou, Z. Shao, Direct evidence of boosted oxygen evolution over perovskite by enhanced lattice oxygen participation. Nat. Commun. 11 (2020) 2002.

[135] Y. Yang, H. Yao, Z. Yu, S.M. Islam, H. He, M. Yuan, Y. Yue, K. Xu, W. Hao, G. Sun, H. Li, S. Ma, P. Zapol, M.G. Kanatzidis, Hierarchical Nanoassembly of MoS_2/Co_9S_8/Ni_3S_2/Ni as a Highly Efficient Electrocatalyst for Overall Water Splitting in a Wide pH Range. J. Am. Chem. Soc. 141 (2019) 10417-10430.

[136] Y. Li, B. Wei, Z. Yu, O. Bondarchuk, A. Araujo, I. Amorim, N. Zhang, J. Xu, I.C. Neves, L. Liu, Bifunctional Porous Cobalt Phosphide Foam for High-Current-Density

Alkaline Water Electrolysis with 4000-h Long Stability. ACS Sustain. Chem. Eng. 8 (2020) 10193-10200.

[137] S. Dresp, F. Dionigi, M. Klingenhof, P. Strasser, Direct Electrolytic Splitting of Seawater: Opportunities and Challenges. ACS Energy Lett. 4 (2019) 933-942.

[138] M. Yang, X. Shu, W. Pan, J. Zhang, Toward Flexible Zinc–Air Batteries with Self-Supported Air Electrodes. Small 17 (2021) 2006773.

[139] P. Wang, T. Jia, B. Wang, Review—Recent Advance in Self-Supported Electrocatalysts for Rechargeable Zinc-Air Batteries. J. Electrochem. Soc. 167 (2020) 110564.

[140] P. Wang, B. Wang, Designing Self-Supported Electrocatalysts for Electrochemical Water Splitting: Surface/Interface Engineering toward Enhanced Electrocatalytic Performance. ACS Appl. Mater. Interfaces 13 (2021) 59593-59617.

[141] W. Li, D. Xiong, X. Gao, L. Liu, The oxygen evolution reaction enabled by transition metal phosphide and chalcogenide pre-catalysts with dynamic changes. Chem. Commun. 55 (2019) 8744-8763.

[142] J. Xu, Y. Liu, J. Li, I. Amorim, B. Zhang, D. Xiong, N. Zhang, S.M. Thalluri, J.P.S. Sousa, L. Liu, Hollow cobalt phosphide octahedral pre-catalysts with exceptionally high intrinsic catalytic activity for electro-oxidation of water and methanol. J. Mater. Chem. A 6 (2018) 20646-20652.

[143] Y. Du, H. Sheng, D. Astruc, M. Zhu, Atomically Precise Noble Metal Nanoclusters as Efficient Catalysts: A Bridge between Structure and Properties. Chem. Rev. 120 (2020) 526-622.

[144] H. Rong, S. Ji, J. Zhang, D. Wang, Y. Li, Synthetic strategies of supported atomic clusters for heterogeneous catalysis. Nat. Commun. 11 (2020) 5884.

[145] E.C. Tyo, S. Vajda, Catalysis by clusters with precise numbers of atoms. Nat. Nanotechnol. 10 (2015) 577-588.

[146] K. Kwak, D. Lee, Electrochemistry of Atomically Precise Metal Nanoclusters. Acc. Chem. Res. 52 (2019) 12-22.

[147] Y. Wang, X. Zheng, D. Wang, Design concept for electrocatalysts. Nano Research 15 (2022) 1730-1752.

[148] Y. Attia, M. Samer, Metal clusters: New era of hydrogen production. Renew. Sust. Energ. Rev. 79 (2017) 878-892.

[149] L. Qin, G. Ma, L. Wang, Z. Tang, Atomically precise metal nanoclusters for (photo)electroreduction of CO2: Recent advances, challenges and opportunities. J. Energy Chem. 57 (2021) 359-370.

[150] Z. Xu, F.S. Xiao, S.K. Purnell, O. Alexeev, S. Kawi, S.E. Deutsch, B.C. Gates, Size-dependent catalytic activity of supported metal clusters. Nature 372 (1994) 346-348.

[151] K. Yamamoto, T. Imaoka, W.J. Chun, O. Enoki, H. Katoh, M. Takenaga, A. Sonoi, Size-specific catalytic activity of platinum clusters enhances oxygen reduction reactions. Nat. Chem. 1 (2009) 397-402.

[152] R. Jin, G. Li, S. Sharma, Y. Li, X. Du, Toward Active-Site Tailoring in Heterogeneous Catalysis by Atomically Precise Metal Nanoclusters with Crystallographic Structures. Chem. Rev. 121 (2021) 567-648.

[153] X. Du, R. Jin, Atomically Precise Metal Nanoclusters for Catalysis. ACS Nano 13 (2019) 7383-7387.

[154] X. Mao, L. Wang, Y. Xu, P. Wang, Y. Li, J. Zhao, Computational high-throughput screening of alloy nanoclusters for electrocatalytic hydrogen evolution. npj Computational Materials 7 (2021) 46.

[155] L. Wang, W. Chen, D. Zhang, Y. Du, R. Amal, S. Qiao, J. Wu, Z. Yin, Surface strategies for catalytic CO_2 reduction: from two-dimensional materials to nanoclusters to single atoms. Chem. Soc. Rev. 48 (2019) 5310-5349.

[156] A.M. Argo, J.F. Odzak, F.S. Lai, B.C. Gates, Observation of ligand effects during alkene hydrogenation catalysed by supported metal clusters. Nature 415 (2002) 623-626.

[157] S. Zhao, R. Jin, R. Jin, Opportunities and Challenges in CO_2 Reduction by Gold- and Silver-Based Electrocatalysts: From Bulk Metals to Nanoparticles and Atomically Precise Nanoclusters. ACS Energy Lett. 3 (2018) 452-462.

[158] D.R. Kauffman, D. Alfonso, C. Matranga, H. Qian, R. Jin, Experimental and Computational Investigation of Au_{25} Clusters and CO_2: A Unique Interaction and Enhanced Electrocatalytic Activity. J. Am. Chem. Soc. 134 (2012) 10237-10243.

[159] W. Zhang, Q. Yao, G. Jiang, C. Li, Y. Fu, X. Wang, A. Yu, Z. Chen, Molecular Trapping Strategy To Stabilize Subnanometric Pt Clusters for Highly Active Electrocatalysis. ACS Catal. 9 (2019) 11603-11613.

[160] L. Liu, A. Corma, Metal Catalysts for Heterogeneous Catalysis: From Single Atoms to Nanoclusters and Nanoparticles. Chem. Rev. 118 (2018) 4981-5079.

[161] C.C. Hou, H.F. Wang, C. Li, Q. Xu, From metal–organic frameworks to single/dual-atom and cluster metal catalysts for energy applications. Energy Environ. Sci. 13 (2020) 1658-1693.

[162] F. Lü, H. Bao, Y. Mi, Y. Liu, J. Sun, X. Peng, Y. Qiu, L. Zhuo, X. Liu, J. Luo, Electrochemical CO_2 reduction: from nanoclusters to single atom catalysts. Sustain. Energy Fuels 4 (2020) 1012-1028.

[163] P. Lettenmeier, L. Wang, U. Golla-Schindler, P. Gazdzicki, N.A. Cañas, M. Handl, R. Hiesgen, S.S. Hosseiny, A.S. Gago, K.A. Friedrich, Nanosized IrO_x–Ir Catalyst with Relevant Activity for Anodes of Proton Exchange Membrane Electrolysis Produced by a Cost-Effective Procedure. Angew. Chem. Int. Ed. 55 (2016) 742-746.

[164] S. Zhao, R.X. Jin, H. Abroshan, C.J. Zeng, H. Zhang, S.D. House, E. Gottlieb, H.J. Kim, J.C. Yang, R.C. Jin, Gold Nanoclusters Promote Electrocatalytic Water Oxidation at the Nanocluster/CoSe2 Interface. J. Am. Chem. Soc. 139 (2017) 1077-1080.

[165] J. Zhang, H. Zhang, Y. Wu, C. Liu, Y. Huang, W. Zhou, B. Zhang, Single-atom catalysts for thermal- and electro-catalytic hydrogenation reactions. J. Mater. Chem. A 10 (2022) 5743-5757.

[166] W. Zang, Z. Kou, S.J. Pennycook, J. Wang, Heterogeneous Single Atom Electrocatalysis, Where “Singles” Are “Married”. Adv. Energy Mater. 10 (2020) 1903181.

[167] X.F. Yang, A. Wang, B. Qiao, J. Li, J. Liu, T. Zhang, Single-Atom Catalysts: A New Frontier in Heterogeneous Catalysis. Acc. Chem. Res. 46 (2013) 1740-1748.

[168] B. Qiao, A. Wang, X. Yang, L.F. Allard, Z. Jiang, Y. Cui, J. Liu, J. Li, T. Zhang, Single-atom catalysis of CO oxidation using Pt_1/FeO_x. Nat. Chem. 3 (2011) 634-641.

[169] Y. Wang, H. Su, Y. He, L. Li, S. Zhu, H. Shen, P. Xie, X. Fu, G. Zhou, C. Feng, D. Zhao, F. Xiao, X. Zhu, Y. Zeng, M. Shao, S. Chen, G. Wu, J. Zeng, C. Wang, Advanced Electrocatalysts with Single-Metal-Atom Active Sites. Chem. Rev. 120 (2020) 12217-12314.

[170] N. Cheng, L. Zhang, K. Doyle-Davis, X. Sun, Single-Atom Catalysts: From Design to Application. Electrochemical Energy Reviews 2 (2019) 539-573.

[171] Y. Chen, S. Ji, C. Chen, Q. Peng, D. Wang, Y. Li, Single-Atom Catalysts: Synthetic Strategies and Electrochemical Applications. Joule 2 (2018) 1242-1264.

[172] K. Maiti, S. Maiti, M.T. Curnan, H.J. Kim, J.W. Han, Engineering Single Atom Catalysts to Tune Properties for Electrochemical Reduction and Evolution Reactions. Adv. Energy Mater. 11 (2021) 2101670.

[173] C. Rivera-Cárcamo, P. Serp, Single Atom Catalysts on Carbon-Based Materials. ChemCatChem 10 (2018) 5058-5091.

[174] Y. Pan, C. Zhang, Z. Liu, C. Chen, Y. Li, Structural Regulation with Atomic-Level Precision: From Single-Atomic Site to Diatomic and Atomic Interface Catalysis. Matter 2 (2020) 78-110.

[175] R. Li, D. Wang, Superiority of Dual-Atom Catalysts in Electrocatalysis: One Step Further Than Single-Atom Catalysts. Adv. Energy Mater. 12 (2022) 2103564.

[176] A.R. Poerwoprajitno, L. Gloag, J. Watt, S. Cheong, X. Tan, H. Lei, H.A. Tahini, A. Henson, B. Subhash, N.M. Bedford, B.K. Miller, P.B. O'Mara, T.M. Benedetti, D.L. Huber, W. Zhang, S.C. Smith, J.J. Gooding, W. Schuhmann, R.D. Tilley, A single-Pt-atom-on-Ru-nanoparticle electrocatalyst for CO-resilient methanol oxidation. Nat. Catal. 5 (2022) 231-237.

[177] M.T.M. Koper, T.E. Shubina, R.A. van Santen, Periodic Density Functional Study of CO and OH Adsorption on Pt−Ru Alloy Surfaces: Implications for CO Tolerant Fuel Cell Catalysts. J. Phys. Chem. B 106 (2002) 686-692.

[178] W. Zhang, Y. Chao, W. Zhang, J. Zhou, F. Lv, K. Wang, F. Lin, H. Luo, J. Li, M. Tong, E. Wang, S. Guo, Emerging Dual-Atomic-Site Catalysts for Efficient Energy Catalysis. Adv. Mater. 33 (2021) 2102576.

[179] A. Pedersen, J. Barrio, A. Li, R. Jervis, D.J.L. Brett, M.M. Titirici, I.E.L. Stephens, Dual-Metal Atom Electrocatalysts: Theory, Synthesis, Characterization, and Applications. Adv. Energy Mater. 12 (2022) 2102715.

[180] T. He, A.R.P. Santiago, Y. Kong, M.A. Ahsan, R. Luque, A. Du, H. Pan, Atomically Dispersed Heteronuclear Dual-Atom Catalysts: A New Rising Star in Atomic Catalysis. Small 18 (2022) 2106091.

[181] Z. He, K. He, A.W. Robertson, A.I. Kirkland, D. Kim, J. Ihm, E. Yoon, G.D. Lee, J.H. Warner, Atomic Structure and Dynamics of Metal Dopant Pairs in Graphene. Nano Lett. 14 (2014) 3766-3772.

[182] M. Xiao, H. Zhang, Y. Chen, J. Zhu, L. Gao, Z. Jin, J. Ge, Z. Jiang, S. Chen, C. Liu, W. Xing, Identification of binuclear Co_2N_5 active sites for oxygen reduction reaction with more than one magnitude higher activity than single atom CoN4 site. Nano Energy 46 (2018) 396-403.

[183] H. Li, L. Wang, Y. Dai, Z. Pu, Z. Lao, Y. Chen, M. Wang, X. Zheng, J. Zhu, W. Zhang, R. Si, C. Ma, J. Zeng, Synergetic interaction between neighbouring platinum monomers in CO_2 hydrogenation. Nat. Nanotechnol. 13 (2018) 411-417.

[184] Z. Zhu, H. Yin, Y. Wang, C.H. Chuang, L. Xing, M. Dong, Y.R. Lu, G. Casillas-Garcia, Y. Zheng, S. Chen, Y. Dou, P. Liu, Q. Cheng, H. Zhao, Coexisting Single-Atomic Fe and Ni Sites on Hierarchically Ordered Porous Carbon as a Highly Efficient ORR Electrocatalyst. Adv. Mater. 32 (2020) 2004670.

[185] X. Zhu, D. Zhang, C.J. Chen, Q. Zhang, R.S. Liu, Z. Xia, L. Dai, R. Amal, X. Lu, Harnessing the interplay of Fe–Ni atom pairs embedded in nitrogen-doped carbon for bifunctional oxygen electrocatalysis. Nano Energy 71 (2020) 104597.

[186] X. Zhong, S. Ye, J. Tang, Y. Zhu, D. Wu, M. Gu, H. Pan, B. Xu, Engineering Pt and Fe dual-metal single atoms anchored on nitrogen-doped carbon with high activity and durability towards oxygen reduction reaction for zinc-air battery. Appl. Catal. B Environ. 286 (2021) 119891.

[187] Z.W. Chen, L.X. Chen, M. Jiang, D. Chen, Z.L. Wang, X. Yao, C.V. Singh, Q. Jiang, A triple atom catalyst with ultrahigh loading potential for nitrogen electrochemical reduction. J. Mater. Chem. A 8 (2020) 15086-15093.

[188] Z.W. Chen, L.X. Chen, C.C. Yang, Q. Jiang, Atomic (single, double, and triple atoms) catalysis: frontiers, opportunities, and challenges. J. Mater. Chem. A 7 (2019) 3492-3515.

[189] D. Zhao, Z. Zhuang, X. Cao, C. Zhang, Q. Peng, C. Chen, Y. Li, Atomic site electrocatalysts for water splitting, oxygen reduction and selective oxidation. Chem. Soc. Rev. 49 (2020) 2215-2264.

[190] J. Wang, Z. Li, Y. Wu, Y. Li, Fabrication of Single-Atom Catalysts with Precise Structure and High Metal Loading. Adv. Mater. 30 (2018) 1801649.

[191] S.K. Kaiser, Z. Chen, D. Faust Akl, S. Mitchell, J. Pérez-Ramírez, Single-Atom Catalysts across the Periodic Table. Chem. Rev. 120 (2020) 11703-11809.

[192] S. Chen, M. Cui, Z. Yin, J. Xiong, L. Mi, Y. Li, Single-Atom and Dual-Atom Electrocatalysts Derived from Metal Organic Frameworks: Current Progress and Perspectives. ChemSusChem 14 (2021) 73-93.

[193] Q. Zhang, J. Guan, Atomically dispersed catalysts for hydrogen/oxygen evolution reactions and overall water splitting. J. Power Sources 471 (2020) 228446.

[194] X. Zhu, X. Zhang, C. Zhao, T. Liao, Y. Zhang, C. Lin, C. Qi, P. Qiu, X. Li, W. Luo, Single, double and triple cobalt atoms confined in 2D regular framework for oxygen electrocatalysis. J. Alloys Compd. 872 (2021) 159689.

[195] H. Zhang, G. Liu, L. Shi, J. Ye, Single-Atom Catalysts: Emerging Multifunctional Materials in Heterogeneous Catalysis. Adv. Energy Mater. 8 (2018) 1701343.

2. Saline water electrolysis over self-supported electrode

2.1 Efficient hydrogen production by saline water electrolysis at high current densities without the interfering chlorine evolution

Abstract

Seawater electrolysis powered by renewable energy sources has been proposed to be a potentially cost-effective approach to green hydrogen production. However, the long-standing issue regarding the chlorine evolution reaction (CER) that deteriorates the performance of electrocatalysts and other components of electrolyzers has been impeding the market adoption of direct seawater electrolyzers. Herein, we demonstrate that coupling the cathodic hydrogen evolution reaction (HER) with the hydrazine oxidation reaction (HzOR) taking place at the anode enables the alkaline-saline water electrolysis to occur at a high current density without the unfavorable, interfering CER. Using the bifunctional carbon paper supported Co-Ni-P nanowires (Co-Ni-P/CP) as the cathode and anode, we have accomplished hydrogen production in alkaline-saline-hydrazine electrolyte at 500 mA cm^{-2} with a small cell voltage of only 0.533 V and outstanding stability of 80 hours with minimal degradation.

2.1.1 Introduction

Green hydrogen (H_2) produced through water electrolysis in combination with renewable energy sources such as solar and wind has become an important vector of decarbonizing the chemical industry and energy sector [1, 2], which will help to achieve the carbon neutrality goals set out by many countries. For widespread deployment of green H_2, the cost of water electrolysis must be substantially reduced to make the electrolyzed H_2 competitive relative to that produced by conventional steam reforming. To this end, considerable efforts have been made in the last decades, for example, to developing efficient and cost-effective electrocatalysts [3-7], optimizing the operation conditions of electrolysis (*e.g.*, pressure, temperature) [8, 9], and using cheap seawater as the feedstock for electrolysis [10-16]. For the commercial alkaline and proton exchange membrane (PEM) electrolyzers currently being deployed, there is generally a stringent requirement for the quality of water fed into the electrolyzer [12]. As a result, ancillary equipment is in most cases needed to desalinate and purify water before it is used for

electrolysis. Such desalination/purification units markedly increase the overall cost of the system and thereby the price of H_2. Therefore, it is highly desirable to develop efficient catalytic materials and membranes as well as to design new electrolyzer configurations to enable direct usage of low-grade or saline water for hydrogen production. This is particularly favorable for large-scale offshore hydrogen production emerged very recently, taking advantage of the largely abundant and free seawater resources and the capability of installing the offshore wind and solar farms on megawatt/gigawatt-scale, as pointed out by the recent techno-economic analyses [17].

However, direct seawater electrolysis faces formidable technological challenges, in particular the chloride evolution reaction (CER) happening at the anode, which competes with the oxygen evolution reaction (OER) and generates unfavorable chlorine and/or hypochlorite that will corrode catalysts, membranes and other components over time and thereby substantially reduce the operational lifetime of the electrolyzer [12, 16]. To alleviate corrosion, precious noble metal catalysts and expensive support materials such as titanium have to be used [18], which increases the production cost of H_2 and hinders market penetration of seawater electrolyzers. According to the Pourbaix diagram of the aqueous saline electrolyte (0.5 M NaCl), when the pH value is above 7.5, the OER is thermodynamically more favorable than the hypochlorite formation reaction [12, 19]. On this basis, Dionigi and co-workers proposed an “alkaline design criterion” in saline water electrolysis, pointing out that an overpotential of up to 480 mV can be applied to drive the OER without any interfering CER [19]. However, the OER is a kinetically demanding process involving four proton-coupled electron transfer steps [20], and within the 480 mV overpotential limit it is unlikely to reach an electrolysis current density that is large enough to enable a high yield of H_2, even the most advanced OER electrocatalysts are employed [15, 19, 21, 22].

Herein, we propose that adding a small-molecule chemical such as hydrazine (N_2H_4) into the alkaline-saline electrolyte can effectively shift the anodic oxidation potential negatively and thereby significantly increase the potential gap between the hypochlorite formation (ca. 1.71 V vs. reversible hydrogen electrode, RHE) [19] and the electro-oxidation reaction (EOR) of small organic molecules, which allows for a large current density to be applied for the cathodic hydrogen evolution reaction (HER) during the saline water electrolysis, without the formation of any environmentally-unfriendly, corrosive hypochlorite species. Coupling EOR with HER has been extensively explored in the last few years as an energy-saving pathway for alkaline water electrolysis, and a number of small molecules such as alcohols [23, 24], amine [25], urea [26, 27] and hydrazine [28-

30], have been demonstrated to enable the anodic oxidation to occur at a potential markedly lower than 1.23 V vs. RHE – the thermodynamic potential for the OER, such that the electrical energy input for water electrolysis can be reduced to a large extent. In particular, substituting the OER with the hydrazine oxidation reaction (HzOR) received considerable attention very recently because the HzOR can take place at a fairly low potential in theory (–0.33 V vs. RHE) and its product is inert, non-toxic nitrogen (N_2), which substantially improves the safety of electrolyzers due to the elimination of the possibility of having the explosive H_2/O_2 mixture [30]. Although introducing hydrazine into the electrolyte and its continuous consumption may to a certain extent increase the cost, it is believed that the economic profit gained from the replacement of CER by HzOR would be much larger for direct seawater electrolysis, given the significantly alleviated corrosion that can largely reduce the balance of plant (BoP) cost and eliminate the need for noble metal catalysts [18], as well as the energy-saving feature that allows for a high H_2 production rate at a markedly lower cell voltage.

Presently, most works reported so far on HzOR-assisted water electrolysis were exclusively focused on the energy-saving aspect as well as catalytic materials design and synthesis [28, 30-32], and there has been no attempt to replace the CER with the HzOR or any other EOR for H_2 production by seawater electrolysis, to the best of our knowledge. In this work, we for the first time report the coupling of HzOR and HER for saline water electrolysis to produce H_2. Using Co-Ni-P nanowires (NWs) coated carbon paper (Co-Ni-P/CP) as a self-supported bifunctional catalytic electrode, we demonstrate that a large anodic current density of 500 mA cm^{-2} can be accomplished at a potential as low as 0.175 V vs. RHE in the alkaline-saline-hydrazine electrolyte (1.0 M KOH + 0.5 M NaCl + 0.1 M N_2H_4), so far away from the onset potential of hypochlorite formation (ca. 1.71 V vs. RHE) that the evolution of OCl^- species is fully blocked even at such a high current density. Moreover, the Co-Ni-P/CP electrode is able to catalyze the HER in the 1.0 M KOH + 0.5 M NaCl + 0.1 M N_2H_4 electrolyte at 500 mA cm^{-2} with a comparatively low overpotential of 0.350 V. Consequently, the overall saline water electrolysis (OSWE) by coupling HER with HzOR can be achieved at a low cell voltage of 0.533 V at 500 mA cm^{-2}, and more impressively, it can be sustained at 500 mA cm^{-2} for at least 80 hours without obvious degradation, which shows great promise for industrial seawater electrolysis.

2.1.2 Results and discussion

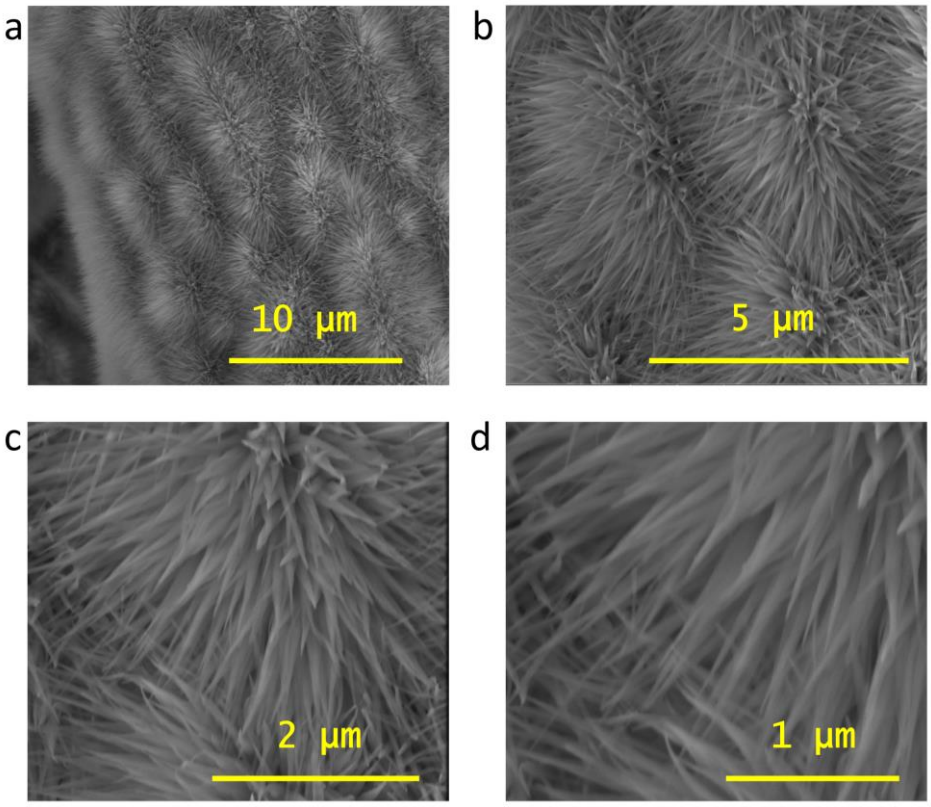

Figure 2.1.1 a, b) Low-magnification and c, d) high-magnification SEM images showing the morphology of the as-prepared cobalt-nickel-carbonate-hydroxide precursor ($CoNi(CO_3)(OH)_2$) nanowires on carbon paper.

The bifunctional Co-Ni-P/CP electrode was fabricated by firstly growing cobalt-nickel-carbonate-hydroxide ($CoNi(CO_3)(OH)_2$) precursor NWs on a piece of carbon paper (CP) through a hydrothermal approach [33], followed by a simple low-temperature phosphorization treatment using sodium hypophosphite (NaH_2PO_2) as the source of phosphorus. The scanning electron microscopy (SEM) examination revealed that a high density of tapered NWs have grown on the entire surface of the CP current collector after the hydrothermal reaction (**Figure 2.1.1**). Upon phosphorization, the NWs were converted to cobalt nickel phosphide consisting of a mixture of orthorhombic CoP (ICDD no. 00-029-0497), hexagonal Ni_5P_2 (ICDD no. 04-018-0215) and hexagonal CoNiP (ICDD no. 04-001-6153) crystal phases, as evidenced by the X-ray diffractometry (XRD) measurements (**Figure 2.1.2a**), and the tapered wire-like morphology did not change notably (**Figure 2.1.2b** and **Figure 2.1.3**). The microstructure of the Co-Ni-P NWs was further investigated by transmission electron microscopy (TEM). The NWs are several micrometers long and composed of interconnected crystallites with sizes in the range of 20 – 50 nm (**Figure 2.1.2c-d**). The high-resolution TEM (HRTEM) images reveal the well-defined crystal lattices that can be assigned to the (100) crystal planes of CoNiP solid solution (**Figure 2.1.2e**), (111) crystal planes of CoP and (211) crystal planes of

Ni_5P_2 (**Figure 2.1.2f**). Furthermore, the elemental distribution was probed in the high-angle annular dark-field scanning transmission electron microscopy (HAADF-STEM) mode. While Co and P are found to distribute uniformly across the whole NW, Co and Ni segregation is observed in several places (**Figure 2.1.2g**), indicating that the NW comprises the mixture of CoP, Ni_5P_2 and CoNiP phases, in agreement with the XRD result.

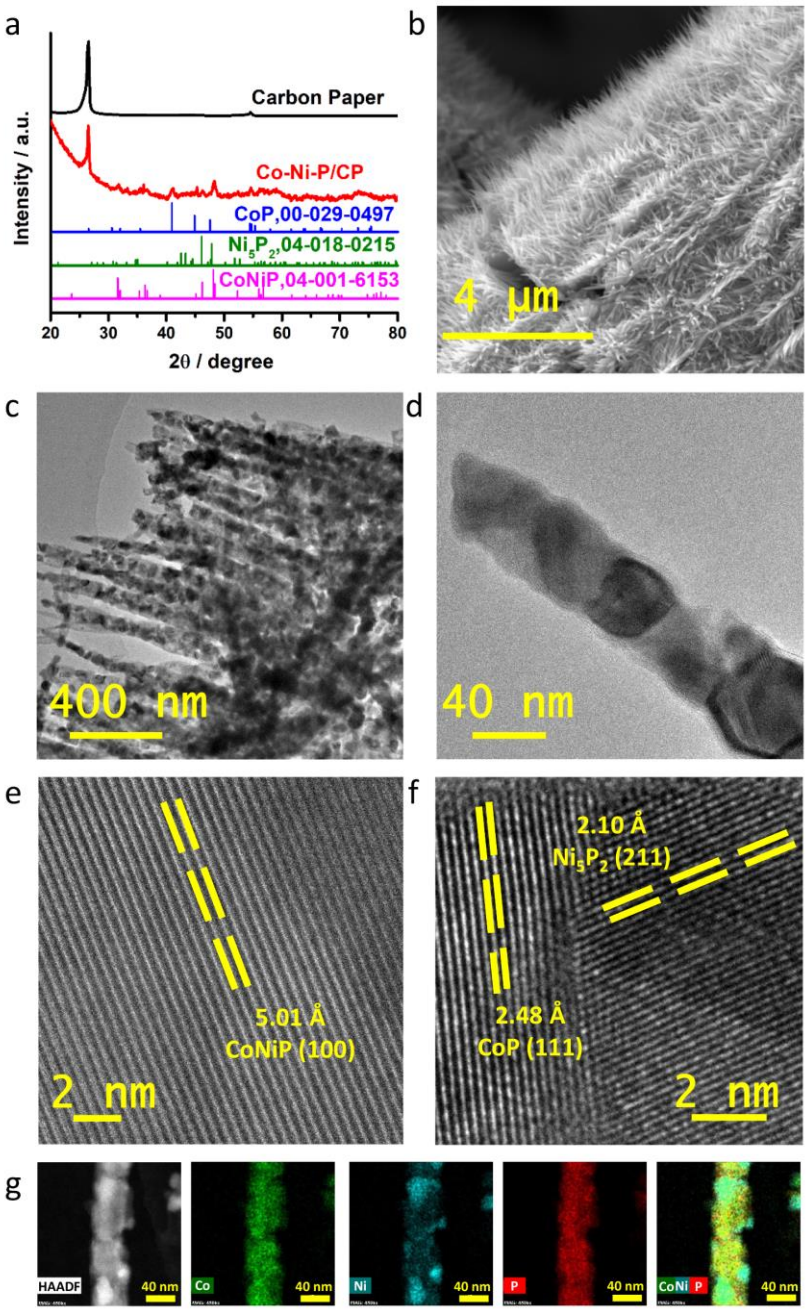

Figure 2.1.2 a) XRD pattern of the Co-Ni-P/CP. For comparison, the XRD patterns of the pristine CP, CoP, Ni_5P_2 and CoNiP solid solution are also presented. b) SEM image showing the morphology of the Co-Ni-P/CP. c-d) TEM images showing the microstructure of Co-Ni-P NWs at different magnifications. e-f) HRTEM images showing the lattice structure of the crystalline domains of Co-Ni-P NWs. g) HADDF-STEM image and the elemental maps of Co, Ni, P and their overlay.

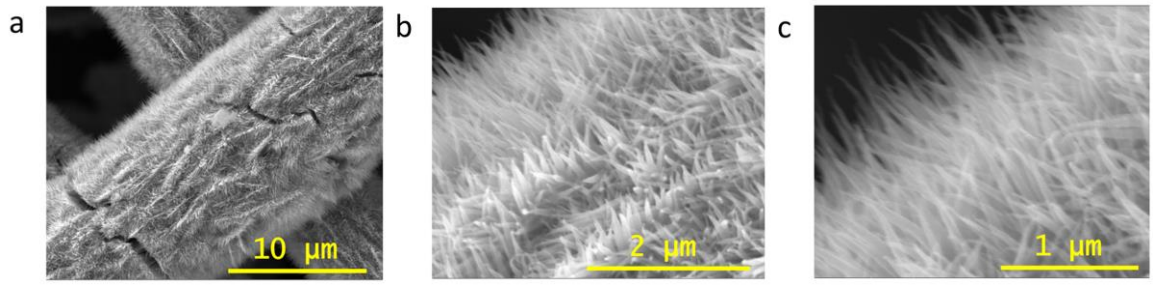

Figure 2.1.3 a) Low- and b, c) high-magnification SEM images showing the morphology of the as-prepared Co-Ni-P/CP electrode.

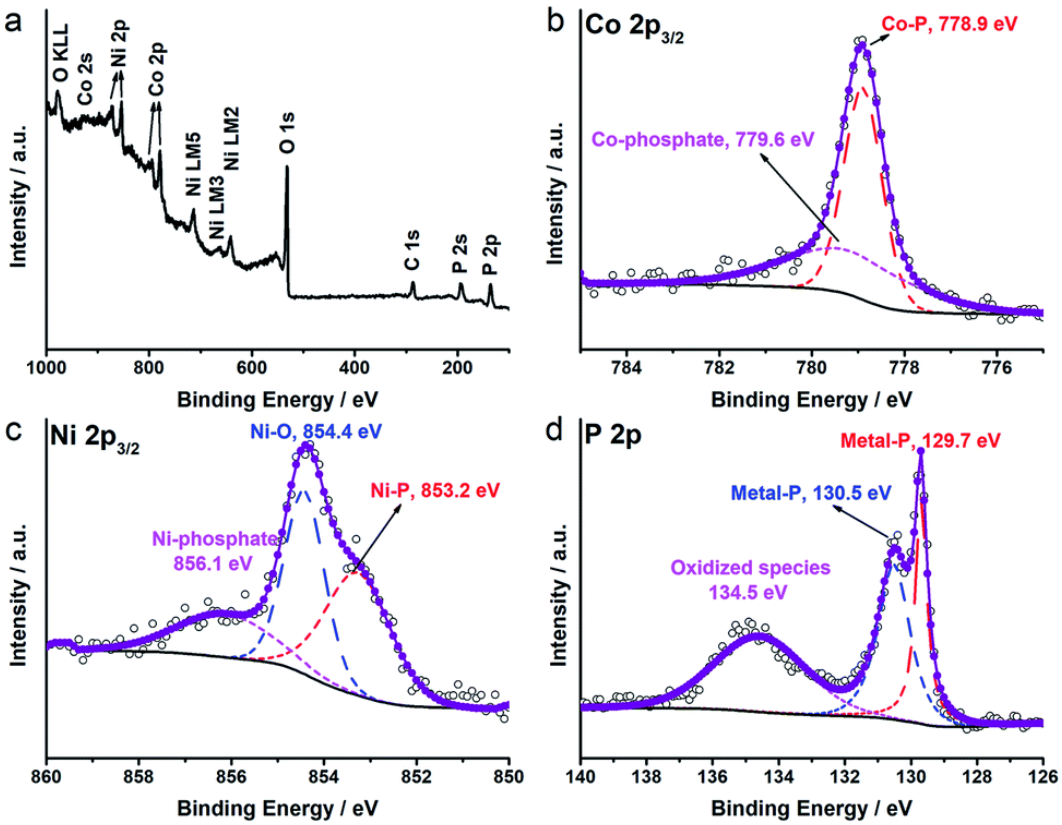

Figure 2.1.4 a) XPS survey spectrum and high-solution b) Co $2p_{3/2}$, c) Ni $2p_{3/2}$ and d) P 2p XPS spectra of the Co-Ni-P/CP electrode.

The surface chemical states of Co-Ni-P/CP were examined by X-ray photoelectron spectroscopy (XPS). The XPS survey spectrum confirms the presence of Co, Ni and P elements in the Co-Ni-P/CP electrode (**Figure 2.1.4a**), and the O signal may result from the surface oxidation of the sample and/or the absorbed oxygenated species. **Figure 2.1.4b** shows the core-level $Co2p_{3/2}$ XPS spectrum, where the peaks at the binding energy of 778.9 and 779.6 eV can be assigned to the Co–P and Co–PO_x bonding [34, 35], respectively. Similarly, in the $Ni2p_{3/2}$ XPS spectrum (**Figure 2.1.4c**), the peaks appearing at 853.2 and 856.1 eV are associated with the characteristic Ni–P and Ni–PO_x

bonding [36, 37]. The peak at 854.4 eV can be ascribed to the Ni–O bonding, which may result from the surface oxidation of Ni_5P_2 [38]. In addition, the formation of metal–P bond is corroborated by the P2p core-level XPS spectrum (**Figure 2.1.4d**), where the peaks located at 130.5 and 129.7 eV arise from low-valence P and P–metal bonding in metal phosphide, respectively [39]. The relatively weak peak at 134.5 eV generally relates to the oxidized phosphorus species due to the oxidation of the sample surface upon contact with air [40].

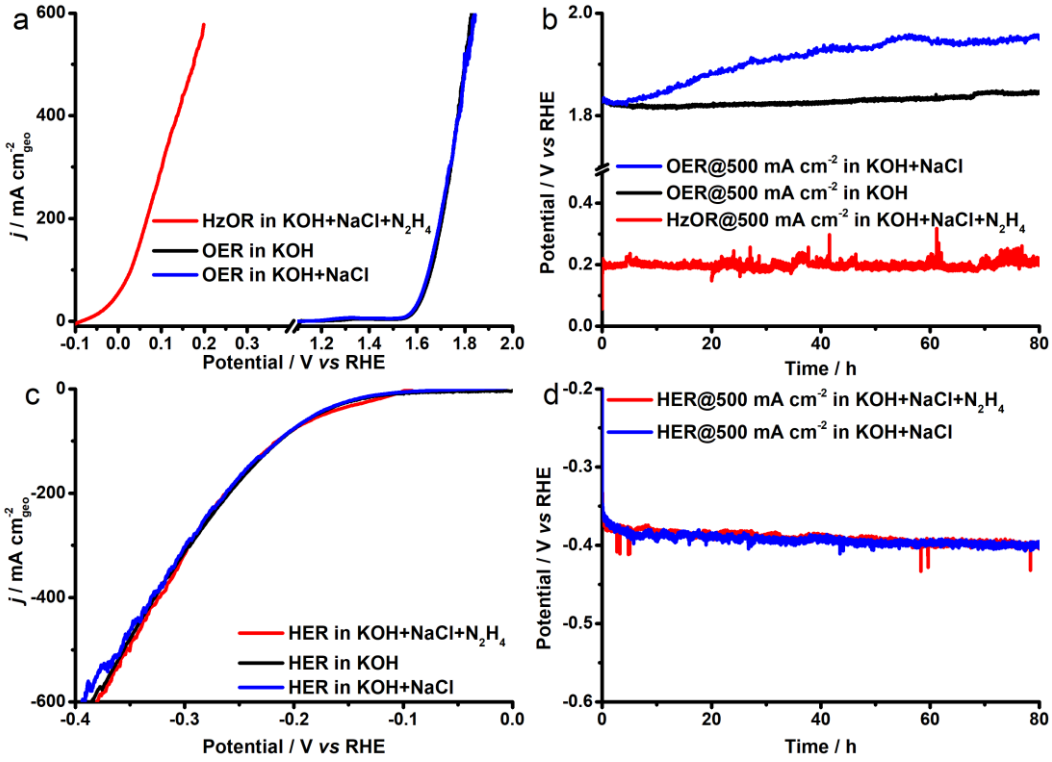

Figure 2.1.5 a) LSV curves showing the electrocatalytic activity of the Co-Ni-P/CP for HzOR and OER. Sweep rate: 5 mV s^{-1}. b) Chronopotentiometric curves recorded at a constant current density of 500 mA cm^{-2} in different electrolytes. c) LSV curves showing the HER activity of the Co-Ni-P/CP. Sweep rate: 5 mV s^{-1}. d) Chronopotentiometric curves recorded at a constant current density of –500 mA cm^{-2} measured in different electrolytes.

The electrocatalytic activity of the as-prepared Co-Ni-P/CP electrode (Co-Ni-P NW loading density: 6 mg cm^{-2}) was firstly evaluated toward the HzOR and OER in a typical three-electrode configuration by linear sweep voltammetry (LSV) in 1.0 M KOH + 0.5 M NaCl + 0.1 M N_2H_4, 1.0 M KOH and 1.0 M KOH + 0.5 M NaCl solutions, respectively. For the OER in 1.0 M KOH (black trace in **Figure 2.1.5a**), the Co-Ni-P/CP electrode can deliver geometric current densities of 10 and 500 mA cm_{geo}^{-2} at potentials of 1.550 V (E_{10}) and 1.791 V (E_{500}) vs. RHE, respectively, showing reasonably good catalytic activity [41-43]. Adding 0.5 M NaCl into the electrolyte does not give rise to an obvious change in the catalytic activity (E_{10} = 1.559 V vs. RHE and E_{500} = 1.794 V vs. RHE, **Figure 2.1.6**),

in agreement with previous reports [44,45]. However, the maximal current density under which the interfering hypochlorite formation would not happen (E = 1.71 V vs. RHE) is only 214 mA cm^{-2} in this case, which is insufficient to produce H_2 with a high yield. When additional 0.1 M N_2H_4 is added into the KOH + NaCl electrolyte, the anodic oxidation reaction onset (defined as the potential at which the anodic current density is 5 mA cm^{-2}, herein) shows a significant negative shift by 1.611 V, due to the preferential oxidation of N_2H_4 that happens much earlier. Consequently, the potentials to deliver 10 and 500 mA cm^{-2} can be reduced to only –0.057 V and 0.175 V vs. RHE, respectively, remarkably lower than the thermodynamic potential of hypochlorite formation in the strongly alkaline solution (*i.e.*, 1.71 V vs. RHE), which completely eliminates the interference of the unfavorable CER. Furthermore, the electrocatalytic performance of the Co-Ni-P/CP electrode was also investigated in the 1.0 M KOH + 0.5 M NaCl electrolytes with different concentrations of N_2H_4 (**Figure 2.1.7a**). There is no anodic current response in the potential window under investigation (–0.1 – 0.2 V vs. RHE) in the absence of N_2H_4. Upon the addition of N_2H_4 into the alkaline-saline electrolyte, the anodic current density markedly increases but does not show further increase when the N_2H_4 concentration reaches 0.1 M and beyond. Since hydrazine is highly toxic (NOTE: all experiments are recommended to be done in a ventilated fume hood. Personal protective equipment such as tight-fitting goggles, face masks, gloves, full suit and boots must be worn), a low N_2H_4 concentration (0.1 M) with which the best electrocatalytic performance can be achieved (**Figure 2.1.7a**) was chosen for all subsequent electrocatalytic tests (*i.e.*, using 1.0 M KOH + 0.5 M NaCl + 0.1 M N_2H_4 as the electrolyte). Furthermore, we also demonstrated that the HzOR is not diffusion-limited and the LSV curves acquired at different scan rates ranging from 5 to 90 mV s^{-1} vary insignificantly (**Figure 2.1.7b**), suggesting the efficient charge and mass transport processes occurring in the free-standing porous Co-Ni-P/CP electrode and that the HzOR itself should take place very fast.

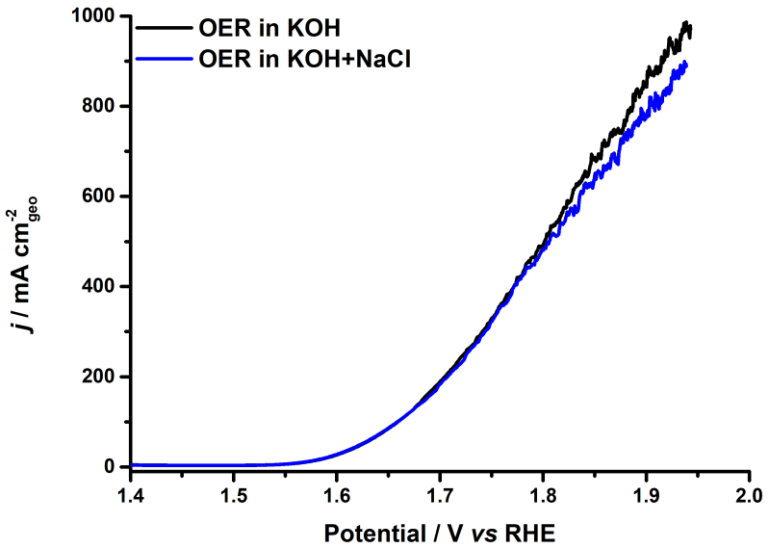

Figure 2.1.6 LSV curves showing the electrocatalytic activity of the Co-Ni-P/CP in 1.0 M KOH and 1.0 M KOH + 0.5 M NaCl solutions (zoomed view of **Figure 2.1.5a**).

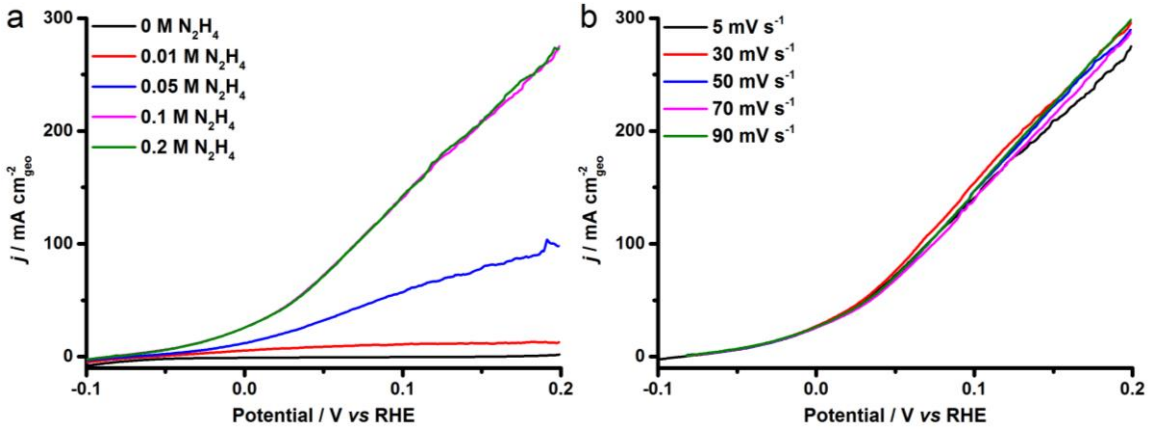

Figure 2.1.7 a) LSV curves of the Co-Ni-P/CP electrode recorded in the 1.0 M KOH + 0.5 M NaCl electrolytes with different concentrations of hydrazine. b) LSV curves of the Co-Ni-P/CP electrode recorded in 1.0 M KOH + 0.5 M NaCl + 0.1 M N_2H_4 at different scan rates.

The reaction kinetics of the Co-Ni-P/CP electrode was evaluated by the Tafel analysis (**Figure 2.1.8a**). The Co-Ni-P/CP exhibits a low Tafel slope of 50.6 mV dec^{-1} in 1.0 M KOH + 0.5 M NaCl + 0.1 M N_2H_4, indicating favorable HzOR kinetics. This is consistent with the electrochemical impedance spectroscopy (EIS) measurements, where the charge transfer resistance (R_{ct}) of the Co-Ni-P/CP in the alkaline-saline-N_2H_4 solution is as small as 3 Ω (**Figure 2.1.8b**), markedly lower than that measured in 1.0 M KOH (R_{ct} = 4.6 Ω) and 1.0 M KOH + 0.5 M NaCl (R_{ct} = 4.8 Ω) electrolytes. Long-term catalytic stability is of vital importance for practical applications of electrocatalysts. The OER stability of the Co-Ni-P/CP electrode for alkaline-saline water electrolysis was assessed by chronopotentiometry (CP) in 1.0 M KOH + 0.5 M NaCl solution at different current

densities ranging from 200 – 500 mA cm^{-2} (**Figure 2.1.9**). At 200 mA cm^{-2}, the Co-Ni-P/CP electrode can continuously catalyze the OER with minimal degradation. However, when the current density reaches 500 mA cm^{-2}, the electrode shows OER performance similar to that measured in the pristine 1.0 M KOH solution (**Figure 2.1.5b**) in the beginning few hours, and then the overpotential needed to maintain 500 mA cm^{-2} increases gradually and the performance continues to degrade in the remaining period of the stability test. As mentioned before, the hypochlorite formation would start to interfere the OER at 214 mA cm^{-2} and likely become predominant at 500 mA cm^{-2}, producing a large amount of corrosive OCl^- species that may deteriorate the performance of catalysts. This may explain the performance decay of the Co-Ni-P/CP at 500 mA cm^{-2} in 1.0 M KOH + 0.5 M NaCl as shown in **Figure 2.1.5b**. In case 0.1 M N_2H_4 is added, the HzOR can take place continuously and much earlier at ca. 0.2 V vs. RHE for 80 h with minimal performance deterioration (**Figure 2.1.5b**), showing outstanding catalytic stability. This also implies that no corrosive species that can potentially cause catalyst degradation are generated in the whole process. It is also worth mentioning that the HzOR has been rarely demonstrated before at such a high industry-relevant current density for a long time (previous HzOR was mainly tested at a current density of below 50 mA cm^{-2} for a limited period of time, see **Table 2.1.1**) [28, 30-32].

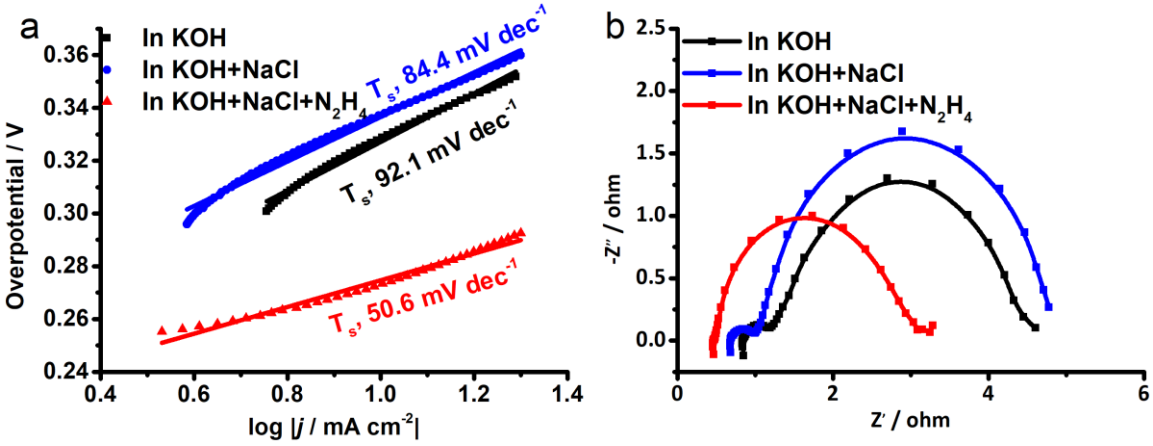

Figure 2.1.8 a) Tafel plots and b) Nyquist plots of the Co-Ni-P/CP electrode measured at –0.057 V vs. RHE toward the HzOR and 1.550 V vs. RHE toward the OER.

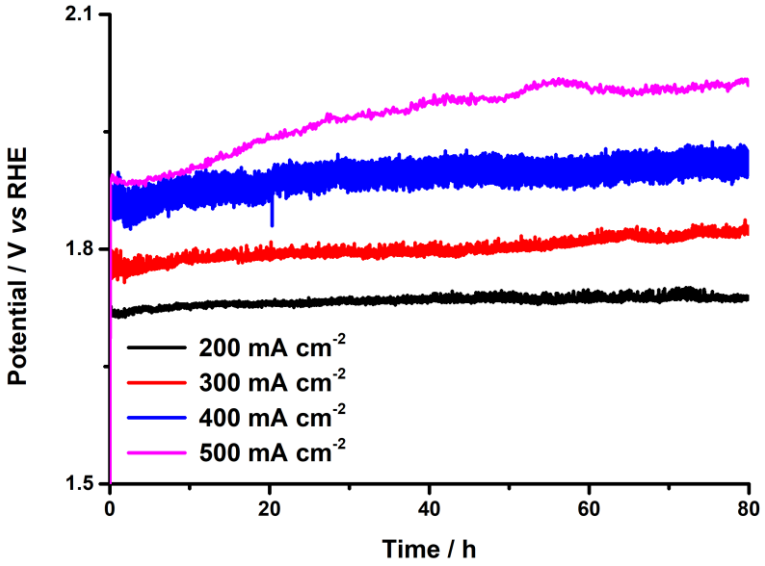

Figure 2.1.9 Chronopotentiometric curves of the Co-Ni-P/CP electrode recorded in 1.0 M KOH + 0.5 M NaCl electrolyte at different current densities.

Table 2.1.1 The comparison of hydrazine electrolysis performance for the Co-Ni-P/CP electrode reported in this work with that of electrocatalysts/catalytic electrodes recently reported in the literature.

Catalysts	Electrolyte	Cell voltage (V)	j (mA cm^{-2})	Stability	Reference
Co-Ni-P/CP	**1 M KOH + 0.5 M NaCl + 0.1 M N_2H_4**	**0.216**	**100**	**500 mA cm^{-2}@80 h, 1000 mA cm^{-2}@40 h**	**This work**
		0.533	**500**		
		1.116	**1000**		
NiCo-$MoNi_4$	1 M KOH+ 0.1 M N_2H_4	0.315	100	0.1 V for 10 h	Chem. Eng. J. 2021, 414, 128818.
Cu_1Ni_2-N	1 M KOH + 0.5 M N_2H_4	0.24	10	10 mA cm^{-2}@75 h	Adv. Energy Mater. 2019, 9, 1900390.
$CoSe_2$	1 M KOH + 0.5 M N_2H_4	0.164	10	10 mA cm^{-2}@14 h	Angew. Chem. Int. Ed. 2018, 57, 7649-7653.
CoP	1 M KOH + 0.1 M N_2H_4	0.2	10	0.1 V for 20 h	ChemElectroChem 2017, 4, 481-484.
CoS_2	1 M KOH + 0.1 M N_2H_4	0.81	100	25 mA cm^{-2}@5.6 h	New J. Chem. 2017, 41, 4754-4757.
Ni(Cu)	1 M KOH + 0.5 M N_2H_4	0.41	100	100 mA cm^{-2}@10 h	ACS Sustain. Chem. Eng. 2018, 6, 12746-12754.

Cu_3P	1 M KOH + 0.5 M N_2H_4	0.72	100	10 mA cm^{-2}@3 h	Inorg. Chem. Front. 2017, 4, 420-423.
CoSe	1 M KOH + 0.5 M N_2H_4	0.5	50	40 mA cm^{-2}@10 h	J. Power Sources 2018, 401, 238-244.
Ni_3S_2	1 M KOH + 0.2 M N_2H_4	0.867	100	20 mA cm^{-2}@11 h	J. Mater. Chem. A 2018, 6, 19201-19209.
Rh-C-N	1 M KOH + 0.5 M N_2H_4	0.2	20	20 mA cm^{-2}@3 h	ACS Appl. Mater. Interfaces 2019, 11, 35039-35049.

The electrocatalytic performance of the Co-Ni-P/CP electrode for the HER was also investigated in different electrolytes. The Co-Ni-P/CP can deliver geometric current densities of –10 and –500 mA cm_{geo}^{-2} at overpotentials (η) of 108 and 350 mV, respectively, in 1.0 M KOH + 0.5 M NaCl + 0.1 M N_2H_4 solution, showing HER performance similar to that measured in 1.0 M KOH and 1.0 M KOH + 0.5 M NaCl solutions (**Figure 2.1.5c**). Besides, a smaller Tafel slope and a lower R_{ct}, compared to those obtained in 1.0 M KOH and 1.0 M KOH + 0.5 M NaCl solutions, are also observed (**Figure 2.1.10**), indicating favorable HER kinetics in the presence of N_2H_4. Impressively, the Co-Ni-P/CP electrode can sustain HER catalysis at –500 mA cm_{geo}^{-2} for 80 h without notable degradation, exhibiting reasonably good catalytic stability (**Figure 2.1.5d**). The initial potential drop might result from the loss of some loosely-bound catalysts upon the violent evolution of H_2 gas bubbles.

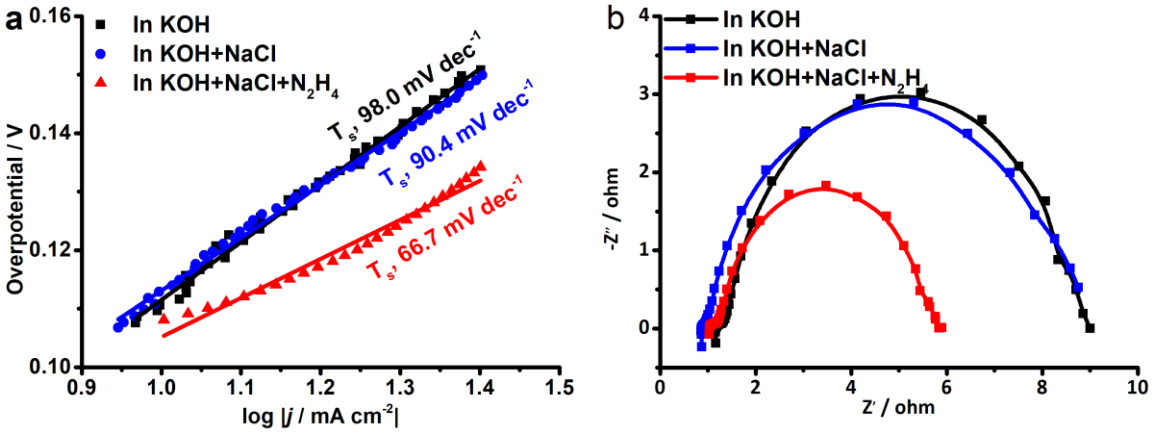

Figure 2.1.10 a) Tafel plots and b) Nyquist plots of the Co-Ni-P/CP electrode measured at –0.110 V vs. RHE toward the HER.

Given the validated remarkable HzOR and HER performance of the bifunctional Co-Ni-P/CP electrode, we managed to test the overall alkaline-saline water electrolysis by

coupling HER with HzOR in 1.0 M KOH + 0.5 M NaCl + 0.1 M N_2H_4 in a two-electrode configuration using two identical Co-Ni-P/CP electrodes as the anode and the cathode, respectively. Compared to the OSWE (HER + OER + CER) taking place in 1.0 M KOH + 0.5 M NaCl, the cell voltage needed at a given current density is significantly reduced for the HzOR + HER coupled saline water electrolysis (**Figure 2.1.11a**), which not only prevents the evolution of the interfering hypochlorite species, but also remarkably reduces the electrical energy input demanded for the H_2 production. The coupled HzOR + HER saline water electrolysis can be accomplished with ultralow cell voltages of 0.216, 0.298, 0.374, 0.450 and 0.533 V to reach the current densities of 100, 200, 300, 400 and 500 mA cm^{-2}, respectively, much lower than the values of 1.811, 1.916, 2.013, 2.093 and 2.153 V required to drive the same corresponding current density for the OSWE in 1.0 M KOH + 0.5 M NaCl (**Figure 2.1.11b**). In addition, the Faradaic efficiency of H_2 and N_2 evolution by the Co-Ni-P/CP electrode was measured (**Figure 2.1.12**). The volume ratio of H_2 over N_2 is close to 2:1, and the total volume of H_2 and N_2 gases experimentally detected matches well with that theoretically calculated, indicating a nearly 100 % Faradaic efficiency. The operational stability of the HzOR + HER coupled alkaline-saline water electrolysis was further assessed at a high current density of 500 mA cm^{-2}. The Co-Ni-P/CP electrode pair shows remarkable long-term durability of at least 80 h toward continuous H_2 production (red trace in **Figure 2.1.11c**), indicating that no interfering hypochlorite, which is detrimental to the operational stability of the saline water electrolyzers, was generated. For comparison, the catalytic stability of Co-Ni-P/CP in 1.0 M KOH + 0.5 M NaCl without the presence of N_2H_4 was also assessed (black trace in **Figure 2.1.11c**). The voltage needed to maintain 500 mA cm^{-2} is markedly higher than that of the HzOR + HER coupled alkaline-saline water electrolysis and gradually increases over time, implying a performance degradation likely resulting from the unfavorable CER. Furthermore, the operational stability of the Co-Ni-P/CP electrode pair was tested at a higher current density of 1000 mA cm^{-2} in the alkaline-saline-N_2H_4 electrolyte. The electrolysis can be accomplished stably under a low voltage of 1.116 V for at least 40 h (**Figure 2.1.13**), indicating outstanding long-time durability at high current densities. Notably, this is the first demonstration of the HzOR + HER coupled electrolysis occurring at such a high current density for a long period of time (**Table 2.1.1**), to the best of our knowledge.

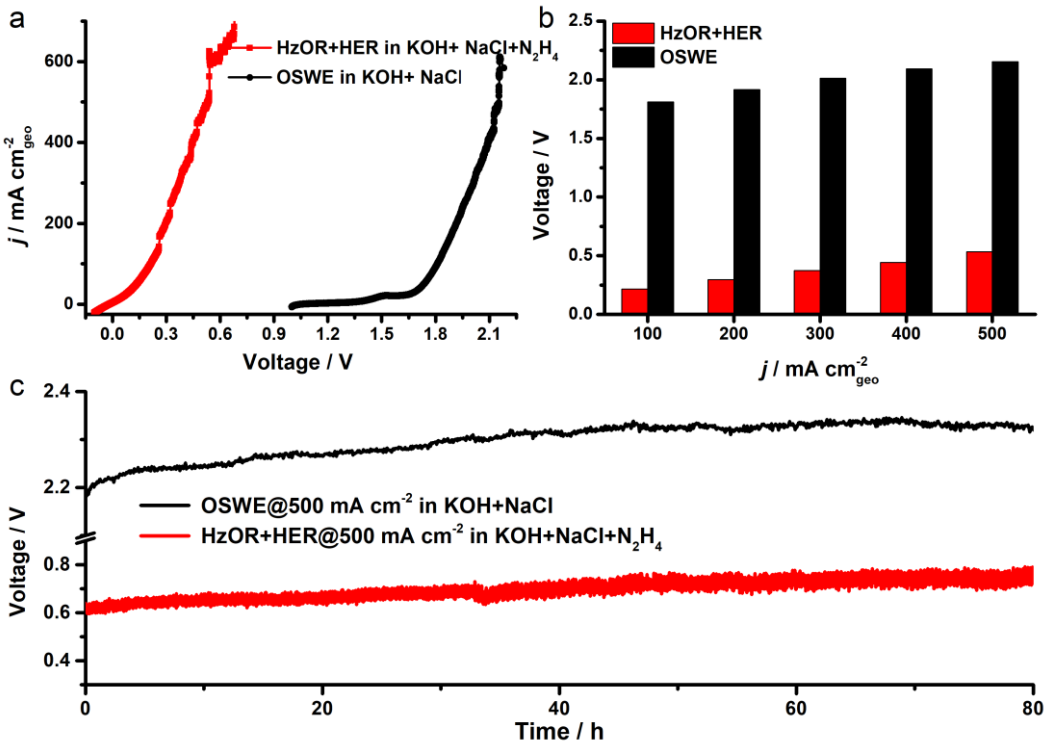

Figure 2.1.11 a) LSV curves of the coupled HzOR + HER measured in 1.0 M KOH + 0.5 M NaCl + 0.1 M N_2H_4 and the OSWE measured in 1.0 M KOH + 0.5 M NaCl. Sweep rate: 5 mV s^{-1}. b) Comparison of the cell voltages at different current densities for HzOR + HER and OSWE. c) Chronopotentiometric curves of the HzOR + HER and OSWE recorded at a constant current density of 500 mA cm^{-2} in 1.0 M KOH + 0.5 M NaCl + 0.1 M N_2H_4 and 1.0 M KOH + 0.5 M NaCl, respectively.

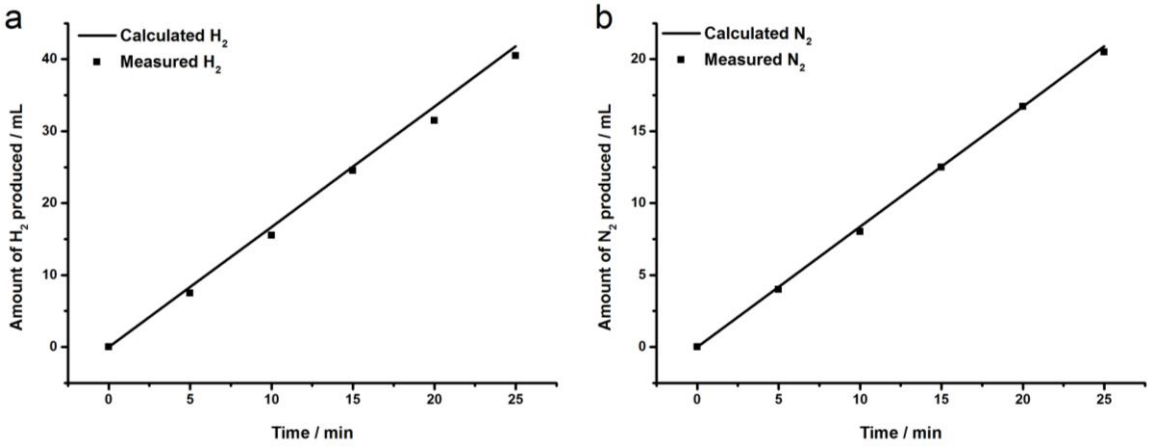

Figure 2.1.12 The volume of a) H_2 gas and b) N_2 gas theoretically evolved (solid line) and experimentally measured (scattered data points) for the HzOR + HER at the current density of 500 mA cm^{-2}.

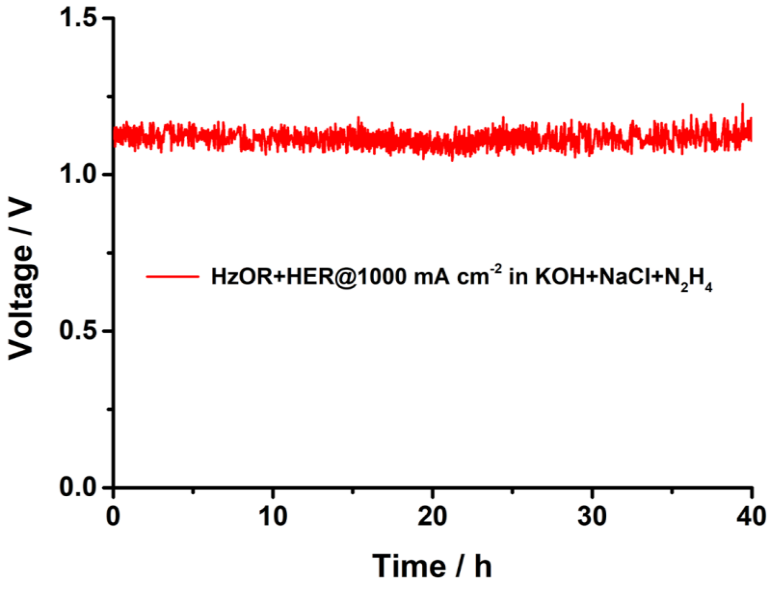

Figure 2.1.13 Chronopotentiometric curve of the HzOR + HER recorded at a constant current density of 1000 mA cm^{-2} in 1.0 M KOH + 0.5 M NaCl + 0.1 M N_2H_4.

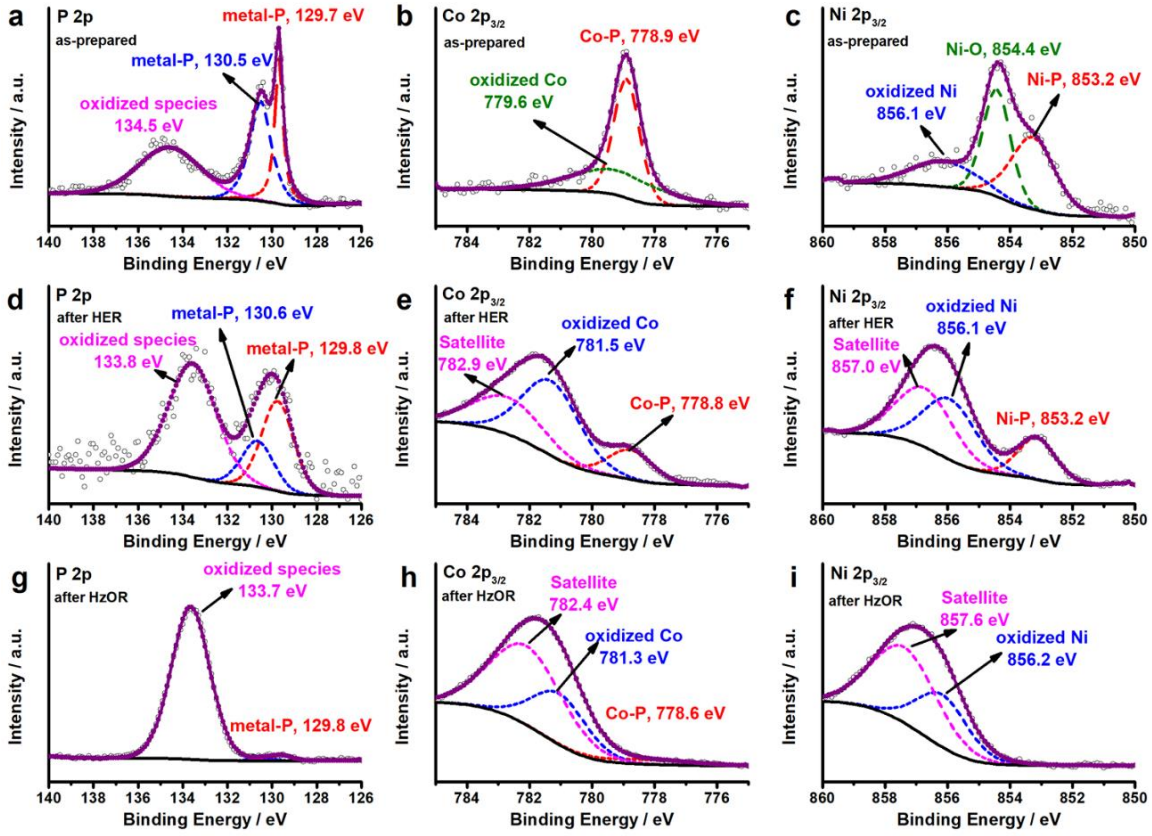

Figure 2.1.14 High-solution a, d, g) P 2p, b, e, h) Co $2p_{3/2}$, and c, f, i) Ni $2p_{3/2}$ XPS spectra of the Co-Ni-P/CP electrode a-c) before and after the d-f) HER and g-i) HzOR at 500 mA cm^{-2} for 80 h in 1.0 M KOH + 0.5 M NaCl + 0.1 M N_2H_4 in the two-electrode configuration.

Furthermore, we performed post-mortem XPS analysis of the Co-Ni-P/CP electrodes after the extended OSWE stability test at 500 mA cm^{-2} in the alkaline-saline-N_2N_4 electrolyte (**Figure 2.1.14**). The signals from metal–P bonding can be still clearly resolved for the cathode (**Figure 2.1.14d-f**), demonstrating good chemical stability of Co-Ni-P NWs toward the HER [46]. For the Co-Ni-P/CP anode subjected to the HzOR at 500 mA cm^{-2} for 80 h, the signals from metal phosphides disappear (**Figure 2.1.14g-i**), indicating that phosphide has been completely transformed to phosphate/oxidized species under the harsh oxidative conditions, as expected [7]. Nevertheless, good catalytic stability still maintained, as shown in **Figure 2.1.11c**, which likely because of the effective surface passivation by the *in-situ* formed catalytically-active oxygenated species (*e.g.*, oxide, hydroxide or oxyhydroxide).

2.1.3 Conclusions

In summary, we demonstrate in this work that adding hydrazine into the alkaline-saline water can help significantly shift the anodic oxidation reaction toward a negative potential and effectively prevent the interfering hypochlorite formation from occurring, even at a large industry-relevant current density. Using the carbon paper supported Co-Ni-P NWs as bifunctional electrocatalysts for HzOR and HER, we have proved that large current densities of 500 and 1000 mA cm^{-2} can be accomplished for the alkaline-saline water electrolysis with small cell voltages of 0.533 V and 1.116 V, respectively, with an outstanding operational stability, remarkably outperforming the conventional alkaline-saline water electrolysis in the absence of hydrazine using the same Co-Ni-P/CP bifunctional electrodes. The strategy we developed here not only provides a promising solution to the long-standing problem of the interfering chlorine evolution reaction in the saline/sea water electrolysis, but also enables the H_2 production *via* alkaline-saline water electrolysis to occur with a substantially reduced energy input, thereby improving the system energy efficiency. Moreover, the bifunctional Co-Ni-P/CP electrode simplifies the system design and eliminates the need for platinum group metal catalysts, which will help reduce production cost. Importantly, the products of the electrolysis, even operating at a high current density, are only non-explosive gaseous mixture of H_2 and N_2, which markedly improve the safety of electrolyzers. It is also worth mentioning that the waste water containing hydrazine from the hydrazinolysis process in chemical and pharmaceutical industry [47] could potentially serve as the feedstock of hydrazine in alkaline-saline water electrolysis, which may further reduce the costs of green hydrogen production and meanwhile help solve the problem of waste water treatment of this sector.

2.1.4 Experimental section

Preparation of the Co-Ni-P/CP electrodes: The carbon paper (CP, FuelCellStore) was firstly treated in a mixed solution of sulfuric acid and nitric acid (v (98% H_2SO_4):v (70% HNO_3):v (H_2O) = 1:1:1) at 60 °C for 6 h under vigorous magnetic stirring, in order to make the surface hydrophilic and to introduce the nucleation sites for the growth of cobalt-nickel-carbonate-hydroxide precursor NWs. The precursor solution was prepared by dissolving 10 mmol urea, 5 mmol NH_4F, 2 mmol $Co(NO_3)_2{\cdot}6H_2O$ and 2 mmol $Ni(NO_3)_2{\cdot}6H_2O$ in 30 ml deionized (DI) water under continuous magnetic stirring until a homogeneous, transparent solution was obtained (typically for 30 min), according to a previous report [33]. Afterwards, the solution was transferred into a Teflon-lined stainless steel autoclave reactor, and a piece of acid-treated CP (4 × 3 cm^2) was completely submerged in the precursor solution. Subsequently, the reactor was sealed and heated up to 120 °C, and maintained at this temperature for 6 h. After the autoclave reactor was cooled down to room temperature, the CP was taken out and thoroughly rinsed several times with DI water and then dried under vacuum at 70°C.

The Co-Ni-P/CP electrode was obtained by phosphorization of the precursor electrode using NaH_2PO_2 as the source of phosphorus at 300°C. Specifically, the CP coated with precursor NWs was loaded in a ceramic boat and 1.0 g of NaH_2PO_2 powders was placed 2 cm away from the CP at the upstream side. Subsequently, the furnace was purged with high-purity N_2 (99.999%) for 1 h to remove air, heated to 300 °C at a ramping rate of 5 °C min^{-1} and held at this temperature for 2 h. Finally, the furnace was naturally cooled down to room temperature. The mass loading of Co-Ni-P NWs on the CP electrode is around 6 mg cm^{-2}.

Materials Characterization: The morphology of Co-Ni-P/CP electrode was characterized by scanning electron microscopy (SEM, FEI Quanta 650 FEG microscope equipped with an INCA 350 spectrometer) and transmission electron microscopy (TEM, FEI ChemiSTEM 80-200, probe corrected). The X-ray diffraction (XRD) experiment was conducted on an X'Pert PRO diffractometer (PANalytical) set at 45 kV and 40 mA, using Cu K_α radiation (λ = 1.541874 Å) and a PIXcel detector. Data were collected with the Bragg–Brentano configuration in the 2θ range of 20 – 80^o at a scan speed of 0.011^o s^{-1}. X-ray photoelectron spectroscopy (XPS) characterization was carried out on an ESCALAB 250Xi instrument with the monochromated Al K_α (1486.6 eV) X-ray source.

Electrocatalytic tests: All electrochemical measurements of the Co-Ni-P/CP electrode was performed in a three-electrode configuration at room temperature using a Biologic

VMP3 potentiostat/galvanostat. The as-synthesized Co-Ni-P/CP electrode, a saturated calomel electrode (SCE), and a graphite rod were employed as the working, reference, and counter electrodes, respectively. The SCE reference was calibrated before each measurement in the H_2-saturated 0.5 M H_2SO_4 solution using a clean Pt wire as the working electrode. All potentials in this study were converted to the reversible hydrogen electrode (RHE) scale according to the following equation:

$$E_{RHE} = E_{SCE} + 0.059 \times pH + 0.244 \quad (1)$$

The HER, OER and HzOR measurements were carried out in the simulated seawater containing 1.0 M KOH + 0.5 M NaCl. For HzOR tests, different concentrations of hydrazine were dissolved in the electrolyte. The linear scan voltammetry (LSV) was performed at a scan rate of 5 mV s^{-1}. An *iR*-correction (85%) was applied to compensate for the voltage drop between the reference and working electrodes, which was measured by the single-point high-frequency impedance test. The electrochemical impedance spectroscopy (EIS) measurements were conducted at −0.110 V vs. RHE for the HER, −0.057 V vs. RHE for the HzOR and 1.550 V for OER in the frequency range of 10^5 – 0.01 Hz with a 10 mV sinusoidal perturbation. The stability of the Co-Ni-P/CP electrode was assessed using chronopotentiometry (CP) at a constant current density of 500 mA cm^{-2} for the OER, HzOR, OSWE and HzOR + HER, and −500 mA cm^{-2} for the HER. Moreover, the stability of the Co-Ni-P/CP pair toward HzOR + HER at 1000 mA cm^{-2} was also assessed.

2.1.5 References

[1] S. Chu, A. Majumdar, Opportunities and challenges for a sustainable energy future. Nature 488 (2012) 294-303.

[2] I. Staffell, D. Scamman, A. Velazquez Abad, P. Balcombe, P.E. Dodds, P. Ekins, N. Shah, K.R. Ward, The role of hydrogen and fuel cells in the global energy system. Energy Environ. Sci. 12 (2019) 463-491.

[3] H. Fei, J. Dong, M.J. Arellano-Jiménez, G. Ye, N. Dong Kim, E.L.G. Samuel, Z. Peng, Z. Zhu, F. Qin, J. Bao, M.J. Yacaman, P.M. Ajayan, D. Chen, J.M. Tour, Atomic cobalt on nitrogen-doped graphene for hydrogen generation. Nat. Commun. 6 (2015) 8668.

[4] W.T. Hong, M. Risch, K.A. Stoerzinger, A. Grimaud, J. Suntivich, Y. Shao-Horn, Toward the rational design of non-precious transition metal oxides for oxygen electrocatalysis. Energy Environ. Sci. 8 (2015) 1404-1427.

[5] J. Xu, T. Liu, J. Li, B. Li, Y. Liu, B. Zhang, D. Xiong, I. Amorim, W. Li, L. Liu, Boosting the hydrogen evolution performance of ruthenium clusters through synergistic coupling with cobalt phosphide. Energy Environ. Sci. 11 (2018) 1819-1827.

[6] Z. Yu, J. Xu, Y. Li, B. Wei, N. Zhang, Y. Li, O. Bondarchuk, H. Miao, A. Araujo, Z. Wang, J.L. Faria, Y. Liu, L. Liu, Ultrafine oxygen-defective iridium oxide nanoclusters for efficient and durable water oxidation at high current densities in acidic media. J. Mater. Chem. A 8 (2020) 24743-24751.

[7] W. Li, D. Xiong, X. Gao, L. Liu, The oxygen evolution reaction enabled by transition metal phosphide and chalcogenide pre-catalysts with dynamic changes. Chem. Commun. 55 (2019) 8744-8763.

[8] G. Tjarks, A. Gibelhaus, F. Lanzerath, M. Müller, A. Bardow, D. Stolten, Energetically-optimal PEM electrolyzer pressure in power-to-gas plants. Appl. Energy 218 (2018) 192-198.

[9] F. Scheepers, M. Stähler, A. Stähler, E. Rauls, M. Müller, M. Carmo, W. Lehnert, Temperature optimization for improving polymer electrolyte membrane-water electrolysis system efficiency. Appl. Energy 283 (2021) 116270.

[10] L. Yu, Q. Zhu, S. Song, B. McElhenny, D. Wang, C. Wu, Z. Qin, J. Bao, Y. Yu, S. Chen, Z. Ren, Non-noble metal-nitride based electrocatalysts for high-performance alkaline seawater electrolysis. Nat. Commun. 10 (2019) 5106.

[11] Y. Kuang, M.J. Kenney, Y. Meng, W.-H. Hung, Y. Liu, J.E. Huang, R. Prasanna, P. Li, Y. Li, L. Wang, M.C. Lin, M.D. McGehee, X. Sun, H. Dai, Solar-driven, highly sustained splitting of seawater into hydrogen and oxygen fuels. Proc. Natl. Acad. Sci. USA 116 (2019) 6624-6629.

[12] W. Tong, M. Forster, F. Dionigi, S. Dresp, R. Sadeghi Erami, P. Strasser, A.J. Cowan, P. Farràs, Electrolysis of low-grade and saline surface water. Nat. Energy 5 (2020) 367-377.

[13] H. Jin, X. Wang, C. Tang, A. Vasileff, L. Li, A. Slattery, S.Z. Qiao, Stable and Highly Efficient Hydrogen Evolution from Seawater Enabled by an Unsaturated Nickel Surface Nitride. Adv. Mater. 33 (2021) 2007508.

[14] F. Yang, Y. Luo, Q. Yu, Z. Zhang, S. Zhang, Z. Liu, W. Ren, H.M. Cheng, J. Li, B. Liu, A Durable and Efficient Electrocatalyst for Saline Water Splitting with Current Density Exceeding 2000 mA cm^{-2}. Adv. Funct. Mater. 31 (2021) 2010367.

[15] Y. Zhao, B. Jin, A. Vasileff, Y. Jiao, S.Z. Qiao, Interfacial nickel nitride/sulfide as a bifunctional electrode for highly efficient overall water/seawater electrolysis. J. Mater. Chem. A 7 (2019) 8117-8121.

[16] J.G. Vos, T.A. Wezendonk, A.W. Jeremiasse, M.T.M. Koper, MnO_x/IrO_x as Selective Oxygen Evolution Electrocatalyst in Acidic Chloride Solution. J. Am. Chem. Soc. 140 (2018) 10270-10281.

[17] R. d'Amore-Domenech, T.J. Leo, Sustainable Hydrogen Production from Offshore Marine Renewable Farms: Techno-Energetic Insight on Seawater Electrolysis Technologies. ACS Sustain. Chem. Eng. 7 (2019) 8006-8022.

[18] Z. Kato, M. Sato, Y. Sasaki, K. Izumiya, N. Kumagai, K. Hashimoto, Electrochemical characterization of degradation of oxygen evolution anode for seawater electrolysis. Electrochim. Acta 116 (2014) 152-157.

[19] F. Dionigi, T. Reier, Z. Pawolek, M. Gliech, P. Strasser, Design Criteria, Operating Conditions, and Nickel–Iron Hydroxide Catalyst Materials for Selective Seawater Electrolysis. ChemSusChem 9 (2016) 962-972.

[20] J. Xu, J. Li, Z. Lian, A. Araujo, Y. Li, B. Wei, Z. Yu, O. Bondarchuk, I. Amorim, V. Tileli, B. Li, L. Liu, Atomic-Step Enriched Ruthenium–Iridium Nanocrystals Anchored Homogeneously on MOF-Derived Support for Efficient and Stable Oxygen Evolution in Acidic and Neutral Media. ACS Catal. 11 (2021) 3402-3413.

[21] F. Cheng, X. Feng, X. Chen, W. Lin, J. Rong, W. Yang, Synergistic action of Co-Fe layered double hydroxide electrocatalyst and multiple ions of sea salt for efficient seawater oxidation at near-neutral pH. Electrochim. Acta 251 (2017) 336-343.

[22] H.J. Song, H. Yoon, B. Ju, D.Y. Lee, D.W. Kim, Electrocatalytic Selective Oxygen Evolution of Carbon-Coated $Na_2Co_{1-x}Fe_xP_2O_7$ Nanoparticles for Alkaline Seawater Electrolysis. ACS Catal. 10 (2020) 702-709.

[23] Y.X. Chen, A. Lavacchi, H.A. Miller, M. Bevilacqua, J. Filippi, M. Innocenti, A. Marchionni, W. Oberhauser, L. Wang, F. Vizza, Nanotechnology makes biomass electrolysis more energy efficient than water electrolysis. Nat. Commun. 5 (2014) 4036.

[24] G.F. Chen, Y. Luo, L.X. Ding, H. Wang, Low-Voltage Electrolytic Hydrogen Production Derived from Efficient Water and Ethanol Oxidation on Fluorine-Modified FeOOH Anode. ACS Catal. 8 (2018) 526-530.

[25] W. Xu, R. Lan, D. Du, J. Humphreys, M. Walker, Z. Wu, H. Wang, S. Tao, Directly growing hierarchical nickel-copper hydroxide nanowires on carbon fibre cloth for efficient electrooxidation of ammonia. Appl. Catal. B Environ. 218 (2017) 470-479.

[26] S. Chen, J. Duan, A. Vasileff, S.Z. Qiao, Size Fractionation of Two-Dimensional Sub-Nanometer Thin Manganese Dioxide Crystals towards Superior Urea Electrocatalytic Conversion. Angew. Chem. Int. Ed. 55 (2016) 3804-3808.

[27] Z.Y. Yu, C.C. Lang, M.R. Gao, Y. Chen, Q.Q. Fu, Y. Duan, S.H. Yu, Ni–Mo–O nanorod-derived composite catalysts for efficient alkaline water-to-hydrogen conversion via urea electrolysis. Energy Environ. Sci. 11 (2018) 1890-1897.

[28] Q. Qian, J. Zhang, J. Li, Y. Li, X. Jin, Y. Zhu, Y. Liu, Z. Li, A. El-Harairy, C. Xiao, G. Zhang, Y. Xie, Artificial Heterointerfaces Achieve Delicate Reaction Kinetics towards Hydrogen Evolution and Hydrazine Oxidation Catalysis. Angew. Chem. Int. Ed. 60 (2021) 5984-5993.

[29] C. Tang, R. Zhang, W. Lu, Z. Wang, D. Liu, S. Hao, G. Du, A.M. Asiri, X. Sun, Energy-Saving Electrolytic Hydrogen Generation: Ni_2P Nanoarray as a High-Performance Non-Noble-Metal Electrocatalyst. Angew. Chem. Int. Ed. 56 (2017) 842-846.

[30] Y. Li, J. Zhang, Y. Liu, Q. Qian, Z. Li, Y. Zhu, G. Zhang, Partially exposed RuP_2 surface in hybrid structure endows its bifunctionality for hydrazine oxidation and hydrogen evolution catalysis. Sci. Adv. 6 (2020) eabb4197.

[31] Q. Qian, Y. Li, Y. Liu, Y. Guo, Z. Li, Y. Zhu, G. Zhang, Hierarchical multi-component nanosheet array electrode with abundant $NiCo/MoNi_4$ heterostructure interfaces enables superior bifunctionality towards hydrazine oxidation assisted energy-saving hydrogen generation. Chem. Eng. J. 414 (2021) 128818.

[32] Y. Liu, J. Zhang, Y. Li, Q. Qian, Z. Li, Y. Zhu, G. Zhang, Manipulating dehydrogenation kinetics through dual-doping Co_3N electrode enables highly efficient hydrazine oxidation assisting self-powered H_2 production. Nat. Commun. 11 (2020) 1853.

[33] I. Amorim, J. Xu, N. Zhang, D. Xiong, S.M. Thalluri, R. Thomas, J.P.S. Sousa, A. Araújo, H. Li, L. Liu, Bi-metallic cobalt-nickel phosphide nanowires for electrocatalysis of the oxygen and hydrogen evolution reactions. Catal. Today 358 (2020) 196-202.

[34] V.V. Nemoshalenko, V.V. Didyk, V.P. Krivitskii, A.I. Senekevich, Study of the Charge State of Atoms in Iron, Cobalt and Nickel Phosphides. Zh. Neorg. Khimii 28 (1983) 2182.

[35] Y. Li, B. Wei, Z. Yu, O. Bondarchuk, A. Araujo, I. Amorim, N. Zhang, J. Xu, I.C. Neves, L. Liu, Bifunctional Porous Cobalt Phosphide Foam for High-Current-Density Alkaline Water Electrolysis with 4000-h Long Stability. ACS Sustain. Chem. Eng. 8 (2020) 10193-10200.

[36] H. Zhang, X. Li, A. Hähnel, V. Naumann, C. Lin, S. Azimi, S.L. Schweizer, A.W. Maijenburg, R.B. Wehrspohn, Bifunctional Heterostructure Assembly of NiFe LDH Nanosheets on NiCoP Nanowires for Highly Efficient and Stable Overall Water Splitting. Adv. Funct. Mater. 28 (2018) 1706847.

[37] J. Xu, I. Amorim, Y. Li, J. Li, Z. Yu, B. Zhang, A. Araujo, N. Zhang, L. Liu, Stable overall water splitting in an asymmetric acid/alkaline electrolyzer comprising a bipolar membrane sandwiched by bifunctional cobalt-nickel phosphide nanowire electrodes. Carbon Energy 2 (2020) 646-655.

[38] A.N. Mansour, Characterization of NiO by XPS. Surface Science Spectra 3 (1994) 231-238.

[39] Z. Yu, X.K. Wei, J. Xu, Y. Li, A. Araujo, J.L. Faria, R.E. Dunin-Borkowski, L. Liu, Multifunctional Noble Metal Phosphide Electrocatalysts for Organic Molecule Electro-Oxidation. ACS Appl. Energy Mater. 4 (2021) 1593-1600.

[40] Z. Yu, J. Xu, I. Amorim, Y. Li, L. Liu, Easy preparation of multifunctional ternary PdNiP/C catalysts toward enhanced small organic molecule electro-oxidation and hydrogen evolution reactions. J. Energy Chem. 58 (2021) 256-263.

[41] D. Li, H. Baydoun, C.N. Verani, S.L. Brock, Efficient Water Oxidation Using CoMnP Nanoparticles. J. Am. Chem. Soc. 138 (2016) 4006-4009.

[42] L. Jiao, Y.X. Zhou, H.L. Jiang, Metal–organic framework-based CoP/reduced graphene oxide: high-performance bifunctional electrocatalyst for overall water splitting. Chem. Sci. 7 (2016) 1690-1695.

[43] X. Wang, X. Huang, W. Gao, Y. Tang, P. Jiang, K. Lan, R. Yang, B. Wang, R. Li, Metal–organic framework derived $CoTe_2$ encapsulated in nitrogen-doped carbon nanotube frameworks: a high-efficiency bifunctional electrocatalyst for overall water splitting. J. Mater. Chem. A 6 (2018) 3684-3691.

[44] L. Yu, Q. Zhu, S. Song, B. McElhenny, D. Wang, C. Wu, Z. Qin, J. Bao, Y. Yu, S. Chen, Z. Ren, Non-noble metal-nitride based electrocatalysts for high-performance alkaline seawater electrolysis. Nat. Commun. 10 (2019) 5106.

[45] B. Wang, M. Lu, D. Chen, Q. Zhang, W. Wang, Y. Kang, Z. Fang, G. Pang,S. Feng, Ni_xFe_yN@C microsheet arrays on Ni foam as an efficient and durable electrocatalyst for electrolytic splitting of alkaline seawater. J. Mater. Chem. A 9 (2021) 13562-13569.

[46] A. Parra-Puerto, K.L. Ng, K. Fahy, A.E. Goode, M.P. Ryan, A. Kucernak, Supported Transition Metal Phosphides: Activity Survey for HER, ORR, OER, and Corrosion Resistance in Acid and Alkaline Electrolytes. ACS Catal. 9 (2019) 11515-11529.

[47] M. Morishita, J. Kobayashi, H. Yamada, T. Yajima, Synthesis of 3-Chloropyridazine-6-carboxylic Acid Hydrazide and Selective Hydrazinolysis of 3, 6-Substituted Pyridazines. Chem. Pharm. Bull. 42 (1994) 371-372.

2.2 Highly efficient and stable saline water electrolysis enabled by self-supported nickel-iron phosphosulfide nanotubes with heterointerfaces and under-coordinated metal active sites

Abstract

Direct seawater electrolysis is proposed to be a potentially low-cost approach to green hydrogen production taking advantage of the vastly available seawater and large-scale offshore renewable energy being deployed. However, developing efficient, earth-abundant electrocatalysts that can survive under harsh corrosive conditions for long time is still a significant technical challenge. Herein, we report the fabrication of self-supported nickel-iron phosphosulfide (NiFeSP) nanotube array electrode through a two-step sulfurization/phosphorization approach. The as-obtained NiFeSP nanotubes comprise abundant NiFeS/NiFeP heterointerfaces and under-coordinated metal sites, which exhibit outstanding activity and durability for the hydrogen and oxygen evolution reactions (HER & OER) in simulated alkaline-seawater solution (KOH + NaCl), with an overpotential of 380 (HER) and 260 mV (OER) at a large current density of 500 mA cm^{-2} and durability of 1000 hours. Theoretical calculations demonstrate that the heterointerface and under-coordinated metal sites synergistically lower the energy barrier to the rate-determining step of reactions, rationally explaining the excellent performance observed experimentally. The NiFeSP electrode also shows good catalytic performance for the urea oxidation reaction (UOR). By coupling UOR with HER, the bifunctional NiFeSP electrode pair can efficiently catalyze the overall alkaline-saline-urea water electrolysis at 500 mA cm^{-2} under 1.938 V for 1000 hours without notable performance degradation, showing significant potential for energy-saving production of green hydrogen.

2.2.1 Introduction

Green hydrogen (H_2) produced by water electrolysis in combination with renewable energy sources such as solar and wind, has been proposed to be a sustainable alternative to fossil fuels and capable of decarbonizing the transport and power sectors as well as hard-to-abate industries, contributing to achieving carbon-neutrality [1]. Compared to the conventional water electrolysis where highly-purified water is used as the feedstock, direct seawater electrolysis recently attracted considerable attention and has shown significant potential for offshore green H_2 production, considering that seawater accounts for 96.5% of the world's water resource and is virtually inexhaustible

[2] and that this approach potentially allows for marked reduction of the H_2 fuel price [3]. Notwithstanding appealing, there are still some technical challenges to overcome for direct seawater electrolysis. On one hand, direct seawater electrolysis usually occurs in a strongly alkaline solution, and operating the electrolyzer at an industry-relevant high current density (*e.g.*, > 500 mA cm^{-2}) requires efficient and stable oxygen evolution reaction (OER) and hydrogen evolution reaction (HER) electrocatalysts [4]. On the other hand, attaining a high current density needs a large overpotential, under which condition the chloride evolution reaction (CER) will come into play and compete with OER, lowering seawater electrolysis efficiency, and more severely, leading to the corrosion of all electrolyzer components over time. This will substantially reduce the operational lifetime of electrolyzers [4].

To address these challenges, attempts have been made to replace OER with the electro-oxidation reaction (EOR) of small organic molecules that happens at an anodic potential much lower than the thermodynamic onset potential of OER (*i.e.*, 1.23 V vs. reversible hydrogen electrode – RHE), such as hydrazine oxidation reaction (HzOR) and urea oxidation reaction (UOR) [5, 6]. For seawater electrolysis, coupling HER with EOR offers a promising approach to produce H_2 at a large current density without the unfavorable, interfering CER. In particular, UOR has recently been reported as a good alternative to OER due to its low thermodynamic potential (0.37 V vs. RHE) and less harmful nature compared to other EOR involving the use of toxic organic molecules (*e.g.*, hydrazine) [7]. Urea is widely existent in urban and industrial wastewater, and therefore urea electrolysis, when coupled with HER, not only favors H_2 production, but meanwhile enables efficient wastewater treatments [8, 9]. However, the complex six-electron transfer steps of UOR typically lead to sluggish reaction kinetics and thereby require a high practical cell voltage to allow the reaction to take place [7, 8].

To make seawater and urea electrolysis energy-efficient and cost-effective, highly active earth-abundant electrocatalysts able to remarkably boost the HER and OER/UOR are critically needed [7, 10]. Various transition metal-based materials, such as nitrides [11, 12], oxides [13, 14], phosphides [15, 16] and chalcogenides [17-19], have been reported lately to show impressive electrocatalytic activity, among which phosphide- and sulfide-based compounds were demonstrated to be very promising HER catalysts and the pre-catalysts for OER/UOR [20, 21]. In the pursuit of achieving better electrocatalytic performance of phosphide- and sulfide-based catalysts, several strategies are being developed. Firstly, multi-component electrocatalysts comprising more than one metals (*e.g.*, Fe, Co, and Ni) and/or non-metals (*e.g.*, S and P) have been demonstrated to show

better performance than monometallic phosphide and sulfide [21], because the co-existence of multiple elements allows for the exposure of more catalytically active sites, and more importantly the tuning of catalyst's electronic structure that enables to enhance the intrinsic catalytic activity [22]. To this end, bimetallic phosphide/sulfide ($Ni_xFe_{1-x}P/S$ [23], $(Co_{1-x}Fe_x)_2P$ [24], NiCoP [25] and Fe-NiS_2 [26]), metal phosphosulfide (CoPS [27], P-NiS_2 [28], CoS|P/CNT [29] and $FePS_3$ [30]) and multi-metal phosphosulfide ($Fe_{0.2}Ni_{0.8}$-$P_{0.5}S_{0.5}$ [31], $Ni_{1-x}Fe_xPS$ [32], P-$CoNi_2S_4$ [17] and $FeCoNiP_xS_y$ [33]), were already reported and exhibited improved electrocatalytic performance thanks to the synergetic interplay of different elements. Secondly, structure engineering turns out to be an effective strategy to achieve high catalytic performance. Notably, heterostructured catalysts consisting of enriched hetero-interfaces between different active phases may show intriguing electronic properties promoting the electrocatalytic performance [18, 34-36]. Moreover, introducing crystal defects can also effectively modulate local charge distribution and thereby the electronic structure of catalysts, boosting the catalytic activity [28, 37, 38]. In this respect, post-phosphorization treatment of sulfide catalysts has recently been illustrated to be able to improve the intrinsic catalytic activity and conductivity [17, 28, 38, 39], because of the increased number of active sites or the newly introduced active sites owing to the distortion of atomic structures of the parent sulfide. Last but not least, the catalytic performance can be enhanced through morphological engineering and design, which help enlarge electrochemically accessible surface area and enable rapid charge/mass transfer. To this end, various structures of phosphide/sulfide catalysts, including nanowires [27], nanosheets [30], nanoflower [34], and hierarchical architectures [28, 39], were already reported.

Herein, we report the fabrication of a self-supported nickel-iron phosphosulfide nanotube array (NiFeSP-NT) electrode *via* hydrothermal sulfurization of commercially available NiFe foam, followed by post-phosphorization treatment. Advanced transmission electron microscopy (TEM) and synchrotron X-ray absorption spectroscopy (XAS) measurements illustrate that the NiFeSP NTs comprise many hetero-interfaces and the metal sites are under-coordinated. When used to catalyze the OER and UOR in alkaline-saline water, the NiFeSP electrode can deliver 500 mA cm^{-2} at low potentials of 1.490 and 1.424 V vs. RHE respectively, effectively avoiding the CER from happening. Moreover, the NiFeSP electrode can accomplish a large cathodic current density of −500 mA cm^{-2} at −380 mV vs. RHE in the same electrolyte. Our density functional theory (DFT) calculations confirm that the NiFeS/NiFeP heterointerfaces and under-coordinated metal sites synergistically promote the electrocatalytic performance. Furthermore, we use the

NiFeSP as a bifunctional electrode and test its performance for the overall saline water electrolysis (OSWE, *i.e.*, OER + HER) and the overall urea-mediated saline water electrolysis (OUSWE, *i.e.*, UOR + HER). Impressively, the OUSWE enabled by bifunctional NiFeSP electrodes can operate at 500 mA cm^{-2} under a low cell voltage of 1.938 V with a long-term stability of 1000 hours, showing minimal performance degradation, which holds substantial promise for industrial seawater electrolysis.

2.2.2 Results and discussion

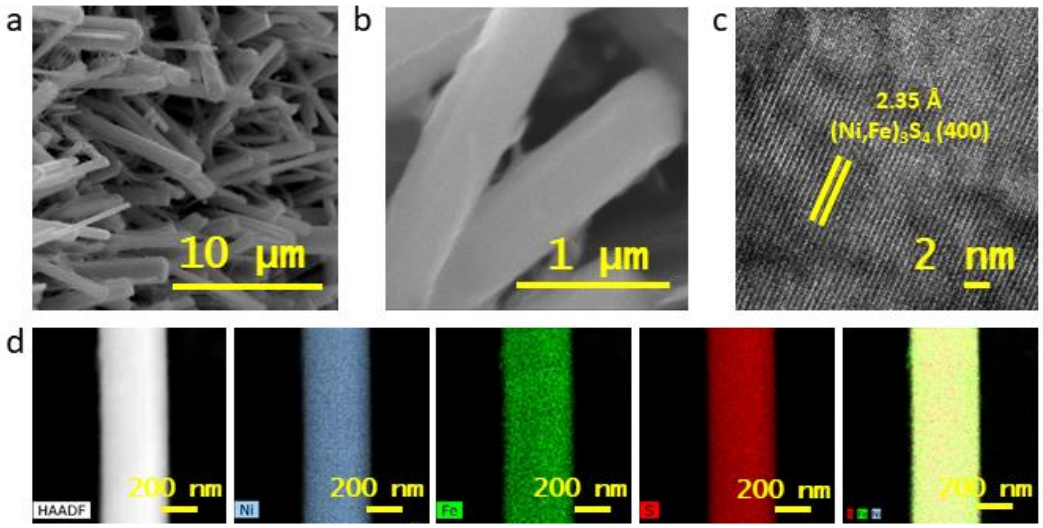

Figure 2.2.1 a-b) SEM images at different magnifications. c) HRTEM image, d) HAADF-STEM image of the NiFeS electrode and the corresponding elemental maps of Ni, Fe, S and their overlay.

As detailed in the **Experimental** section, the NiFeSP electrode was prepared by hydrothermal sulfurization of commercially available NiFe foam, followed by post-phosphorization using NaH_2PO_2 as the source of phosphorous. Scanning electron microscopy (SEM) examination showed that hydrothermal sulfurization led to the formation of a high density of vertically-aligned nanorods (NRs) with a smooth surface on the NiFe foam surface (**Figure 2.2.1**), which was a crucial step to obtain the NiFeSP-NT electrode subsequently. Both X-ray diffraction (XRD, **Figure 2.2.2a**) and high-resolution transmission electron microscopy (HRTEM, **Figure 2.2.1c**) confirmed that the NRs are composed of cubic $(Ni,Fe)_3S_4$ crystal phase (ICDD no. 04-001-4563). Moreover, Ni, Fe and S elements distribute uniformly along the NRs (**Figure 2.2.1d**). Upon a simple low-temperature phosphorization treatment at 300 °C for 2 h, the NiFeS electrode was converted into a self-supported NiFeSP-NT electrode. SEM revealed that the morphology of the vertically-aligned NR-like structure was well preserved after phosphorization, but the surface became rough (**Figure 2.2.2b**). A close inspection

under TEM disclosed that the original solid NRs were all converted into hollow NTs with unsmooth surfaces (**Figure 2.2.2c-d**), whose diameters and length are 300 – 500 nm and several micrometers, respectively. This structural transformation should result from the Kirkendall effect, which was also observed and reported previously [40-42]. The relatively large inner diameter of NTs allows the electrolyte to readily access the inner surface, exposing more catalyticallyactive sites; meanwhile, it facilitates the escape of gaseous product. For comparison, the NiFeP electrode was also fabricated by one-step phosphorization of the commercial NiFe foam, which only generated short vertically-aligned hexagonal NiFeP (ICDD no. 04-001-4563) nanostructures with ill-defined shape on the NiFe foam surface (**Figure 2.2.2a**; **Figure 2.2.3**). This highlights the importance of the order of the sulfurization and phosphorization processes in attaining well-defined, vertically-aligned NiFeSP-NT arrays.

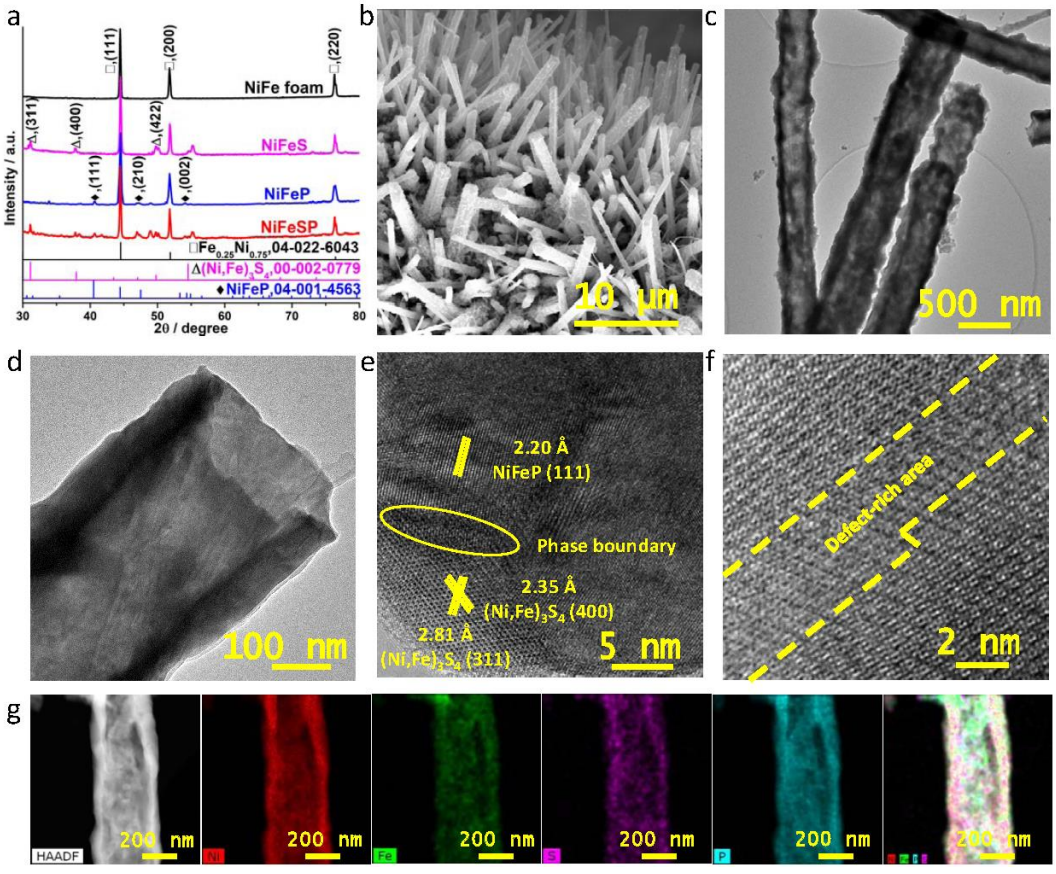

Figure 2.2.2 Morphology and microstructure characterization of NiFeSP-NT electrodes. a) XRD patterns of the NiFeSP-NT electrode and the reference samples. b) SEM image showing the vertically-standing nanotubes on the electrode surface. Inset: bird view of the NiFeSP electrode. c-d) TEM images and e-f) high-resolution TEM images taken at different magnifications. g) HAADF-STEM image and the corresponding elemental maps of Ni, Fe, S, P and their overlay.

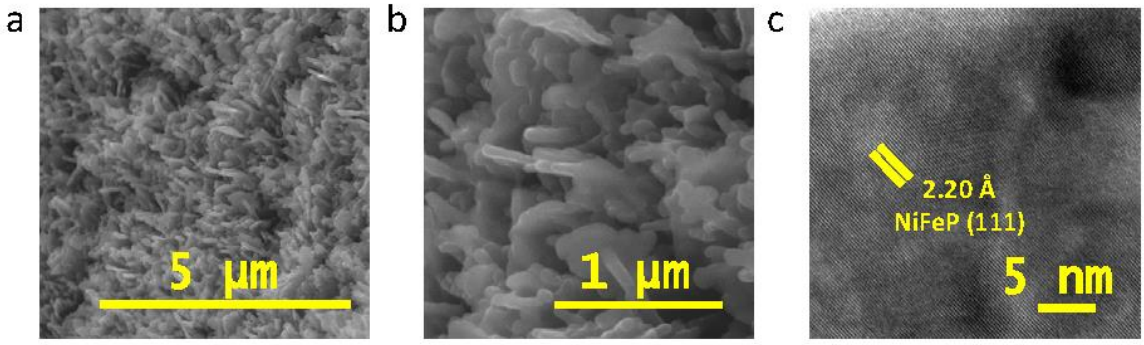

Figure 2.2.3 a-b) SEM images at different magnifications. c) HRTEM image of the NiFeP electrode.

XRD examination confirmed that the NiFeSP NTs consist of a composite of crystalline $(Ni,Fe)_3S_4$ and NiFeP phases (**Figure 2.2.2a**). Furthermore, diffraction peaks from $Fe_{0.25}Ni_{0.75}$ (ICDD no. 04-022-6043) are predominant in all samples, suggesting that the sulfurization and phosphorization only took place on the outermost surface and the crystal structure of the bulk NiFe foam remains unchanged, which helps maintain the mechanical strength of the electrode (pure sulfide, phosphide and phosphosulfide are all brittle) and facilitates charge transfer during electrocatalysis. The co-existence of $(Ni,Fe)_3S_4$ and NiFeP crystallites were further corroborated by HRTEM (**Figure 2.2.2e**), where the (311) and (400) crystal planes of $(Ni,Fe)_3S_4$ and the (111) crystal planes of NiFeP can be clearly distinguished, consistent with our XRD result. In addition, local lattice distortion (**Figure 2.2.2e**) and defect-rich areas with disordered lattice structure (**Figure 2.2.2f**) were also observed, particularly at $(Ni,Fe)_3S_4$/NiFeP phase boundaries, which might be introduced during the inter-diffusion of different phases upon phosphorization (Kirkendall effect). The formed uncoordinated defects may boost the electrocatalytic activity and reaction kinetics, according to previous reports [28, 38]. Nevertheless, on nanometer scale, the Ni, Fe, S and P elements are evenly distributed along and across individual NTs, as illustrated by the elemental maps taken in the high-angle annular dark-field scanning transmission electron microscopy (HAADF-STEM) mode (**Figure 2.2.2g**).

The surface chemical composition and oxidation state of the NiFeSP NTs and other control samples were analyzed by X-ray photoelectron spectroscopy (XPS). The XPS survey spectra (**Figure 2.2.4a**) confirm the existence of Ni, Fe, S and P in the NiFeSP-NT electrode, Ni, Fe and S in the NiFeS electrode, and Ni, Fe and P in the NiFeP electrode. The S:P atomic ratio in NiFeSP was determined to be ca. 1:3, which agrees with the energy-dispersive X-ray spectroscopy (EDX) analysis (**Figure 2.2.4b**), indicating that about 75% of S sites were substituted by P during the phosphorization. To

investigate the chemical bonding of S and P species with Ni/Fe atoms, we analyzed the high-resolution S2p and P2p XPS spectra of NiFeSP and other control samples. Three components that are assigned to metal sulfide (located at 161.7 and 163.0 eV) and oxidized sulfur (167.8 eV) [35, 39], respectively, can be observed in the S2p XPS spectra of both NiFeS and NiFeSP (**Figures 2.2.5a** and **2.2.5c**). The signal of S–O bonding is significantly attenuated for NiFeSP, suggesting that phosphorization can effectively mitigate surface oxidation of sulphides [17, 39]. In addition, the formation of metal–P bond in NiFeSP and NiFeP is corroborated by the P2p core-level XPS spectra (**Figures 2.2.5b** and **2.2.5d**). The peaks located at 129.6 and 130.5 eV arise from the low-valence P and P–metal bonding in metal phosphides [5, 43], respectively, and another peak appearing at 133.6 eV generally relates to the oxidized phosphorus species due to surface oxidation of samples in air, which were commonly observed in metal phosphides [44, 45].

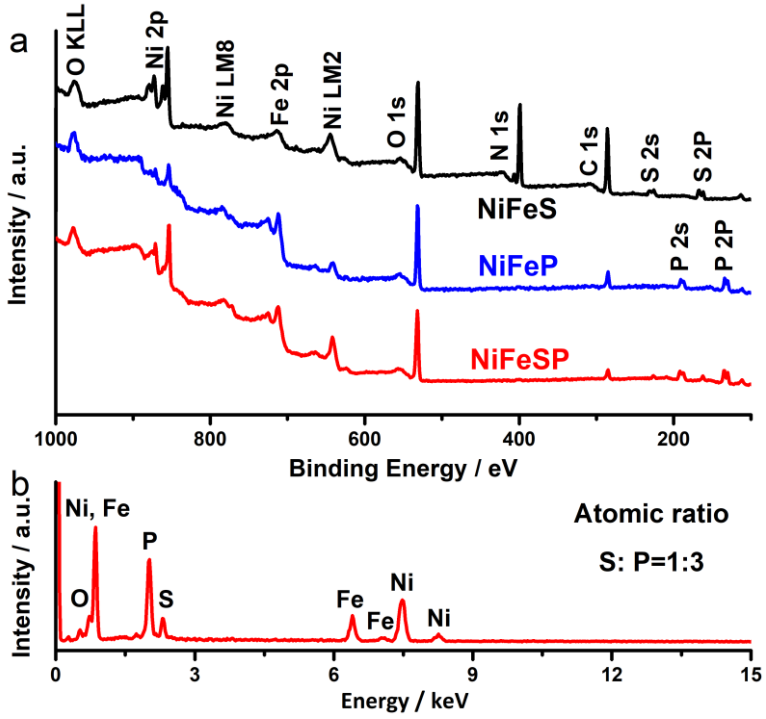

Figure 2.2.4 a) XPS survey spectrum of NiFeSP and other control samples, b) A representative EDX spectrum of the NiFeSP electrode.

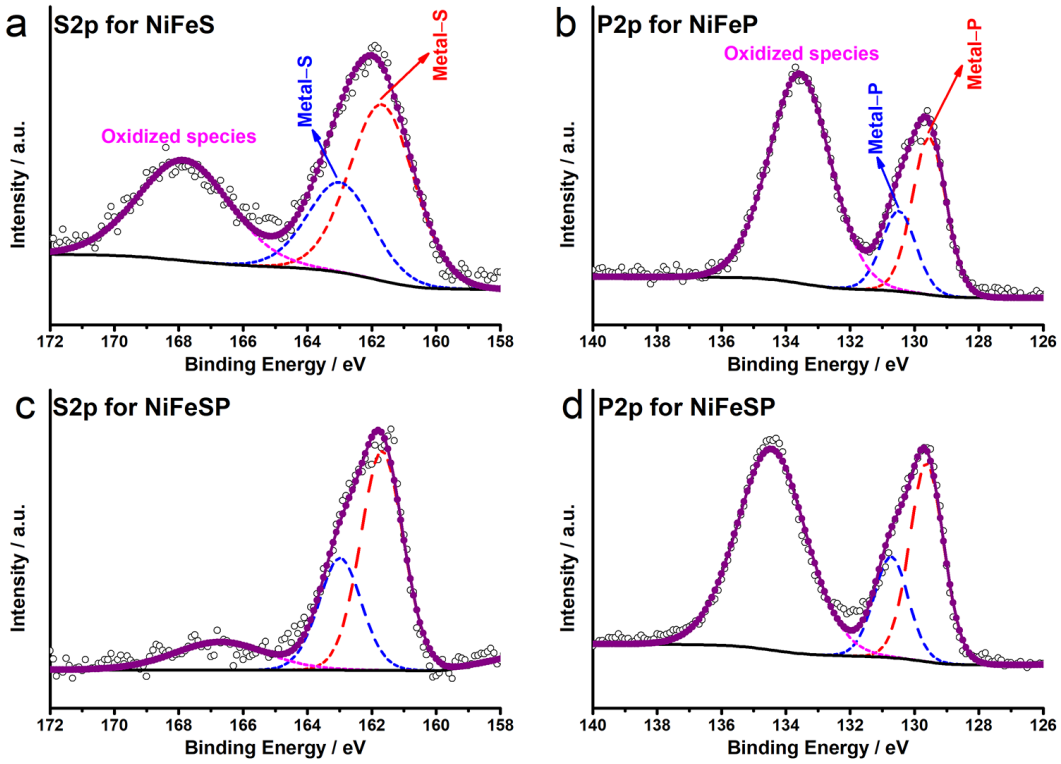

Figure 2.2.5 High-solution (a) S2p XPS spectrum of the NiFeS electrode, (b) P2p XPS spectrum of the NiFeP electrode, (c) S2p and d) P2p XPS spectra of the NiFeSP electrode.

Figure 2.2.6a shows the core-level Fe2p$_{3/2}$ XPS spectrum of the NiFeS electrode, where components resulting from Fe^{3+} (711.3 eV), Fe^{2+} (709.9 eV) and Fe–S (707.5 eV) can be observed [46]. The peak located at 713.2 eV is assigned to the satellite. Similarly, for the NiFeP electrode, the peaks appearing at 709.9, 711.3 and 714.1 eV are associated with Fe^{2+}, Fe^{3+} species and the satellite, while the peak at 707.1 eV can be ascribed to Fe–P bonding (**Figure 2.2.6b**) [15], in which Fe–P accounts for 18.3 at%. The NiFeSP electrode shows a Fe2p$_{3/2}$ XPS spectrum similar to that of NiFeS and NiFeP, but the peak at 707.3 eV should contain the contribution from both Fe–S and Fe–P bonding (**Figure 2.2.6c**). Quantitative XPS analysis revealed that the ratio of Fe–S: Fe–P is approximately 1:3 (**Table 2.2.1**), which agrees well with the EDX result (**Figure 2.2.4**). Additionally, the electronic structures of Ni in all samples were also investigated by XPS. For the Ni2p$_{3/2}$ XPS spectrum of NiFeS (**Figure 2.2.7a**), the two peaks at 852.6 and 856.0 eV originate from metallic Ni and Ni^{2+} species, respectively, while the signal centered at 862.0 eV is assigned to the satellite peak [35]. For the NiFeP and NiFeSP electrodes (**Figures 2.2.7b** and **2.2.7c**), a new peak that is ascribed to Ni–P bonding appears at 853.3 eV, which arises from the phosphorization process [5, 45]. It is noted that the Ni–P peak shows a significantly higher signal compared to the Ni^{2+} and the satellite, indicating

that phosphorization substantially reduced the amount of oxide/sulfide on the electrode surface. This was confirmed by XPS quantitative analysis of the NiFeSP electrode, where the ratio of Ni–S component over Ni–P component is close to 1:3, consistent with the above XPS (based on S2p and P2p spectra) and EDX analyses (**Figure 2.2.4**).

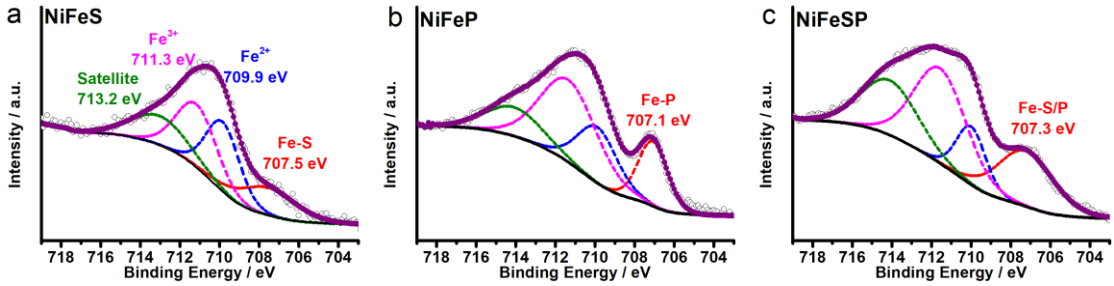

Figure 2.2.6 High-solution $Fe2p_{3/2}$ XPS spectra of the a) NiFeS b) NiFeP and c) NiFeSP electrodes.

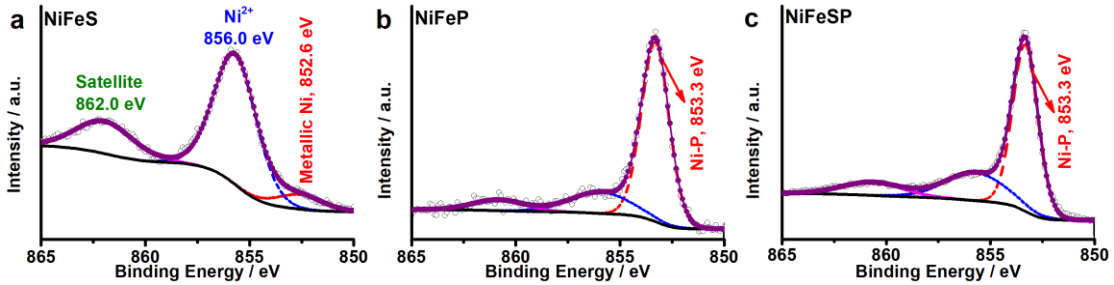

Figure 2.2.7 High-solution $Ni2p_{3/2}$ XPS spectra of the a) NiFeS b) NiFeP and c) NiFeSP electrodes.

Table 2.2.1. Fitting results of the $Fe2p_{3/2}$ and $Ni2p_{3/2}$ XPS spectra of the prepared self-supported electrodes.

	$Fe2p_{3/2}$				**$Ni2p_{3/2}$**		
NiFeS							
BE (eV)	707.5	709.9	711.3	713.2	852.6	856.0	862.0
Area (%)	19.3	28.8	31.6	20.3	8.7	67.6	23.7
Species	Fe–S	Fe^{2+}	Fe^{3+}	satellite	Ni^{0}	Ni^{2+}	satellite
NiFeP							
BE (eV)	707.1	709.9	711.3	714.1	853.3	855.9	860.8
Area (%)	18.3	21.4	44.6	15.7	73.0	19.0	8.0
Species	Fe–P	Fe^{2+}	Fe^{3+}	satellite	Ni–P	Ni^{2+}	satellite
NiFeSP							

BE (eV)	707.3	710.2	711.6	713.3	853.3	855.8	860.7
Area (%)	24.2	14.0	37.7	24.1	62.9	25.2	11.9
Species	Fe–S/ Fe–P	Fe^{2+}	Fe^{3+}	satellite	Ni–P	Ni^{2+}	satellite

Furthermore, X-ray absorption spectroscopy (XAS) at the Fe and Ni K-edges was conducted to investigate the local electronic and structural properties of the prepared NiFeSP and other reference electrodes around the metal centers. The Fe and Ni K-edge X-ray absorption near-edge structure (XANES) spectra are reported in **Figure 2.2.8a,c**. Having the XAS spectra bulk sensitivity in the investigated energy ranges, the reported signals corresponds to the overlap of the NiFe foam and $(Ni,Fe)_3S_4$ and/or NiFeP phases, together with other eventual amorphous contributions. Both the Ni and Fe K-edge XANES of NiFeSP are globally close to that of NiFeP, consistent with conclusions from XPS and EDX analysis were P dominates S as the principal ligand. More in details, all the XANES spectra present a weaker absorption feature located at lower energy, which correspond to quadrupolar 1s → 3d transition, where the metal 3d state are hybridized with the ligand or metal p states, and stronger dipolar transitions (1s → 4p) at higher energy (white-line). The quadrupolar pre-peak is expected more intense with increased 3d-4p orbital mixing resulting from an eventual broken centrosymmetric environment, which can be related to defects/edge sites [33].

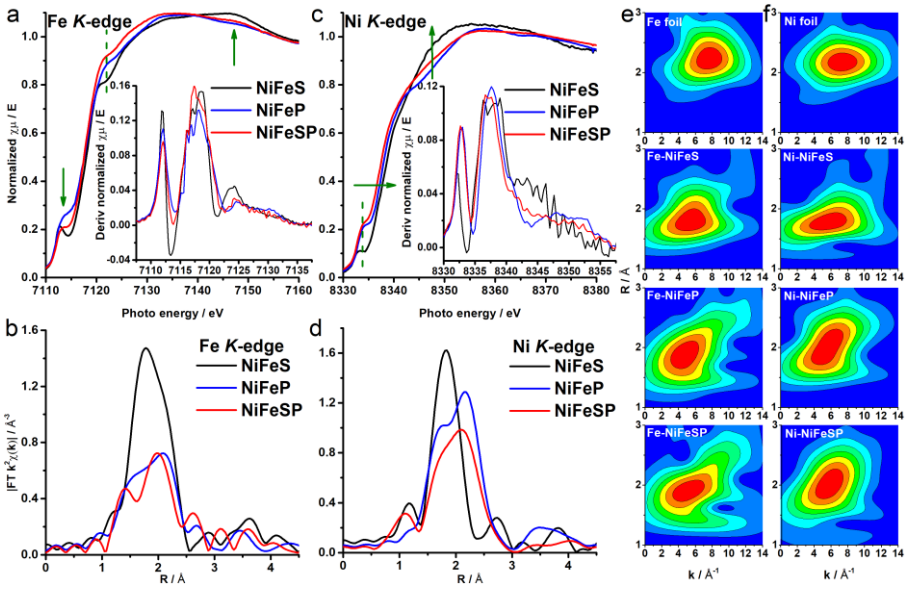

Figure 2.2.8 Local electronic and structural analyses of the NiFeSP and other control electrodes. a) Fe and c) Ni K-edge XANES spectra, and the corresponding (panels b and d) Fourier transforms of the k^2 weighted EXAFS oscillations in *R*-space, for the NiFeS, NiFeP and NiFeSP electrodes (k-range from 2.8 to 11.5 with Hanning window). Cauchy Wavelet EXAFS contour maps of metal foils and NiFeS, NiFeP and NiFeSP electrodes collected at the Fe e) and Ni f) K-edge, respectively.

The presence of metal-P instead of metal-S bonds seems to increase the feeling in between the quadrupolar pre-peak and the white-line gap, both for the Fe and Ni K-edge XANES spectra, suggesting a variation of the 3d-p mixing, and rearrangement of the 3d electrons or intra-site quadrupolar excitations by changing the ligand. In particular, the evident increase in intensity of the Ni K-edge absorption pre-peak for the NiFeP and NiFePS electrodes suggests an increase of vacancies around the Ni site in these systems respect the NiFeS counterpart. At higher energies, in average, a transfer of spectral weight from lower to higher energies seems the signature of the metal-S bonds. Globally, the position of the Fe K rising edge indicate that the Fe oxidation state is close to 2+ in all the systems, while the Ni center seems closer to an averaged monovalent state. Moreover, the Ni K-edge white-line shift toward higher energy for the NiFeS and even more for the NiFeSP electrode, compatibly with an increase of the Ni oxidations state. This suggest a more reduced environment in NiFeSP, accompanied by under-coordinated Ni sites.

The XANES results are supported by the Fourier transform (FT) of the k^2-weighted extended X-ray absorption fine structure (EXAFS) region collected at the Fe and Ni K-edge and reported in **Figure 2.2.8b,d**. At both edges two main features appear at around 1.7 and 2.1 Å, corresponding to the M-S/P and M-M bonds (M = Fe, Ni). The intensity of the feature at 2.1 Å mainly corresponds to the NiFe foam contribution. As for the XANES region, both edges the NiFeSP spectra approach that of NiFeP. Furthermore, phosphorizations at both Ni and Fe seems to lead to higher disorder, ascribable to a lower metal coordination number, as suggested by the decrease in the FT signal intensity of the 1.7 Å feature respect to the NiFeS electrode.

Additional insight is offered by inspection of the Cauchy wavelet transforms (WT) which allows deconvolution of the EXAFS signal based on both bond distance and the speciation of the scattering atoms. It is interesting then to note, that comparison to Fe and Ni foil spectra, showing a main contribution around 2.2 Å and 8 $Å^{-1}$ in R and k space, respectively, confirms the presence of various degrees of metal-metal interactions presumably resulting from the residual NiFe foam (**Figure 2.2.8e,f**). Patterns similar to the metallic foils are particularly evident at the Ni K-edge and for samples containing phosphide, in agreement with the XRD data, showing a typical higher residual NiFe foam fraction for such electrodes. Moreover, the samples exhibit a pronounced feature at ~1.9 - 2.0 Å in r-space with a maximum at 5 $Å^{-1}$ in k-space consistent with the presence of M-S and/or M-P bonds. Finally, a weaker signal at ~1.4 Å in r-space centered at a k of 4 $Å^{-1}$, indicate the presence of a minority fraction of M-O bonds as also suggested by XPS

data. These comprehensive atomic structure analyses indicate that the phosphorization of NiFeS electrodes notably changed the coordination environment of Ni/Fe atoms and accordingly altered the electronic structure of NiFeSP. As will be discussed below, the under-coordinated metal helps enhance the electrocatalytic performance for water splitting.

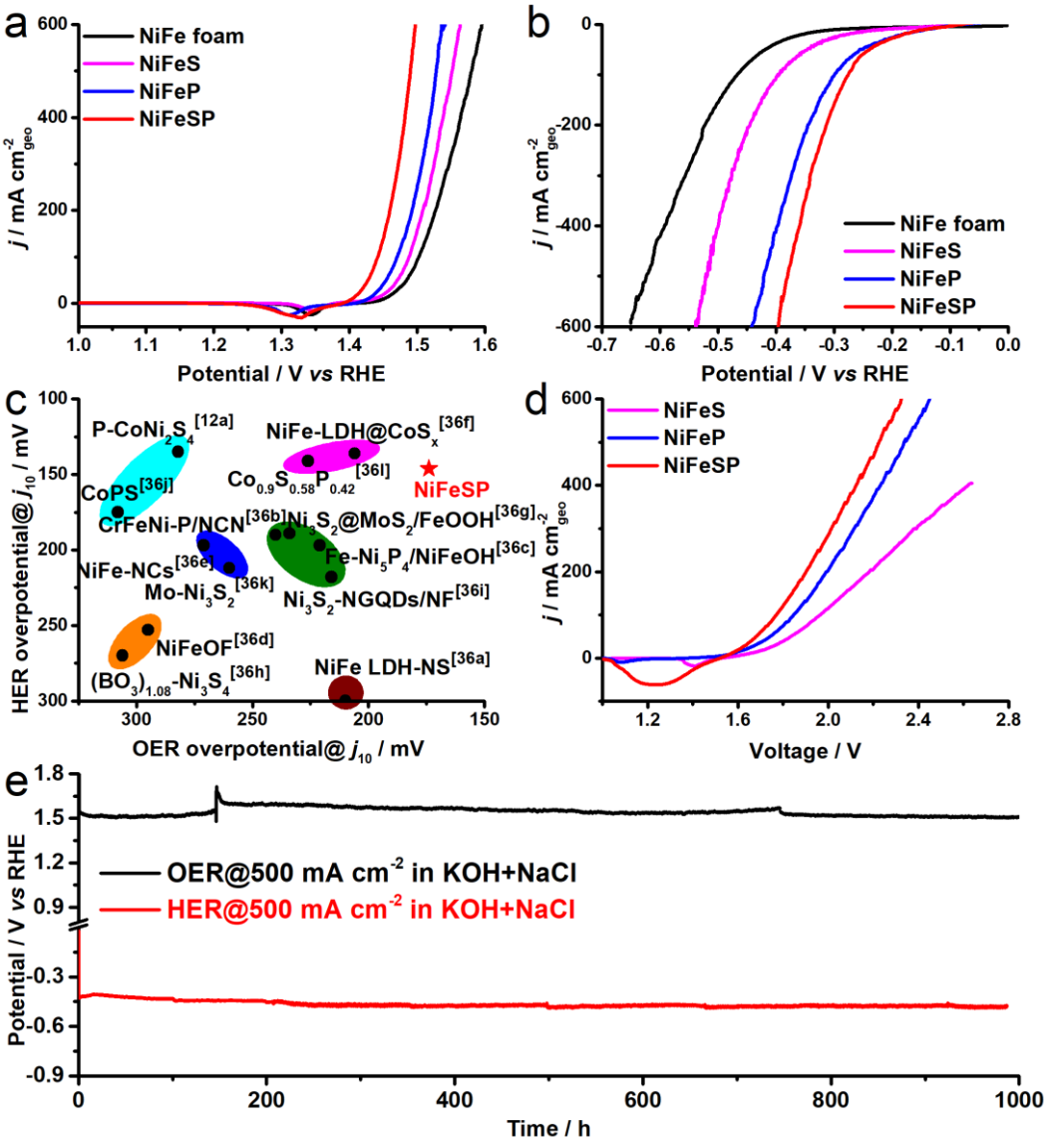

Figure 2.2.9 Electrocatalytic performance of NiFeSP and other control electrodes for OER, HER and OSWE. Polarization curves of the a) OER and b) HER, recorded at 5 mV s^{-1}. c) Comparison of OER and HER overpotentials at 10 mA cm^{-2} of various bifunctional electrocatalysts. d) Polarization curves of the OSWE. Scan rate: 5 mV s^{-1}. e) Chronopotentiometric curves recorded at a constant current density of 500 mA cm^{-2} toward OER and HER. The electrolyte used in all measurements was in 1.0 M KOH + 0.5 M NaCl.

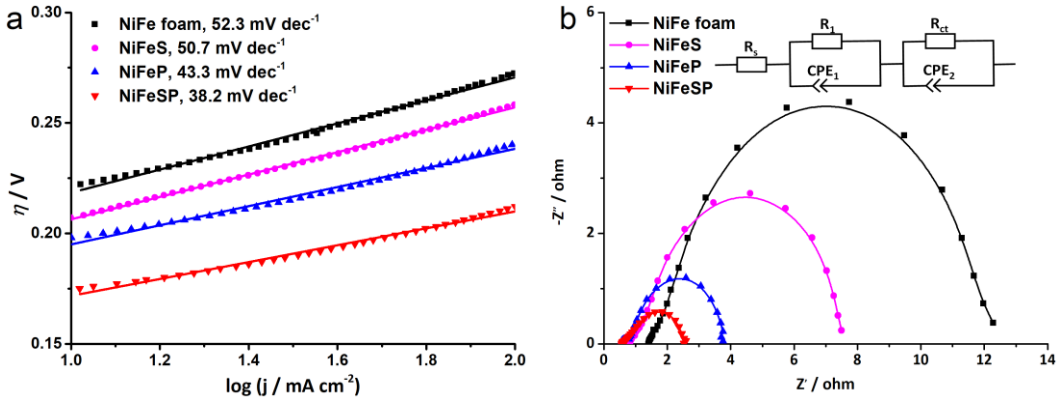

Figure 2.2.10 a) Tafel plots, b) Nyquist plots, measured at 1.41 V vs. RHE, of the NiFeS, NiFeP and NiFeSP electrodes for the OER.

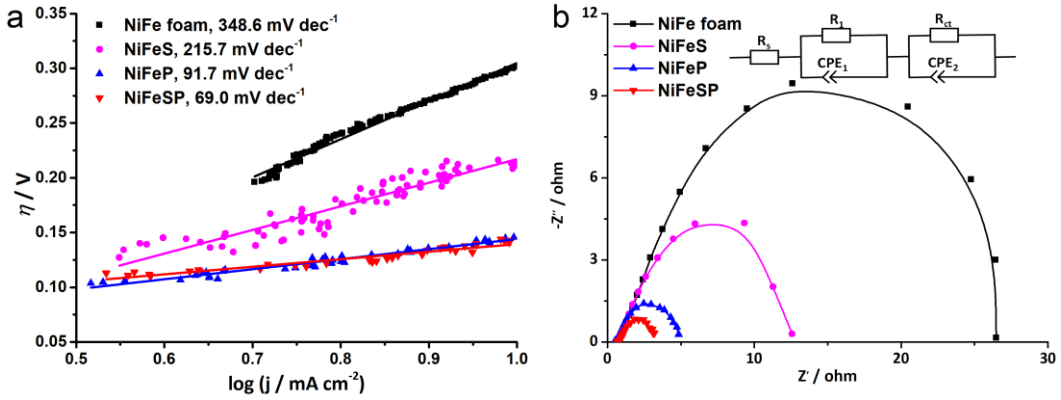

Figure 2.2.11 a) Tafel plots, b) Nyquist plots, measured at −0.15 V vs. RHE, of the NiFeS, NiFeP and NiFeSP electrodes for the HER.

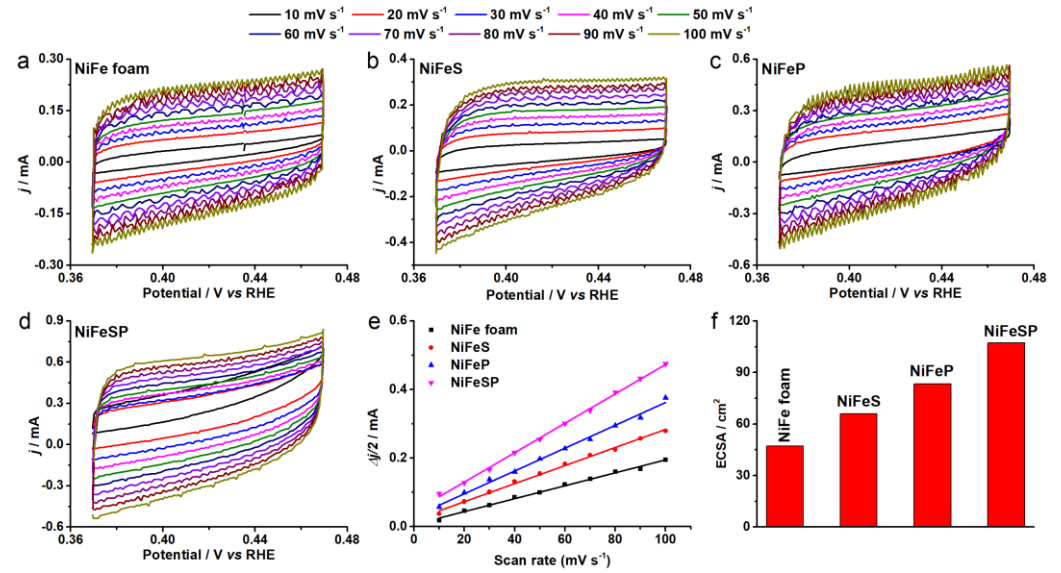

Figure 2.2.12 Electrochemical CV curves of a) NiFe foam, b) NiFeS, c) NiFeP and d) NiFeSP electrodes recorded at diffrent scan rates of 10, 20, 30, 40, 50, 60, 70, 80, 90 and 100 mV s^{-1}. e) Plots of the capacitive current density as a funtion of the scan rate for all catalysts. f) ECSAs of all catalysts.

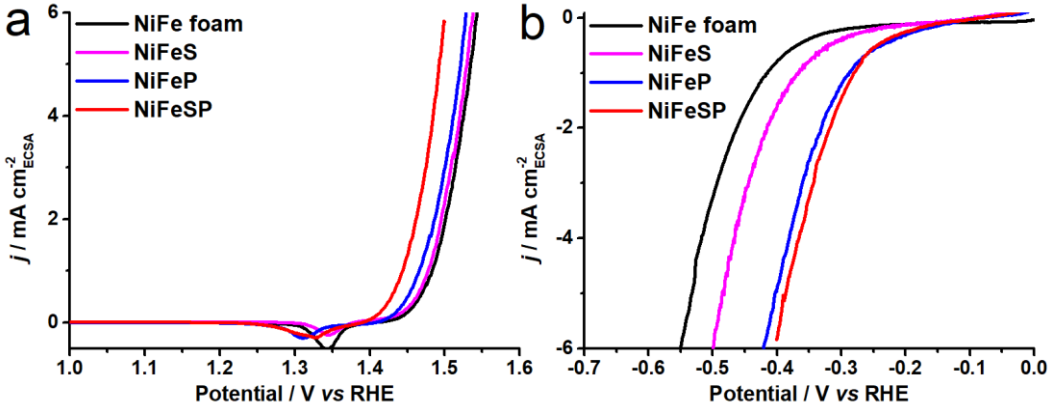

Figure 2.2.13 Specific activity of NiFeSP and other control electrodes toward a) OER and b) HER.

The electrocatalytic activity of these self-supported electrodes toward the OER and HER was firstly evaluated in a typical three-electrode configuration by linear sweep voltammetry (LSV) in a simulated seawater solution (1.0 M KOH + 0.5 M NaCl). For OER testing, all LSV curves were recorded by sweeping the potential negatively to avoid possible overestimation of performance, which is particularly prominent for self-supported electrodes. As shown in **Figure 2.2.9a**, the NiFeSP electrode exhibits significantly enhanced OER activity compared to the NiFeS, NiFeP and bare NiFe foam references. It needs low overpotentials (η) of 174, 212 and 260 mV to drive current densities of 10, 100 and 500 mA cm^{-2}, lower than those of NiFeS (207, 258 and 321 mV), NiFeP (198, 241 and 298 mV) and NiFe foam (222, 273 and 351 mV). The OER reaction kinetics of all catalysts was studied by Tafel analysis (**Figure 2.2.10a**). The NiFeSP electrode shows a Tafel slope (38.2 mV dec^{-1}), markedly smaller than NiFeS (50.7 mV dec^{-1}), NiFeP (43.3 mV dec^{-1}) and NiFe foam (52.3 mV dec^{-1}), indicating that introducing two *p*-block elements simultaneously in NiFe can accelerate the reaction kinetics. The electrochemical impedance spectroscopy (EIS) measurements also confirmed the efficient charge transfer of NiFeSP during the OER, as evidenced by its much smaller charge transfer resistance (R_{ct}) than that of other control electrodes (**Figure 2.2.10b**). Furthermore, the catalytic activity of NiFeSP electrodes for the HER was evaluated in the same electrolyte. As seen in **Figure 2.2.9b**, the NiFeSP electrode can deliver geometric current densities of 10, 100 and 500 mA cm^{-2} at low η values of 146, 276 and 380 mV, remarkably lower than NiFeS (228, 396 and 519 mV), NiFeP (147, 300 and 422 mV), and NiFe foam (302, 467 and 624 mV). Similarly, the NiFeSP electrode shows the lowest Tafel slope and R_{ct} value compared to other controls, indicating rapid catalytic reaction kinetics (**Figure 2.2.11**). To further assess the intrinsic catalytic activity, the electrochemically active surface area (ECSA) of all self-supported electrodes, which is

proportional to the double-layer capacitance (C_{dl}), was measured to calculate the specific activity. The NiFeSP electrode was found to shows the highest ECSA value of 107.3 cm^2, implying that it has substantially more active sites exposed (**Figure 2.2.12**). Nevertheless, the NiFeSP electrode still exhibits the largest specific activity for both OER and HER activity (**Figure 2.2.13**), suggesting that the excellent catalytic performance observed in NiFeSP is intrinsic, irrelevant to its large accessible surface area. It is also worth noting that the NiFeSP electrode outperforms many other self-supported electrodes for OER and HER (**Figure 2.2.9c** and **Table 2.2.2**), showing excellent bifunctionality [17, 47-58]. On this basis, we further tested the overall seawater water electrolysis (OSWE) performance using two symmetric NiFeSP electrodes as the anode and cathode in simulated seawater (*i.e.*, 1.0 M KOH + 0.5 M NaCl). Our NiFeSP electrode pair can deliver current densities of 10, 100 and 500 mA cm^{-2} at voltages of 1.494, 1.667 and 1.938 V, exhibiting the best OSWE performance (**Figure 2.2.9d**) and favorably comparing to many other bifunctional electrodes reported recently in the literature (**Table 2.2.3**).

Table 2.2.2 Comparison of the OER and HER activity of the NiFeSP electrode to that of other recently reported bifunctional OER/HER electrocatalysts measured in 1.0 M KOH.

Catalytic electrode	OER overpotential@ j_{10} / mV	HER overpotential@ j_{10}/ mV	Reference
NiFeSP	**174**	**146**	**This work**
NiFe LDH-NS	210	300	Adv. Mater. 2017, 29, 1700017.
CrFeNi–P/NCN	240	190	Adv. Mater. 2019, 31, 1900178.
Fe-Ni_5P_4/NiFeOH	221	197	Appl. Catal. B: Environ. 2021, 291, 119987.
NiFeOF	295	253	ACS Catal. 2017, 7, 8406-8412.
NiFe-NCs	271	197	ACS Appl. Mater. Interfaces, 2017, 9, 41906-41915.
NiFe-LDH@CoS_x	206	136	Chem. Eng. J. 2021, 419, 129512.
Ni_3S_2@MoS_2/FeOOH	234	189	Appl. Catal. B: Environ. 2019, 244, 1004-1012.

$(BO_3)_{1.08}$-Ni_3S_4	306	270	ChemElectroChem 2019, 6, 1443-1449.
Ni_3S_2-NGQDs/NF	216	218	Small 2017, 13, 1700264.
CoPS	308	175	J. Catal. 2019, 371, 126-134.
P-$CoNi_2S_4$	282	135	Angew. Chem. Int. Ed. 2021, 60, 22885–22891.
Mo-Ni_3S_2	260	212	Appl. Surf. Sci. 2018, 441, 1024-1033.
$Co_{0.9}S_{0.58}P_{0.42}$	226	141	ACS Nano 2017, 11, 11031.

Table 2.2.3 Comparison of the voltage needed to reach 10 mA cm^{-2} for the bifunctional NiFeSP electrode pairs to that achieved by other bifunctional electrode pairs reported in the literature (tested in 1.0 M KOH solution).

Bifunctional electrode pair	Voltage (V)	Reference
NiFeSP	**1.565**	**This work**
$NiCo_2S_4$ NW/NF	1.63	Adv. Funct. Mater. 2016, 26, 4661.
Exfoliated graphene-Ni_3Se_2@Co_9S_8	1.62	Nano Lett. 2017, 17, 4202.
$Co_{0.9}S_{0.58}P_{0.42}$	1.59	ACS Nano 2017, 11, 11031.
EG/H-$Co_{0.85}Se$|P	1.64	Adv. Mater. 2017, 29, 1701589.
$Co(S_{0.22}Se_{0.78})_2$||$Co(S_{0.71}Se_{0.29})_2$	1.63	Adv. Funct. Mater. 2017, 27, 1701008.
$(Co_{1-x}Ni_x)(S_{1-y}P_y)_2$/G	1.65	Adv. Energy Mater. 2018, 8, 1802319.
CoPS	1.59	J. Catal. 2019, 371, 126.
CoFeO@BP	1.58	Angew. Chem. Int. Ed. 2020, 59, 21106.
Fe_2CoPS_3	1.59	Int. J. Hydrogen Energy 2021, 46, 3354.
Fe-Ni_2P@PC/Cu_xS	1.62	Nano Energy 2021, 84, 105861.
Ni/NiCoP	1.57	Appl. Catal. B Environ. 2019, 259, 118039.
Co_xNi_yP	1.59	Adv. Funct. Mater. 27 (2017) 1703455.
NiFeS-2	1.64	Small 2017, 13, 1700610.

Ni/Mo2C-PC	1.66	Chem. Sci. 2017, 8, 968-973.
NiSe nanowire film	1.63	Angew. Chem., Int. Ed. 2015, 54, 9351-9355.
NiFe LDH@NiCoP	1.57	Adv. Funct. Mater. 2018, 28, 1706847.
FeNi-P	1.57	ACS Sustainable Chem. Eng. 2018, 6, 9640-9648.

Long-term catalytic durability is of particular importance to practical seawater electrolysis. The durability of the NiFeSP electrode toward OER and HER was evaluated by chronopotentiometry in the saline electrolyte at 500 mA cm^{-2}, a current density sufficiently high for practical applications. As shown in **Figure 2.2.9e**, the NiFeSP electrode is able to continuously catalyze OER and HER at such a high current density for 1000 h with minimal degradation. We believe that the excellent long-term durability may, on one hand, originate from the improved corrosion resistance and chemical stability of sulfide/phosphide;[59, 60] on the other hand, be due to the fact that the corrosive hypochlorite is not considerably evolved under 2 V. XPS was used to investigate the surface chemistry after the OER and HER stability tests at a current density of 500 mA cm^{-2} for 10 h. XPS inspection revealed that after extended OER at a high current density, signals arising from high oxidation state (*i.e.*, Fe^{3+} and Ni^{3+}) appeared (**Figure 2.2.14**), suggesting that NiFeSP was oxidized into Fe-/Ni-oxyhydroxide under anodic OER conditions [32, 61]. No metal–S and metal–P bonding could be detected anymore in the S2p and P2p XPS spectra, and there was only a weak peak centered at 132.8 eV that can be attributed to PO_4^{3-} species. This indicates that substantial compositional change occurred during the OER, consistent with previous reports [20, 62]. The formed phosphate and sulfate may help passivate electrode surface, suppressing chemical dissolution in subsequent electrolysis [60, 63, 64]. Likewise, after the HER, the metal–P bonding disappeared and the metal–S was significantly attenuated, suggesting that surface re-construction happened as well in the strongly alkaline medium under reductive HER conditions. This is further supported by a shift to higher energy after OER/HER electrocatalysis in the XANES spectra at both the Fe and Ni K-edges. In particular, the oxidation state in the post-OER electrode is higher in energy with a more intense whiteline consistent with the formation of high valence metal-oxo species as determined by XPS (**Figure 2.2.15**).

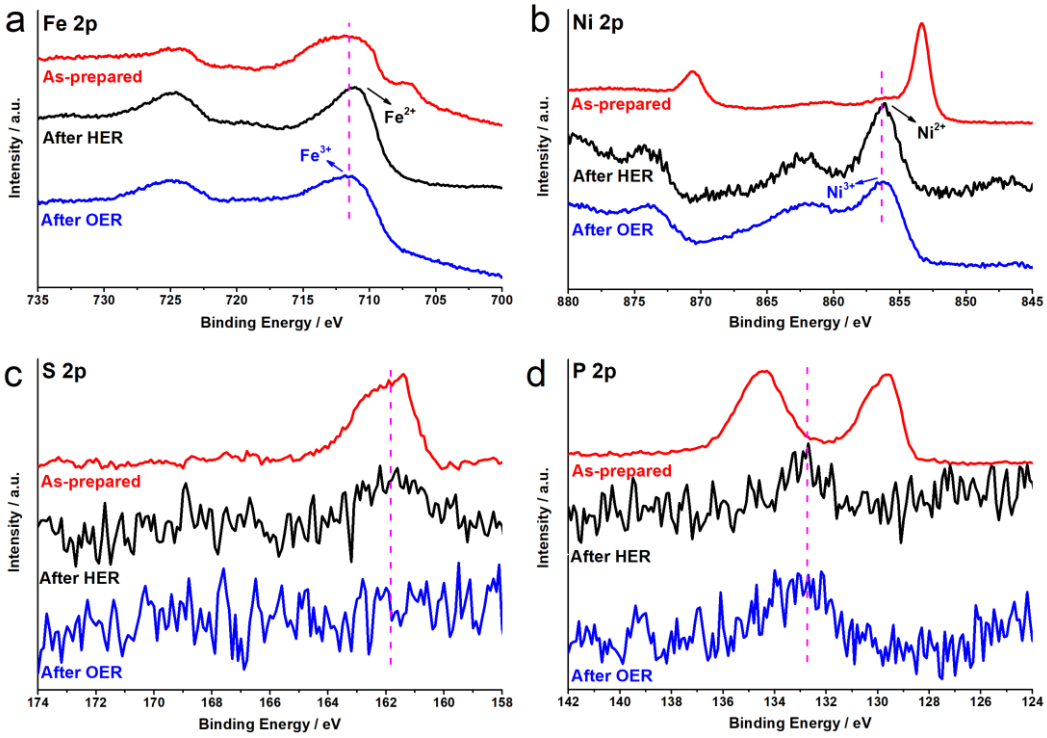

Figure 2.2.14 High resolution XPS spectra of a) Fe2p, b) Ni2p, c) S2p and d) P2p of the NiFeSP electrode before and after the HER and OER at a current density of 500 mA cm^{-2} for 10 h in alkaline-saline solution.

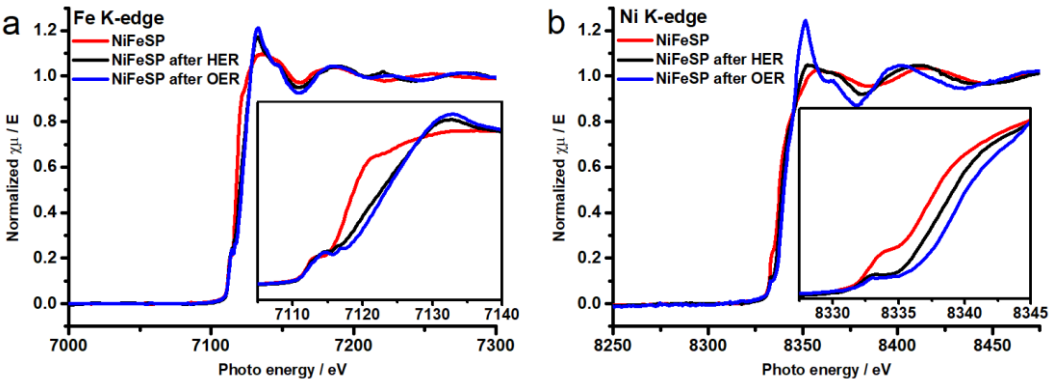

Figure 2.2.15 a) Fe and b) Ni K-edge XANES spectra of the NiFeSP electrode before and after the HER and OER at a current density of 500 mA cm^{-2} for 10 h in alkaline-saline solution.

In order to gain further insight into the catalytic mechanism of the NiFeSP electrode toward HER and OER, DFT calculations were carried out using $(Ni,Fe)_3S_4$ (311) and NiFeP (111) as the model catalysts, given that they are prevail in the samples according to our TEM observation. The NiFeSP model catalyst was constructed by interfacing $(Ni,Fe)_3S_4$ (311) facet with NiFeP (111) facet (**Figure 2.2.16c**). To investigate how under-coordination influences the catalytic performance, a model catalyst of NiFeSP containing vacancy was also constructed (**Figure 2.2.16d**). We firstly calculated the density of

states (DOS) of these model catalysts. As shown in **Figure 2.2.17a**, the total DOS of NiFeS and NiFeP is non-zero at the Fermi level, suggesting that NiFeS and NiFeP are metalloid in nature, which is conducive to rapid electron transfer in the electrocatalytic process [65, 66]. Moreover, the DOS distribution shows a notable spin polarization, and the DOS of all P-containing catalysts at the Fermi level mainly comes from the contribution of spin-down electrons of Fe. This manifests that Fe element may play an important role in charge transfer [66]. The charge density difference was further analyzed for the heterostructured NiFeSP with and without vacancy, where more positive charges are found to appear at Fe sites and electrons are enriched at Ni sites (**Figures 2.2.17b** and **2.2.17c**), in agreement with the DOS results. This further proves that Fe is more prone to accepting electrons in the OER process, boosting the electrocatalytic activity.

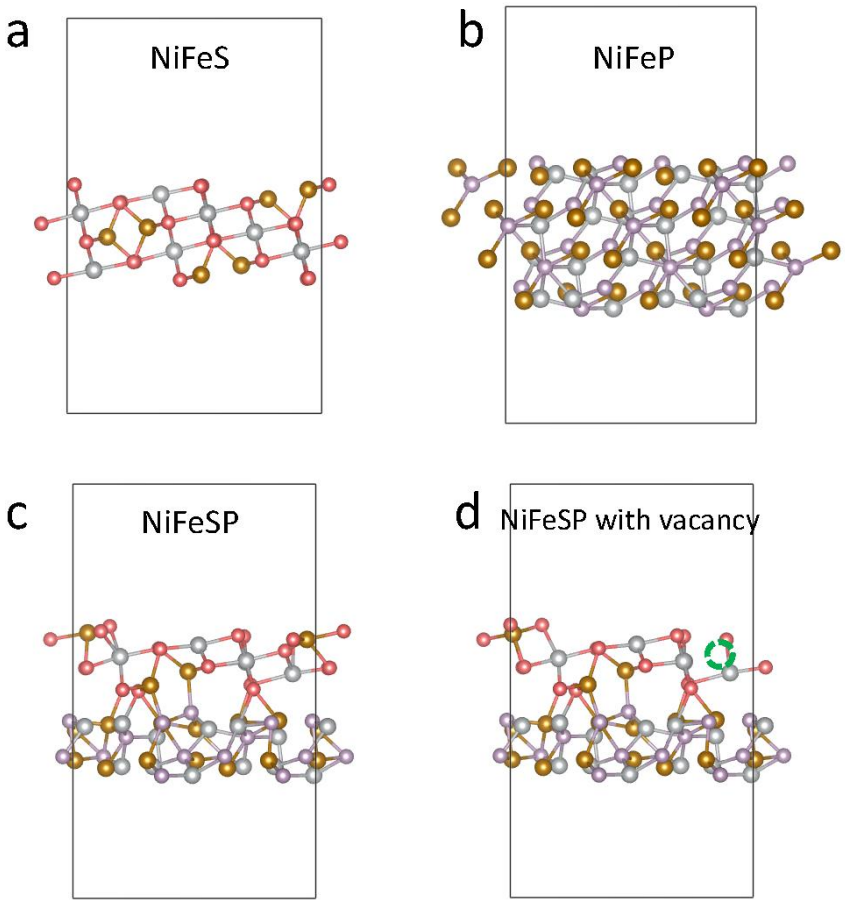

Figure 2.2.16 Optimized model catalysts. a) $(Ni,Fe)_3S_4$ (311), b) NiFeP (111), c) $(Ni,Fe)_3S_4$ (311)/NiFeP (111) heterostructure, and d) $(Ni,Fe)_3S_4$ (311)/NiFeP (111) heterostructure with vacancy (marked by green dash circle).. The gray, wine, red and pink spheres represent Ni, Fe, S and P atoms, respectively.

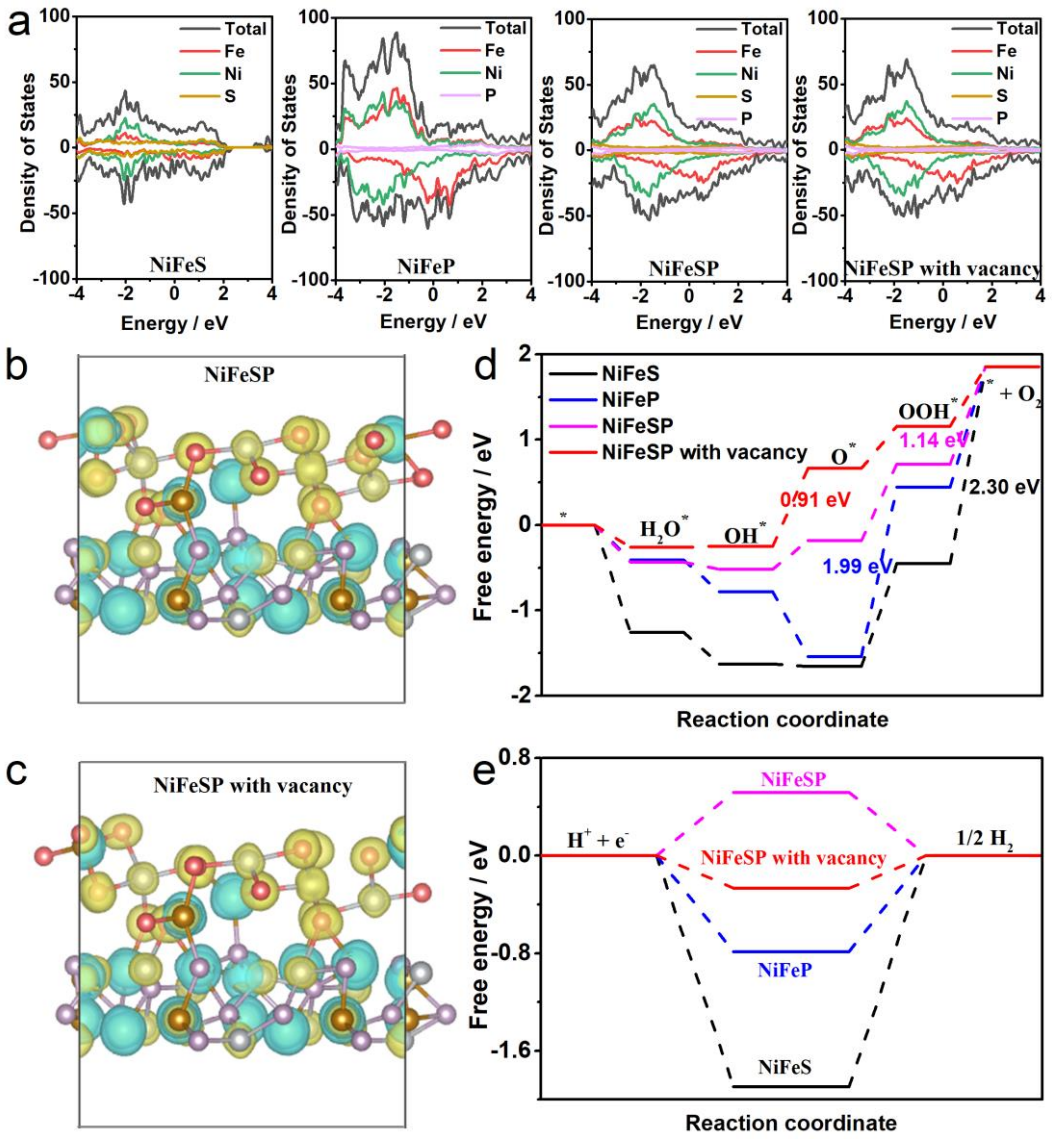

Figure 2.2.17 Computational analyses of the NiFeSP electrode for OER and HER. a) Calculated DOS profiles; Charge density difference of b) NiFeSP and c) NiFeSP with vacancy. The gray, wine, red and pink spheres represent Ni, Fe, S and P atoms, respectively. The yellow and blue colors denote the accumulation and depletion of electrons. Gibbs free-energy diagrams of d) OER and e) HER.

Furthermore, the Gibbs free energy diagrams of the OER for different model catalysts were also calculated. The computation takes into account the Gibbs free energy of intermediate adsorption in each step for both Fe sites and Ni sites. For P-containing catalysts, the energy barrier to the rate-determining step (RDS) on Fe sites is similar to or smaller than that on Ni sites (**Figure 2.2.18**), implying that Fe sites might be more active. Therefore, the OER performance comparison is made based on the Fe site of each model. While the NiFeS and NiFeP show a high energy barrier to the RDS (2.30 eV for NiFeS and 1.99 eV for NiFeP), the heterostructured NiFeSP exhibits a substantially lower energy barrier of 1.14 V (**Figure 2.2.17d**), indicating that the formation

of the heterojunction significantly improves the OER performance. Introducing vacancy further helps decrease the barrier to 0.91 eV, demonstrating that the under-coordination also boosts the intrinsic activity of OER, besides heterostructuring. Likewise, the Gibbs free energy changes (ΔG) during the HER were investigated. It's known that the Gibbs free energy (ΔG_{H^*}) of hydrogen adsorption is a primary descriptor of the HER activity. The closer the value of $|\Delta G_{H^*}|$ is to zero, the higher the activity [67, 68]. As displayed in **Figure 2.2.17e**, the NiFeS and NiFeP show a $|\Delta G_{H^*}|$ value of 1.89 and 0.79 eV, respectively. Upon heterostructuring NiFeS and NiFeP, the $|\Delta G_{H^*}|$ value is markedly reduced to 0.52 eV. If vacancy (*i.e.*, under-coordination) is introduced, then the $|\Delta G_{H^*}|$ value can be further decreased to 0.27 eV. This indicates that both heterostructure and under-coordination can help expedite the reaction process, resulting in a low overpotential and facilitating H_2 evolution. Our DFT calculations unambiguously demonstrate that both NiFeS/NiFeP heterostructuring and under-coordinated metal sites substantially contribute to the OER and HER activity, thanks to the electron transfer from Fe atoms to adjacent Ni atoms, resulting in favorable reaction pathways.

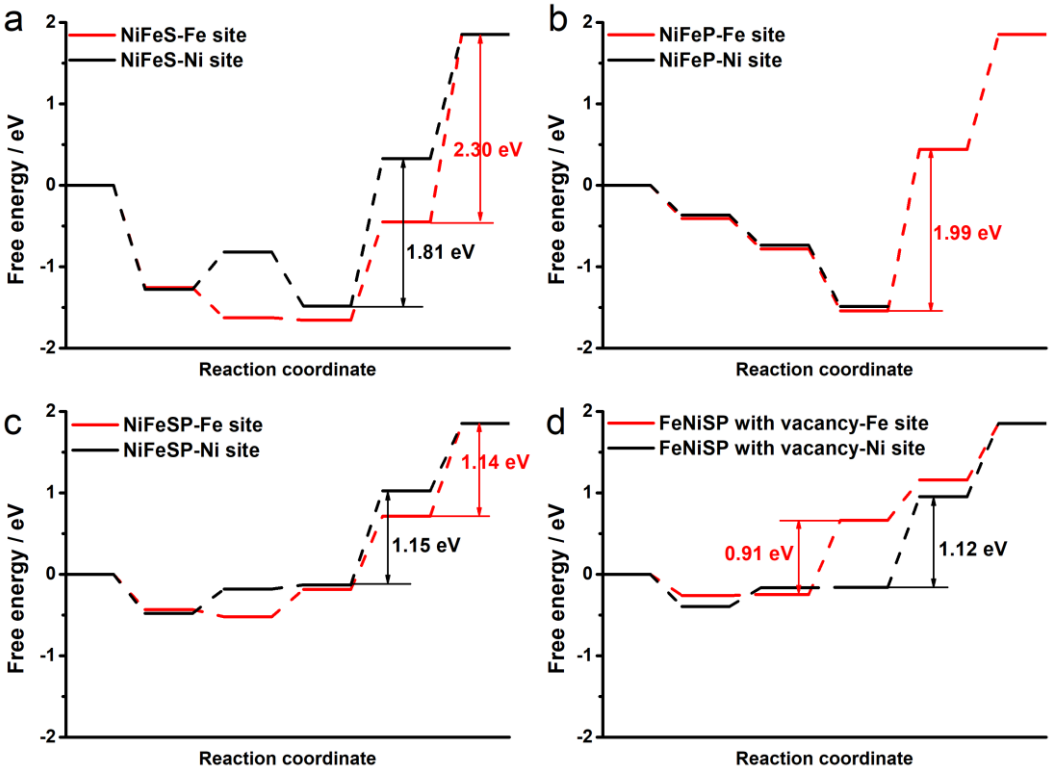

Figure 2.2.18 Gibbs free energy diagrams of the OER pathways on different catalysts of a) NiFeS, b) NiFeP, c) NiFeSP, and d) NiFeSP with vacancy. The free energy of both Fe site and Ni site are calculated.

Although the NiFeSP electrode demonstrated outstanding performance in OSWE, further improvement in energy efficiency for H_2 production is still preferred. A promising

means to such improvement is to substitute the energy-demanding OER with UOR, in such a way that the total energy input can be reduced. To this end, we evaluated the UOR performance of the self-supported NiFeSP electrode. As shown in **Figure 2.2.19a**, the NiFeSP electrode can deliver geometric current densities of 10 and 500 mA cm^{-2} at potentials of 1.264 (E_{10}) and 1.424 V (E_{500}) vs. RHE, respectively, better than NiFeS (E_{10} = 1.303 V, E_{500} = 1.476 V), NiFeP (E_{10} = 1.300, E_{500} = 1.458 V) and NiFe foam (E_{10} = 1.333 V, E_{500} = 1.520 V), also outperforming most previously reported UOR electrocatalysts (**Table 2.2.4**). Moreover, the NiFeSP exhibits a Tafel slope of 76.8 mV dec^{-1} (**Figure 2.2.19b**), smaller than that of other reference electrodes, confirming that the multi-step UOR occurs faster on the NiFeSP, which was also corroborated by the EIS study (**Figure 2.2.20**). The presence of urea in the electrolyte negatively shifts the polarization curve to a large extent (**Figure 2.2.19c**), and the potential needed to afford 100 mA cm^{-2} can be reduced by 116 mV. However, we found that the addition of urea (0.5 M) did not influence the HER activity of the NiFeSP electrode in the alkaline-saline electrolyte (**Figure 2.2.21**).

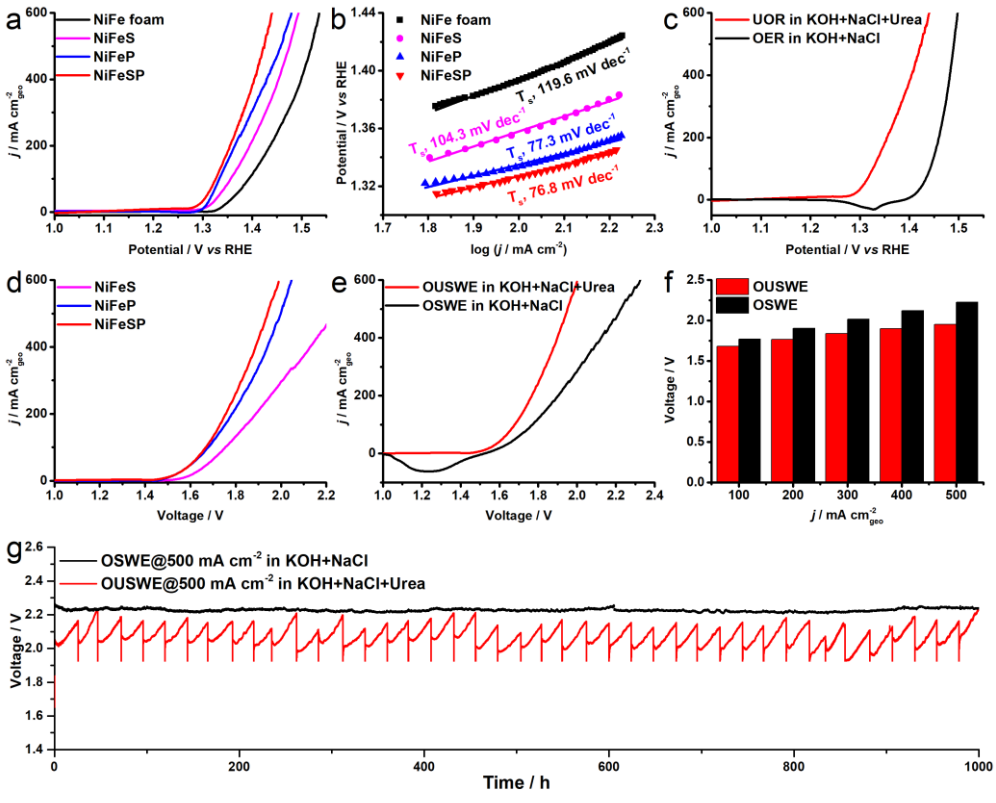

Figure 2.2.19 Electrocatalytic UOR and OUSWE performance of the NiFeSP and other control electrodes. a) Polarization curves and b) Tafel analysis of the UOR, recorded at a scan rate of 5 mV s^{-1} in 1.0 M KOH + 0.5 M NaCl + 0.5 M urea. c) LSV curves of the NiFeSP electrode for UOR and OER. d) LSV curves of the OUSWE (*i.e.*, UOR + HER) for different electrodes, measured in 1.0 M KOH + 0.5 M NaCl + 0.5 M Urea. e) LSV curves of the OUSWE and OSWE of the NiFeSP electrode, measured at 5 mV s^{-1}. f) Comparison of the cell voltages of the NiFeSP at different current densities for OUSWE and OSWE. g) Chronopotentiometric curves of the OSUWE and OSWE for the NiFeSP electrode pair, recorded at a constant current density of 500 mA cm^{-2} in 1.0 M KOH + 0.5 M NaCl + 0.5 M Urea and 1.0 M KOH + 0.5 M NaCl, respectively.

Table 2.2.4 Comparison of the electrocatalytic UOR activity of the NiFeSP electrode to that of other representative electrocatalysts reported recently, tested in 1.0 M KOH solution containing different concentrations of urea.

Catalyst/electrode	Urea contentration (mol L^{-1})	E@J (V vs. RHE@mA cm^{-2})	Reference
NiFeSP	**0.5**	**1.264@10** **1.326@100**	**This work**
P-$CoNi_2S_4$	0.5	1.306@10 1.367@100	Angew. Chem. Int. Ed. 2021, 60, 22885–228915.
Metallic $Ni(OH)_2$	0.33	1.42@10	Angew. Chem. Int. Ed. 2016, 55, 12465.
NF-MnO_2	0.5	1.33@10	Angew. Chem. Int. Ed. 2016, 55, 3804.
NF/NiMoO-Ar	0.5	1.37@10	Energy Environ. Sci. 2018, 11, 1890.
CoS_2-MoS_2	0.5	1.29@10	Adv. Energy Mater. 2018, 8, 1801775.
1% Cu:a-$Ni(OH)_2$/NF	0.33	1.405@100	J. Mater. Chem. A 2019, 7, 13577.
Ni-MOF-0.5	0.5	1.381@10	Chem. Eng. J. 2020, 395, 125166.
MoS_2/Ni_3S_2/NiFe-LDH/NF	0.5	1.396@100	Int. J. Hydrogen Energy 2020, 45, 23.
Mn-Ni_3S_2/NF-0.2	0.5	1.303@10 1.397@100	ACS Sustainable Chem. Eng. 2020, 8, 8348.
MoP@NiCo-LDH/NF	0.5	1.392@100	J. Mater. Chem. A 2020, 8, 18106.
CoMn/$CoMn_2O_4$	0.5	1.32@10 1.36@100	Adv. Funct. Mater. 2020, 30, 2000556.
Ni/FeOOH	0.5	1.373@10 1.407@100	Chem. Commun. 2020, 56, 14713.
Ni@NCNT-3	0.5	1.38@10	Appl. Catal. B: Environ. 2021, 280, 119436.
Ni-WO_x	0.33	1.40@100	Angew. Chem. Int. Ed. 2021, 60, 10577.

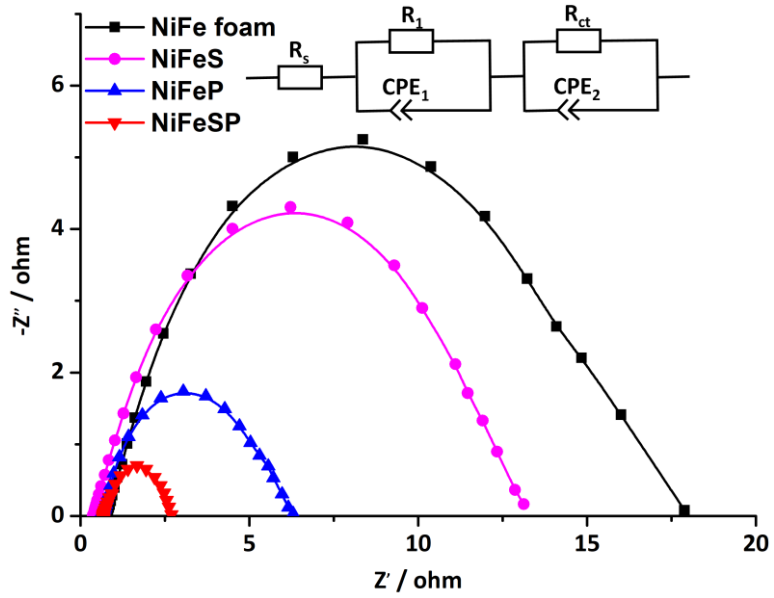

Figure 2.2.20 Nyquist plots of different electrodes for the UOR, measured at 1.27 V vs. RHE.

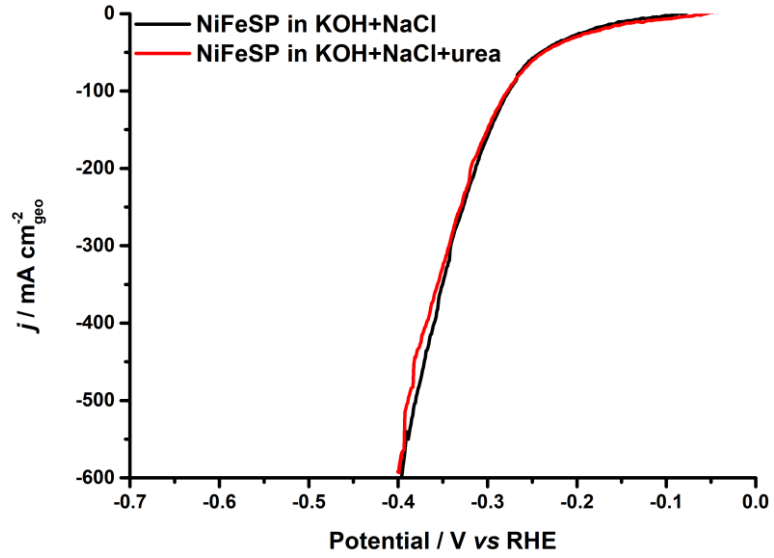

Figure 2.2.21 LSV curves of the NiFeSP electrode for the HER, recorded in 1.0 M KOH + 0.5 M NaCl with and without urea.

Figure 2.2.19d compares the OUSWE performance of different electrodes. The NiFeSP electrode still outperforms the NiFeS and NiFeP electrodes in the presence of urea. Moreover, compared to the OSWE, the cell voltage needed at a given current density is notably reduced for the OSUWE (**Figure 2.2.19e**), proving that the UOR can help save energy for electrolysis and meanwhile avoid the formation of unfavorable hypochlorite species. The NiFeSP electrode pair requires 1.667 and 1.938 V to deliver 100 and 500 mA cm^{-2}, respectively, for the OUSWE, much lower than the voltages of

1.771 and 2.225 V required to drive the same current densities for the OSWE (**Figure 2.2.19f**). Besides, the NiFeSP electrode pair also demonstrates excellent long-term durability for the OUSWE, able to produce H_2 at 500 mA cm^{-2} for at least 1000 h (**Figure 2.2.19g**), at a cell voltage smaller than that is needed for OSWE. The gradual voltage increase over time resulted from the consumption of urea during electrolysis, and the cell voltage can be restored after replenishment of the electrolyte.

2.2.3 Conclusions

In summary, we fabricated self-supported NiFeSP nanotube array electrode by hydrothermal sulfurization of commercially available NiFe foam and subsequent post-phosphorization treatment. Advanced transmission electron microscopy and X-ray absorption spectroscopy characterization confirmed that the NiFeSP nanotubes are enriched with NiFeS/NiFeP heterointerfaces and under-coordinated metal sites. Thus-fabricated electrode combines several merits including multiple metal/non-metal components, 3D hierarchical architecture, and abundant heterointerfaces and under-coordinated active sites, which can work in synergy boosting the electrocatalytic performance. Consequently, the self-supported NiFeSP electrode shows a low overpotential of 380 mV for HER and 260 mV for OER at a large industry-relevant current density of 500 mA cm^{-2} in alkaline-saline water solution. To prevent the interfering chlorine evolution reaction from happening, we further substituted the OER with urea oxidation reaction, which meanwhile lowers the need for overall energy input in alkaline-saline water electrolysis. In this case, the bifunctional NiFeSP electrode, active for both HER and UOR, can deliver 500 mA cm^{-2} under a low cell voltage of 1.938 V, and more impressively, survive for continuous electrolysis at such a high current density for 1000 hours without notable degradation. This work provides an effective strategy for the design and synthesis of highly-active and stable catalytic electrodes for saline water electrolysis, which will find applications in massive production of low-cost renewable hydrogen.

2.2.4 Experimental section

Reagents: NiFe foam (110 PPI, 1 mm thick) was purchased from Heze Jiaotong Xinda Import & Export Co., Ltd, China. Sulfur powders, sodium hypophosphite (NaH_2PO_2), absolute ethanol, urea, sodium chloride (NaCl), potassium hydroxide (KOH) and hydrochloric acid (HCl) were all purchased from Sigma-Aldrich. Ethylenediamine was acquired from Fluka Analytical. All reagents were used as received without further purification.

Synthesis of self-supported NiFeS electrodes: Before usage, the NiFe foam was ultrasonically cleaned in 3 M HCl, deionized (DI) water and ethanol to remove inorganic and organic impurities from the surface. 128 mg of sulfur powders were dissolved into a mixture of ethanol and ethylenediamine (v/v = 1:1) under continuous magnetic stirring until a homogeneous solution was obtained. Afterward, the solution was transferred into a Teflon-lined stainless-steel reactor. After putting a piece of pretreated NiFe foam, the reactor was sealed and maintained at 180 °C in an oven for 12 h. After naturally cooled down to room temperature, the foam was washed thoroughly with DI water and then dried in an oven at 60 °C.

Synthesis of self-supported NiFeP electrodes: The NiFeP electrode was synthesized by a one-step phosphorization method reported in our previous work [62, 69]. Typically, the pretreated NiFe foam was loaded in a ceramic boat, and 1.0 g of NaH_2PO_2 powders was placed 2 cm away from the foam at the upstream side. Subsequently, the furnace was purged with high-purity N_2 (99.9995%) for 1 h to get rid of air, heated to 300 °C at a ramping rate of 5 °C min^{-1}, and held at this temperature for 2 h. Finally, the furnace was naturally cooled down to room temperature.

Synthesis of self-supported NiFeSP electrodes: The NiFeSP electrode was prepared by hydrothermal sulfurization of the NiFe foam, followed by a phosphorization process. In brief, the obtained NiFeS electrode was phosphorized at 300°C for 2 h in a tube furnace, as mentioned before, using NaH_2PO_2 as the source of phosphorus. A high-purity N_2 flow was maintained during the whole process.

Materials characterization: Powder XRD examinations were conducted on a X'Pert PRO diffractometer (PANalytical) working at 45 kV and 40 mA with Cu K_α radiation (λ = 1.541874 Å) and a PIXcel detector. Data were collected with the Bragg-Brentano configuration in the 2θ range of 30^o – 80^o at a scan speed of 0.01^o s^{-1}. The morphology and microstructure of NiFeSP electrodes were characterized by scanning electron microscopy (SEM, FEI Quanta 650 FEG microscope equipped with an INCA 350 spectrometer) and transmission electron microscopy (TEM, FEI ChemiSTEM 80-200, probe corrected). XPS characterization was performed on an ESCALAB 250Xi instrument with an Mg K_α X-ray source (1253.6 eV). The X-ray absorption spectroscopy (XAS) was conducted at the BL22-CLAESS beamline, ALBA Synchrotron (Barcelona, Spain) [70]. The NiFeSP NTs were scratched off the NiFe foam support, mixed with cellulose, and mechanically pressed into solid pellets. Data were acquired at room temperature using a Si111 double crystal monochromator. Fe and Ni K-edge spectra

were collected in transmission mode. Several repeats were made before recording the spectra to ensure reproducibility and statistics. The averaged spectra were treated with the Athena software package [71]. The energy scale was calibrated by setting the first inflection point of Fe foil to 7112 eV in the case of Fe data and to the first inflection point of Ni foil taken as 8333 eV for Ni data.

DFT calculations: The spin-polarized DFT calculations were performed using Vienna Ab-initio Simulation Package (VASP) with the projector augmented wave (PAW) pseudopotential and Perdew-Burke-Ernzerhof (PBE) functional [72-74]. The energy cutoff was set to 450 eV, and the atomic positions were allowed to relax until the energy and force were less than 10^{-5} eV and 10^{-2} eV $Å^{-1}$, respectively. The slab lattice parameters of the FeNiS (311) model catalyst are a = 13.41 Å and b = 6.70 Å, and those of the FeNiP (111) model catalyst are a = 14.83 Å and b = 6.63 Å. The FeNiS (311) – FeNiP (111) heterostructure was constructed and optimized by adjusting the arrangement between two surfaces. Vacuum space above all surfaces was kept to >10 Å. The Brillouin zone was sampled using 3 × 5 × 1 and 9 × 15 × 1 Monkhorst-Pack k-point grid for structure optimization and electronic property calculation, respectively. Vaspkit was used for data processing [75].

The HER proceeds through the two-electron pathway with the following reaction steps:

$$M^* + H^+ + e^- \rightarrow H^* \quad (1)$$

$$H^* + H^+ + e^- \rightarrow H_2\,(g) + M^* \quad (2)$$

where M^* represents the active site, and H^* is the hydrogen intermediate adsorbed on the active sites during the HER. The adsorption energy was calculated according to the following equation:

$$G_{ad} = G_{sys} - G_{sur} - G_{spe} \quad (3)$$

where G_{ad}, G_{sys}, G_{sur} and G_{spe} denote the adsorption free energy, the free energy of the adsorption system, the free energy of a clean surface and the free energy of the isolated adsorption species, respectively.

The overall OER process includes five steps:

$$H_2O\,(aq) + M^* \rightarrow H_2O^* \quad (4)$$

$$H_2O^* + OH^- \rightarrow OH^* + H_2O\,(l) + e^- \quad (5)$$

$$OH^* + OH^- \rightarrow O^* + H_2O\,(l) + e^- \quad (6)$$

$$O^* + OH^- \rightarrow OOH^* + e^- \quad (7)$$

$$OOH^* + OH^- \rightarrow M^* + O_2\,(g) + H_2O\,(l) + e^- \quad (8)$$

where M* represents the active site, and H_2O*, OH*, O*, and OOH* are the intermediates adsorbed on the active sites during the OER. The Gibbs free energy changes of these steps were calculated as follows [76]:

$$\Delta G_1 = G(H_2O^*) - G(^*) - G(H_2O) \quad (9)$$

$$\Delta G_2 = G(OH^*) - G(H_2O^*) + \tfrac{1}{2}\,G(H_2(g)) - |e|U - 0.059 \times pH \quad (10)$$

$$\Delta G_3 = G(O^*) - G(OH^*) + \tfrac{1}{2}\,G(H_2(g)) - |e|U - 0.059 \times pH \quad (11)$$

$$\Delta G_4 = G(OOH^*) - G(O^*) - G(H_2O) + \tfrac{1}{2}\,G(H_2(g)) - |e|U - 0.059 \times pH \quad (12)$$

$$\Delta G_5 = G(^*) + G(O_2(g)) - G(OOH^*) + \tfrac{1}{2}\,G(H_2(g)) - |e|U - 0.059 \times pH \quad (13)$$

All Gibbs free energy in reactions were calculated under zero potential as follows:

$$G = E + ZPE - TS \quad (14)$$

where *E* is the intermediate energy obtained from DFT calculations, *ZPE* represents the zero point energy, *T* stands for the reaction temperature which is considered to be 300 K, and *S* denotes the entropy. For reaction steps that involved H^+ and e^-, the computational hydrogen electrode model developed by Nørskov *et al.* was used [76, 77]. All Gibbs free energy analysis was performed under standard conditions (pH = 0, 298.15 K, 1 atm).

Electrode preparation and electrocatalytic tests. Half-cell electrocatalytic tests were carried out in a three-electrode configuration at room temperature using a Biologic VMP-3 potentiostat/galvanostat. For HER, OER and UOR tests, the as-synthesized NiFeSP electrode, a saturated calomel electrode (SCE), and a graphite rod were employed as the working, reference, and counter electrodes, respectively. The SCE reference was calibrated before each measurement in the H_2-saturated 0.5 M H_2SO_4 solution using a clean Pt wire as the working electrode. All potentials in this work were converted to the reversible hydrogen electrode (RHE) scale according to the following equation:

$$E_{RHE} = E_{SCE} + 0.059 \times pH + 0.241 \quad (15)$$

The HER, OER and UOR measurements were further carried out in the simulated seawater containing 1.0 M KOH + 0.5 M NaCl. For UOR tests, 0.5 M urea was dissolved in the electrolyte. The apparent activity was assessed using cyclic voltammetry (CV) at

a scan rate of 5 mV s^{-1}, and an *iR*-correction (85%) was applied to compensate the voltage drop between the reference and working electrodes, which was measured by a single-point high-frequency impedance test. The reduction branch of the CV curves was used for performance comparison of all catalysts. Electrochemical impedance spectroscopy (EIS) measurements were conducted at −0.15 V vs. RHE for the HER, 1.27 V vs. RHE for the UOR and 1.41 V for the OER in the frequency range of 10^5 – 0.01 Hz with a 10 mV sinusoidal perturbation.

The double layer capacitance (C_{dl}) of catalysts was estimated by performing CV in the potential range of 0.37 − 0.47 V vs. RHE (non-Faradaic potential range) at different scan rates (v) of 10, 20, 30, 40, 50, 60, 70, 80, 90 and 100 mV s^{-1}, followed by extracting the slope from the resulting $|j_a-j_c|/2$ vs. v plots (j_a and j_c represent the anodic and cathodic current density at −0.42 V vs. RHE). The ECSAs were then calculated according to the following equation [78]:

$$ECSA = C_{dl} / 0.04\ mF\ cm^{-2} \quad (16)$$

The stability of the NiFeSP electrodes was assessed at a constant current density of 500 mA cm^{-2} for OER and UOR and −500 mA cm^{-2} for HER. For full-cell tests, *i.e.*, OSWE and OUSWE, two symmetric self-supported NiFeSP electrodes were used as the anode and the cathode, respectively.

2.2.5 References

[1] A. Buttler, H. Spliethoff, Current status of water electrolysis for energy storage, grid balancing and sector coupling via power-to-gas and power-to-liquids: A review. Renew. Sust. Energ. Rev. 82 (2018) 2440-2454.

[2] S. Dresp, F. Dionigi, M. Klingenhof, P. Strasser, Direct Electrolytic Splitting of Seawater: Opportunities and Challenges. ACS Energy Lett. 4 (2019) 933-942.

[3] R. d'Amore-Domenech, T.J. Leo, Sustainable Hydrogen Production from Offshore Marine Renewable Farms: Techno-Energetic Insight on Seawater Electrolysis Technologies. ACS Sustain. Chem. Eng. 7 (2019) 8006-8022.

[4] W. Tong, M. Forster, F. Dionigi, S. Dresp, R. Sadeghi Erami, P. Strasser, A.J. Cowan, P. Farràs, Electrolysis of low-grade and saline surface water. Nat. Energy 5 (2020) 367-377.

[5] Z. Yu, J. Xu, L. Meng, L. Liu, Efficient hydrogen production by saline water electrolysis at high current densities without the interfering chlorine evolution. J. Mater. Chem. A 9 (2021) 22248-22253.

[6] Y. Li, X. Wei, L. Chen, J. Shi, Electrocatalytic Hydrogen Production Trilogy. Angew. Chem. Int. Ed. 60 (2021) 19550-19571.

[7] B. Zhu, Z. Liang, R. Zou, Designing Advanced Catalysts for Energy Conversion Based on Urea Oxidation Reaction. Small 16 (2020) 1906133.

[8] B.K. Boggs, R.L. King, G.G. Botte, Urea electrolysis: direct hydrogen production from urine. Chem. Commun. (2009) 4859-4861.

[9] D. Liu, T. Liu, L. Zhang, F. Qu, G. Du, A.M. Asiri, X. Sun, High-performance urea electrolysis towards less energy-intensive electrochemical hydrogen production using a bifunctional catalyst electrode. J. Mater. Chem. A 5 (2017) 3208-3213.

[10] F. Zhang, L. Yu, L. Wu, D. Luo, Z. Ren, Rational design of oxygen evolution reaction catalysts for seawater electrolysis. Trends Chem. 3 (2021) 485-498.

[11] H. Jin, X. Wang, C. Tang, A. Vasileff, L. Li, A. Slattery, S.-Z. Qiao, Stable and Highly Efficient Hydrogen Evolution from Seawater Enabled by an Unsaturated Nickel Surface Nitride. Adv. Mater. 33 (2021) 2007508.

[12] J. Li, C. Yao, X. Kong, Z. Li, M. Jiang, F. Zhang, X. Lei, Boosting Hydrogen Production by Electrooxidation of Urea over 3D Hierarchical Ni4N/Cu3N Nanotube Arrays. ACS Sustain. Chem. Eng. 7 (2019) 13278-13285.

[13] L. Bigiani, D. Barreca, A. Gasparotto, T. Andreu, J. Verbeeck, C. Sada, E. Modin, O.I. Lebedev, J.R. Morante, C. Maccato, Selective anodes for seawater splitting via functionalization of manganese oxides by a plasma-assisted process. Appl. Catal. B Environ. 284 (2021) 119684.

[14] Y. Tong, P. Chen, M. Zhang, T. Zhou, L. Zhang, W. Chu, C. Wu, Y. Xie, Oxygen Vacancies Confined in Nickel Molybdenum Oxide Porous Nanosheets for Promoted Electrocatalytic Urea Oxidation. ACS Catal. 8 (2018) 1-7.

[15] L. Wu, L. Yu, F. Zhang, B. McElhenny, D. Luo, A. Karim, S. Chen, Z. Ren, Heterogeneous Bimetallic Phosphide Ni_2P-Fe_2P as an Efficient Bifunctional Catalyst for Water/Seawater Splitting. Adv. Funct. Mater. 31 (2021) 2006484.

[16] H. Jiang, M. Sun, S. Wu, B. Huang, C.S. Lee, W. Zhang, Oxygen-Incorporated NiMoP Nanotube Arrays as Efficient Bifunctional Electrocatalysts For Urea-Assisted Energy-Saving Hydrogen Production in Alkaline Electrolyte. Adv. Funct. Mater. 31 (2021) 2104951.

[17] X.F. Lu, S.L. Zhang, W.L. Sim, S. Gao, X.W. Lou, Phosphorized $CoNi_2S_4$ Yolk-Shell Spheres for Highly Efficient Hydrogen Production via Water and Urea Electrolysis. Angew. Chem. Int. Ed. 60 (2021) 22885-22891.

[18] C. Wang, M. Zhu, Z. Cao, P. Zhu, Y. Cao, X. Xu, C. Xu, Z. Yin, Heterogeneous bimetallic sulfides based seawater electrolysis towards stable industrial-level large current density. Appl. Catal. B Environ. 291 (2021) 120071.

[19] Y. Zhao, B. Jin, Y. Zheng, H. Jin, Y. Jiao, S.Z. Qiao, Charge State Manipulation of Cobalt Selenide Catalyst for Overall Seawater Electrolysis. Adv. Energy Mater. 8 (2018) 1801926.

[20] W. Li, D. Xiong, X. Gao, L. Liu, The oxygen evolution reaction enabled by transition metal phosphide and chalcogenide pre-catalysts with dynamic changes. Chem. Commun. 55 (2019) 8744-8763.

[21] J. Xu, J. Li, D. Xiong, B. Zhang, Y. Liu, K.-H. Wu, I. Amorim, W. Li, L. Liu, Trends in activity for the oxygen evolution reaction on transition metal (M = Fe, Co, Ni) phosphide pre-catalysts. Chem. Sci. 9 (2018) 3470-3476.

[22] J.S. Kim, B. Kim, H. Kim, K. Kang, Recent Progress on Multimetal Oxide Catalysts for the Oxygen Evolution Reaction. Adv. Energy Mater. 8 (2018) 1702774.

[23] Q. Han, Y. Luo, J. Li, X. Du, S. Sun, Y. Wang, G. Liu, Z. Chen, Efficient NiFe-based oxygen evolution electrocatalysts and origin of their distinct activity. Appl. Catal. B Environ. 304 (2022) 120937.

[24] Y. Tan, H. Wang, P. Liu, Y. Shen, C. Cheng, A. Hirata, T. Fujita, Z. Tang, M. Chen, Versatile nanoporous bimetallic phosphides towards electrochemical water splitting. Energy Environ. Sci. 9 (2016) 2257-2261.

[25] H. Liang, A.N. Gandi, D.H. Anjum, X. Wang, U. Schwingenschlögl, H.N. Alshareef, Plasma-Assisted Synthesis of NiCoP for Efficient Overall Water Splitting. Nano Lett. 16 (2016) 7718-7725.

[26] J. Yan, H. Wu, P. li, H. Chen, R. Jiang, S. Liu, Fe(iii) doped NiS_2 nanosheet: a highly efficient and low-cost hydrogen evolution catalyst. J. Mater. Chem. A 5 (2017) 10173-10181.

[27] M. Cabán-Acevedo, M.L. Stone, J.R. Schmidt, J.G. Thomas, Q. Ding, H.C. Chang, M.L. Tsai, J.H. He, S. Jin, Efficient hydrogen evolution catalysis using ternary pyrite-type cobalt phosphosulphide. Nat. Mater. 14 (2015) 1245-1251.

[28] S. Huang, Z. Jin, P. Ning, C. Gao, Y. Wu, X. Liu, P. Xin, Z. Chen, Y. Jiang, Z. Hu, Z. Chen, Synergistically modulating electronic structure of NiS_2 hierarchical architectures by phosphorus doping and sulfur-vacancies defect engineering enables efficient electrocatalytic water splitting. Chem. Eng. J. 420 (2021) 127630.

[29] W. Liu, E. Hu, H. Jiang, Y. Xiang, Z. Weng, M. Li, Q. Fan, X. Yu, E.I. Altman, H. Wang, A highly active and stable hydrogen evolution catalyst based on pyrite-structured cobalt phosphosulfide. Nat. Commun. 7 (2016) 10771.

[30] D. Mukherjee, P.M. Austeria, S. Sampath, Two-Dimensional, Few-Layer Phosphochalcogenide, $FePS_3$: A New Catalyst for Electrochemical Hydrogen Evolution over Wide pH Range. ACS Energy Lett. 1 (2016) 367-372.

[31] L. Wan, Z. Xu, P. Wang, P.F. Liu, Q. Xu, B. Wang, Dual regulation both intrinsic activity and mass transport for self-supported electrodes using in anion exchange membrane water electrolysis. Chem. Eng. J. 431 (2022) 133942.

[32] W. Peng, J. Li, K. Shen, L. Zheng, H. Tang, Y. Gong, J. Zhou, N. Chen, S. Zhao, M. Chen, F. Gao, H. Gou, Iron-regulated NiPS for enhanced oxygen evolution efficiency. J. Mater. Chem. A 8 (2020) 23580-23589.

[33] X. Wang, W. Ma, C. Ding, Z. Xu, H. Wang, X. Zong, C. Li, Amorphous Multi-elements Electrocatalysts with Tunable Bifunctionality toward Overall Water Splitting. ACS Catal. 8 (2018) 9926-9935.

[34] Y. Men, S. Jia, P. Li, Y. Tan, J. Wang, P. Zhao, G. Cheng, S. Chen, W. Luo, Boosting alkaline hydrogen evolution electrocatalysis through electronic communicating vessels on Co_2P/Co_4N heterostructure catalyst. Chem. Eng. J. (2021) 133831.

[35] Y. Zhao, B. Jin, A. Vasileff, Y. Jiao, S.Z. Qiao, Interfacial nickel nitride/sulfide as a bifunctional electrode for highly efficient overall water/seawater electrolysis. J. Mater. Chem. A 7 (2019) 8117-8121.

[36] I. Amorim, J. Xu, N. Zhang, Z. Yu, A. Araújo, F. Bento, L. Liu, Dual-phase CoP−$CoTe_2$ nanowires as an efficient bifunctional electrocatalyst for bipolar membrane-assisted acid-alkaline water splitting. Chem. Eng. J. 420 (2021) 130454.

[37] Z. Yu, J. Xu, Y. Li, B. Wei, N. Zhang, Y. Li, O. Bondarchuk, H. Miao, A. Araujo, Z. Wang, J.L. Faria, Y. Liu, L. Liu, Ultrafine oxygen-defective iridium oxide nanoclusters for efficient and durable water oxidation at high current densities in acidic media. J. Mater. Chem. A 8 (2020) 24743-24751.

[38] H. Fei, T. Guo, Y. Xin, L. Wang, R. Liu, D. Wang, F. Liu, Z. Wu, Sulfur vacancy engineering of MoS_2 via phosphorus incorporation for improved electrocatalytic N2 reduction to NH_3. Appl. Catal. B Environ. 300 (2022) 120733.

[39] H.J. Song, H. Yoon, B. Ju, G.H. Lee, D.W. Kim, 3D Architectures of Quaternary Co-Ni-S-P/Graphene Hybrids as Highly Active and Stable Bifunctional Electrocatalysts for Overall Water Splitting. Adv. Energy Mater. 8 (2018) 1802319.

[40] X.Q. Bao, M. Fatima Cerqueira, P. Alpuim, L. Liu, Silicon nanowire arrays coupled with cobalt phosphide spheres as low-cost photocathodes for efficient solar hydrogen evolution. Chem. Commun. 51 (2015) 10742-10745.

[41] J. Xu, Y. Liu, J. Li, I. Amorim, B. Zhang, D. Xiong, N. Zhang, S.M. Thalluri, J.P.S. Sousa, L. Liu, Hollow cobalt phosphide octahedral pre-catalysts with exceptionally high intrinsic catalytic activity for electro-oxidation of water and methanol. J. Mater. Chem. A 6 (2018) 20646-20652.

[42] J. Xu, D. Xiong, I. Amorim, L. Liu, Template-Free Synthesis of Hollow Iron Phosphide–Phosphate Composite Nanotubes for Use as Active and Stable Oxygen Evolution Electrocatalysts. ACS Appl. Nano Mater. 1 (2018) 617-624.

[43] Z. Yu, J. Xu, I. Amorim, Y. Li, L. Liu, Easy preparation of multifunctional ternary PdNiP/C catalysts toward enhanced small organic molecule electro-oxidation and hydrogen evolution reactions. J. Energy Chem. (2020).

[44] Z. Yu, X.K. Wei, J. Xu, Y. Li, A. Araujo, J.L. Faria, R.E. Dunin-Borkowski, L. Liu, Multifunctional Noble Metal Phosphide Electrocatalysts for Organic Molecule Electro-Oxidation. ACS Appl. Energy Mater. 4 (2021) 1593-1600.

[45] J. Xu, I. Amorim, Y. Li, J. Li, Z. Yu, B. Zhang, A. Araujo, N. Zhang, L. Liu, Stable overall water splitting in an asymmetric acid/alkaline electrolyzer comprising a bipolar

membrane sandwiched by bifunctional cobalt-nickel phosphide nanowire electrodes. Carbon Energy 2 (2020) 646-655.

[46] I. Uhlig, R. Szargan, H.W. Nesbitt, K. Laajalehto, Surface states and reactivity of pyrite and marcasite. Appl. Surf. Sci. 179 (2001) 222-229.

[47] Y. Jia, L. Zhang, G. Gao, H. Chen, B. Wang, J. Zhou, M.T. Soo, M. Hong, X. Yan, G. Qian, J. Zou, A. Du, X. Yao, A Heterostructure Coupling of Exfoliated Ni–Fe Hydroxide Nanosheet and Defective Graphene as a Bifunctional Electrocatalyst for Overall Water Splitting. Adv. Mater. 29 (2017) 1700017.

[48] Y. Wu, X. Tao, Y. Qing, H. Xu, F. Yang, S. Luo, C. Tian, M. Liu, X. Lu, Cr-Doped FeNi–P Nanoparticles Encapsulated into N-Doped Carbon Nanotube as a Robust Bifunctional Catalyst for Efficient Overall Water Splitting. Adv. Mater. 31 (2019) 1900178.

[49] C.F. Li, J.W. Zhao, L.J. Xie, J.Q. Wu, G.R. Li, Fe doping and oxygen vacancy modulated Fe-Ni_5P_4/NiFeOH nanosheets as bifunctional electrocatalysts for efficient overall water splitting. Appl. Catal. B Environ. 291 (2021) 119987.

[50] K. Liang, L. Guo, K. Marcus, S. Zhang, Z. Yang, D.E. Perea, L. Zhou, Y. Du, Y. Yang, Overall Water Splitting with Room-Temperature Synthesized NiFe Oxyfluoride Nanoporous Films. ACS Catal. 7 (2017) 8406-8412.

[51] A. Kumar, S. Bhattacharyya, Porous NiFe-Oxide Nanocubes as Bifunctional Electrocatalysts for Efficient Water-Splitting. ACS Appl. Mater. Interfaces 9 (2017) 41906-41915.

[52] Y. Yang, Y. Xie, Z. Yu, S. Guo, M. Yuan, H. Yao, Z. Liang, Y.R. Lu, T.S. Chan, C. Li, H. Dong, S. Ma, Self-supported NiFe-LDH@CoS_x nanosheet arrays grown on nickel foam as efficient bifunctional electrocatalysts for overall water splitting. Chem. Eng. J. 419 (2021) 129512.

[53] M. Zheng, K. Guo, W.J. Jiang, T. Tang, X. Wang, P. Zhou, J. Du, Y. Zhao, C. Xu, J.S. Hu, When MoS_2 meets FeOOH: A “one-stone-two-birds’’ heterostructure as a bifunctional electrocatalyst for efficient alkaline water splitting. Appl. Catal. B Environ. 244 (2019) 1004-1012.

[54] Z. Zhang, T. Zhang, J.Y. Lee, Electrochemical Performance of Borate-Doped Nickel Sulfide: Enhancement of the Bifunctional Activity for Total Water Splitting. ChemElectroChem 6 (2019) 1443-1449.

[55] J.J. Lv, J. Zhao, H. Fang, L.P. Jiang, L.L. Li, J. Ma, J.J. Zhu, Incorporating Nitrogen-Doped Graphene Quantum Dots and Ni_3S_2 Nanosheets: A Synergistic Electrocatalyst with Highly Enhanced Activity for Overall Water Splitting. Small 13 (2017) 1700264.

[56] G. Hu, J. Xiang, J. Li, P. Liu, R.N. Ali, B. Xiang, Urchin-like ternary cobalt phosphosulfide as high-efficiency and stable bifunctional electrocatalyst for overall water splitting. J. Catal. 371 (2019) 126-134.

[57] C. Wu, B. Liu, J. Wang, Y. Su, H. Yan, C. Ng, C. Li, J. Wei, 3D structured Mo-doped Ni_3S_2 nanosheets as efficient dual-electrocatalyst for overall water splitting. Appl. Surf. Sci. 441 (2018) 1024-1033.

[58] Z. Dai, H. Geng, J. Wang, Y. Luo, B. Li, Y. Zong, J. Yang, Y. Guo, Y. Zheng, X. Wang, Q. Yan, Hexagonal-Phase Cobalt Monophosphosulfide for Highly Efficient Overall Water Splitting. ACS Nano 11 (2017) 11031-11040.

[59] Y. Guo, T. Park, J.W. Yi, J. Henzie, J. Kim, Z. Wang, B. Jiang, Y. Bando, Y. Sugahara, J. Tang, Y. Yamauchi, Nanoarchitectonics for Transition-Metal-Sulfide-Based Electrocatalysts for Water Splitting. Adv. Mater. 31 (2019) 1807134.

[60] A. Parra-Puerto, K.L. Ng, K. Fahy, A.E. Goode, M.P. Ryan, A. Kucernak, Supported Transition Metal Phosphides: Activity Survey for HER, ORR, OER, and Corrosion Resistance in Acid and Alkaline Electrolytes. ACS Catal. 9 (2019) 11515-11529.

[61] M. Wang, L. Zhang, J. Pan, M. Huang, H. Zhu, A highly efficient Fe-doped Ni3S2 electrocatalyst for overall water splitting. Nano Research 14 (2021) 4740-4747.

[62] X. Wang, W. Li, D. Xiong, L. Liu, Fast fabrication of self-supported porous nickel phosphide foam for efficient, durable oxygen evolution and overall water splitting. J. Mater. Chem. A 4 (2016) 5639-5646.

[63] T. Ma, W. Xu, B. Li, X. Chen, J. Zhao, S. Wan, K. Jiang, S. Zhang, Z. Wang, Z. Tian, Z. Lu, L. Chen, The Critical Role of Additive Sulfate for Stable Alkaline Seawater Oxidation on Nickel-Based Electrodes. Angew. Chem. Int. Ed. 60 (2021) 22740-22744.

[64] Y. Kuang, M.J. Kenney, Y. Meng, W.H. Hung, Y. Liu, J.E. Huang, R. Prasanna, P. Li, Y. Li, L. Wang, M.C. Lin, M.D. McGehee, X. Sun, H. Dai, Solar-driven, highly sustained splitting of seawater into hydrogen and oxygen fuels. Proc. Natl. Acad. Sci. USA 116 (2019) 6624-6629.

[65] P. Wang, T. Wang, R. Qin, Z. Pu, C. Zhang, J. Zhu, D. Chen, D. Feng, Z. Kou, S. Mu, J. Wang, Swapping Catalytic Active Sites from Cationic Ni to Anionic S in Nickel Sulfide Enables More Efficient Alkaline Hydrogen Generation. Adv. Energy Mater. 12 (2022) 2103359.

[66] S. Shen, Z. Wang, Z. Lin, K. Song, Q. Zhang, F. Meng, L. Gu, W. Zhong, Crystalline-Amorphous Interfaces Coupling of $CoSe_2$/CoP with Optimized d-band Center and Boosted Electrocatalytic Hydrogen Evolution. Adv. Mater. 34 (2022) 2110631.

[67] J. Wei, M. Zhou, A. Long, Y. Xue, H. Liao, C. Wei, Z.J. Xu, Heterostructured Electrocatalysts for Hydrogen Evolution Reaction Under Alkaline Conditions. Nano-Micro Letters 10 (2018) 75.

[68] J. Xu, T. Liu, J. Li, B. Li, Y. Liu, B. Zhang, D. Xiong, I. Amorim, W. Li, L. Liu, Boosting the hydrogen evolution performance of ruthenium clusters through synergistic coupling with cobalt phosphide. Energy Environ. Sci. 11 (2018) 1819-1827.

[69] X. Wang, Y.V. Kolen'ko, X.Q. Bao, K. Kovnir, L. Liu, One-Step Synthesis of Self-Supported Nickel Phosphide Nanosheet Array Cathodes for Efficient Electrocatalytic Hydrogen Generation. Angew. Chem. Int. Ed. 54 (2015) 8188-8192.

[70] L. Simonelli, C. Marini, W. Olszewski, M. Ávila Pérez, N. Ramanan, G. Guilera, V. Cuartero, K. Klementiev, CLÆSS: The hard X-ray absorption beamline of the ALBA CELLS synchrotron. Cogent Physics 3 (2016) 1231987.

[71] B. Ravel, M. Newville, ATHENA, ARTEMIS, HEPHAESTUS: data analysis for X-ray absorption spectroscopy using IFEFFIT. J. Synchrotron Radiat. 12 (2005) 537-541.

[72] P.E. Blöchl, Projector augmented-wave method. Phys. Rev. B 50 (1994) 17953-17979.

[73] G. Kresse, J. Furthmüller, Efficient iterative schemes for ab initio total-energy calculations using a plane-wave basis set. Phys. Rev. B 54 (1996) 11169-11186.

[74] J.P. Perdew, K. Burke, M. Ernzerhof, Generalized Gradient Approximation Made Simple. Phys. Rev. Lett. 77 (1996) 3865-3868.

[75] V. Wang, N. Xu, J.C. Liu, G. Tang, W.T. Geng, VASPKIT: A user-friendly interface facilitating high-throughput computing and analysis using VASP code. Comput. Phys. Commun. 267 (2021) 108033.

[76] J.K. Nørskov, J. Rossmeisl, A. Logadottir, L. Lindqvist, J.R. Kitchin, T. Bligaard, H. Jónsson, Origin of the Overpotential for Oxygen Reduction at a Fuel-Cell Cathode. J. Phys. Chem. B 108 (2004) 17886-17892.

[77] J.K. Nørskov, T. Bligaard, A. Logadottir, J.R. Kitchin, J.G. Chen, S. Pandelov, U. Stimming, Trends in the Exchange Current for Hydrogen Evolution. J. Electrochem. Soc. 152 (2005) J23.

[78] C.C.L. McCrory, S. Jung, I.M. Ferrer, S.M. Chatman, J.C. Peters, T.F. Jaramillo, Benchmarking Hydrogen Evolving Reaction and Oxygen Evolving Reaction Electrocatalysts for Solar Water Splitting Devices. J. Am. Chem. Soc. 137 (2015) 4347-4357.

3. Ultrafine oxygen-defective iridium oxide nanoclusters for efficient and durable water oxidation at high current densities in acidic media

Abstract

Iridium oxide (IrO_2) is one of the best known electrocatalysts for the oxygen evolution reaction (OER) taking place in a strongly acidic solution. IrO_2 nanocatalysts with high activity as well as long-term catalytic stability, particularly at high current densities, are highly desirable for proton exchange membrane water electrolysis (PEMWE). Here, we report a simple and cost-effective strategy for depositing ultrafine oxygen-defective IrO_x nanoclusters (1–2 nm) on a high-surface-area, acid-stable titanium current collector (H-Ti@IrO_x), through a repeated impregnation–annealing process. The high catalytically active surface area resulting from the small size of IrO_x and the preferable electronic structure originating from the presence of oxygen defects enable the outstanding OER performance of H-Ti@IrO_x, with low overpotentials of 277 and 336 mV to deliver 10 and 200 mA cm^{-2} in 0.5 M H_2SO_4. Moreover, H-Ti@IrO_x also shows an intrinsic specific activity of 0.04 mA $cm_{catalyst}^{-2}$ and superior mass activity of 1500 A g_{Ir}^{-1} at an overpotential of 350 mV. Comprehensive experimental studies and density functional theory calculations confirm the important role of oxygen defects in the enhanced OER performance. Remarkably, H-Ti@IrO_x can continuously catalyze the OER in 0.5 M H_2SO_4 at 200 mA cm^{-2} for 130 hours with minimal degradation, and with a higher IrO_x loading, it can sustain at such a high current density for over 500 hours without significant performance decay, holding substantial promise for use in PEMWE.

3.1 Introduction

Developing electrochemical energy conversion devices, such as fuel cells and water electrolyzers, is of paramount importance to the future energy sustainability and environmental remediation [1]. Electrocatalytic water splitting has recently regained considerable research interest as a sustainable and carbon-neutral approach to the production of hydrogen (H_2) – a promising energy carrier that has the potential to replace conventional fossil fuels [2-4]. In particular, proton exchange membrane water

electrolysis (PEMWE) has shown significant advantages over the conventional alkaline water electrolysis (AWE) technology, because PEMWE allows for higher energy efficiency, production of purer H_2 gas, compact system design, and dynamic flexibility of operation [5-7]. However, the development of PEM electrolyzers is largely hindered by the lack of highly active and stable electrocatalysts to efficiently catalyze the oxygen evolution reaction (OER) in acidic solutions [8]. Up to now, iridium (Ir)-based materials are the best known OER electrocatalysts with both high activity and reasonably good stability in acidic media [8-13]. However, large-scale deployment of PEM electrolyzers is restricted by the low earth abundance and high cost of iridium [10, 14-16].

To enable widespread deployment of PEM water electrolyzers, the OER catalytic performance of Ir-based catalysts must be drastically improved and meanwhile the Ir utilization should be kept as minimal as possible. To this end, much research effort has been dedicated to nanostructuring Ir and doping Ir with non-precious transition metals, aiming to enhance the intrinsic catalytic activity and to better utilize the precious Ir [17]. For example, nanoclusters of IrO_x–Ir and IrRu alloy [18, 19], bimetallic IrNi [20], nanoporous [21] and ultra-small IrO_2 [22] have been reported to show good OER performance in acid media, with a low overpotential to deliver the benchmark current density of 10 mA cm^{-2} [18-22]. In addition, a number of studies have shown that structural defects have a significant impact on the electronic structure and surface properties of catalysts, and intentional or accidental introduction of defects into catalysts may enhance their catalytic activity, which has been verified in a few nonprecious metal based catalysts [23, 24]. Recent studies have also demonstrated that non-stoichiometric and defective oxygen in the lattice of iridium oxide or ruthenium oxide may markedly boost the intrinsic activity of these catalysts for the OER [25-29]. This makes defect engineering a useful strategy to enhance the catalytic activity.

While various strategies have been developed to improve the activity of Ir-based catalysts, achieving long-term stability in strongly acidic media, particularly at a high current density, remains a great challenge. The harsh, corrosive and oxidative environment may give rise to dissolution and/or over-oxidation of catalytically active species, leading to the rapid loss of OER catalytic activity [30-32]. For these reasons, most Ir-based OER catalysts reported so far can only survive at a low current density (typically ≤10 mA cm^{-2}) for a limited period of time (a few to tens of hours) [14, 15, 25-29], which is far from what is required for practical industry-relevant PEMWE.

Herein, we develop iridium oxide (IrO_x) nanoclusters combining the advantages of an ultrafine cluster size (1–2 nm), which leads to the exposure of a large active surface area, and an oxygen-defective feature, which results in an electronic structure favorable for the OER. By loading IrO_x nanoclusters on hydrothermally treated high-surface-area titanium foam (H-Ti foam), outstanding OER catalytic activity has been achieved in a strongly acidic solution (*i.e.*, 0.5 M H_2SO_4), with low overpotentials (η) of 277 and 336 mV to deliver current densities of 10 and 200 mA cm^{-2}, respectively. Moreover, the intimate contact between IrO_x and H-Ti foam significantly stabilizes the IrO_x nanocluster catalysts. As a result, the H-Ti foam supported IrO_x (H-Ti@IrO_x) is able to continuously catalyze the OER at a high current density of 200 mA cm^{-2} in 0.5 M H_2SO_4 for 130 hours without notable degradation. Moreover, density functional theory (DFT) calculations confirm that the oxygen defects in IrO_x result in a low binding energy of oxygenated intermediates, especially of the oxygen atoms, leading to a markedly decreased energy barrier to the catalytic reaction and thus higher OER performance in the IrO_x.

3.2 Results and discussion

The H-Ti@IrO_x catalyst was prepared by soaking H-Ti foam in 0.1 M aqueous solution of $IrCl_3$ for 30 min, followed by thermal annealing at 400 °C in air for 30 min. The IrO_x loading density can be adjusted by repeating the impregnation–annealing cycles. Using a similar process, IrO_x was also loaded on pristine Ti foam (P-Ti@IrO_x) and a carbon paper substrate (C@IrO_x) for use as controls.

Hydrothermal treatment of Ti foam in high-concentration KOH solution (10 M) led to the formation of a high density of cross-linked nanowires (NWs, 20–30 nm in diameter) on the foam surface (**Figure 3.1**), which may significantly increase the number of sites that can immobilize IrO_x nanoclusters. The same morphology was observed as well on hydrothermally treated Ti foam in a recent report [33]. According to the X-ray diffractometry (XRD) examination results, only a very weak diffraction peak from $KHTi_4O_9{\cdot}0.5H_2O$ (PHT, ICDD no. 00-038-0173) was detected for H-Ti (**Figure 3.1a**), besides those from metallic Ti (ICDD no. 04-015-0276). This indicates that the formed PHT NWs have poor crystallinity. Furthermore, the formation of $KHTi_4O_9{\cdot}0.5H_2O$ was confirmed by Raman spectroscopy (**Figure 3.2a**), where the Raman peaks at 200, 280, 440, and 650 cm^{-1} can be well assigned to the Ti-OH vibration in $KHTi_4O_9{\cdot}0.5H_2O$ [34, 35].

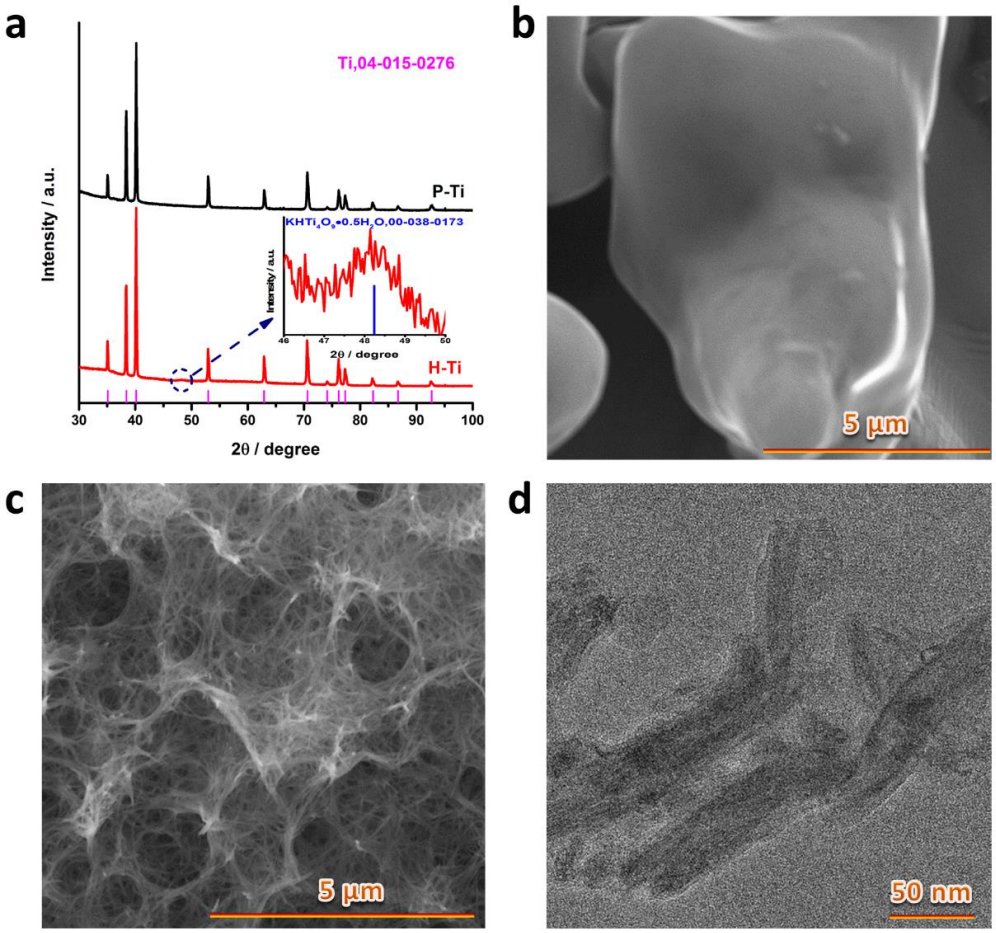

Figure 3.1 a) XRD patterns of P-Ti foam and H-Ti foam. SEM images of b) P-Ti foam and c) H-Ti foam. d) TEM image of H-Ti foam. PHT nanowires were obtained upon the hydrothermal treatment.

Figure 3.2b shows the XRD patterns of the as-prepared H-Ti@IrO_x catalyst and the control samples of C@IrO_x and P-Ti@IrO_x. No diffraction peaks from IrO_2 can be resolved for H-Ti@IrO_x and P-Ti@IrO_x, suggesting that the deposited iridium oxide may either be poorly crystallized or consist of tiny crystallites that significantly widen the diffraction peaks.

The morphology and microstructure of H-Ti@IrO_x catalysts were further examined by scanning electron microscopy (SEM) and transmission electron microscopy (TEM). Loading IrO_x nanoclusters on H-Ti foam did not markedly alter its morphology, as revealed by SEM examination (**Figure 3.3**). **Figure 3.2c** shows a representative low-magnification TEM image of PHT NWs loaded with IrO_x catalysts, where a high density of nanoclusters are found to distribute on the surface of NWs (representative nanoclusters marked with yellow circles). These nanoclusters have a typical size of 1–2 nm and are crystallized, as shown in the high resolution TEM (HRTEM) image in **Figure 3.2d**. The measured lattice fringe of 0.258 nm corresponds to the (101) crystal planes of

tetragonal IrO_2 (ICDD no. 00-015-0870). The crystal structure of nanoclusters was further examined in the high-angle annular dark field scanning transmission electron microscopy (HAADF-STEM) mode, where a dense distribution of nanoclusters on the NW surface can be distinguished more clearly (**Figure 3.2e-f**). The atomic-resolution HAADF-STEM imaging (**Figure 3.2g**) confirmed that the lattice of nanoclusters matches well the atomic model of tetragonal IrO_2 with defective oxygen, viewed along the [100] direction (**Figure 3.2h**), which can be further corroborated by the fast Fourier transformation electron diffraction (FFT-ED) analyses (**Figure 3.2g**, inset). Furthermore, STEM elemental mapping (**Figure 3.2i**) illustrated that Ir covers on the PHT NWs with a very high density.

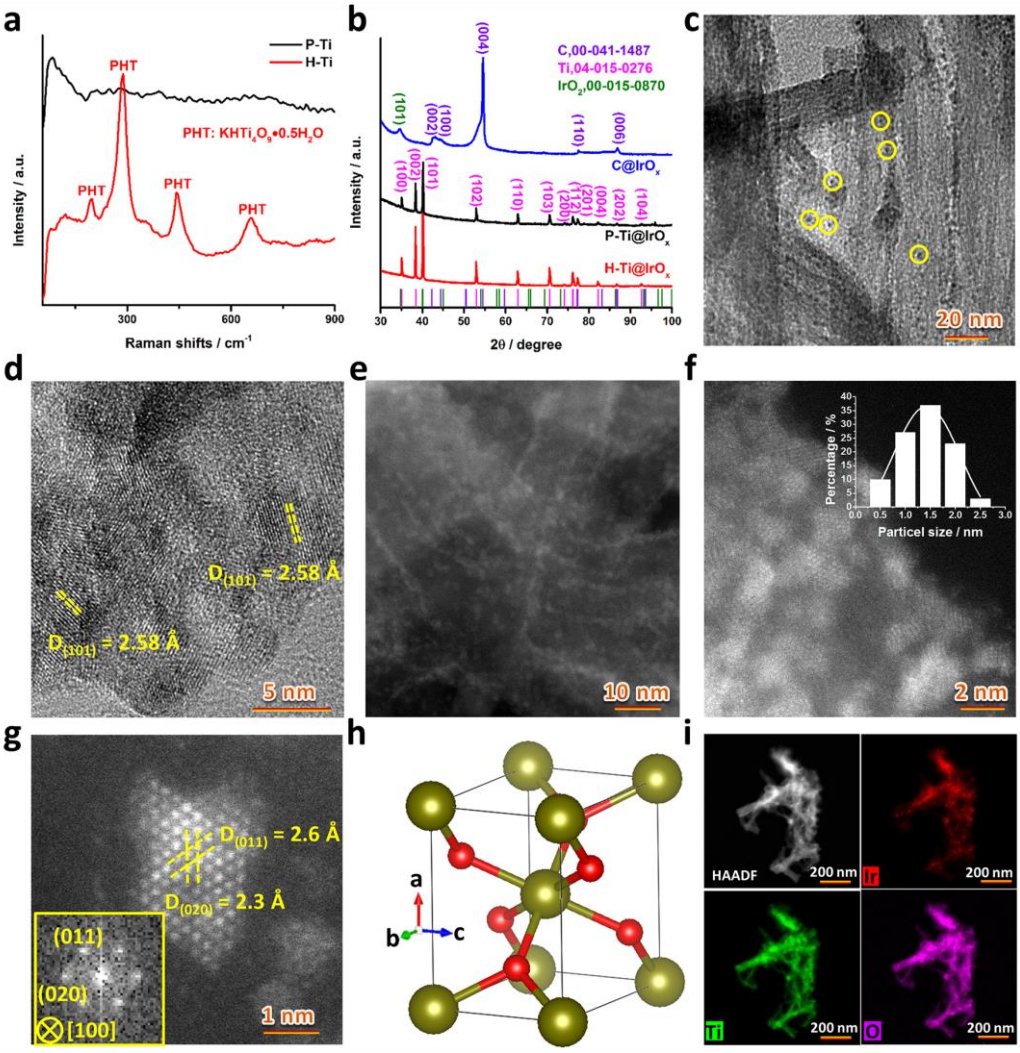

Figure 3.2 a) Raman spectra of H-Ti foam and P-Ti foam. b) XRD patterns of H-Ti@IrO_x, P-Ti@IrO_x, and C@IrO_x. c) Bright-field TEM image and d) HRTEM image of H-Ti@IrO_x. e) Low-magnification and f) high-magnification HAADF-STEM image of IrO_x catalysts. g) Atomic-resolution STEM image of an individual IrO_x nanocluster. Inset: the corresponding FFT-ED pattern. h) Schematic illustration of the crystal structure in g). Yellow and red spheres represent Ir and O atoms, respectively. i) HAADF-STEM image and the corresponding elemental maps of Ir, Ti and O.

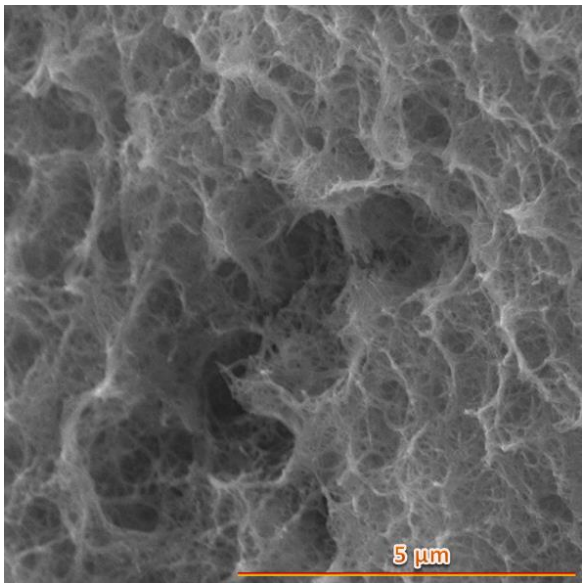

Figure 3.3 SEM image of H-Ti@IrO_x catalysts.

We also examined the crystal structure and morphology of H-Ti@IrO_x with different IrO_x loading densities. No XRD peaks from any polymorph of iridium oxides were detected even if the loading density was increased to 0.6 mg cm^{-2} (**Figure 3.4**). Moreover, the morphology did not change as the loading density varied (**Figure 3.5**). Furthermore, we investigated the microstructure of IrO_x clusters deposited on the P-Ti foam and carbon paper substrate. In P-Ti@IrO_x, IrO_x exhibits the same tetragonal crystal structure, but has a bigger cluster size and broader size distribution (4–10 nm, **Figure 3.6**); while for C@IrO_x, the deposited IrO_x is interconnected forming a porous structure where the size of ligaments falls in the range of 2–3 nm (**Figure 3.7**), similar to the morphology of cluster beam deposited Ru clusters we reported previously [36]. This suggests that both the size and uniformity of the deposited IrO_x nanoclusters are influenced by the catalyst support. When the H-Ti foam was immersed in $IrCl_3$ solution, Ir^{3+} cations tended to bond with the hydroxyl groups on the surface of PHT NWs *via* electrostatic interaction [34]. The subsequent thermal annealing in air oxidized the chemisorbed iridium and immobilized the formed IrO_x nanoclusters on the H-Ti foam. Simultaneous nucleation at multiple sites resulted in the formation of size-uniform ultrafine nanoclusters. A similar nucleation process also happened on the oxidized carbon paper, where a large quantity of hydroxyl functional groups exist on the surface [37, 38], leading to the formation of small IrO_x clusters. In contrast, the pristine P-Ti foam does not have as many oxyl or hydroxyl groups on its surface as the H-Ti foam or carbon paper, and therefore, the IrO_x deposited on the P-Ti foam is larger in size and shows a wider size distribution.

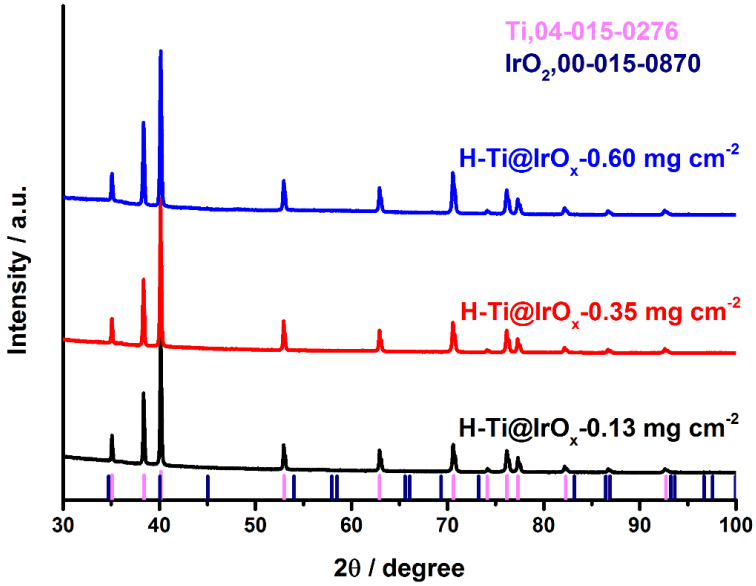

Figure 3.4 XRD patterns of H-Ti@IrO_x-0.13 mg cm^{-2}, H-Ti@IrO_x-0.35 mg cm^{-2} and H-Ti@IrO_x-0.60 mg cm^{-2}.

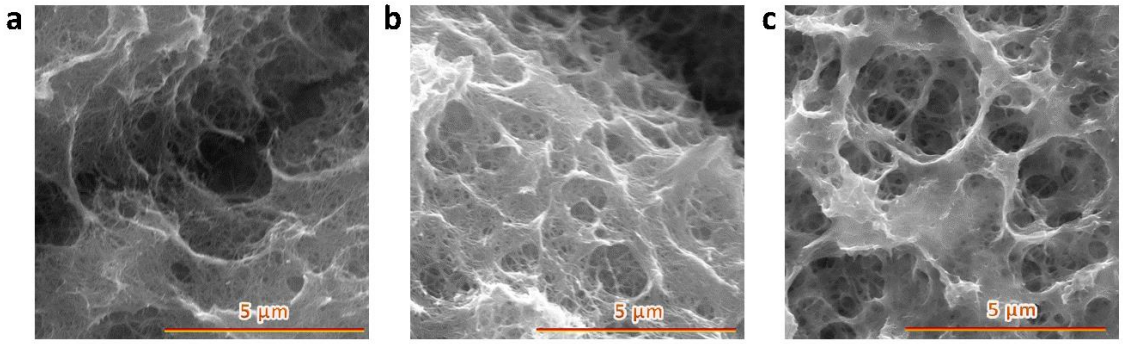

Figure 3.5 SEM images of a) H-Ti@IrO_x-0.13 mg cm^{-2}, b) H-Ti@IrO_x-0.35 mg cm^{-2} and c) H-Ti@IrO_x-0.60 mg cm^{-2}.

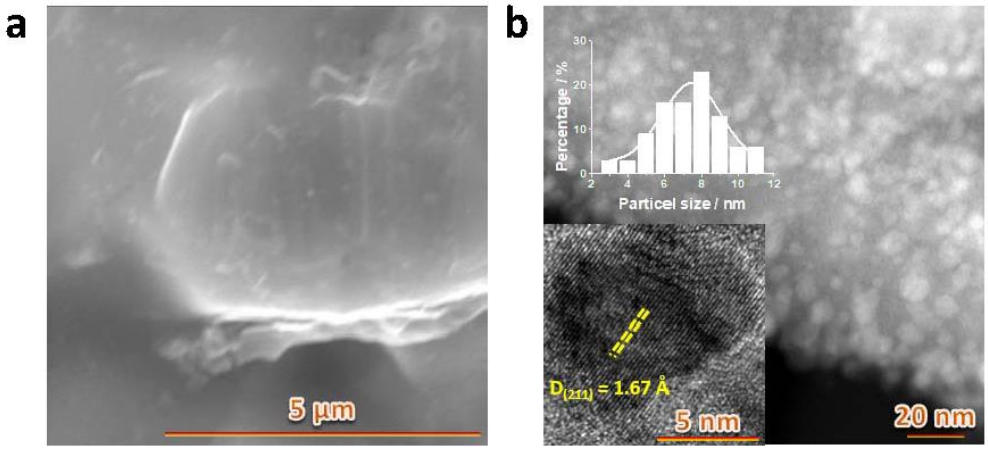

Figure 3.6 Morphology and microstructure characterization of P-Ti@IrO_x catalyst. a) SEM image. b) HAADF-STEM image. Bottom left inset is the HRTEM image of individual IrO_x nanoclusters, and the marked lattice fringe of 0.167 nm corresponds to the (211) crystal planes of tetragonal IrO_2 (ICDD No. 00-015-0870). Upper left inset is a histogram illustrating the size distribution of IrO_x nanoclusters.

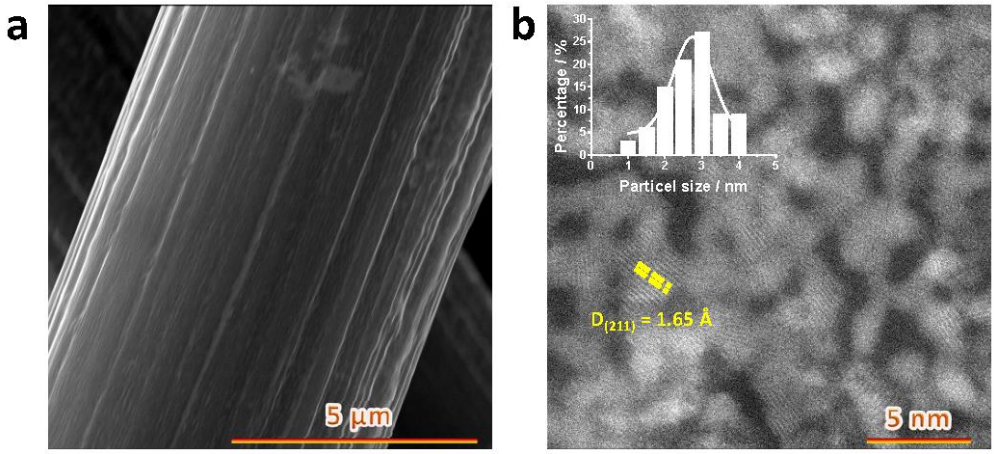

Figure 3.7 Morphology and microstructure characterization of C@IrO_x. a) SEM image. b) HAADF-STEM image. The marked lattice fringe of 0.165 nm corresponds to the (211) crystal planes of tetragonal IrO_2 (ICDD No. 00-015-0870). Inset: histogram illustrating the size distribution of ligaments.

We have investigated the surface chemical states of H-Ti@IrO_x, P-Ti@IrO_x, C@IrO_x, and commercial IrO_2 particles using X-ray photoelectron spectroscopy (XPS). The XPS survey spectra confirm the presence of corresponding elements in each catalyst (**Figure 3.8**). Given that XPS allows the investigation of the local chemical (ionic) environment of materials [39], it has been used to characterize the degree of oxygen deficiency and related valence state change of metal cations in metal oxides [23, 24]. **Figure 3.9** shows the O 1s XPS spectra of H-Ti@IrO_x and other control catalysts, which can be de-convoluted into four components. The binding energy (BE) peak at *ca.* 529.8 eV (O1) generally relates to metal–oxygen bonding, the BE peak at 531.4 eV (O3) can be assigned to surface –OH groups, and the BE peak at 532.6 eV (O4) is associated with water [40]. In the literature, the BE peak centered around 530.4 eV (O2) has been proposed to correlate with surface oxygen defects, reflecting the degree of oxygen deficiency (*i.e.*, the stoichiometry of oxygen with metal cations) [24, 25]. XPS quantitative analysis manifests that the content of the surface defective oxygen is 37.0%, 34.4%, 28.5%, and 20.5% in H-Ti@IrO_x, C@IrO_x, P-Ti@IrO_x, and commercial IrO_2 particles, respectively (**Table 3.1**), indicating that the Ir/O stoichiometry in H-Ti@IrO_x deviates heavily from 1 : 2 and the IrO_x nanoclusters in H-Ti@IrO_x are severely oxygen-defective. The high-resolution Ir 4f XPS spectra of all the catalysts are compared in **Figure 3.10**. There exist two spin–orbit components in the spectra, corresponding to the Ir $4f_{5/2}$ and Ir $4f_{7/2}$ components, respectively, which can be further de-convoluted into nine components characteristic of Ir^{IV}, Ir^{III}, Ir^{IV} satellite 1, Ir^{IV} satellite 2 and Ir^{III} satellite, respectively (**Figure 3.10**, **Tables 3.2** and **3.3**) [41, 42]. Notably, we found that the ratio of Ir^{III}/Ir^{IV} increases as the content of surface defective oxygen increases, following the order H-Ti@IrO_x >

C@IrO_x > P-Ti@IrO_x > commercial IrO_2, in consistence with the degree of oxygen deficiency in these catalysts, which indicates that the Ir^{III} valence state correlates with the O2 component in O 1s spectra. The Ir^{III} valence state likely results from the transfer of electrons trapped at the oxygen-defective sites to Ir^{IV} cations [41, 42].

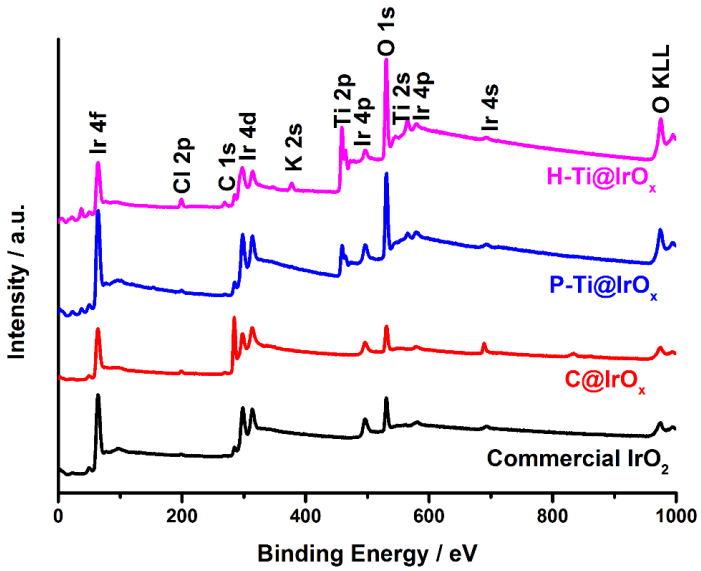

Figure 3.8 XPS survey spectra of H-Ti@IrO_x, P-Ti@IrO_x, C@IrO_x, and commercial IrO_2 catalysts.

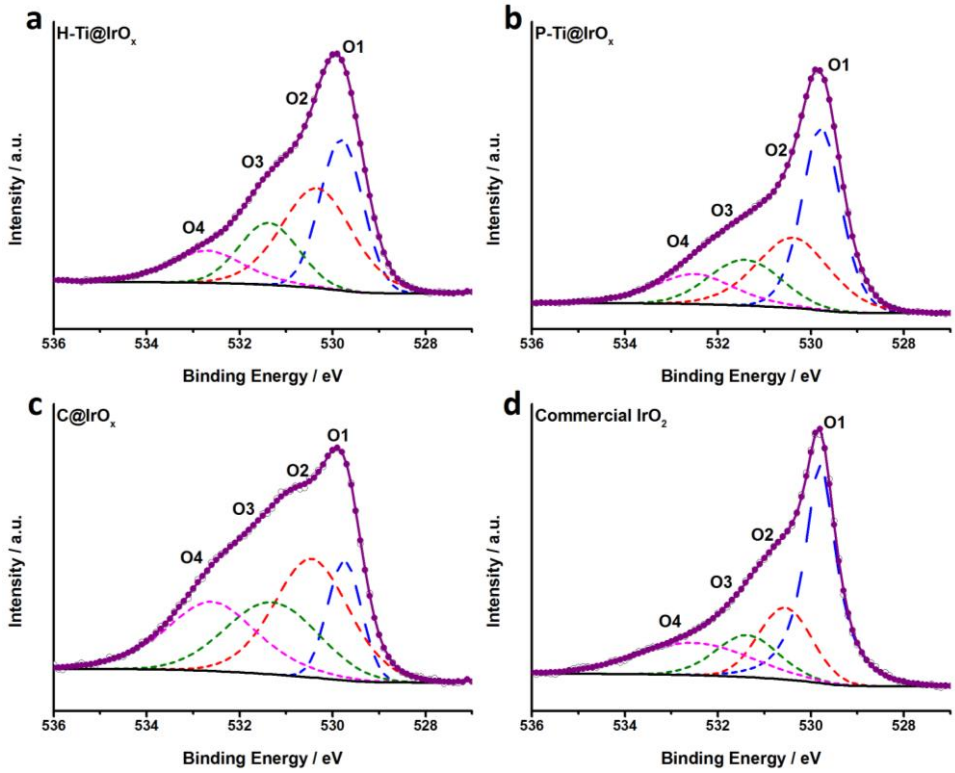

Figure 3.9 O 1s spectra of a) H-Ti@IrO_x, b) P-Ti@IrO_x, c) C@IrO_x, and d) commercial IrO_2 particles.

Table 3.1 Fitting parameters of O1s spectra of H-Ti@IrO_x, P-Ti@IrO_x, C@IrO_x, commercial IrO_2, H-Ti@IrO_x-air-0.5 h and H-Ti@IrO_x-air-5 h.

	O1	**O2**	**O3**	**O4**
H-Ti@IrO_x				
BE (eV)	529.8	530.4	531.4	532.7
Area (%)	33.0	37.0	18.5	11.5
FWHM (eV)	1.1	1.9	1.5	1.9
P-Ti@IrO_x				
BE (eV)	529.8	530.4	531.4	532.6
Area (%)	40.1	28.5	17.7	13.7
FWHM (eV)	1.0	1.9	1.9	2.1
C@IrO_x				
BE (eV)	529.8	530.4	531.4	532.6
Area (%)	15.4	34.4	25.1	25.1
FWHM (eV)	0.9	1.9	2.4	2.4
Commercial IrO_2				
BE (eV)	529.8	530.5	531.4	532.6
Area (%)	45.5	20.5	14.5	19.5
FWHM (eV)	0.8	1.4	1.7	2.9
H-Ti@IrO_x-air-0.5 h				
BE (eV)	529.8	530.3	531.3	532.3
Area (%)	28.3	32.6	18.2	20.9
FWHM (eV)	1.3	2.0	1.4	2.0
H-Ti@IrO_x-air-5 h				
BE (eV)	529.8	530.3	531.3	532.4
Area (%)	36.5	27.0	23.4	13.1
FWHM (eV)	1.2	1.2	1.9	2.5

BE: binding energy; FWHM: full width at half maximum.

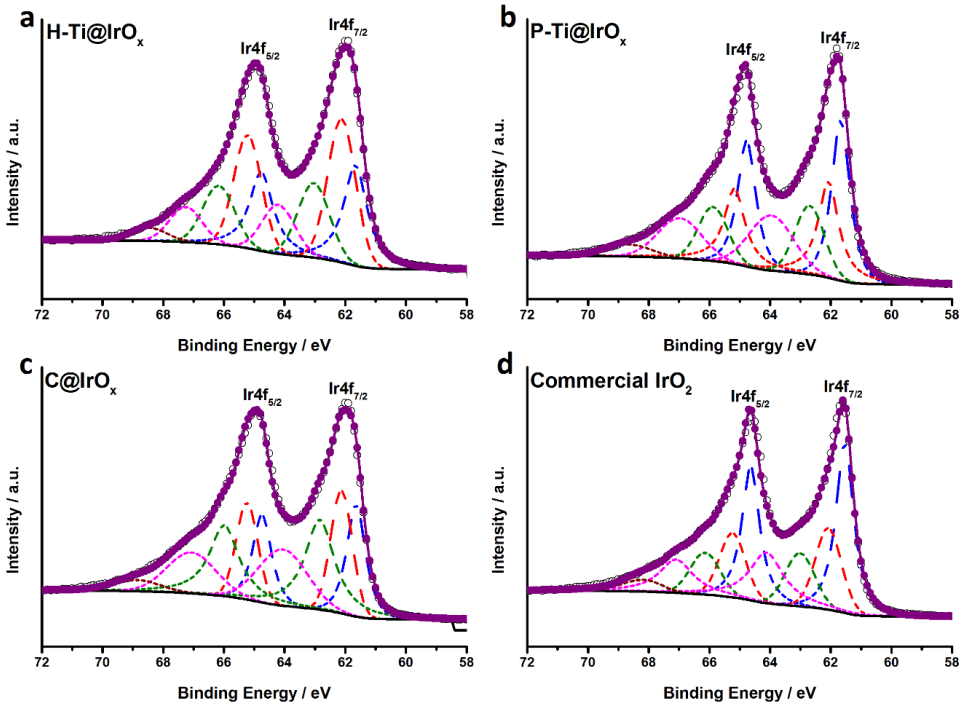

Figure 3.10 Ir 4f XPS spectrum of a) H-Ti@IrO_x, b) P-Ti@IrO_x, c) C@IrO_x and d) commercial IrO_2 catalysts. Blue and red curves represent Ir^{IV} and Ir^{III}, respectively; olive, wine and orange curves represent Ir^{IV} satellite 1, satellite 2 and Ir^{III} satellite, respectively.

Table 3.2 Fitting parameters of Ir 4f spectra of H-Ti@IrO_x, P-Ti@IrO_x, C@IrO_x, commercial IrO_2, H-Ti@IrO_x-air-0.5 h and H-Ti@IrO_x-air-5 h.

Catalysts	Content of Ir species (%)	
	Ir^{3+}	Ir^{4+}
H-Ti@IrO_x	56.4	43.6
P-Ti@IrO_x	45.1	54.9
C@IrO_x	53.2	46.8
Commercial IrO_2	36.8	63.2
H-Ti@IrO_x-air-0.5 h	48.2	51.8
H-Ti@IrO_x-air-5 h	40.8	59.2

Table 3.3 Fitting parameters of Ir 4f spectra of H-Ti@IrO_x, P-Ti@IrO_x, C@IrO_x, commercial IrO_2, H-Ti@IrO_x-air-0.5 h and H-Ti@IrO_x-air-5 h.

	Ir4f$_{7/2}$ Ir^{IV}	Ir4f$_{5/2}$ Ir^{IV}	Ir4f$_{7/2}$ Ir^{IV} sat 1	Ir4f$_{5/2}$ Ir^{IV} sat 1	Ir4f$_{5/2}$ Ir^{IV} sat 2	Ir4f$_{7/2}$ Ir^{III}	Ir4f$_{5/2}$ Ir^{III}	Ir4f$_{7/2}$ Ir^{III} sat 1	Ir f$_{5/2}$ Ir^{III} sat 1
H-Ti@IrO_x									

BE (eV)	61.7	64.8	62.9	66.1	68.4	62.1	65.2	64.1	67.2
Area (%)	15.3	11.9	11.7	9.3	2.6	19.8	15.7	7.9	5.8
FWHM (eV)	0.9	0.9	1.2	1.2	1.4	1.1	1.1	1.3	1.3
P-Ti@IrO_x									
BE (eV)	61.7	64.8	62.7	65.9	68.7	62.1	65.2	64.0	67.0
Area (%)	17.4	13.7	10.4	8.2	3.0	14.3	11.3	12.5	9.2
FWHM (eV)	0.7	0.7	1.1	1.1	1.8	0.8	0.8	1.7	1.7
C@IrO_x									
BE (eV)	61.7	64.8	62.9	66.0	68.8	62.1	65.2	64.1	67.1
Area (%)	11.5	9.2	17.0	13.4	2.5	13.1	10.2	13.4	9.7
FWHM (eV)	0.8	0.8	1.2	1.2	1.8	0.9	0.9	1.9	1.9
Commercial IrO_2									
BE (eV)	61.6	64.7	63.0	66.1	68.2	62.1	65.2	64.1	67.1
Area (%)	21.3	16.8	9.0	7.0	2.8	12.4	9.6	12.8	8.3
FWHM (eV)	0.7	0.7	1.2	1.2	1.3	1.1	1.1	1.3	1.3
H-Ti@IrO_x-air-0.5 h									
BE (eV)	61.7	64.8	62.9	66.1	68.9	62.2	65.3	64.0	67.1
Area (%)	14.4	11.4	12.9	10.2	2.0	13.4	10.5	14.1	11.1
FWHM (eV)	1.2	1.2	1.4	1.4	1.8	1.2	1.2	1.9	1.9
H-Ti@IrO_x-air-5 h									
BE (eV)	61.7	64.8	62.9	66.0	68.9	62.2	65.3	63.9	67.1
Area (%)	18.4	14.5	10.8	8.5	1.3	12.7	10.1	13.2	10.5

FWHM (eV)	1.1	1.1	1.2	1.2	1.5	1.1	1.1	1.8	1.8

BE: binding energy; FWHM: full width at half maximum.

The OER activity of H-Ti@IrO_x with different IrO_x loading densities was first assessed at room temperature in 0.5 M H_2SO_4 (pH = 0.3), and H-Ti@IrO_x loaded with 0.25 mg cm^{-2} IrO_x was found to outperform all others under the same testing conditions in terms of not only the apparent catalytic activity but also the Ir-mass based activity and the intrinsic specific activity obtained through normalizing the catalytic current with the electrocatalytically active surface area, *i.e.*, ECSA (**Figures 3.11–13**). Therefore, the H-Ti@IrO_x-0.25 mg cm^{-2} sample (denoted as H-Ti@IrO_x for simplicity hereafter) was used in further investigation and comparison with other control catalysts.

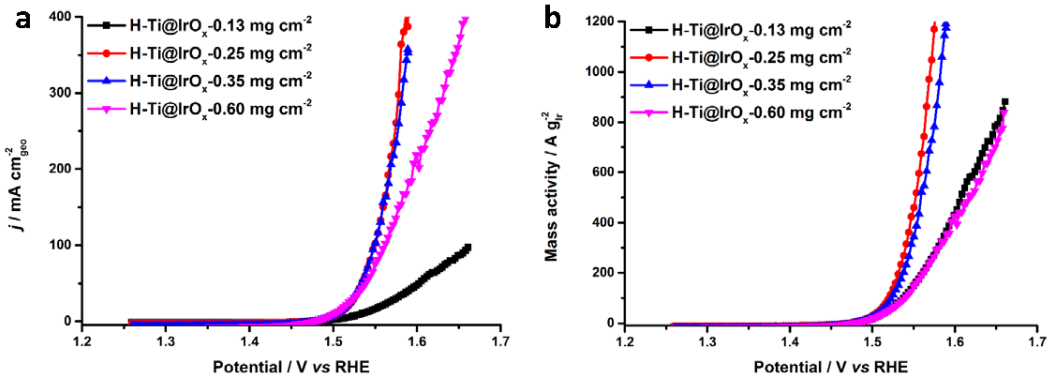

Figure 3.11 a) *iR*-corrected polarization curves and b) mass activity of H-Ti@IrO_x with different IrO_x loading densities, recorded at a scan rates of 5 mV s^{-1}. The H-Ti@IrO_x-0.25 mg cm^{-2} (denoted as H-Ti@IrO_x in the main text for simplicity) shows the best apparent and mass activities and therefore was used in further investigation and the comparison with other control catalysts.

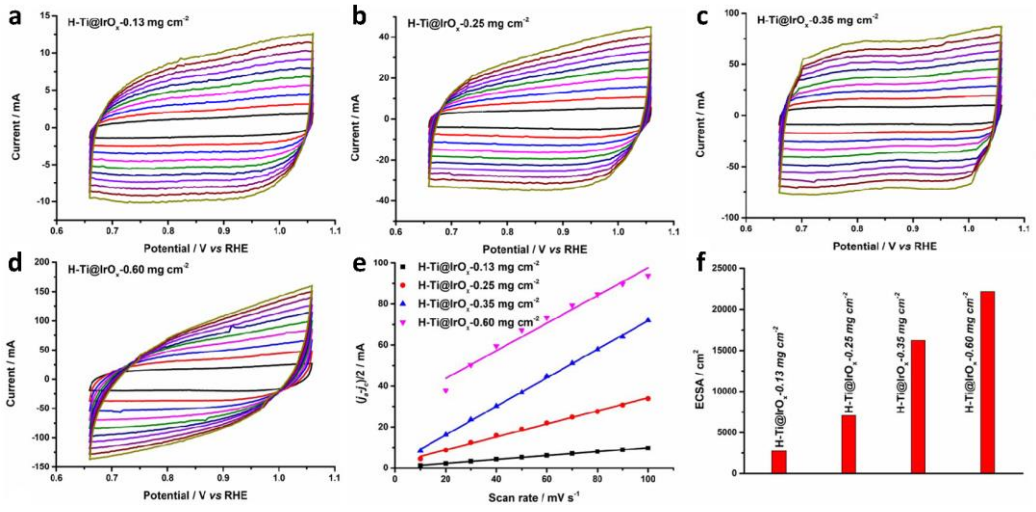

Figure 3.12 Electrochemical CV curves of a) H-Ti@IrO_x-0.13 mg cm^{-2}, b) H-Ti@IrO_x-0.25 mg cm^{-2}, c) H-Ti@IrO_x-0.35 mg cm^{-2} and d) H-Ti@IrO_x-0.60 mg cm^{-2}, recorded at different scan rates of 10, 20, 30, 40, 50, 60, 70, 80, 90 and 100 mV s^{-1}. e) Plots of the capacitive currents as a function of the scan rate for all the catalysts. f) ECSA of all the catalysts.

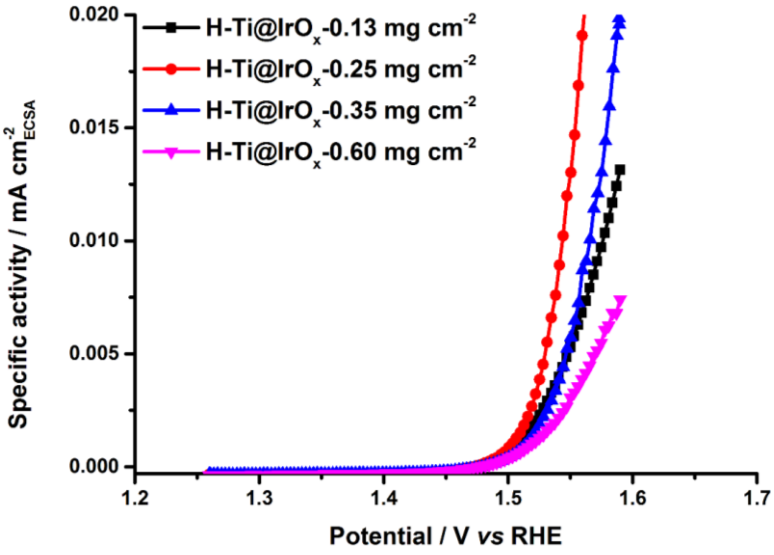

Figure 3.13 Specific activity H-Ti@IrO_x with different IrO_x loading densities, recorded at a scan rates of 5 mV s^{-1}.

Figure 3.14a shows the polarization curves of H-Ti@IrO_x and control catalysts including P-Ti@IrO_x, C@IrO_x, and commercial IrO_2, which were recorded in 0.5 M H_2SO_4 at a scan rate of 5 mV s^{-1}. The H-Ti foam subjected to thermal annealing treatment the same as that for preparing H-Ti@IrO_x does not show appreciable anodic current density (**Figure 3.15**). Upon loading IrO_x, the OER catalytic current density of H-Ti@IrO_x is significantly enhanced. The H-Ti@IrO_x can deliver geometric current densities of 10, 100, and 200 mA cm_{geo}^{-2} at low overpotentials (η) of 277, 318 and 336 mV, respectively (**Figure 3.14a**), remarkably lower than those of P-Ti@IrO_x (η_{10} = 343 mV), C@IrO_x (η_{10} = 328 mV), and commercial IrO_2 (η_{10} = 556 mV), even if the loading densities of iridium oxide are similar to or lower than these control catalysts (0.39 mg cm^{-2} for P-Ti@IrO_x, 0.24 mg cm^{-2} for C@IrO_x, and 0.39 mg cm^{-2} for commercial IrO_2 particles).

To assess the intrinsic catalytic performance, the ECSA-normalized specific activities of H-Ti@IrO_x and other control catalysts, which reflect the reactivity of each active site, were calculated and compared. The ECSA was obtained by cyclic voltammetry measurements in the non-faradaic potential region (see **Experimental** details), and it shows the following order: H-Ti@IrO_x (7086 $cm_{catalyst}^2$) > C@IrO_x (828 $cm_{catalyst}^2$) > P-Ti@IrO_x (357 $cm_{catalyst}^2$) > commercial IrO_2 (37 $cm_{catalyst}^2$), as revealed in **Figure 3.16**. The exceptionally high ECSA of H-Ti@IrO_x may result, on the one hand, from the ultra-small size feature of IrO_x nanoclusters and ultra-high specific surface area of the PHT NW support, and on the other hand, likely from the high number of oxygen defects in H-Ti@IrO_x [23]. Despite the exceptionally high surface area, after normalization the H-Ti@IrO_x catalyst still exhibits a higher specific activity, able to deliver 0.04 mA $cm_{catalyst}^{-2}$

at η = 350 mV (**Figure 3.14b**), 2.4, 2.0 and 6.5 times more active than P-Ti@IrO_x, C@IrO_x, and commercial IrO_2, respectively.

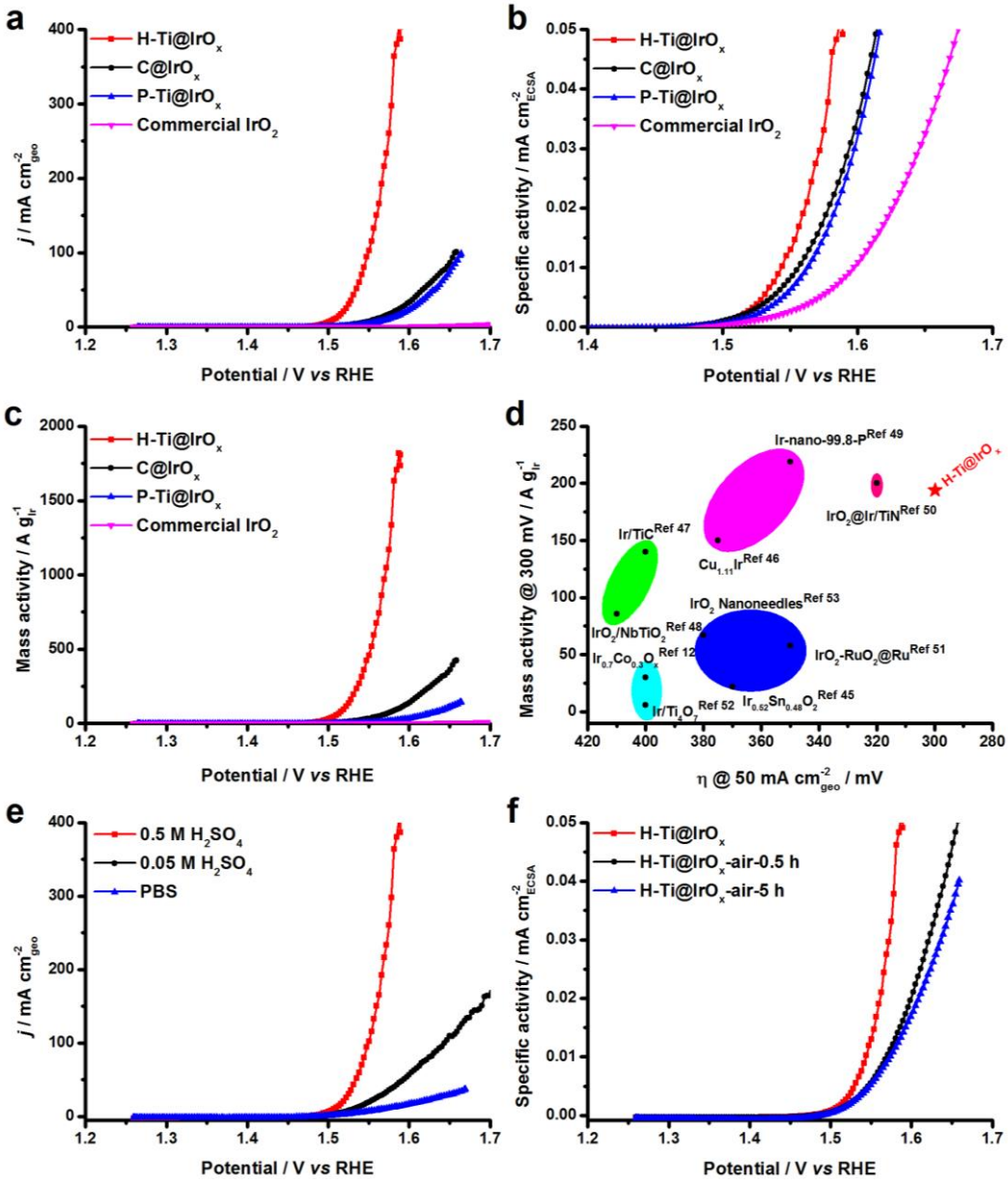

Figure 3.14 OER performance of H-Ti@IrO_x and other control catalysts. a) *iR*-corrected polarization curves of H-Ti@IrO_x, C@IrO_x, P-Ti@IrO_x and commercial IrO_2 catalysts, recorded at a scan rate of 5 mV s^{-1} in 0.5 M H_2SO_4. b) Specific activities and c) mass activities of H-Ti@IrO_x, C@IrO_x, P-Ti@IrO_x and commercial IrO_2 catalysts in 0.5 M H_2SO_4. d) Comparison of the OER performance of H-Ti@IrO_x catalysts to that of other state-of-the-art OER catalysts. e) *iR*-corrected polarization curves of H-Ti@IrO_x catalysts, recorded at a scan rate of 5 mV s^{-1} in electrolytes with different pH values. f) Specific activities of H-Ti@IrO_x, H-Ti@IrO_x-air-0.5 h and H-Ti@IrO_x-air-5 h in 0.5 M H_2SO_4.

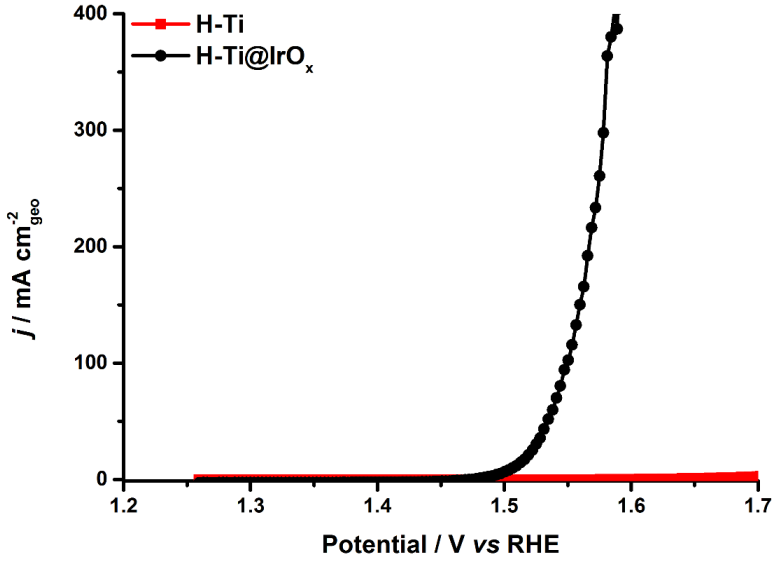

Figure 3.15 *iR*-corrected polarization curve of the porous H-Ti foam after the annealing process, recorded in 0.5 M H_2SO_4 at a scan rate of 5 mV s^{-1}.

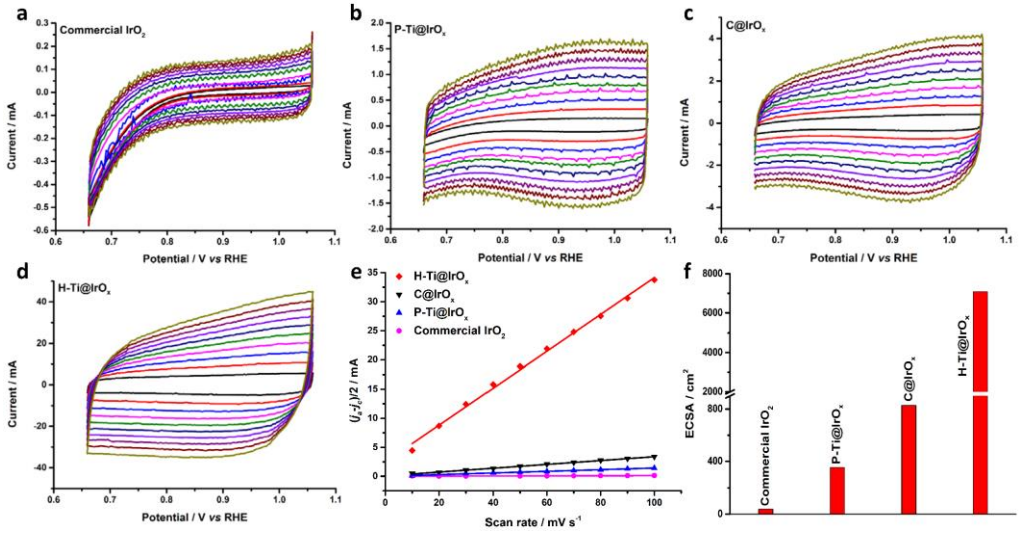

Figure 3.16 Electrochemical CV curves of a) commercial IrO_2, b) P-Ti@IrO_x, c) C@IrO_x and d) H-Ti@IrO_x, recorded at different scan rates of 10, 20, 30, 40, 50, 60, 70, 80, 90 and 100 mV s^{-1}. e) Plots of the capacitive currents as a function of the scan rate for all the catalysts. f) ECSA of all the catalysts.

The mass activities of all catalysts, an important consideration for practical applications, were also calculated and are compared in **Figure 3.14c**. The H-Ti@IrO_x catalyst outperforms all control catalysts, capable of delivering a mass activity as high as 1500 A g_{Ir}^{-1} at η = 350 mV, which is 20, 89 and 2041 higher than that of C@IrO_x, P-Ti@IrO_x and commercial IrO_2, respectively. The mass activity of H-Ti@IrO_x is also higher than that of commercial Ir-based catalysts from different industrial suppliers [43]. To better reflect the utilization of precious Ir, the mass activity of H-Ti@IrO_x at η = 300 mV is further plotted against the apparent catalytic activity η_{50} and compared to that of

previously reported state-of-the-art Ir-based catalysts, as shown in **Figure 3.14d**. An optimal catalyst should show both high apparent activity (*i.e.*, low overpotential at a given current density) and high mass activity, namely, utilization of the minimum possible precious metal(s) without sacrificing the apparent catalytic current density (positioned in the upper right region in **Figure 3.14d**) [14, 44]. In this respect, our H-Ti@IrO_x catalyst indeed outperforms many other Ir-based OER catalysts [12, 45-53], indicating that the Ir in H-Ti@IrO_x is optimally utilized.

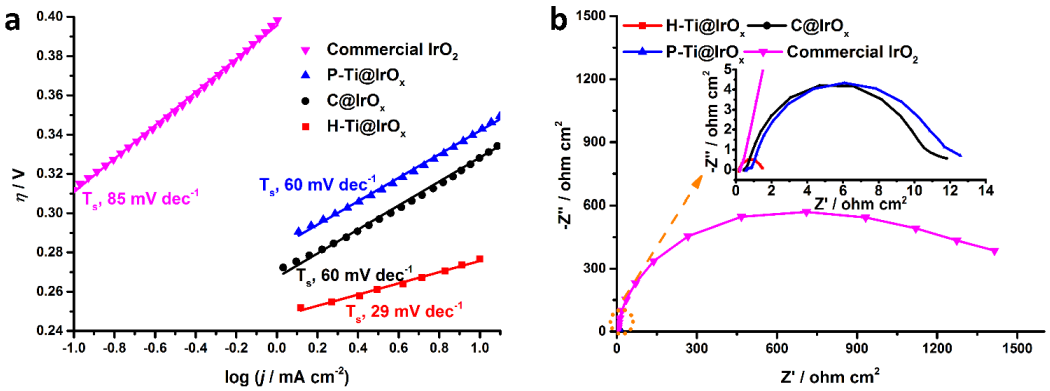

Figure 3.17 a) Tafel plots and b) Nyquist plots measured at 1.51 V vs. RHE of all catalysts.

The reaction kinetics of all catalysts was studied by Tafel analysis. As shown in **Figure 3.17a**, the H-Ti@IrO_x catalyst exhibits a small Tafel slope of 29 mV dec^{-1}, which is markedly smaller than that of C@IrO_x (60 mV dec^{-1}), P-Ti@IrO_x (60 mV dec^{-1}) and commercial IrO_2 (85 mV dec^{-1}), indicating more favorable OER kinetics. The electrochemical impedance spectroscopy (EIS) measurements also confirmed the fast reaction rate of H-Ti@IrO_x for the OER, as evidenced by its much smaller charge transfer resistance (R_{ct}) than that of other control catalysts (**Figure 3.17b**). It is hypothesized that the oxygen defects might give rise to reactive oxygen species such as O^{I-} reported by Schlögl and co-workers [41, 42, 54], the electrophilic nature of which would help accelerate the formation of the OOH intermediates, leading to fast OER kinetics [54].

Given the corrosive nature of strong acids, it is preferable to perform PEMWE in weak acids or environmentally more friendly neutral media. However, developing OER electrocatalysts active in weak acids and neutral solutions remains a great challenge [2]. We have tested the OER performance of H-Ti@IrO_x in 0.05 M H_2SO_4 and phosphate buffered saline (PBS) solution (pH = 7.2), respectively. Interestingly, H-Ti@IrO_x likewise exhibits very good OER activity in these electrolytes (**Figure 3.14e**). For instance, it only needs an overpotential of 414 mV to generate a high catalytic current density of 100 mA

cm^{-2} in 0.05 M H_2SO_4. Furthermore, in PBS electrolyte it can deliver 10 mA cm^{-2} at a low overpotential of 339 mV, showing substantial promise for use in PEMWE in neutral solutions.

We hypothesize that the content of oxygen-defective sites in the H-Ti@IrO_x catalysts may play an important role in their outstanding OER performance. To validate this hypothesis, we managed to anneal H-Ti@IrO_x in air for 0.5 and 5 h (denoted as H-Ti@IrO_x-air-0.5 h and H-Ti@IrO_x-air-5 h, respectively). XPS analyses proved that the content of oxygen-defective sites was decreased to 32.6% and 27.0% for H-Ti@IrO_x-air-0.5 h and H-Ti@IrO_x-air-5 h, respectively, from the initial 37.0%, and meanwhile, the ratio of Ir^{III}/Ir^{IV} in the catalysts decreased accordingly (**Figure 3.18**, **Tables 3.1** and **3.2**). Moreover, the ECSA of thermally annealed H-Ti@IrO_x was remarkably reduced as well (**Figure 3.19a–c**). Accordingly, the apparent catalytic activities of H-Ti@IrO_x-air-0.5 h and H-Ti@IrO_x-air-5 h become poorer, and larger overpotentials of 372 and 381 mV are needed to afford 100 mA cm^{-2} for H-Ti@IrO_x-air-0.5 h and H-Ti@IrO_x-air-5 h, respectively (**Figure 3.19d**). Furthermore, the specific activity of H-Ti@IrO_x becomes deteriorated upon thermal annealing (**Figure 3.14f**), which suggests that the intrinsic catalytic performance of H-Ti@IrO_x is indeed closely related to the content of oxygen-defective sites in IrO_x.

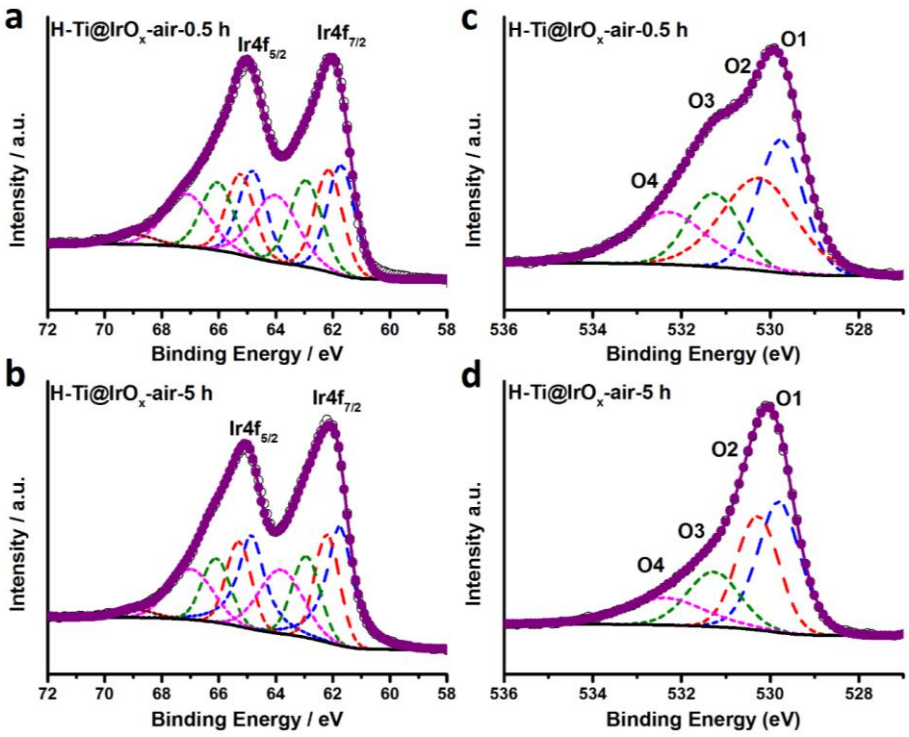

Figure 3.18 High resolution a, b) Ir 4f and c, d) O 1s spectra of H-Ti@IrO_x-air-0.5 h and H-Ti@IrO_x-air-5 h. (Blue and red curves represent Ir^{IV} and Ir^{III}, respectively; olive, wine and orange curves represent Ir^{IV} satellite 1, satellite 2 and Ir^{III} satellite, respectively.)

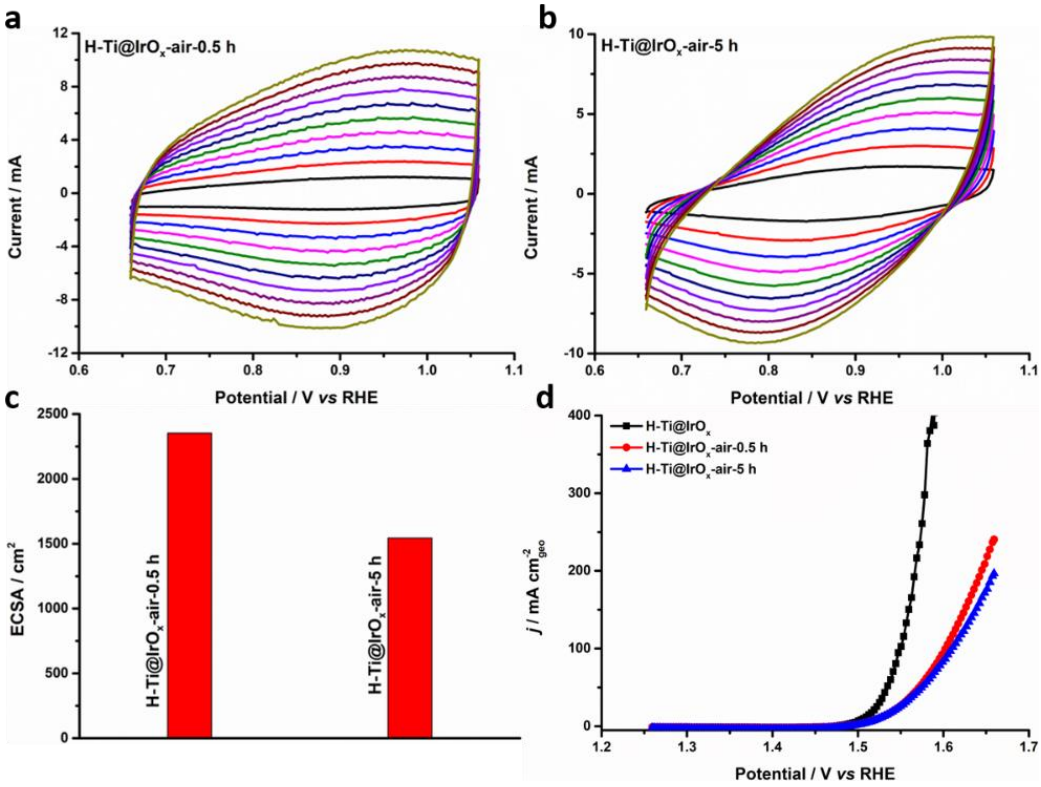

Figure 3.19 Electrochemical CV curves of a) H-Ti@IrO$_x$-air-0.5 h and b) H-Ti@IrO$_x$-air-5 h, recorded at different scan rates of 10, 20, 30, 40, 50, 60, 70, 80, 90 and 100 mV s^{-1} in the non-Faradaic potential region. c) ECSA of H-Ti@IrO$_x$-air-0.5 h and H-Ti@IrO$_x$-air-5 h. d) *iR*-corrected polarization curves of H-Ti@IrO$_x$, H-Ti@IrO$_x$-air-0.5 h and H-Ti@IrO$_x$-air-5 h, recorded at a scan rates of 5 mV s^{-1}.

Density functional theory (DFT) calculations were performed to gain further insight into the role of oxygen defects in promoting the OER performance. The (110) facet of the tetragonal (rutile-phase) IrO_2 without (perfect IrO_2, denoted as p-IrO_2) and with oxygen defects (*i.e.*, IrO_x) was used as a model surface, in accordance with the previous reports [55-57]. **Figure 3.20a** shows the reaction steps during the OER with the related oxygenated intermediates of OH*, O*, OOH* and OO*, based on the conventional adsorbate evolution mechanism (AEM). To study how the number of oxygen defects influences the catalytic performance, IrO_x models with a single oxygen-defective site at five possible sites (denoted as mono-IrO_x, **Figure 3.21**) and with double oxygen-defective sites at seven possible sites (denoted as bi-IrO_x, **Figure 3.22**) were developed and the thermodynamically most stable models were identified (**Figures 3.21** and **3.22**). The OER Gibbs free energy diagrams of p-IrO_2, mono-IrO_x, and bi-IrO_x were calculated at a potential of U = 1.50 V based on the optimized models (**Figure 3.20b–d**). For p-IrO_2 and mono-IrO_x, the calculations reveal that the last elementary reaction step (OO* → O_2↑ + *) is the rate determining step (RDS), and the energy barrier (2.23 eV) is significantly higher for the Ir site in p-IrO_2 (labelled with a light blue circle in **Figure 3.20b**,

inset) than that (1.21 eV) for the Ir site in mono-IrO_x (labelled with a light blue circle in **Figure 3.20c**, inset). This indicates that introducing an oxygen-defective site into IrO_x indeed decreases the energy barrier in the RDS and enhances the OER activity. Interestingly, for bi-IrO_x the RDS has been altered to the second elementary step (OH* → O* + H^+ + e^-) with a much lower energy barrier of 0.51 eV, suggesting that the OER activity is further improved as the number of oxygen defects increases. The Gibbs energy calculations agree well with the experimental observation where the intrinsic OER activity increases with the increasing content of oxygen defects (**Figures 3.14b** and **f**). It is worth noting that the same trend is also valid for the Gibbs free energy diagrams calculated at U = 1.23 V (**Figure 3.23**).

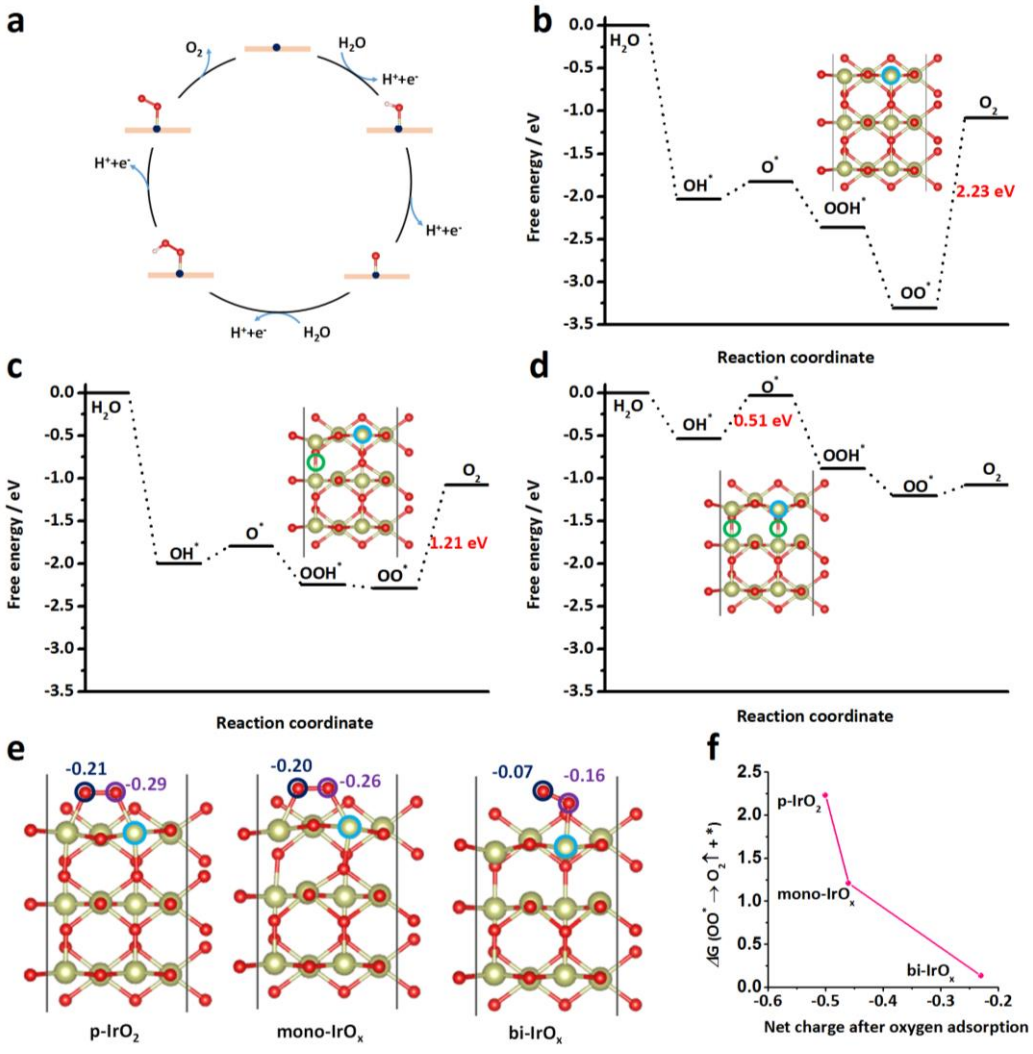

Figure 3.20 a) The proposed 4e^- OER mechanism in the present work. Calculated Gibbs free-energy diagrams for the OER on b) p-IrO_2, c) mono-IrO_x and d) bi-IrO_x at U = 1.50 V. The inset shows the corresponding calculation model of each catalyst. The catalyst models of mono-IrO_x and bi-IrO_x are the optimized ones. e) Net charge analysis of oxygen atoms adsorbed on p-IrO_2 (left), mono-IrO_x (middle) and bi-IrO_x (right). f) The net charge relative to the Gibbs energy barrier of the oxygen desorption step in p-IrO_2, mono-IrO_x and bi-IrO_x. The yellow and red spheres represent Ir and O atoms, respectively, in all models. The active site, oxygen-defective site and adsorbed oxygen atoms are labelled with light blue, green, violet and navy circles in the each model used for calculation.

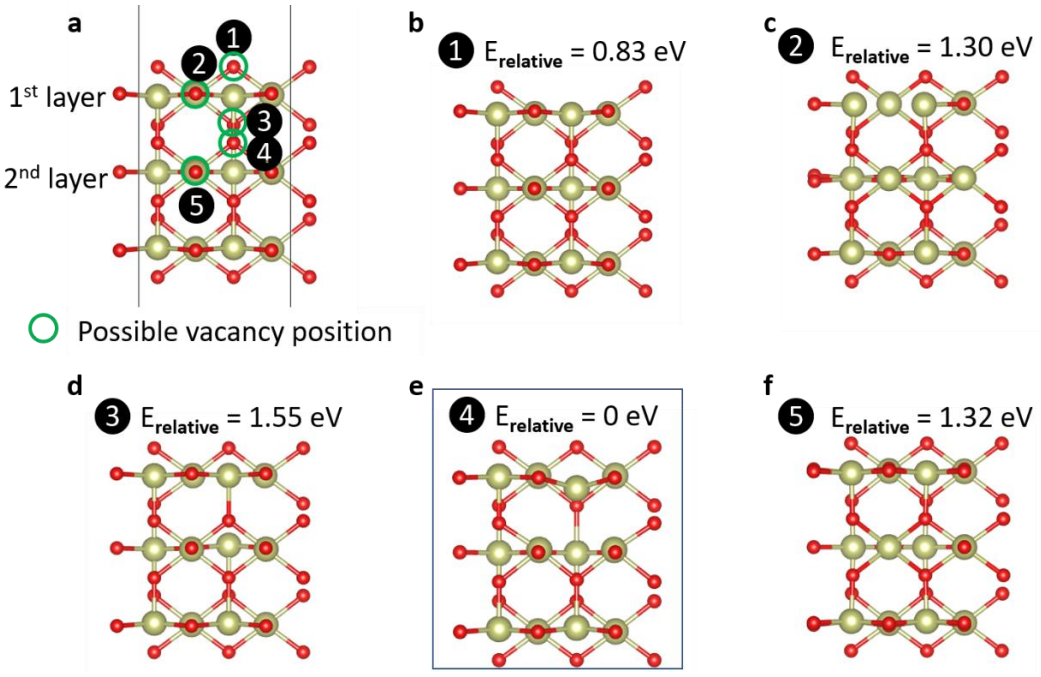

Figure 3.21 a) The five possible oxygen-defective sites introduced on the (110) surface of mono-IrO_x, as indicated by green circles. Yellow and red spheres represent Ir and O atoms, respectively. b-f) mono-IrO_x with an oxygen-defective site at different sites and the relative energy of different models. The relative energy is the difference between the energy of the current structure and the energy of the optimal structure (configuration 4).

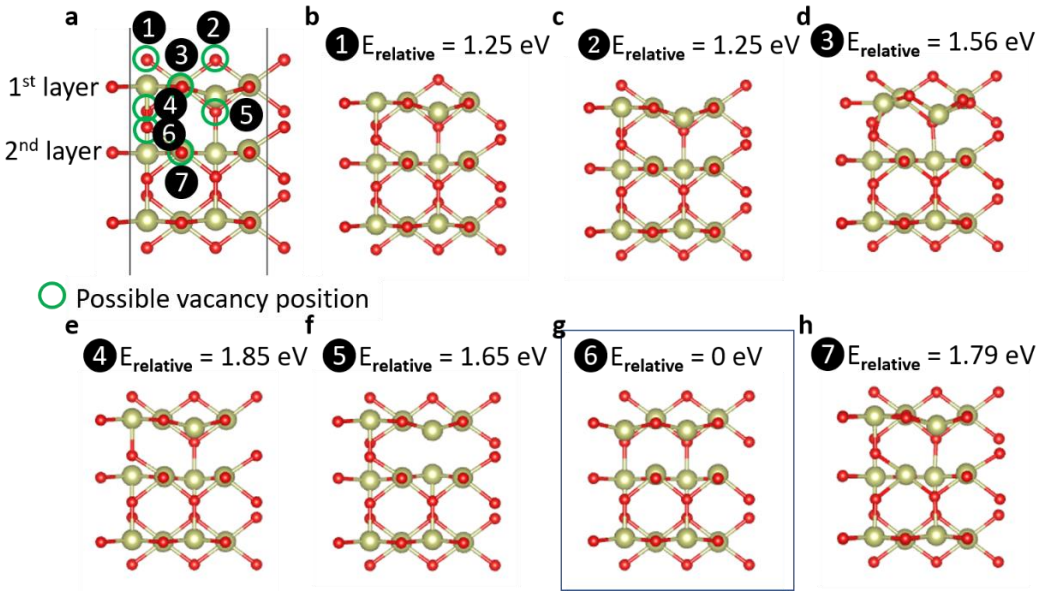

Figure 3.22 a) The seven possible oxygen-defective sites introduced on the (110) surface of bi-IrO_x, as indicated by green circles. Yellow and red spheres represent Ir and O atoms, respectively. b-h) bi-IrO_x with two oxygen-defective sites at different sites and the relative energy of different models. The relative energy is the difference between the energy of the current structure and the energy of the optimal structure (configuration 6).

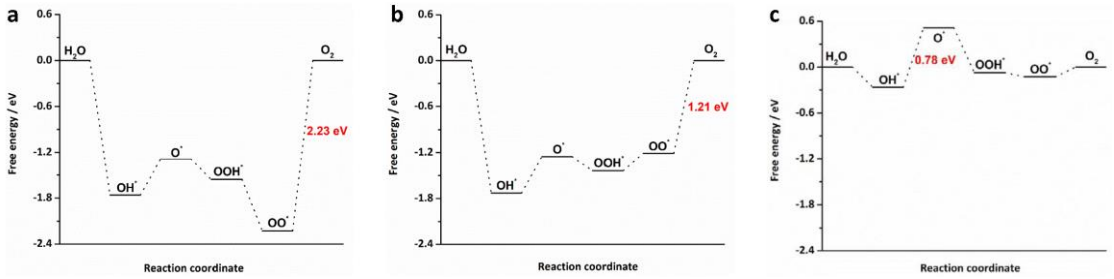

Figure 3.23 Gibbs free-energy diagrams for the OER on a) p-IrO_2, b) mono-IrO_x and c) bi-IrO_x calculated at U = 1.23 V based on the adsorbate evolution mechanism (AEM).

To further scrutinize the oxygen defect induced enhancement in OER performance, the optimal adsorption structures of all reaction intermediates were identified and the binding energy of the reaction intermediates to the model catalysts was calculated. As shown in **Figure 3.24a**, all the reaction intermediates bind strongly to the p-IrO_2 surface, which causes high energy barriers for the OER [55]. Incorporation of an oxygen-defective site (*i.e.*, mono-IrO_x) weakens the binding of all intermediates to IrO_x, especially that of the adsorbed oxygen atoms (**Figure 3.24b**), thus decreasing the energy barrier of the RDS (OO* → O_2↑ + *). Incorporating one more oxygen-defective site further reduces the binding energy of OO*, and the oxygen desorption step is not the RDS any more in bi-IrO_x; moreover, the energy barrier of the RDS in bi-IrO_x markedly diminishes due to the optimized adsorption of all reaction intermediates (**Figure 3.24c**). All these results suggest that the enhanced OER performance could be largely attributed to the decreased binding energy of reaction intermediates to the catalyst as the oxygen defects are introduced.

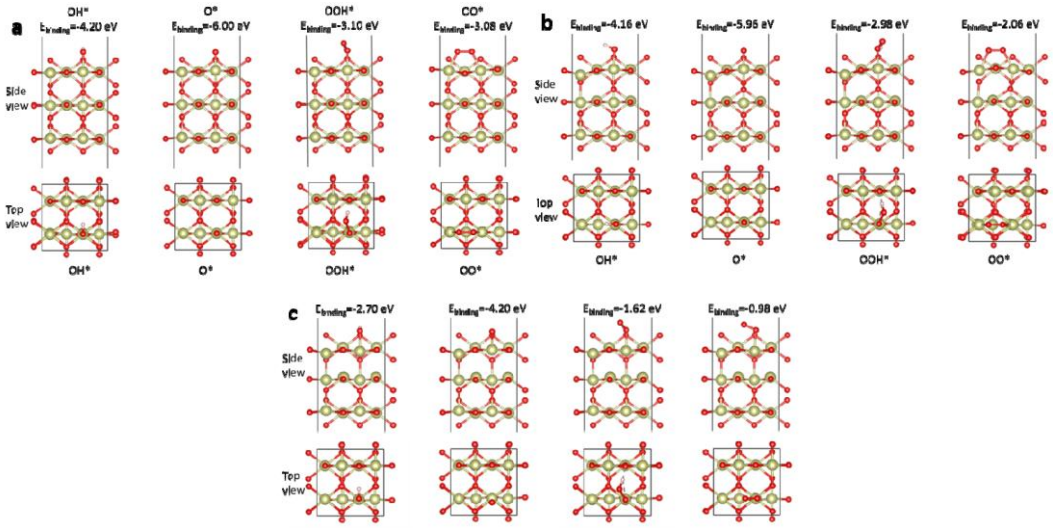

Figure 3.24 Optimized geometry of adsorption structure of OH, O, OOH and OO intermediates with the corresponding binding energy on a) p-IrO_2, b) mono-IrO_x and c) bi-IrO_x. Yellow, red and white spheres represent Ir, O and H atoms, respectively.

Furthermore, the net charge induced by the adsorbed oxygen atoms at the Ir site was calculated and compared (**Figure 3.20e**). The net charge is −0.46 e in mono-IrO_x, lower than that of −0.50 e in p-IrO_2, which implies that the oxygen adsorption is weakened around the Ir site, and accordingly, the energy barrier of the RDS is reduced and the OER performance is promoted (**Figure 3.20f**). The net charge further decreases to −0.23 e in bi-IrO_x, and in this case, the oxygen molecule release step (OO* → O_2↑ + *) shows an even lower energy barrier (**Figure 3.20f**). Meanwhile, the partial density of states (PDOS) calculations reveal markedly reduced overlay of the Ir d-orbital and O p-orbital in defect-rich catalysts (**Figure 3.25**), corroborating the decreased adsorption of oxygen atoms in mono-IrO_x and bi-IrO_x.

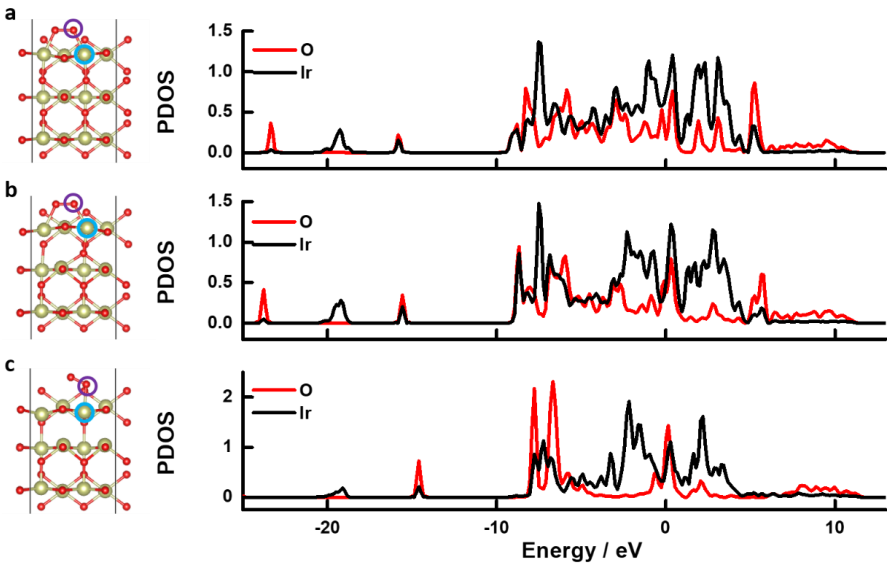

Figure 3.25 Calculated PDOS of a) p-IrO_2, b) mono-IrO_x and c) bi-IrO_x after oxygen atoms adsorption. The yellow and red spheres represent Ir and O atoms in all models. The active site and adsorbed oxygen atoms on the active site are labelled by light blue and violet circles, respectively, in the each calculation model.

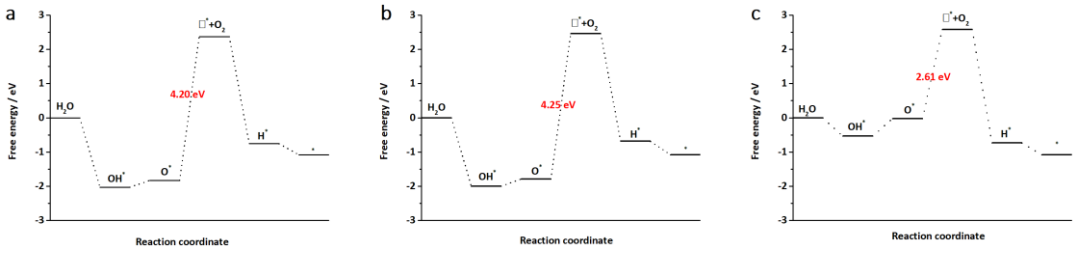

Figure 3.26 Gibbs free-energy diagrams for the OER on a) p-IrO_2, b) mono-IrO_x and c) bi-IrO_x calculated at U = 1.50 V based on the lattice oxygen mechanism (LOM).

While the above calculations are made based on the conventional adsorbate evolution mechanism, it was recently reported that the lattice oxygen may also participate in the OER generating oxygen through the lattice oxygen mechanism (LOM), especially

in hydrous IrO_x [10, 58, 59]. To assess to which degree the LOM would contribute to the OER, we calculated the Gibbs free energy of reaction intermediates on p-IrO_2, mono-IrO_x, and bi-IrO_x based on the LOM at U = 1.50 V (see **Experimental** details) [60]. As shown by the free energy diagrams (**Figure 3.26**), the energy barrier to overcome for the $O^* + O_{lat} \rightarrow O_2\uparrow + V_o$ step (RDS) for all model catalysts *via* the LOM, where O_{lat} and V_o represent the lattice oxygen and the oxygen vacancy (defect), respectively, is much higher than that of the RDS of the catalysts *via* the AEM (**Figures 3.20b–d**), suggesting that the desorption of the evolved oxygen from the catalyst lattice would be difficult and the OER on our IrO_x catalysts is unlikely to occur *via* the LOM. Our calculations are consistent with the recent theoretical research on the AEM and LOM of IrO_2, where oxygen-defective IrO_2 is demonstrated to be less LOM active than RuO_2 [60]. In fact, even for the previously reported electrodeposited hydrous IrO_x where the LOM works toward the OER, the contribution of oxygen evolution from the lattice oxygen is fairly small, compared to the oxygen evolved through the AEM [58].

Overall, our DFT calculations are in good agreement with the experimental data of OER tests (**Figure 3.14**), highlighting the prominent role of oxygen defects in the improvement of OER catalytic performance by weakening the binding of all intermediates to IrO_x. This is also consistent with previous studies on IrO_x [41, 42], in which “O holes” are proposed to contribute to higher catalytic activity.

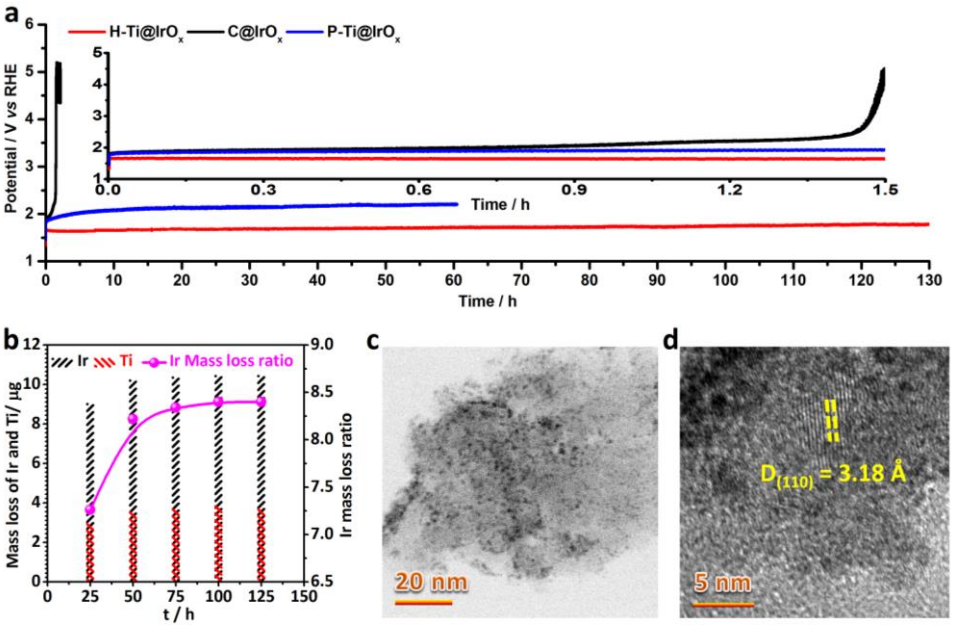

Figure 3.27 a) Chronopotentiometric curves of H-Ti@IrO_x and other control catalysts, recorded at a constant current density of 200 mA cm^{-2} in 0.5 M H_2SO_4. The inset shows the zoomed in view of the initial 1.5 h. b) ICP analysis of the dissolution of Ir and Ti in H-Ti@IrO_x during the OER electrolysis at 200 mA cm^{-2} after different time intervals. c) Low-magnification TEM image and d) HRTEM image of H-Ti@IrO_x after the extended stability test at 200 mA cm^{-2} for 130 h.

Stability is a critically important indicator of electrocatalysts for practical applications in water electrolyzers, especially in a strongly acidic environment. Many catalysts are subjected to fast dissolution and/or loss of active phases under corrosive and highly oxidative conditions, leading to poor stability of only a few hours [14, 15, 25-30, 57, 61]. We have examined the catalytic stability of H-Ti@IrO_x and other control catalysts in 0.5 M H_2SO_4 using chronopotentiometry (CP) at a large current density of 200 mA cm^{-2} relevant to practical applications. As illustrated in **Figure 3.27a**, C@IrO_x shows a gradual degradation initially and a sharp increase in potential when the OER is going on for only about 1.5 h (**Figure 3.27a**, inset). The failure might result from the significant corrosion of the carbon paper during the OER at a high current density, which led to the detachment of IrO_x nanoclusters from the carbon microfiber surface. This was confirmed by our energy-dispersive X-ray (EDX) spectroscopy, where it showed that *ca.* 82% of the initial Ir loading is lost after the stability test in only a short period of time (*i.e.*, 1.5 h, **Figure 3.28**). The Ir loss can be suppressed in case IrO_x is loaded on a corrosion-resistant, acid-stable support such as Ti foam, as verified by the stability test of P-Ti@IrO_x catalysts at 200 mA cm^{-2} for 60 h, where only 55% of the initial Ir got lost in 60 h (**Figure 3.29**). Compared to C@IrO_x and P-Ti@IrO_x, the H-Ti@IrO_x catalyst exhibited superior stability and was able to sustain at 200 mA cm^{-2} for continuous OER electrolysis of 130 h with minimal degradation. According to EDX analysis, merely 22% of the initial Ir is lost in this case (**Figure 3.30**). Meanwhile, the Ir dissolution in the electrolyte was monitored using inductively coupled plasma-optical emission spectroscopy (ICP-OES) (**Figure 3.27b**), where we found an Ir loss of only 8.4% after the stability test. The discrepancy in EDX and ICP results can be explained by the fact that some physically detached yet undissolved IrO_x nanoclusters cannot be detected by ICP [30]. We further examined the microstructure of H-Ti@IrO_x after the extended stability test at 200 mA cm^{-2}. Remarkably, a high density of uniformly distributed IrO_x nanoclusters with sizes of 1–2 nm still remained on the surface of PHT NWs and remained crystalline (**Figure 3.27c-d**). Furthermore, using XPS we investigated the chemical states of the H-Ti@IrO_x catalyst subjected to the extended stability test, and we found that both Ir 4f and O 1s spectra (**Figure 3.31**) show features pretty similar to those of freshly prepared H-Ti@IrO_x (**Figures 3.9a** and **3.10a**). All the above analyses verify that the corrosion-resistant H-Ti support (as proved by the trace amounts of Ti dissolution observed by ICP, **Figure 3.27b**) indeed substantially stabilizes IrO_x and significantly suppresses its loss under harsh conditions, thereby giving rise to excellent catalytic stability. Moreover, the stability number as a metric for electrocatalyst stability benchmarking is also calculated [59, 62], and our H-Ti@IrO_x catalysts show a stability number of 4.27×10^6, which is

much higher than that of IrO_x nanoparticles (5–6.5 × 10^4) [59], $SrCo_{0.9}Ir_{0.1}O_{3-\delta}$ (8 × 10^4) [62], Ba_2PrIrO_6 (0.7–2.5 × 10^4) [63], and comparable to that of crystalline IrO_2 (0.7–3 × 10^6) [59]. In fact, with a higher IrO_x loading density (*e.g.*, H-Ti@IrO_x-0.60 mg cm^{-2}), the H-Ti@IrO_x can survive for a significantly longer period of time (above 500 h) at 200 mA cm^{-2} (**Figure 3.32**), even though the catalytic activity is compromised a bit. In addition, the faradaic efficiency of O_2 evolution by H-Ti@IrO_x was measured (**Figure 3.33**). The volume of O_2 detected matches well with that calculated, indicating a nearly 100% faradaic efficiency in the process of the OER.

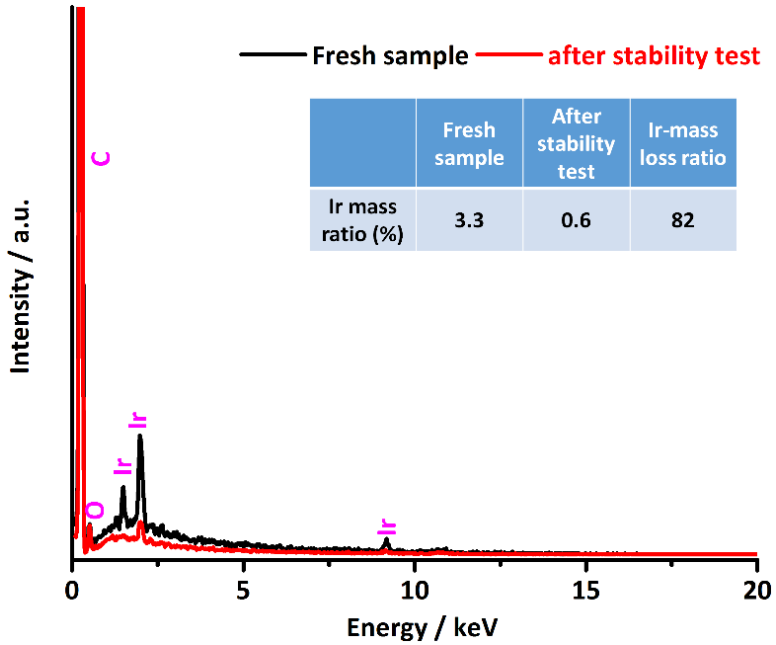

Figure 3.28 EDX spectra of C@IrO_x before and after the stability test at 200 mA cm^{-2} for 1.5 h, showing that ca. 82 % of initial IrO_x has lost during the stability test.

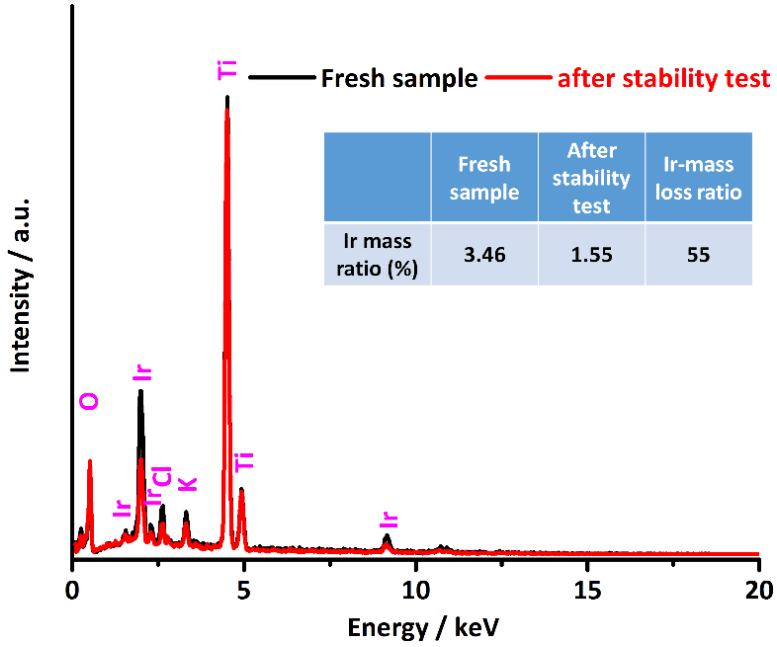

	Fresh sample	After stability test	Ir-mass loss ratio
Ir mass ratio (%)	3.46	1.55	55

Figure 3.29 EDX spectra of P-Ti@IrO_x before and after the extended stability test at 200 mA cm^{-2} for 60 h, showing that ca. 55 % of initial IrO_x has lost during the stability test.

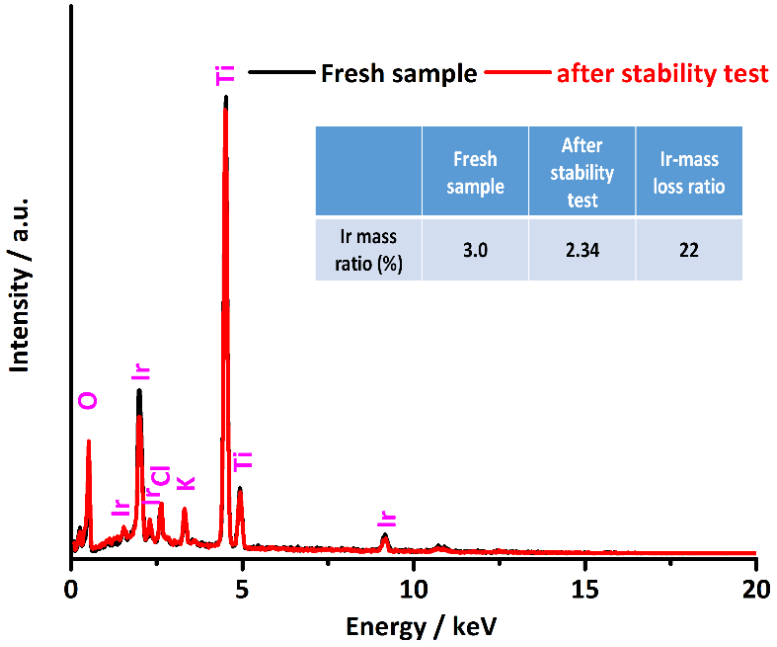

	Fresh sample	After stability test	Ir-mass loss ratio
Ir mass ratio (%)	3.0	2.34	22

Figure 3.30 EDX spectra of H-Ti@IrO_x before and after the extended stability test at 200 mA cm^{-2} for 130 h, showing that only ca. 22 % of initial IrO_x lost during the stability test.

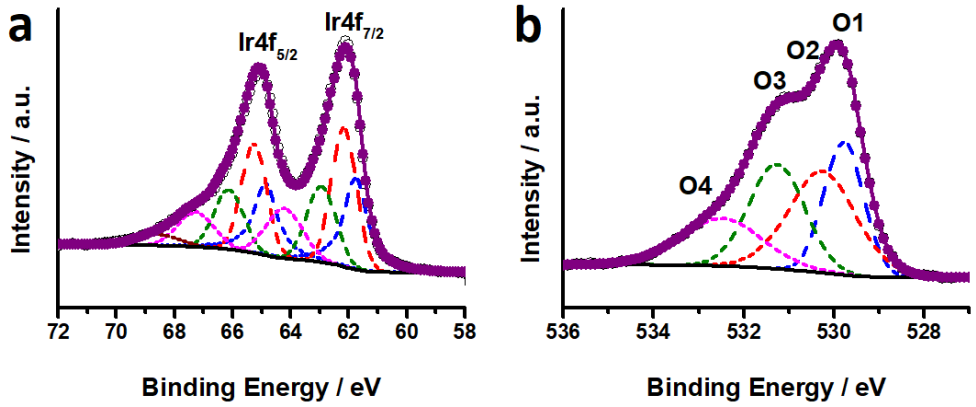

Figure 3.31 a) Ir 4f (Blue and red curves represent Ir^{IV} and Ir^{III}, respectively; olive, wine and orange curves represent Ir^{IV} satellite 1, satellite 2 and Ir^{III} satellite, respectively). b) O 1s spectra of H-Ti@IrO_x after the extended stability test at 200 mA cm^{-2} for 130 h.

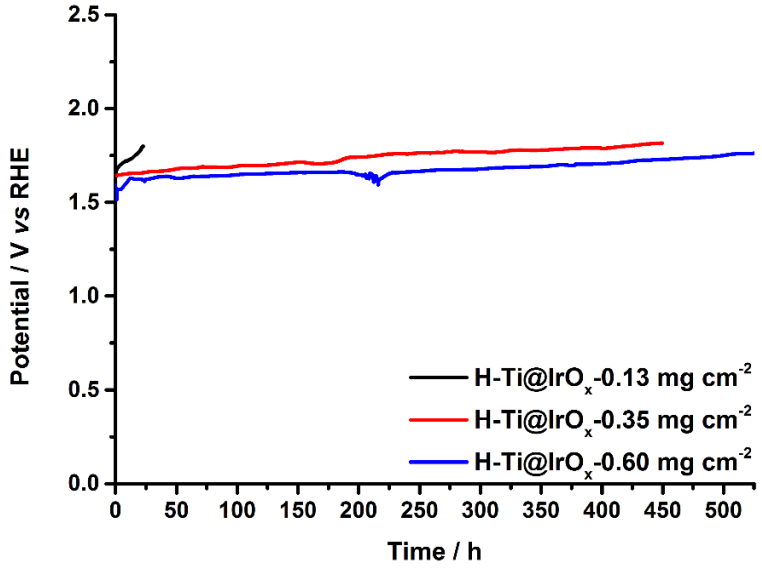

Figure 3.32 Chronopotentiometric curves recorded at a constant current density of 200 mA cm^{-2} for H-Ti@IrO_x-0.13 mg cm^{-2}, H-Ti@IrO_x-0.35 mg cm^{-2} and H-Ti@IrO_x-0.60 mg cm^{-2}.

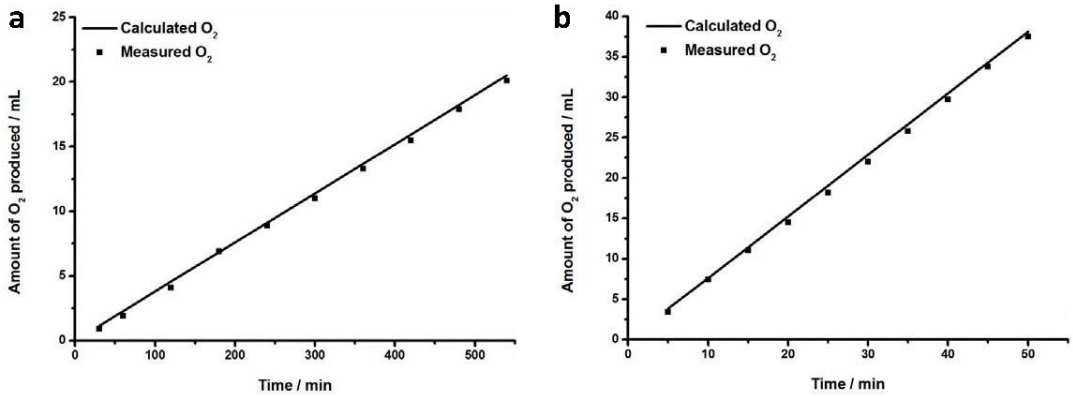

Figure 3.33 Experimentally measured and calculated volumes of O_2 gas evolved from H-Ti@IrO_x at a fixed current density of a) 10 mA cm^{-2} and b) 200 mA cm^{-2}. Electrolyte: 0.5 M H_2SO_4.

3.3 Conclusions

In summary, we have deposited ultrafine oxygen-defective iridium oxide nanoclusters on a hydrothermally treated, high-surface-area, acid-stable porous titanium current collector, using a repetitive impregnation–annealing process. Benefiting from the large electrocatalytically accessible surface area and intrinsically high activity arising from the oxygen defects, the obtained H-Ti@IrO_x electrode exhibits excellent apparent, specific, and mass activities for the OER in both acidic and neutral electrolytes, outperforming most of the Ir-based OER catalysts reported before. Comprehensive experimental and theoretical studies confirm that oxygen defects play an important role in the enhanced OER performance. More importantly, we demonstrate that the H-Ti@IrO_x electrode can sustain continuous acidic OER electrolysis at a high current density of 200 mA cm^{-2} for 130 hours without notable degradation, and increasing IrO_x loading to a certain level allows the electrode to catalyze the OER at such a high current density over 500 hours with little performance decay. Given the simplicity of the fabrication procedures and the high mass activity and excellent long-term stability, the porous titanium foam loaded with ultrafine oxygen-defective iridium oxide nanoclusters holds substantial promise for use as a high-performance anode in proton exchange membrane water electrolyzers.

3.4 Experimental section

Reagents: All reagents were used as received without further purification. Ti foam was purchased from Xiamen Tmax Battery Equipments Limited. China. Nafion® perfluorinated resin solution (5 wt %) were purchased from Sigma-Aldrich. Potassium hydroxide (KOH), Iridium(III) chloride hydrate ($IrCl_3 \cdot x\ H_2O$) and IrO_2 powders were acquired from Alfa Aesar.

Synthesis of H-Ti foam: The H-Ti foam was prepared using a hydrothermal method similar to that reported previously with some modification [64]. In a typical procedure, a piece of Ti foam was cleaned by ultra-sonication in acetone, ethanol and deionized (DI) water for 30 min each time, and then dried under vacuum at 70 °C. The dried Ti foam (1 × 1 cm^2) was then immersed into 20 mL of 10 M KOH solution in a Teflon-lined stainless steel autoclave. The autoclave was sealed, heated up to 90 °C, and maintained at this temperature for 6 h in an oven. After cooling down to room temperature naturally, the obtained H-Ti foam was washed with DI water several times and dried under vacuum at 70 °C for further use [65].

Oxidization of carbon paper: The oxidation of carbon paper was conducted using a mixed acid solution as described in our previous work with some modification [66]. Typically, a piece of carbon paper (1 × 1 cm^2) was immersed in a mixed solution of sulfuric acid, nitric acid and water (v(98% H_2SO_4):v(70% HNO_3):v(H_2O) = 1:1:1) at 70 ^oC for 2 h under vigorous magnetic stirring. The obtained carbon paper was washed with DI water several times and dried under vacuum at 70 ^oC for further use.

Synthesis of H-Ti@IrO_x: To load IrO_x on H-Ti foam, 89.6 mg of $IrCl_3 \cdot xH_2O$ was firstly added to 3 mL of H_2O, and the solution was sonicated for 1 h to form 100 mM aqueous solution of $IrCl_3$. Then a piece of dried H-Ti foam (1 × 1 cm^2) was soaked in the $IrCl_3$ solution for 30 min to obtain H-Ti@$IrCl_3$. Afterwards, H-Ti@$IrCl_3$ was thermally annealed at 400 ^oC for 30 min in air [67, 68]. The loading density of IrO_x on H-Ti could be adjusted by repeating the above-mentioned soaking-annealing process, and 1 – 4 repeats gave rise to a loading density of 0.13, 0.25, 0.35, and 0.60 mg cm^{-2} (denoted as H-Ti@IrO_x-0.13 mg cm^{-2}, H-Ti@IrO_x-0.25 mg cm^{-2}, H-Ti@IrO_x-0.35 mg cm^{-2}, and H-Ti@IrO_x-0.60 mg cm^{-2}), respectively. According to the electrocatalytic tests, H-Ti@IrO_x-0.25 mg cm^{-2} showed the best catalytic performance for OER, and therefore most physicochemical characterization was carried out based on H-Ti@IrO_x-0.25 mg cm^{-2} (denoted as H-Ti@IrO_x in the main text for simplicity).

The C@IrO_x and P-Ti@IrO_x control samples were prepared according to the procedures similar to those described above with two soaking-annealing cycles. However, in these cases $IrCl_3$ precursor solution with a lower concentration (25 mM for C@IrO_x and 6.25 mM for P-Ti@IrO_x) was used. This led to an IrO_x loading density of 0.24 mg cm^{-2} for C@IrO_x and 0.39 mg cm^{-2} for P-Ti@IrO_x.

The IrO_x loading was measured using a high precision micro-balance (Sartorius, readability: 0.001 mg) by subtracting the mass of the catalyst support (H-Ti, P-Ti, or carbon paper) subjected to the annealing treatment under the same conditions as those for preparing the catalysts (H-Ti@IrO_x, P-Ti@IrO_x or C@IrO_x) from the mass of the final catalysts. Measurements from three batches of samples were carried out and an average value was used to denote the loading mass.

Materials characterization: XRD experiments were conducted on an X'Pert PRO diffractometer (PANalytical) set at 45 kV and 40 mA, using Cu *K*α radiation (λ = 1.541874 Å) and a PIXcel detector. Data were collected with the Bragg–Brentano configuration in the 2θ range of 30 – 100^o at a scan speed of 0.011^o s^{-1}. XPS characterization was carried out on an ESCALAB 250 instrument with Al *K*α X-rays (1486.6 eV). SEM examination

was performed on a FEI Quanta 650 FEG microscope equipped with INCA 350 spectrometer (Oxford Instruments) for EDX. TEM, HRTEM and EDX elemental mapping studies were conducted on a probe-corrected transmission electron microscope operating at 200 kV (FEI Themis 60-300). Raman spectroscopy examination was done on a confocal Raman spectrometer (Witec Alpha 300R). The mass loss of Ir and Ti was detected by the inductively coupled plasma – optical emission spectroscopy (ICP–OES, ICPE-9000 spectrometer, Shimadzu) after different time intervals. Electrolyte solution was sampled every 25 h during the stability test, and was filtrated prior to each ICP-OES analysis.

DFT calculations: Density functional theory calculations were performed using Vienna Ab-initio Simulation Package (VASP), with projector augmented wave (PAW) pseudopotential and Perdew–Burke–Ernzerhof (PBE) exchange-correlation functional [69-71]. A kinetic energy cut-off of 450 eV was adopted for the plane-wave expansion, and 5×5×1 K-point mesh was used. All structures were fully relaxed until the final energy and force on each atom were less than 10^{-5} eV and 0.02 eV $Å^{-1}$, respectively. Vacuum space above the IrO_2 (110) surface was kept to >15 Å. The overall OER likely proceeds through two pathways, namely the conventional adsorbate evolution mechanism (AEM) and the lattice oxygen mechanism (LOM), both including the following reaction steps [72]:

AEM – adsorbate evolution mechanism		LOM – lattice oxygen mechanism	
$H_2O\ (aq) + {}^* \rightarrow OH^* + e^- + H^+$	(1)	$H_2O\ (aq) + {}^* \rightarrow OH^* + e^- + H^+$	(1')
$OH^* \rightarrow O^* + e^- + H^+$	(2)	$OH^* \rightarrow O^* + e^- + H^+$	(2')
$O^* + H_2O\ (aq) \rightarrow OOH^* + e^- + H^+$	(3)	$O^* + O_{lat} \rightarrow O_2 \uparrow + V_o$	(3')
$OOH^* \rightarrow OO^* + e^- + H^+$	(4)	$V_o + H_2O\ (aq) \rightarrow H^* + e^- + H^+$	(4')
$OO^* \rightarrow {}^* + O_2 \uparrow$	(5)	$H^* \rightarrow {}^* + e^- + H^+$	(5')

where *, O_{lat}, V_o represent the Ir active site, lattice oxygen and lattice oxygen vacancy, respectively, and OH^*, O^*, OOH^*, OO^* and $H^*$are the intermediates absorbed on the active sites during the OER. The adsorption energy was calculated according to the formula $E_{ad} = E_{sys} - E_{sur} - E_{spe}$, in which E_{ad}, E_{sys}, E_{sur} and E_{spe} denote the adsorption energy, the energy of adsorption system, the energy of clean surface and the energy of isolated adsorption species. The Gibbs free energy changes of these steps were calculated as follows [73]:

AEM – adsorbate evolution mechanism	LOM – lattice oxygen mechanism

$\Delta G_1 = G(OH^*) - G(^*) - G(H_2O) + ½\ G(H_2(g)) - \lvert e\rvert U$ (6)	$\Delta G_1 = G(OH^*) - G(^*) - G(H_2O) + ½\ G(H_2(g)) - \lvert e\rvert U$ (6')
$\Delta G_2 = G(O^*) - G(OH^*) + ½\ G(H_2(g)) - \lvert e\rvert U$ (7)	$\Delta G_2 = G(O^*) - G(OH^*) + ½\ G(H_2(g)) - \lvert e\rvert U$ (7')
$\Delta G_3 = G(OOH^*) - G(O^*) - G(H_2O) + ½\ G(H_2(g)) - \lvert e\rvert U$(8)	$\Delta G_3 = G(O_2(g)) + G(V_o) - G(O^*) - G(O_{lat})$ (8')
$\Delta G_4 = G(OO^*) - G(OOH^*) + ½\ G(H_2(g)) - \lvert e\rvert U$ (9)	$\Delta G_4 = G(H^*) - G(V_o) - G(H_2O) + ½\ G(H_2(g)) - \lvert e\rvert U$ (9')
$\Delta G_5 = G(^*) + G(O_2(g)) - G(OO^*)$ (10)	$\Delta G_5 = G(^*) - G(H^*) + ½\ G(H_2(g)) - \lvert e\rvert U$ (10')

Electrode preparation and electrocatalytic tests: All the electrocatalytic tests were carried out in a three electrode configuration at room temperature using a Biologic VMP-3 potentiostat/galvanostat. The as-fabricated of H-Ti@IrO_x, C@IrO_x or P-Ti@IrO_x (1 × 1 cm^2) was directly used as the working electrode. A Pt wire and a saturated calomel electrode (SCE) were utilized as the counter and reference electrodes, respectively. The SCE reference was calibrated prior to each measurement in Ar/H_2-saturated 0.5 M H_2SO_4 solution using a clean Pt wire as the working electrode. Unless otherwise stated, all potentials are reported versus RHE by converting the measured potentials according to the following equation:

$$E_{RHE} = E_{SCE} + 0.059 \times pH + 0.241 \quad (11)$$

For commercial IrO_2 powders, the catalyst ink was prepared by ultrasonically dispersing 10 mg of IrO_2 into 950 µL of ethanol containing 50 µL of Nafion® solution. 30 µL of the catalyst ink was loaded on a piece of glassy carbon (GC) substrate (0.78 cm^2), leading to a catalyst loading density of 0.39 mg cm^{-2}. The electrode was then dried at room temperature naturally in air.

The apparent OER activity was appraised using cyclic voltammetry (CV) at a scan rate of 5 mV s^{-1}, and an *iR*-correction (85%) was applied to compensate for the voltage drop between the reference and working electrodes, which was measured by a single-point high-frequency impedance measurement. The reduction branches of the CV curves were used to compare the performance of all catalysts.

The ECSAs were estimated from the electrochemical double-layer capacitance of the catalytic surface. The double-layer capacitance (C_{dl}) of catalysts was derived by performing CV in the potential range of 0.66 to 1.06 V vs. RHE (non-Faradaic potential range) at different scan rates (v) of 10, 20, 30, 40, 50, 60, 70, 80, 90 and 100 mV s^{-1},

followed by extracting the slope from the resulting $|j_a-j_c|/2$ vs. v plots (j_a and j_c represent the anodic and cathodic current at 0.86 V vs. RHE). The ECSA can be then calculated by dividing the measured C_{dl} by the capacitance of a model catalyst over a unit surface area (0.04 mF cm_{geo}^{-2} for metal oxide) [74].

$$ECSA = C_{dl} / 0.04\ mF\ cm^{-2} \quad (12)$$

EIS measurements were carried out at 1.51 V vs. RHE in the frequency range of 10^5 to 0.01 Hz with a 10 mV sinusoidal perturbation. The stability of catalysts was assessed at a constant current density of 200 mA cm^{-2} using chronopotentiometry (CP).

3.5 References

[1] G.M. Wang, Y. Yang, D.D. Han, Y. Li, Oxygen defective metal oxides for energy conversion and storage. Nano Today 13 (2017) 23-39.

[2] N.T. Suen, S.F. Hung, Q. Quan, N. Zhang, Y.J. Xu, H.M. Chen, Electrocatalysis for the oxygen evolution reaction: recent development and future perspectives. Chem. Soc. Rev. 46 (2017) 337-365.

[3] W. Li, D.H. Xiong, X.F. Gao, L.F. Liu, The oxygen evolution reaction enabled by transition metal phosphide and chalcogenide pre-catalysts with dynamic changes. Chem. Commun. 55 (2019) 8744-8763.

[4] X.W. Li, X.G. Hao, A. Abudula, G.Q. Guan, Nanostructured catalysts for electrochemical water splitting: current state and prospects. J. Mater. Chem. A 4 (2016) 11973-12000.

[5] M. Carmo, D.L. Fritz, J. Mergel, D. Stolten, A comprehensive review on PEM water electrolysis. Int. J. Hydrog. Energy 38 (2013) 4901-4934.

[6] J.Y. Xu, D. Aili, Q.F. Li, E. Christensen, J.O. Jensen, W. Zhang, M.K. Hansen, G.Y. Liu, X.D. Wang, N.J. Bjerrum, Oxygen evolution catalysts on supports with a 3-D ordered array structure and intrinsic proton conductivity for proton exchange membrane steam electrolysis. Energy Environ. Sci. 7 (2014) 820-830.

[7] M. Bernt, H.A. Gasteiger, Influence of Ionomer Content in IrO_2/TiO_2 Electrodes on PEM Water Electrolyzer Performance. J. Electrochem. Soc. 163 (2016) F3179-F3189.

[8] T. Reier, M. Oezaslan, P. Strasser, Electrocatalytic Oxygen Evolution Reaction (OER) on Ru, Ir, and Pt Catalysts: A Comparative Study of Nanoparticles and Bulk Materials. ACS Catal. 2 (2012) 1765-1772.

[9] J.Y. Xu, M. Wang, G.Y. Liu, J.L. Li, X.D. Wang, The physical–chemical properties and electrocatalytic performance of iridium oxide in oxygen evolution. Electrochim. Acta. 56 (2011) 10223-10230.

[10] A. Grimaud, A. Demortière, M. Saubanère, W. Dachraoui, M. Duchamp, M.L. Doublet, J.M. Tarascon, Activation of surface oxygen sites on an iridium-based model catalyst for the oxygen evolution reaction. Nat. Energy 2 (2016) 16189.

[11] D.F. Abbott, D. Lebedev, K. Waltar, M. Povia, M. Nachtegaal, E. Fabbri, C. Copéret, T.J. Schmidt, Iridium Oxide for the Oxygen Evolution Reaction: Correlation between Particle Size, Morphology, and the Surface Hydroxo Layer from Operando XAS. Chem. Mater. 28 (2016) 6591-6604.

[12] W. Hu, H.W. Zhong, W. Liang, S.L. Chen, Ir-Surface Enriched Porous Ir–Co Oxide Hierarchical Architecture for High Performance Water Oxidation in Acidic Media. ACS Appl. Mater. Interfaces 6 (2014) 12729-12736.

[13] E. Oakton, D. Lebedev, M. Povia, D.F. Abbott, E. Fabbri, A. Fedorov, M. Nachtegaal, C. Copéret, T. J. Schmidt, IrO_2-TiO_2: A High-Surface-Area, Active, and Stable Electrocatalyst for the Oxygen Evolution Reaction. ACS Catal. 7 (2017) 2346-2352.

[14] L.C. Seitz, C.F. Dickens, K. Nishio, Y. Hikita, J. Montoya, A. Doyle, C. Kirk, A. Vojvodic, H.Y. Hwang, J.K. Norskov, T.F. Jaramillo, A highly active and stable IrO_x/$SrIrO_3$ catalyst for the oxygen evolution reaction. Science 353 (2016) 1011-1014.

[15] L. Yang, G.T. Yu, X. Ai, W.S. Yan, H.L. Duan, W. Chen, X.T. Li, T. Wang, C.H. Zhang, X.R. Huang, J.S. Chen, X.X. Zou, Efficient oxygen evolution electrocatalysis in acid by a perovskite with face-sharing IrO_6 octahedral dimers. Nat. Commun. 9 (2018) 5236.

[16] C.V. Pham, M. Bühler, J. Knöppel, M. Bierling, D. Seeberger, D. Escalera-López, K.J.J. Mayrhofer, S. Cherevko, S. Thiele, IrO_2 coated TiO_2 core-shell microparticles advance performance of low loading proton exchange membrane water electrolyzers. Appl. Catal. B: Environ. 269 (2020) 118762.

[17] C. Wang, F.L. Lan, Z.F. He, X.F. Xie, Y.H. Zhao, H. Hou, L. Guo, V. Murugadoss, H. Liu, Q. Shao, Q. Gao, T. Ding, R.B. Wei, Z.H. Guo, Iridium-Based Catalysts for Solid Polymer Electrolyte Electrocatalytic Water Splitting. ChemSusChem 12 (2019) 1576-1590.

[18] P. Lettenmeier, L. Wang, U. Golla-Schindler, P. Gazdzicki, N.A. Cañas, M. Handl, R. Hiesgen, S.S. Hosseiny, A.S. Gago, K.A. Friedrich, Nanosized IrO_x–Ir Catalyst with Relevant Activity for Anodes of Proton Exchange Membrane Electrolysis Produced by a Cost-Effective Procedure. Angew. Chem. Int. Ed. 55 (2016) 742-746.

[19] J.Y. Xu, Z. Lian, B. Wei, Y. Li, O. Bondarchuk, N. Zhang, Z.P. Yu, A. Araujo, I. Amorim, Z.C. Wang, B. Li, L.F. Liu, Strong Electronic Coupling between Ultrafine Iridium–Ruthenium Nanoclusters and Conductive, Acid-Stable Tellurium Nanoparticle Support for Efficient and Durable Oxygen Evolution in Acidic and Neutral Media. ACS Catal. 10 (2020) 3571-3579.

[20] T. Reier, Z. Pawolek, S. Cherevko, M. Bruns, T. Jones, D. Teschner, S. Selve, A. Bergmann, H.N. Nong, R. Schlögl, K.J.J. Mayrhofer, P. Strasser, Molecular Insight in Structure and Activity of Highly Efficient, Low-Ir Ir–Ni Oxide Catalysts for Electrochemical Water Splitting (OER). J. Am. Chem. Soc. 137 (2015) 13031-13040.

[21] Q. Li, J.J. Li, J.Y. Xu, N. Zhang, Y.P. Li, L.F. Liu, D. Pan, Z.C. Wang, F.L. Deepak, Ultrafine-Grained Porous Ir-Based Catalysts for High-Performance Overall Water Splitting in Acidic Media. ACS Appl. Energy Mater. 3 (2020) 3736-3744.

[22] J.Q. Guan, D. Li, R. Si, S. Miao, F.X. Zhang, C. Li, Synthesis and Demonstration of Subnanometric Iridium Oxide as Highly Efficient and Robust Water Oxidation Catalyst. ACS Catal. 7 (2017) 5983-5986.

[23] D.F. Yan, Y.X. Li, J. Huo, R. Chen, L.M. Dai, S.Y. Wang, Defect Chemistry of Nonprecious-Metal Electrocatalysts for Oxygen Reactions. Adv. Mater. 29 (2017) 1606459.

[24] T. Zhang, M.Y. Wu, D.Y. Yan, J. Mao, H. Liu, W.B. Hu, X.W. Du, T. Ling, S.Z. Qiao, Engineering oxygen vacancy on NiO nanorod arrays for alkaline hydrogen evolution. Nano Energy 43 (2018) 103-109.

[25] R.X. Ge, L. Li, J.W. Su, Y.C. Lin, Z.Q. Tian, L. Chen, Ultrafine Defective RuO2 Electrocatayst Integrated on Carbon Cloth for Robust Water Oxidation in Acidic Media. Adv. Energy Mater. 9 (2019) 1901313.

[26] Y.C. Pi, J. Guo, Q. Shao, X.Q. Huang, Highly Efficient Acidic Oxygen Evolution Electrocatalysis Enabled by Porous Ir–Cu Nanocrystals with Three-Dimensional Electrocatalytic Surfaces. Chem. Mater. 30 (2018) 8571-8578.

[27] B.M. Tackett, W.C. Sheng, S. Kattel, S.Y. Yao, B.H. Yan, K. A. Kuttiyiel, Q.Y. Wu, J.G. Chen, Reducing Iridium Loading in Oxygen Evolution Reaction Electrocatalysts Using Core–Shell Particles with Nitride Cores. ACS Catal. 8 (2018) 2615-2621.

[28] J.W. Su, R.X. Ge, K.M. Jiang, Y. Dong, F. Hao, Z.Q. Tian, G.X. Chen, L. Chen, Assembling Ultrasmall Copper-Doped Ruthenium Oxide Nanocrystals into Hollow Porous Polyhedra: Highly Robust Electrocatalysts for Oxygen Evolution in Acidic Media. Adv. Mater. 30 (2018) 1801351.

[29] Q. Feng, Q. Wang, Z. Zhang, Y.Y.H. Xiong, H.Y. Li, Y. Yao, X.Z. Yuan, M.C. Williams, M. Gu, H. Chen, H. Li, H.J. Wang, Highly active and stable ruthenate pyrochlore for enhanced oxygen evolution reaction in acidic medium electrolysis. Appl. Catal. B: Environ. 244 (2019) 494-501.

[30] H.S. Oh, H.N. Nong, T. Reier, A. Bergmann, M. Gliech, J. Ferreira de Araújo, E. Willinger, R. Schlögl, D. Teschner, P. Strasser, Electrochemical Catalyst–Support Effects and Their Stabilizing Role for IrO_x Nanoparticle Catalysts during the Oxygen Evolution Reaction. J. Am. Chem. Soc. 138 (2016) 12552-12563.

[31] C. Spöri, J.T.H. Kwan, A. Bonakdarpour, D.P. Wilkinson, P. Strasser, The Stability Challenges of Oxygen Evolving Catalysts: Towards a Common Fundamental Understanding and Mitigation of Catalyst Degradation. Angew. Chem. Int. Ed. 56 (2017) 5994-6021.

[32] S. Cherevko, T. Reier, A.R. Zeradjanin, Z. Pawolek, P. Strasser, K.J.J. Mayrhofer, Stability of nanostructured iridium oxide electrocatalysts during oxygen evolution reaction in acidic environment. Electrochem. Commun. 48 (2014) 81-85.

[33] L.L. Zhao, Q. Cao, A.L. Wang, J.Z. Duan, W.J. Zhou, Y.H. Sang, H. Liu, Iron oxide embedded titania nanowires – An active and stable electrocatalyst for oxygen evolution in acidic media. Nano Energy 45 (2018) 118-126.

[34] T. Kokubo, S. Yamaguchi, Novel Bioactive Titanate Layers Formed on Ti Metal and Its Alloys by Chemical Treatments. Materials 3 (2010) 48-63.

[35] C. Caparrós, M. Ortiz-Hernandez, M. Molmeneu, M. Punset, J.A. Calero, C. Aparicio, M. Fernández-Fairén, R. Perez, F.J. Gil, Bioactive macroporous titanium implants highly interconnected. J. Mater. Sci.: Mater. Med. 27 (2016) 151.

[36] J.Y. Xu, S. Murphy, D.H. Xiong, R.S. Cai, X.K. Wei, M. Heggen, E. Barborini, S. Vinati, R.E. Dunin-Borkowski, R.E. Palmer, L.F. Liu, Cluster Beam Deposition of Ultrafine Cobalt and Ruthenium Clusters for Efficient and Stable Oxygen Evolution Reaction. ACS Appl. Energy Mater. 1 (2018) 3013-3018.

[37] J.Y. Xu, T.F. Liu, J.J. Li, B. Li, Y.F. Liu, B.S. Zhang, D.H. Xiong, I. Amorim, W. Li, L.F. Liu, Boosting the hydrogen evolution performance of ruthenium clusters through synergistic coupling with cobalt phosphide. Energy Environ. Sci. 11 (2018) 1819-1827.

[38] J.Y. Xu, J.J. Li, D.H. Xiong, B.S. Zhang, Y.F. Liu, K.H. Wu, I. Amorim, W. Li, L.F. Liu, Trends in activity for the oxygen evolution reaction on transition metal (M = Fe, Co, Ni) phosphide pre-catalysts. Chem. Sci. 9 (2018) 3470-3476.

[39] A. Sarkar, G.G. Khan, The formation and detection techniques of oxygen vacancies in titanium oxide-based nanostructures. Nanoscale 11 (2019) 3414-3444.

[40] R. Kötz, H. Neff, S. Stucki, Anodic Iridium Oxide Films: XPS-Studies of Oxidation State Changes and O2 Evolution. J. Electrochem. Soc. 131 (1984) 72-77.

[41] V. Pfeifer, T.E. Jones, J.J. Velasco Vélez, C. Massué, M.T. Greiner, R. Arrigo, D. Teschner, F. Girgsdies, M. Scherzer, J. Allan, M. Hashagen, G. Weinberg, S. Piccinin, M. Hävecker, A. Knop-Gericke, R. Schlögl, The electronic structure of iridium oxide electrodes active in water splitting. Phys. Chem. Chem. Phys. 18 (2016) 2292-2296.

[42] V. Pfeifer, T.E. Jones, J.J. Velasco Vélez, C. Massué, R. Arrigo, D. Teschner, F. Girgsdies, M. Scherzer, M.T. Greiner, J. Allan, M. Hashagen, G. Weinberg, S. Piccinin, M. Hävecker, A. Knop-Gericke, R. Schlögl, The electronic structure of iridium and its oxides. Surf. Interface Anal. 48 (2016) 261-273.

[43] S.M. Alia, B. Rasimick, C. Ngo, K.C. Neyerlin, S.S. Kocha, S. Pylypenko, H. Xu, B.S. Pivovar, Activity and Durability of Iridium Nanoparticles in the Oxygen Evolution Reaction. J. Electrochem. Soc. 163 (2016) F3105-F3112.

[44] H.N. Nong, T. Reier, H.S. Oh, M. Gliech, P. Paciok, T.H.T. Vu, D. Teschner, M. Heggen, V. Petkov, R. Schlögl, T. Jones, P. Strasser, A unique oxygen ligand environment facilitates water oxidation in hole-doped IrNiOx core–shell electrocatalysts. Nat. Catal. 1 (2018) 841-851.

[45] G.F. Li, H.M. Yu, X.Y. Wang, S.C. Sun, Y.K. Li, Z.G. Shao, B.L. Yi, Highly effective $Ir_xSn_{1-x}O_2$ electrocatalysts for oxygen evolution reaction in the solid polymer electrolyte water electrolyser. Phys. Chem. Chem. Phys. 15 (2013) 2858-2866.

[46] C. Wang, Y.M. Sui, G.J. Xiao, X.Y. Yang, Y.J. Wei, G.T. Zou, B. Zou, Synthesis of Cu–Ir nanocages with enhanced electrocatalytic activity for the oxygen evolution reaction. J. Mater. Chem. A 3 (2015) 19669-19673.

[47] R.E. Fuentes, H.R. Colón-Mercado, M.J. Martínez-Rodríguez, Pt-Ir/TiC Electrocatalysts for PEM Fuel Cell/Electrolyzer Process. J. Electrochem. Soc. 161 (2014) F77-F82.

[48] W. Hu, S.L. Chen, Q.H. Xia, IrO_2/Nb–TiO_2 electrocatalyst for oxygen evolution reaction in acidic medium. Int. J. Hydrogen Energy. 39 (2014) 6967-6976.

[49] P. Lettenmeier, J. Majchel, L. Wang, V.A. Saveleva, S. Zafeiratos, E.R. Savinova, J.J. Gallet, F. Bournel, A.S. Gago, K.A. Friedrich, Highly active nano-sized iridium catalysts: synthesis and operando spectroscopy in a proton exchange membrane electrolyzer. Chem. Sci. 9 (2018) 3570-3579.

[50] G.Q. Li, K. Li, L. Yang, J.F. Chang, R.P. Ma, Z.J. Wu, J.J. Ge, C.P. Liu, W. Xing, Boosted Performance of Ir Species by Employing TiN as the Support toward Oxygen Evolution Reaction. ACS Appl. Mater. Inter. 10 (2018) 38117-38124.

[51] G.Q. Li, S.T. Li, J.J. Ge, C.P. Liu, W. Xing, Discontinuously covered IrO_2–RuO_2@Ru electrocatalysts for the oxygen evolution reaction: how high activity and long-term durability can be simultaneously realized in the synergistic and hybrid nano-structure. J. Mater. Chem. A 5 (2017) 17221-17229.

[52] L. Wang, P. Lettenmeier, U. Golla-Schindler, P. Gazdzicki, N.A. Cañas, T. Morawietz, R. Hiesgen, S.S. Hosseiny, A.S. Gago, K.A. Friedrich, Nanostructured Ir-supported on Ti_4O_7 as a cost-effective anode for proton exchange membrane (PEM) electrolyzers. Phys. Chem. Chem. Phys. 18 (2016) 4487-4495.

[53] J. Lim, D. Park, S.S. Jeon, C.W. Roh, J. Choi, D. Yoon, M. Park, H. Jung, H. Lee, Ultrathin IrO_2 Nanoneedles for Electrochemical Water Oxidation. Adv. Funct. Mater. 28 (2018) 1704796.

[54] V. Pfeifer, T.E. Jones, S. Wrabetz, C. Massué, J.J. Velasco Vélez, R. Arrigo, M. Scherzer, S. Piccinin, M. Hävecker, A. Knop-Gericke, R. Schlögl, Reactive oxygen species in iridium-based OER catalysts. Chem. Sci. 7 (2016) 6791-6795.

[55] J.R. Feng, F. Lv, W.Y. Zhang, P.H. Li, K. Wang, C. Yang, B. Wang, Y. Yang, J.H. Zhou, F. Lin, G.C. Wang, S.J. Guo, Iridium-Based Multimetallic Porous Hollow Nanocrystals for Efficient Overall-Water-Splitting Catalysis. Adv. Mater. 29 (2017) 1703798.

[56] Q.R. Shi, C.Z. Zhu, H. Zhong, D. Su, N. Li, M.H. Engelhard, H.B. Xia, Q. Zhang, S. Feng, S.P. Beckman, D. Du, Y.H. Lin, Nanovoid Incorporated Ir_xCu Metallic Aerogels for Oxygen Evolution Reaction Catalysis. ACS Energy Lett. 3 (2018) 2038-2044.

[57] Y.C. Lin, Z.Q. Tian, L.J. Zhang, J.Y. Ma, Z. Jiang, B.J. Deibert, R.X. Ge, L. Chen, Chromium-ruthenium oxide solid solution electrocatalyst for highly efficient oxygen evolution reaction in acidic media. Nat. Commun. 10 (2019) 162.

[58] O. Kasian, S. Geiger, T. Li, J.P. Grote, K. Schweinar, S.Y. Zhang, C. Scheu, D. Raabe, S. Cherevko, B. Gault, K.J.J. Mayrhofer, Degradation of iridium oxides via oxygen evolution from the lattice: correlating atomic scale structure with reaction mechanisms. Energy Environ. Sci. 12 (2019) 3548-3555.

[59] S. Geiger, O. Kasian, M. Ledendecker, E. Pizzutilo, A.M. Mingers, W.T. Fu, O. Diaz-Morales, Z.Z. Li, T. Oellers, L. Fruchter, A. Ludwig, K.J.J. Mayrhofer, M.T.M. Koper, S. Cherevko, The stability number as a metric for electrocatalyst stability benchmarking. Nat. Catal. 1 (2018) 508-515.

[60] A. Zagalskaya, V. Alexandrov, Role of Defects in the Interplay between Adsorbate Evolving and Lattice Oxygen Mechanisms of the Oxygen Evolution Reaction in RuO2 and IrO2. ACS Catal. 10 (2020) 3650-3657.

[61] J.Y. Chen, P.X. Cui, G.Q. Zhao, K. Rui, M.M. Lao, Y.P. Chen, X.S. Zheng, Y.Z. Jiang, H.G. Pan, S.X. Dou, W.P. Sun, Low-Coordinate Iridium Oxide Confined on Graphitic Carbon Nitride for Highly Efficient Oxygen Evolution. Angew. Chem. Int. Ed. 58 (2019) 12540-12544.

[62] Y.B. Chen, H.Y. Li, J.X. Wang, Y.H. Du, S.B. Xi, Y.M. Sun, M. Sherburne, J.W. Ager, A.C. Fisher, Z.C.J. Xu, Exceptionally active iridium evolved from a pseudo-cubic perovskite for oxygen evolution in acid. Nat. Commun. 10 (2019) 572.

[63] O. Diaz-Morales, S. Raaijman, R. Kortlever, P.J. Kooyman, T. Wezendonk, J. Gascon, W.T. Fu, M.T.M. Koper, Iridium-based double perovskites for efficient water oxidation in acid media. Nat. Commun. 7 (2016) 12363.

[64] W.J. Zhou, X.J. Liu, Y.H. Sang, Z.H. Zhao, K. Zhou, H. Liu, S.W. Chen, Enhanced Performance of Layered Titanate Nanowire-Based Supercapacitor Electrodes by Nickel Ion Exchange. ACS Appl. Mater. Interfaces 6 (2014) 4578-4586.

[65] L.L. Zhao, Q. Cao, A.L. Wang, J.Z. Duan, W.J. Zhou, Y.H. Sang, H. Liu, Iron oxide embedded titania nanowires – An active and stable electrocatalyst for oxygen evolution in acidic media. Nano Energy 45 (2018) 118-126.

[66] X.G. Wang, W. Li, D.H. Xiong, D.Y. Petrovykh, L.F. Liu, Bifunctional Nickel Phosphide Nanocatalysts Supported on Carbon Fiber Paper for Highly Efficient and Stable Overall Water Splitting. Adv. Funct. Mater. 26 (2016) 4067-4077.

[67] V.V. Gorodetskii, V.A. Neburchilov, Titanium Anodes with Active Coatings Based on Iridium Oxides: The Chemical Composition of the Coatings and the Distribution of Their Components over Depth on Anodes Made of IrO_2, $IrO_2 + TiO_2$, $IrO_2 + RuO_2 + TiO_2$, and $IrO_2 + RuO_2 + TiO_2 + Ta_2O_5$. Russ. J. Electrochem. 39 (2003) 1116-1123.

[68] S. Geiger, O. Kasian, B.R. Shrestha, A.M. Mingers, K.J.J. Mayrhofer, S. Cherevko, Activity and Stability of Electrochemically and Thermally Treated Iridium for the Oxygen Evolution Reaction. J. Electrochem. Soc. 163 (2016) F3132-F3138.

[69] G. Kresse, J. Furthmüller, Efficient iterative schemes for ab initio total-energy calculations using a plane-wave basis set. Phys. Rev. B, 1996, 54, 11169-11186.

[70] J.P. Perdew, K. Burke, M. Ernzerhof, Generalized Gradient Approximation Made Simple. Phys. Rev. Lett. 77 (1996) 3865-3868.

[71] P.E. Blöchl, Projector augmented-wave method. Phys. Rev. B 50 (1994) 17953-17979.

[72] Z. Alexandra, A. Vitaly, Role of Defects in the Interplay between Adsorbate Evolving and Lattice Oxygen Mechanisms of the Oxygen Evolution Reaction in RuO_2 and IrO_2. ACS Catal. 10 (2020) 3650-3657.

[73] J.K. Nørskov, J. Rossmeisl, A. Logadottir, L. Lindqvist, J.R. Kitchin, T. Bligaard, H. Jónsson, Origin of the Overpotential for Oxygen Reduction at a Fuel-Cell Cathode. J. Phys. Chem. B 108 (2004) 17886-17892.

[74] C.C.L. McCrory, S.H. Jung, I.M. Ferrer, S.M. Chatman, J.C. Peters, T.F. Jaramillo, Benchmarking Hydrogen Evolving Reaction and Oxygen Evolving Reaction Electrocatalysts for Solar Water Splitting Devices. J. Am. Chem. Soc. 137 (2015) 4347-4357.

4. Efficient hydrogen production over atomically dispersed catalysts

4.1 Rhodium single-atom catalysts with enhanced electrocatalytic hydrogen evolution performance

Abstract

The hydrogen evolution reaction (HER) is crucially important for “green” hydrogen production from water electrolysis. While platinum (Pt) has been the state-of-the-art HER catalysts with good activity and durability, rhodium (Rh)-based nanostructures have recently shown reasonably good electrocatalytic performance for the HER and are drawing increasing attention for usage as HER catalysts. However, the mass activity of Rh-based HER catalysts still needs to be significantly improved considering the high price and scarcity of Rh. Herein, we report the outstanding HER performance of Rh single-atom catalysts (SACs) supported on activated carbon (Rh_1/AC) synthesized *via* a “top-down” chemical reaction induced dispersion process using Rh nanoparticles as the starting materials. The as-obtained Rh_1/AC exhibits a mass activity of 2367 mA mg_{Rh}^{-1} and a turnover frequency (TOF) value of 1.26 s^{-1} at η = 100 mV in an alkaline solution with a low loading density of only 15 μg cm^{-2}. Besides, we demonstrate that Rh_1/AC can sustain continuous HER electrolysis at −10 mA cm^{-2} for 290 hours with little degradation, showing much better performance than those of the state-of-the-art Pt/C catalysts tested under the same conditions.

4.1.1 Introduction

Developing electrochemical energy conversion devices such as water electrolysers is of paramount importance to the widespread deployment of renewable energy, which is intermittent and has to be transformed into storable fuels for long-term usage [1-3]. In particular, the “green hydrogen (H_2)” produced by water electrolysis using renewable energy as power input has been proposed to be a promising energy carrier able to decarbonise the transportation sector and chemical industry. While the electricity from renewables has recently become more and more affordable, the key to enabling large-scale production of “green hydrogen” is to improve the energy efficiency and reduce production costs of electrolysers. To this end, electrocatalysts play an essential role in boosting the hydrogen evolution reaction (HER) performance (*e.g.*, activity, and kinetics)

and constitute an indispensable component in a water electrolyser [4], and therefore much research effort has been dedicated to developing efficient and durable electrocatalysts in recent years.

Very recently, rhodium (Rh)-based materials have drawn increasing attention for use to catalyse the HER, and have been demonstrated both theoretically and experimentally to possess good HER performance [5-18]. To date, a variety of Rh nanostructures (*e.g.*, nanoparticles [6, 7], nanoclusters [8], nanosheets [9], and nanodendrites [10]), compounds (*e.g.*, Rh_2P [11], RhO_2 [12], and RhCoB [13]) and composites (*e.g.*, $MoSe_2$/Rh [14], Rh–MoS_2 [15, 16], CoP–Rh [17], and Rh–Rh_2P [18]) have been synthesised, and HER performance comparable to that of the commercial Pt/C benchmark catalysts has been reported. Notwithstanding some process, the mass activity of Rh-based HER catalysts still needs to be significantly improved considering that Rh is a precious metal and too scarce to be used on a large scale commensurate with the global demand.

Single-atom catalysts (SACs), consisting of metal atoms individually dispersed on a given support, have lately emerged as a new class of catalysts potentially allowing the catalytic materials to be utilised to a maximal extent. SACs were firstly developed for use in gas-phase heterogeneous reactions [19], and they have been recently demonstrated to show good electrocatalytic performance in several electrochemical reactions including the HER [20], oxygen evolution reaction (OER) [21], oxygen reduction reaction (ORR) [22], CO_2 reduction reaction (CO_2RR) [23], and nitrogen reduction reaction (NRR) [24-26]. Although Rh SACs have been reported to catalyse the hydroformylation of olefins [27], ammonia–borane hydrolysis [28], methane transformation [29, 30], methanol carbonylation [31], CO oxidation [32, 33], and very recently formic acid electro-oxidation [34], they have been rarely explored as electrocatalysts to accelerate the HER [35].

Herein, we report the electrocatalytic performance of Rh SACs supported on activated carbon (Rh_1/AC) towards the HER, which can deliver current densities of 10 and 100 mA cm^{-2} at low overpotentials (η) of 48 and 199 mV, respectively, in an alkaline solution with a low loading density of 15 μg cm^{-2}. Importantly, Rh_1/AC exhibits a mass activity of 2367 mA mg_{Rh}^{-1} and a turnover frequency (TOF) value of 1.26 s^{-1} at η = 100 mV, significantly higher than those of the state-of-the-art commercial Pt/C benchmark catalysts. Besides, Rh_1/AC can sustain continuous HER electrolysis at −10 mA cm^{-2} for 290 hours with little degradation, showing much better catalytic stability than that of Pt/C.

4.1.2 Results and discussion

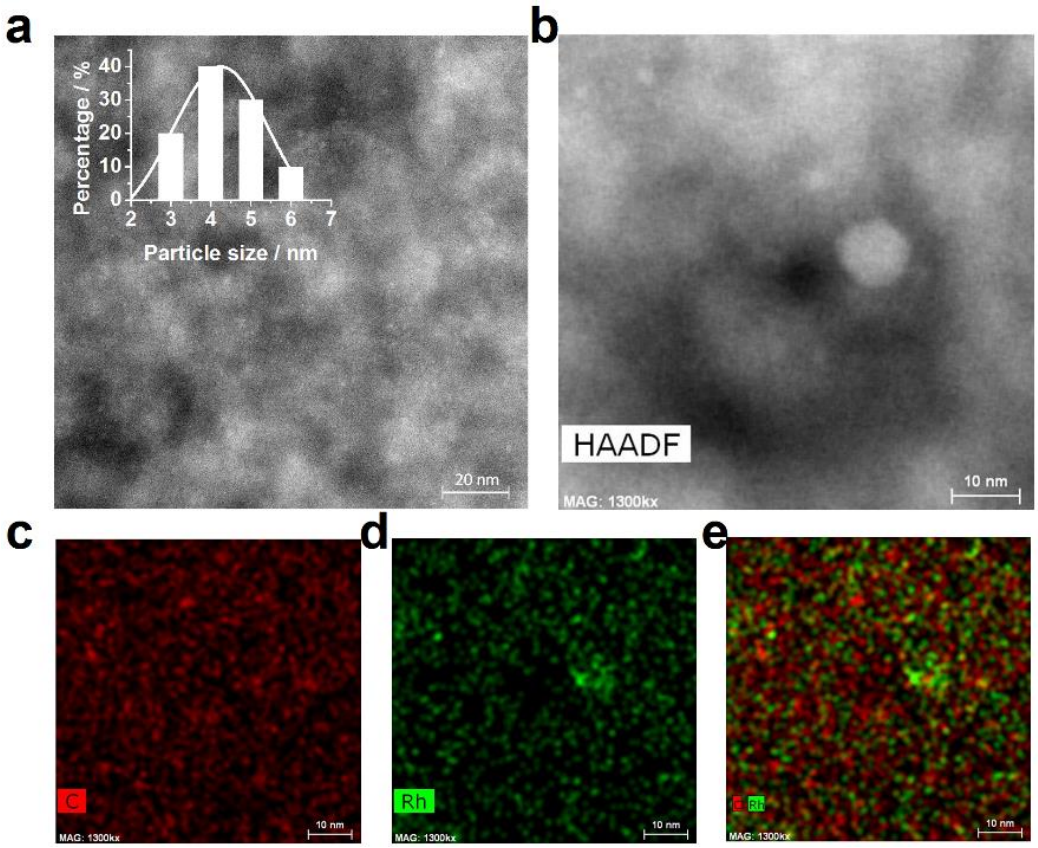

Figure 4.1.1 a, b) HAADF-STEM images of the as-prepared Rh/AC catalysts. c-e) EDX elemental maps of c) C, d) Rh, and e) their overlay.

Presently, most SACs reported in the literature were synthesised based on “bottom-up” approaches, namely, the metal precursors undergo adsorption, reduction and/or activation in a wet chemical synthesis process. In contrast, our Rh_1/AC SACs were prepared through a new “top-down” approach developed by some co-authors of this work [36]. In this case, Rh nanoparticles (NPs) were firstly dispersed on activated carbon support (Rh/AC) *via* solution-based impregnation in the presence of $RhCl_3 \cdot nH_2O$ and AC powders, followed by a post-annealing treatment at 300 °C to reduce Rh^{3+} to metallic Rh (see **Experimental** details,). The as-prepared Rh NPs have an average diameter of 4 nm with a high degree of coverage on the surface of the AC support (**Figure 4.1.1**), and the loading of Rh NPs was measured to be *ca.* 5 wt% by energy-dispersive X-ray (EDX) spectroscopy (**Figure 4.1.2**). To achieve atomic dispersion of Rh, the Rh/AC was subjected to a chemical etching/redispersion process in a mixture of CH_3I and CO at 240 °C for 6 h (**Figure 4.1.3**), which resulted in the formation of Rh_1/AC with a virtually unchanged Rh loading (*i.e.*, ~5 wt%, **Figure 4.1.2**), as also confirmed by the inductively coupled plasma – optical emission spectroscopy (ICP–OES) in the previous work [36]. The atomic dispersion was firstly examined by X-ray diffractometry (XRD, **Figure 4.1.4**).

While broad diffraction peaks from cubic Rh (ICDD no. 01-075-3848) could be clearly observed in the Rh/AC, all these peaks vanished in the sample after the chemical reaction with CH_3I/CO, indicating that the long-range order of Rh atoms disappears, a characteristic of SACs.

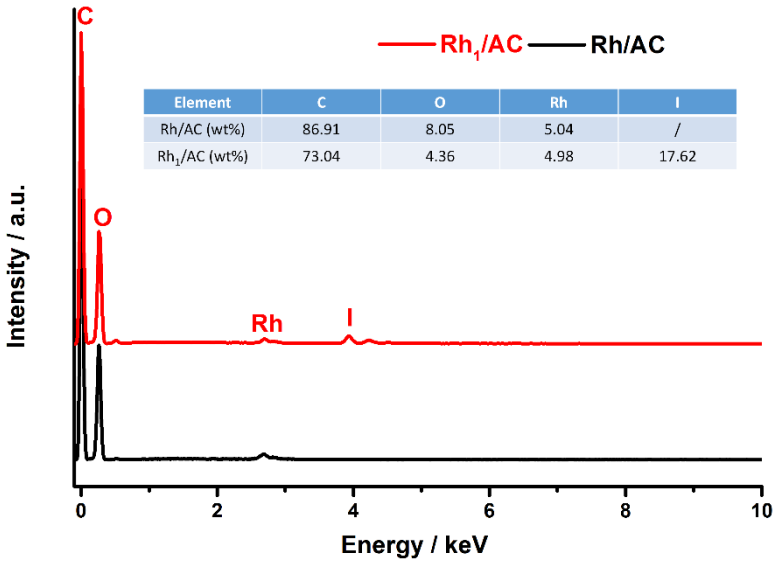

Element	C	O	Rh	I
Rh/AC (wt%)	86.91	8.05	5.04	/
Rh_1/AC (wt%)	73.04	4.36	4.98	17.62

Figure 4.1.2 SEM-EDX spectra of the as-prepared Rh/AC and Rh_1/AC catalysts. The quantitative analysis confirmed the mass loading of Rh on AC (ca. 5 wt%).

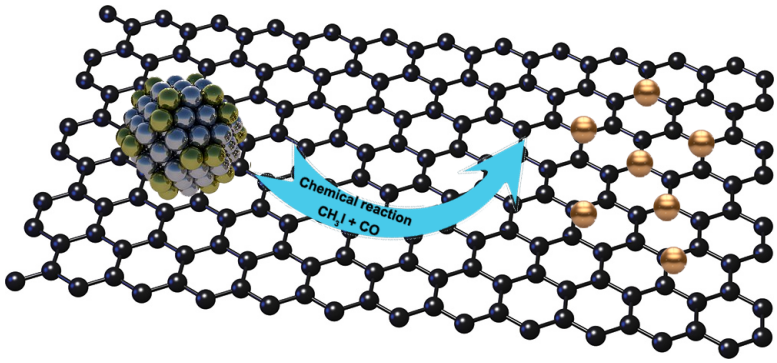

Figure 4.1.3 Schematic illustration of the preparation of Rh_1/AC.

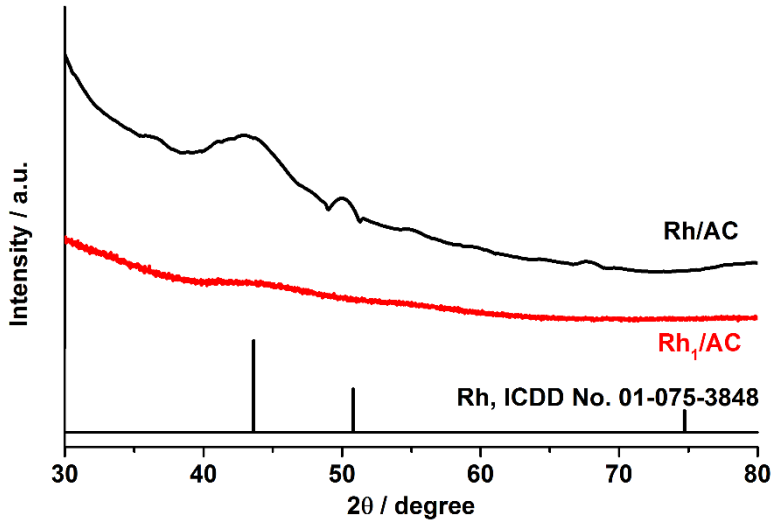

Figure 4.1.4 XRD patterns of the as-prepared Rh/AC and Rh_1/AC catalysts.

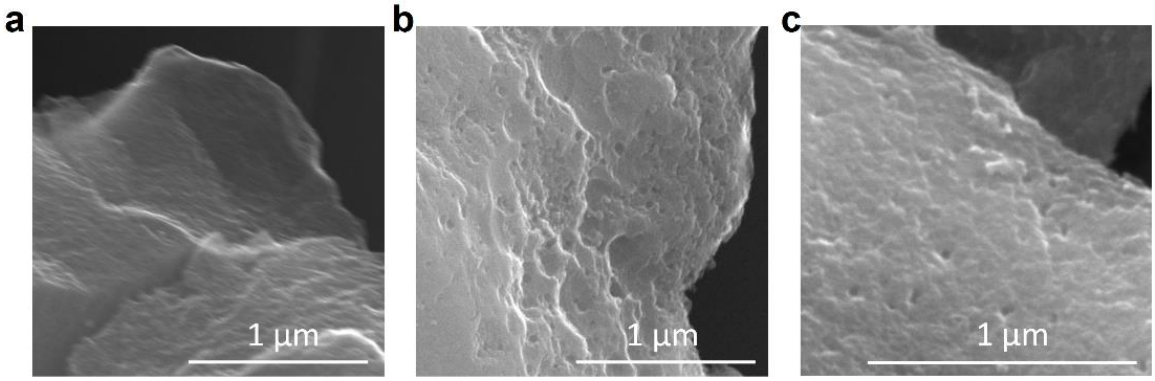

Figure 4.1.5 SEM images of the as-prepared a) AC, b) Rh/AC and c) Rh_1/AC.

Figure 4.1.5 shows scanning electron microscopy (SEM) images of the as-obtained as-prepared AC, Rh/AC and Rh_1/AC. There is no discernible morphology change for Rh_1/AC after the redispersion, in comparison to those of the Rh/AC and AC supports. **Figure 4.1.6a** shows a high-resolution transmission electron microscopy (HRTEM) image of Rh/AC, where the Rh nanoparticles (NPs) can be resolved clearly. After the chemical reaction, these NPs were not visible anymore (**Figure 4.1.6b**), implying that Rh may have been redispersed on the AC support in the form of single atoms. This was confirmed by high angle annular dark-field scanning transmission electron microscopy (HAADF-STEM) examination (**Figure 4.1.6c**), where individual Rh atoms were clearly observed to disperse on the AC support with a high density, and no NPs could be seen anymore, indicating that Rh SACs have been exclusively obtained upon the chemical redispersion process. The atomic dispersion nature of Rh_1/AC was also confirmed previously by extended X-ray absorption fine structure (EXAFS) spectroscopy, which

proved that isolated Rh mononuclear complexes are immobilised by the oxygen-containing functional groups. The detailed information can be found in the previous publication [36].

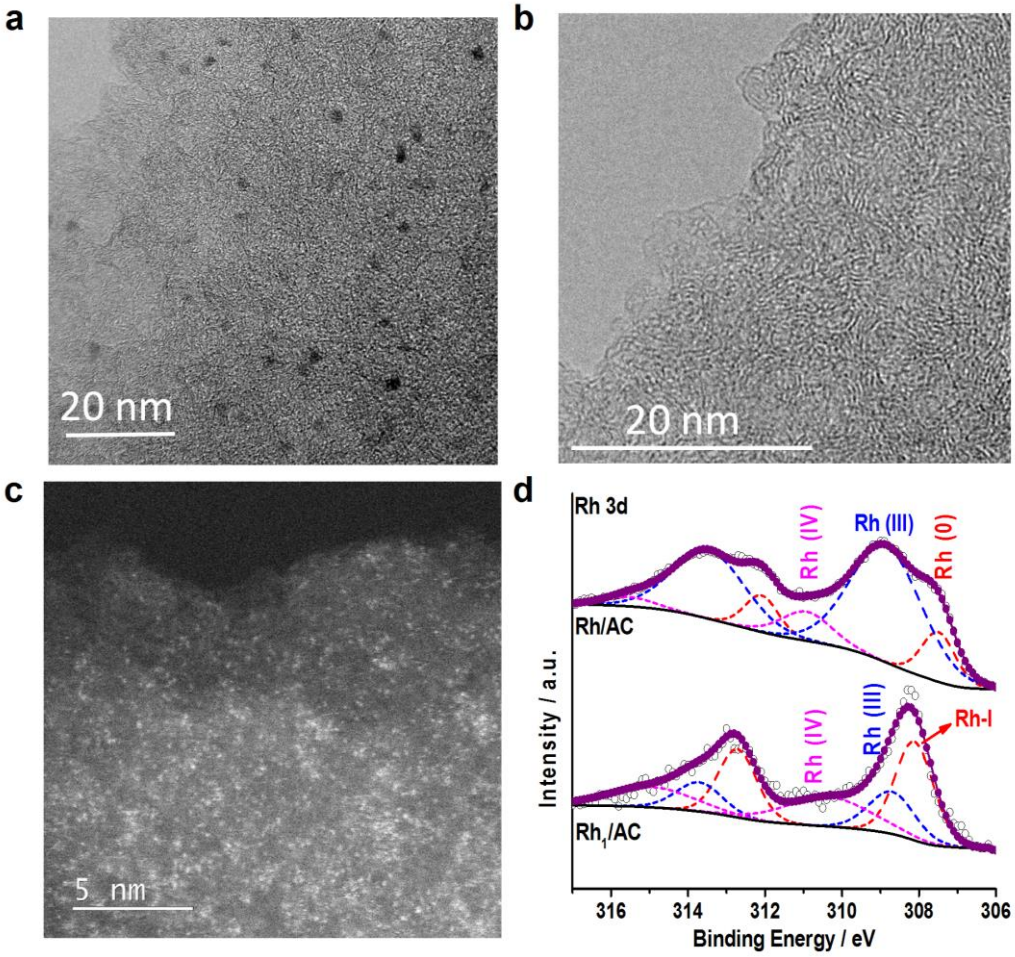

Figure 4.1.6 a) HRTEM image of Rh/AC, b) HRTEM and c) HADDF-STEM images of Rh_1/AC, and d) comparison of Rh3d XPS spectra for Rh/AC and Rh_1/AC. The scattered dots are experimental data, the dashed lines represent fitting curves of each component, and the thick purple line is the fitting envelope.

X-ray photoelectron spectroscopy (XPS) was employed to analyse the surface chemical states of Rh/AC and Rh_1/AC. The XPS survey spectra confirm the presence of the corresponding elements in each catalyst (**Figure 4.1.7**). **Figure 4.1.6d** shows the high-resolution Rh3d XPS spectra of Rh/AC and Rh_1/AC, respectively. For Rh/AC, the two peaks represent the spin–orbit components of the Rh3d core level, *i.e.*, $Rh3d_{5/2}$ and $Rh3d_{3/2}$. The $Rh3d_{5/2}$ peak can be deconvoluted into three components centred at 307.5, 308.9, and 310.9 eV, which can be assigned to metallic Rh(0), Rh(iii), and Rh(iv) oxidation states, respectively [37, 38]. The oxidisation may result from the long-term exposure of the fine NPs to air before XPS inspection. Compared to Rh/AC, Rh_1/AC shows a new component (RhI_3) located at 308.2 eV, which is owing to chemical reaction

with I^- during the chemical etching/redispersion process in the presence of CH_3I/CO [38]. Furthermore, the presence of iodine was also confirmed by the I3d XPS spectrum, where the binding energy peaks at 619.1 and 630.7 eV can be assigned to Rh–I bonding (**Figure 4.1.8**) [39].

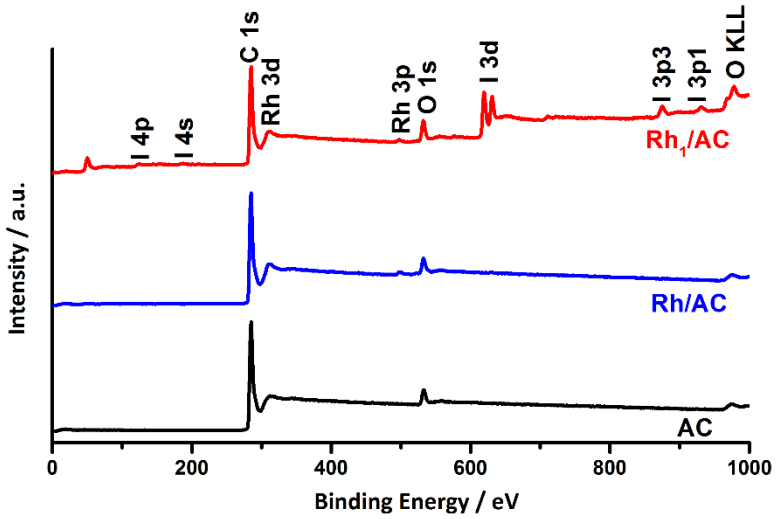

Figure 4.1.7 XPS survey spectra of the AC, Rh/AC and Rh_1/AC.

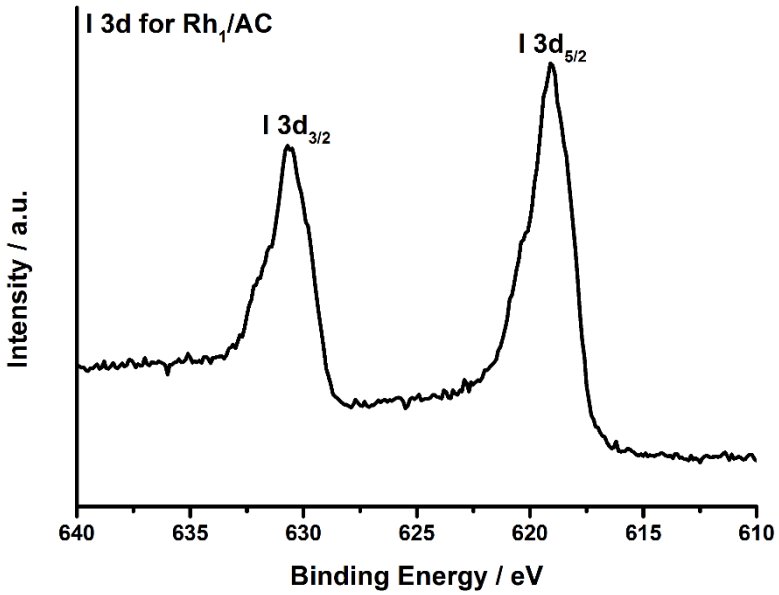

Figure 4.1.8 XPS spectrum of I3d for Rh_1/AC.

The HER electrocatalytic activities of Rh_1/AC and control catalysts including Rh/AC, commercial Pt/C and AC support, were investigated by linear sweep voltammetry (LSV) in N_2-saturated 1.0 M NaOH at a sweep rate of 5 mV s^{-1}. The Rh_1/AC can deliver geometric current densities of 10 and 100 mA cm_{geo}^{-2} at low overpotentials (η) of 48 and

199 mV, respectively (**Figure 4.1.9a**), remarkably lower than those of Rh/AC (η_{10} = 99 mV and η_{100} = 322 mV) and commercial Pt/C (η_{10} = 75 mV and η_{100} = 298 mV). The reaction kinetics of all catalysts was studied by the Tafel analysis (**Figure 4.1.9b**). The Rh_1/AC exhibits a low Tafel slope of 33 mV dec^{-1}, which is markedly smaller than that of Rh/AC (70 mV dec^{-1}) and commercial Pt/C (43 mV dec^{-1}), indicating more favourable HER kinetics. The HER may proceed through the Volmer–Tafel mechanism, in which the two chemisorbed hydronium ions (H_3O^+) may readily combine releasing one H_2 molecule, owing to the high-density dispersion of Rh single atoms (**Figure 4.1.6c**). Furthermore, the electrochemical impedance spectroscopy (EIS) measurements also confirmed the fast reaction rate of Rh_1/AC for the HER, as evidenced by its much smaller charge transfer resistance (R_{ct}) compared to that of other control catalysts (**Figure 4.1.10**). Besides, the Rh_1/AC catalysts show markedly higher catalytic activity than many previously reported single-atom electrocatalysts (**Table 4.1.1**), such as SANi-PtNWs (η_{10} = 70 mV, and 60.3 mV dec^{-1}) [40] and Co_1/PCN (η_{10} = 89 mV, and 52 mV dec^{-1}) [41], although they are slightly less active than the Rh@NG SACs (η_{10} = 33 mV, and 30 mV dec^{-1}) reported recently [35].

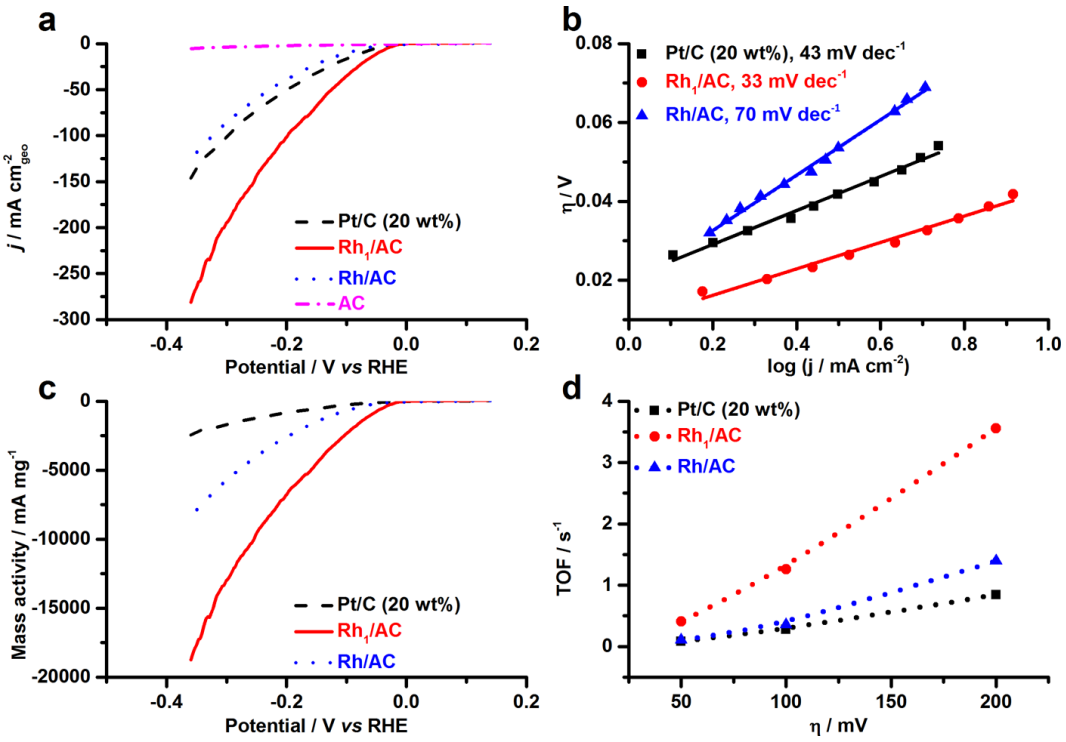

Figure 4.1.9 Electrocatalytic HER performance of Rh_1/AC and other control catalysts. a) LSV curves, b) Tafel slopes, c) mass activity, and d) comparison of the TOF values calculated at η = 50, 100 and 200 mV for Rh_1/AC, Rh/AC and commercial Pt/C, respectively. All tests were carried out in 1.0 M NaOH at room temperature.

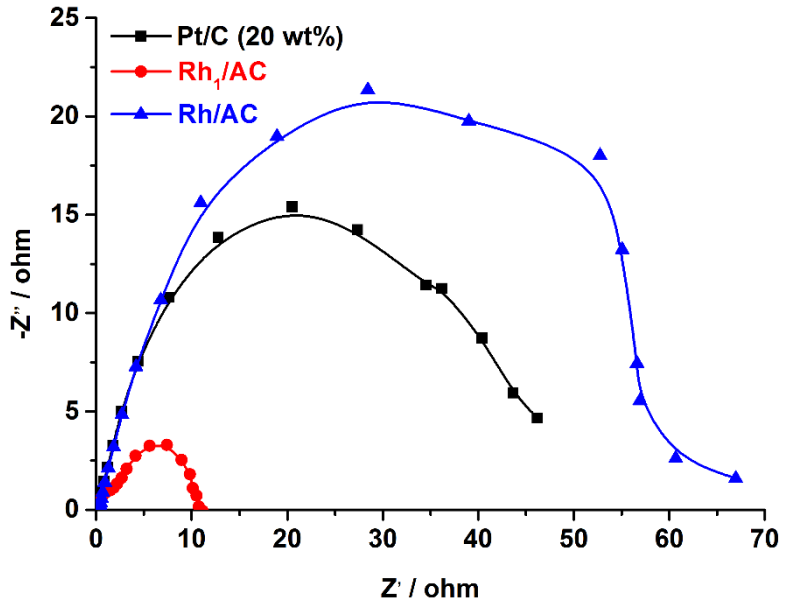

Figure 4.1.10 Nyquist plots of all catalysts measured at an overpotential of 50 mV.

Table 4.1.1 Summary of the HER activity of SACs in alkaline solutions.

Catalysts	η at j=10 mA cm^{-2} / mV	Tafel slope / mV dec^{-1}	Reference
Rh_1/AC	**48**	**33**	**This work**
Pt@PCM	139	73.6	Sci. Adv. 2018, 4, eaao6657.
SANi-PtNWs	70	60.3	Nat. Catal. 2019, 2, 495-503.
Ru@Co SAs/N–C	7	30	Nano Energy 2019, 59, 472-480.
Ru-MoS_2/CC	41	114	Appl. Catal. B Environ. 2019, 249, 91-97.
Rh@NG	33	30	Carbon 2020, 164, 121-128.
Co_1/PCN	89	52	Nat. Catal. 2019, 2, 134-141.
$Mo_1N_1C_2$	132	90	Angew. Chem. Int. Ed. 2017, 56, 16086-16090.
Co_1N_x/C	170	75	Nat. Commun. 2015, 6, 7992.
Pt/np-$Co_{0.85}Se$	58	39	Nat. Commun. 2019, 10, 1743.
Ru-NC-700	47	14	Nat. Commun. 2019, 10, 631.
Pt_1/N-C	46	36.8	Nat. Commun. 2020, 11, 1029.
Ni_{SA}-MoS_2/CC	95	75	Nano Energy 2018, 53, 458-467.

SA-Ru-MoS_2	76	21	Small Methods 2019, 3, 1900653.
Ru_{SA}-N-S-$Ti_3C_2T_x$	99	/	Adv. Mater. 2019, 31, 1903841.
W-SAC	85	53	Adv. Mater. 2018, 30, 1800396.

For noble metal electrocatalysts, the mass activity is a fundamental metric for practical applications, reflecting the effectiveness of noble metal utilisation and therefore closely related to the production costs of electrolysers [42-45]. The Rh_1/AC can deliver an exceptionally high mass activity of 2367 mA mg^{-1} at η = 100 mV, which is 3.6 and 8.7 times higher than that of Rh/AC and commercial Pt/C, respectively (**Figure 4.1.9c**). Meanwhile, the Rh_1/AC exhibits the highest activity among all the catalysts under study, able to deliver a mass activity of 1000 mA mg^{-1} at η = 60 mV, showing an overpotential significantly lower than those of Rh/AC (122 mV) and commercial Pt/C (224 mV).

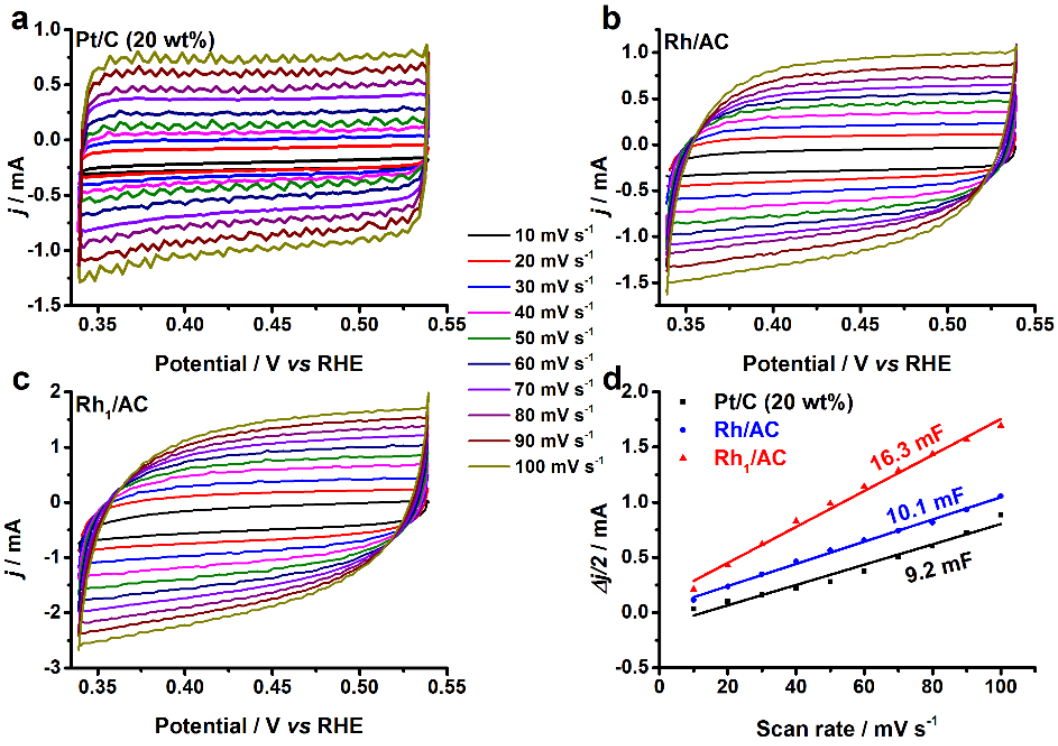

Figure 4.1.11 Electrochemical CV curves of a) Pt/C, b) Rh/AC and c) Rh_1/AC, recorded at different scan rates of 10, 20, 30, 40, 50, 60, 70, 80, 90 and 100 mV s^{-1}. d) Plots of the capacitive currents as a function of the scan rate for all the catalysts.

To obtain more information on the excellent performance of Rh_1/AC for the HER, the electrochemically active surface area (ECSA), which is considered a critical factor influencing the catalytic performance, was measured. The ECSA was obtained by cyclic

voltammetry (CV) measurements in the non-faradaic potential region (see **Experimental** details). As revealed in **Figure 4.1.11**, the Rh_1/AC shows the highest ECSA value of 408 cm^2, followed by Rh/AC (253 cm^2) and commercial Pt/C (230 cm^2). The intrinsic HER activity of Rh_1/AC, Rh/AC and commercial Pt/C was further evaluated based on the ECSA-normalized specific activities (**Figure 4.1.12**). Despite its large ECSA, after normalization, the Rh_1/AC still exhibits higher specific activity than that of Rh/AC and commercial Pt/C, suggesting that its activity is intrinsically high. The HER activity of all catalysts was further assessed using the turnover frequency (TOF), and the TOF values are compared at η = 50, 100, and 200 mV in **Figure 4.1.9d**. The Rh_1/AC shows a TOF value of 1.26 s^{-1} at η = 100 mV, substantially outperforming both Rh/AC and commercial Pt/C, which corroborates that the Rh_1/AC is intrinsically more active for the HER.

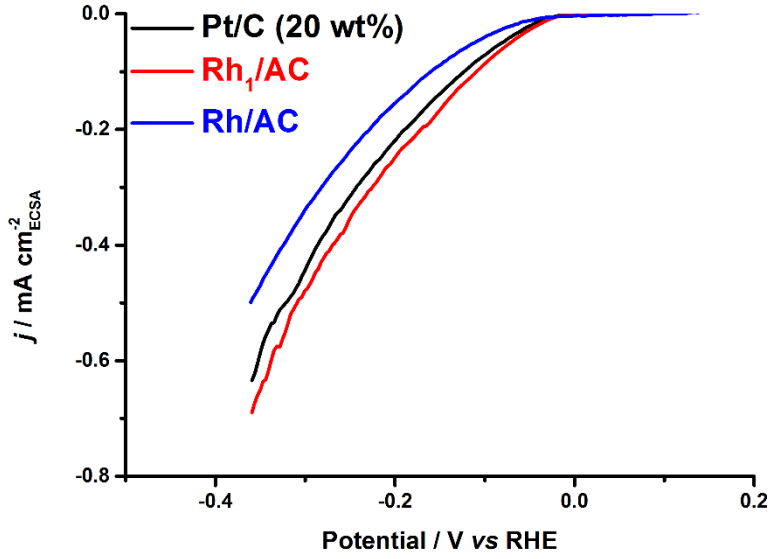

Figure 4.1.12 Specific activity Rh_1/AC and other control catalysts.

The electrocatalytic stability is another significant performance indicator of an HER catalyst. The stability of Rh_1/AC and control catalysts was firstly assessed by performing repetitive CV scans in a potential range of −0.36 – 0.14 V vs. RHE at a rate of 100 mV s^{-1} for 45 000 CV cycles. **Figure 4.1.13a** shows the polarisation curves recorded before and after the cycling, where it is seen that the polarisation curve of Rh_1/AC nearly remains unchanged after 45 000 cycles, suggesting excellent stability. In contrast, Rh/AC and commercial Pt/C exhibit marked degradation after CV cycling. Furthermore, chronopotentiometry (CP) was applied to evaluate the long-term durability of the catalysts in 1.0 M NaOH at a current density of −10 mA cm^{-2}. As illustrated in **Figure 4.1.13b**, the overpotential needed to maintain −10 mA cm^{-2} for commercial Pt/C catalysts quickly increases in a few hours, and then continuously degrades over the course of 120

hours. Similar performance decay was also observed for Rh/AC, and the overpotential went up to 420 mV after the 290 hour test. In comparison, Rh_1/AC can continuously catalyse the HER for 290 h with little performance deterioration, indicating outstanding durability towards the HER in alkaline medium.

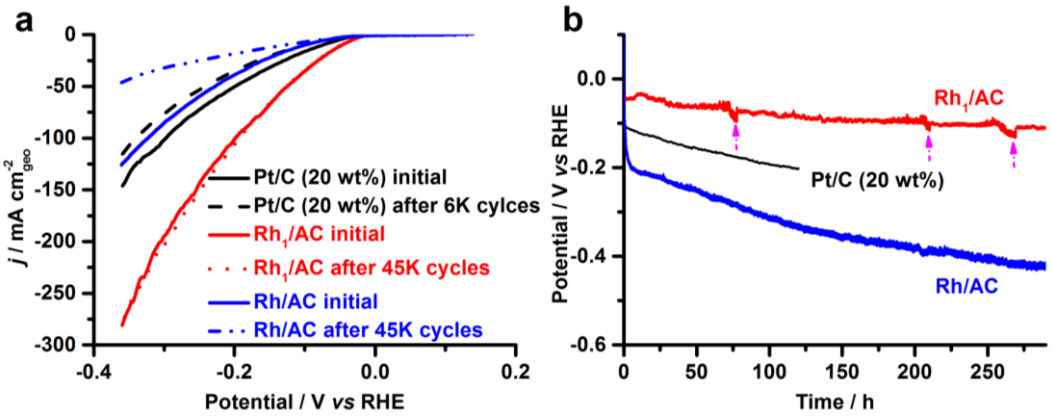

Figure 4.1.13 Stability of the Rh_1/AC and control catalysts. a) Cyclic durability and b) long-term catalytic stability tested at −10 mA cm^{-2}. All tests were carried out in 1.0 M NaOH at room temperature. The polarisation curves in panel a) were recorded at 5 mV s^{-1}. The pink arrows in panel b) show the potential variations from the replenishment of the electrolyte.

We further examined the morphology, structure and chemical state changes of Rh_1/AC after the extended stability test. As illustrated in **Figure 4.1.14**, Rh nanoclusters appeared after 290 h of HER electrolysis, and the SACs could be hardly seen (**Figure 4.1.14a**). Accordingly, diffraction peaks from cubic metallic Rh could be resolved in the XRD pattern of the tested sample (**Figure 4.1.14.b**), confirming the agglomeration of single atoms into fine nanoclusters. This explains why a performance decay, despite being little, was observed in Rh_1/AC during the HER durability test (**Figure 4.1.13b**). Further XPS analysis demonstrated that the agglomerated Rh nanoclusters are virtually in a metallic state, as evidenced by the two peaks appearing at 307.8 and 312.6 eV in the Rh3d XPS spectrum of the tested sample (**Figure 4.1.15a**). This implies that the oxidised Rh species were reduced during the HER. Moreover, we found that the surface iodine species could not be detected any longer (**Figure 4.1.15b**). The disappearance of iodine species might destroy the coordination environment of singly dispersed Rh, causing agglomeration. Further investigation will be carried out in the future to figure out how to maintain the atomic dispersion of Rh_1/AC during the HER and if Rh_1/AC could be regenerated after the durability test through heat treatment in the mixture of CH_3I/CO. In addition, the faradaic efficiency of H_2 evolution by Rh_1/AC was measured (**Figure 4.1.16**). The volume of H_2 detected matches well with that calculated, indicating a nearly 100% faradaic efficiency in the process of the HER.

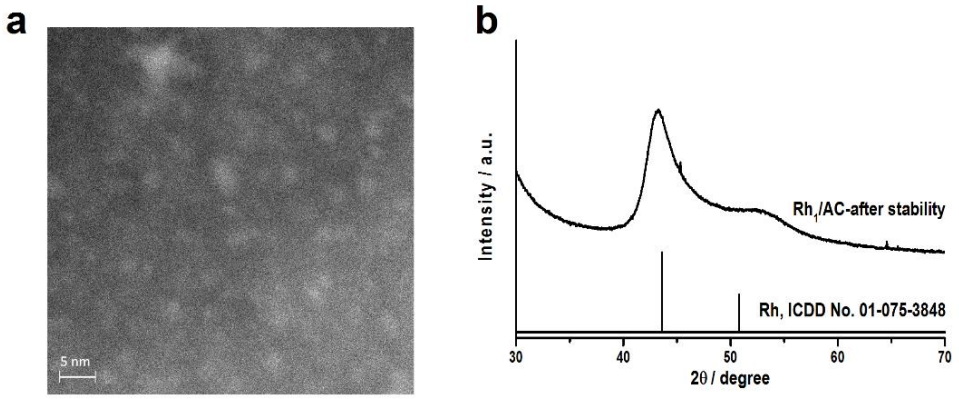

Figure 4.1.14 a) STEM image of b) XRD pattern of Rh_1/AC after the extended stability test at –10 mA cm^{-2} for 290 h.

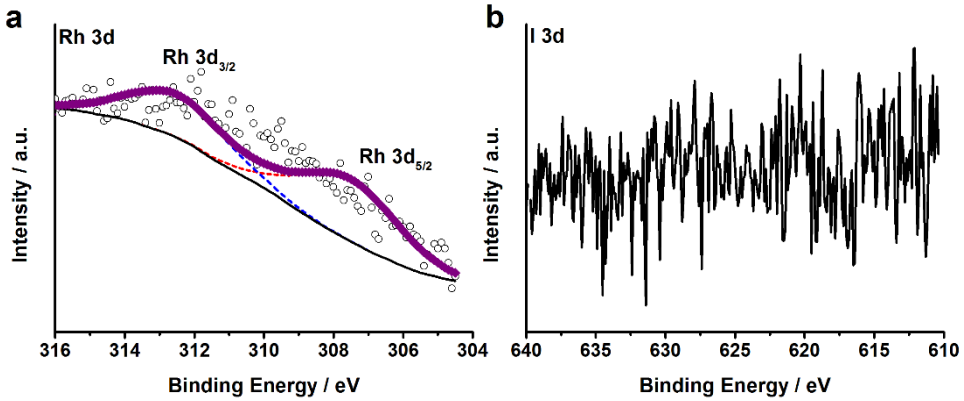

Figure 4.1.15 XPS spectra of a) Rh3d and b) I3d for Rh_1/AC after the extended stability test at –10 mA cm^{-2} for 290 h.

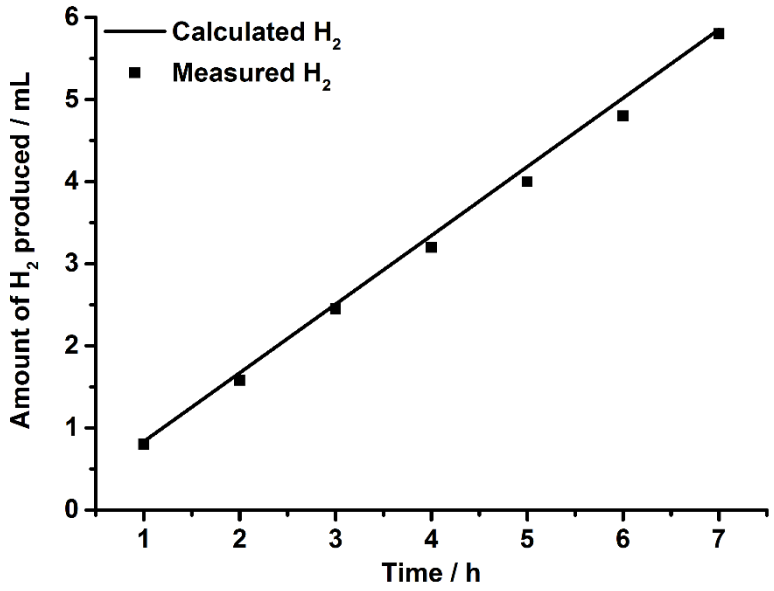

Figure 4.1.16 Experimentally measured and calculated volumes of H_2 gas evolved from Rh_1/AC at a fixed current density of -10 mA cm^{-2}.

4.1.3 Conclusions

In summary, we demonstrate that atomically dispersed Rh_1/AC catalysts prepared by a scalable “top-down” approach exhibit outstanding electrocatalytic performance for the hydrogen evolution reaction in alkaline medium, significantly better than that of the state-of-the-art commercial Pt/C catalysts in terms of apparent activity, mass activity, reaction kinetics, turnover frequency, catalytic stability and durability. The Rh_1/AC shows substantial promise for use as high-performance HER catalysts for alkaline water electrolysis to produce hydrogen.

4.1.4 Experimental section

Preparation of the Rh_1/AC catalysts: The Rh_1/AC catalysts were prepared according to the “top-down” approach reported previously [36]. Firstly, the coconut activated carbon (AC) was ground to 40-60 mesh and washed with deionized (DI) water at 80 °C. The electrical conductivity of the DI water is below 20 μs cm^{-1}. The AC powders were then dried in static air at 120 °C for 12 h to obtain AC support ready for use to prepare Rh_1/AC. Secondly, 1.35 g $RhCl_3 \cdot nH_2O$ with 37 wt% metal content was dissolved in 15 mL deionized water to obtain precursor solutions. Subsequently, 10 g dried AC powders were added in, and the mixture was stirred continuously until no bubbles could be discerned by naked eyes. Afterwards, the mixture of the solution and AC was statically dried at 90 °C until all the solvent was volatilized, followed by further drying at 120 °C overnight to completely remove the residual water. Thirdly, the collected powders were loaded in a quartz tubular reactor, calcined at 300 °C for 2 h in a flow of N_2 (100 mL/min), and then continuously reduced in high-purity H_2 at the same temperature for 2 h, which resulted in the formation of Rh NPs supported on AC (Rh/AC). Lastly, the as-obtained Rh/AC was treated in a mixture of CO/CH_3I at 240 °C for 6 h (CO passed through a bottle filled with CH_3I at 25 °C with a flow rate of 30 mL/min), during which the re-dispersion of Rh happened that led to the formation of Rh SACs (Rh_1/AC). The reactor was cooled down to room temperature in a flow of CO after the chemical reaction.

Materials Characterization: The morphology of AC, Rh/AC, Rh_1/AC catalysts was characterized by scanning electron microscopy (SEM, FEI Quanta 650 FEG microscope equipped with INCA 350 spectrometer) and transmission electron microscopy (TEM, FEI ChemiSTEM 80-200, probe corrected). The X-ray diffraction (XRD) experiment was conducted on an X’Pert PRO diffractometer (PANalytical) set at 45 kV and 40 mA, using Cu K_α radiation (λ = 1.541874 Å) and a PIXcel detector. Data were collected with the Bragg–Brentano configuration in the 2θ range of 30 – 80° at a scan speed of 0.011° s^{-1}.

X-ray photoelectron spectroscopy (XPS) characterization was carried out on an ESCALAB 250Xi instrument with monochromated Al K_α (1486.6 eV) X-ray source.

Electrocatalytic tests: The catalyst ink was prepared by ultrasonically dispersing 5 mg of Rh_1/AC catalysts with Rh loading of 5 wt% into 500 μL of ethanol + 50 μL of Nafion® (Sigma, 5 wt%) solution. To prepare an electrode for electrocatalytic tests, 6.6 μL of catalyst ink was loaded on a polished glassy carbon (GC) electrode with an exposed area of 0.2 cm^2. The Rh loading can be calculated as follows:

$$C = \frac{5\ mg \times 6.6\ \mu L \times 5\%}{(500\ \mu L + 50\ \mu L) \times 0.2\ cm^2} = 15\ \mu g\ cm^2 \quad (1)$$

For comparison, the HER performances of commercial Pt/C (20 wt%, Johnson Matthey) catalysts, Rh/AC and AC support control samples were also investigated. The working electrode was prepared according to the procedures similar to what described above. The metal loadings of Pt/C and Rh/AC were 60 and 15 μg cm^{-2}, respectively. The electrodes loaded with catalysts were dried at room temperature (ca. 25 °C) naturally in the air.

All the electrocatalytic tests were carried out in a three-electrode configuration at room temperature using a Biologic VMP-3 potentiostat/galvanostat. A graphite rod and a saturated calomel electrode (SCE) were utilized as counter and reference electrodes, respectively. The SCE reference was calibrated before each measurement in pure H_2-saturated 0.5 M H_2SO_4 solution using a clean Pt wire as the working electrode. Unless otherwise stated, all potentials are reported versus RHE by converting the measured potentials to the RHE scale according to the following equation:

$$E_{RHE} = E_{SCE} + 0.059 \times pH + 0.244 \quad (2)$$

Linear scan voltammetry (LSV) was performed at a scan rate of 5 mV s^{-1} in 1.0 M NaOH. *iR*-correction (85%) was made to compensate for the voltage drop between the reference and working electrodes, which was measured by single-point high-frequency impedance measurement. The cyclic durability of Rh_1/AC, Rh/AC and commercial Pt/C catalysts were studied and compared by repetitive cyclic voltammetry (CV) scans. The potential was scanned between −0.36 and 0.14 V vs. RHE at a scan rate of 100 mV s^{-1}. After 45000 cycles, a CV curve was recorded at 5 mV s^{-1}. Furthermore, the stability of Rh_1/AC, Rh/AC and commercial Pt/C catalysts was assessed using chronopotentiometry (CP) at a constant current density of −10 mA cm^{-2}. All LSV, CV and CP curves were recorded in the electrolyte constantly bubbled with Ar/H_2 (5% H_2, v/v).

The electrochemically active surface area (ECSAs) of the catalysts was estimated from the electrochemical double-layer capacitance (C_{dl}) of the catalysts' surface. The C_{dl} value was derived by performing CV in the potential range of 0.34 – 0.54 V vs. RHE (non-Faradaic potential range) at different scan rates (ν) of 10, 20, 30, 40, 50, 60, 70, 80, 90 and 100 mV s^{-1}, followed by extracting the slope from the resulting $|j_a-j_c|/2$ vs. ν plots, where j_a and j_c represent the anodic and cathodic current at 0.44 V vs. RHE. The ECSA can be then calculated by dividing the measured C_{dl} by the specific capacitance (C_S=0.04 mF cm^{-2}) [46].

$$\text{ECSA} = C_{dl} / 0.04 \text{ mF cm}^{-2} \quad \text{(S3)}$$

The electrochemical impedance spectroscopy (EIS) measurements were carried out at an overpotential of 50 mV in the frequency range of 10^5 – 0.01 Hz with a 10 mV sinusoidal perturbation.

The turnover frequency (TOF) of the catalysts was calculated according to the following formula:

$$\text{TOF}\ (s^{-1}) = \frac{j \times A}{2 \times F \times n} \quad \text{(S4)}$$

where j (A cm^{-2}) is the current density at a given overpotential, A = 0.2 cm^2 is the geometric surface area of the electrode, F = 96500 C mol^{-1} stands for the Faraday constant, n (mol) is mole number of Rh or Pt loaded on the GC electrode. All metal cations in the catalyst were assumed to be catalytically active, so the calculated values represent the lower limits of TOF.

4.1.5 References

[1] S. Chu, A. Majumdar, Opportunities and challenges for a sustainable energy future, Nature 488 (2012) 294-303.

[2] Z.J. Chen, X.G. Duan, W. Wei, S.B. Wang, B.J. Ni, Recent advances in transition metal-based electrocatalysts for alkaline hydrogen evolution, J. Mater. Chem. A 7 (2019) 14971-15005.

[3] W. Li, D.H. Xiong, X.F. Gao, L.F. Liu, The oxygen evolution reaction enabled by transition metal phosphide and chalcogenide pre-catalysts with dynamic changes, Chem. Commun. 55 (2019) 8744-8763.

[4] Y.J. Li, Y.J. Sun, Y.N. Qin, W.Y. Zhang, L. Wang, M.C. Luo, H. Yang, S.J. Guo, Recent Advances on Water-Splitting Electrocatalysis Mediated by Noble-Metal-Based Nanostructured Materials, Adv. Energy Mater. 10 (2020) 1903120.

[5] G. Soldano, E.N. Schulz, D.R. Salinas, E. Santos, W. Schmickler, Hydrogen electrocatalysis on overlayers of rhodium over gold and palladium substrates—more active than platinum?, Phys. Chem. Chem. Phys. 13 (2011) 16437-16443.

[6] Q. Wang, M. Ming, S. Niu, Y. Zhang, G.Y. Fan, J.S. Hu, Scalable Solid-State Synthesis of Highly Dispersed Uncapped Metal (Rh, Ru, Ir) Nanoparticles for Efficient Hydrogen Evolution, Adv. Energy Mater. 8 (2018) 1801698.

[7] J. Du, X.L. Wang, C. Li, X.Y. Liu, L. Gu, H.P. Liang, Hollow Rh nanoparticles with nanoporous shell as efficient electrocatalyst for hydrogen evolution reaction, Electrochim. Acta 282 (2018) 853-859.

[8] M. Hu, Q. Chen, R. Ding, J. Wu, Y. Wang, Y. Zhang, G.Y. Fan, Spatially localized fabrication of uniform Rh nanoclusters on nanosheet-assembled hierarchical carbon architectures as excellent electrocatalysts for boosting alkaline hydrogen evolution, Int. J. Hydrogen Energy 45 (2020) 8118-8125.

[9] Y. Zhao, S.H. Xing, X.Y. Meng, J.H. Zeng, S.B. Yin, X.F. Li, Y. Chen, Ultrathin Rh nanosheets as a highly efficient bifunctional electrocatalyst for isopropanol-assisted overall water splitting, Nanoscale 11 (2019) 9319-9326.

[10] Z. Han, R.L. Zhang, J.J. Duan, A.J. Wang, Q.L. Zhang, H. Huang, J.J. Feng, Platinum-rhodium alloyed dendritic nanoassemblies: An all-pH efficient and stable electrocatalyst for hydrogen evolution reaction, Int. J. Hydrogen Energy 45 (2020) 6110-6119.

[11] F.L. Yang, Y.M. Zhao, Y.S. Du, Y.T. Chen, G.Z. Cheng, S.L. Chen, W. Luo, A Monodisperse Rh_2P-Based Electrocatalyst for Highly Efficient and pH-Universal Hydrogen Evolution Reaction, Adv. Energy Mater. 8 (2018) 1703489.

[12] Z. Li, Y. Feng, Y.L. Liang, C.Q. Cheng, C.K. Dong, H. Liu, X.W. Du, Stable Rhodium (IV) Oxide for Alkaline Hydrogen Evolution Reaction, Adv. Mater. 32 (2020) 1908521.

[13] K. Deng, T.L. Ren, Y. Xu, S.L. Liu, Z.C. Dai, Z.Q. Wang, X.N. Li, L. Wang, H.J. Wang, Transition metal M (M = Co, Ni, and Fe) and boron co-modulation in Rh-based

aerogels for highly efficient and pH-universal hydrogen evolution electrocatalysis, J. Mater. Chem. A 8 (2020) 5595-5600.

[14] M.D. Sharma, C. Mahala, M. Basu, Nanosheets of $MoSe_2$@M (M = Pd and Rh) function as widespread pH tolerable hydrogen evolution catalyst, J. Colloid Interface Sci. 534 (2019) 131-141.

[15] Y.F. Cheng, S.K. Lu, F. Liao, L.B. Liu, Y.Q. Li, M.W. Shao, Rh-MoS_2 Nanocomposite Catalysts with Pt-Like Activity for Hydrogen Evolution Reaction, Adv. Funct. Mater. 27 (2017) 1700359.

[16] X.Y. Meng, C. Ma, L.Z. Jiang, R. Si, X.G. Meng, Y.C. Tu, L. Yu, X.H. Bao, D.H. Deng, Distance Synergy of MoS_2-Confined Rhodium Atoms for Highly Efficient Hydrogen Evolution, Angew. Chem. Int. Ed. 59 (2020) 10502-10507.

[17] H.Y. Zheng, X.B. Huang, H.Y. Gao, W.J. Dong, G.L. Lu, X. Chen, G. Wang, Decorating cobalt phosphide and rhodium on reduced graphene oxide for high-efficiency hydrogen evolution reaction, J. Energy Chem. 34 (2019) 72-79.

[18] F. Luo, L. Guo, Y.H. Xie, J.X. Xu, W.W. Cai, K.G. Qu, Z.H. Yang, Robust hydrogen evolution reaction activity catalyzed by ultrasmall Rh–Rh_2P nanoparticles, J. Mater. Chem. A 8 (2020) 12378-12384.

[19] B.T. Qiao, A.Q. Wang, X.F. Yang, L.F. Allard, Z. Jiang, Y.T. Cui, J.Y. Liu, J. Li, T. Zhang, Single-atom catalysis of CO oxidation using Pt_1/FeO_x, Nat. Chem. 3 (2011) 634-641.

[20] T.T. Chao, X. Luo, W.X. Chen, B. Jiang, J.J. Ge, Y. Lin, G. Wu, X.Q. Wang, Y.M. Hu, Z.B. Zhuang, Y.E. Wu, X. Hong, Y.D. Li, Atomically Dispersed Copper–Platinum Dual Sites Alloyed with Palladium Nanorings Catalyze the Hydrogen Evolution Reaction, Angew. Chem. Int. Ed. 56 (2017) 16047-16051.

[21] P.Z. Chen, T.P. Zhou, L.L. Xing, K. Xu, Y. Tong, H. Xie, L.D. Zhang, W.S. Yan, W.S. Chu, C.Z. Wu, Y. Xie, Atomically Dispersed Iron–Nitrogen Species as Electrocatalysts for Bifunctional Oxygen Evolution and Reduction Reactions, Angew. Chem. Int. Ed. 56 (2017) 610-614.

[22] Y.H. Han, Y.G. Wang, W.X. Chen, R.R. Xu, L.R. Zheng, J. Zhang, J. Luo, R.A. Shen, Y.Q. Zhu, W.C. Cheong, C. Chen, Q. Peng, D.S. Wang, Y.D. Li, Hollow N-Doped Carbon Spheres with Isolated Cobalt Single Atomic Sites: Superior Electrocatalysts for Oxygen Reduction, J. Am. Chem. Soc. 139 (2017) 17269-17272.

[23] C.M. Zhao, X.Y. Dai, T. Yao, W.X. Chen, X.Q. Wang, J. Wang, J. Yang, S.Q. Wei, Y.E. Wu, Y.D. Li, Ionic Exchange of Metal–Organic Frameworks to Access Single Nickel Sites for Efficient Electroreduction of CO_2, J. Am. Chem. Soc. 139 (2017) 8078-8081.

[24] J.X. Zhao, Z.F. Chen, Single Mo Atom Supported on Defective Boron Nitride Monolayer as an Efficient Electrocatalyst for Nitrogen Fixation: A Computational Study, J. Am. Chem. Soc. 139 (2017) 12480-12487.

[25] D. Zhao, Z.W. Zhuang, X. Cao, C. Zhang, Q. Peng, C. Chen, Y.D. Li, Atomic site electrocatalysts for water splitting, oxygen reduction and selective oxidation, Chem. Soc. Rev. 49 (2020) 2215-2264.

[26] Y.J. Chen, S.F. Ji, C. Chen, Q. Peng, D.S. Wang, Y.D. Li, Single-Atom Catalysts: Synthetic Strategies and Electrochemical Applications, Joule 2 (2018) 1242-1264.

[27] C.Y. Li, L. Yan, L.L. Lu, K. Xiong, W.L. Wang, M. Jiang, J. Liu, X.G. Song, Z.P. Zhan, Z. Jiang, Y.J. Ding, Single atom dispersed Rh-biphephos&PPh_3@porous organic copolymers: highly efficient catalysts for continuous fixed-bed hydroformylation of propene, Green Chem. 18 (2016) 2995-3005.

[28] L.B. Wang, H.L. Li, W.B. Zhang, X. Zhao, J.X. Qiu, A.W. Li, X.S. Zheng, Z.P. Hu, R. Si, J. Zeng, Supported Rhodium Catalysts for Ammonia–Borane Hydrolysis: Dependence of the Catalytic Activity on the Highest Occupied State of the Single Rhodium Atoms, Angew. Chem. Int. Ed. 56 (2017) 4712-4718.

[29] Y. Tang, Y.T. Li, V. Fung, D.E. Jiang, W.X. Huang, S.R. Zhang, Y. Iwasawa, T. Sakata, L. Nguyen, X.Y. Zhang, A.I. Frenkel, F. Tao, Single rhodium atoms anchored in micropores for efficient transformation of methane under mild conditions, Nat. Commun. 9 (2018) 1231.

[30] S.X. Bai, F.F. Liu, B.L. Huang, F. Li, H.P. Lin, T. Wu, M.Z. Sun, J.B. Wu, Q. Shao, Y. Xu, X.Q. Huang, High-efficiency direct methane conversion to oxygenates on a cerium dioxide nanowires supported rhodium single-atom catalyst, Nat. Commun. 11 (2020) 954.

[31] Z. Ren, Y. Liu, Y. Lyu, X.G. Song, C.Y. Zheng, S.Q. Feng, Z. Jiang, Y.J. Ding, Single-atom Rh based bipyridine framework porous organic polymer: A high active and superb stable catalyst for heterogeneous methanol carbonylation, J. Catal. 369 (2019) 249-256.

[32] M.J. Hülsey, B. Zhang, Z.R. Ma, H. Asakura, D.A. Do, W. Chen, T. Tanaka, P. Zhang, Z.L. Wu, N. Yan, In situ spectroscopy-guided engineering of rhodium single-atom catalysts for CO oxidation, Nat. Commun. 10 (2019) 1330.

[33] B. Han, T.B. Li, J.Y. Zhang, C.B. Zeng, H. Matsumoto, Y. Su, B.T. Qiao, T. Zhang, A highly active Rh_1/CeO_2 single-atom catalyst for low-temperature CO oxidation, Chem. Commun. 56 (2020) 4870-4873.

[34] Y. Xiong, J.C. Dong, Z.Q. Huang, P.Y. Xin, W.X. Chen, Y. Wang, Z. Li, Z. Jin, W. Xing, Z.B. Zhuang, J.Y. Ye, X. Wei, R. Cao, L. Gu, S.G. Sun, L. Zhuang, X.Q. Chen, H. Yang, C. Chen, Q. Peng, C.R. Chang, D.S. Wang, Y.D. Li, Single-atom Rh/N-doped carbon electrocatalyst for formic acid oxidation, Nat. Nanotechnol. 15 (2020) 390-397.

[35] J.Q. Guan, X.D. Wen, Q.Q. Zhang, Z.Y. Duan, Atomic rhodium catalysts for hydrogen evolution and oxygen reduction reactions. Carbon 164 (2020) 121-128

[36] S.Q. Feng, X.G. Song, Y. Liu, X.S. Lin, L. Yan, S.Y. Liu, W.R. Dong, X.M. Yang, Z. Jiang, Y.J. Ding, In situ formation of mononuclear complexes by reaction-induced atomic dispersion of supported noble metal nanoparticles, Nat. Commun. 10 (2019) 5281.

[37] S. Yacob, S. Park, B.A. Kilos, D.G. Barton, J.M. Notestein, Vapor-phase ethanol carbonylation with heteropolyacid-supported Rh, J. Catal. 325 (2015) 1-8.

[38] C.E. Vallet, A. Choudhury, P.E. Sobol, C.W. White, XPS characterization of anodic layers grown on Ir- and Rh-implanted titanium, Electrochim. Acta 38 (1993) 1313-1320.

[39] M.W. Peterson, B.A. Parkinson, Photoelectrochemical Characterization of Novel Rhodium Iodide Photoconductors, J. Electrochem. Soc. 135 (1988) 1424-1431.

[40] M.F. Li, K.N. Duanmu, C.Z. Wan, T. Cheng, L. Zhang, S. Dai, W.X. Chen, Z.P. Zhao, P. Li, H.L. Fei, Y.M. Zhu, R. Yu, J. Luo, K.T. Zang, Z.Y. Lin, M.N. Ding, J. Huang, H.T. Sun, J.H. Guo, X.Q. Pan, W.A. Goddard, P. Sautet, Y. Huang, X.F. Duan, Single-atom tailoring of platinum nanocatalysts for high-performance multifunctional electrocatalysis. Nat. Catal. 2 (2019) 495-503.

[41] L.L. Cao, Q.Q. Luo, W. Liu, Y. Lin , X.K. Liu, Y.J. Cao, W. Zhang, Y. Wu, J.L. Yang, T. Yao, S.Q. Wei, Identification of single-atom active sites in carbon-based cobalt catalysts during electrocatalytic hydrogen evolution. Nat. Catal. 2 (2019) 134-141.

[42] J.Y. Xu, T.F. Liu, J.J. Li, B. Li, Y.F. Liu, B.S. Zhang, D.H. Xiong, I. Amorim, W. Li, L.F. Liu, Boosting the hydrogen evolution performance of ruthenium clusters through synergistic coupling with cobalt phosphide, Energy Environ. Sci. 11 (2018) 1819-1827.

[43] J.Y. Xu, Z. Lian, B. Wei, Y. Li, O. Bandarchuk, N. Zhang, Z.P. Yu, A. Araujo, I. Amorim, Z.C. Wang, B. Li, L.F. Liu, Strong Electronic Coupling between Ultrafine Iridium–Ruthenium Nanoclusters and Conductive, Acid-Stable Tellurium Nanoparticle Support for Efficient and Durable Oxygen Evolution in Acidic and Neutral Media. ACS Catal. 10 (2020) 3571-3579.

[44] Z.P. Yu, J.Y. Xu, Y.F. Li, B. Wei, N. Zhang, Y. Li, O. Bandarchuk, H.W. Miao, A. Araujo, Z.C. Wang, J.L. Faria, Y.Y. Liu, L.F. Liu, Ultrafine oxygen-defective iridium oxide nanoclusters for efficient and durable water oxidation at high current densities in acidic media. J. Mater. Chem. A 8 (2020) 24743-24751.

[45] J.Y. Xu, J.J. Li, Z. Lian, Y. Li, B. Wei, Z.P. Yu, O. Bondarchuk, I. Amorim, V. Tileli, B. Li, L.F. Liu, Atomic-Step Enriched Ruthenium–Iridium Nanocrystals Anchored Homogeneously on MOF-Derived Support for Efficient and Stable Oxygen Evolution in Acidic and Neutral Media. ACS Catalysis 11 (2021) 3402-3413.

[46] C.C.L. McCrory, S.H. Jung, I.M. Ferrer, S.M. Chatman, J.C. Peters, T.F. Jaramillo, Benchmarking Hydrogen Evolving Reaction and Oxygen Evolving Reaction Electrocatalysts for Solar Water Splitting Devices. J. Am. Chem. Soc. 137 (2015) 4347-4357.

4.2 Bifunctional atomically dispersed ruthenium electrocatalysts with ultralow metal loading for efficient bipolar membrane water electrolysis

Abstract

Atomically dispersed catalysts (ADCs) have recently drawn considerable interest for use in water electrolysis to produce hydrogen, because they allow for maximal utilization of metal species, particularly the expensive and scarce platinum group metals. Herein, we report the electrocatalytic performance of atomically dispersed ruthenium catalysts (Ru ADCs) with ultralow Ru loading (0.2 wt%). The as-obtained Ru ADCs (Ru (0.2)-NC) are active for both hydrogen evolution reaction (HER) and oxygen evolution reaction (OER), which only require a low overpotential (η) of 47.1 and 72.8 mV to deliver 10 mA cm^{-2} for HER in 0.5 M H_2SO_4 and 1.0 M KOH, respectively, and of 300 mV for OER in 1.0 M KOH, showing favorable bifunctionality. Density functional theory (DFT) calculations reveal that the Ru-N bonding plays an important role in lowering the energy barrier of the reactions, boosting the HER and OER activities. Furthermore, the bipolar membrane (BPM) water electrolysis using the bifunctional Ru (0.2)-NC as both HER and OER catalysts can afford 10 mA cm^{-2} under a low cell voltage of only 0.89 V, and does not show any performance decay upon 100-h continuous operation, showing great potential for energy-saving hydrogen production.

4.2.1 Introduction

Hydrogen (H_2) has now been broadly accepted to be an important alternative to the conventional fossil fuels, and its widespread usage is crucial for achieving global carbon neutrality [1]. Water electrolysis, powered by renewable energy like solar and wind, is proposed to be the most promising approach to “green” hydrogen production [2], and many countries have recently launched initiatives aiming to accelerate the deployment of electrolyzers to produce green hydrogen [3]. However, for large-scale deployment of electrolyzers on gigawatt (GW) scale or beyond, it is essential to address some major challenges in terms of, for example, the availability of key materials and components, costs and energy demand, such that massive production of green hydrogen will become technically viable and economically competitive.

Electrocatalysts are key components of water electrolyzers and critically determine their electrochemical performance toward the hydrogen evolution reaction (HER) and oxygen evolution reaction (OER). In the last two decades, considerable efforts have been

made to developing efficient and stable electrocatalysts with reduced utilization of metal species taken into account [4-8]. In particular, atomically dispersed catalysts (ADCs) have drawn significant attention in recent years and were demonstrated to be promising electrocatalysts for water electrolysis [9-11]. ADCs allow for maximal utilization of metal species and can help markedly reduce the metal loading in the catalyst layers without compromising the electrocatalytic performance. To some extent, this will enable high-performance platinum group metal (PGM) catalysts to be used in electrolyzers, but meanwhile not notably increase the materials costs, especially for the relatively less expensive PGM such as ruthenium (Ru). Indeed, Ru-based materials have recently been extensively studied for use to catalyze the HER and OER [4, 12, 13]. They were long known to be active for the OER in both acidic and alkaline solutions, and were lately also demonstrated to be good electrocatalysts for the HER [14-16]. Particularly, Ru ADCs with a Ru loading of 0.2 – 1.0 wt% have shown electrocatalytic performance comparable to that of the commercial benchmark catalysts (*e.g.*, Pt/C for HER and RuO_2 for OER) [14-19]. It has now generally accepted that the RuN_x species in Ru ADCs are electrocatalytically active sites and play an important role in improving the catalytic performance [16, 18, 20]. The nitrogen groups on the catalyst support can not only impart uniform dispersion of Ru species [7], but also alter the electronic structure of Ru, prompting the electrocatalytic reaction [16, 18]. Notwithstanding some progress, the intrinsic catalytic performance and stability of Ru ADCs still need to be further improved.

While ADCs with reduced amount of metal species in electrocatalysts may contribute to cost reduction, for large-capacity electrolyzers lowering the energy demand is also an effective approach to saving system costs. To this end, the recently developed bipolar membrane water electrolysis (BPMWE) seems promising [21]. A bipolar membrane (BPM) consists of a cation exchange membrane (CEM) permselective to cations adjoining with an anion exchange membrane (AEM) permselective to anions. It enables the HER to occur in kinetically favorable acidic solution in the cathodic compartment and the OER to simultaneously take place in kinetically favorable alkaline solution in the anodic compartment. Moreover, when used in the “forward-bias” configuration (*e.g.*, CEM side facing the cathode and AEM side facing the anode) [21, 22], the external electrical energy needed to drive water electrolysis can be significantly diminished due to the assistance of electrochemical neutralization of acid and alkaline. BPMWE has been recently reported to be enabled with a number of earth-abundant electrocatalysts [21-23], and showed preferable energy-saving feature in comparison to the conventional

proton exchange membrane water electrolysis (PEMWE) or anion exchange membrane water electrolysis (AEMWE).

Herein, we report the electrocatalytic performance of Ru ADCs with an ultralow Ru loading of only 0.2 wt% (Ru (0.2)-NC) synthesized through a two-step wet chemical impregnation – pyrolysis method. We show that the ammonium salt treated activated carbon may offer abundant pyrrolic and pyridinic nitrogen that can bind Ru species during thermal pyrolysis. The as-prepared Ru (0.2)-NC exhibits outstanding HER and OER performance in 1.0 M KOH, with a high turnover frequency (TOF) of 11.5 s^{-1} at η = 100 mV for HER and 4.89 s^{-1} at η = 300 mV for OER as well as good catalytic stability of at least 100 h at a current density of 10 mA cm^{-2}. Density functional theory (DFT) calculations confirm that the Ru atoms bonding with either pyrrolic or pyridinic nitrogen indeed markedly decrease the energy barrier to the catalytic reactions, boosting the activity. Furthermore, we demonstrate that the Ru (0.2)-NC can be used as bifunctional electrocatalysts in BPMWE in the forward-bias configuration, where the cell only demands a low voltage of 0.89 V to deliver 10 mA cm^{-2} and can stably operate for 100 h without any performance decay, showing great promise for low-cost, energy-saving production of green hydrogen.

4.2.2 Results and discussion

Figure 4.2.1a shows the X-ray diffractometry (XRD) patterns of as-prepared Ru (0.2)-NC and the pristine nitrogen-doped carbon (NC) control sample. No diffraction peaks from any metallic ruthenium or ruthenium compounds can be resolved for the Ru (0.2)-NC, suggesting that ruthenium may either be atomically dispersed on NC or consist of tiny crystallites that significantly widen the diffraction peaks. The surface chemical states of Ru (0.2)-NC and pristine NC were investigated by X-ray photoelectron spectroscopy (XPS). The high-resolution N1s spectra of both samples can be deconvoluted into several peaks (**Figure 4.2.1b**), corresponding to pyridinic-N (398.0 eV), pyrrolic-N (399.8 eV), graphitic-N (400.9 eV) and oxidized-N (402.9 eV), respectively [24, 25]. Notably, different from the pristine NC, the Ru (0.2)-NC shows a component arising from metal–nitrogen (M–N) bonding at 399.0 eV, indicating that Ru atoms are anchored by uncoordinated nitrogen species. Further XPS quantitative analysis manifests that the content of the M–N bond is 10.7 % for Ru (0.2)-NC (**Table 4.2.1**).

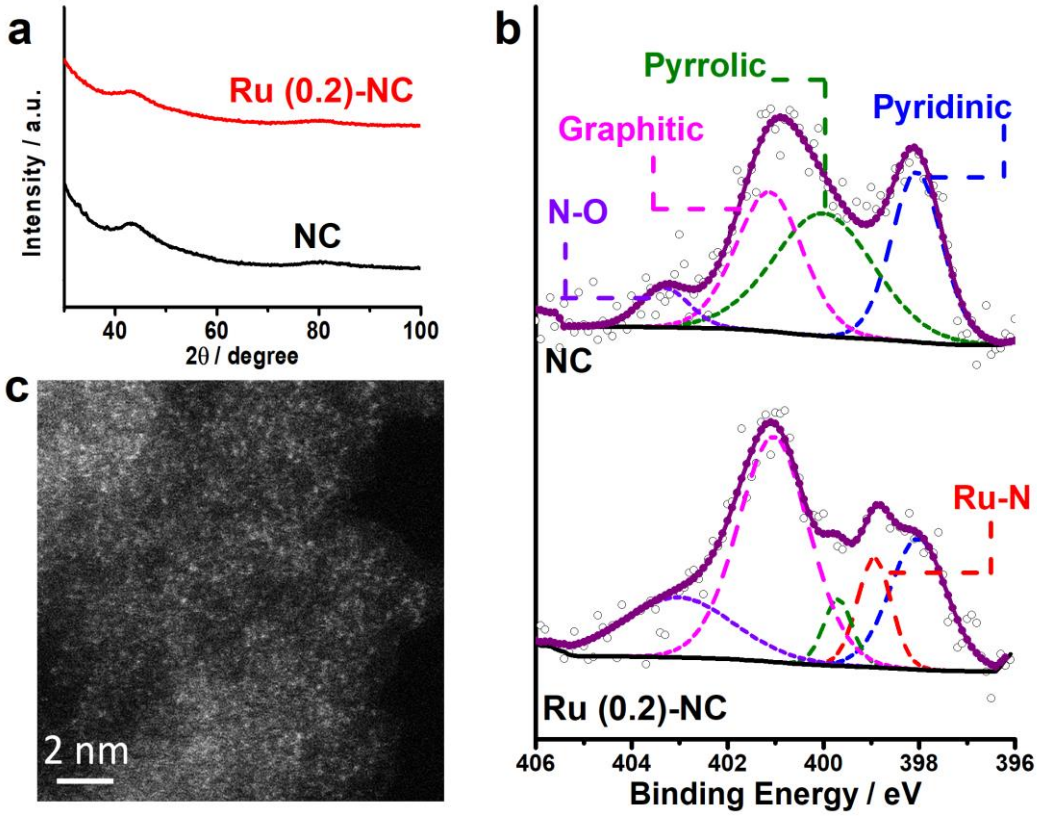

Figure 4.2.1 a) XRD patterns and b) high-resolution N1s spectrum of Ru (0.2)-NC and pristine NC. c) HAADF-STEM image of Ru (0.2)-NC.

Table 4.2.1 Fitting results of the N1s spectrum in pristine NC and Ru (0.2)-NC.

Samples	Pyridinic N	M-N	Pyrrolic N	Graphitic N	Oxidized N
NC	26.3	/	38.8	29.1	5.8
Ru (0.2)-NC	20.9	10.7	5.3	44.4	18.7

The morphology and microstructure of Ru (0.2)-NC catalysts were further examined by scanning electron microscopy (SEM) and transmission electron microscopy (TEM). Loading Ru on the NC support did not markedly alter its morphology, as revealed by SEM examination (**Figure 4.2.2**). **Figure 4.2.3a-b** show the high resolution TEM (HRTEM) images of Ru (0.2)-NC, where only amorphous microstructure is observed and no large Ru nanoparticles are visible. Further the high-angle annular dark field scanning transmission electron microscopy (HAADF-STEM) imaging revealed a high degree of atomic dispersion of Ru on the NC support (**Figure 4.2.1c**). However, some ultrafine

clusters with sub-nanometric sizes were also occasionally found along with the ADCs (**Figures 4.2.3c** and **4.2.3d**).

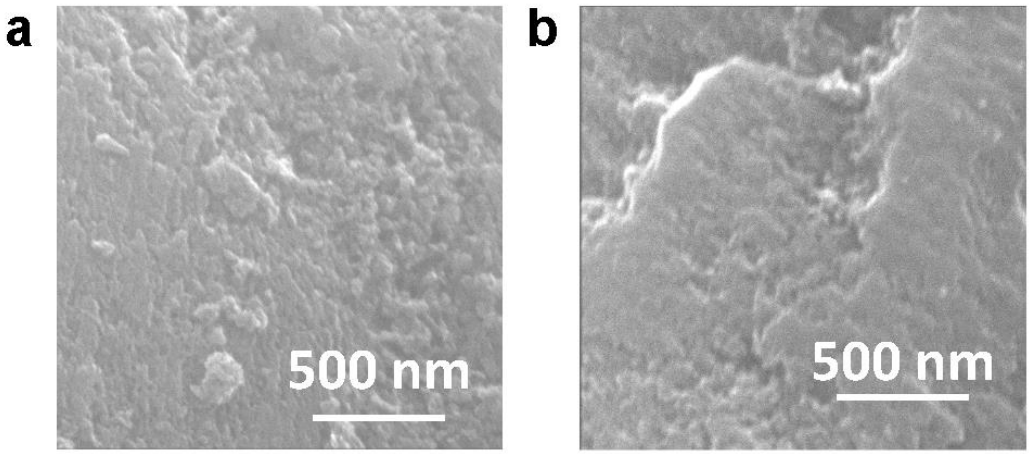

Figure 4.2.2 SEM images of a) pristine NC and b) Ru (0.2)-NC.

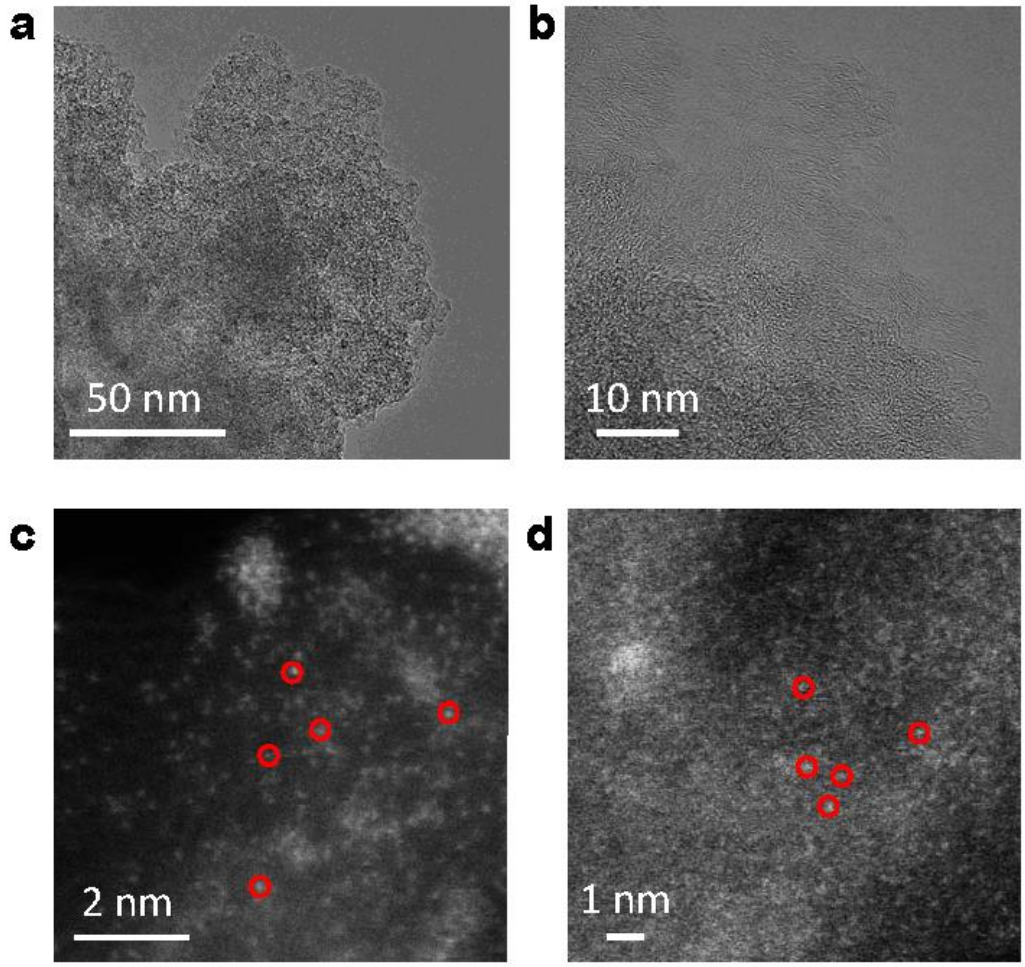

Figure 4.2.3 a) Low- and b) high-magnification HRTEM images of Ru (0.2)-NC. (c, d) HAADF-STEM images of Ru (0.2)-NC, where some nanometric clusters can be distinguished.

The electrocatalytic HER performance of the Ru (0.2)-NC and other control catalysts including pristine NC and commercial Pt/C was investigated in both 0.5 M H_2SO_4 and 1.0 M KOH in a three-electrode configuration at room temperature. The pristine NC support exhibits inferior HER performance in both acidic and alkaline solutions and only delivers a current density of –5.56 and –6.76 mA cm^{-2} in 0.5 M H_2SO_4 and 1.0 M KOH (**Figures 4.2.4a** and **4.2.4b**), respectively, when an overpotential (η) of 250 mV is applied. Upon loading Ru, the HER catalytic current density is significantly enhanced and becomes favorably comparable to that of the commercial Pt/C benchmark, merely requiring a low overpotential of 47.1 and 72.8 mV to deliver a cathodic current density of 10 mA cm^{-2} in 0.5 M H_2SO_4 and 1.0 M KOH, respectively. This indicates that the atomically dispersed Ru will be a good low-cost alternative to Pt/C for HER, particularly for PEM water electrolysis in acidic environment where non-PGM catalysts, though existing, do not show sufficiently good catalytic performance [26-28]. The reaction kinetics of all catalysts was studied by the Tafel analysis (**Figure 4.2.5**). The Ru (0.2)-NC exhibits a Tafel slope of 72 mV dec^{-1} in 0.5 M H_2SO_4, higher than that of Pt/C (34 mV dec^{-1}), indicating that the HER proceeds on Ru (0.2)-NC through the Volmer-Heyrovsky mechanism. In 1.0 M KOH, The Ru (0.2)-NC shows a Tafel slope of 74 mV dec^{-1}, close to that of Pt/C (77 mV dec^{-1}). Similar trend for HER kinetics was also confirmed by the EIS studies, where Ru (0.2)-NC shows the same and even smaller charge transfer resistance (R_{ct}) than that of Pt/C in 0.5 M H_2SO_4 and 1.0 M KOH, respectively (**Figure 4.2.6**). For PGM electrocatalysts, mass activity is a critical performance indicator toward practical applications reflecting the effectiveness of PGM utilization [7, 10]. Ru (0.2)-NC can deliver an exceptionally large mass activity of 18.0 and 13.8 A mg^{-1} at η = 50 mV in 0.5 M H_2SO_4 and 1.0 M KOH, respectively (**Figure 4.2.7**), which is 92 and 153 times higher than that of commercial Pt/C, suggesting that dispersing metal catalysts on atomic scale is indeed an effective strategy of maximizing metal utilization without compromising the catalytic activity.

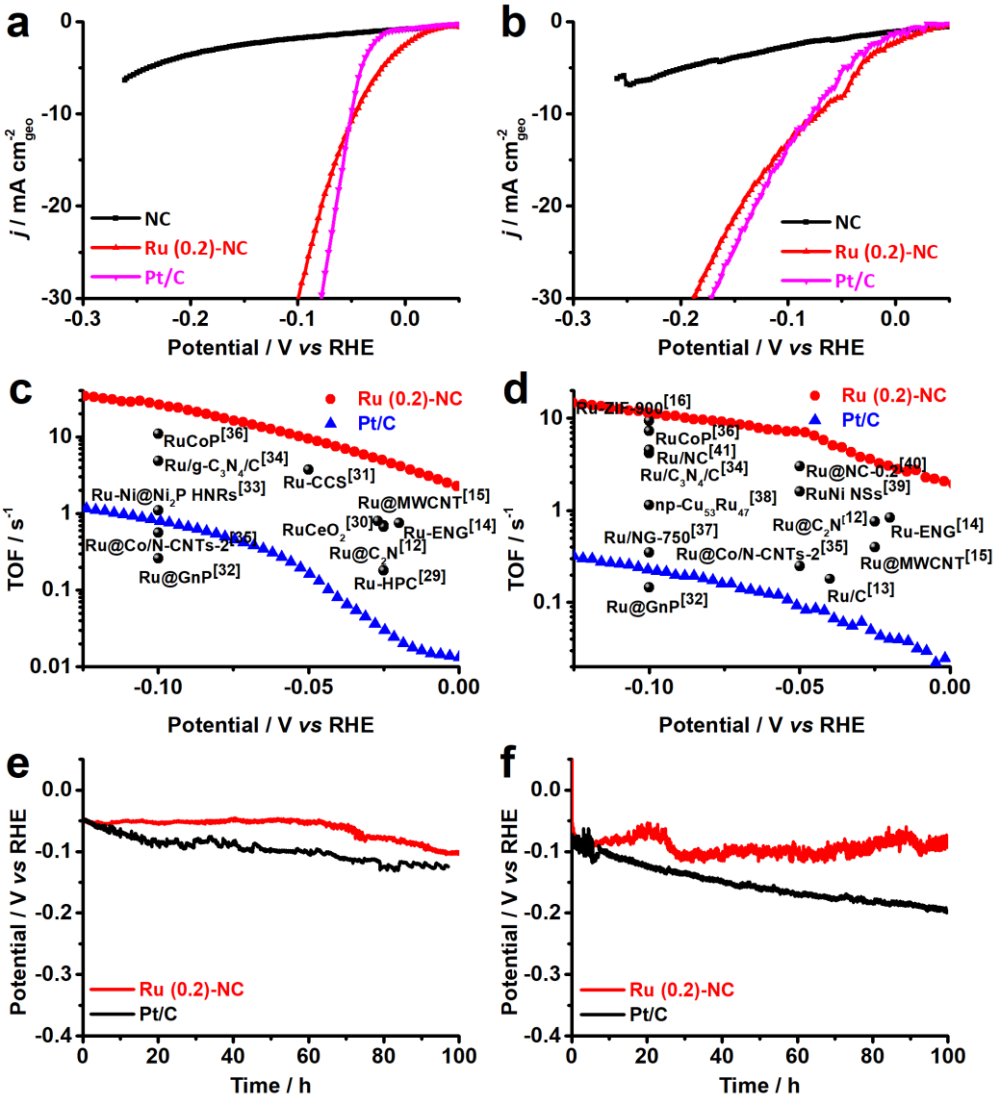

Figure 4.2.4 Electrocatalytic HER performance of Ru (0.2)-NC and other control catalysts. a, b) LSV curves. Scan rate: 5 mV s^{-1}. c, d) Comparison of the TOF values with other start-of-the-art Ru-based HER catalysts. e, f) Long-term catalytic stability test at –10 mA cm^{-2}. Data were acquired in a, c, e) 0.5 M H_2SO_4 and b, d, f) 1.0 M KOH, respectively.

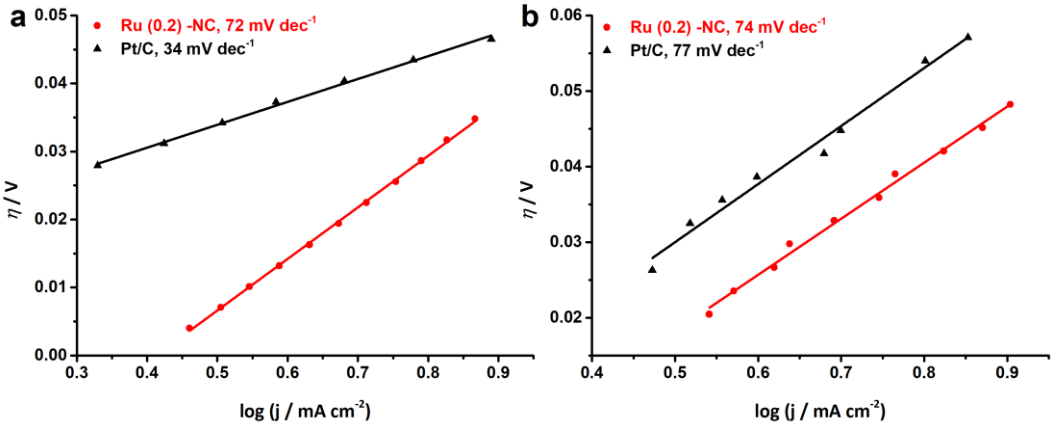

Figure 4.2.5 Tafel slopes of the catalysts derived from electrocatalytic tests in a) 0.5 M H_2SO_4 and b) 1.0 M KOH.

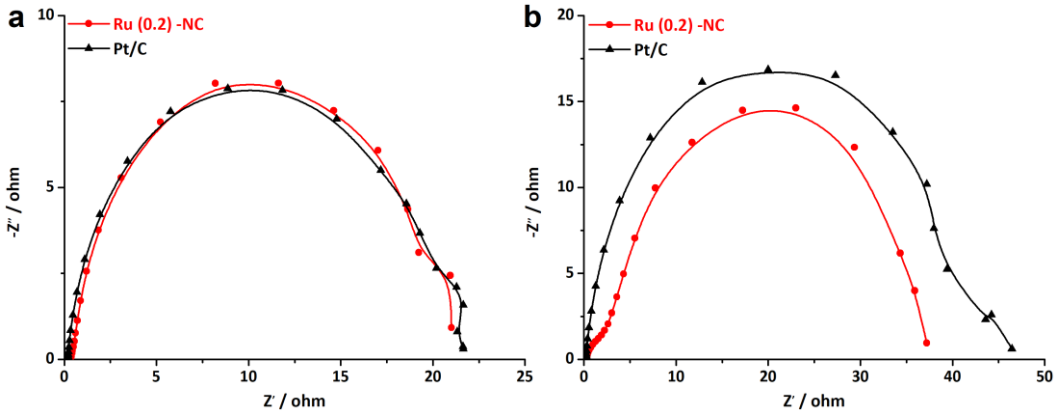

Figure 4.2.6 Nyquist plots of the catalysts toward HER tested in a) 0.5 M H_2SO_4 and b) 1.0 M KOH.

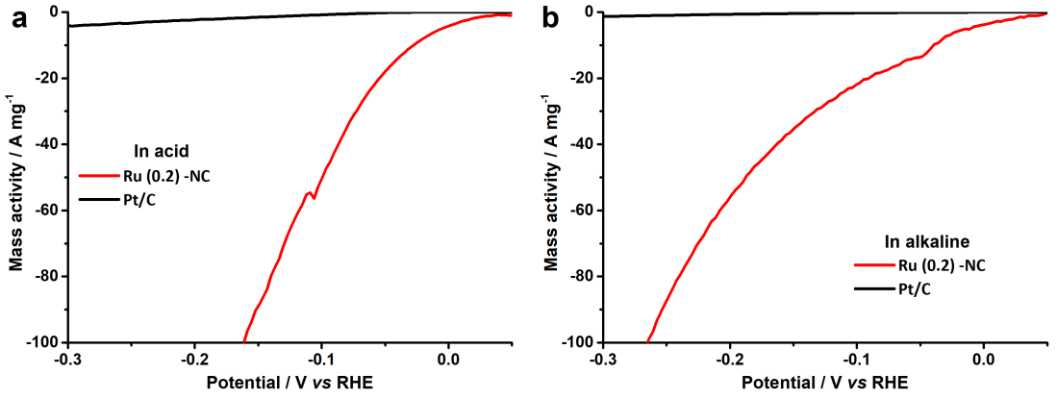

Figure 4.2.7 Mass activities of Ru (0.2)-NC and commercial Pt/C catalysts toward HER tested in a) 0.5 M H_2SO_4 and b) 1.0 M KOH.

To gain more insight into the good activity, the electrochemically active surface area (ECSA) of all catalysts was measured. As revealed in **Figure 4.2.8**, Ru (0.2)-NC shows an ECSA value of 334.6 cm^2, higher than that of the commercial Pt/C (258.9 cm^2), which indicates that the highly dispersed Ru provides more active sites for the HER. The intrinsic HER catalytic activity of Ru (0.2)-NC was assessed by turnover frequency (TOF) and compared to that of some other Ru-based electrocatalysts reported recently (**Figures 4.2.4c** and **4.2.4d**). The Ru (0.2)-NC shows a TOF value of 26.2 and 11.5 s^{-1} at η = 100 mV in 0.5 M H_2SO_4 and 1.0 M KOH, respectively, substantially outperforming commercial Pt/C and many other Ru-based electrocatalysts [12-16, 29-41] (**Tables 4.2.2** and **4.2.3**), which corroborates that Ru (0.2)-NC is intrinsically more active for the HER. Moreover, the Ru (0.2)-NC catalysts reveal outstanding catalytic stability for the HER activity in both acidic and alkaline electrolytes (**Figures 4.2.4e** and **4.2.4f**), able to sustain at −10 mA cm^{-2} for 100-h continuous electrolysis without significant performance degradation. The slight potential increase might stem from the active site loss [42, 43].

In contrast, Pt/C exhibits a notable performance decay, consistent with previous reports in the literature, which may result from to weak interactions between the Pt NPs and the carbon support [36, 44, 45].

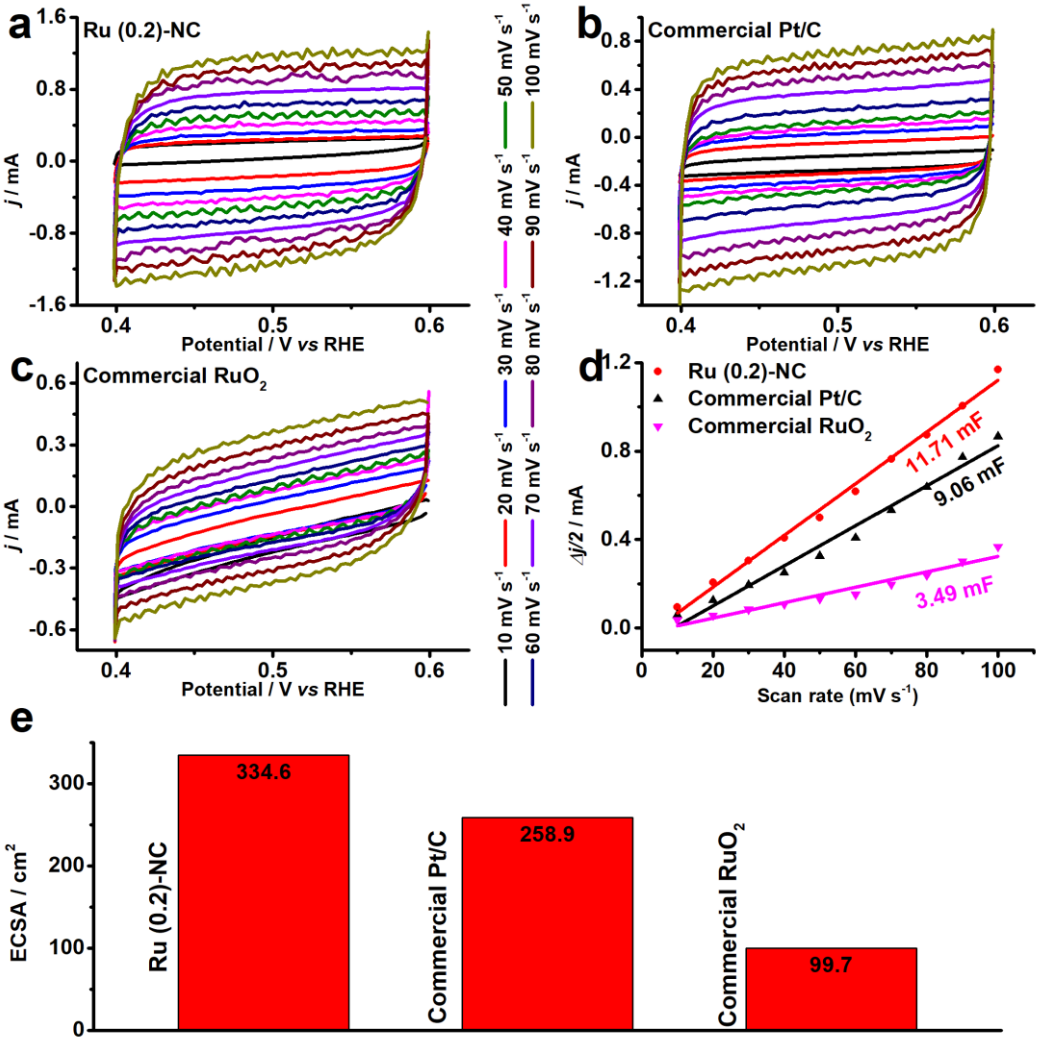

Figure 4.2.8 Electrochemical CV curves of a) Ru (0.2)-NC, b) commercial Pt/C and c) commercial RuO_2, recorded at different scan rates of 10, 20, 30, 40, 50, 60, 70, 80, 90 and 100 mV s^{-1}. d) Plots of the capacitive currents as a function of the scan rate for all catalysts. e) ECSA of all catalysts.

Table 4.2.2 Comparison of the turnover frequencies (TOFs) of Ru (0.2)-NC to those of other recently reported Ru-based HER catalysts tested in acidic condition.

Catalyst	Overpotential (V)	TOF (s^{-1})	Reference
Ru (0.2)-NC	**0.1**	**26.2**	**This work**
Ru-HPC	0.025	0.18	Nano Energy 2019, 58, 1–10.
Ru@C_2N	0.025	0.67	Nat. Nanotechnol. 2017, 12, 441-446.

Ru@MWCNT	0.025	0.70	Nat. Commun. 2020, 11, 1278.
$RuCeO_2$	0.027	0.8	ACS Appl. Mater. Interfaces 2018, 10, 6299–6308.
Ru-CCS	0.05	3.7	J. Mater. Chem. A 2018, 6, 2311–2317.
Ru@GnP	0.1	0.26	Adv. Mater. 2018, 30, 1803676.
Ru-Ni@Ni_2P-HNRs	0.1	1.1	J. Am. Chem. Soc. 2018, 140, 2731–2734.
Ru/g-C_3N_4/C	0.1	4.85	J. Am. Chem. Soc. 2016, 138, 16174–16181.
Ru-ENG	0.02	0.75	Nano Energy 2020, 76, 105114.
Ru@Co/N-CNTs-2	0.1	0.56	ACS Sustainable Chem. Eng. 2020, 8, 9136–9144.
RuCoP	0.1	10.95	Energy Environ. Sci. 2018, 11, 1819.

Table 4.2.3 Comparison of the turnover frequencies (TOFs) of Ru (0.2)-NC to those of other recently reported Ru-based HER catalysts tested in alkaline condition.

Catalyst	**Overpotential (V)**	**TOF (s^{-1})**	**Reference**
Ru (0.2)-NC	**0.1**	**11.5**	**This work**
Ru@MWCNT	0.025	0.40	Nat. Commun. 2020, 11, 1278.
Ru@C_2N	0.025	0.76	Nat. Nanotechnol. 2017, 12, 441-446.
Ru/C	0.04	0.18	Adv. Energy Mater. 2018, 8, 1801698.
Ru@GnP	0.1	0.145	Adv. Mater. 2018, 30, 1803676.
Ru/NG-750	0.1	0.35	ACS Appl. Mater. Interfaces 2017, 9, 3785–3791.
Ru-ENG	0.02	0.84	Nano Energy 2020, 76, 105114.
Ru@Co/N-CNTs-2	0.05	0.25	ACS Sustainable Chem. Eng. 2020, 8, 9136–9144.
np-$Cu_{53}Ru_{47}$	0.1	1.139	ACS Energy Lett. 2020, 5, 192−199.
RuNi NSs	0.05	1.60	Nano Energy 2019, 66, 104173.
Ru-ZIF-900	0.1	9.38	J. Mater. Chem. A 2020, 8, 3203-3210.
Ru/g-C_3N_4/C	0.1	4.2	J. Am. Chem. Soc. 2016, 138, 16174-16181.

Ru@NC-0.2	0.05	3.02	Angew. Chem. Int. Ed. 2018, 57, 5848-5852.
Ru/NC	0.1	4.55	J. Mater. Chem. A 2017, 5, 25314-25318.
RuCoP	0.1	7.26	Energy Environ. Sci. 2018, 11, 1819.

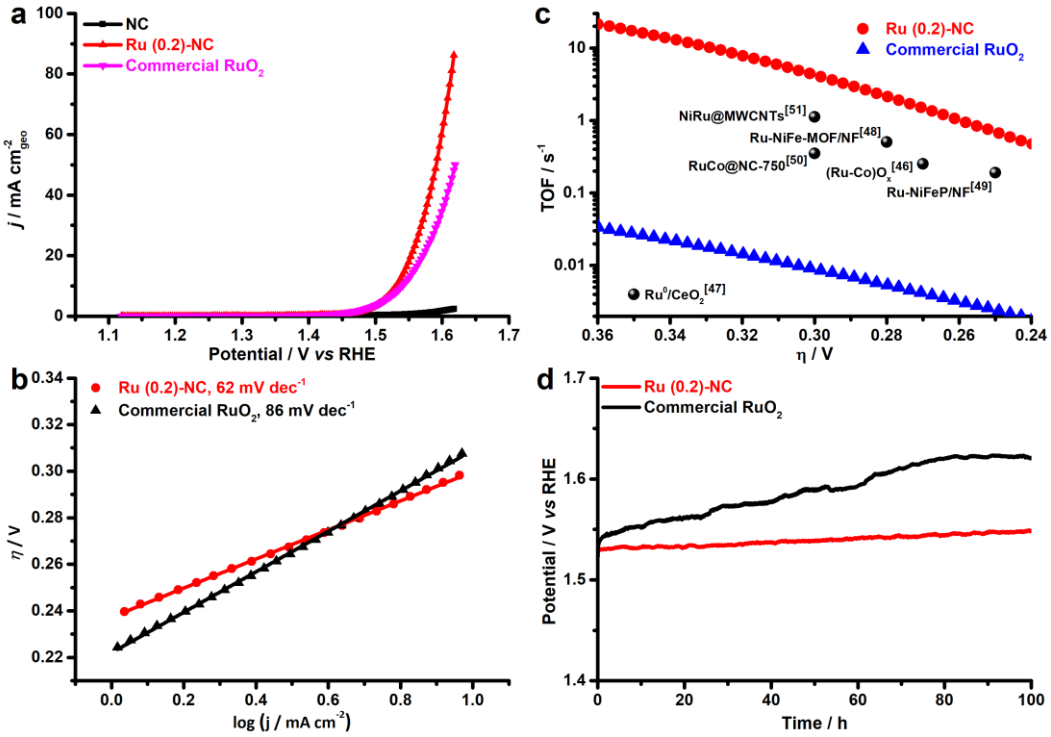

Figure 4.2.9 Electrocatalytic OER performance of Ru (0.2)-NC and other control catalysts. a) LSV curves. Scan rate: 5 mV s^{-1}. b) Tafel slopes. c) Comparison of the TOF values with other start-of-the-art OER catalysts. d) Long-term catalytic stability test at 10 mA cm^{-2} in 1.0 M KOH.

The electrocatalytic activity of Ru (0.2)-NC and other control catalysts toward the OER was further studied in 1.0 M KOH. Ru (0.2)-NC shows a comparatively low η_{10} value of 300 mV (**Figure 4.2.9a**), outperforming the commercial RuO_2 nanoparticle benchmark catalysts (η_{10} = 310 mV). Moreover, Ru (0.2)-NC exhibits a Tafel slope of 62 mV dec^{-1} (**Figure 4.2.9b**), much smaller than that of commercial RuO_2 nanoparticles (86 mV dec^{-1}), indicating more favorable OER kinetics. The EIS measurements also confirmed the faster reaction kinetics of Ru (0.2)-NC compared to the control sample, as evidenced by its smaller R_{ct} (**Figure 4.2.10**). The Ru (0.2)-NC can deliver a superior mass activity of 16.9 A mg^{-1} at η = 300 mV, which is 563 times higher than that of commercial RuO_2 in 1.0 M KOH (**Figure 4.2.11**). Meanwhile, the TOF values of Ru (0.2)-NC and other start-of-the-art Ru-based OER catalysts are compared in **Figure 4.2.9c**. The Ru (0.2)-NC exhibits an impressive TOF value of 4.89 s^{-1} at η = 300 mV, remarkably higher than that

of commercial RuO_2 and many other Ru-based OER catalysts reported recently [46-51] (see details in **Table 4.2.4**). The long-term stability of Ru (0.2)-NC and the RuO_2 reference catalyst were evaluated by CP at 10 mA cm^{-2} (**Figure 4.2.9d**). The potential required to maintain 10 mA cm^{-2} for Ru (0.2)-NC does not show an obvious increase after the 100-h continuous test, revealing very good durability. In comparison, RuO_2 needs a higher potential to deliver 10 mA cm^{-2} and the potential needed continues to increase over time, due probably to the gradual dissolution of high-valence Ru species [52, 53].

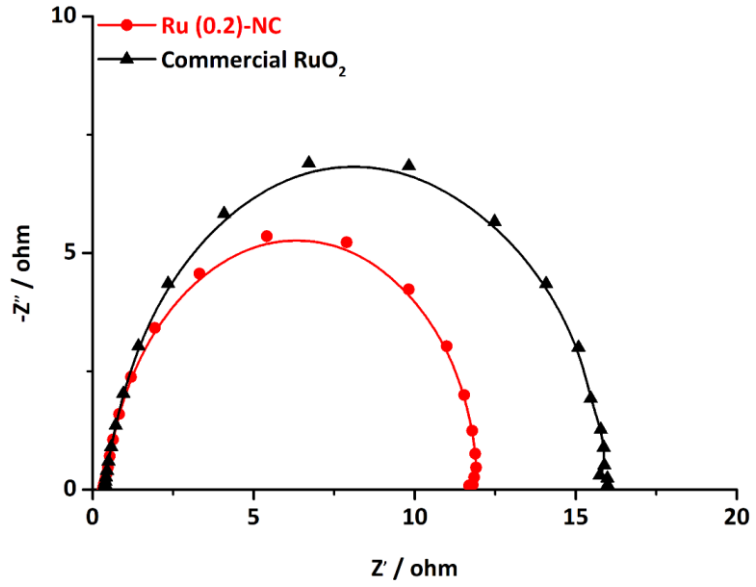

Figure 4.2.10 Nyquist plots of the catalysts toward OER, measured at 1.53 V vs. RHE in 1.0 M KOH.

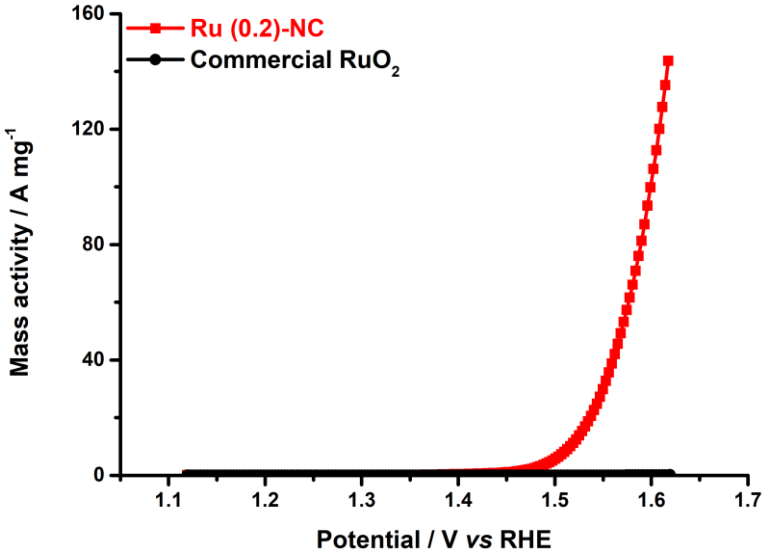

Figure 4.2.11 Mass activities of Ru (0.2)-NC and commercial Pt/C catalysts toward OER tested in 1.0 M KOH.

Table 4.2.4 Comparison of turnover frequencies (TOFs) of Ru (0.2)-NC to those of other recently reported Ru-based OER catalysts tested in alkaline condition.

Catalyst	Overpotential (V)	TOF (s^{-1})	Reference
Ru (0.2)-NC	**0.30**	**4.89**	**This work**
(Ru-Co)O_x	0.27	0.252	Angew. Chem. Int. Ed. 2020, 59, 17219–17224.
Ru^0/CeO_2	0.35	0.004	J. Colloid Interface Sci. 2019, 534, 704-710.
Ru-NiFe-MOF/NF	0.28	0.506	Dalton Trans. 2021, 50, 4280-4287.
Ru-NiFeP/NF	0.25	0.190	Appl. Surf. Sci. 2021, 536, 147952.
RuCo@NC-750	0.30	0.35	Electrochimica Acta 2019, 327, 134958.
NiRu@MWCNTs	0.30	1.12	ACS Appl. Mater. Interfaces 2020, 12, 13842–13851.

In order to gain insight into the catalytically active sites and reaction mechanisms of the Ru (0.2)-NC catalyst, we performed DFT calculations and obtained the Gibbs free energy diagrams for the OER and the HER. **Figure 4.2.12a** shows the adsorption configurations of the reaction intermediates on the pyrrole-type Ru (0.2)-NC model catalysts during the OER, which involves successive electron transfer steps with the related oxygenated intermediates of OH*, O* and OOH*. The OER Gibbs free energy diagrams of Ru (0.2)-NC and RuO_2 were calculated at the potential of U = 1.23 V (**Figure 4.2.12b**). For RuO_2, the calculations reveal that the elementary reaction step $^*O + OH^- \rightarrow {}^*OOH + e^-$ is the rate determining step (RDS) with a high energy barrier of 2.10 eV. In comparison, for Ru (0.2)-NC, the RDS has been altered to the last elementary step $OOH^* + OH^- \rightarrow {}^* + O_2\ (g) + H_2O\ (l) + e^-$ with a much lower energy barrier of 0.86 eV, revealing a more favorable OER kinetics. The Gibbs free energy diagrams of Ru (0.2)-NC and Pt/C for the HER were also derived from the DFT calculations (**Figure 4.2.12c**). The Ru (0.2)-NC exhibits a ΔG_H value (−0.38 eV) comparable to Pt (−0.19 eV), indicating appropriate H adsorption on the Ru sites of Ru (0.2)-NC. The band-order and Bader charge analyses confirm that there is 0.89 e charge transferred from the Ru site to the N atoms when Ru forms chemical bonds with the N atoms (**Figures 4.2.12d** and **4.2.12e**). This indicates that the Ru sites lose their electrons and thus are positively charged, which are expected to be able to regulate their interaction with the reaction intermediates,

promoting the activity. Furthermore, the crystal orbital Hamilton populations (COHP) analysis reveals that the peaks of the antibonding orbital are close to the Fermi level, suggesting that the Ru atoms in Ru (0.2)-NC catalysts are easy to form bonds with the adsorbed species, reducing the energy barrier of the reaction (**Figure 4.2.12f**).

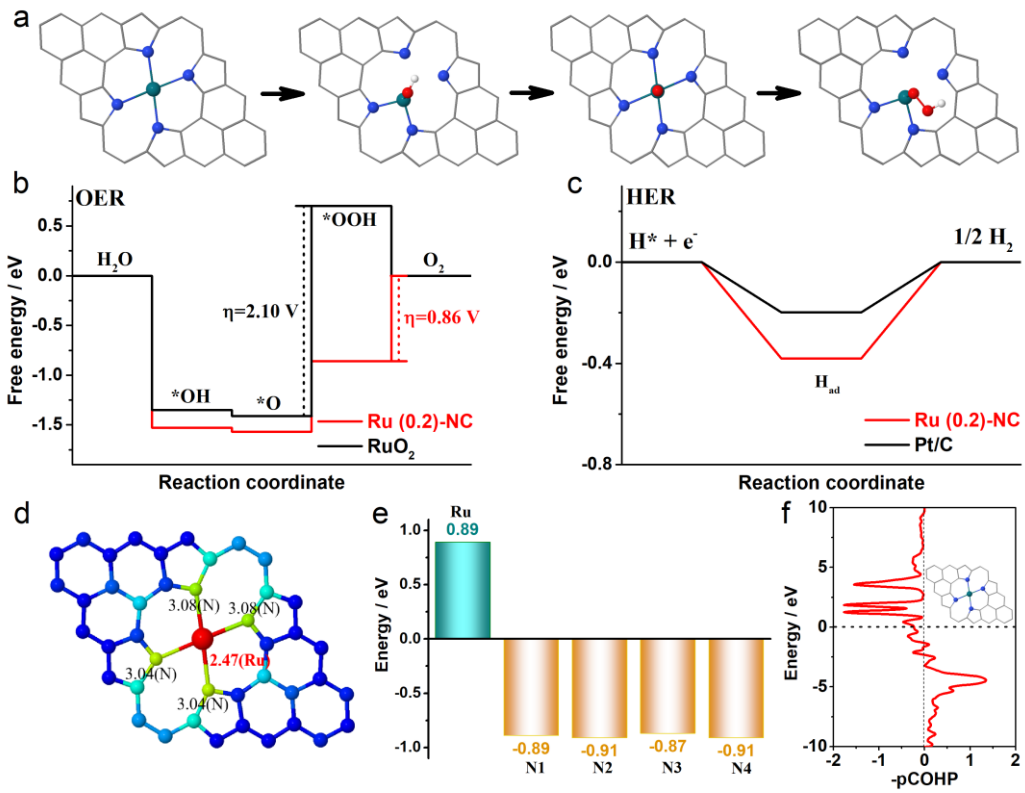

Figure 4.2.12 a) Adsorption configurations of the intermediates during the OER process on pyrrole-type Ru (0.2)-NC (the balls in cyan, blue, red and white represent Ru, N, O and H atoms, respectively). Gibbs free-energy diagram for b) the four steps of OER and c) the two steps of HER on pyrrole-type Ru (0.2)-NC. The dotted lines in panel b) denote the RDS. d) The band-order, e) Bader charge and f) COHP analysis of pyrrole-type Ru (0.2)-NC.

While the above calculations were made based on the pyrrole-type Ru (0.2)-NC catalyst model, it was also reported that the pyridinic-type metal moieties are active sites toward the electrocatalysis [54]. Therefore, we further calculated the Gibbs free energy of the reaction intermediates on pyridinic-type Ru (0.2)-NC at U = 1.23 V. As shown from the free energy diagrams for the OER and HER (**Figure 4.2.13**), our Ru (0.2)-NC catalyst exhibits the lower energy barrier for both model reactions relative to RuO_2 and comparable with Pt/C. Overall, the Gibbs energy calculations agree well with our experimental observation, demonstrating that the atomically dispersed Ru sites on Ru (0.2)-NC indeed help decrease the energy barrier in the RDS step and enhance the electrocatalytic activity for both OER and HER.

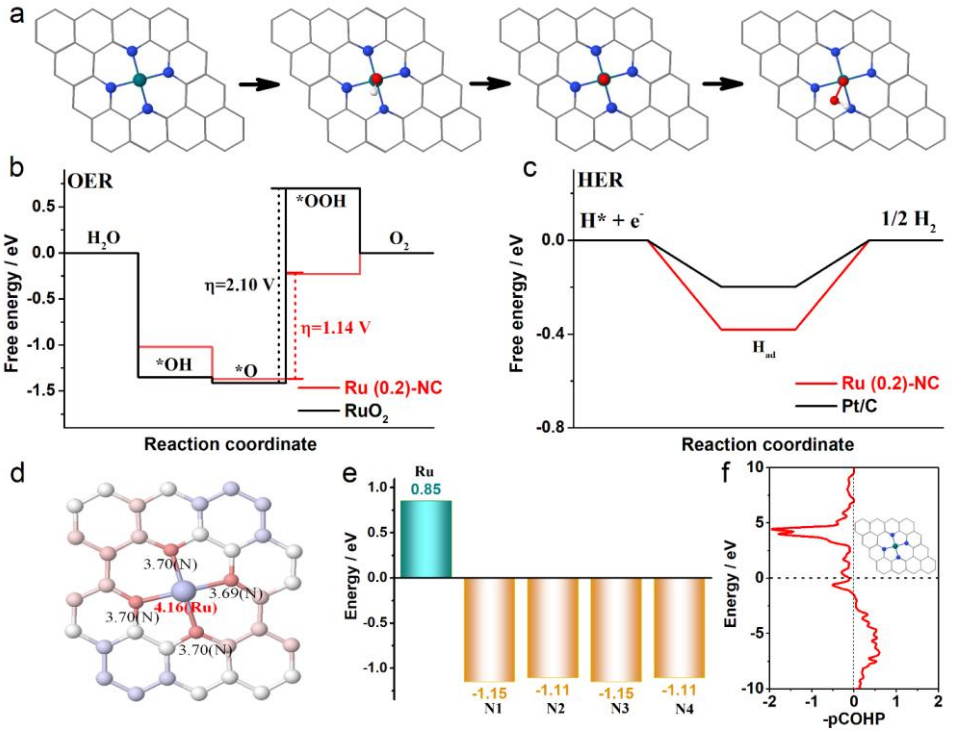

Figure 4.2.13 a) Adsorption configurations of the intermediates during the OER process on pyridinic-type Ru (0.2)-NC (the balls in cyan, blue, red and white represent Ru, N, O and H atoms, respectively). b) Gibbs free-energy diagram for the four steps of OER and c) two steps of HER on pyridinic-type Ru (0.2)-NC. d) The band-order, e) Bader charge and f) COHP analysis in pyridinic-type Ru (0.2)-NC.

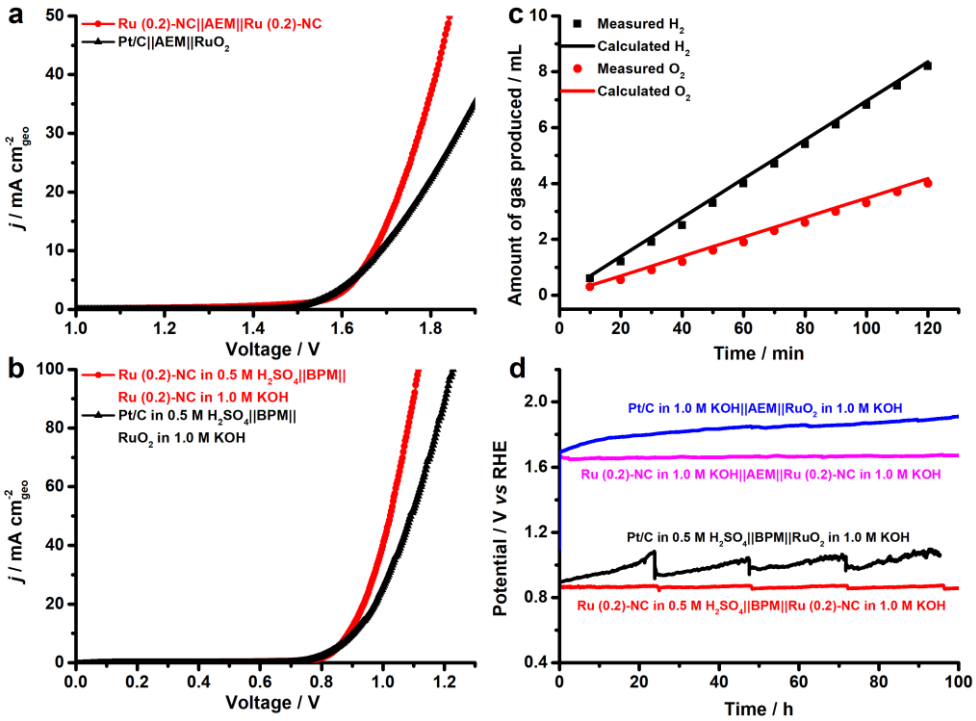

Figure 4.2.14 Overall water electrolysis tests of Ru (0.2)-NC and other control catalysts, performed in a two-compartment Teflon cell separated by a) the anion exchange membrane (AEM) and b) the bipolar membrane (BPM). c) Faradaic efficiency of Ru (0.2)-NC in the BPM-based water electrolysis measured a fixed current density of 10 mA cm^{-2}. d) Operational stability of AEMWE and BPMWE for Ru (0.2)-NC and other control catalysts at 10 mA cm^{-2}.

On the basis of the excellent electrocatalytic performance of Ru (0.2)-NC illustrated in the HER and OER, we further used Ru (0.2)-NC as the bifunctional electrocatalysts to perform overall water electrolysis in a two-electrode configuration in 1.0 M KOH in the presence of an anion exchange membrane (AEM). The result shows that the Ru (0.2)-NC electrode pair needs a cell voltage of 1.67 V to achieve 10 mA cm^{-2}, outperforming the the electrode pair comprising commercial Pt/C and RuO_2 catalysts (**Figure 4.2.14a**). Given that the electrical energy demand is high in this case, we further employed a bipolar membrane (BPM) to improve the overall water electrolysis performance. Working in the "forward-bias" configuration, a BPM allows the HER and OER to be accomplished in kinetically favorable acidic and alkaline environments, respectively, at a markedly lowered cell voltage thanks to the assistance of electrochemical neutralization energy [21-23]. Such asymmetric acid-alkaline BPM water electrolysis (BPMWE) using Ru (0.2)-NC as both cathode and anode catalysts can operate under a low cell voltage (V_{10}) of only 0.89 V to deliver 10 mA cm^{-2} (**Figure 4.2.14b**). Moreover, a high current density of 100 mA cm^{-2} can be achieved at a cell voltage of merely 1.12 V. The BPMWE based on the commercial Pt/C || RuO_2 also exhibits a dramatic negative shift in the cell voltage to reach a given current density (V_{10} = 0.91 V), but it is not as good as the BPMWE based on the Ru (0.2)-NC || Ru (0.2)-NC electrode pair. The Faradaic efficiency of the HER and OER in the BPMWE was measured (**Figure 4.2.14c**), and the volumes of the H_2 and O_2 gases collected matched well with those calculated, showing an efficiency of close to 100%. This indicates that there was no side reaction occurring during the BPMWE. Stability is a critically important indicator of electrocatalysts for practical applications in water electrolyzers. We examined the catalytic stability of the Ru (0.2)-NC || Ru (0.2)-NC electrode pair and commercial Pt/C || RuO_2 electrode pair in the AEM water electrolysis (AEMWE) and BPMWE at a constant current density of 10 mA cm^{-2} (**Figure 4.2.14d**). In both cases, the Pt/C || RuO_2 electrode pair suffered a notable performance decay in the course of 100-h water splitting. In contrast, the Ru (0.2)-NC || Ru (0.2)-NC pair exhibited outstanding stability and was able to sustain continuous AEMWE and BPMWE at 10 mA cm^{-2} for 100 h without degradation. In particular, the BPMWE was accomplished at a low, stable voltage of 0.89 V, which shows great potential for energy-saving hydrogen production.

4.2.3 Conclusions

In summary, we have successfully proved a higher activity of atomically dispersed Ru supported on nitrogen-doped carbon with an ultralow Ru loading (0.2 wt%) through a two-step deposition-pyrolysis method. The as-prepared Ru (0.2)-NC catalysts exhibit

superior electrocatalytic activity and better stability for both HER and OER in comparison to the state-of-the-art commercial Pt/C and RuO_2 catalysts as well as many other Ru-based HER and OER catalysts reported in the literature. Comprehensive DFT calculations confirm that the chemical bonding formed between Ru and N atoms can effectively lower the energy barrier of the rate determining step of the OER and that the Ru-N4 moieties can more easily absorb the reaction intermediates, both contributing to the enhanced OER performance. Furthermore, we accessed the suitability of using Ru (0.2)-NC as the bifunctional catalysts in AEM and BPM water electrolysis. A significant reduction in the applied external cell voltage can be achieved in the "forward-bias" BPM configuration, owing to the assistance of electrochemical neutralization energy. In particular, the BPM electrolyzer using Ru (0.2)-NC as the bifunctional catalysts is able to afford a current density of 10 mA cm^{-2} at a low cell voltage of merely 0.89 V and can continuously and stably produce hydrogen at this voltage up to 100 hours without performance decay, holding substantial potential for use in low-cost hydrogen production.

4.2.4 Experimental section

Reagents: All reagents were used as received without further purification. Alginate acid, ammonia solution (NH_4OH), and Nafion® perfluorinated resin solution (5 wt %) were purchased from Sigma-Aldrich. Activated carbon (Norit CN-1) was bought from Fisher Scientific. Ruthenium chloride hydrate ($RuCl_3 \cdot xH_2O$) was acquired from Johnson Matthey. Potassium hydroxide (KOH) and ruthenium dioxide (RuO_2) powders were purchased from Alfa Aesar.

Synthesis of atomically dispersed Ru ADCs: The Ru ADCs were prepared through a two-step process involving the introduction of nitrogen groups by dispersing ammonium alginate onto a carbonaceous support, followed by the incorporation of the ruthenium precursor in an alcoholic solution and subsequent pyrolysis treatment [55-57]. Typically, 0.2 g of alginate acid was dissolved in 20 mL of deionized Milli-Q water (resistivity: 18.2 $M\Omega \cdot cm$), and 2 mL of NH_4OH (28 %) was then added in order to transform the insoluble acid to the soluble ammonium salt (NH_4A). Subsequently, 0.8 g of the activated carbon support (Norit CN-1) was added and the mixture was vigorously stirred for 1 h. The solvent was evaporated under vacuum at 65 °C and the dried product was ground into powders. The ground support (20 % NH_4A/C) composed of 20 wt% ammonium alginate was then dispersed in 10 mL of 1-butanol containing 5.3 mg of $RuCl_3 \cdot xH_2O$ (40 %) and kept at the reflux temperature of the alcohol (117.7 °C) for 16 h. Afterwards, the Ru-impregnated solid was filtered, washed three times with 50 mL of ethanol and dried under

reduced pressure at room temperature for 12 h. Finally, the as-prepared sample (0.2 wt% Ru-20 % NH_4A/C) was subjected to a pyrolysis treatment at 800 °C for 2 h under a N_2 flow of 50 mL min^{-1} with a ramping rate of 25 ºC min^{-1} to yield the Ru ADCs with 0.2 wt% Ru loading (*i.e.*, Ru (0.2)-NC). Likewise, pristine nitrogen-doped carbon (denoted as NC hereafter) was prepared as a control sample, according to a similar procedure as described above, in the absence of ruthenium precursors.

Materials characterization: X-ray diffractometry (XRD) examinations were performed on an X'Pert PRO diffractometer (PANalytical) set at 45 kV and 40 mA with Cu K_α radiation (λ = 1.541874 Å) and a PIXcel detector. Data were collected in the Bragg-Brentano configuration in the 2θ range of 30 – 100º at a scan speed of 0.011º s^{-1}. X-ray photoelectron spectroscopy (XPS) characterization was carried out on an ESCALAB 250 instrument (Thermo Scientific) with Al K_α X-rays (1486.6 eV). Scanning electron microscopy (SEM) examination was conducted on a FEI Quanta 650 FEG microscope. Transmission electron microscopy (TEM), high-resolution TEM (HRTEM), and scanning transmission electron microscopy (STEM) elemental mapping investigations were carried out on a probe-corrected transmission electron microscope operating at 200 kV (FEI Themis 60-300). The Ru loading of Ru ADCs was determined by inductively coupled plasma-optical emission spectroscopy (ICP-OES, ICPE-9000 spectrometer, Shimadzu).

DFT calculations: DFT calculations were performed using Vienna Ab-initio Simulation Package (VASP) with the projector augmented wave (PAW) pseudopotential and Revised Perdew-Burke-Ernzerhof (RPBE) functional [58-60]. A kinetic energy cut-off of 400 eV was adopted for the plane-wave expansion. A Gamma point was used to sample the Brillouin zone in energy and structure relaxation calculation. A 3 × 3 × 1 Monkhorst-Pack k-point mesh was utilized in electronic structure calculations. All structures were fully relaxed until the final energy and force on each atom were less than 10^{-6} eV and 0.02 eV $Å^{-1}$, respectively. A 5 × 6 supercell including 62 C, 4 N and 1 Ru atoms, was chosen for modelling atomically dispersed Ru, while in the N-doped graphene sheet model, the graphene supercell is 14.76 × 12.75 × 15.00 $Å^3$ in the x, y and z directions and the periodic condition is applied along z direction. The following catalyst models were used for the calculations: Ru single atom with the pyrrolic N coordination configuration; Ru single atom with the pyridinic N coordination configuration; Pt (111) surface for the HER; RuO_2 (110) surface for the OER. The HER proceeds through the two-electron pathways with the following reaction steps:

$$* + H^+ + e^- \rightarrow H* \quad (1)$$

$$H^* + H^+ + e^- \rightarrow H_2\,(g) + {}^* \quad (2a)$$

$$\text{or} \quad H^* + H^* \rightarrow H_2\,(g) + 2^* \quad (2b)$$

The OER process includes the following steps:

$$^* + OH^- \rightarrow OH^* + e^- \quad (3)$$

$$OH^* + OH^- \rightarrow O^* + H_2O\,(l) + e^- \quad (4)$$

$$O^* + OH^- \rightarrow OOH^* + e^- \quad (5)$$

$$OOH^* + OH^- \rightarrow {}^* + O_2\,(g) + H_2O\,(l) + e^- \quad (6)$$

where * represents the Ru active site, and OH^*, O^*, OOH^* and H^* are the intermediates absorbed on the active sites during the OER and HER. The adsorption energy was calculated as follows: $E_{ad} = E_{sys} - E_{sur} - E_{spe}$, in which E_{ad}, E_{sys}, E_{sur} and E_{spe} denote the adsorption energy, the energy of adsorption system, the energy of clean surface and the energy of insulated adsorption species.

Electrode preparation and electrocatalytic tests: To prepare the working electrode, 5 mg of Ru (0.2)-NC catalysts was first ultrasonically dispersed into 500 µL of ethanol and 50 µL of Nafion® (Sigma, 5 wt%) solution to form a homogeneous ink. Subsequently, 6.6 µL of catalyst ink was loaded on a polished glassy carbon (GC) electrode with an exposed area of 0.2 cm^2, resulting in a Ru loading density of 0.6 µg cm^{-2}. For comparison, the electrocatalytic performance of commercial Pt/C (FuelCellStore, 20 wt% Pt), RuO_2 nanoparticles (Alfa Aesar) and pristine NC support control samples was also investigated. The working electrode was prepared according to the procedure similar to that described above. The metal loading density of Pt/C and RuO_2 was 60 and 300 µg cm^{-2}, respectively.

All electrocatalytic tests were performed in a three-electrode configuration at room temperature using a Biologic VMP-3 potentiostat/galvanostat. A graphite rod and a saturated calomel electrode (SCE) were utilized as the counter and reference electrodes, respectively. Unless otherwise stated, all potentials are reported versus the reversible hydrogen electrode (RHE) by converting the measured potentials according to the following equation:

$$E_{RHE} = E_{SCE} + 0.059 \times pH + 0.241 \quad (7)$$

The apparent HER and OER activities were appraised using linear scan voltammetry (LSV) at a scan rate of 5 mV s^{-1}, and an *iR*-correction (85%) was applied to compensate

for the voltage drop between the reference and working electrodes, which was measured by a single-point high-frequency impedance measurement.

The electrocatalytically-active surface areas (ECSAs) were estimated from the electrochemical double-layer capacitance (C_{dl}) of the catalysts. The C_{dl} values were derived by performing cyclic voltammetry (CV) in the non-Faradaic potential range of 0.4 – 0.6 V vs. RHE at different scan rates (v) of 10, 20, 30, 40, 50, 60, 70, 80, 90 and 100 mV s^{-1}, followed by extracting the slope from the resulting $|j_a - j_c|/2$ vs. v plots (j_a and j_c represent the anodic and cathodic current at 0.5 V vs. RHE). The ECSA was computed according to the following formula [7];

$$ECSA = \frac{C_{dl}}{C_s} \quad (8)$$

where C_s represents the areal capacitance of a flat surface (35 μF cm^{-2}) [61].

Electrochemical impedance spectroscopy (EIS) measurements were carried out at –0.047 V vs. RHE for HER in 0.5 M H_2SO_4, –0.073 V vs. RHE for HER in 1.0 M KOH and 1.530 V vs. RHE for OER in 1.0 M KOH in the frequency range of 10^5 – 0.01 Hz with a 10 mV sinusoidal perturbation. The stability of catalysts was assessed at a constant current density of –10 mA cm^{-2} for HER and 10 mA cm^{-2} for OER using chronopotentiometry (CP).

For HER and OER, the turnover frequency (TOF) of the catalysts was calculated according to the following formula [22]:

HER: $$TOF = \frac{j}{2nF} \quad (9)$$

OER: $$TOF = \frac{j}{4nF} \quad (10)$$

where j (A) is the current at a given overpotential, F = 96500 C mol^{-1} stands for the Faraday constant, and n (mol) is mole number of Ru or Pt loaded on the GC electrode. All metal species in catalysts were assumed to be catalytically active, so the calculated values represent the lower limits of TOF.

Overall water splitting performance: The overall water electrolysis performance was firstly investigated in a two-compartment Teflon cell using Ru ADCs as both HER and OER catalysts in the presence of an anion exchange membrane (AEM). 1.0 M KOH solution was used as the electrolyte. Furthermore, asymmetric water electrolysis in acid-alkaline dual electrolytes was also demonstrated using a bipolar membrane (BPM) to separate the cathodic compartment from the anodic one. In this case, 1.0 M KOH and

0.5 M H_2SO_4 were supplied as the anolyte and catholyte, respectively. For comparison, commercial Pt/C and RuO_2 were also utilized as HER and OER catalysts, respectively, and tested in the same asymmetric configuration. The Faradaic efficiency of the hydrogen and oxygen evolution was measured during the continuous BPM water electrolysis at 10 mA cm^{-2}. The stability of overall water electrolysis was assessed in the two-compartment Teflon cell using CP at a constant current density of 10 mA cm^{-2}.

4.2.5 References

[1] I. Staffell, D. Scamman, A. Velazquez Abad, P. Balcombe, P.E. Dodds, P. Ekins, N. Shah, K.R. Ward, The role of hydrogen and fuel cells in the global energy system. Energy Environ. Sci. 12 (2019) 463-491.

[2] S.E. Hosseini, M.A. Wahid, Hydrogen production from renewable and sustainable energy resources: Promising green energy carrier for clean development. Renew. Sust. Energ. Rev. 57 (2016) 850-866.

[3] S. Furfari, A. Clerici, Green hydrogen: the crucial performance of electrolysers fed by variable and intermittent renewable electricity. Eur. Phys. J. Plus 136 (2021) 509.

[4] J. Yu, Q. He, G. Yang, W. Zhou, Z. Shao, M. Ni, Recent Advances and Prospective in Ruthenium-Based Materials for Electrochemical Water Splitting. ACS Catal. 9 (2019) 9973-10011.

[5] S. Sultan, J.N. Tiwari, A.N. Singh, S. Zhumagali, M. Ha, C.W. Myung, P. Thangavel, K.S. Kim, Single Atoms and Clusters Based Nanomaterials for Hydrogen Evolution, Oxygen Evolution Reactions, and Full Water Splitting. Adv. Energy Mater. 9 (2019) 1900624.

[6] Z. Yu, J. Xu, Y. Li, B. Wei, N. Zhang, Y. Li, O. Bondarchuk, H. Miao, A. Araujo, Z. Wang, J.L. Faria, Y. Liu, L. Liu, Ultrafine oxygen-defective iridium oxide nanoclusters for efficient and durable water oxidation at high current densities in acidic media. J. Mater. Chem. A 8 (2020) 24743-24751.

[7] J. Xu, J. Li, Z. Lian, A. Araujo, Y. Li, B. Wei, Z. Yu, O. Bondarchuk, I. Amorim, V. Tileli, B. Li, L. Liu, Atomic-Step Enriched Ruthenium–Iridium Nanocrystals Anchored Homogeneously on MOF-Derived Support for Efficient and Stable Oxygen Evolution in Acidic and Neutral Media. ACS Catal. 11 (2021) 3402-3413.

[8] J. Xu, Z. Lian, B. Wei, Y. Li, O. Bondarchuk, N. Zhang, Z. Yu, A. Araujo, I. Amorim, Z. Wang, B. Li, L. Liu, Strong Electronic Coupling between Ultrafine Iridium–Ruthenium

Nanoclusters and Conductive, Acid-Stable Tellurium Nanoparticle Support for Efficient and Durable Oxygen Evolution in Acidic and Neutral Media. ACS Catal. 10 (2020) 3571-3579.

[9] C. Zhu, S. Fu, Q. Shi, D. Du, Y. Lin, Single-Atom Electrocatalysts. Angew. Chem. Int. Ed. 56 (2017) 13944-13960.

[10] Z. Yu, J. Xu, S. Feng, X. Song, O. Bondarchuk, J.L. Faria, Y. Ding, L. Liu, Rhodium single-atom catalysts with enhanced electrocatalytic hydrogen evolution performance. New J. Chem. 45 (2021) 5770-5774.

[11] T. Sun, L. Xu, D. Wang, Y. Li, Metal organic frameworks derived single atom catalysts for electrocatalytic energy conversion. Nano Research 12 (2019) 2067-2080.

[12] J. Mahmood, F. Li, S.M. Jung, M.S. Okyay, I. Ahmad, S.J. Kim, N. Park, H.Y. Jeong, J.B. Baek, An efficient and pH-universal ruthenium-based catalyst for the hydrogen evolution reaction. Nat. Nanotechnol. 12 (2017) 441-446.

[13] Q. Wang, M. Ming, S. Niu, Y. Zhang, G. Fan, J.S. Hu, Scalable Solid-State Synthesis of Highly Dispersed Uncapped Metal (Rh, Ru, Ir) Nanoparticles for Efficient Hydrogen Evolution. Adv. Energy Mater. 8 (2018) 1801698.

[14] Y. Yang, J. Kim, C. Kim, A. Seong, O. Kwon, J.H. Lee, I. Kristanto, L. Zhang, J. Zhou, J.Q. Wang, J.B. Baek, S.K. Kwak, G. Kim, Edge-selective decoration with ruthenium at graphitic nanoplatelets for efficient hydrogen production at universal pH. Nano Energy 76 (2020) 105114.

[15] D.H. Kweon, M.S. Okyay, S.J. Kim, J.P. Jeon, H.J. Noh, N. Park, J. Mahmood, J.B. Baek, Ruthenium anchored on carbon nanotube electrocatalyst for hydrogen production with enhanced Faradaic efficiency. Nat. Commun. 11 (2020) 1278.

[16] L. Xing, H. Gao, G. Hai, Z. Tao, J. Zhao, D. Jia, X. Chen, M. Han, S. Hong, L. Zheng, X. Huang, W. Dong, G. Wang, X. Shu, Atomically dispersed ruthenium sites on whisker-like secondary microstructure of porous carbon host toward highly efficient hydrogen evolution. J. Mater. Chem. A 8 (2020) 3203-3210.

[17] X. Peng, S. Zhao, Y. Mi, L. Han, X. Liu, D. Qi, J. Sun, Y. Liu, H. Bao, L. Zhuo, H.L. Xin, J. Luo, X. Sun, Trifunctional Single-Atomic Ru Sites Enable Efficient Overall Water Splitting and Oxygen Reduction in Acidic Media. Small 16 (2020) 2002888.

[18] L. Cao, Q. Luo, J. Chen, L. Wang, Y. Lin, H. Wang, X. Liu, X. Shen, W. Zhang, W. Liu, Z. Qi, Z. Jiang, J. Yang, T. Yao, Dynamic oxygen adsorption on single-atomic

Ruthenium catalyst with high performance for acidic oxygen evolution reaction. Nat. Commun. 10 (2019) 4849.

[19] D. Wang, Q. Li, C. Han, Z. Xing, X. Yang, Single-atom ruthenium based catalyst for enhanced hydrogen evolution. Appl. Catal. B Environ. 249 (2019) 91-97.

[20] L. Duan, F. Bozoglian, S. Mandal, B. Stewart, T. Privalov, A. Llobet, L. Sun, A molecular ruthenium catalyst with water-oxidation activity comparable to that of photosystem II. Nat. Chem. 4 (2012) 418-423.

[21] Y. Ding, P. Cai, Z. Wen, Electrochemical neutralization energy: from concept to devices. Chem. Soc. Rev. 50 (2021) 1495-1511.

[22] I. Amorim, J. Xu, N. Zhang, Z. Yu, A. Araújo, F. Bento, L. Liu, Dual-phase CoP−$CoTe_2$ nanowires as an efficient bifunctional electrocatalyst for bipolar membrane-assisted acid-alkaline water splitting. Chem. Eng. J. 420 (2021) 130454.

[23] J. Xu, I. Amorim, Y. Li, J. Li, Z. Yu, B. Zhang, A. Araujo, N. Zhang, L. Liu, Stable overall water splitting in an asymmetric acid/alkaline electrolyzer comprising a bipolar membrane sandwiched by bifunctional cobalt-nickel phosphide nanowire electrodes. Carbon Energy 2 (2020) 646-655.

[24] K. Artyushkova, B. Kiefer, B. Halevi, A. Knop-Gericke, R. Schlogl, P. Atanassov, Density functional theory calculations of XPS binding energy shift for nitrogen-containing graphene-like structures. Chem. Commun. 49 (2013) 2539-2541.

[25] W. Ren, X. Tan, W. Yang, C. Jia, S. Xu, K. Wang, S.C. Smith, C. Zhao, Isolated Diatomic Ni-Fe Metal–Nitrogen Sites for Synergistic Electroreduction of CO_2. Angew. Chem. Int. Ed. 58 (2019) 6972-6976.

[26] X. Wang, Y.V. Kolen'ko, X.Q. Bao, K. Kovnir, L. Liu, One-Step Synthesis of Self-Supported Nickel Phosphide Nanosheet Array Cathodes for Efficient Electrocatalytic Hydrogen Generation. Angew. Chem. Int. Ed. 54 (2015) 8188-8192.

[27] W. Li, X. Wang, D. Xiong, L. Liu, Efficient and durable electrochemical hydrogen evolution using cocoon-like MoS_2 with preferentially exposed edges. Int. J. Hydrogen Energy 41 (2016) 9344-9354.

[28] W. Li, D. Xiong, X. Gao, W.G. Song, F. Xia, L. Liu, Self-supported Co-Ni-P ternary nanowire electrodes for highly efficient and stable electrocatalytic hydrogen evolution in acidic solution. Catal. Today 287 (2017) 122-129.

[29] T. Qiu, Z. Liang, W. Guo, S. Gao, C. Qu, H. Tabassum, H. Zhang, B. Zhu, R. Zou, Y. Shao-Horn, Highly exposed ruthenium-based electrocatalysts from bimetallic metal-organic frameworks for overall water splitting. Nano Energy 58 (2019) 1-10.

[30] E. Demir, S. Akbayrak, A.M. Önal, S. Özkar, Nanoceria-Supported Ruthenium(0) Nanoparticles: Highly Active and Stable Catalysts for Hydrogen Evolution from Water. ACS Appl. Mater. Interfaces 10 (2018) 6299-6308.

[31] D. Luo, B. Zhou, Z. Li, X. Qin, Y. Wen, D. Shi, Q. Lu, M. Yang, H. Zhou, Y. Liu, Biomimetic organization of a ruthenium-doped collagen-based carbon scaffold for hydrogen evolution. J. Mater. Chem. A 6 (2018) 2311-2317.

[32] F. Li, G.F. Han, H.J. Noh, I. Ahmad, I.Y. Jeon, J.B. Baek, Mechanochemically Assisted Synthesis of a Ru Catalyst for Hydrogen Evolution with Performance Superior to Pt in Both Acidic and Alkaline Media. Adv. Mater. 30 (2018) 1803676.

[33] Y. Liu, S. Liu, Y. Wang, Q. Zhang, L. Gu, S. Zhao, D. Xu, Y. Li, J. Bao, Z. Dai, Ru Modulation Effects in the Synthesis of Unique Rod-like Ni@Ni_2P–Ru Heterostructures and Their Remarkable Electrocatalytic Hydrogen Evolution Performance. J. Am. Chem. Soc. 140 (2018) 2731-2734.

[34] Y. Zheng, Y. Jiao, Y. Zhu, L.H. Li, Y. Han, Y. Chen, M. Jaroniec, S.Z. Qiao, High Electrocatalytic Hydrogen Evolution Activity of an Anomalous Ruthenium Catalyst. J. Am. Chem. Soc. 138 (2016) 16174-16181.

[35] Z. Liu, X. Yang, G. Hu, L. Feng, Ru Nanoclusters Coupled on Co/N-Doped Carbon Nanotubes Efficiently Catalyzed the Hydrogen Evolution Reaction. ACS Sustain. Chem. Eng. 8 (2020) 9136-9144.

[36] J. Xu, T. Liu, J. Li, B. Li, Y. Liu, B. Zhang, D. Xiong, I. Amorim, W. Li, L. Liu, Boosting the hydrogen evolution performance of ruthenium clusters through synergistic coupling with cobalt phosphide. Energy Environ. Sci. 11 (2018) 1819-1827.

[37] R. Ye, Y. Liu, Z. Peng, T. Wang, A.S. Jalilov, B.I. Yakobson, S.H. Wei, J.M. Tour, High Performance Electrocatalytic Reaction of Hydrogen and Oxygen on Ruthenium Nanoclusters. ACS Appl. Mater. Interfaces 9 (2017) 3785-3791.

[38] Q. Wu, M. Luo, J. Han, W. Peng, Y. Zhao, D. Chen, M. Peng, J. Liu, F.M.F. de Groot, Y. Tan, Identifying Electrocatalytic Sites of the Nanoporous Copper–Ruthenium Alloy for Hydrogen Evolution Reaction in Alkaline Electrolyte. ACS Energy Lett. 5 (2020) 192-199.

[39] G. Liu, W. Zhou, B. Chen, Q. Zhang, X. Cui, B. Li, Z. Lai, Y. Chen, Z. Zhang, L. Gu, H. Zhang, Synthesis of RuNi alloy nanostructures composed of multilayered nanosheets for highly efficient electrocatalytic hydrogen evolution. Nano Energy 66 (2019) 104173.

[40] Z.L. Wang, K. Sun, J. Henzie, X. Hao, C. Li, T. Takei, Y.M. Kang, Y. Yamauchi, Spatially Confined Assembly of Monodisperse Ruthenium Nanoclusters in a Hierarchically Ordered Carbon Electrode for Efficient Hydrogen Evolution. Angew. Chem. Int. Ed. 57 (2018) 5848-5852.

[41] J. Zhang, P. Liu, G. Wang, P.P. Zhang, X.D. Zhuang, M.W. Chen, I.M. Weidinger, X.L. Feng, Ruthenium/nitrogen-doped carbon as an electrocatalyst for efficient hydrogen evolution in alkaline solution. J. Mater. Chem. A 5 (2017) 25314-25318.

[42] S.M. Alia, S. Stariha, R.L. Borup, Electrolyzer Durability at Low Catalyst Loading and with Dynamic Operation. J. Electrochem. Soc. 166 (2019) F1164-F1172.

[43] S. Siracusano, V. Baglio, N. Van Dijk, L. Merlo, A.S. Aricò, Enhanced performance and durability of low catalyst loading PEM water electrolyser based on a short-side chain perfluorosulfonic ionomer. Appl. Energy 192 (2017) 477-489.

[44] P. Paciok, M. Schalenbach, M. Carmo, D. Stolten, On the mobility of carbon-supported platinum nanoparticles towards unveiling cathode degradation in water electrolysis. J. Power Sources 365 (2017) 53-60.

[45] Z. Pu, I.S. Amiinu, Z. Kou, W. Li, S. Mu, RuP2-Based Catalysts with Platinum-like Activity and Higher Durability for the Hydrogen Evolution Reaction at All pH Values. Angew. Chem. Int. Ed. 56 (2017) 11559-11564.

[46] C. Wang, L. Qi, Heterostructured Inter-Doped Ruthenium–Cobalt Oxide Hollow Nanosheet Arrays for Highly Efficient Overall Water Splitting. Angew. Chem. Int. Ed. 59 (2020) 17219-17224.

[47] E. Demir, S. Akbayrak, A.M. Önal, S. Özkar, Ceria supported ruthenium(0) nanoparticles: Highly efficient catalysts in oxygen evolution reaction. J. Colloid Interface Sci. 534 (2019) 704-710.

[48] Y. Lin, L. Zhao, L. Wang, Y. Gong, Ruthenium-doped NiFe-based metal–organic framework nanoparticles as highly efficient catalysts for the oxygen evolution reaction. Dalton Trans. 50 (2021) 4280-4287.

[49] Y. Lin, M. Zhang, L. Zhao, L. Wang, D. Cao, Y. Gong, Ru doped bimetallic phosphide derived from 2D metal organic framework as active and robust electrocatalyst for water splitting. Appl. Surf. Sci. 536 (2021) 147952.

[50] C. Gao, H. Wang, S. Li, B. Liu, J. Yang, J. Gao, Z. Peng, Z. Zhang, Z. Liu, Enhanced cobalt-based catalysts through alloying ruthenium to cobalt lattice matrix as an efficient catalyst for overall water splitting. Electrochim. Acta 327 (2019) 134958.

[51] Z. Peng, J. Liu, B. Hu, Y. Yang, Y. Guo, B. Li, L. Li, Z. Zhang, B. Cui, L. He, M. Du, Surface Engineering on Nickel–Ruthenium Nanoalloys Attached Defective Carbon Sites as Superior Bifunctional Electrocatalysts for Overall Water Splitting. ACS Appl. Mater. Interfaces 12 (2020) 13842-13851.

[52] S. Cherevko, S. Geiger, O. Kasian, N. Kulyk, J.-P. Grote, A. Savan, B.R. Shrestha, S. Merzlikin, B. Breitbach, A. Ludwig, K.J.J. Mayrhofer, Oxygen and hydrogen evolution reactions on Ru, RuO_2, Ir, and IrO_2 thin film electrodes in acidic and alkaline electrolytes: A comparative study on activity and stability. Catal. Today 262 (2016) 170-180.

[53] N. Hodnik, P. Jovanovič, A. Pavlišič, B. Jozinović, M. Zorko, M. Bele, V.S. Šelih, M. Šala, S. Hočevar, M. Gaberšček, New Insights into Corrosion of Ruthenium and Ruthenium Oxide Nanoparticles in Acidic Media. J. Phys. Chem. C 119 (2015) 10140-10147.

[54] L. Bai, Z. Duan, X. Wen, R. Si, Q. Zhang, J. Guan, Highly Dispersed Ruthenium-Based Multifunctional Electrocatalyst. ACS Catal. 9 (2019) 9897-9904.

[55] A. Corma, P. Concepción, I. Domínguez, V. Forné, M.J. Sabater, Gold supported on a biopolymer (chitosan) catalyzes the regioselective hydroamination of alkynes. J. Catal. 251 (2007) 39-47.

[56] M.J. Sabater, T. Ródenas, A. Heredia, Handbook of Biopolymer-Based Materials, pp. 37-86.

[57] F.J. Escobar-Bedia, M. Lopez-Haro, J.J. Calvino, V. Martin-Diaconescu, L. Simonelli, V. Perez-Dieste, M.J. Sabater, P. Concepción, A. Corma, Active and Regioselective Ru Single-Site Heterogeneous Catalysts for Alpha-Olefin Hydroformylation. ACS Catal. (2022) 4182-4193.

[58] G. Kresse, J. Furthmüller, Efficient iterative schemes for ab initio total-energy calculations using a plane-wave basis set. Phys. Rev. B 54 (1996) 11169-11186.

[59] P.E. Blöchl, Projector augmented-wave method. Phys. Rev. B 50 (1994) 17953-17979.

[60] J.P. Perdew, K. Burke, M. Ernzerhof, Generalized Gradient Approximation Made Simple. Phys. Rev. Lett. 77 (1996) 3865-3868.

[61] C.C.L. McCrory, S. Jung, J.C. Peters, T.F. Jaramillo, Benchmarking Heterogeneous Electrocatalysts for the Oxygen Evolution Reaction. J. Am. Chem. Soc. 135 (2013) 16977-16987.

4.3 Single-atom Ir and Ru anchored on graphitic carbon nitride for efficient and stable electrocatalytic/photocatalytic hydrogen evolution

Abstract

Renewable energy-powered water electrolysis and photocatalytic water splitting are two promising approaches to green hydrogen production. Electrocatalysts and photocatalysts are essential components determining the performance of water electrolyzers and photocatalytic reactors, respectively. Currently, there is a pressing need to develop efficient and stable electrocatalysts and photocatalysts for large-scale deployment of these devices to reach carbon neutrality. Herein, we report the synthesis of single-atom Ir and Ru anchored on mesoporous graphitic carbon nitride (Ir-g-CN and Ru-g-CN), which can be used as electrocatalysts and photocatalysts for the hydrogen evolution reaction (HER). Remarkably, Ru-g-CN shows a high turnover frequency (TOF) of 12.9 and 5.1 s^{-1} at an overpotential (η) of 100 mV in 0.5 M H_2SO_4 and 1.0 M KOH, respectively, outperforming Ir-g-CN, commercial Pt/C benchmark and many other advanced HER catalysts reported recently. Moreover, Ru-g-CN can deliver an exceptionally high mass activity of 24.55 and 8.78 A mg^{-1} at η = 100 mV in acidic and alkaline solutions, meanwhile exhibiting a high apparent current density, which is favorable for practical applications. Additionally, both Ru-g-CN and Ir-g-CN show outstanding catalytic stability, continuously catalyzing the HER in acidic and alkaline conditions for 120 h with minimal degradation. Besides, when used for photocatalytic water splitting, Ru-g-CN can achieve a high hydrogen production rate of 489.7 mmol H_2 g_{Ru}^{-1} h^{-1}, and shows good photocatalytic stability. Our density functional theory (DFT) calculations demonstrate that loading Ir and Ru single-atoms on g-CN alters the electronic structure, resulting in a reduced bandgap and improved electrical conductivity, facilitating electron transfer during the catalysis. Moreover, the Gibbs free energy of hydrogen adsorption on Ru-g-CN and Ir-g-CN is also substantially lowered, enhancing HER performance.

4.3.1 Introduction

Hydrogen (H_2), as a carbon-free energy carrier with a high gravimetric energy density, has shown significant potential for decarbonizing the transport sector and hard-to-abate industries [1], contributing to reaching the carbon-neutral goals pledged by many countries in the world. Water electrolysis coupled with renewable sources [2-4] and direct

solar-driven photocatalysis [5-8] have been considered the most promising approaches to “green” H_2 production. To turn the blueprint into reality, water electrolyzers and photocatalytic reactors must be deployed on a large scale commensurate with the global demand. Given that hydrogen evolution reaction (HER) catalysts and photocatalysts are crucial components governing the performance of electrochemical and photocatalytic water splitting, respectively, there is a pressing need to develop efficient, stable and cost-effective HER electrocatalysts and photocatalysts to enable fast, widespread deployment of water electrolyzers and photocatalytic reactors across different sectors where H_2 is needed.

Since its report in 2009 [9], graphitic carbon nitride (g-CN) has been intensively investigated as a metal-free photocatalyst for H_2 production [5, 6, 10, 11]. Despite being active, the H_2 production rate of pure g-CN is, in general, not sufficiently high, and it was demonstrated that loading co-catalysts on g-CN can markedly enhance the H_2 evolution performance [3, 12]. Besides, g-CN was also explored as an electrocatalyst for electrochemical water splitting [13]. However, g-CN is a polymer semiconductor having a bandgap of ~2.7 eV. It has poor electrical conductivity, and therefore pure g-CN by nature is not a suitable electrocatalyst [13]. Nevertheless, recent theoretical studies and experimental investigations have demonstrated that g-CN loaded with noble or transition metal species can serve as an outstanding electrocatalyst toward the HER in acidic and alkaline electrolytes [14-16]. For example, Zheng et al. reported that anomalous face-centered cubic (fcc) Ru nanoparticles supported on g-CN exhibited 2.5 times higher hydrogen evolution turnover frequency (TOF) under alkaline conditions than the state-of-the-art commercial Pt/C catalysts [15], which can be attributed to the favorable water dissociation dictated by the combination of Ru and g-CN. In particular, metal species atomically dispersed on the surface of g-CN have recently emerged as a new class of electrocatalysts, which can optimize the utilization of metals, especially the costly platinum group metals (PGMs), and also enable notably improved catalytic performance [12, 17-21]. To this end, g-CN emerges as an excellent supporting material because of its abundant uncoordinated nitrogen groups that can firmly anchor metal species, resulting in improved atomic dispersion [13].

Recent density functional theory (DFT) calculations revealed that introducing single metal (M) atoms onto the surface of g-CN may remarkably lower the bandgap [22], improving the conductivity of the resulting M-g-CN. Moreover, this will cause a drastic change in the electronic structure and alter the ratio of ionic to covalent bonding, thereby changing the adsorption energy of intermediates, the free energy of hydrogen adsorption

and accordingly, the HER overpotential [17, 18]. Experimentally, M-g-CN has recently been demonstrated to be active for both electrochemical and photocatalytic water splitting. For instance, Peng et al. reported that Ru ion-complexed g-CN nanosheets could catalyze the HER with an overpotential (η) of 140 mV to achieve a current density of 10 mA cm^{-2} and a Tafel slope of 57 mV dec^{-1} [23]. Liu and co-workers lately demonstrated that by introducing only 0.1 wt% of palladium clusters and single-atoms on g-CN, the photocatalytic H_2 production rate of g-CN could increase from 1.4 to 728 μmol g^{-1} h^{-1} under visible light irradiation [24]. Notwithstanding some progress, most of the previous reports were mainly focused on g-CN supported Pt single-atom catalysts [12, 13]; moreover, the electrocatalytic and photocatalytic properties of M-g-CN toward hydrogen evolution were usually investigated separately. More importantly, both the electrocatalytic and photocatalytic performance of these catalysts need to be further improved to explore possible synergies between the processes.

This work reports the synthesis of single-atom Ir and Ru anchored on mesoporous g-CN (denoted as Ir-g-CN and Ru-g-CN) by a simple hydrothermal method. Both Ir-g-CN and Ru-g-CN are comprehensively characterized, and the dispersion of Ir and Ru species on the g-CN support is evidenced by advanced scanning transmission electron microscopy. The obtained Ir-g-CN and Ru-g-CN show outstanding electrocatalytic performance for HER. Notably, the Ru-g-CN exhibits a high TOF value of 12.9 and 5.1 s^{-1} at η = 100 mV in 0.5 M H_2SO_4 and 1.0 M KOH, respectively, which outperforms Ir-g-CN, commercial Pt/C benchmark and many other advanced HER catalysts recently reported in the literature. In addition, Ru-g-CN affords an exceptionally high mass activity of 24.55 and 8.78 A mg^{-1} at η = 100 mV in acidic and alkaline solutions, meanwhile exhibiting a high apparent current density, which is favorable for practical applications. Impressively, Ru-g-CN also reveals outstanding photocatalytic HER activity showing a high H_2 production rate of 489.7 mmol H_2 g_{Ru}^{-1} h^{-1}, along with good catalytic stability. Our DFT calculations disclose that the atomic dispersion of Ir and Ru on g-CN reduces the bandgap and increases electrical conductivity. Moreover, DFT results can also explain the improved HER activity through the lowering of the Gibbs free energy of hydrogen adsorption on Ir-g-CN and Ru-g-CN.

4.3.2 Results and discussion

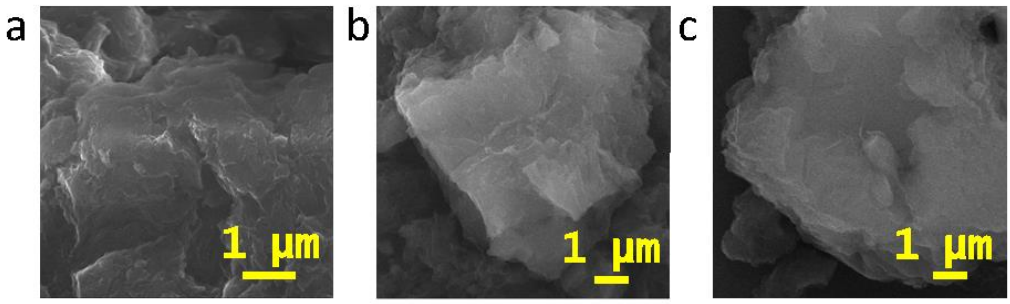

Figure 4.3.1 SEM images of a) pristine g-CN support, b) Ir-g-CN and c) Ru-g-CN catalysts.

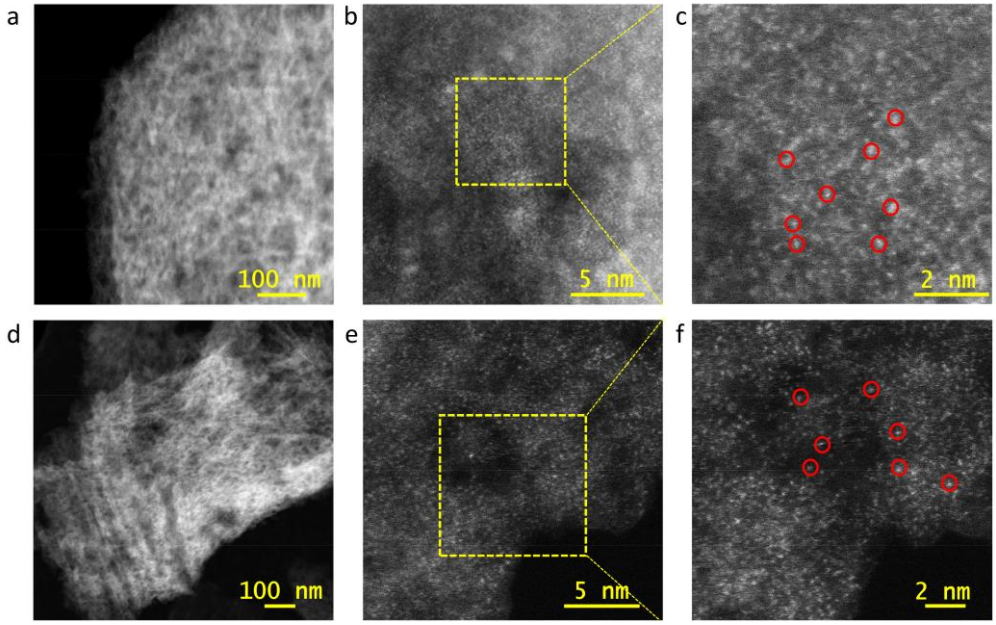

Figure 4.3.2 Aberration-corrected HAADF-STEM images of a-c) Ir-g-CN and d-f) Ru-g-CN. Red circles in c) and f) spotlight representative Ir and Ru single-atoms, respectively.

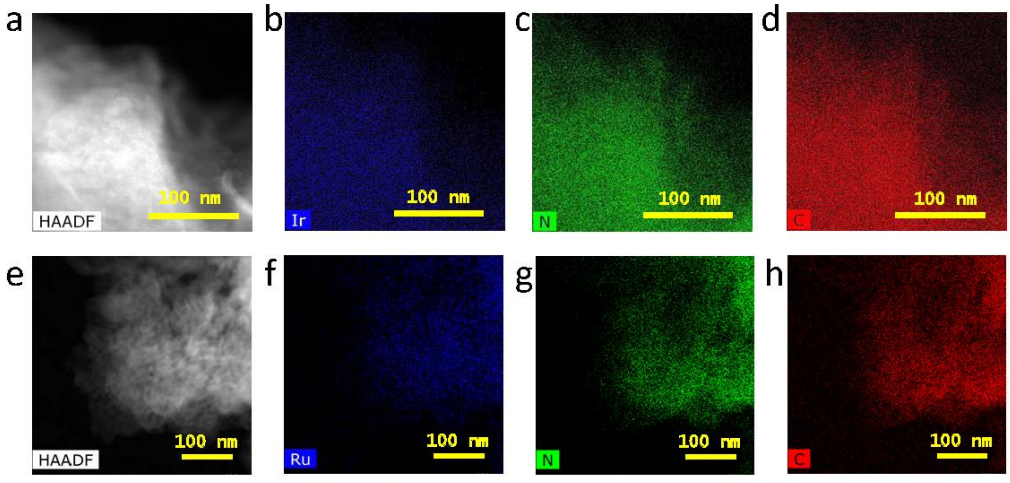

Figure 4.3.3 a, e) HAADF-STEM images, and b-d, f-h) elemental maps of a-d) Ir-g-CN and e-h) Ru-g-CN catalysts. Ultrafine Ir and Ru clusters can be found to distribute sparsely in both samples.

As detailed in the **Experimental** section, the Ir-g-CN and Ru-g-CN catalysts were prepared by wet chemical reduction of Ir- and Ru-containing precursors on the mesoporous g-CN support under hydrothermal conditions. g-CN is known to have abundant uncoordinated N groups on its surface [19, 20], which can anchor metal cations firmly, leading to a high degree of dispersion of Ir and Ru species. Scanning electron microscopy (SEM) examination showed that the as-prepared g-CN consists of carbon nitride thin layers stacked together into micrometer-sized particles, and loading Ir or Ru on g-CN did not change its morphology (**Figure 4.3.1**). The aberration-corrected high-angle annular dark-field scanning transmission electron microscopy (HAADF-STEM) was further carried out to investigate the microstructure of Ir-g-CN and Ru-g-CN, where numerous mesopores were found in the g-CN support of both samples (**Figures 4.3.2a** and **4.3.2d**), which are expected to offer high surface areas and enable the exposure of more catalytically active sites. Further HAADF-STEM imaging at higher magnification revealed a high degree of atomic dispersion of Ir and Ru atoms on the g-CN support (See the bright spots in **Figures 4.3.2b** and **4.3.2e**. Some of them are marked with red cycles in **Figures 4.3.2c** and **4.3.2f**). While most metal species were found in the form of single-atoms, sparse ultrafine nanoclusters with a subnanometer diameter were also observed in some places of both samples. Elemental mapping over Ir-g-CN and Ru-g-CN further corroborated that Ir or Ru element is distributed relatively uniformly over the g-CN with a high density (**Figures 4.3.3b-d** and **4.3.3f-h**).

The crystal structure and chemical composition of Ir-g-CN and Ru-g-CN catalysts were further investigated by X-ray diffractometry (XRD), Fourier transform infrared spectroscopy (FT-IR) and X-ray photoelectron spectroscopy (XPS). According to the XRD results (**Figure 4.3.4a**), only one strong diffraction peak at 27.6° and another very weak one at 12.9°, which can be assigned to the diffractions of (002) and (100) planes of g-CN, are observed for all samples, and no other diffraction peaks from any polymorphs of Ir, Ru or their compounds can be identified. Therefore, no crystalline structures, such as big nanoparticles or clusters, are formed when loading Ir or Ru on the g-CN support. As such, Ir or Ru should virtually be atomically dispersed, consistent with the HAADF-STEM examination (**Figure 4.3.2**). The diffraction intensity of sparsely dispersed subnanometric Ir and Ru clusters (**Figure 4.3.3**) is not strong enough to show any peaks in the XRD patterns, implying that the quantity of such clusters is insignificant. The FT-IR spectra of Ir-g-CN and Ru-g-CN catalysts closely resemble that of as-prepared g-CN, indicating that introducing Ir and Ru atoms onto g-CN did not alter the bulk molecular structure of the g-CN (**Figure 4.3.4b**). The Brunauer-Emmett-Teller (BET)

specific surface area of the Ir-g-CN catalysts was measured to be 64.9 m^2 g^{-1}, slightly lower than that of Ru-g-CN (79.0 m^2 g^{-1}), but both are almost two times higher than that of the original g-CN (34.7 m^2 g^{-1}). This increase suggests that loading Ir or Ru atoms onto g-CN remarkably enlarges the specific surface area of samples, which is beneficial for exposing more active sites and promoting mass transport [25].

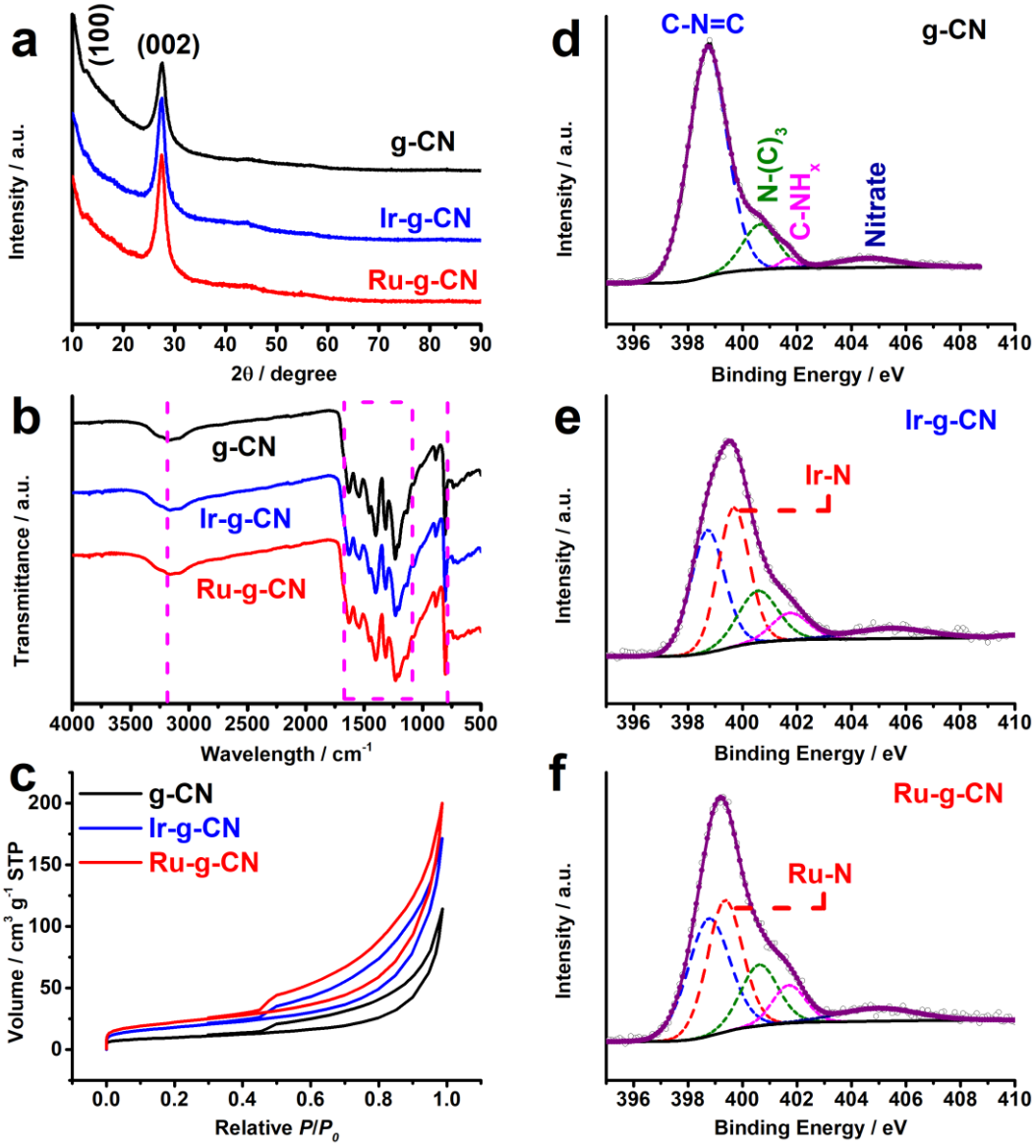

Figure 4.3.4 a) XRD patterns, b) FT-IR spectra, c) Nitrogen adsorption-desorption isotherms of all catalysts. The high-resolution N 1 s spectrum of d) g-CN, e) Ir-g-CN and f) Ru-g-CN catalysts.

The surface chemistry of Ir-g-CN and Ru-g-CN was further analyzed by XPS. The XPS survey spectra of samples confirm the presence of corresponding elements in each catalyst, as shown in **Figure 4.3.5**. The high-resolution N 1 s spectra of g-CN, Ir-g-CN and Ru-g-CN are shown in **Figure 4.3.4d-f**. The N 1 s XPS spectrum of g-CN can be

deconvoluted into four components (**Figure 4.3.4d**), corresponding to triazine rings (C–N=C, 398.7 eV), tertiary nitrogen ($N–(C)_3$, 400.7 eV), amino function groups (401.9 eV) and the nitrate group (404.5 eV) [26], respectively. Compared to the pristine g-CN, Ir-g-CN and Ru-g-CN have one more component appearing at 399.6 eV, which can be assigned to the metal–nitrogen (M–N) bonding [27, 28] resulting from the anchoring of Ir and Ru atoms on the g-CN surface. Meanwhile, the C 1 s XPS spectra of these samples were also compared. The C 1 s XPS spectrum of g-CN is deconvoluted into three components (**Figure 4.3.6a**), corresponding to the sp^2-bonded carbon in N-containing aromatic rings (N–C=N, 288.6 eV), amino functional groups (286.3 eV) and $C(–N)_3$ planar trigonal carbon geometry (284.9 eV) [29]. After loading Ir and Ru onto g-CN, the intensity of N–C=N signals relative to that of the other two components is decreased (**Figure 4.3.6b**-**c**), which can be attributed to the N bonding with Ir and Ru species, consistent with the results for N 1 s spectra (**Figure 4.3.4d-f**). In addition, inductively coupled plasma – optical emission spectroscopy (ICP-OES) measurements were performed, which revealed that the loading mass of Ir and Ru on g-CN is 1.71 wt% and 0.24 wt% for Ir-g-CN and Ru-g-CN, respectively.

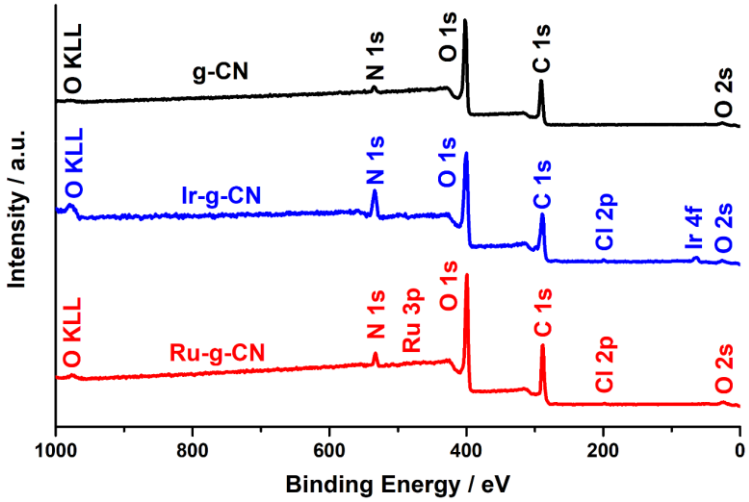

Figure 4.3.5 XPS survey spectra of pristine g-CN, Ir-g-CN and Ru-g-CN.

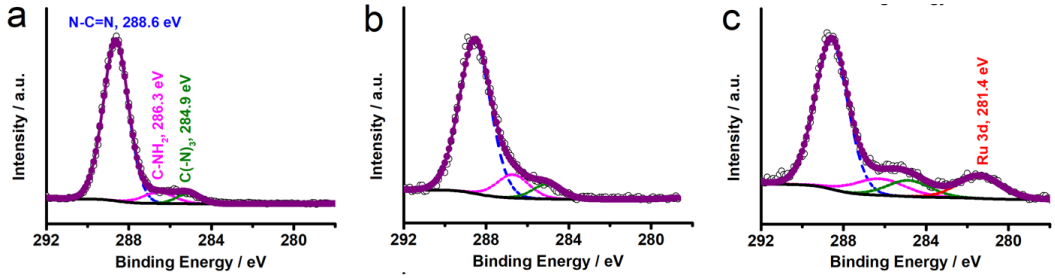

Figure 4.3.6 High-resolution C 1s XPS spectra of a) g-CN, b) Ir-g-CN and c) Ru-g-CN.

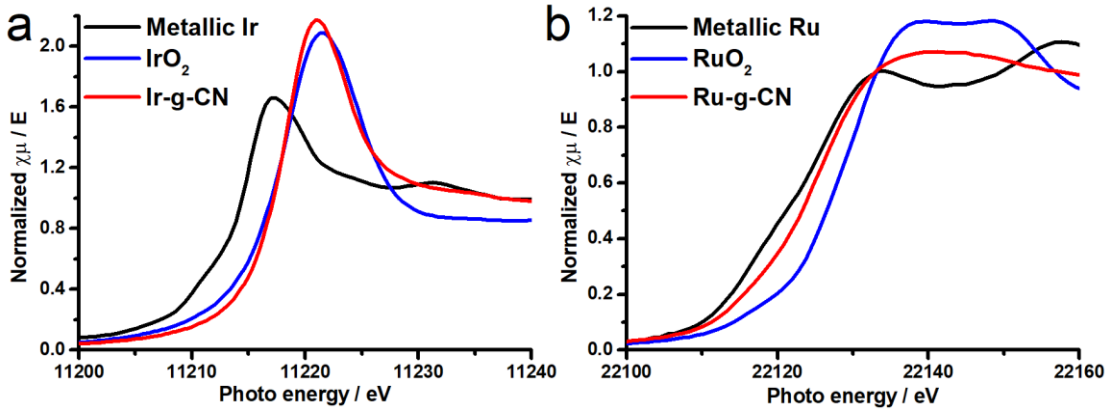

Figure 4.3.7 a) Ir L_3-edge XANES spectra of commercial Ir/C, IrO_2 and Ir-g-CN. b) Ru K-edge XANES spectra of commercial $RuCl_3$, RuO_2 and Ru-g-CN.

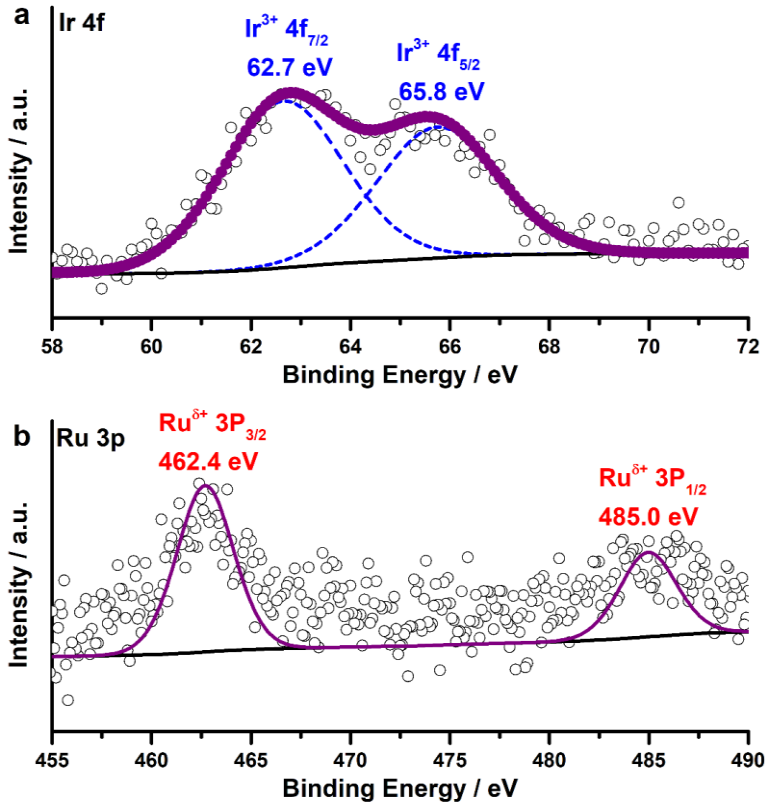

Figure 4.3.8 a) Ir 4f XPS spectrum of Ir-g-CN. b) Ru 3p XPS spectrum of Ru-g-CN.

Moreover, X-ray absorption near-edge structure (XANES) spectroscopy measurements were carried out to gain more insight into the chemical state. **Figure 4.3.7a** shows the Ir L_3-edge XANES spectra of metallic Ir, commercial IrO_2 and Ir-g-CN. The absorption white-line of Ir-g-CN stands in the middle of that of metallic Ir and IrO_2 references, indicating an average Ir oxidation state lower than + 4 but higher than 0. This is in good agreement with the XPS results, where no components from metallic Ir^0 are

observed, and the oxidation state of Ir has been found close to 3 + (**Figure 4.3.8a**). **Figure 4.3.7b** reveals the Ru K-edge XANES spectra of metallic Ru, commercial RuO_2 and Ru-g-CN, respectively, where the Ru in Ru-g-CN is more reduced than that in RuO_2 (4 +) but more oxidized than that in metallic Ru, indicating that the Ru in Ru-g-CN carries positive charges, consistent with the XPS results (**Figure 4.3.8b**). The absence of reduced metallic forms in Ir-g-CN and Ru-g-CN implies that Ir and Ru are predominantly dispersed atomically on the g-CN support [30, 31], agreeing with the above XRD and HAADF-STEM results.

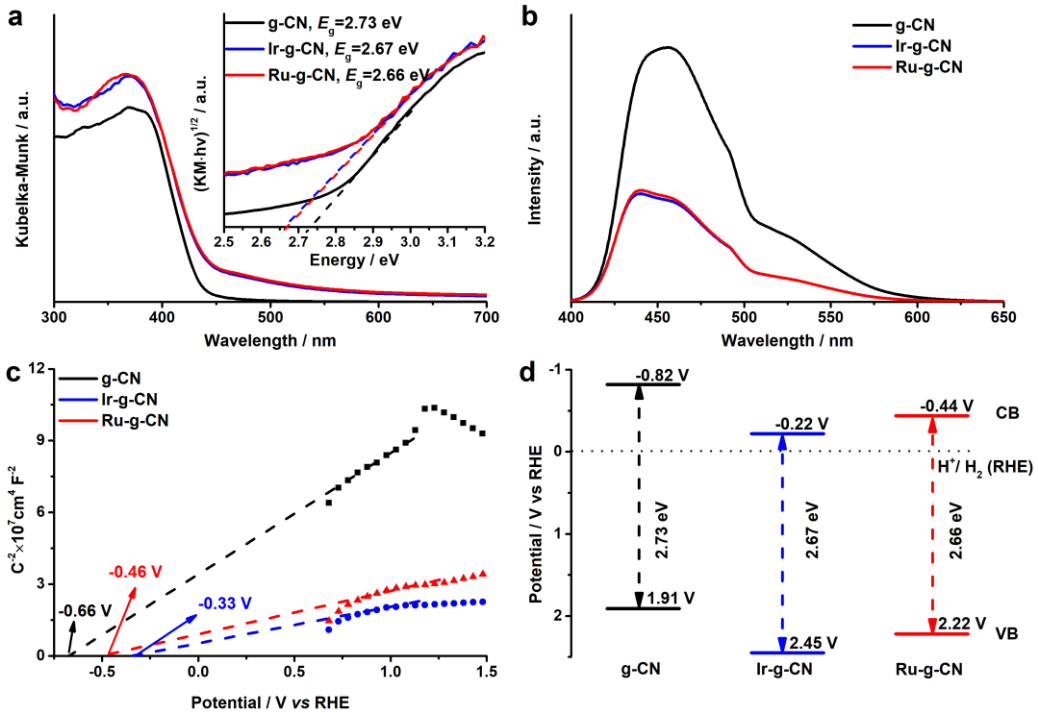

Figure 4.3.9 a) UV–vis absorption spectra and the corresponding Tauc plots (inset), b) PL spectra, c) Mott-Schottky plots and d) the corresponding electronic band structure of g-CN, Ir-g-CN and Ru-g-CN catalysts.

g-CN is known to be a polymeric semiconductor [13], and therefore the effect of introducing Ir and Ru co-catalysts on the optical properties of g-CN was further investigated. According to the Diffuse Reflectance Ultraviolet-Visible (DR UV–vis) spectra measured in the wavelength range of 300 – 700 nm (**Figure 4.3.9a**), the light absorption of both Ir-g-CN and Ru-g-CN exhibits an increase over the whole spectral range, accompanied by a slight red shift in the absorption edge with respect to the as-obtained g-CN support. This indicates that the interaction between Ir or Ru atoms and g-CN enhances light absorption, which improves photocatalytic activity [12, 32]. Furthermore, the optical band gap (E_g) of Ir-g-CN and Ru-g-CN was estimated from the Tauc plot (**Figure 4.3.9a** inset), which shows a very similar value for Ir-g-CN (2.67 eV)

and Ru-g-CN (2.66 eV), slightly lower than that of the as-prepared g-CN (2.73 eV). This was also confirmed by photoluminescence (PL) measurements (**Figure 4.3.9b**), where the PL signals of Ir-g-CN and Ru-g-CN are significantly lower in comparison with that of g-CN, suggesting that the photo-carrier collection in Ir-g-CN and Ru-g-CN works efficiently and that the incorporation of atomically dispersed Ir or Ru can effectively suppress the electron-hole recombination, promoting the separation and transfer of photo-carriers [11, 22, 33].

To further investigate the band structure of the Ir-g-CN and Ru-g-CN catalysts, Mott-Schottky analyses were conducted at a frequency of 1000 Hz. All samples show the n-type semiconductor characteristics, with a positive slope in the Mott-Schottky plots (**Figure 4.3.9c**). The flat band potentials of g-CN, Ir-g-CN and Ru-g-CN can be extrapolated to be −0.66 V, −0.33 V and −0.46 V vs. RHE, respectively [34]. Considering the energy gap (E_{vb}) between the Fermi level (E_f) and the valence band maximum (E_v) of different samples obtained by the ultraviolet photoelectron spectroscopy – valence band maximum (UPS-VBM) spectrum (**Figure 4.3.10**), the valence band position (E_v) and conduction band position (E_c) could be estimated [33] (**Figure 4.3.9d** and **Table 4.3.1**). Since the conduction band of Ir-g-CN and Ru-g-CN is much closer to the Fermi level than that of the original g-CN, the Ir or Ru atoms serve as electron acceptors. In this case, the electron transfer from the support to Ir or Ru co-catalysts will be promoted under photo-irradiation, and thus the electron-hole recombination can be effectively suppressed [11].

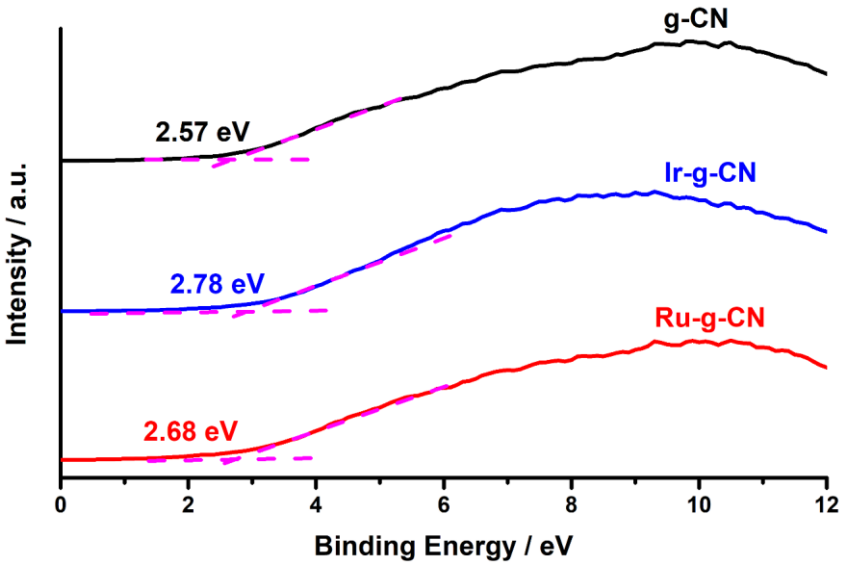

Figure 4.3.10 XPS-VBM spectra of pristine g-CN, Ir-g-CN and Ru-g-CN.

Table 4.3.1 Detailed energy band position of g-CN, Ir-g-CN and Ru-g-CN.

Sample	E_g[a] (eV)	E_f[b] (V)	E_{vb}[c] (eV)	E_v[d] (eV)	E_c[e] (eV)
g-CN	2.73	–0.66	2.57	1.91	–0.82
Ir-g-CN	2.67	–0.33	2.78	2.45	–0.22
Ru-g-CN	2.66	–0.46	2.68	2.22	–0.44

[a] E_g represents the bandgap values that are obtained by extraploating the linear region in the Tauc plots.
[b] E_f represents the Fermi level, approximate to the flat band potential, derived from the Mott-Schottky plots.
[c] E_{vb} represents the energy gap values between the Fermi level (E_f) and the position of the valence band maximum (E_v), derived from its XPS-VBM spectrum.
[d] E_v represents the position of the valence band maximum calculated by the equation $E_v = E_{vb} + E_f$.
[e] E_c represents the position of the conduction band minimum calculated by the equation $E_c = E_v - E_g$.

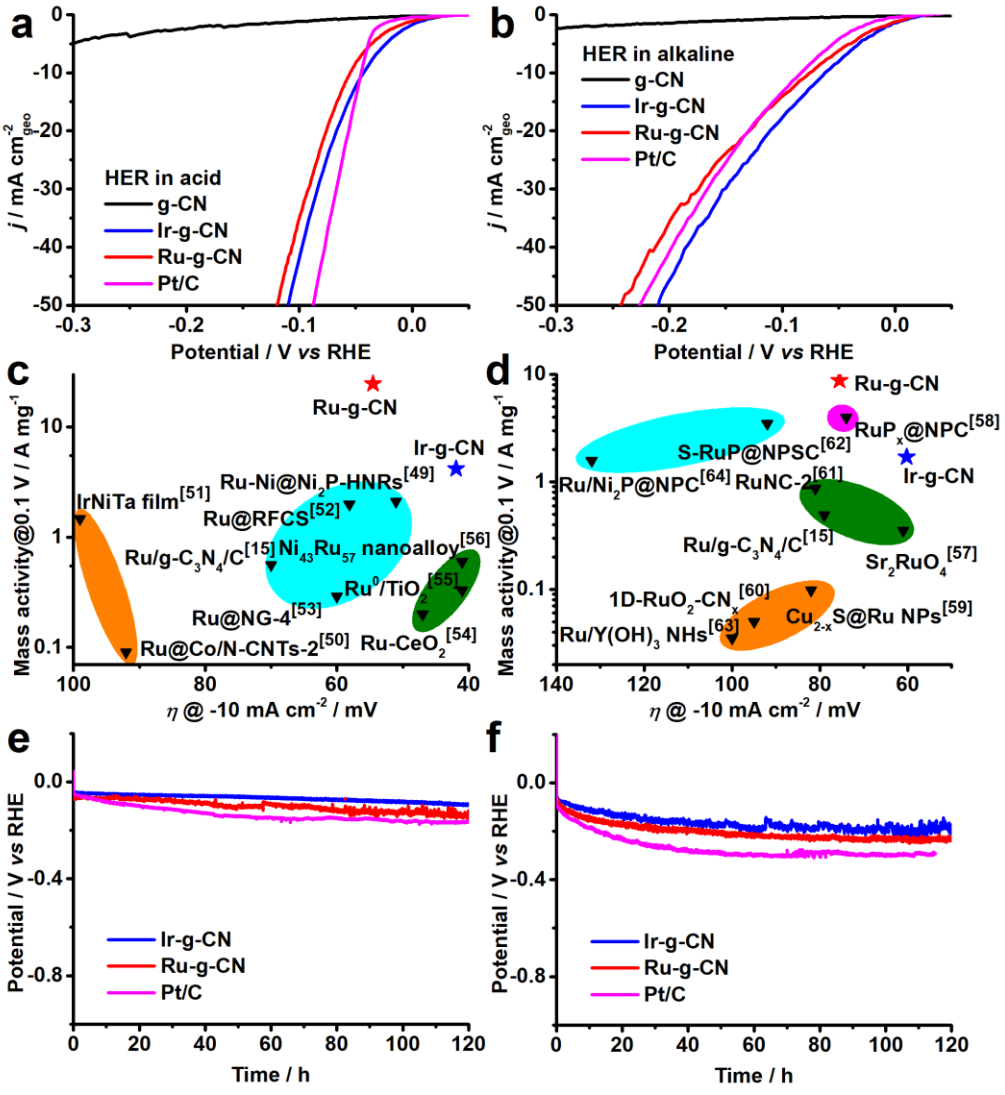

Figure 4.3.11 Electrocatalytic HER performance of g-CN, Ir-g-CN and Ru-g-CN catalysts. a, b) LSV curves. Scan rate: 5 mV s^{-1}. c, d) Comprehensive comparison of the mass activity versus apparent activity of Ir-g-CN and Ru-g-CN to those of other start-of-the-art Ir- and Ru-based catalysts reported recently. See Supporting Information for details. e, f) Long-term catalytic stability tests at −10 mA cm^{-2}. Data were acquired in a, c, e) 0.5 M H_2SO_4 and b, d, f) 1.0 M KOH, respectively.

The electrocatalytic HER activities of Ir-g-CN and Ru-g-CN catalysts were investigated by linear sweep voltammetry (LSV) in both 0.5 M H_2SO_4 and 1.0 M KOH solutions. Pristine g-CN and commercial 20% Pt/C catalysts were used as references. **Figures 4.3.11a** and **4.3.11b** show that the pristine g-CN support exhibits inferior HER performance in acidic and alkaline solutions. Upon loading a tiny amount of Ir or Ru (1.71 wt% for Ir-g-CN and 0.24 wt% for Ru-g-CN), the apparent HER activity is significantly enhanced in both cases, even outperforming the commercial Pt/C benchmark, particularly in the low overpotential (η) region. This performance indicates that dispersing Ir or Ru in the form of single-atoms is an effective strategy to reduce the utilization of precious metals while retaining adequately sound HER performance. The flat portion of LSV curve for Pt/C might result from the hydrogen buildup at low overpotentials, which is likely related to the mass-transport limitations, according to a recent report [35]. The reaction kinetics of all catalysts was studied by the Tafel analysis (**Figures 4.3.12a** and **4.3.12b**). The Ir-g-CN and Ru-g-CN catalysts exhibit a Tafel slope of 47.6 and 54.0 mV dec^{-1}, respectively, in 0.5 M H_2SO_4, slightly higher than that of commercial Pt/C (32.2 mV dec^{-1}), indicating that the HER proceeds on Ir-g-CN and Ru-g-CN through the Volmer-Heyrovsky mechanism, where the electrochemical desorption is fast, but the discharge step is slow. In 1.0 M KOH, the Ir-g-CN shows a Tafel slope of 49.3 mV dec^{-1}, followed by commercial Pt/C (61.0 mV dec^{-1}) and Ru-g-CN (63.5 mV dec^{-1}), suggesting more favorable HER kinetics on Ir-g-CN. Furthermore, the EIS measurements also confirmed the fast reaction rate of the Ir-g-CN and Ru-g-CN for the HER, as evidenced by their small charge transfer resistance (R_{ct}, **Figure 4.3.12c-d**).

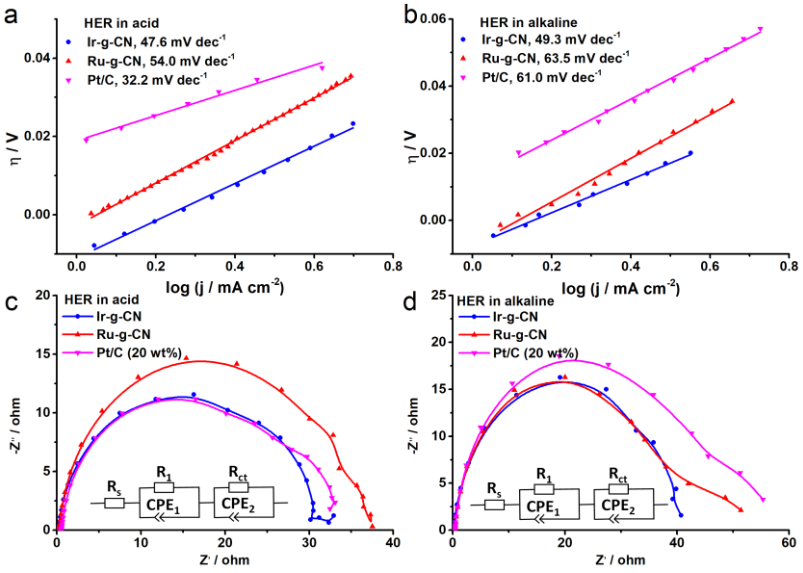

Figure 4.3.12 a, b) Tafel plots, c, d) Nyquist plots of all catalysts towards the HER tested in acidic and alkaline media, respectively. The insets in c) and d) show the equivalent circuit diagrams used for fitting.

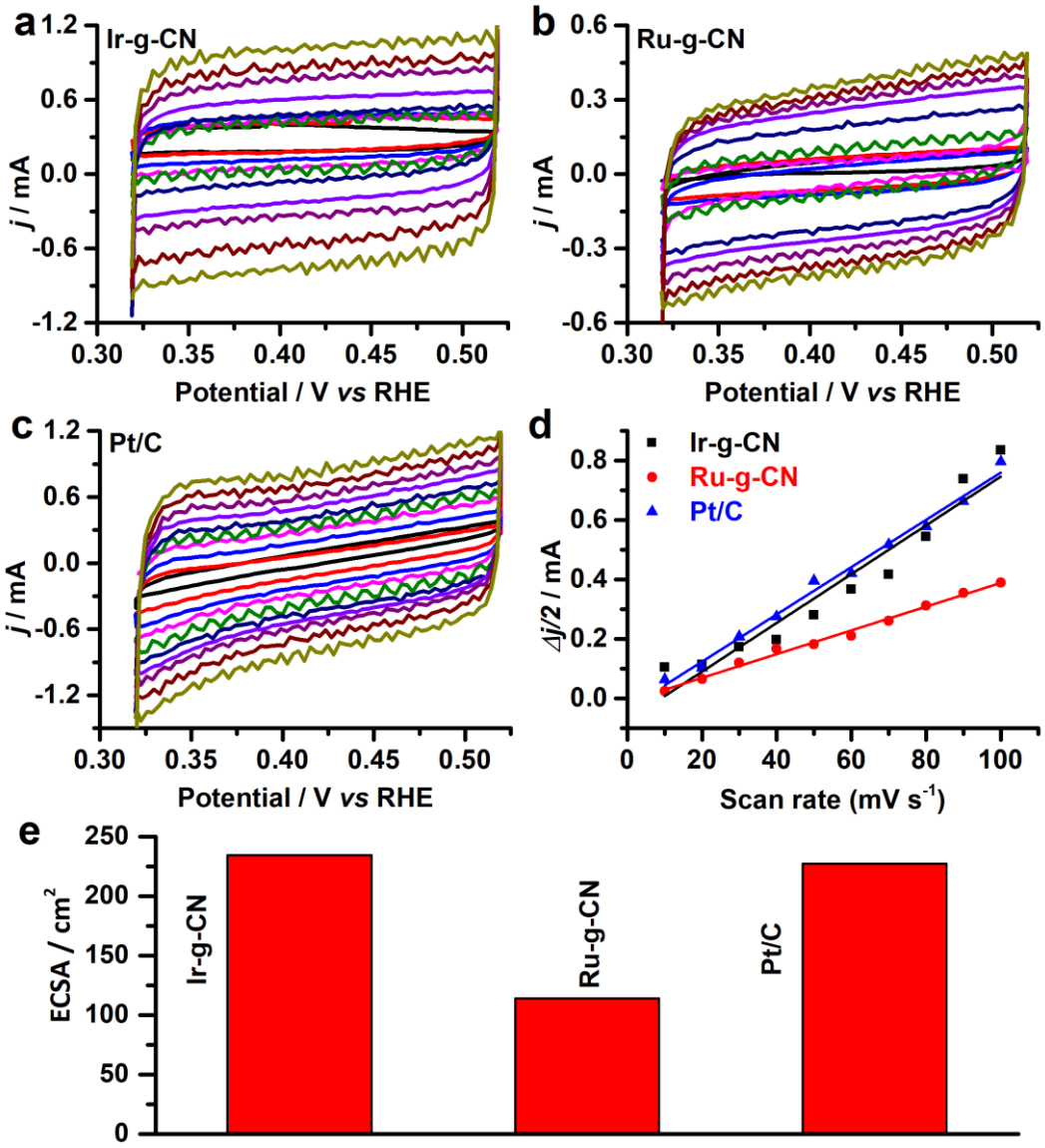

Figure 4.3.13 Electrochemical CV curves of a) Ir-g-CN, b) Ru-g-CN and c) commercial Pt/C, recorded at different scan rates of 10, 20, 30, 40, 50, 60, 70, 80, 90 and 100 mV s^{-1}. d) Plots of the capacitive current as a function of the scan rate for all catalysts. e) ECSA of all catalysts.

To further assess the intrinsic catalytic performance, the ECSAs of Ir-g-CN, Ru-g-CN and reference catalysts were estimated and compared through the electrochemical double-layer capacitance (C_{dl}) measurements [36]. As revealed in **Figure 4.3.13**, Ir-g-CN shows an ECSA value of 234.3 cm^2, higher than the commercial Pt/C (227.1 cm^2) and Ru-g-CN (114.0 cm^2). The ECSA normalized specific activity of Ru-g-CN outperforms that of Ir-g-CN and Pt/C in both acidic and alkaline electrolytes (**Figure 4.3.14**), indicating the intrinsically high HER activity of Ru-g-CN. Furthermore, the TOF values of Ir-g-CN and Ru-g-CN were also calculated and compared to those of other advanced Ir- and Ru-based HER electrocatalysts reported recently (**Figure 4.3.15**). The

Ru-g-CN shows a TOF value of 12.9 and 5.1 s^{-1} at η = 100 mV in 0.5 M H_2SO_4 and 1.0 M KOH, respectively, substantially outperforming commercial Pt/C and many other Ir-/Ru-based electrocatalysts (**Tables 4.3.2** and **4.3.3**), such as Ru/g-C_3N_4/C (4.85 s^{-1} at η = 100 mV in acid) [15], RuCoP (10.95 s^{-1} at η = 100 mV in acid) [37], and np-$Cu_{53}Ru_{47}$ (1.139 s^{-1} at η = 100 mV in alkaline) [38].

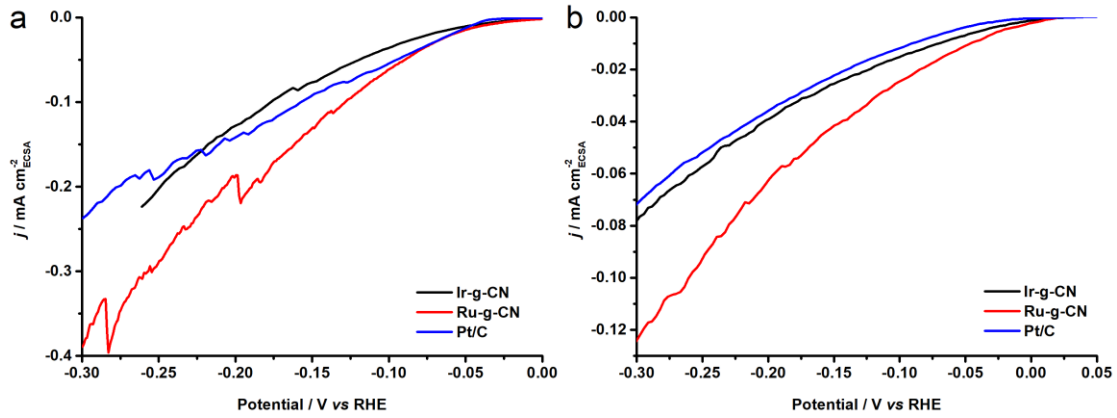

Figure 4.3.14 Specific activity of Ir-g-CN, Ru-g-CN and commercial Pt/C catalysts towards the HER tested in a) 0.5 M H_2SO_4 and b) 1.0 M KOH.

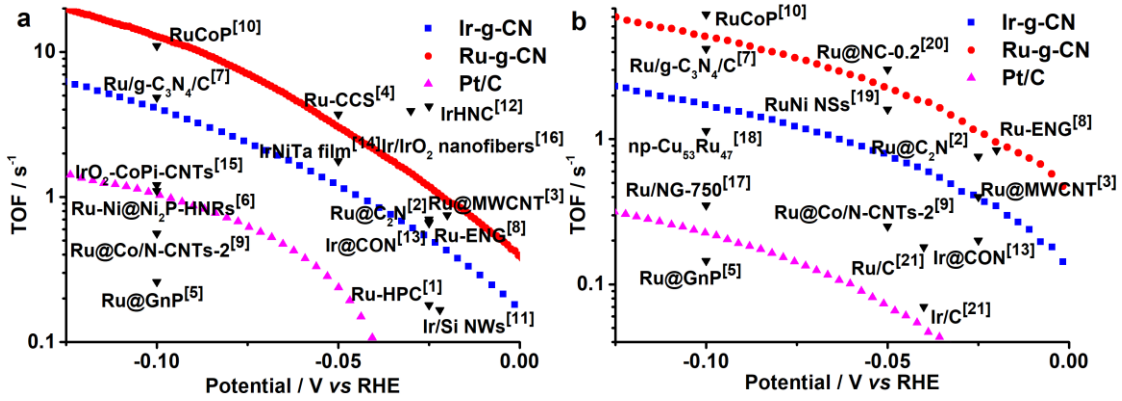

Figure 4.3.15 Comparison of the TOF values of Ir-g-CN and Ru-g-CN catalysts to those of other Ir- and Ru-based catalysts reported recently in the literature. The measurements were conducted in a) 0.5 M H_2SO_4 and b) 1.0 M KOH (Data acquired from the **Tables 4.3.2-4.3.3**).

Table 4.3.2 Comparison of the turnover frequency (TOF) values of Ru-g-CN samples to those of other recently reported Ru-based HER catalysts tested in acidic condition.

Catalyst	Loading of Metal (μg cm^{-2})	Overpotential (V)	TOF (s^{-1})	Reference
Ru-g-CN	**1.5**	**0.1**	**12.9**	**This work**

Ir-g-CN	**10.3**	**0.1**	**4.1**	**This work**
Ru-HPC	11.1	0.025	0.18	[1]Nano Energy 2019, 58, 1–10.
Ru@C_2N	81.8	0.025	0.67	[2]Nat. Nanotechnol. 2017, 12, 441-446.
Ru@MWCNT	89.6	0.025	0.70	[3]Nat. Commun. 2020, 11, 1278.
Ru-CCS	10.6	0.05	3.7	[4]J. Mater. Chem. A 2018, 6, 2311–2317.
Ru@GnP	80.3	0.1	0.26	[5]Adv. Mater. 2018, 30, 1803676.
Ru-Ni@Ni_2P-HNRs	23.4	0.1	1.1	[6]J. Am. Chem. Soc. 2018, 140, 2731–2734.
Ru/g-C_3N_4/C	48.0	0.1	4.85	[7]J. Am. Chem. Soc. 2016, 138, 16174–16181.
Ru-ENG	16.2	0.02	0.75	[8]Nano Energy 2020, 76, 105114.
Ru@Co/N-CNTs-2	/	0.1	0.56	[9]ACS Sustainable Chem. Eng. 2020, 8, 9136–9144.
RuCoP	53.1	0.1	10.95	[10]Energy Environ. Sci. 2018, 11, 1819.
Ir/Si NWs	60.0	0.022	0.166	[11]ACS Nano 2019, 13, 2786–2794.
IrHNC	18.0	0.025	4.21	[12]Nat Commun. 2019, 10, 4060.
Ir@CON	102.5	0.025	0.66	[13]Adv. Mater. 2018, 30, 1805606.
IrNiTa film	8.2	0.05	1.76	[14]Adv. Mater. 2020, 32, 1906384.
IrO_2-CoPi-CNTs	1.9	0.10	1.21	[15]J. Mater. Chem. A 2020,8, 8273-8280.
Ir/IrO_2 nanofibers	/	0.03	3.92	[16]ACS Sustainable Chem. Eng. 2019, 7, 8613–8620.

Table 4.3.3 Comparison of the turnover frequency (TOF) values of Ru-g-CN samples to those of other recently reported Ru-based HER catalysts tested in alkaline condition.

Catalyst	**Loading of Metal ($\mu g\ cm^{-2}$)**	**Overpotential (V)**	**TOF (s^{-1})**	**Reference**
Ru-g-CN	**1.5**	**0.1**	**5.1**	**This work**

Ir-g-CN	**10.3**	**0.1**	**1.7**	**This work**
Ru@C_2N	81.8	0.025	0.76	[2]Nat. Nanotechnol. 2017, 12, 441-446.
Ru@MWCNT	20.5	0.025	0.40	[3]Nat. Commun. 2020, 11, 1278.
Ru@GnP	26.8	0.1	0.145	[5]Adv. Mater. 2018, 30, 1803676.
Ru/C_3N_4/C	48.0	0.1	4.2	[7]J. Am. Chem. Soc. 2016, 138, 16174-16181.
Ru-ENG	16.2	0.02	0.84	[8]Nano Energy 2020, 76, 105114.
Ru@Co/N-CNTs-2	/	0.05	0.25	[9]ACS Sustainable Chem. Eng. 2020, 8, 9136–9144.
RuCoP	53.1	0.1	7.26	[10]Energy Environ. Sci. 2018, 11, 1819.
Ir@CON	102.5	0.025	0.20	[13]Adv. Mater. 2018, 30, 1805606.
Ru/NG-750	14.9	0.1	0.35	[17]ACS Appl. Mater. Interfaces 2017, 9, 3785–3791
np-$Cu_{53}Ru_{47}$	173.0	0.1	1.139	[18]ACS Energy Lett. 2020, 5, 192−199.
RuNi NSs	1.9	0.05	1.60	[19]Nano Energy 2019, 66, 104173.
Ru@NC-0.2	6.0	0.05	3.02	[20]Angew. Chem. Int. Ed. 2018, 57, 5848-5852.
Ru/C	138.0	0.04	0.18	[21]Adv. Energy Mater. 2018, 8, 1801698.
Ir/C	135.7	0.04	0.07	[21]Adv. Energy Mater. 2018, 8, 1801698.

For PGM electrocatalysts, both mass activity and apparent activity are crucial metrics for practical applications in electrolyzers [21, 39]. For single-atom catalysts, the low metal loading would lead to a high normalized mass activity, but this advantage in many cases cannot be fully translated into practical applications. For catalysts with a relatively low PGM loading density, the catalyst layer must be thick enough to deliver a given high catalytic current (not current density), which would hinder efficient mass and charge transport within the electrode, eventually compromising the overall catalytic performance

of the electrode. Therefore, a more comprehensive assessment considering both mass and apparent activities is critically needed, especially for single-atom catalysts. To this end, the mass activity of Ru-g-CN at $\eta = 100$ mV versus its apparent activity at -10 mA cm^{-2} is plotted and compared to that of other advanced Ru-based electrocatalysts reported recently. Ru-g-CN can deliver an exceptionally high mass activity of 24.55 and 8.78 A mg^{-1} at $\eta = 100$ mV in 0.5 M H_2SO_4 and 1.0 M KOH, respectively, and meanwhile afford an apparent current density of -10 mA cm^{-2} at a low overpotential (positioned in the upper right corner in **Figures 4.3.11c** and **4.3.11d**), outperforming many other catalysts tested under the same conditions (**Tables 4.3.4** and **4.3.5**). In addition, the Faradaic efficiency of Ir-g-CN and Ru-g-CN toward the HER was measured (**Figure 4.3.16**), and the volume of H_2 gases collected matches well with that calculated, indicating a near 100% Faradaic efficiency.

Table 4.3.4 Comparison of the mass activity and overpoential of Ru-g-CN samples to those of other recently reported Ru-based HER catalysts tested in acidic condition.

Catalyst	Overpotential @10 mAcm^{-2}	Overpotential (V)	Mass activity (A mg^{-1})	Reference
Ru-gCN	**54.5**	**0.1**	**24.55**	**This work**
Ir-gCN	**41.9**	**0.1**	**4.16**	**This work**
Ru-Ni@Ni_2P-HNRs	51	0.1	~2.1	J. Am. Chem. Soc. 2018, 140, 2731–2734
Ru@Co/N-CNTs-2	92	0.1	~0.09	ACS Sustainable Chem. Eng. 2020, 8, 9136–9144
IrNiTa film	99	0.1	~1.47	Adv. Mater. 2020, 32, 1906384
Ru@RFCS	58.1	0.1	~1.99	Energy Environ. Sci. 2018,11, 1232-1239
Ru/g-C_3N_4/C	70	0.1	~0.56	J. Am. Chem. Soc. 2016, 138, 16174–16181
Ru@NG-4	60	0.1	~0.29	Sustain. Energy Fuels 2017, 1, 1028−1033
Ru-CeO_2	47	0.1	~0.2	ACS Appl. Mater. Interfaces 2018, 10, 6299–6308

Ru^0/TiO_2	41	0.1	~0.33	J. Colloid Interface Sci. 2018, 531, 570-577
$Ni_{43}Ru_{57}$ nanoalloy	41	0.1	~0.6	ACS Appl. Mater. Interfaces 2017, 9, 17326–17336

Table 4.3.5 Comparison of the mass activity and overpoential of Ru-g-CN samples to those of other recently reported Ru-based HER catalysts tested in alkaline condition.

Catalyst	**Overpotential @10 mAcm^{-2}**	**Overpotential (V)**	**Mass activity (A mg^{-1})**	**Reference**
Ru-gCN	**75.5**	**0.1**	**8.78**	**This work**
Ir-gCN	**60.2**	**0.1**	**1.71**	**This work**
$Ru/C_3N_4/C$	79	0.1	~0.49	J. Am. Chem. Soc. 2016, 138, 16174-16181
Sr_2RuO_4	61	0.10	~0.35	Nat. Commun. 2019, 10, 149
RuP_x@NPC	74	0.1	3.97	ChemSusChem 2018, 11, 743
$Cu_{2-x}S$@Ru NPs	82	0.1	0.098	Small 2017, 13, 1700052
1D-RuO_2-CN_x	95	0.1	0.05	ACS Appl. Mater. Interfaces 2016, 8, 28678–28688
RuNC-2	81	0.1	0.87	Chem. Commun. 2018, 54, 13076-13079
S-RuP@NPSC	92	0.1	3.47	Adv. Sci. 2020, 7, 2001526
$Ru/Y(OH)_3$ NHs	100	0.1	0.035	Chem. Commun. 2018, 54, 12202-12205
Ru/Ni_2P@NPC	132	0.1	1.567	ACS Sustainable Chem. Eng. 2019, 7, 17714–17722

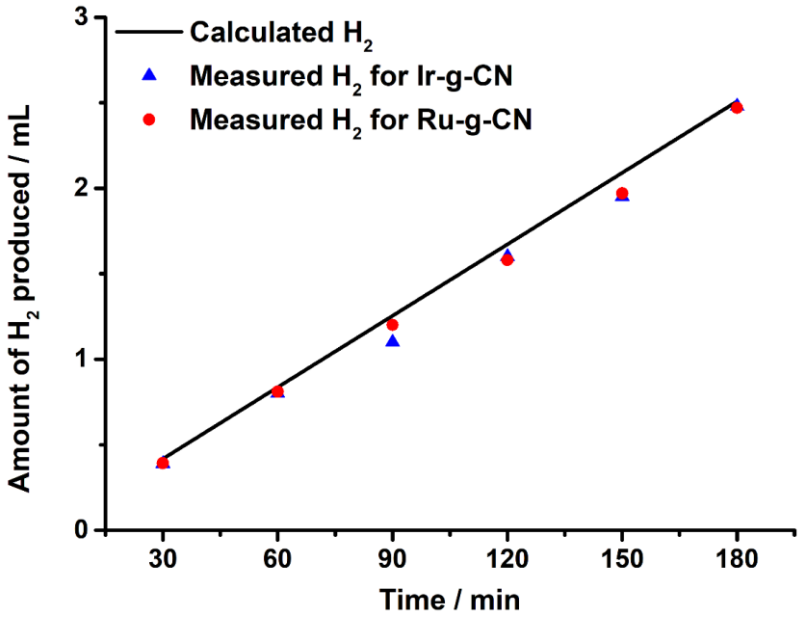

Figure 4.3.16 Experimentally measured and calculated volumes of H_2 gas evolved from Ir-g-CN and Ru-g-CN at a fixed current density of -10 mA cm^{-2}.

The electrocatalytic stability is another significant performance indicator of an HER catalyst in practical applications. The commercial Pt/C catalysts display a gradually decreased activity upon continuous HER electrolysis at −10 mA cm^{-2} for 120 h in both acidic and alkaline solutions (**Figures 4.3.11e** and **4.3.11f**), in agreement with previous reports [37, 40], which likely results from the weak binding between Pt nanoparticles and the carbon support. In contrast, although Ir-g-CN and Ru-g-CN also exhibit slow degradation in HER activity, this happens to a much lesser extent compared to the commercial Pt/C catalysts, which may originate from the strong chemical bonding between Ir/Ru atoms and uncoordinated N in g-CN that has much better electrochemical stability even in anodic oxidation conditions [39, 41, 42]. The degradation rate of Ir-g-CN is only 0.45 and 0.87 mV h^{-1} in 0.5 M H_2SO_4 and 1.0 M KOH, respectively, and that of Ru-g-CN is 0.66 and 1.11 mV h^{-1}, both lower than that of the commercial Pt/C benchmark (0.96 and 1.58 mV h^{-1}).

Besides electrocatalytic performance, the photocatalytic H_2 evolution performance of Ir-g-CN and Ru-g-CN was also investigated in a suspension system, given that g-CN itself is a photocatalyst with a suitable bandgap for visible light water splitting [10, 43]. According to the photocatalytic tests (**Figure 4.3.17a**), where methanol was used as the sacrificial agent, the pristine g-CN exhibits an H_2 production rate of 58 μmol H_2 $g_{catalyst}^{-1}$ h^{-1}, similar to and even higher than that in some previous reports on g-CN [11, 44, 45]. According to the DR UV–vis and PL results discussed above (**Figures 4.3.9a** and **4.3.9b**),

this relatively low H_2 evolution rate might result from rapid recombination of photo-generated charge carriers. Once Ir or Ru single-atoms are loaded as the co-catalysts, even only with an ultralow loading mass (1.71 wt% for Ir-g-CN and 0.24 wt% for Ru-g-CN), significant enhancement in the H_2 production rate has been observed, amounting to 2122 μmol H_2 $g_{catalyst}^{-1}$ h^{-1} for Ir-g-CN and 1175 μmol H_2 $g_{catalyst}^{-1}$ h^{-1} for Ru-g-CN, much higher than that of atomic palladium on g-CN (728 μmol H_2 $g_{catalyst}^{-1}$ h^{-1}) [24], g-C_3N_4-Pt^{2+} (605 μmol H_2 $g_{catalyst}^{-1}$ h^{-1}) [32], and 3Ru/TiO_2 (1000 μmol H_2 $g_{catalyst}^{-1}$ h^{-1}) [46]. If only normalized to the mass and mole of noble metals, the Ru-g-CN catalyst shows a remarkably high photocatalytic H_2 production rate of 489.7 mmol H_2 g_{Ru}^{-1} h^{-1} or a photocatalytic TOF value of 50.4 h^{-1} (**Figures 4.3.17b** and **4.3.17c**), greater than that of Ir-g-CN (124.1 mmol H_2 g_{Ir}^{-1} h^{-1}, TOF: 25.2 h^{-1}) and other Ru-based photocatalysts (**Table 4.3.6**), due likely to the ultralow loading of Ru (0.24 wt%) on g-CN. The photocatalytic stability and re-usability of Ir-g-CN and Ru-g-CN catalysts were further examined by repeating the photocatalytic reaction cycles. The H_2 evolution rate of both catalysts remained constant during the tests for at least three cycles (**Figure 4.3.17d**), illustrating their good stability and re-usability.

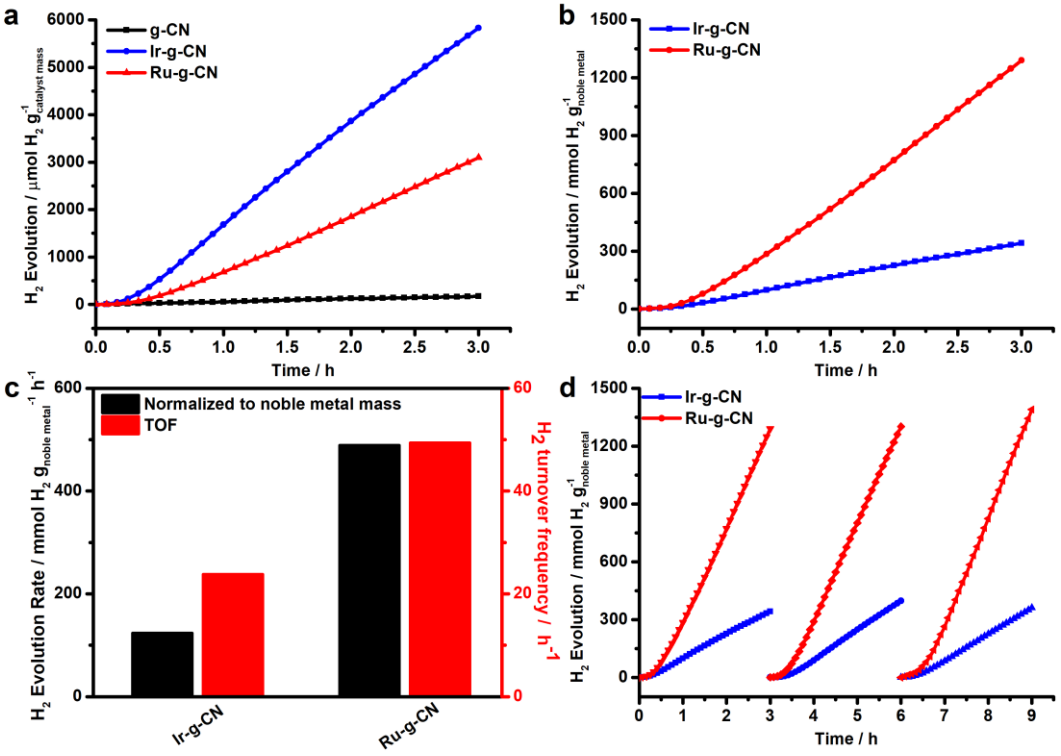

Figure 4.3.17 Photocatalytic H_2 evolution tests of pristine g-CN, Ir-g-CN and Ru-g-CN catalysts. a) H_2 evolution normalized to the catalyst mass vs. photocatalytic reaction duration. b) H_2 evolution normalized only to the mass of noble metal vs. photocatalytic reaction duration. c) Comparison of mass-based hydrogen evolution rate and the TOF values. d) Photocatalytic test cycles of Ir-g-CN and Ru-g-CN under light irradiation.

Table 4.3.6 Comparison of photocatalytic HER performance of Ru-g-CN samples to those of other recently reported Ru-based HER catalysts**.**

Samples	Loading (wt%)	Activity relative to total mass[a]	Activity relative to metal[b]	Reference
g-CN	**/**	**0.058**	**/**	**This work**
Ir-g-CN	**1.71**	**2.122**	**124.1**	**This work**
Ru-g-CN	**0.24**	**1.175**	**489.7**	**This work**
g-C_3N_4-Pt^{2+}	0.18	0.605	336.1	Adv. Mater. 2016, 28, 6959–6965.
PtSA-CN620	1.72	3.02	175.5	Nano Energy 2019, 56,127–137.
RuP/g-CN	0.1	2.11	2110	Appl. Catal. B Environ. 2018, 239, 578-585.
Ru-NPs/SAs@N-TC	0.457	5	1094.09	Adv. Funct. Mater. 2020, 30, 2003007.
RuNPs@CNH/mpg-CN	0.26	0.42	161.5	Renew. Energ. 2021, 168, 668-675.
U-1Ru/3DpCN	2.69	2.945	109.5	Dalton Trans. 2021, 50, 2414-2425.
3Ru/TiO_2	3	≈1	33.3	Appl. Catal. B Environ. 2018, 238, 434-443.
g-C_3N_4-Pd20	1.2	0.105	8.75	ACS Appl. Energy Mater. 2018, 1, 2866–2873.
0.1 Pd/C_3N_4	0.1	0.728	728	Commun. Chem. 2019, 2, 18
Ag-N_2C_2/CN	3.8	1.866	49.1	Angew. Chem. Int. Ed. 2020, 59, 23112–23116.
AgTCM-mpg-CN	2	0.79	39.5	ACS Nano 2016, 10, 3166-3175.
MoS_2/mpg-CN	2	0.969	48.45	Angew. Chem. Int. Ed. 2013, 52, 3621–3625.

[a] $mmol_{(H2)}\ g_{(catalysts)}^{-1}\ h^{-1}$
[b] $mmol_{(H2)}\ g_{(metal)}^{-1}\ h^{-1}$

To gain further insights into the markedly enhanced electrocatalytic and photocatalytic performance of Ir-g-CN and Ru-g-CN with respect to the pristine g-CN, we performed DFT calculations. The proposed atomic models of the pristine g-CN, Ir-g-CN and Ru-g-CN catalysts are illustrated in **Figure 4.3.18**. As shown in **Figure 4.3.19a**, the g-CN has

an indirect bandgap of 2.7 eV, which is in good agreement with our experimental data (**Figure 4.3.9a**) and previous reports [17, 18]. According to the optimal models we obtained (**Figure 4.3.18**), introducing Ir or Ru single-atoms onto g-CN dramatically changes the electronic structure of the resulting Ir-g-CN and Ru-g-CN (**Figures 4.3.19a** and **4.3.19b**), which show significantly reduced bandgaps and increased projected density of states (PDOS) near the Fermi level. Such modification may result in a higher carrier density and facilitate the charge transfer on and near the surface [20, 47], where the electrocatalytic and photocatalytic reactions are taking place, eventually enhancing the electrocatalytic and photocatalytic activity. Note that the theoretically calculated bandgaps of Ir-g-CN and Ru-g-CN are smaller than the experimentally measured (**Figure 4.3.9**), owing to the fact that the Ir/Ru density on g-CN in our models (34.3 wt% for Ir-g-CN and 21.6 wt% for Ru-g-CN) is much higher than the measured Ir/Ru loading density (1.71 wt% for Ir-g-CN and 0.24 wt% for Ru-g-CN). Nevertheless, it is unambiguous that loading single-atoms on g-CN can decrease the bandgap, and this has been confirmed by other groups as well [17, 18].

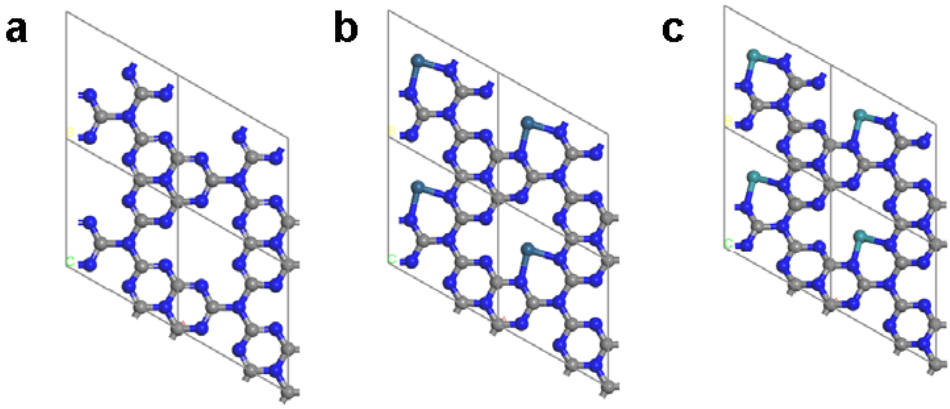

Figure 4.3.18 Top view of the optimized structures of a) g-CN, b) Ir-g-CN and c) Ru-g-CN. Cyan, dark cyan, blue and gray balls represent Ru, Ir, N and C atoms, respectively.

Furthermore, the Gibbs free energy (ΔG_H) diagrams of pristine g-CN, Ir-g-CN and Ru-g-CN catalysts for the HER were calculated (**Figure 4.3.19c**). The ΔG_H of hydrogen adsorption has been proposed to be a suitable descriptor of the HER activity, and the closer ΔG_H value is to zero, the better the HER activity. According to **Figure 4.3.19c**, Ru-g-CN exhibits a ΔG_H value (−0.08 eV) much closer to zero than Ir-g-CN (−0.16 eV), Pt (111) surface (−0.19 eV) and g-CN (−0.73 eV). This indicates that the Ru sites in Ru-g-CN provide optimal adsorption for H* intermediates, compared to the Ir-g-CN and Pt/C controls, which rationally explains the intrinsically high specific activity of Ru-g-CN (**Figure 4.3.14**). Overall, our DFT calculations consistently support the experimental

results, demonstrating that introducing Ir and Ru atoms onto the g-CN support alters the electronic structures and results in remarkably improved electrocatalytic and photocatalytic HER activity.

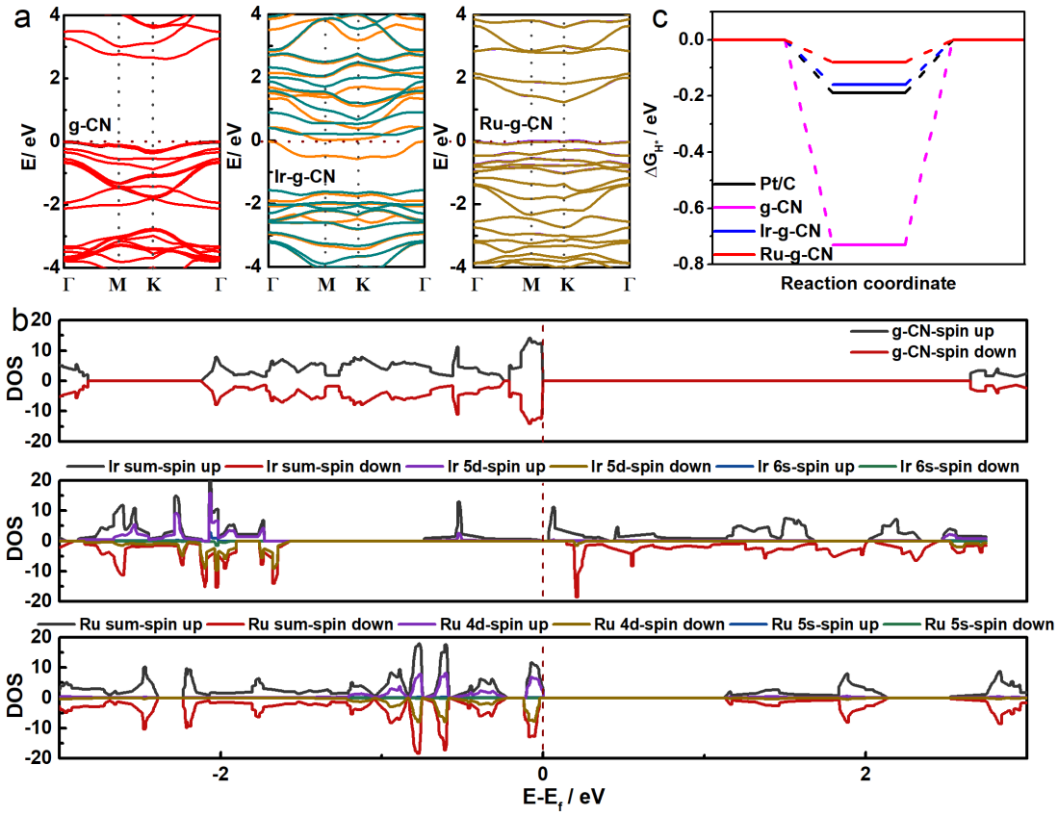

Figure 4.3.19 a) Energy band structures, b) Projected density of states, and c) The Gibbs free-energy diagram towards the HER of the pristine g-CN, Ir-g-CN and Ru-g-CN catalysts.

4.3.3 Conclusions

In summary, we synthesized single-atom Ir and Ru catalysts supported on mesoporous graphitic carbon nitride, which can act as efficient and stable HER catalysts for electrocatalytic and photocatalytic water splitting. In particular, Ru-g-CN shows outstanding electrocatalytic performance in terms of specific activity, mass activity, and catalytic stability. It exhibits a high TOF value of 12.9 and 5.1 s^{-1} at $\eta = 100$ mV in 0.5 M H_2SO_4 and 1.0 M KOH, respectively, which outperforms Ir-g-CN, commercial Pt/C benchmark and many other advanced HER catalysts recently reported in the literature. In addition, Ru-g-CN affords an exceptionally high mass activity of 24.55 and 8.78 A mg^{-1} at $\eta = 100$ mV in acidic and alkaline solutions, meanwhile exhibiting a high apparent current density, which is favorable for practical applications. Impressively, Ru-g-CN also reveals outstanding photocatalytic HER activity showing a high H_2 production rate of 489.7 mmol H_2 g_{Ru}^{-1} h^{-1}, along with good catalytic stability. For single-atom catalysts with

a low metal loading density, the catalytic performance should be comprehensively assessed in the context of practical application. The mass activity alone should not be overemphasized without considering the catalyst's apparent activity. To this end, our Ru-g-CN catalysts exhibit a high mass activity, and at the same time, a high apparent activity. All in all, our experimental results are supported by the theoretical calculations, in which introducing Ir or Ru onto the surface of g-CN has been demonstrated to be able to promote the electron transfer and lead to optimal Gibbs free energy of hydrogen adsorption, contributing to the remarkable improvement of the electrocatalytic and photocatalytic HER performance.

4.3.4 Experimental section

Reagents: Dicyandiamide (99 wt%), ethylene glycol (EG), iridium chloride hydrate ($IrCl_3 \cdot xH_2O$) and Nafion® perfluorinated resin solution (5 wt%) were purchased from Sigma-Aldrich. Ruthenium chloride hydrate ($RuCl_3 \cdot xH_2O$) and commercial Pt/C (20 wt%) were acquired from Johnson Matthey. All reagents were used as received without further purification.

Synthesis of Ir-g-CN and Ru-g-CN: Firstly, the mesoporous g-CN was synthesized by a simple thermal decomposition process of dicyandiamide under a static air atmosphere at 550 °C, using a Phoenix Microwave Muffle Furnace (CEM Corporation) according to the pre-established thermal muffle furnace procedure [26]. The resulting solids were ground and washed, followed by filtration, and dried overnight at 120 °C. The obtained powders were then collected and loaded in an open crucible, calcined in air at 500 ^oC for 2 h. The as-prepared product is labeled as g-CN. In the synthesis of Ir-g-CN and Ru-g-CN, 100 mg of g-CN was added to 16 mL of EG, followed by ultrasonication for 1 h to obtain a homogeneous solution. Subsequently, 4 mL of 2 mg L^{-1} $IrCl_3$/EG or $RuCl_3$/EG mixture was added to the g-CN/EG solution and the solution was then mixed homogeneously by ultrasonication. Afterward, the solution was continuously stirred for 12 h to disperse the Ir or Ru precursors into the mesoporous g-CN adequately. In the next step, the mixed solution was transferred into a Teflon-lined stainless steel autoclave reactor, heated to 130 °C, and maintained at this temperature for 3 h. After the reactor was naturally cooled down to 25 °C, the obtained precipitates were centrifuged, washed twice with deionized water and ethanol sequentially, and then dried under vacuum at 60 °C for further use.

Materials characterization: Scanning electron microscopy (SEM) was performed on an FEI Quanta 650 FEG microscope. The high-angle annular dark-field scanning

transmission electron microscopy (HAADF-STEM) was carried out on an image- and probe-corrected transmission electron microscope operating at 200 kV (FEI Themis 60-300). X-ray diffractometry (XRD) examination was conducted on an X'Pert PRO diffractometer (PANalytical) set at 45 kV and 40 mA, using Cu K_α radiation (λ = 1.5406 Å) and a PIXcel detector. Experimental data were obtained with the Bragg-Brentano configuration in the 2θ range of 10 – 90º at a scan speed of 0.011º s^{-1}. Fourier transform infrared spectroscopy (FT-IR) was performed on an ERTEX 80v vacuum FT-IR spectrometer (Bruker). Nitrogen adsorption/desorption porosimetry measurements were conducted at 77 K using a Quantachrome Autosorb IQ_2 system, and the surface area of samples was derived by the Brunauer-Emmett-Teller (BET) method. X-ray photoelectron spectroscopy (XPS) experiments were carried out on an ESCALAB 250 instrument with Al K_α X-rays (1486.6 eV), and ultraviolet photoelectron spectroscopy (UPS) measurements were conducted with an unfiltered He I (21.22 eV) gas discharge lamp to calculate the valence band maximum (VBM). The loading mass of Ir and Ru on g-CN was determined by the inductively coupled plasma – optical emission spectroscopy (ICP-OES, ICPE-9000 spectrometer, Shimadzu). The Diffuse Reflectance Ultraviolet-Visible (DR UV–vis) spectra were recorded on a UV–vis spectrophotometer (Jasco V-560) equipped with an integrating sphere attachment (Jasco ISV-469), with data being converted to equivalent absorption Kubelka-Munk units to construct the respective Tauc plot. Photoluminescence (PL) spectra were acquired between 400 and 650 nm, using a spectrofluorometer (Jasco FP-8300) with a 150 W Xenon lamp under 370 nm excitation while fixing the emission and excitation bandwidths at 2.5 nm. The X-ray adsorption spectroscopy (XAS) experiments were carried out at the CLAESS beamline, of the ALBA Synchrotron [48]. Samples were prepared as solid pellets diluted in cellulose. Data were acquired at room temperature using a Si311 double crystal monochromator. Ir L_3-edge spectra was collected in transmission mode, while Ru K-edge was measured in transmission for the references and in fluorescence mode for the catalyst by means of a multi-channel SDD detector. Several XAS repeats were collected to ensure reproducibility and statistics. The averaged spectra were treated with the Athena software package [49]. The energy scale was calibrated by setting the first inflection point of Pt foil to 11564 eV in the case of Ir data and to the first inflection point of RuO_2 taken as 22129 eV for Ru data

Electrocatalytic tests: The electrocatalytic experiments were performed in a three-electrode configuration at room temperature using a Biologic VMP-3 potentiostat/galvanostat. The catalyst ink was prepared by ultrasonically dispersing 5 mg

of Ir-g-CN and Ru-g-CN catalysts into 500 µL of isopropanol + 50 µL of Nafion® (Sigma, 5 wt%) solution. Afterward, 13.2 µL of catalyst ink was evenly drop-cast on the glassy carbon (GC) electrode with an exposed area of 0.2 cm^2. For comparison, the commercial Pt/C (20 wt%, Johnson Matthey) catalysts and g-CN support as control samples were also investigated. The catalyst-loaded GC, a graphitic rod, and a saturated calomel electrode (SCE) were used, respectively, as the working, counter, and reference electrodes. All potentials are converted to the reversible hydrogen electrode (RHE) scale according to the following formula:

$$E_{RHE} = E_{SCE} + 0.059 \times pH + 0.241 \quad (1)$$

Cyclic voltammetry (CV) was carried out at a scan rate of 5 mV s^{-1} to evaluate the apparent HER activity of catalysts, and an *iR*-correction (85 %) was made to compensate for the voltage drop between the reference and working electrodes. The electrochemical double-layer capacitance (C_{dl}) was measured to calculate the catalysts' electrochemically active surface area (ECSA). The C_{dl} value of catalysts was estimated by performing CV in the non-Faradaic potential range of 0.32 to 0.52 V vs. RHE in 1.0 M KOH at different scan rates (v) of 10, 20, 30, 40, 50, 60, 70, 80, 90 and 100 mV s^{-1}, followed by extracting the slope from the resulting $|j_a-j_c|/2$ vs. v plots, where j_a and j_c represent the anodic and cathodic currents obtained at 0.42 V vs. RHE, respectively. The ECSA was estimated upon dividing C_{dl} by the capacitance of a model catalyst over a unit surface area (usually 0.035 mF cm^{-2} for noble metals) [36, 39], as follows:

$$ECSA = C_{dl} / 0.035 \text{ mF cm}^{-2} \quad (2)$$

Furthermore, the TOF values were calculated through the following equation [50]:

$$TOF = \frac{j}{2nF} \quad (3)$$

where j (A) is the current at a given overpotential, F = 96500 C mol^{-1} stands for the Faraday constant, and n (mol) represents the mole number of Ir or Ru loaded on the g-CN support calculated from the ICP-OES measurements. All metal species in catalysts are assumed to be catalytically active, so the calculated values represent the lower limit of TOF.

Electrochemical impedance spectroscopy (EIS) tests were performed at −0.075 V vs. RHE in the frequency range of 10^5 – 0.01 Hz with a 10 mV sinusoidal perturbation. The stability of catalysts was assessed at a constant current density of −10 mA cm^{-2} using chronopotentiometry (CP). Mott-Schottky (M-S) plots were acquired in 0.5 M Na_2SO_4 at

the frequency of 1000 Hz, where the initial potential, final potential and amplitude of perturbation were set to 0.66 V, 1.5 V vs. RHE and 0.01 V, respectively.

Photocatalytic tests: The photocatalytic H_2 production tests were carried out at room temperature in a cylindrical glass immersion photo-reactor coupled with a DURAN® glass cooling jacket. The irradiation system consisted of four near-UV light-emitting diodes (LEDs) as the light source (λ_{max} = 417 nm), placed equidistantly at 3.5 cm from the reactor wall. The LED intensity reaching the reactor wall was ca. 450 W m^{-2} determined by a spectroradiometer (USB2000+, Ocean Optics, USA). The reactor was charged with 150 mL of the aqueous solution, containing 75 mg of catalysts and 10% v/v methanol as the sacrificial agent. The suspension was first degassed by a nitrogen flow for 20 min, after which the light was turned on. During measurements, the N_2 flow was maintained at a rate of 10 cm^3 min^{-1}. H_2 was detected in-line using an Inficon Micro GC 3000 gas chromatograph equipped with a molecular sieve column and a micro-TCD detector. Argon (Ar) was used as the carrier gas. The photocatalytic durability tests used the same catalysts recycled by filtration, followed by washing and drying, after finishing one photocatalytic cycle and before using them in the next cycle.

DFT calculations: The first-principles density functional theory (DFT) calculations were performed using Vienna Ab-initio Simulation Package (VASP) with the projector augmented wave (PAW) pseudopotential [51-53]. Since the generalized gradient approximation (GGA) functionals such as PBE tend to underestimate the bandgap of materials, the electronic properties were calculated by using hybrid HSE06 functional [54]. The energy cutoff was set to 450 eV, and the atomic positions were allowed to relax until the energy and force were less than 10^{-5} eV and 10^{-2} eV $Å^{-1}$, respectively. The crystal lattices of g-CN used for computation are *a* = 7.13 Å and *b* = 7.13 Å, and a double layer periodic slab of g-CN with a 15 Å separation in the *z*-direction was used to model the experimental work. The Brillouin zone was sampled using 5 × 5 × 1 and 9 × 9 × 1 Monkhorst–Pack k-point grid for structure optimization and electronic property calculation, respectively. For Ir-g-CN and Ru-g-CN, the optimized most stable structural models are Ir_1N_x or Ru_1N_x single-site/g-CN, where the Ir or Ru atom is embedded in the plane and forms chemical bonds with two N atoms.

The HER proceeds through two-electron pathways with the following reaction steps:

$$M^* + H^+ + e^- \rightarrow H^* \quad (4)$$

$$H^* + H^+ + e^- \rightarrow H_2\,(g) + M^* \quad (5a)$$

or $H^* + H^* \rightarrow H_2(g) + 2M^*$ (5b)

where M^* represents the Ir or Ru active site, and H^* is the hydrogen intermediate absorbed on the active sites during the HER. The adsorption energy was calculated according to the following equation:

$$G_{ad} = G_{sys} - G_{sur} - G_{spe} \quad (6)$$

where G_{ad}, G_{sys}, G_{sur} and G_{spe} denote the adsorption free energy, the free energy of the adsorption system, the free energy of a clean surface and the free energy of the isolated adsorption species, respectively.

4.3.5 References

[1] M. De Simón-Martín, B.R. Cortes-Nava, R. Rodriguez-Parra, F. Carro-De Lorenzo, The role of green hydrogen in the energy transition of the industry. DYNA 96 (2021) 200-206.

[2] S. Furfari, A. Clerici, Green hydrogen: the crucial performance of electrolysers fed by variable and intermittent renewable electricity. Eur. Phys. J. Plus 136 (2021) 509.

[3] L. Liu, Platinum group metal free nano-catalysts for proton exchange membrane water electrolysis. Curr. Opin. Chem. Eng. 34 (2021) 100743.

[4] J. Xu, I. Amorim, Y. Li, J. Li, Z. Yu, B. Zhang, A. Araujo, N. Zhang, L. Liu, Stable overall water splitting in an asymmetric acid/alkaline electrolyzer comprising a bipolar membrane sandwiched by bifunctional cobalt-nickel phosphide nanowire electrodes. Carbon Energy 2 (2020) 646-655.

[5] S.J. Mun, S. J. Park, Graphitic Carbon Nitride Materials for Photocatalytic Hydrogen Production via Water Splitting: A Short Review. Catalysts 9 (2019) 805.

[6] X. Xiao, L. Zhang, H. Meng, B. Jiang, H. Fu, Single Metal Atom Decorated Carbon Nitride for Efficient Photocatalysis: Synthesis, Structure, and Applications. Solar RRL 5 (2021) 2000609.

[7] M.G. Walter, E.L. Warren, J.R. McKone, S.W. Boettcher, Q. Mi, E.A. Santori, N.S. Lewis, Solar Water Splitting Cells. Chem. Rev. 110 (2010) 6446-6473.

[8] S.M. Thalluri, L. Bai, C. Lv, Z. Huang, X. Hu, L. Liu, Strategies for Semiconductor/Electrocatalyst Coupling toward Solar-Driven Water Splitting. Adv. Sci. 7 (2020) 1902102.

[9] X. Wang, K. Maeda, A. Thomas, K. Takanabe, G. Xin, J.M. Carlsson, K. Domen, M. Antonietti, A metal-free polymeric photocatalyst for hydrogen production from water under visible light. Nat. Mater. 8 (2009) 76-80.

[10] M.S. Nasir, G. Yang, I. Ayub, S. Wang, L. Wang, X. Wang, W. Yan, S. Peng, S. Ramakarishna, Recent development in graphitic carbon nitride based photocatalysis for hydrogen generation. Appl. Catal. B Environ. 257 (2019) 117855.

[11] W. Li, X.S. Chu, F. Wang, Y.Y. Dang, X.Y. Liu, X.C. Wang, C.Y. Wang, Enhanced cocatalyst-support interaction and promoted electron transfer of 3D porous g-C_3N_4/GO-M (Au, Pd, Pt) composite catalysts for hydrogen evolution. Appl. Catal. B Environ. 288 (2021) 120034.

[12] X. Li, W. Bi, L. Zhang, S. Tao, W. Chu, Q. Zhang, Y. Luo, C. Wu, Y. Xie, Single-Atom Pt as Co-Catalyst for Enhanced Photocatalytic H_2 Evolution. Adv. Mater. 28 (2016) 2427-2431.

[13] W. Niu, Y. Yang, Graphitic Carbon Nitride for Electrochemical Energy Conversion and Storage. ACS Energy Lett. 3 (2018) 2796-2815.

[14] Y. Yang, J. Kim, C. Kim, A. Seong, O. Kwon, J.H. Lee, I. Kristanto, L. Zhang, J. Zhou, J.Q. Wang, J.B. Baek, S.K. Kwak, G. Kim, Edge-selective decoration with ruthenium at graphitic nanoplatelets for efficient hydrogen production at universal pH. Nano Energy 76 (2020) 105114.

[15] Y. Zheng, Y. Jiao, Y. Zhu, L.H. Li, Y. Han, Y. Chen, M. Jaroniec, S.Z. Qiao, High Electrocatalytic Hydrogen Evolution Activity of an Anomalous Ruthenium Catalyst. J. Am. Chem. Soc. 138 (2016) 16174-16181.

[16] J. Mahmood, F. Li, S.M. Jung, M.S. Okyay, I. Ahmad, S.J. Kim, N. Park, H.Y. Jeong, J.B. Baek, An efficient and pH-universal ruthenium-based catalyst for the hydrogen evolution reaction. Nat. Nanotechnol. 12 (2017) 441-446.

[17] T. Tong, B. He, B. Zhu, B. Cheng, L. Zhang, First-principle investigation on charge carrier transfer in transition-metal single atoms loaded g-C_3N_4. Appl. Surf. Sci. 459 (2018) 385-392.

[18] T. Tong, B. Zhu, C. Jiang, B. Cheng, J. Yu, Mechanistic insight into the enhanced photocatalytic activity of single-atom Pt, Pd or Au-embedded g-C_3N_4. Appl. Surf. Sci. 433 (2018) 1175-1183.

[19] J. Fu, S. Wang, Z. Wang, K. Liu, H. Li, H. Liu, J. Hu, X. Xu, H. Li, M. Liu, Graphitic carbon nitride based single-atom photocatalysts. Front. Phys. 15 (2020) 33201.

[20] X. H. Jiang, L.S. Zhang, H.Y. Liu, D.S. Wu, F.Y. Wu, L. Tian, L.L. Liu, J.P. Zou, S.L. Luo, B.B. Chen, Silver Single Atom in Carbon Nitride Catalyst for Highly Efficient Photocatalytic Hydrogen Evolution. Angew. Chem. Int. Ed. 59 (2020) 23112-23116.

[21] Z. Yu, J. Xu, S. Feng, X. Song, O. Bondarchuk, J.L. Faria, Y. Ding, L. Liu, Rhodium single-atom catalysts with enhanced electrocatalytic hydrogen evolution performance. New J. Chem. 45 (2021) 5770-5774.

[22] P. Zhou, F. Lv, N. Li, Y. Zhang, Z. Mu, Y. Tang, J. Lai, Y. Chao, M. Luo, F. Lin, J. Zhou, D. Su, S. Guo, Strengthening reactive metal-support interaction to stabilize high-density Pt single atoms on electron-deficient g-C_3N_4 for boosting photocatalytic H2 production. Nano Energy 56 (2019) 127-137.

[23] Y. Peng, B. Lu, L. Chen, N. Wang, J.E. Lu, Y. Ping, S. Chen, Hydrogen evolution reaction catalyzed by ruthenium ion-complexed graphitic carbon nitride nanosheets. J. Mater. Chem. A 5 (2017) 18261-18269.

[24] L. Liu, X. Wu, L. Wang, X. Xu, L. Gan, Z. Si, J. Li, Q. Zhang, Y. Liu, Y. Zhao, R. Ran, X. Wu, D. Weng, F. Kang, Atomic palladium on graphitic carbon nitride as a hydrogen evolution catalyst under visible light irradiation. Commun. Chem. 2 (2019) 18.

[25] A. Walcarius, Mesoporous materials and electrochemistry. Chem. Soc. Rev. 42 (2013) 4098-4140.

[26] A. Torres-Pinto, M.J. Sampaio, C.G. Silva, J.L. Faria, A.M.T. Silva, Metal-free carbon nitride photocatalysis with in situ hydrogen peroxide generation for the degradation of aromatic compounds. Appl. Catal. B Environ. 252 (2019) 128-137.

[27] J. Feng, H. Gao, L. Zheng, Z. Chen, S. Zeng, C. Jiang, H. Dong, L. Liu, S. Zhang, X. Zhang, A Mn-N_3 single-atom catalyst embedded in graphitic carbon nitride for efficient CO_2 electroreduction. Nat. Commun. 11 (2020) 4341.

[28] P. Yang, S. Zuo, F. Zhang, B. Yu, S. Guo, X. Yu, Y. Zhao, J. Zhang, Z. Liu, Carbon Nitride-Based Single-Atom Cu Catalysts for Highly Efficient Carboxylation of Alkynes with Atmospheric CO_2. Ind. Eng. Chem. Res. 59 (2020) 7327-7335.

[29] M.J. Lima, A.M.T. Silva, C.G. Silva, J.L. Faria, Graphitic carbon nitride modified by thermal, chemical and mechanical processes as metal-free photocatalyst for the selective synthesis of benzaldehyde from benzyl alcohol. J. Catal. 353 (2017) 44-53.

[30] L. Bai, Z. Duan, X. Wen, R. Si, Q. Zhang, J. Guan, Highly Dispersed Ruthenium-Based Multifunctional Electrocatalyst. ACS Catal. 9 (2019) 9897-9904.

[31] Z. Li, Y. Chen, S. Ji, Y. Tang, W. Chen, A. Li, J. Zhao, Y. Xiong, Y. Wu, Y. Gong, T. Yao, W. Liu, L. Zheng, J. Dong, Y. Wang, Z. Zhuang, W. Xing, C.T. He, C. Peng, W.C. Cheong, Q. Li, M. Zhang, Z. Chen, N. Fu, X. Gao, W. Zhu, J. Wan, J. Zhang, L. Gu, S. Wei, P. Hu, J. Luo, J. Li, C. Chen, Q. Peng, X. Duan, Y. Huang, X.M. Chen, D. Wang, Y. Li, Iridium single-atom catalyst on nitrogen-doped carbon for formic acid oxidation synthesized using a general host–guest strategy. Nat. Chem. 12 (2020) 764-772.

[32] Y. Li, Z. Wang, T. Xia, H. Ju, K. Zhang, R. Long, Q. Xu, C. Wang, L. Song, J. Zhu, J. Jiang, Y. Xiong, Implementing Metal-to-Ligand Charge Transfer in Organic Semiconductor for Improved Visible-Near-Infrared Photocatalysis. Adv. Mater. 28 (2016) 6959-6965.

[33] W. Luo, Y. Li, J. Wang, J. Liu, N. Zhang, M. Zhao, J. Wu, W. Zhou, L. Wang, Asymmetric structure engineering of polymeric carbon nitride for visible-light-driven reduction reactions. Nano Energy 87 (2021) 106168.

[34] D. Zhu, Q. Zhou, Nitrogen doped g-C_3N_4 with the extremely narrow band gap for excellent photocatalytic activities under visible light. Appl. Catal. B Environ. 281 (2021) 119474.

[35] J.N. Hansen, H. Prats, K.K. Toudahl, N. Mørch Secher, K. Chan, J. Kibsgaard, I. Chorkendorff, Is There Anything Better than Pt for HER? ACS Energy Lett. 6 (2021) 1175-1180.

[36] C.C.L. McCrory, S. Jung, J.C. Peters, T.F. Jaramillo, Benchmarking Heterogeneous Electrocatalysts for the Oxygen Evolution Reaction. J. Am. Chem. Soc. 135 (2013) 16977-16987.

[37] J. Xu, T. Liu, J. Li, B. Li, Y. Liu, B. Zhang, D. Xiong, I. Amorim, W. Li, L. Liu, Boosting the hydrogen evolution performance of ruthenium clusters through synergistic coupling with cobalt phosphide. Energy Environ. Sci. 11 (2018) 1819-1827.

[38] Q. Wu, M. Luo, J. Han, W. Peng, Y. Zhao, D. Chen, M. Peng, J. Liu, F.M.F. de Groot, Y. Tan, Identifying Electrocatalytic Sites of the Nanoporous Copper–Ruthenium Alloy for Hydrogen Evolution Reaction in Alkaline Electrolyte. ACS Energy Lett. 5 (2020) 192-199.

[39] J. Xu, J. Li, Z. Lian, A. Araujo, Y. Li, B. Wei, Z. Yu, O. Bondarchuk, I. Amorim, V. Tileli, B. Li, L. Liu, Atomic-Step Enriched Ruthenium–Iridium Nanocrystals Anchored Homogeneously on MOF-Derived Support for Efficient and Stable Oxygen Evolution in Acidic and Neutral Media. ACS Catal. 11 (2021) 3402-3413.

[40] Z. Pu, I.S. Amiinu, Z. Kou, W. Li, S. Mu, RuP_2-Based Catalysts with Platinum-like Activity and Higher Durability for the Hydrogen Evolution Reaction at All pH Values. Angew. Chem. Int. Ed. 56 (2017) 11559-11564.

[41] J. Yang, W. Li, D. Wang, Y. Li, Electronic Metal–Support Interaction of Single-Atom Catalysts and Applications in Electrocatalysis. Adv. Mater. 32 (2020) 2003300.

[42] J. Yang, B. Chen, X. Liu, W. Liu, Z. Li, J. Dong, W. Chen, W. Yan, T. Yao, X. Duan, Y. Wu, Y. Li, Efficient and Robust Hydrogen Evolution: Phosphorus Nitride Imide Nanotubes as Supports for Anchoring Single Ruthenium Sites. Angew. Chem. Int. Ed. 57 (2018) 9495-9500.

[43] I.F. Teixeira, E.C.M. Barbosa, S.C.E. Tsang, P.H.C. Camargo, Carbon nitrides and metal nanoparticles: from controlled synthesis to design principles for improved photocatalysis. Chem. Soc. Rev. 47 (2018) 7783-7817.

[44] S. Gao, X. Wang, C. Song, S. Zhou, F. Yang, Y. Kong, Engineering carbon-defects on ultrathin g-C_3N_4 allows one-pot output and dramatically boosts photoredox catalytic activity. Appl. Catal. B Environ. 295 (2021) 120272.

[45] L. Zhang, R. Long, Y. Zhang, D. Duan, Y. Xiong, Y. Zhang, Y. Bi, Direct Observation of Dynamic Bond Evolution in Single-Atom Pt/C3N4 Catalysts. Angew. Chem. Int. Ed. 59 (2020) 6224-6229.

[46] W. Ouyang, M.J. Muñoz-Batista, A. Kubacka, R. Luque, M. Fernández-García, Enhancing photocatalytic performance of TiO_2 in H_2 evolution via Ru co-catalyst deposition. Appl. Catal. B Environ. 238 (2018) 434-443.

[47] D. Zhao, C.L. Dong, B. Wang, C. Chen, Y.C. Huang, Z. Diao, S. Li, L. Guo, S. Shen, Synergy of Dopants and Defects in Graphitic Carbon Nitride with Exceptionally Modulated Band Structures for Efficient Photocatalytic Oxygen Evolution. Adv. Mater. 31 (2019) 1903545.

[48] L. Simonelli, C. Marini, W. Olszewski, M. Ávila Pérez, N. Ramanan, G. Guilera, V. Cuartero, K. Klementiev, CLÆSS: The hard X-ray absorption beamline of the ALBA CELLS synchrotron. Cogent Physics 3 (2016) 1231987.

[49] B. Ravel, M. Newville, ATHENA, ARTEMIS, HEPHAESTUS: data analysis for X-ray absorption spectroscopy using IFEFFIT. J. Synchrotron Radiat. 12 (2005) 537-541.

[50] I. Amorim, J. Xu, N. Zhang, Z. Yu, A. Araújo, F. Bento, L. Liu, Dual-phase CoP−$CoTe_2$ nanowires as an efficient bifunctional electrocatalyst for bipolar membrane-assisted acid-alkaline water splitting. Chem. Eng. J. 420 (2021) 130454.

[51] G. Kresse, J. Furthmüller, Efficient iterative schemes for ab initio total-energy calculations using a plane-wave basis set. Phys. Rev. B 54 (1996) 11169-11186.

[52] P.E. Blöchl, Projector augmented-wave method. Phys. Rev. B 50 (1994) 17953-17979.

[53] J.P. Perdew, K. Burke, M. Ernzerhof, Generalized Gradient Approximation Made Simple. Phys. Rev. Lett. 77 (1996) 3865-3868.

[54] J. Heyd, G.E. Scuseria, M. Ernzerhof, Hybrid functionals based on a screened Coulomb potential. J. Chem. Phys. 118 (2003) 8207-8215.

[55] Y. Bai, L. Ye, T. Chen, L. Wang, X. Shi, X. Zhang, D. Chen, Facet-Dependent Photocatalytic N_2 Fixation of Bismuth-Rich Bi_5O_7I Nanosheets. ACS Appl. Mater. Interfaces 8 (2016) 27661–27668.

5. Iridium-iron diatomic active sites for efficient bifunctional oxygen electrocatalysis

Abstract

Diatomic catalysts, particularly those having heteronuclear active sites, have lately attracted considerable attention for their advantages over single-atom catalysts in reactions involving multi-electron transfers. We report the first bimetallic iridium-iron diatomic catalysts (IrFe-N-C), derived from metal organic frameworks in a facile wet chemical synthesis followed by post-pyrolysis. We use various advanced characterization techniques to comprehensively confirm the atomic dispersion of Ir and Fe on the nitrogen-doped carbon support and the presence of atomic pairs. The as-obtained IrFe-N-C shows substantially higher electrocatalytic performance for both oxygen reduction reaction (ORR) and oxygen evolution reaction (OER) when compared to the single-atom counterparts (*i.e.*, Ir-N-C and Fe-N-C), revealing favorable bifunctionality. Consequently, the IrFe-N-C is used as an air cathode in zinc-air batteries, which displays much better performance than the batteries containing commercial Pt/C+RuO_2 benchmark catalysts. Our synchrotron-based X-ray absorption spectroscopy (XAS) experiments and density functional theory (DFT) calculations suggest that the IrFe dual-atoms exist likely in an $IrFeN_6$ configuration where both Ir and Fe coordinate with four N atoms without the formation of an Ir-Fe bonding. The Fe site contributes mainly to the ORR, while the Ir site plays a more important role in the OER. The dual-atom sites work synergistically, reducing the energy barrier of the rate-determining step and eventually boosting the reversible oxygen electrocatalysis. The IrFe-N-C catalysts hold great potential for use in various electrochemical energy storage and conversion devices.

5.1 Introduction

Developing high-efficiency electrochemical energy conversion and storage devices, such as electrolyzers, fuel cells, and metal-air batteries, is paramount to future energy sustainability and environmental remediation [1]. The oxygen reduction reaction (ORR) and the oxygen evolution reaction (OER) are two essential half-reactions in the aforementioned energy storage and conversion devices, and play crucial roles in determining the device's performance [2, 3]. Both the ORR and OER involve four successive proton-coupled electron transfer steps, and therefore show sluggish kinetics and high activation overpotentials, being the bottleneck of the energy efficiency

improvement [4-6]. Although substantial research efforts have recently been dedicated to developing platinum group metal (PGM) free ORR/OER catalysts [7-10], for practical applications, PGMs such as Pt, Ir and Ru are currently still the most reliable and efficient electrocatalysts for the ORR and OER [11-13]. In this context, the high cost, the scarcity, and the current low uptake of recycling, of PGM catalysts will pose considerable challenges for large-scale deployment of electrochemical energy storage and conversion devices in the future, and therefore developing electrocatalysts containing significantly reduced PGM without compromised performance becomes a pressing need. Additionally, few of the commercially available PGM catalysts show desired bifunctional properties, able to simultaneously promote ORR and OER with satisfactory performance, though such ORR/OER bifunctional catalysts are interesting and vital for use in metal-air batteries [14, 15].

In the pursuit of downsizing electrocatalysts to reduce the utilization of PGMs and expose more catalytically active sites, single-atom catalysts (SACs) have emerged as an outstanding and promising candidate [16, 17]. Besides the maximized metal utilization efficiency, SACs also possess unique electronic structures owing to their unique coordination environment and strong interaction with the support material, which may drastically change catalytic performance. While a variety of SACs has been reported in the past few years [18, 19], for reactions involving multi-electron transfers like the ORR and OER, diatomic active sites that can work in synergy to help break the scaling relationships for the adsorption energy of intermediates [20], are highly preferred in order to lower the reaction barrier and accelerate the reaction kinetics [20-24]. Recent density functional theory (DFT) calculations have predicted that hydroxyl group modified transition metal (M = Ni, Co and Fe) diatomic active sites show markedly higher ORR activity than the single-atom active sites, thanks to the high valence state in diatomic catalysts [25]. Experimentally, both homonuclear and heteronuclear diatomic catalysts were reported. For instance, Zhao et al. immobilized Ir homodimers on the surface of α-Fe_2O_3 photoanodes, which exhibited notably increased OER activity with respect to the Ir SAC modified α-Fe_2O_3 under solar irradiation [26]. Zeng and co-workers reported that by grafting Pt single-atoms onto Fe-N_4 moieties through a bridging oxygen molecule, the obtained bi-metallic Pt_1-O_2-Fe_1-N_4 active sites showed enhanced electrocatalytic performance toward both ORR and OER [27]. Notwithstanding some progress, the research on diatomic electrocatalysts, particularly the heteronuclear ones, is still in its early stage, and the potential of diatomic catalysts for promoting both ORR and OER has not been fully unleashed yet.

Herein, we report the first example of atomically dispersed bimetallic iridium-iron diatomic active sites dispersed on nitrogen-doped carbon (denoted as IrFe-N-C), which were derived by wet chemical synthesis of a metal organic framework (zeolitic imidazolate framework, *i.e.*, ZIF-8) in the presence of Ir and Fe salts, followed by post-pyrolysis. Our aberration-corrected scanning transmission electron microscopy (STEM) and synchrotron X-ray absorption spectroscopy (XAS) characterization unambiguously confirmed the atomic dispersion of Ir and Fe and the presence of IrFe atomic pairs. Compared to the single-atom control catalysts (Ir-N-C and Fe-N-C) prepared using the same method, the bimetallic IrFe-N-C diatomic catalysts show markedly improved electrocatalytic performance for both ORR and OER, and outperform many state-of-the-art bifunctional ORR/OER catalysts reported in the literature. When tested as an air cathode in a rechargeable Zn-air battery, IrFe-N-C endows a much higher power density and better cycle stability than the cathode comprising the commercial benchmark Pt/C ORR catalysts mixed with the benchmark RuO_2 OER catalysts (denoted as "Pt/C+RuO_2"). Our DFT calculations disclose that the atomic dispersion and the synergistic interaction of the diatomic IrFe catalytic sites can decrease the energy barrier of the rate-determining step (RDS) of reactions and enable the optimization of the adsorption of reaction intermediates, in comparison to the Ir-N-C and Fe-N-C controls, thereby substantially boosting the reversible oxygen electrocatalysis.

5.2 Results and discussion

As detailed in the **Experimental** section, the IrFe-N-C catalysts were prepared *via* a cage-encapsulated precursor pyrolysis approach. Typically, ZIF-8, with a microporous structure showing the space-confinement effect and abundant uncoordinated N atoms able to anchor metal species strongly, was used as the host to *in situ* encapsulate $Ir(acac)_3$ and $Fe(TMHD)_3$ precursor molecules within its cavities. The ZIF-8@IrFe precursor was then subjected to pyrolysis, resulting in the formation of IrFe-N-C. For comparison, the Ir-N-C and Fe-N-C catalysts with single-atom active sites were also prepared as controls through a similar method using only $Ir(acac)_3$ or $Fe(TMHD)_3$ as the metal precursor. Scanning electron microscopy (SEM) examination confirmed the successful synthesis of ZIF-8, ZIF-8@Ir, ZIF-8@Fe and ZIF-8@IrFe precursor nanoparticles, which show uniform sizes and well-defined dodecahedral shape (**Figure 5.1**). X-ray diffraction (XRD) measurements revealed the highly crystalline structure of the ZIF-8 framework, which does not change upon loading metal species (**Figure 5.2**). After the pyrolysis at 900 °C, the sharp XRD peaks of all samples disappeared, and only broad bumps centered at 25° and 43°, characteristic of carbon, can be observed (**Figure**

5.3a), indicating that there were no crystalline IrFe, Ir, Fe or their compounds formed. In addition, the obtained N-C, Ir-N-C, Fe-N-C and IrFe-N-C virtually inherit the dodecahedral morphology of the ZIF-8, ZIF-8@Ir, ZIF-8@Fe and ZIF-8@IrFe precursors, respectively, except that their surfaces become rough and porous (**Figures 5.3b** and **5.3c**; **Figure 5.4**).

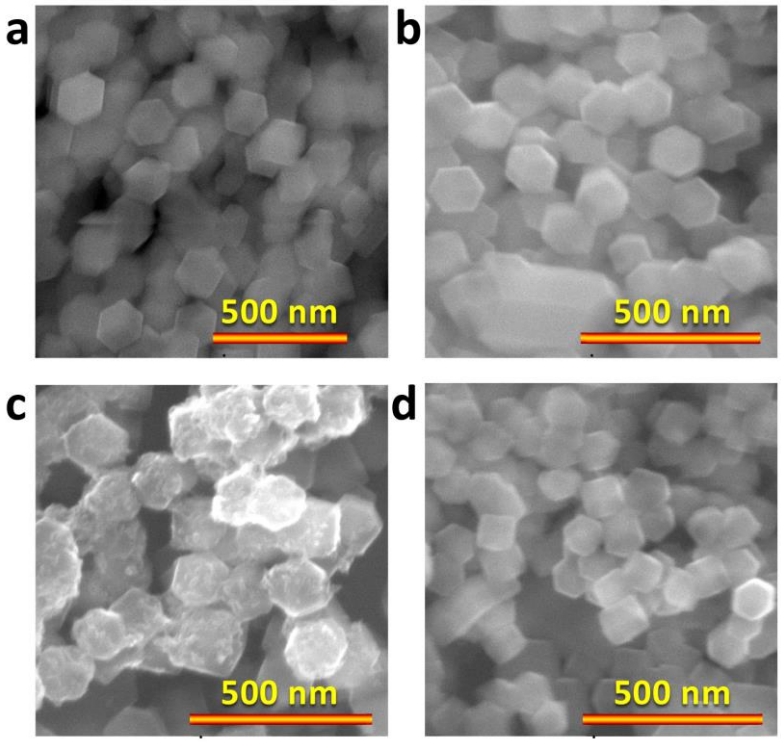

Figure 5.1 a) SEM images showing the morphology of a) ZIF-8, b) ZIF-8@Ir, c) ZIF-8@Fe and d) ZIF-8@IrFe.

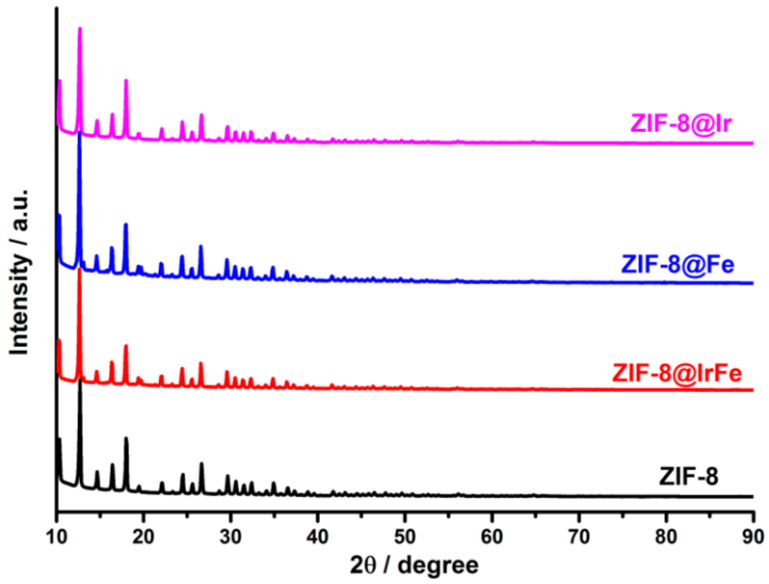

Figure 5.2 XRD patterns of ZIF-8, ZIF-8@Ir, ZIF-8@Fe and ZIF-8@IrFe.

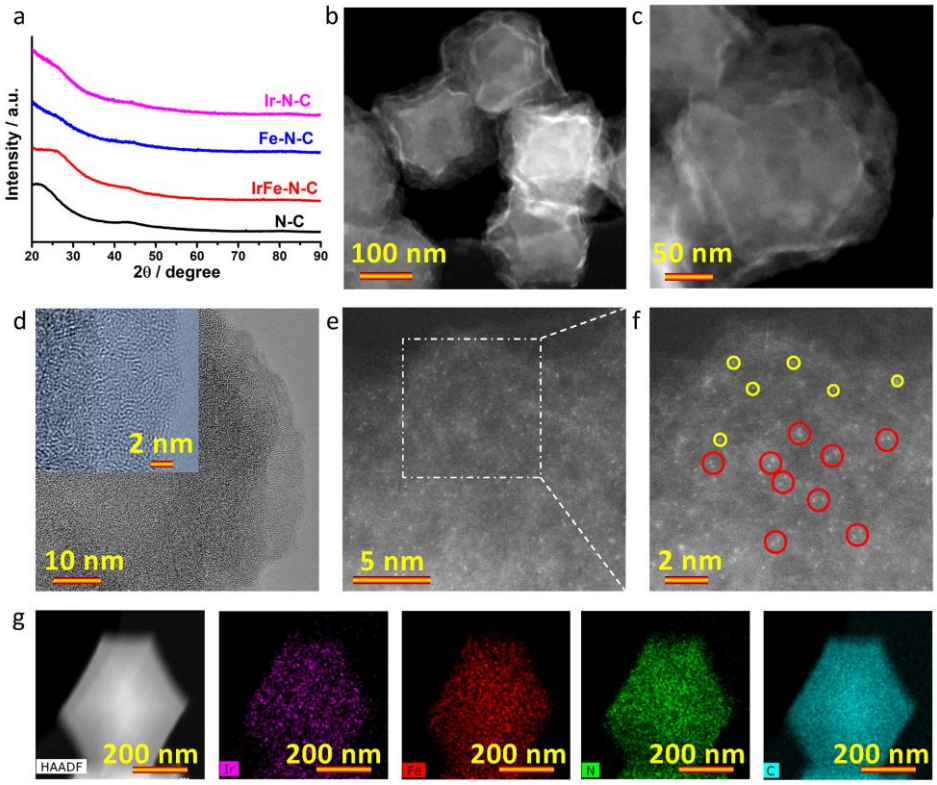

Figure 5.3 Morphology and microstructure characterization of IrFe-N-C catalysts. a) XRD patterns of IrFe-N-C and other control catalysts. b-c) HAADF-STEM images at different magnifications. d) HRTEM images. e-f) High-resolution HAADF-STEM images. In panel f), some representative bimetallic IrFe dual-atom sites are marked with red circles, and some representative single-atom sites are marked with yellow circles. g) HAADF-STEM image and the corresponding elemental maps of Ir, Fe, N and C.

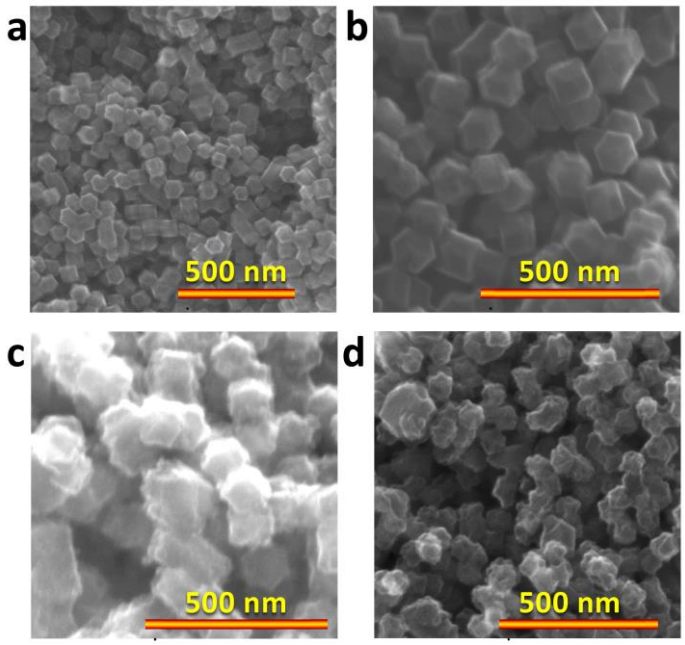

Figure 5.4 SEM images of a) N-C, b) Ir-N-C, c) Fe-N-C and d) IrFe-N-C.

The morphology and microstructure of IrFe-N-C catalysts were further examined by transmission electron microscopy (TEM) and high-angle annular dark-field scanning

transmission electron microscopy (HAADF-STEM). As shown in **Figure 5.3d**, micropores are visible at the edges of the carbon matrix with distinct graphitic carbon domains and defect sites. The microporous nature of the N-C support and all catalysts was further characterized by N_2 adsorption and desorption isotherms (**Figure 5.5**), where all samples show a typical type-IV isotherm and a multimodal pore distribution below 2 nm. The specific surface area of IrFe-N-C is 423 m^2 g^{-1}, larger than that of other control catalysts (324 m^2 g^{-1} for Ir-N-C and 309 m^2 g^{-1} for Fe-N-C), which would be beneficial to boost mass transport [28, 29]. The Raman spectrum of IrFe-N-C (**Figure 5.6**) shows a relatively high intensity ratio (I_D/I_G) of the disordered carbon induced peak (D) over the graphitic carbon peak (G), suggesting a higher content of defects, which are associated with the high degree of microporosity as revealed by the sorption isotherm and also likely related to the etching effect of metals during the carbonization. Moreover, the difference in I_D/I_G values between the pristine N-C and metal loaded N-C (*i.e.*, M-N-C) is marginal, indicating that introducing metal species does not influence the graphitization degree of the N-C framework. From the HAADF-STEM images shown in **Figures 5.3e** and **5.3f**, bright spots can be clearly discerned, corresponding to the dispersed metal atoms. A closer inspection (**Figure 5.3f**) further confirms that some Ir or Fe atoms are present individually on the N-C surface (marked with yellow circles), while some others appear in pair (marked with red circles). STEM elemental mapping demonstrates that Ir and Fe are distributed evenly on N-C (**Figure 5.3g**). Additionally, the morphology and microstructure of Ir-N-C and Fe-N-C control catalysts were also characterized by HAADF-STEM (**Figures 5.7** and **5.8**), and the atomic dispersion of Ir and Fe was unambiguously confirmed. Further ICP-OES measurements revealed that there is 0.7 wt% Ir in Ir-N-C, 2.3 wt% Fe in Fe-N-C, and 1.4 wt% Ir and 1.9 wt% Fe in IrFe-N-C (**Figure 5.9**).

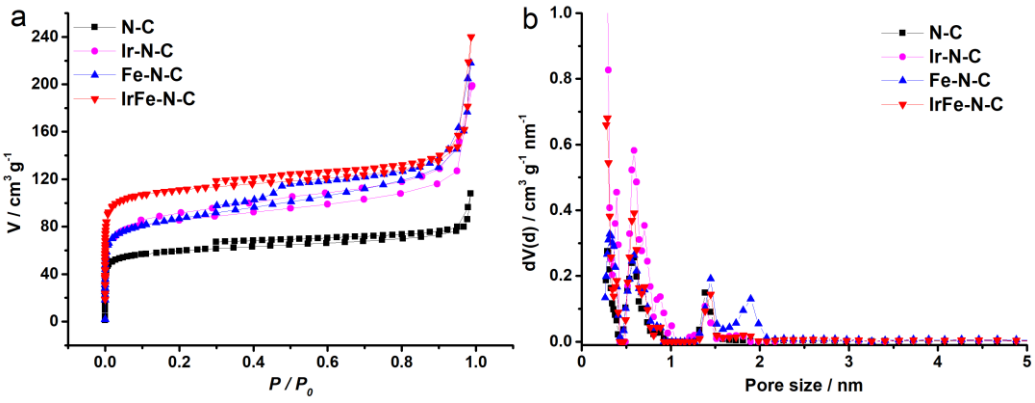

Figure 5.5 N_2 adsorption and desorption isotherms at 77 K of IrFe-N-C and other control catalysts.

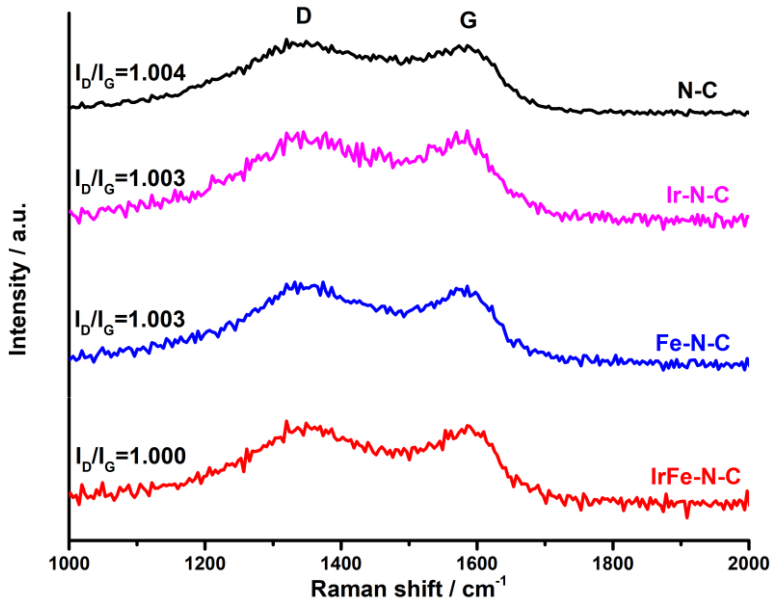

Figure 5.6 Raman spectra of IrFe-N-C and other control catalysts.

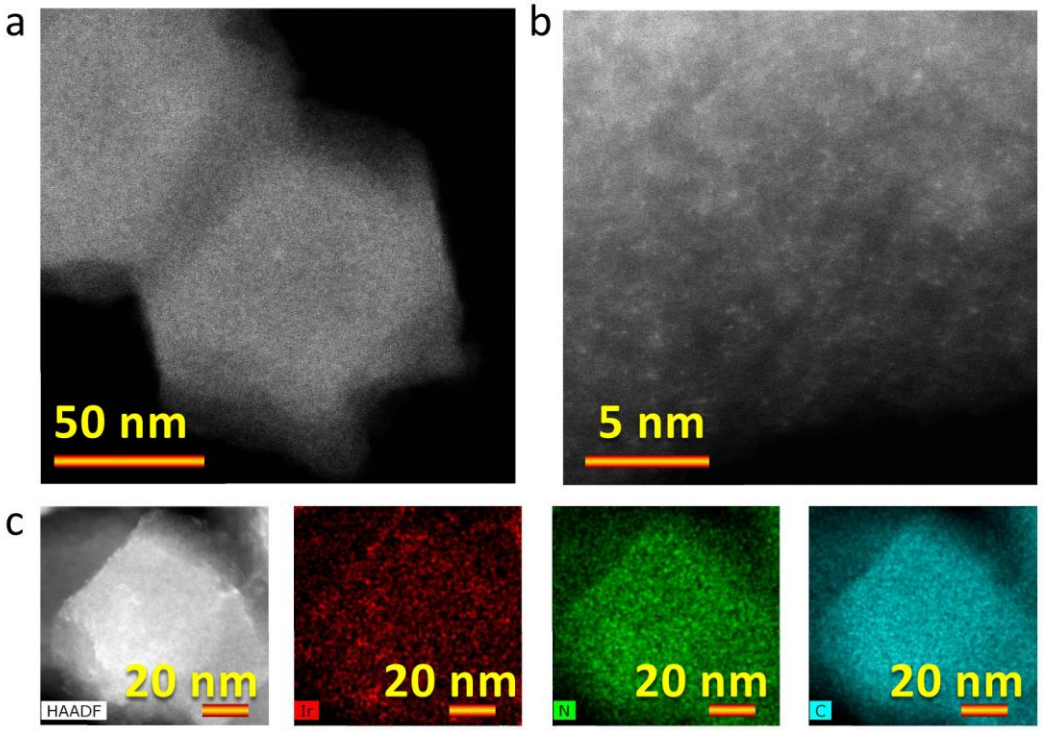

Figure 5.7 a-b) HAADF-STEM images at different magnifications and c) EDS mapping of Ir-N-C.

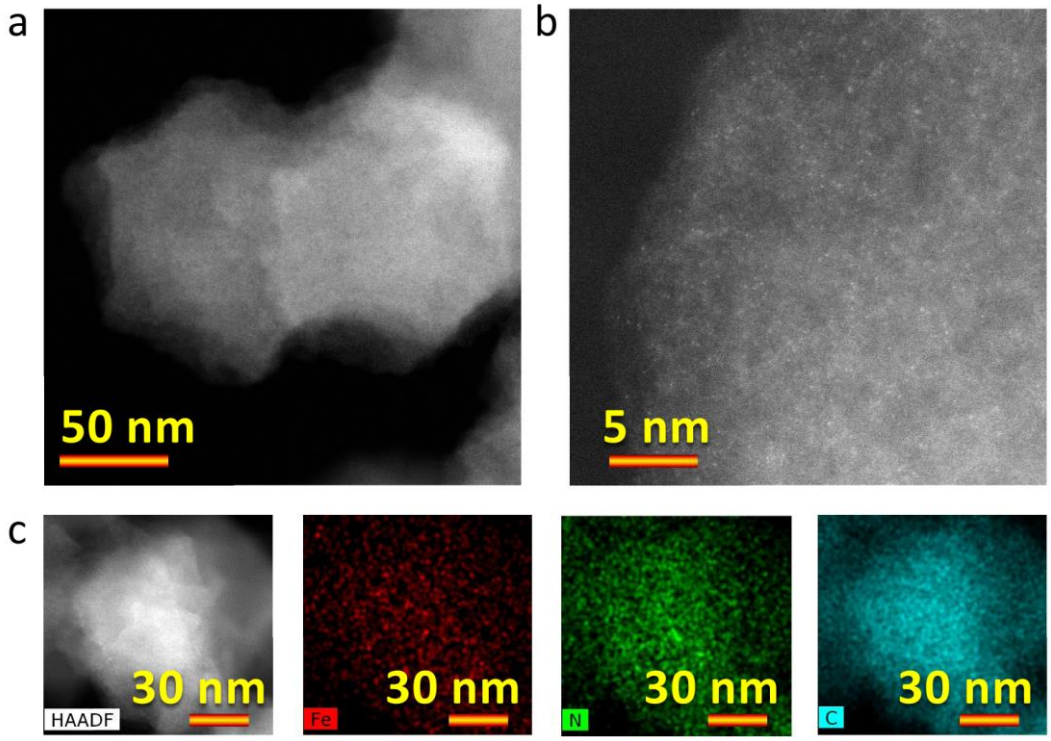

Figure 5.8 a-b) HAADF-STEM images at different magnifications and c) EDS mapping of Fe-N-C.

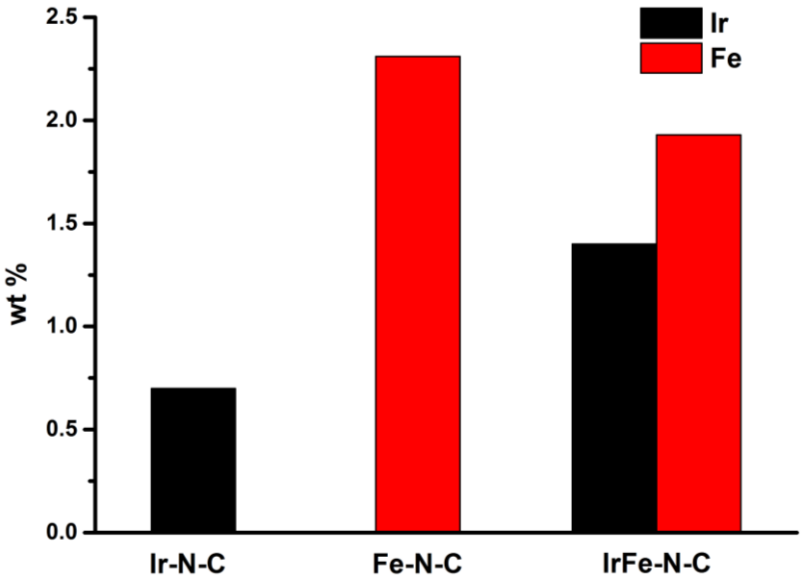

Figure 5.9 The actual metal contents in Ir-N-C, Fe-N-C and IrFe-N-C.

We have investigated the surface chemistry of N-C, Ir-N-C, Fe-N-C and IrFe-N-C using X-ray photoelectron spectroscopy (XPS). The high-resolution N1s spectra (**Figure 5.10a**) of all samples can be de-convoluted into several peaks, corresponding to pyridinic-N (398.2 eV), pyrrolic-N (399.7 eV), graphitic-N (400.8 eV) and oxyl-N (404.0 eV) [30], respectively. Besides these functional groups, metal–nitrogen (M–N) bonding at 399.0 eV is ubiquitously observed in all M-N-C samples, implying that the uncoordinated N groups serve as the anchoring points of metal species, consistent with previous reports [31-33]. XPS quantitative analysis manifested that the content of the M–N bonding is 10.7 %, 8.7 % and 5.0 % in IrFe-N-C, Fe-N-C and Ir-N-C, respectively (**Table 5.1**), indicating that Fe is possibly easier to coordinate with N and that both Ir and Fe tend to coordinate with N, instead of forming IrFe clusters or nanoparticles, which agrees with our HAADF-STEM results. The valance state of Ir and Fe in IrFe-N-C was further examined and compared to that of reference materials (**Figure 5.11**). There is no metal–metal bonding detected, suggesting the absence of agglomerated metal species on the N-C surface, which corroborates the atomic dispersion of Ir and Fe.

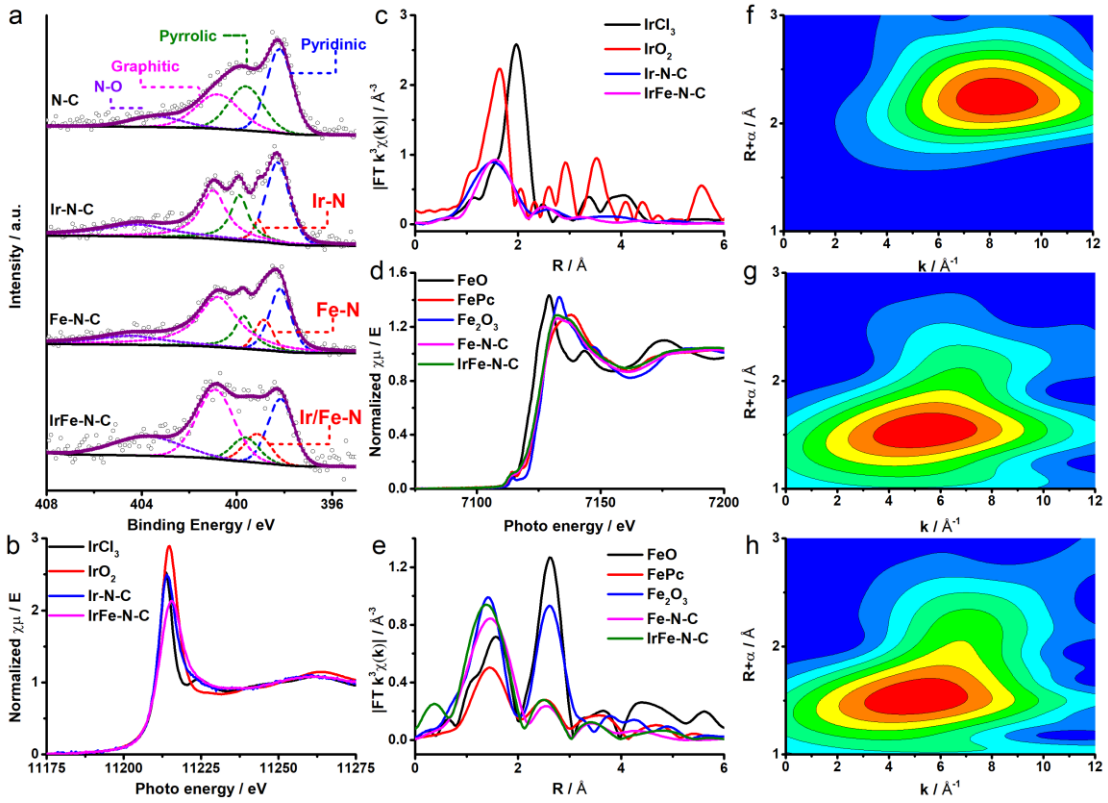

Figure 5.10 Electronic structure analyses of IrFe-N-C and other control catalysts. a) High-resolution N1s XPS spectrum of samples. b) Ir L_3-edge XANES spectra of $IrCl_3$, IrO_2, Ir-N-C and IrFe-N-C. c) Fourier transformation of the EXAFS spectra in real (R) space. d) Fe K-edge XANES spectra of FeO, FePc, Fe_2O_3, Fe-N-C and IrFe-N-C. e) Fourier transformation of the EXAFS spectra in real (R) space. Wavelet transform contours of the Fe K-edge from f) Fe foil, g) Fe-N-C, and h) IrFe-N-C.

Table 5.1. Fitting results of the N1s spectra of the pristine N-C and Ir-N-C, Fe-N-C and IrFe-N-C catalysts.

Sample	De-convoluted peaks				
	Pyridinic N	**M–N**	**Pyrrolic N**	**Graphitic N**	**Oxyl-N**
NC	37.6	/	26.3	26.3	9.8
Ir-N-C	31.1	5.0	18.4	28.7	16.8
Fe-N-C	22.1	8.7	13.4	43.3	12.5
IrFe-N-C	24.4	10.7	9.2	36.9	18.8

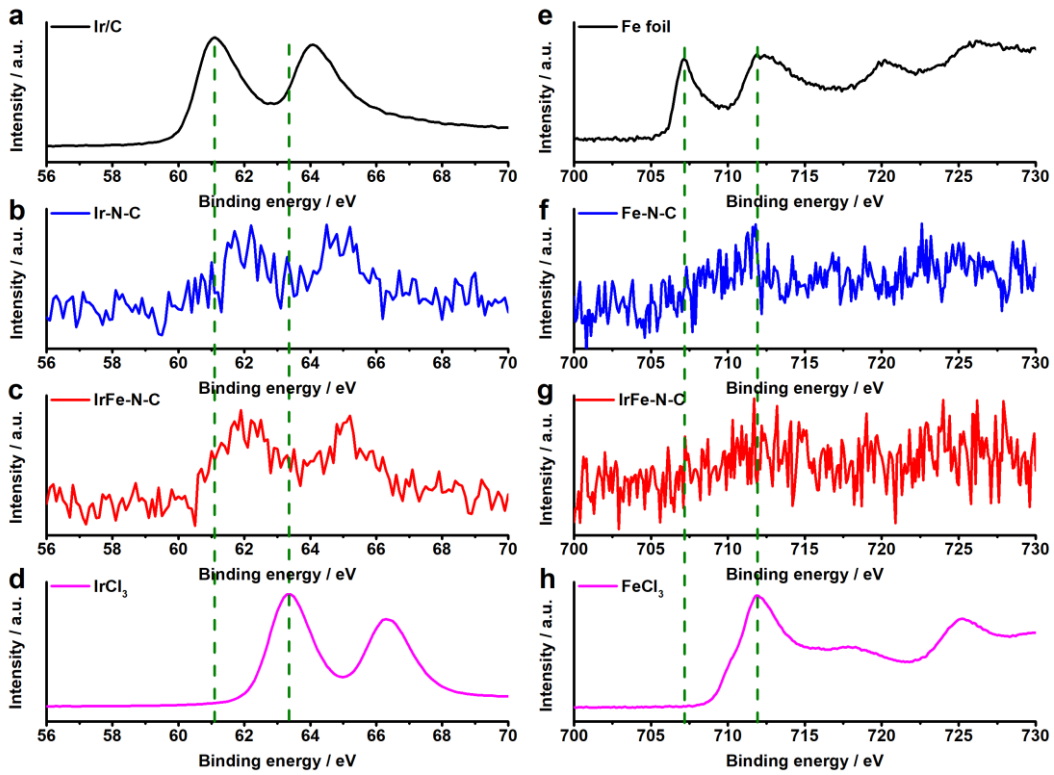

Figure 5.11 XPS high-resolution Ir 4f spectra of a) Ir/C, b) Ir-N-C, c) IrFe-N-C and d) $IrCl_3$. XPS high-resolution Fe 2p spectra of e) Fe foil, f) Fe-N-C, g) IrFe-N-C and h) $FeCl_3$. No signals of metallic bonding were detected, illustrating the absence of agglomerated metal species on the surface of N-C.

Moreover, X-ray absorption near-edge structure (XANES) and extended X-ray absorption fine structure (EXAFS) spectroscopy measurements were carried out to gain more insight into the chemical state and local coordination environments. **Figure 5.10b** shows the Ir L_3-edge XANES spectra of Ir-N-C, IrFe-N-C, and $IrCl_3$ and IrO_2 references. The white-line absorption of Ir-N-C and IrFe-N-C is close to that of $IrCl_3$, but lower than

that of IrO_2, indicating that the Ir atoms in Ir-N-C and IrFe-N-C carry positive charges, consistent with the XPS results (**Figure 5.11**). **Figure 5.10c** displays the Fourier transform (FT) k^3-weighted χ(k)-function curves of the non-phase corrected Ir L_3-edge EXAFS spectra. Both IrFe-N-C and Ir-N-C show an intense peak at 1.53 Å (2.01 Å after phase correction and fitting, see **Table 5.2**), which can be assigned to Ir–N bonding. As for the Fe K-edge XANES spectra (**Figure 5.10d**), the white-line absorption of Fe-N-C and IrFe-N-C is very similar to that of Fe_2O_3 and higher than that of FeO, indicating that the oxidation state of Fe atoms in these samples is close to Fe^{3+}. Likewise, one peak appears dominantly at 1.47 Å (1.98 Å after phase correction and fitting, see **Table 5.2**) that can be attributed to the Fe–N coordination in Fe-N-C and IrFe-N-C (**Figure 5.10e**). It is worth mentioning that when fitting the EXAFS spectra, we also managed to include metal–metal coordination, but this resulted in unreasonably large bond length. Therefore, we conclude that only M–N coordination is present in IrFe-N-C, Ir-N-C and Fe-N-C, and the Ir–Ir, Fe–Fe, and Ir–Fe coordination is unlikely to exist. To further scrutinize the coordination states of Ir and Fe atoms in IrFe-N-C, quantitative fitting of the EXAFS spectra was performed. The mean coordination number of both Ir and Fe with N in IrFe-N-C is 3.9, which is similar to that in Ir-N-C and Fe-N-C (**Figures 5.12-5.14** and **Table 5.2**). This indicates that each Ir or Fe atom is coordinated with four adjacent N atoms [34]. Besides, the wavelet transform (WT) of the Fe K-edge EXAFS oscillations was obtained [35]. The location of the intensity maxima of IrFe-N-C shows a down- and left-shift in the wave vector *k* and the bond length R, relative to that of Fe foil (**Figures 5.10f-h**), illustrating that Fe single atoms are successfully introduced into IrFe-N-C by forming the Fe–N coordination.

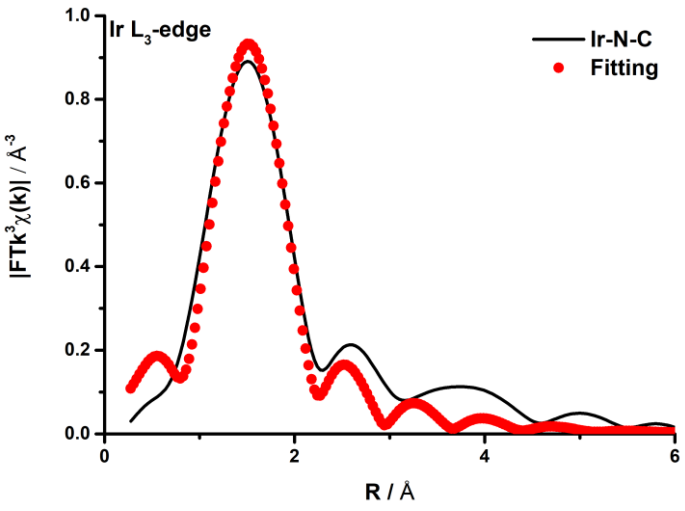

Figure 5.12 EXAFS fitting curve of Ir-N-C at Ir L_3-edge.

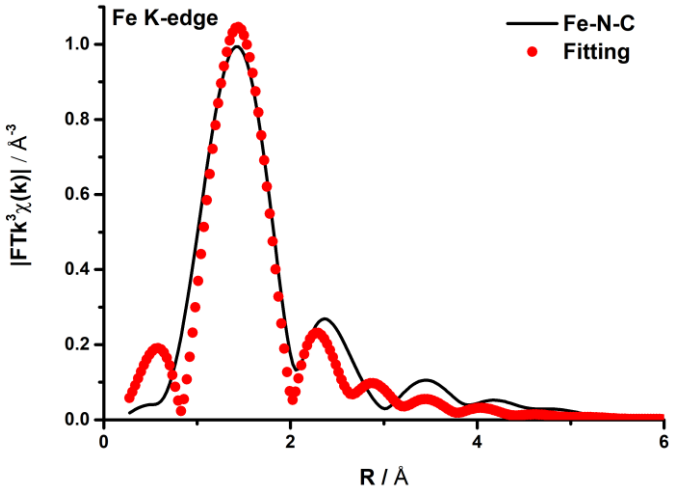

Figure 5.13 EXAFS fitting curve of Fe-N-C at Fe K-edge.

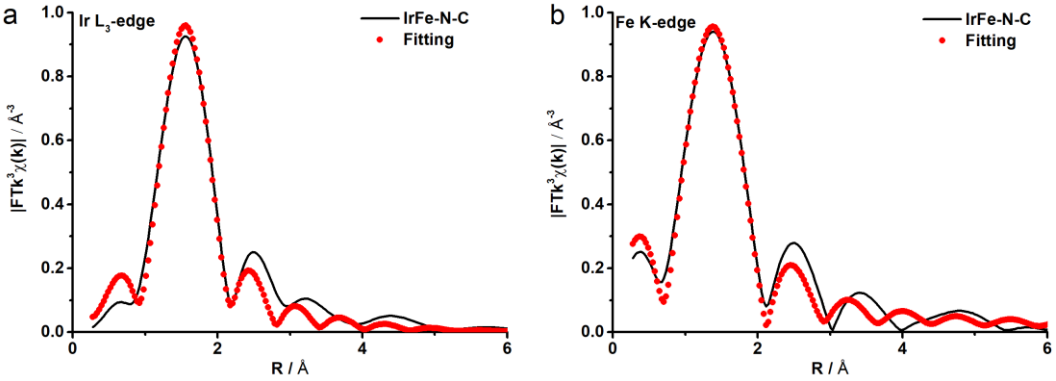

Figure 5.14 EXAFS fitting curves of IrFe-N-C at a) Ir L_3-edge and b) Fe K-edge.

Table 5.2 Fitting results of the Ir L_3-edge and Fe K-edge EXAFS spectra of the prepared catalysts.

Sample	Shell	CN	R (Å)	σ^2(Å^2)	ΔE_0	R factor
Ir-N-C	Ir-N	4.2	1.99	0.007	6.44	0.016
IrFe-N-C (Ir)	Ir-N	3.9	2.01	0.003	8.13	0.011
Fe-N-C	Fe-N	4.1	2.00	0.006	3.25	0.017
IrFe-N-C (Fe)	Fe-N	3.9	1.98	0.003	5.59	0.018

CN: coordination numbers; **R:** bond distance; **σ^2:** Debye-Waller factors; **ΔE_0:** the inner potential correction. **R factor:** goodness of fit.

The electrocatalytic performance of the as-synthesized IrFe-N-C and other control catalysts toward ORR was investigated using a rotating disc electrode (RDE) in O_2-saturated 1.0 M KOH and 0.5 M H_2SO_4 solutions. The linear sweep voltammograms (LSVs, **Figure 5.15**) show that the pristine N-C, despite being active, exhibits much

inferior activity compared to the IrFe-N-C, indicating that the activity of IrFe-N-C is ascribed mainly to the M-N-C sites rather than the N-C sites. By introducing IrFe diatomic sites, the IrFe-N-C delivers an outstanding ORR activity with an onset potential (E_{on}) of 1.02 V vs. reversible hydrogen electrode (RHE) and a half-wave potential ($E_{1/2}$) of 0.92 V vs. RHE in 1.0 M KOH (**Figure 5.16a**), remarkably higher than those of commercial Pt/C (20 wt% Pt on Vulcan XC-72, Fuel Cell Store, E_{on} = 0.98 V and $E_{1/2}$ = 0.86 V), Ir-N-C (E_{on} = 0.97 V and $E_{1/2}$ = 0.85 V), and Fe-N-C (E_{on} = 0.99 V and $E_{1/2}$ = 0.90 V). Even in the strongly acidic medium (0.5 M H_2SO_4, **Figure 5.16b**), the IrFe-N-C exhibits a high half-wave potential (0.77 V), outperforming both Ir-N-C (0.71 V) and Fe-N-C (0.75 V) and comparable to commercial Pt/C (0.80 V). The IrFe-N-C's superior activity is further verified by its smaller Tafel slope (63 and 86 mV dec^{-1} in 1.0 M KOH and 0.5 M H_2SO_4, respectively, **Figure 5.17**), compared to that of Ir-N-C (75 and 120 mV dec^{-1}), Fe-N-C (72 and 94 mV dec^{-1}) and commercial Pt/C (89 and 144 mV dec^{-1}), suggesting the synergistic coupling between Ir and Fe atoms may play a critical role in improving the ORR activity. Notably, the IrFe-N-C can afford high mass activities of 376.7 and 366.7 A g_{metal}^{-1} in alkaline and acid solutions, which are about 6.3 and 6.1 times, respectively, higher than commercial Pt/C (**Figure 5.16c**). When comparing with previous reports in the literature (**Figure 5.16d**; **Tables 5.3**-**5.4**), our IrFe-N-C catalysts indeed outperform many other Fe-based atomically dispersed catalysts under both alkaline and acidic conditions [36-54], which hold great potential for the application in proton exchange membrane (PEMFC) and anion exchange membrane (AEMFC) fuel cells.

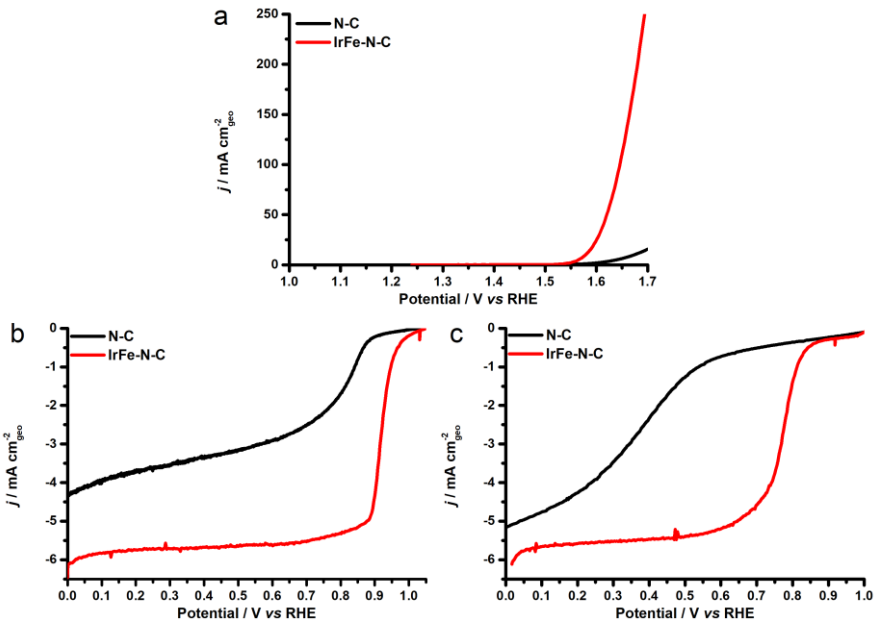

Figure 5.15 a) *iR*-corrected OER polarization curves of IrFe-N-C and N-C in 1.0 M KOH solution. ORR polarization curves of IrFe-N-C and N-C in O_2-saturated b) 1.0 M KOH and c) 0.5 M H_2SO_4, recorded at a rotation rate of 1600 rpm.

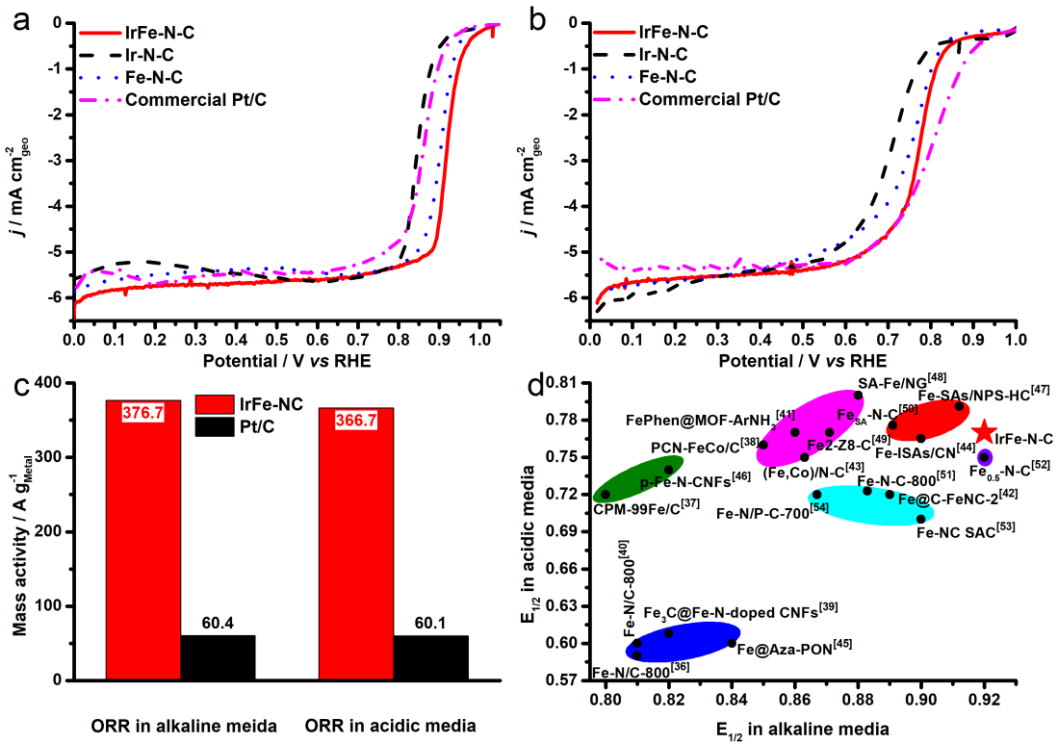

Figure 5.16 Electrocatalytic ORR performance of IrFe-N-C and other control catalysts. ORR polarization curves, recorded at a scan rate of 5 mV s^{-1} at 1600 rpm in a) 1.0 M KOH and b) 0.5 M H_2SO_4. c) Comparison of the ORR mass activity of IrFe-N-C and commercial Pt/C. d) Comparison of the half-wave potential of IrFe-N-C and other recently reported Fe-based atomically dispersed ORR catalysts.

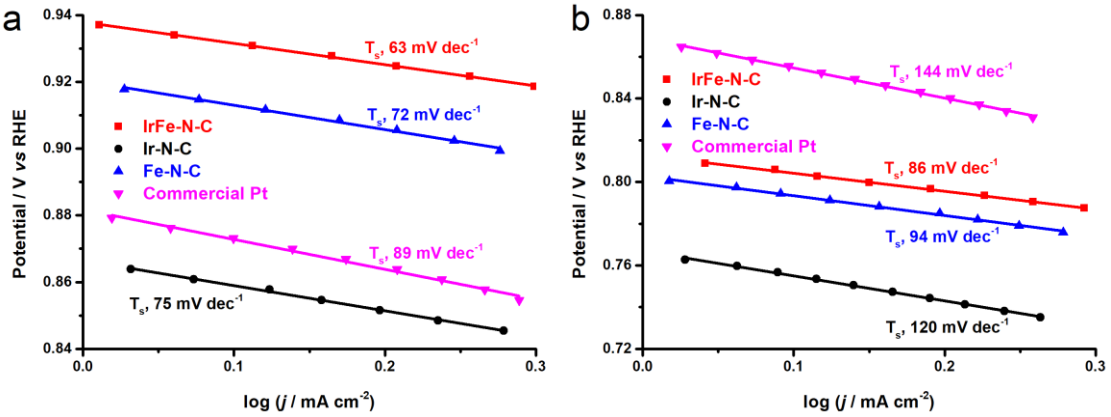

Figure 5.17 Tafel plots of IrFe-N-C, Ir-N-C, Fe-N-C and commercial Pt/C for ORR, measured in a) 1.0 M KOH and b) 0.5 M H_2SO_4.

Table 5.3 Comparison of the IrFe-N-C's ORR performance with other state-of-the-art atomically dispersed catalysts reported recently in the literature, all measured in alkaline media.

Electrocatalyst	**Electrolyte**	**E_{onset}** (V vs. RHE)	**$E_{1/2}$** (V vs. RHE)	**Loading** (mg cm^{-2})	**Reference**

IrFe-N-C	**1.0 M KOH**	**1.02**	**0.92**	**0.45**	**This work**
Fe-ISAs/CN	0.1 M KOH	0.986	0.900	0.408	Angew. Chem. Int. Ed. 2017, 56, 6937.
Fe-N_x/C	0.1 M NaOH	0.95	0.837	0.1	J. Am. Chem. Soc. 2013, 135, 15443.
Fe_3C/C-800	0.1 M KOH	1.05	0.83	0.6	Angew. Chem. Int. Ed. 2014, 53, 3675.
(Fe,Mn)-N-C	0.1 M KOH	0.98	0.90	0.8	Nat. Commun. 2015, 6, 8618.
BCNFNHs	0.1 M KOH	/	0.861	1.2	J. Am. Chem. Soc. 2015, 137, 1436.
Fe-N/C-800	0.1 M KOH	0.98	0.81	0.08	J. Am. Chem. Soc. 2015, 137, 5555.
FeCo/C-800	0.1 M KOH	1.00	0.85	0.2	Adv. Mater. 2015, 27, 3431-3436.
FePhen@MOFArNH_3	0.1 M KOH	1.03	0.86	0.6	Nat. Commun. 2015, 6, 7343.
Fe@C-FeNCs-2	0.1 M KOH	/	0.899	0.7	J. Am. Chem. Soc. 2016, 138, 3570.
S,N-Fe/N/C-CNT	0.1 M KOH	/	0.85	0.6	Angew. Chem. Int. Ed. 2017, 56, 610.
Fe/SNC	0.1 M KOH	/	0.86	0.6	Angew. Chem. Int. Ed. 2017, 56, 13800-13804.
SA-Fe-N nanosheets	0.1 M KOH	0.941	0.910	0.6	Adv. Energy Mater. 2018, 8.1801226.
Fe-NC SAC	0.1 M KOH	0.98	0.90	0.6	Nat. Commun. 2019, 10, 1278.
Fe-N/P-C-700	0.1 M KOH	0.941	0.867	0.6	J. Am. Chem. Soc. 2020, 142, 2404–2412.
Fe-N-C HNSs	0.1 M KOH	1.046	0.87	0.26	Adv. Mater. 2019, 31, e1806312.
$Fe_{0.5}$-N-C	0.1 M KOH	/	0.92	0.274	J. Am. Chem. Soc. 2019, 141, 2035.
SC-Fe	0.1 M KOH	/	0.869	0.25	Angew. Chem. Int. Ed. 2019, 58, 4963.
CNT/PC	0.1 M KOH	/	0.88	0.8	J. Am. Chem. Soc. 2016, 138, 15046-15056.
Co SAs/N-C(900)	0.1 M KOH	0.982	0.881	0.408	Angew. Chem. Int. Ed. 2016, 55, 10800.

Co/N/C	0.1 M KOH	0.94	0.83	0.2	Adv. Mater. 2016, 28, 2337–2344.
Co-N-GA	0.1 M KOH	0.99	0.85	0.6	Acs. Appl. Mater. Inter. 2016, 8, 6488-6495.
Pt_1-N/BP	0.1 M KOH	/	0.87	0.39	Nat. Commun. 2017, 8. 15938.

Table 5.4 Comparison of the IrFe-N-C's ORR performance with other state-of-the-art atomically dispersed catalysts reported recently in the literature, all measured in acidic media.

Electrocatalyst	**Electrolyte**	**E_{onset}** (V vs. RHE)	**$E_{1/2}$** (V vs. RHE)	**Loading** (mg cm^{-2})	**Reference**
IrFe-N-C	**0.5 M H_2SO_4**	**0.89**	**0.77**	**0.45**	**This work**
Ir-SAC	0.1 M $HClO_4$	0.97	0.864	0.4	Angew. Chem. Int. Ed. 2019, 58, 9640.
Pt_1-N/BP	0.1 M $HClO_4$	/	0.76	0.39	Nat. Commun. 2017, 8. 15938.
Ru-G-750	0.1 M $HClO_4$	0.89	0.75	0.32	Acs Nano 2017, 11, 6930-6941.
CNT/PC	0.1 M $HClO_4$	/	0.79	0.8	J. Am. Chem. Soc. 2016, 138, 15046-15056.
SA-Fe-N nanosheets	0.5 M H_2SO_4	0.831	0.812	0.6	Adv. Energy Mater. 2018, 8.1801226.
$Zn(elm)_2TPIP$	0.1 M $HClO_4$	0.914	0.78	0.4	Adv. Mater. 2014, 26, 1093-1097.
Fe/SNC	0.5 M H_2SO_4	/	0.77	0.6	Angew. Chem. Int. Ed. 2017, 56, 13800-13804.
CAPANI-Fe-NaCl	0.1 M $HClO_4$	/	0.73	0.6	J. Am. Chem. Soc. 2015, 137, 5414-5420.
FeCo/C-800	0.1 M $HClO_4$	0.90	0.76	0.2	Adv. Mater. 2015, 27, 3431-3436.
$(Fe, Fe)_2+N_2/H_2$	0.5 M H_2SO_4	0.88	0.75	0.13	J. Am. Chem. Soc. 2016, 138, 635-640.

Co-N-GA	0.5 M H_2SO_4	0.88	0.73	0.6	Acs. Appl. Mater. Inter. 2016, 8, 6488-6495.
Fe-N-C	0.1 M $HClO_4$	/	0.74	0.8	Angew. Chem. Int. Ed. 2015, 54, 12753-12757.
PpPD-Fe-C	0.5 M H_2SO_4	0.826	0.718	0.9	Angew. Chem. Int. Ed. 2014, 53, 10673-10677.
Fe-N_X/C	0.1 M $HClO_4$	0.80	0.667	0.1	J. Am. Chem. Soc. 2013, 135, 15443.
Fe_3C/C-700	0.1 M $HClO_4$	0.90	0.73	0.6	Angew. Chem. Int. Ed. 2014, 53, 3675.
(Fe,Mn)-N-C	0.1 M $HClO_4$	0.92	0.82	0.8	Nat. Commun. 2015, 6, 8618.
BCNFNHs	0.5 M H_2SO_4	0.886	/	1.2	J. Am. Chem. Soc. 2015, 137, 1436.
FePhen@MOFArNH_3	0.1 M $HClO_4$	0.93	0.77	0.6	Nat. Commun. 2015, 6, 7343.
Fe-N/P-C-700	0.1 M $HClO_4$	0.89	0.72	0.6	J. Am. Chem. Soc. 2020, 142, 2404–2412.

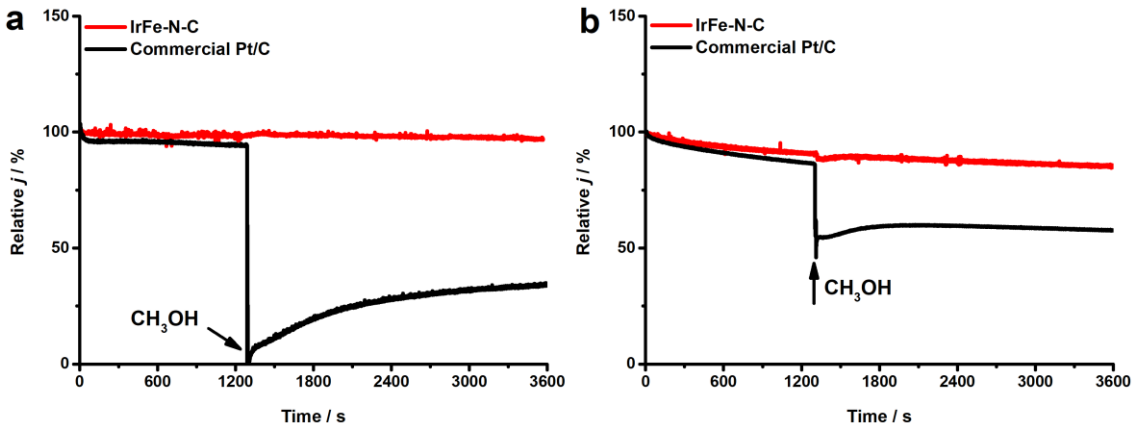

Figure 5.18 Chronoamperometric response of commercial Pt/C and IrFe-N-C measured at 0.6 V vs. RHE after the introduction of 3.0 M methanol in a) 1.0 M KOH and b) 0.5 M H_2SO_4.

Apart from catalytic activity, the poison tolerance and stability are also important indicators for practical applications. To assess the influence of fuel crossover, we performed a chronoamperometry (CA) test at 0.6 V vs. RHE in both alkaline and acid media using an RDE rotating at 1600 rpm. In this course, a solution of 3.0 M methanol

was added into the electrolyte, upon which the commercial Pt/C catalysts exhibit a sharp decrease in current density (**Figure 5.18**). In stark contrast, our IrFe-N-C catalysts show no current density decay in 1.0 M KOH and only a very small attenuation in 0.5 M H_2SO_4. Furthermore, our IrFe-N-C catalysts can sustain at 0.6 V vs. RHE for continuous ORR of 3600 s with minimal degradation, indicating outstanding stability and tolerance to the poisoning of organic solvents.

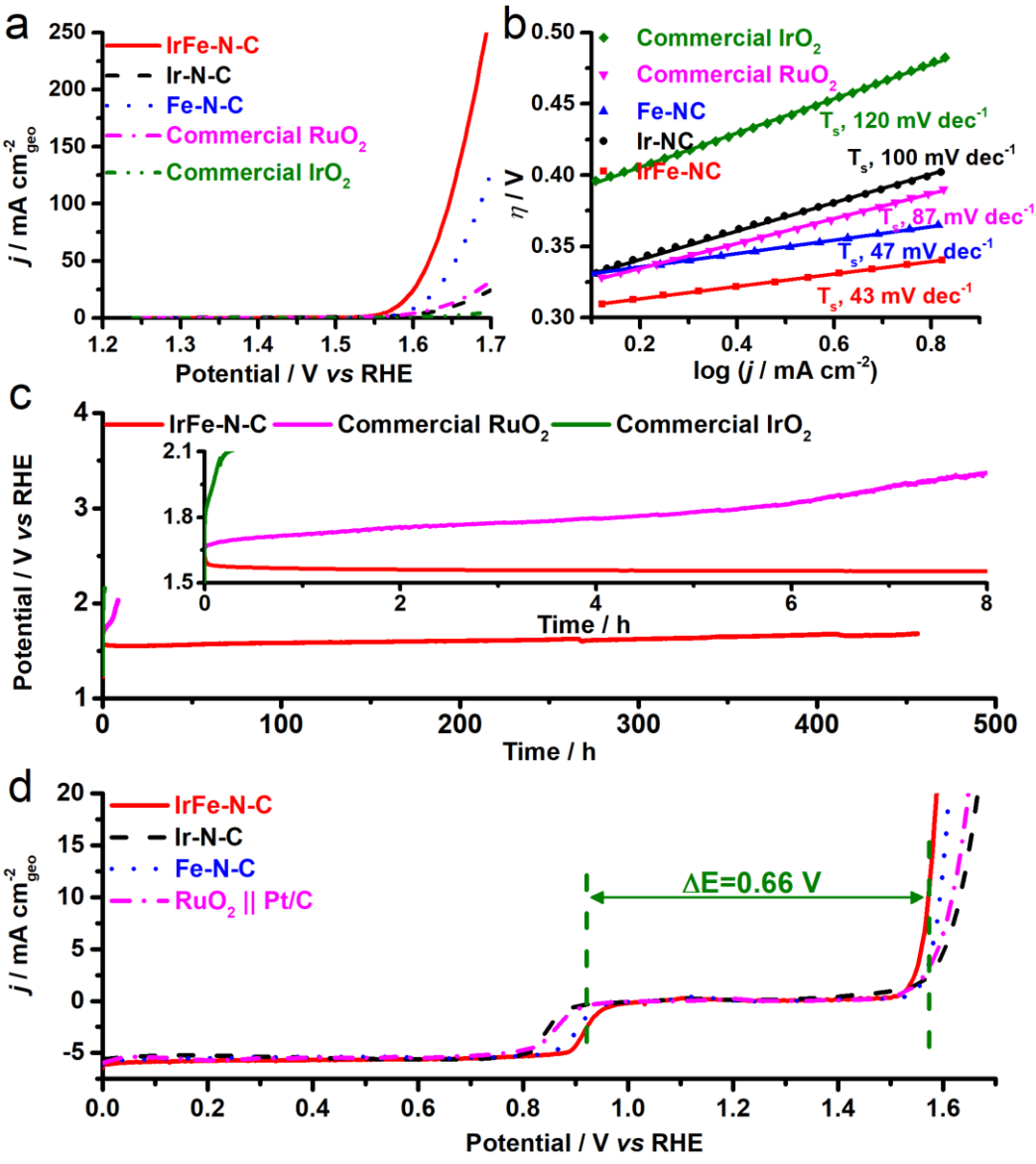

Figure 5.19 Electrocatalytic OER performance of IrFe-N-C and other control catalysts. a) *iR*-corrected OER polarization curves, recorded at a scan rate of 5 mV s^{-1} in 1.0 M KOH. b) Tafel analysis. c) Chronopotentiometric curves of IrFe-N-C and other control catalysts, recorded at a constant current density of 10 mA cm^{-2} in 1.0 M KOH. The inset shows the zoomed view of the initial 8 h. d) Comparison of ORR and OER bifunctional activities of IrFe-N-C, Ir-N-C, Fe-N-C and Pt/C+RuO_2.

To explore the viability of bifunctional oxygen electrocatalysis, the OER activities of IrFe-N-C and other control catalysts were also investigated in 1.0 M KOH. As shown in

Figure 5.19a, the IrFe-N-C can deliver a geometric current density of 10 mA cm_{geo}^{-2} at a low overpotential (η) of 350 mV, remarkably lower than Ir-N-C (η_{10} = 420 mV), Fe-N-C (η_{10} = 370 mV), commercial RuO_2 (η_{10} = 410 mV), and commercial IrO_2 (η_{10} = 500 mV), which also outperforms many other recently reported advanced OER catalysts (**Table 5.5**). The specific activities of IrFe-N-C and other controls, obtained by normalizing the catalytic current to the electrochemically active surface area (ECSA), were calculated and compared to assess the intrinsic catalytic performance. The ECSA was derived from the double-layer capacitances (C_{dl}) of catalysts (see details in **Experiment** section). As shown in **Figures 5.20**, all M-N-C samples exhibit ECSAs (374.6 – 548.3 cm^2) higher than the commercial nanoparticulate catalysts, suggesting that dispersed single- and dual-atoms can expose more active sites for electrocatalysis. As displayed in **Figure 5.21a**, the IrFe-N-C catalysts show the highest specific activity, demonstrating that they are intrinsically more active. Besides, the IrFe-N-C also reveals a mass activity as high as 1.72 A mg^{-1} at η = 350 mV, which is 1.4, 2.6, 78 and 344 times higher than Ir-N-C, Fe-N-C, commercial RuO_2 and commercial IrO_2, respectively (**Figure 5.21b**).

Table 5.5 Comparison of the IrFe-N-C's OER performance with the state-of-the-art catalysts reported recenty in the literature, all measured in alkaline media.

Electrocatalyst	Electrolyte	$\eta_{j=10}$ （mV）	Loading (mg cm^{-2})	Reference
IrFe-N-C	**1.0 M KOH**	**350**	**0.19**	**This work**
Fe_2/Co_1-GNCL	0.1 M KOH	350	0.268	Angew. Chem. Int. Ed. 2020, 59, 16013.
Fe-NHGF	1 M KOH	488	0.275	Nat.Catal. 2018, 1, 63.
Fe-N_4 SAs/NPC	0.1 M KOH	430	0.51	Angew. Chem. Int. Ed. 2018, 57, 8614.
Co-NHGF	1 M KOH	402	0.275	Nat.Catal. 2018, 1, 63.
S,N-Fe/N/C-CNT	0.1 M KOH	370	0.6	Angew. Chem. Int. Ed. 2016, 55, 610.
SS/Co-SAC	0.1 M KOH	348	0.2	Adv. Funct. Mater. 2019, 1906477.
SCoNC	0.1 M KOH	310	0.25	Adv. Energy Mater. 2019, 1900149
NiFe LDH/CNT	1 M KOH	300	2.4	J. Am. Chem. Soc. 2013, 135, 8452.

NiFe LDH	1 M KOH	302	1	Nat. Commun. 2014, 5, 4477.
NiV LDH	1 M KOH	318	0.14	Nat. Commun. 2016, 7, 11981.
CoMn LDH	1 M KOH	324	0.14	J. Am. Chem. Soc. 2014, 136, 16481.
NiCo–$NiCoO_2$@NC	1 M KOH	318	0.14	J. Mater. Chem. A 2017, 5, 15901.
$CoFe_2O_4$ NFs	0.1 M KOH	360	\	Nanoscale, 2015, 7, 8920.
CoP-GNCLNHP	1 M KOH	310	0.397	J. Am. Chem. Soc. 2018, 140, 2610.
CoP/C	0.1 M KOH	358	0.4	ACS Catal. 2015, 5, 4066.
Co_2P	1 M KOH	370	0.284	J. Am.Chem. Soc. 2016, 138, 4006.

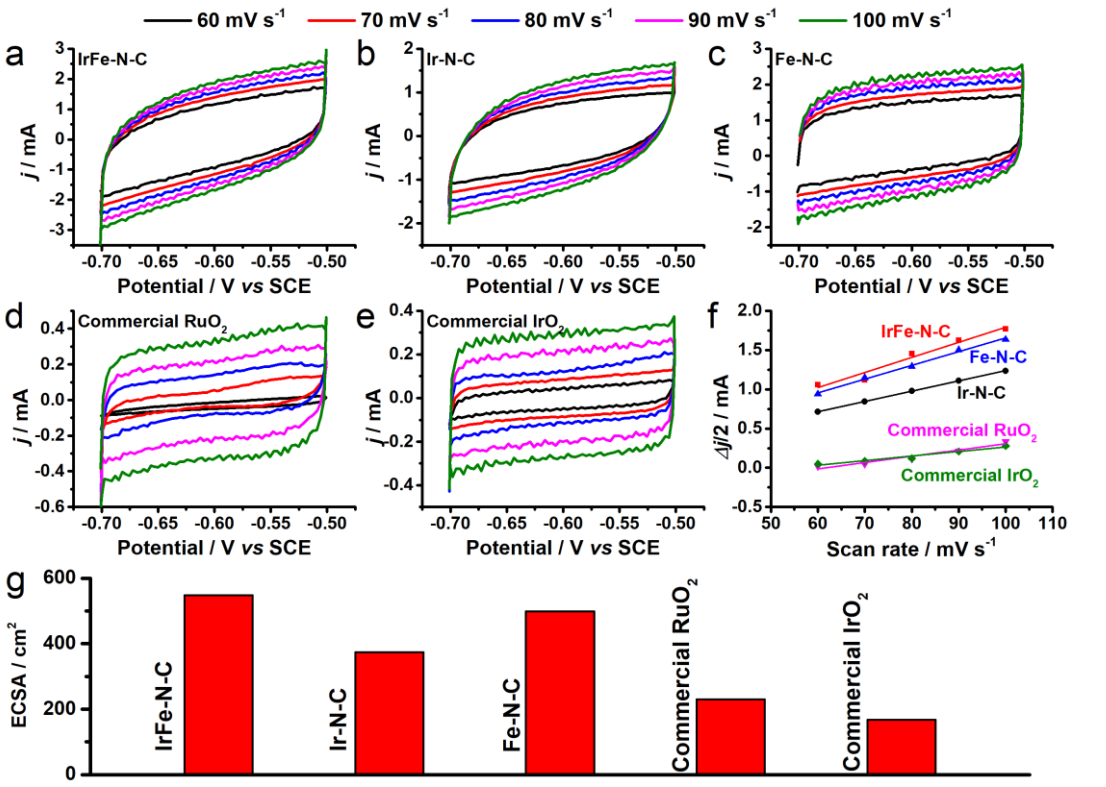

Figure 5.20 Electrochemical CV curves of a) IrFe-N-C, b) Ir-N-C, c) Fe-N-C, d) commercial RuO_2 and e) commercial IrO_2, recorded at diffrent scan rates of 60, 70, 80, 90, and 100 mV s^{-1}. f) Plots of the capacitive current as a funtion of the scan rate for all catalysts. g) ECSAs of all catalysts.

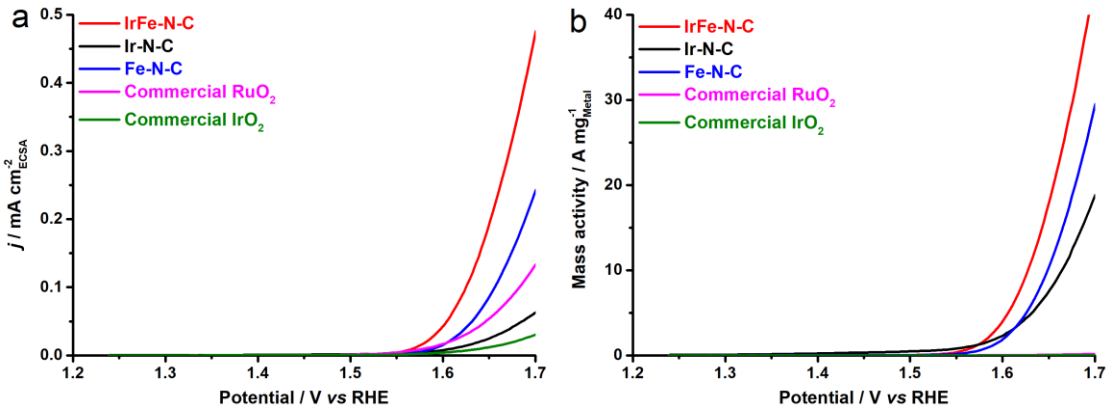

Figure 5.21 a) Specific activity and b) mass activity of IrFe-N-C, Ir-N-C, Fe-N-C, commercial RuO_2 and commercial IrO_2 in 1.0 M KOH solution.

The OER reaction kinetics of all catalysts was evaluated by Tafel analysis (**Figure 5.19b**). The IrFe-N-C shows a Tafel slope of 43 mV dec^{-1}, smaller than other control catalysts, confirming that the presence of IrFe diatomic sites can expedite the OER. The electrochemical impedance spectroscopy (EIS) measurements also verified the efficient charge transfer of IrFe-N-C during the OER, as evidenced by its much smaller charge transfer resistance (R_{ct}) than that of other control catalysts (**Figure 5.22**).

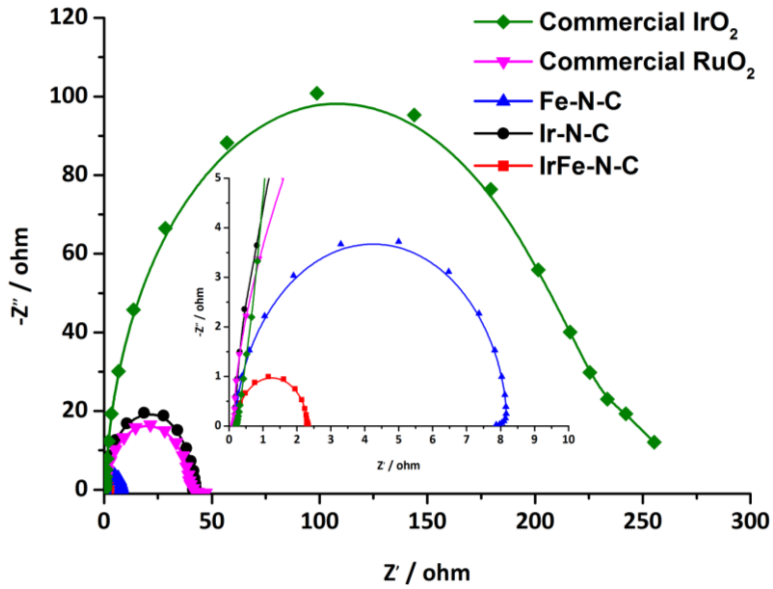

Figure 5.22 Nyquist plots of all catalysts measured at 1.58 V vs. RHE.

Furthermore, we have assessed the catalytic stability of IrFe-N-C in 1.0 M KOH using chronopotentiometry (CP) at a constant current density of 10 mA cm^{-2}, and compared it to that of commercial RuO_2 and IrO_2 catalysts. As illustrated in **Figure 5.19c**, the IrFe-N-C catalyst shows outstanding stability and can catalyze OER continuously at 10 mA cm^{-}

^{2} for 460 h with minimal degradation. In contrast, the potential for maintaining 10 mA cm^{-2} for the commercial RuO_2 and IrO_2 sharply increases in several hours, exhibiting rapid degradation. Besides, the overall electrocatalytic ORR/OER performance of all prepared catalysts was compared by the overvoltage (ΔE), which is the difference between the half-wave potential of ORR and the OER potential at 10 mA cm^{-2}. Remarkably, the IrFe-N-C catalyst shows a small overvoltage of 0.66 V, much lower than the controls and most of the recently reported bifunctional oxygen electrocatalysts (**Figure 5.19d**, **Table 5.6**).

Table 5.6 Comparison of the IrFe-N-C's electrocatalytic performance with the state-of-the-art multi-functional catalysts reported recently in the literature, all measured in the alkaline media.

Electrocatalyst	**$E_{j=10}$ OER** (V vs. RHE)	**$E_{1/2}$ ORR** (V vs. RHE)	**ΔE** (V)	**Reference**
IrFe-N-C	**1.58**	**0.92**	**0.66**	**This work**
Fe_2/Co_1-GNCL	1.58	0.846	0.734	Angew. Chem. Int. Ed. 2020, 59, 16013.
Fe-N_4 SAs/NPC	1.66	0.885	0.775	Angew. Chem. Int. Ed. 2018, 57, 8614.
SS/Co-SAC	1.58	0.81	0.77	Adv. Funct. Mater. 2019, 1906477.
Co/CoP-HNC	1.62	0.83	0.79	Mater. Horiz. 2018, 5, 108.
CF-NG/Co	1.63	0.85	0.78	J. Mater. Chem. A 2018, 6, 489.
N,P,F-tri-doped Graphene	1.8	0.72	1.08	Angew. Chem. Int. Ed. 2016, 55, 13296.
Fe_3C@NG800-0.2	1.59	0.81	0.78	ACS Appl. Mater. Interfaces 2015, 7, 21511.
Co/N-C-800	1.6	0.74	0.86	Nanoscale 2014, 6, 15080.
S,N-Fe/N/C-CNT	1.6	0.85	0.75	Angew. Chem. Int. Ed. 2017, 56, 610.
3D-CNTA	1.54	0.81	0.73	Nano Energy 2017, 39, 626.
Co_3O_4-GNCLMTs	1.58	0.778	0.802	J. Mater. Chem. A 2017, 5, 20170.
CoS_2(400)/N,S-GO	1.61	0.79	0.82	ACS Catal. 2015, 5, 3625.
Co/HNCP	1.613	0.845	0.768	ACS Catal. 2018, 8, 7879.
N/Co_9S_8/G	1.64	0.76	0.88	Energy Environ. Sci. 2016, 9, 1320.

$Co@Co_3O_4$-GNCL-1	1.65	0.8	0.85	Angew. Chem. Int. Ed. 2016, 55, 4087.
N-graphene/CNT	1.65	0.69	0.96	Angew. Chem. Int. Ed. 2014, 53, 6496.
Fe/Fe_2O_3@Fe-N-C-1000	1.66	0.79	0.87	Nano Res. 2016, 9, 2123.
N/Co-doped PCP//NRGO	1.66	0.86	0.8	Adv. Funct. Mater. 2015, 25, 872.
Fe@N-C-700	1.71	0.83	0.88	Nano Energy 2015, 13, 387.
S/N-Fe-27	1.78	0.87	0.91	J. Am. Chem. Soc. 2014, 136, 14486.
NPMC-1000	>1.75	0.85	>0.9	Nat. Nano. 2015, 10, 444.

Given the excellent activity and stability achieved by IrFe-N-C, we further explored its potential application in a rechargeable Zn-air battery, which was assembled using a Zn foil as the anode and the IrFe-N-C catalysts loaded carbon paper as the cathode, as schematically illustrated in **Figure 5.23a**. A mixture of commercial Pt/C and RuO_2 with a mass ratio of 1:1 (denoted as "Pt/C+RuO_2"), which are the state-of-the-art catalysts for the ORR and OER, respectively, was employed as the benchmark. The homemade Zn-air battery based on the IrFe-N-C air cathode exhibits an impressive open-circuit voltage of 1.50 V (**Figure 5.23b**), which is higher than the battery containing the Pt/C+RuO_2 cathode (1.41 V), in line with the high ORR/OER performance of IrFe-N-C (**Figures 5.16** and **5.19**). **Figure 5.23c** shows the discharge polarization curves and the corresponding power density of Zn-air batteries. Remarkably, the battery with the IrFe-N-C cathode can deliver a maximum power density of 113.9 mW cm^{-2} at a current density of 187.7 mA cm^{-2}, much higher than that comprising the Pt/C+RuO_2 cathode (peak power density of 59.6 mW cm^{-2} @ 124.7 mA cm^{-2}). In addition, the IrFe-N-C cathode possesses a lower charge/discharge voltage gap than the Pt/C+RuO_2 cathode (**Figure 5.23d**), suggesting enhanced rechargeability for use in Zn-air batteries, which is consistent with the excellent bifunctionality observed in IrFe-N-C (**Figure 5.19d**). Moreover, the cycling performance of the Zn-air battery made from the IrFe-N-C air cathode was further investigated at 5 mA cm^{-2} with a duration of 30 min per cycle and compared to that of the Pt/C+RuO_2 counterpart (**Figure 5.23e**). The performance of Zn-air batteries consisting of the Pt/C+RuO_2 cathode gradually degraded from the fifth cycle onward. In contrast, negligible performance fading was observed after 60 cycles for the IrFe-N-C based Zn-

air battery, demonstrating the outstanding potential of IrFe-N-C for use as the air cathode in Zn-air batteries.

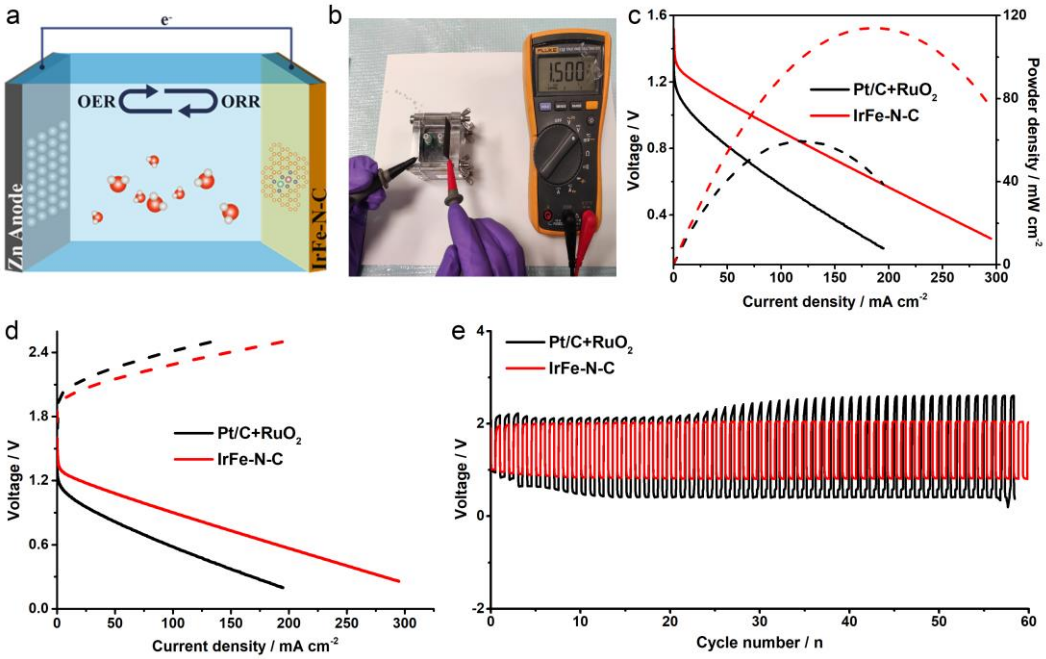

Figure 5.23 Zn-air battery performance of IrFe-N-C and Pt/C+RuO2 catalysts. a) Schematic illustration of the Zn-air battery set-up. b) Digital photograph of the Zn-air battery assembled using IrFe-N-C as the air cathode with an open-circuit voltage of 1.50 V. c) Polarization and power density curves of the IrFe-N-C and Pt/C+RuO_2 catalysts. d) Charge/discharge profiles of the rechargeable Zn-air batteries based on the IrFe-N-C and Pt/C+RuO_2 air cathodes. e) Cycling performance of two-electrode rechargeable Zn-air batteries with the IrFe-N-C air cathode, measured at 5 mA cm^{-2}.

To further elucidate the origin of the high ORR/OER catalytic activity of IrFe-N-C, we performed DFT calculations. Eight possible coordination configurations including single-nuclear (IrN_4, FeN_4), heteronuclear ($IrFeN_6$, $IrFeN_8$) and homonuclear sites (Ir_2N_6, Ir_2N_8, Fe_2N_6, Fe_2N_8) were constructed and optimized to mimic the single-atom and diatomic active sites, based on the EXAFS results and calculated formation energy (**Figure 5.24**, **Table 5.2** and **5.7**). According to the free energy diagrams of the ORR/OER of the six diatomic configurations (**Figure 5.25**), including both heteronuclear ($IrFeN_6$, $IrFeN_8$) and homonuclear sites (Ir_2N_6, Ir_2N_8, Fe_2N_6, Fe_2N_8), we found that the $IrFeN_6$ configuration reveals comparatively lower energy barrier at each step of the reactions. Therefore, $IrFeN_6$ was chosen as the subsequent ORR and OER computation model. The ORR Gibbs free energy diagrams of the IrN_4 and FeN_4 single-atom sites as well the $IrFeN_6$ diatomic sites were calculated at the potential of U = 1.23 V (**Figure 5.26a**). Remarkably, the Fe site in $IrFeN_6$ (0.56 eV) displays the lowest energy barrier for the rate-determining step (RDS), with respect to the FeN_4 (0.60 eV), IrN_4 (0.67 eV) and the Ir site in $IrFeN_6$ (1.24 eV), suggesting that the Fe site in $IrFeN_6$ most likely plays a predominant role in the ORR. The OER is a reverse process of the ORR with four elementary steps as

outlined in **Figure 5.26b**. Our calculations reveal that the $O^* + OH^- \rightarrow OOH^* + e^-$ process is the RDS for IrN_4, FeN_4, and the Fe site in $IrFeN_6$, with relatively higher energy barriers (0.82 V for IrN_4, 0.63 V for FeN_4, and 0.67 V for Fe in $IrFeN_6$), compared to the RDS for the Ir site in $IrFeN_6$ that has an energy barrier of only 0.43 eV. It is noted that the energy barrier of the RDS in homonuclear sites (*i.e.*, Ir_2N_6, Ir_2N_8, Fe_2N_6, Fe_2N_8) is larger than or very close to that of single-nuclear (*i.e.*, IrN_4, FeN_4) sites for both ORR and OER, suggesting that the contribution to performance enhancement from homonuclear sites, if any, would be marginal. The calculated overpotentials were further drawn as a function of the adsorption energy difference, *i.e.*, $\Delta G_{O^*} - \Delta G_{OH^*}$ [31, 55], and a volcano-type plot can be derived (**Figure 5.26c**). The Ir site in $IrFeN_6$ is located at the top of the volcano, indicating its best OER performance. The predicted activity order in this plot agrees well with our experimental observations, *i.e.*, IrFe-N-C > Fe-N-C > Ir-N-C.

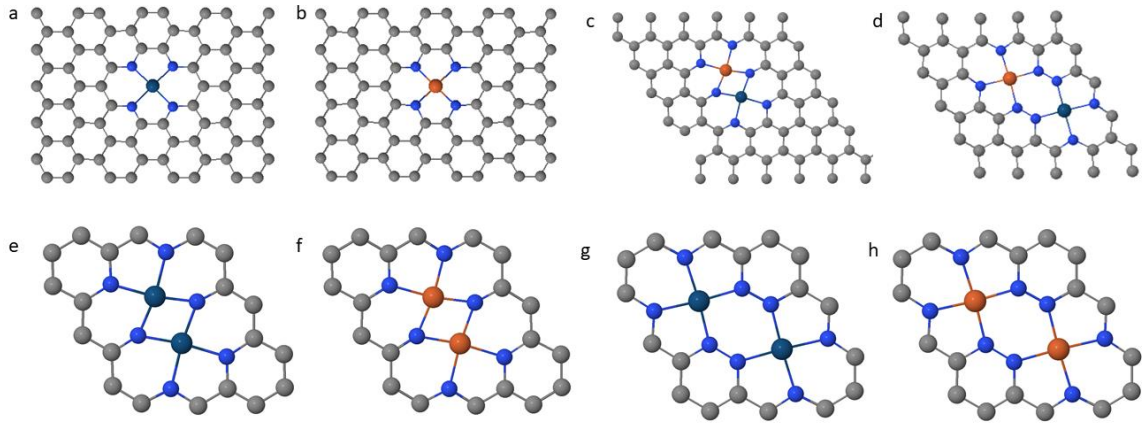

Figure 5.24 Optimized configurations for a) IrN_4, b) FeN_4, c) $IrFeN_6$, d) $IrFeN_8$, e) Ir_2N_6, f) Fe_2N_6, g) Ir_2N_8 and h) Fe_2N_8.

Table 5.7 Calculated Ir–Fe formation energies (E_f) for the optimized configurations.

Configuration	E_f / eV
IrN_4	–1.66
FeN_4	–2.00
$IrFeN_6$	–3.51
$IrFeN_8$	–4.02
IrN_6	-3.70
FeN_6	-4.21

IrN_8	-2.62
FeN_8	-3.26

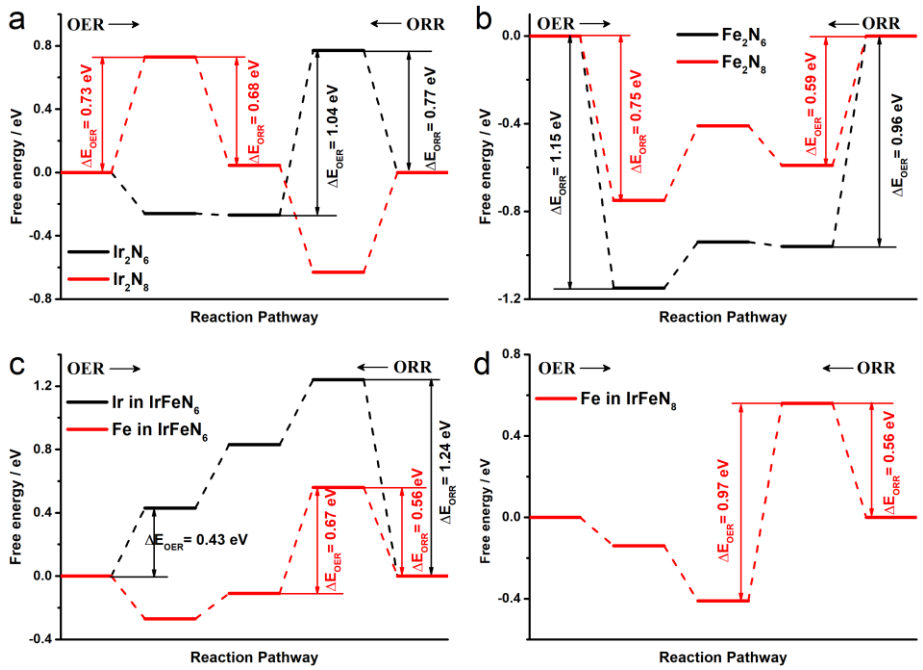

Figure 5.25 Free energy diagrams of the ORR/OER pathways on a) Ir_2N_6, Ir_2N_8, b) Fe_2N_6, Fe_2N_8, c) $IrFeN_6$ and d) $IrFeN_8$ configurations.

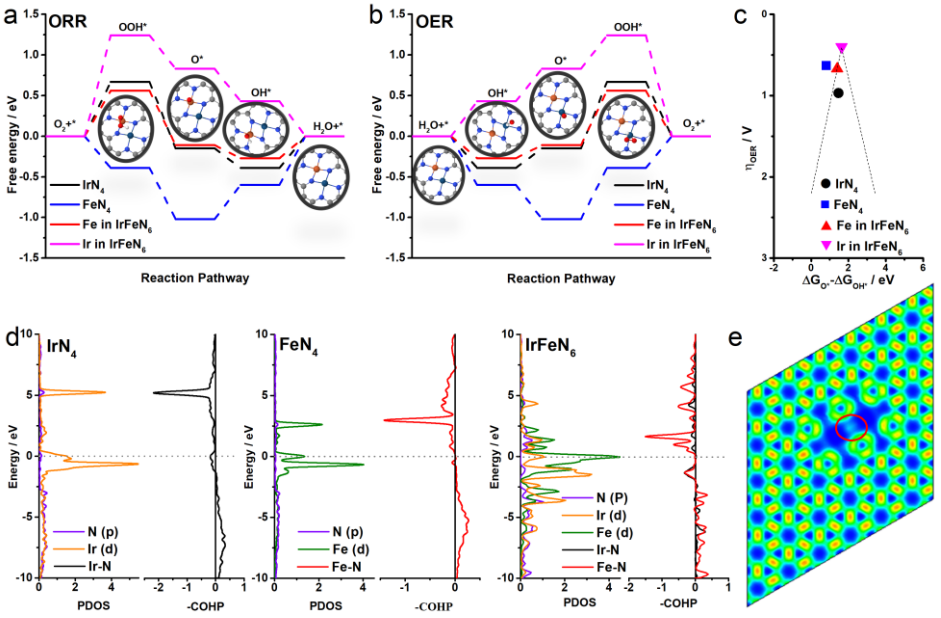

Figure 5.26 Computational analysis of the $IrFeN_6$ diatomic sites for ORR and OER. The Gibbs free energy diagrams for the four reaction steps of a) ORR and b) OER. c) Volcano plots of the OER overpotential (η) versus (ΔG_{O^*}–ΔG_{OH^*}) for the IrN_4, FeN_4 and $IrFeN_6$ configurations. d) PDOS and COHP analyses of the IrN_4, FeN_4 and $IrFeN_6$ configurations. e) ELF maps of $IrFeN_6$.

Furthermore, we calculated the projected density of states (PDOS) and the crystal orbital Hamilton populations (COHP) of IrN_4, FeN_4 and $IrFeN_6$ models (**Figure 5.26d**). The results show that the $IrFeN_6$ has a much higher PDOS at the Fermi level, relative to IrN_4 and FeN_4, which would result in an increased antibonding orbital filling, attenuating the interaction between the active sites and the adsorbates and thus contributing to the enhancement in ORR and OER kinetics [56]. The COHP analysis further corroborates that the antibonding state of Ir/Fe in $IrFeN_6$ is significantly decreased compared to that of the single-atom IrN_4 and FeN_4 sites, which is expected to be able to regulate the interaction of Ir/Fe with reaction intermediates, promoting the activity. To further confirm this electronic interaction, we investigated the electron localization function (ELF) of the single-atom sites of IrN_4 and FeN_4 and the dual-atom sites of $IrFeN_6$ (**Figure 5.26e**; **Figure 5.27**). An electron-gas-like distribution is found between the Ir and Fe atoms in $IrFeN_6$ (marked in a red cycle in **Figure 5.26e**) [57], proving the existence of the electronic interaction between Ir and Fe atoms in $IrFeN_6$. In addition, the band-order and Bader charge analyses were also used to verify the electronic structure features of the IrN_4, FeN_4 and $IrFeN_6$ active sites. The results show that when Ir and Fe atoms form chemical bonds with the N atoms respectively, the Ir site in IrFe-N-C possesses 0.11 more electrons than the Ir site in single-atom Ir-N-C, and the Fe site in IrFe-N-C has 0.17 more electrons than the Fe site in Fe-N-C (**Figure 5.28**). This subtle electronic structure modulation is beneficial and can moderately reduce the binding interaction of oxygen intermediates, which is in full consistency with the above PDOS and COHP analyses. In fact, our XANES experimental results already qualitatively proved that both Ir and Fe in IrFe-N-C gained more electrons, compared to the Ir in Ir-N-C and the Fe in Fe-N-C, as evidenced by the lower peak intensity of IrFe-N-C in the Ir L_3-edge XANES spectra (**Figure 5.10b**) and the lower white-line absorption energy of IrFe-N-C in the Fe K-edge XANES spectra (**Figure 5.10d**). Overall, our comprehensive theoretical analyses demonstrate that the Fe and Ir atoms in the $IrFeN_6$ dual-atom active sites work synergistically, leading to excellent catalytic activity toward both ORR and OER.

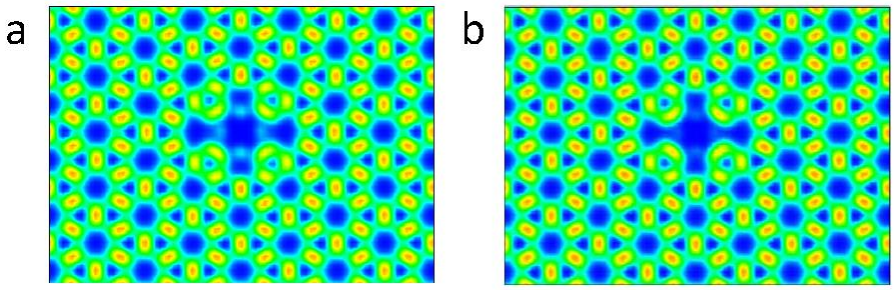

Figure 5.27 The electron localization function (ELF) of a) IrN_4 and b) FeN_4.

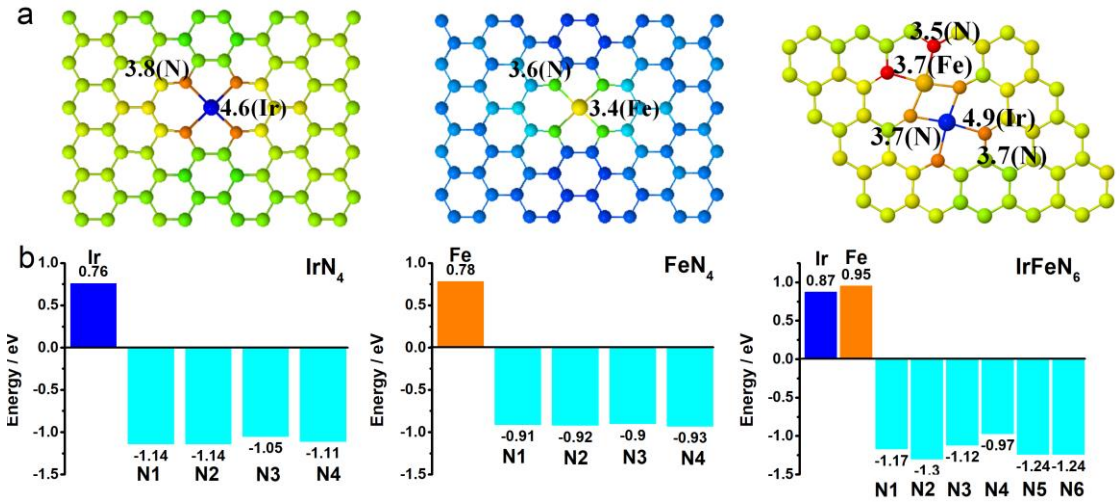

Figure 5.28 a) The band-order and b) Bader charge analysis of IrN_4, FeN_4 and $IrFeN_6$.

5.3 Conclusions

In summary, we, for the first time, report the synthesis of bimetallic IrFe diatomic active sites dispersed on nitrogen-doped carbon *via* a cage-encapsulated precursor pyrolysis strategy. Advanced materials characterization techniques including HAADF-STEM, XPS and synchrotron-based XAS have unambiguously confirmed the atomic dispersion of Ir and Fe and the presence of IrFe dual-atoms. Compared to the single-atom Ir-N-C and Fe-N-C control catalysts, the IrFe-N-C shows outstanding catalytic activity for ORR in both acidic and alkaline media. Especially, it exhibits an onset potential of 1.02 V vs. RHE and a half-wave potential as high as 0.92 V vs. RHE in 1.0 M KOH, rendering it one of the best ORR catalysts reported by far. Moreover, the IrFe-N-C also reveals superior OER performance with a high mass activity of 1.72 A mg^{-1} at η = 350 mV and a long-term stability of 460 h at 10 mA cm^{-2}. The excellent bifunctionality of IrFe-N-C for ORR and OER enables it to serve as a high-performance air cathode in Zn-air batteries, which shows substantially enhanced performance with respect to the commercial Pt/C+RuO_2 benchmarks. Our DFT calculations demonstrate that the diatomic configuration leads to subtle electronic structure modulation. Fe of the diatomic sites contributes more to the ORR, while Ir of the diatomic sites plays a more important role in the OER. The two work in synergy and altogether promote oxygen electrocatalysis. We believe that our work provides an in-depth understanding of the catalytic mechanism of bimetallic diatomic active sites, and the IrFe-N-C catalysts we developed will find important applications in metal-air batteries, fuel cells and electrolyzers.

5.4 Experimental section

Reagents: $Zn(NO_3)_2 \cdot 6H_2O$, 2-methylimidazole (2-MeIM), methanol, isopropanol, H_2SO_4, KOH, iridium(III) acetylacetonate ($Ir(acac)_3$), Iron(III) tris(2,2,6,6-tetramethyl-3,5-heptanedionate) ($Fe(TMHD)_3$) and Nafion® perfluorinated resin solution (5 wt %) were all purchased from Sigma-Aldrich. RuO_2 and IrO_2 powders were acquired from Alfa Aesar. Pt/C (20 wt%) catalysts were bought from FuelCell Store. All reagents and materials were used as received without further purification.

Synthesis of ZIF-8: The ZIF-8 materials were synthesized *via* a method reported previously with some modification [44]. Typically, 594 mg of $Zn(NO_3)_2 \cdot 6H_2O$ were dissolved in 20 mL methanol under vigorous magnetic stirring to form a homogeneous solution A. In the meantime, 659 mg of 2-MeIM were dissolved in 15 mL methanol forming a solution B. Then, Solutions A and B were mixed under vigorous stirring for 1 h. Subsequently, the mixed solution was transferred into a Teflon-lined stainless steel autoclave and maintained at 120 °C for 4 h. The obtained product was centrifuged, washed five times with methanol, and dried under vacuum at 60 °C for further use.

Synthesis of ZIF-8@IrFe, ZIF-8@Ir, and ZIF-8@Fe: The ZIF-8@IrFe catalysts were synthesized using the same procedure as described above with the addition of $Ir(acac)_3$ and $Fe(TMHD)_3$. Specifically, 594 mg of $Zn(NO_3)_2 \cdot 6H_2O$, 97.9 mg $Ir(acac)_3$ and 121.1 mg $Fe(TMHD)_3$ were dissolved in 20 mL methanol under vigorous magnetic stirring to form a homogeneous solution A. Meanwhile, 659 mg of 2-MeIM were dissolved in 15 mL methanol to obtain a solution B. Afterward, solutions A and B were mixed under vigorous stirring for 1 h. The mixed solution was then transferred into a Teflon-lined stainless steel autoclave and kept at 120 °C for 4 h. The obtained products were centrifuged, washed five times with methanol, and then dried under vacuum at 60 °C for further use. ZIF-8@Ir and ZIF-8@Fe were prepared through a similar procedure but using only 97.9 mg $Ir(acac)_3$ or 121.1 mg $Fe(TMHD)_3$, respectively, in each case.

Synthesis of the N-C support: The obtained ZIF-8 powders were loaded in a ceramic boat and placed in a tube furnace filled with high-purity N_2 (99.999%). The furnace was heated to 900 °C at a rate of 5 °C min^{-1}, held at this temperature for 3 h, and then naturally cooled down to room temperature under a constant N_2 flow in the whole process. The obtained material was subsequently dispersed in 0.5 M H_2SO_4 solution at 80 °C for 8 h, under magnetic stirring. After etching, the N-C was centrifuged, rinsed with deionized (DI) water, and dried under vacuum at 60 °C.

Synthesis of IrFe-N-C, Ir-N-C, and Fe-N-C: The IrFe-N-C, Ir-N-C and Fe-N-C catalysts were obtained through a similar procedure as that used to synthesize N-C, except that the starting material was replaced by ZIF-8@IrFe, ZIF-8@Ir, and ZIF-8@Fe.

Materials characterization: Powder XRD examinations were conducted on an X'Pert PRO diffractometer (PANalytical) working at 45 kV and 40 mA with Cu K_α radiation (λ = 1.541874 Å) and a PIXcel detector. Data were collected with the Bragg-Brentano configuration in the 2θ range of 20 – 90° at a scan speed of 0.01° s^{-1}. XPS characterization was performed on an ESCALAB 250Xi instrument with an Al K_α X-ray source (1486.6 eV). The actual Ir and Fe loadings in catalysts were determined by ICP-OES (ICPE-9000 spectrometer, Shimadzu). Raman spectroscopy examination was done on a confocal Raman spectrometer (Witec Alpha 300R). Nitrogen adsorption/desorption porosimetry was performed using a Quantachrome Autosorb IQ_2 system at 77 K. The morphology was characterized by scanning electron microscopy (SEM, FEI Quanta 650 FEG microscope equipped with an INCA 350 spectrometer). TEM, HRTEM, and STEM investigations were carried out on a probe-corrected transmission electron microscope operating at 200 kV (FEI Themis 60 – 300). The actual metal contents of Ir and Fe was detected by the inductively coupled plasma – optical emission spectroscopy (ICP-OES, ICPE-9000 spectrometer, Shimadzu). The X-ray absorption spectroscopy (XAS) was investigated at the Ir-L_3 edges and Fe-K edges in Deutsches Elektronen-Synchrotron DESY.

DFT calculations: DFT calculations using the Vienna Ab-initio Simulation Package (VASP) were performed to optimize geometry structures, and the projector augmented wave (PAW) pseudopotential and Revised Perdew-Burke-Ernzerhof (RPBE) exchange-correlation functional were employed to calculate all geometry optimizations and self-consistent total-energy [58-60]. Zero damping DFT-D3 method of Grimme for van der Waals correlation correction was used. A kinetic energy cut-off of 400 eV was set for the plane-wave expansion. The convergence criteria of final energy and force of all structures were less than 10^{-6} eV and 0.02 eV $Å^{-1}$, respectively. The Brillouin zone was sampled with 1 × 1 × 1 Gamma k-point mesh for energy and 3 × 3 × 1 Monkhorst-Pack k-point meshelectronic structure calculation. The dimension of the hexagonal graphene supercell is 14.76×12.78×15.00 $Å^3$ along x-, y- and z-direction and the periodic condition is employed along z-direction. The distance between neighboring cells is 15.00Å. The following active-site models were used for the calculations: IrN_4, FeN_4, $IrFeN_6$, $IrFeN_8$, Fe_2N_6, Fe_2N_8, Ir_2N_6 and Ir_2N_8.

The overall OER process includes the following four steps:

$M^* + OH^- \rightarrow OH^* + e^-$ (1)

$OH^* + OH^- \rightarrow O^* + H_2O\ (l) + e^-$ (2)

$O^* + OH^- \rightarrow OOH^* + e^-$ (3)

$OOH^* + OH^- \rightarrow M^* + O_2\ (g) + H_2O\ (l) + e^-$ (4)

where M^* represents the Ir or Fe active site, and OH^*, O^* and OOH^* are the intermediates adsorbed on the active sites during the OER or ORR.

For the active-site models, the formation energy (E_b) of the single metal atom is defined in the following Eq. (5):

$$E_b = E_M + E_{graphene} - E_{(graphene + M)} \quad (5)$$

where E_M, $E_{graphene}$ and $E_{(graphene + M)}$ are the energies of the isolated single metal atom, the N-doped graphene and the single-metal-atom adsorbed N-doped graphene, respectively.

Electrode preparation and electrocatalytic tests: The catalyst ink was prepared by ultrasonically dispersing 5 mg of catalysts into 0.5 mL of isopropanol containing 50 µL of Nafion® solution. To prepare an electrode for catalytic tests, 10 or 20 µL of catalyst ink was loaded on a fine-polished glassy carbon (GC) electrode with an exposed area of 0.20 and 0.95 cm^2, leading to a loading density of ca. 0.45 and 0.19 mg cm^{-2} for the ORR and OER, respectively. The electrode was then dried at room temperature (ca. 25 ^oC) naturally in air. For the commercial reference catalysts, 5 mg Pt/C, RuO_2 or IrO_2 were dispersed in 0.5 mL of isopropanol containing 50 µL of Nafion® solution, forming a homogeneous ink upon ultrasonication. The ink was then drop-cast on the GC electrode with the loading density of about 0.45 mg cm^{-2} for Pt/C and 0.19 mg cm^{-2} for RuO_2 and IrO_2.

All electrocatalytic tests were carried out in a three-electrode configuration at room temperature (23 °C) using a Biologic VMP-3 potentiostat/galvanostat. The catalyst-loaded GC, a graphite rod and a saturated calomel electrode (SCE) were used as working, counter, and reference electrodes, respectively. The SCE reference electrode was calibrated prior to each measurement in an Ar/H_2-saturated 0.5 M H_2SO_4 solution using a clean Pt wire as the working electrode. 0.5 M H_2SO_4 and 1.0 M KOH were used

as the electrolyte. Unless otherwise stated, all potentials are reported versus RHE by converting the measured potentials according to the following equation:

$$E_{RHE} = E_{SCE} + 0.059 \times pH + 0.241 \quad (6)$$

The ORR performance of catalysts was measured by linear sweep voltammetry (LSV) from 1.1 V to 0 V *vs.* RHE in O_2-saturated 1.0 M KOH and 0.5 M H_2SO_4 solutions with a scanning rates of 5 mV s^{-1}. The catalyst ink was drop-cast on a GC electrode which was then mounted on a rotating disk electrode (RDE). The revoluiton speed was set to 1600 rpm.

The apparent OER activity was characterized using CV at a scan rate of 5 mV s^{-1}, and an *iR*-correction (85%) was made to compensate for the voltage drop between the reference and working electrodes, which was measured by a single-point high-frequency impedance test. The reduction branch of the CV curves was used for the performance comparison of all the catalysts. Electrochemical impedance spectroscopy (EIS) measurements of OER were carried out at 1.58 V *vs.* RHE in the frequency range of 10^5 – 0.01 Hz with a 10 mV sinusoidal perturbation.

The ECSAs were calculated from the electrochemical double-layer capacitance of the catalytic surface. The double-layer capacitance (C_{dl}) of catalysts was estimated by performing CV in the potential range of –0.50 to –0.70 V *vs.* SCE (non-Faradaic potential range) at different scan rates (v) of 60, 70, 80, 90 and 100 mV s^{-1}, followed by extracting the slope from the resulting $|j_a\text{-}j_c|/2$ vs. v plots (j_a and j_c represent the anodic and cathodic current at –0.60 V *vs.* SCE) [61].

The OER stability was assessed at a constant current density of 10 mA cm^{-2}. The ORR stability was investigated by the chronoamperometric response of catalysts at 0.6 V *vs.* RHE after introducing 3 M methanol in O_2-saturated 1.0 M KOH and 0.5 M H_2SO_4 solutions, using the RDE at a rotation rate of 1600 rpm.

Testing of zinc-air battery: The performance and stability measurements of the aqueous zinc-air battery were carried out in a homemade zinc-air cell using a Biologic VMP-3 potentiostat/galvanostat. The zinc-air battery (ZAB) was composed of a Zn plate as the anode, a 6.0 M KOH and 0.2 M $ZnCl_2$ aqueous solution as the electrolyte, and the IrFe-N-C catalysts as the cathode. Carbon paper was used as the current collector for the cathode. The catalyst ink was prepared by ultrasonically dispersing 10 mg of the IrFe-N-C catalysts into 5 mL of isopropanol containing 200 µL of Nafion® solution. To prepare a cathode for catalytic tests, 2.5 mL of catalyst ink were loaded on the carbon

paper with a catalyst's loading mass of ca. 1.0 mg cm^{-2}. For comparison, 5 mg Pt/C and 5 mg RuO_2 were dissolved in 5 mL isopropanol solution containing 200 µL 5 wt% Nafion®. The catalyst ink was then loaded on the carbon paper with the same Pt/C+RuO_2 loading mass of around 1.0 mg cm^{-2}.

5.5 References

[1] X. Zhang, X. Cheng, Q. Zhang, Nanostructured energy materials for electrochemical energy conversion and storage: A review. J. Energy Chem. 25 (2016) 967-984.

[2] S. Liu, Z. Wang, S. Zhou, F. Yu, M. Yu, C.Y. Chiang, W. Zhou, J. Zhao, J. Qiu, Metal–Organic-Framework-Derived Hybrid Carbon Nanocages as a Bifunctional Electrocatalyst for Oxygen Reduction and Evolution. Adv. Mater. 29 (2017) 1700874.

[3] Y. Pan, S. Liu, K. Sun, X. Chen, B. Wang, K. Wu, X. Cao, W.C. Cheong, R. Shen, A. Han, Z. Chen, L. Zheng, J. Luo, Y. Lin, Y. Liu, D. Wang, Q. Peng, Q. Zhang, C. Chen, Y. Li, A Bimetallic Zn/Fe Polyphthalocyanine-Derived Single-Atom Fe-N_4 Catalytic Site:A Superior Trifunctional Catalyst for Overall Water Splitting and Zn–Air Batteries. Angew. Chem. Int. Ed. 57 (2018) 8614-8618.

[4] Z. Yu, J. Xu, L. Meng, L. Liu, Efficient hydrogen production by saline water electrolysis at high current densities without the interfering chlorine evolution. J. Mater. Chem. A 9 (2021) 22248-22253.

[5] Z.W. Seh, J. Kibsgaard, C.F. Dickens, I. Chorkendorff, J.K. Nørskov, T.F. Jaramillo, Combining theory and experiment in electrocatalysis: Insights into materials design. Science 355 (2017) eaad4998.

[6] Y. Jiao, Y. Zheng, M. Jaroniec, S.Z. Qiao, Design of electrocatalysts for oxygen- and hydrogen-involving energy conversion reactions. Chem. Soc. Rev. 44 (2015) 2060-2086.

[7] M.P. Browne, C. Domínguez, P.E. Colavita, Emerging trends in metal oxide electrocatalysis: Bifunctional oxygen catalysis, synergies and new insights from in situ studies. Curr. Opin. Electrochem. 7 (2018) 208-215.

[8] L. Liu, Platinum group metal free nano-catalysts for proton exchange membrane water electrolysis. Curr. Opin. Chem. Eng. 34 (2021) 100743.

[9] W. Li, D. Xiong, X. Gao, L. Liu, The oxygen evolution reaction enabled by transition metal phosphide and chalcogenide pre-catalysts with dynamic changes. Chem. Commun. 55 (2019) 8744-8763.

[10] S. Gupta, W. Kellogg, H. Xu, X. Liu, J. Cho, G. Wu, Bifunctional Perovskite Oxide Catalysts for Oxygen Reduction and Evolution in Alkaline Media. Chem. Asian J. 11 (2016) 10-21.

[11] Y. Nie, L. Li, Z. Wei, Recent advancements in Pt and Pt-free catalysts for oxygen reduction reaction. Chem. Soc. Rev. 44 (2015) 2168-2201.

[12] J. Xu, Z. Lian, B. Wei, Y. Li, O. Bondarchuk, N. Zhang, Z. Yu, A. Araujo, I. Amorim, Z. Wang, B. Li, L. Liu, Strong Electronic Coupling between Ultrafine Iridium–Ruthenium Nanoclusters and Conductive, Acid-Stable Tellurium Nanoparticle Support for Efficient and Durable Oxygen Evolution in Acidic and Neutral Media. ACS Catal. 10 (2020) 3571-3579.

[13] L. Zhang, K. Doyle-Davis, X. Sun, Pt-Based electrocatalysts with high atom utilization efficiency: from nanostructures to single atoms. Energy Environ. Sci. 12 (2019) 492-517.

[14] X. Han, X. Ling, D. Yu, D. Xie, L. Li, S. Peng, C. Zhong, N. Zhao, Y. Deng, W. Hu, Atomically Dispersed Binary Co-Ni Sites in Nitrogen-Doped Hollow Carbon Nanocubes for Reversible Oxygen Reduction and Evolution. Adv. Mater. 31 (2019) 1905622.

[15] C.Y. Su, H. Cheng, W. Li, Z.Q. Liu, N. Li, Z. Hou, F.Q. Bai, H.X. Zhang, T.Y. Ma, Atomic Modulation of FeCo–Nitrogen–Carbon Bifunctional Oxygen Electrodes for Rechargeable and Flexible All-Solid-State Zinc–Air Battery. Adv. Energy Mater. 7 (2017) 1602420.

[16] Y. Chen, S. Ji, C. Chen, Q. Peng, D. Wang, Y. Li, Single-Atom Catalysts: Synthetic Strategies and Electrochemical Applications. Joule 2 (2018) 1242-1264.

[17] Z. Yu, J. Xu, S. Feng, X. Song, O. Bondarchuk, J.L. Faria, Y. Ding, L. Liu, Rhodium single-atom catalysts with enhanced electrocatalytic hydrogen evolution performance. New J. Chem. 45 (2021) 5770-5774.

[18] D. Zhao, Z. Zhuang, X. Cao, C. Zhang, Q. Peng, C. Chen, Y. Li, Atomic site electrocatalysts for water splitting, oxygen reduction and selective oxidation. Chem. Soc. Rev. 49 (2020) 2215-2264.

[19] Y. Wang, H. Su, Y. He, L. Li, S. Zhu, H. Shen, P. Xie, X. Fu, G. Zhou, C. Feng, D. Zhao, F. Xiao, X. Zhu, Y. Zeng, M. Shao, S. Chen, G. Wu, J. Zeng, C. Wang, Advanced Electrocatalysts with Single-Metal-Atom Active Sites. Chem. Rev. 120 (2020) 12217-12314.

[20] A. Pedersen, J. Barrio, A. Li, R. Jervis, D.J.L. Brett, M.M. Titirici, I.E.L. Stephens, Dual-Metal Atom Electrocatalysts: Theory, Synthesis, Characterization, and Applications. Adv. Energy Mater. 12 (2022) 2102715.

[21] W. Zhang, Y. Chao, W. Zhang, J. Zhou, F. Lv, K. Wang, F. Lin, H. Luo, J. Li, M. Tong, E. Wang, S. Guo, Emerging Dual-Atomic-Site Catalysts for Efficient Energy Catalysis. Adv. Mater. 33 (2021) 2102576.

[22] S. Chen, M. Cui, Z. Yin, J. Xiong, L. Mi, Y. Li, Single-Atom and Dual-Atom Electrocatalysts Derived from Metal Organic Frameworks: Current Progress and Perspectives. ChemSusChem 14 (2021) 73-93.

[23] M. Fan, J. Cui, J. Wu, R. Vajtai, D. Sun, P.M. Ajayan, Improving the Catalytic Activity of Carbon-Supported Single Atom Catalysts by Polynary Metal or Heteroatom Doping. Small 16 (2020) 1906782.

[24] Z. Wang, X. Jin, C. Zhu, Y. Liu, H. Tan, R. Ku, Y. Zhang, L. Zhou, Z. Liu, S.-J. Hwang, H.J. Fan, Atomically Dispersed Co_2–N_6 and Fe–N_4 Costructures Boost Oxygen Reduction Reaction in Both Alkaline and Acidic Media. Adv. Mater. 33 (2021) 2104718.

[25] X. Zhao, X. Liu, B. Huang, P. Wang, Y. Pei, Hydroxyl group modification improves the electrocatalytic ORR and OER activity of graphene supported single and bi-metal atomic catalysts (Ni, Co, and Fe). J. Mater. Chem. A 7 (2019) 24583-24593.

[26] Y. Zhao, K.R. Yang, Z. Wang, X. Yan, S. Cao, Y. Ye, Q. Dong, X. Zhang, J.E. Thorne, L. Jin, K.L. Materna, A. Trimpalis, H. Bai, S.C. Fakra, X. Zhong, P. Wang, X. Pan, J. Guo, M. Flytzani-Stephanopoulos, G.W. Brudvig, V.S. Batista, D. Wang, Stable iridium dinuclear heterogeneous catalysts supported on metal-oxide substrate for solar water oxidation. Proc. Natl. Acad. Sci. USA 115 (2018) 2902-2907.

[27] X. Zeng, J. Shui, X. Liu, Q. Liu, Y. Li, J. Shang, L. Zheng, R. Yu, Single-Atom to Single-Atom Grafting of Pt_1 onto Fe-N_4 Center: Pt_1@Fe-N-C Multifunctional Electrocatalyst with Significantly Enhanced Properties. Adv. Energy Mater. 8 (2018) 1701345.

[28] Z. Li, H. He, H. Cao, S. Sun, W. Diao, D. Gao, P. Lu, S. Zhang, Z. Guo, M. Li, R. Liu, D. Ren, C. Liu, Y. Zhang, Z. Yang, J. Jiang, G. Zhang, Atomic Co/Ni dual sites and Co/Ni alloy nanoparticles in N-doped porous Janus-like carbon frameworks for bifunctional oxygen electrocatalysis. Appl. Catal. B Environ. 240 (2019) 112-121.

[29] A. Walcarius, Mesoporous materials and electrochemistry. Chem. Soc. Rev. 42 (2013) 4098-4140.

[30] K. Artyushkova, B. Kiefer, B. Halevi, A. Knop-Gericke, R. Schlogl, P. Atanassov, Density functional theory calculations of XPS binding energy shift for nitrogen-containing graphene-like structures. Chem. Commun. 49 (2013) 2539-2541.

[31] Y. Wang, Z. Li, P. Zhang, Y. Pan, Y. Zhang, Q. Cai, S.R.P. Silva, J. Liu, G. Zhang, X. Sun, Z. Yan, Flexible carbon nanofiber film with diatomic Fe-Co sites for efficient oxygen reduction and evolution reactions in wearable zinc-air batteries. Nano Energy 87 (2021) 106147.

[32] W. Ren, X. Tan, W. Yang, C. Jia, S. Xu, K. Wang, S.C. Smith, C. Zhao, Isolated Diatomic Ni-Fe Metal–Nitrogen Sites for Synergistic Electroreduction of CO_2. Angew. Chem. Int. Ed. 58 (2019) 6972-6976.

[33] Z. Zeng, L.Y. Gan, H. Bin Yang, X. Su, J. Gao, W. Liu, H. Matsumoto, J. Gong, J. Zhang, W. Cai, Z. Zhang, Y. Yan, B. Liu, P. Chen, Orbital coupling of hetero-diatomic nickel-iron site for bifunctional electrocatalysis of CO_2 reduction and oxygen evolution. Nat. Commun. 12 (2021) 4088.

[34] B. Ravel, M. Newville, ATHENA, ARTEMIS, HEPHAESTUS: data analysis for X-ray absorption spectroscopy using IFEFFIT. J. Synchrotron Radiat. 12 (2005) 537-541.

[35] H. Funke, A.C. Scheinost, M. Chukalina, Wavelet analysis of extended x-ray absorption fine structure data. Phys. Rev. B 71 (2005) 094110.

[36] L. Lin, Q. Zhu, A.-W. Xu, Noble-Metal-Free Fe–N/C Catalyst for Highly Efficient Oxygen Reduction Reaction under Both Alkaline and Acidic Conditions. J. Am. Chem. Soc. 136 (2014) 11027-11033.

[37] Q. Lin, X. Bu, A. Kong, C. Mao, X. Zhao, F. Bu, P. Feng, New Heterometallic Zirconium Metalloporphyrin Frameworks and Their Heteroatom-Activated High-Surface-Area Carbon Derivatives. J. Am. Chem. Soc. 137 (2015) 2235-2238.

[38] Q. Lin, X. Bu, A. Kong, C. Mao, F. Bu, P. Feng, Heterometal-Embedded Organic Conjugate Frameworks from Alternating Monomeric Iron and Cobalt Metalloporphyrins

and Their Application in Design of Porous Carbon Catalysts. Adv. Mater. 27 (2015) 3431-3436.

[39] Z.Y. Wu, X.X. Xu, B.C. Hu, H.W. Liang, Y. Lin, L.F. Chen, S.H. Yu, Iron Carbide Nanoparticles Encapsulated in Mesoporous Fe-N-Doped Carbon Nanofibers for Efficient Electrocatalysis. Angew. Chem. Int. Ed. 54 (2015) 8179-8183.

[40] W. Niu, L. Li, X. Liu, N. Wang, J. Liu, W. Zhou, Z. Tang, S. Chen, Mesoporous N-Doped Carbons Prepared with Thermally Removable Nanoparticle Templates: An Efficient Electrocatalyst for Oxygen Reduction Reaction. J. Am. Chem. Soc. 137 (2015) 5555-5562.

[41] K. Strickland, E. Miner, Q. Jia, U. Tylus, N. Ramaswamy, W. Liang, M.T. Sougrati, F. Jaouen, S. Mukerjee, Highly active oxygen reduction non-platinum group metal electrocatalyst without direct metal–nitrogen coordination. Nat. Commun. 6 (2015) 7343.

[42] W.J. Jiang, L. Gu, L. Li, Y. Zhang, X. Zhang, L.J. Zhang, J.Q. Wang, J.S. Hu, Z. Wei, L.J. Wan, Understanding the High Activity of Fe–N–C Electrocatalysts in Oxygen Reduction: Fe/Fe_3C Nanoparticles Boost the Activity of $Fe–N_x$. J. Am. Chem. Soc. 138 (2016) 3570-3578.

[43] J. Wang, Z. Huang, W. Liu, C. Chang, H. Tang, Z. Li, W. Chen, C. Jia, T. Yao, S. Wei, Y. Wu, Y. Li, Design of N-Coordinated Dual-Metal Sites: A Stable and Active Pt-Free Catalyst for Acidic Oxygen Reduction Reaction. J. Am. Chem. Soc. 139 (2017) 17281-17284.

[44] Y. Chen, S. Ji, Y. Wang, J. Dong, W. Chen, Z. Li, R. Shen, L. Zheng, Z. Zhuang, D. Wang, Y. Li, Isolated Single Iron Atoms Anchored on N-Doped Porous Carbon as an Efficient Electrocatalyst for the Oxygen Reduction Reaction. Angew. Chem. Int. Ed. 56 (2017) 6937-6941.

[45] S.J. Kim, J. Mahmood, C. Kim, G.F. Han, S.W. Kim, S.M. Jung, G. Zhu, J.J. De Yoreo, G. Kim, J.B. Baek, Defect-Free Encapsulation of Fe_0 in 2D Fused Organic Networks as a Durable Oxygen Reduction Electrocatalyst. J. Am. Chem. Soc. 140 (2018) 1737-1742.

[46] B.C. Hu, Z.Y. Wu, S.Q. Chu, H.W. Zhu, H.W. Liang, J. Zhang, S.H. Yu, SiO_2-protected shell mediated templating synthesis of Fe–N-doped carbon nanofibers and their enhanced oxygen reduction reaction performance. Energy Environ. Sci. 11 (2018) 2208-2215.

[47] Y. Chen, S. Ji, S. Zhao, W. Chen, J. Dong, W.C. Cheong, R. Shen, X. Wen, L. Zheng, A.I. Rykov, S. Cai, H. Tang, Z. Zhuang, C. Chen, Q. Peng, D. Wang, Y. Li, Enhanced oxygen reduction with single-atomic-site iron catalysts for a zinc-air battery and hydrogen-air fuel cell. Nat. Commun. 9 (2018) 5422.

[48] L. Yang, D. Cheng, H. Xu, X. Zeng, X. Wan, J. Shui, Z. Xiang, D. Cao, Unveiling the high-activity origin of single-atom iron catalysts for oxygen reduction reaction. Proc. Natl. Acad. Sci. USA 115 (2018) 6626-6631.

[49] Q. Liu, X. Liu, L. Zheng, J. Shui, The Solid-Phase Synthesis of an Fe-N-C Electrocatalyst for High-Power Proton-Exchange Membrane Fuel Cells. Angew. Chem. Int. Ed. 57 (2018) 1204-1208.

[50] L. Jiao, G. Wan, R. Zhang, H. Zhou, S.H. Yu, H.L. Jiang, From Metal–Organic Frameworks to Single-Atom Fe Implanted N-doped Porous Carbons: Efficient Oxygen Reduction in Both Alkaline and Acidic Media. Angew. Chem. Int. Ed. 57 (2018) 8525-8529.

[51] D. Wang, L. Xiao, P. Yang, Z. Xu, X. Lu, L. Du, O. Levin, L. Ge, X. Pan, J. Zhang, M. An, Dual-nitrogen-source engineered Fe–N_x moieties as a booster for oxygen electroreduction. J. Mater. Chem. A 7 (2019) 11007-11015.

[52] S.H. Lee, J. Kim, D.Y. Chung, J.M. Yoo, H.S. Lee, M.J. Kim, B.S. Mun, S.G. Kwon, Y.E. Sung, T. Hyeon, Design Principle of Fe–N–C Electrocatalysts: How to Optimize Multimodal Porous Structures? J. Am. Chem. Soc. 141 (2019) 2035-2045.

[53] L. Zhao, Y. Zhang, L.B. Huang, X.Z. Liu, Q.H. Zhang, C. He, Z.Y. Wu, L.J. Zhang, J. Wu, W. Yang, L. Gu, J.S. Hu, L.J. Wan, Cascade anchoring strategy for general mass production of high-loading single-atomic metal-nitrogen catalysts. Nat. Commun. 10 (2019) 1278.

[54] K. Yuan, D. Lützenkirchen-Hecht, L. Li, L. Shuai, Y. Li, R. Cao, M. Qiu, X. Zhuang, M.K.H. Leung, Y. Chen, U. Scherf, Boosting Oxygen Reduction of Single Iron Active Sites via Geometric and Electronic Engineering: Nitrogen and Phosphorus Dual Coordination. J. Am. Chem. Soc. 142 (2020) 2404-2412.

[55] C.Y. Lin, L. Zhang, Z. Zhao, Z. Xia, Design Principles for Covalent Organic Frameworks as Efficient Electrocatalysts in Clean Energy Conversion and Green Oxidizer Production. Adv. Mater. 29 (2017) 1606635.

[56] J.K. Nørskov, F. Abild-Pedersen, F. Studt, T. Bligaard, Density functional theory in surface chemistry and catalysis. Proc. Natl. Acad. Sci. USA 108 (2011) 937-943.

[57] Y. Li, B. Wei, M. Zhu, J. Chen, Q. Jiang, B. Yang, Y. Hou, L. Lei, Z. Li, R. Zhang, Y. Lu, Adv. Mater. 33 (2021) 2102212.

[58] P.E. Blöchl, Projector augmented-wave method. Phys. Rev. B 50 (1994) 17953-17979.

[59] G. Kresse, J. Furthmüller, Efficient iterative schemes for ab initio total-energy calculations using a plane-wave basis set. Phys. Rev. B 54 (1996) 11169-11186.

[60] J.P. Perdew, K. Burke, M. Ernzerhof, Generalized Gradient Approximation Made Simple. Phys. Rev. Lett. 77 (1996) 3865-3868.

[61] C.C.L. McCrory, S. Jung, J.C. Peters, T.F. Jaramillo, Benchmarking Heterogeneous Electrocatalysts for the Oxygen Evolution Reaction. J. Am. Chem. Soc. 135 (2013) 16977-16987.

6. Conclusions and outlook

6.1 General conclusions

In summary, this PhD thesis developed serials of effective electrocatalyst/photocatalyst based on self-supported electrode, NCs and ADCs. The physical-chemical properties and electro/photochemical behaviors of these materials towards to energy conversion were investigated both experimentally and by theoretical calculations. The main conclusions were list as below:

Saline water electrolysis over self-supported electrode

In **Chapter 2**, the carbon paper was firstly used as the substrate to load Co-Ni-P nanowires (Co-Ni-P/CP). The as-prepared Co-Ni-P/CP exhibit high electrocatalytic activity for HzOR, delieving a large anodic current density of 500 mA cm^{-2} at a potential as low as 0.175 V vs. RHE in the alkaline-saline-hydrazine electrolyte, where the evolution of OCl^- species is fully blocked even at such a high current density. Consequently, by coupling the cathodic HER with the HzOR taking place at the anode using the Co-Ni-P/CP as bifunctional electrode, the overall saline water electrolysis (OSWE) can be achieved at a low cell voltage of 0.533 V at 500 mA cm^{-2} without the unfavorable, interfering CER, and more impressively, it can be sustained at 500 mA cm^{-2} for at least 80 hours without obvious degradation, which shows great promise for industrial seawater electrolysis.

Furthermore, the nickel/iron foam with more mechanical flexibility was designed and fabricated to *in situ* grow nickel-iron phosphosulfide (NiFeSP) nanotube array through a two-step sulfurization/phosphorization approach. When used to catalyze the OER and UOR in alkaline-saline water, the NiFeSP electrode can deliver 500 mA cm^{-2} at low potentials of 1.490 and 1.424 V vs. RHE respectively, effectively avoiding the CER from happening. Moreover, the NiFeSP electrode can exhibit high HER activity, showing the multifuctionalty. Advanced materials characterization techniques (including TEM and synchrotron-based XAS) and theoretical DFT calculations confirm that the NiFeS/NiFeP heterointerfaces and under-coordinated metal sites synergistically promote the electrocatalytic performance. Furthermore, the OSWE and the overall urea-mediated saline water electrolysis (OUSWE) enabled by bifunctional NiFeSP electrodes can operate at 500 mA cm^{-2} under a low cell voltage with a long-term stability of 1000 hours.

Ultrafine oxygen-defective iridium oxide nanoclusters for efficient and durable water oxidation at high current densities in acidic media

In **Chapter 3**, the ultrafine IrO_x NCs was designed to catalyze the acidic OER. By optimizing the loading densities and type of substrate, an ultrafine oxygen-defective IrO_x NCs (1 – 2 nm) can be deposited on a high-surface-area, acid-stable titanium current collector (H-Ti@IrO_x), through a repeated impregnation-annealing process. Benefiting from the advantages of small cluster size, which leads to the exposure of a large active surface area, and oxygen-defective feature, which results in an electronic structure favorable for the OER, the obtained H-Ti@IrO_x electrode exhibits excellent electrocatalytic OER activity, with low overpotentials of 277 and 336 mV to deliver 10 and 200 mA cm^{-2} in 0.5 M H_2SO_4. With the aids of intimate contact between IrO_x NCs and acid-stable H-Ti foam, the H-Ti@IrO_x is able to continuously catalyze the OER at a high current density of 200 mA cm^{-2} in 0.5 M H_2SO_4 for 130 hours without notable degradation. Comprehensive experimental studies and density functional theory calculations confirm the important role of oxygen defects in the enhanced OER performance. Thus-fabricated electrode combines several merits including the small size, oxygen defects and high-surface-area, acid-stable support, which can work in synergy boosting the electrocatalytic acidic OER activity and long-term stability.

Efficient hydrogen production over atomically dispersed catalysts

In **Chapter 4**, a series of ADCs were designed and fabricated to promote the hydrogen production. Firstly, the Rh SACs supported on activated carbon (Rh_1/AC) towards the electrocatalytic HER was reported. Using Rh NPs as the starting materials, the Rh_1/AC synthesized *via* a “top-down” chemical reaction induced dispersion process, which exhibited the outstanding electrocataltic HER activity and durability in alkaline medium due to the a atomic dispersion. Secordly, atomically dispersed ruthenium catalysts (Ru (0.2)-NC) with ultralow Ru loading was synthesized through a two-step wet chemical impregnation – pyrolysis method. The as-prepared Ru (0.2)-NC exhibits outstanding HER and OER performance in alkaline medium, as well as good catalytic stability of at least 100 h at a current density of 10 mA cm^{-2}, showing favorable bifunctionality. DFT calculations reveal that the Ru-N bonding plays an important role in lowering the energy barrier of the reactions, boosting the HER and OER activities. Furthermore, with the aids of BPM, the BPMWE using the bifunctional Ru (0.2)-NC as both HER and OER catalysts can afford 10 mA cm^{-2} under a low cell voltage of only 0.89 V, and does not show any performance decay upon 100-h continuous operation, showing

great promise for low-cost, energy-saving production of green hydrogen. Finally, Ir/Ru SACs were designed to be anchored on mesoporous graphitic carbon nitride (Ir-g-CN and Ru-g-CN), which can act as efficient and stable HER catalysts for electrocatalytic and photocatalytic water splitting. Remarkably, Ru-g-CN reveals outstanding electro/photocatalytic HER activity and stability, respectively. DFT calculations disclose that the atomic dispersion of Ir and Ru on g-CN reduces the bandgap and increases electrical conductivity. Moreover, introducing Ir or Ru onto the surface of g-CN has been demonstrated to be able to promote the electron transfer and lead to optimal Gibbs free energy of hydrogen adsorption, contributing to the remarkable improvement of the electrocatalytic and photocatalytic HER performance.

Iridium-iron diatomic active sites for efficient bifunctional oxygen electrocatalysis

In **Chapter 5**, based on the research of **Chapter 4**, the IrFe DACs (IrFe-N-C), with their advantages over SACs in reactions involving multi-electron transfers, were designed and fabricated, derived from MOFs in a facile wet chemical synthesis followed by post-pyrolysis. Various advanced characterization techniques including the HAADF-STEM and synchrotron-based XAS unambiguously confirmed the atomic dispersion of Ir and Fe and the presence of IrFe atomic pairs. The as-obtained IrFe-N-C shows substantially higher electrocatalytic performance for both ORR and OER when compared to the single-atom counterparts (*i.e.*, Ir-N-C and Fe-N-C), revealing favorable bifunctionality, and outperform many state-of-the-art bifunctional ORR/OER catalysts reported in the literature. The excellent bifunctionality of IrFe-N-C enables it to serve as a high-performance air cathode in ZABs. Moreover, our DFT calculations demonstrate that the diatomic configuration leads to subtle electronic structure modulation. Fe in the diatomic sites contributes more to the ORR, while Ir in the diatomic sites plays a more important role in the OER. The two active sites work in synergy and altogether promote oxygen electrocatalysis.

6.2 Outlook for future

The rational design of advanced catalysts with high activity and low cost is of paramount significance for renewable and sustainable energy storage and conversion systems. Considering the enormous potential of self-supported electrode, NCs and ADCs, plenty of opportunities may push the rapid development further. Nevertheless, despite tremendous progress in recent years, further development in the following aspects is envisioned to be essential for advancing the practical implementation: 1) explore pH-universal self-supported catalysts; 2) explore more kinds of NC catalysts; 3) improve the

loading amounts and stability of ADCs; 4) explore the real process for the energy conversion.

1) Due to several remarkable traits, that is, binder-free, large surface area and rapid delivery of charge and mass, considerable efficient and low-cost self-supported TM-based electrocatalysts have been developed in the past few years. However, the majority of currently explored self-supported TM-based catalysts displayed outstanding performance only for the alkaline environment, which limits their practical application under wide-pH conditions. In other words, in acid or neutral media, such efficient catalysts were rarely reported, especially for full water splitting, at large current density, and within long-term working period. This may be mainly attributed to the poor OER activity, unstable chemical and structural properties of electrocatalysts in the acid environment, as well as low solution conductivity of the neutral electrolyte [1-3]. To deal with it, some points are suggested to be considered. First, some compositions with relatively great inherent corrosion resistance in acid media should be favorably selected to synthesize electrocatalysts, such as nitrides, phosphides, alloys, and intermetallics [4-8]. Second, the “anti-corrosion coating,” which will simultaneously keep or even boost the activity of inner catalytic species in an acid environment can be utilized, for example, FTO, carbon-based and Ti-based materials [9-11]. Third, for low-conductive neutral electrolytes, the emphasis should be given to the improvement of intrinsic conductivity and increment of electrochemically active sites of the electrocatalysts themselves.

2) Downsizing the metal particles from nano-meter to sub-nano-meter scale has proven to be an efficient strategy to obtain attractive catalytic properties [12, 13]. For NCs, increasing or decreasing the number of atoms results in different catalytic behaviors [13-15]. So far, numbers of metals NCs have been studied using DFT simulations [16]. But only a small portion of them have been validated by experiments, the variety of materials screened so far is remarkably small. In fact, the preparation of metal NCs with a few atoms in a controllable manner is still a challenge, which is hardly achievable using the traditional preparation methods [17]. Therefore, in future work, more novel synthesis strategies are needed for developing effective NC catalysts. In addition, the combination of theoretical model studies and experiment analysis will also promote the exploration of catalysts with high catalytic activities.

3) Further reducing the size of metal catalysts to isolated atoms is a major breakthrough for energy conversion [18]. Because of its unique electronic and structural properties of isolated active sites, the ADCs could achieve excellent catalytic

performance and selectivity in various chemical reactions [19-21]. For practical applications, high performance will require a high density of single metal atoms for abundant active sites; therefore, the limited loading of metal single atoms in the ADCs still need to be further increased to meet the requirement for the practical application [21, 22]. Even this loading value has been significantly enhanced in recent years, there are still full of opportunities and challenges need to be addressed for the SACs field: i) synthesis of high metal loading SACs; ii) design and synthesis of DACs and TACs, in this ways, it not only increases the mass loading of metal atom but also alter more efficiently geometrical configurations and electronic structures, further promoting the excellent catalytic performance [22, 23].

Moreover, stability remains a major challenges for ADCs due to the high surface energies, which result in the possible aggregation and leaching during the catalytic process, especially at high metal loading [22]. To address this problem, selecting the appropriate metal and suitable supports and strengthening their interaction are among the most effective strategies. Constructing a SMSIs can ensure the stability by mitigating the aggregation of isolated reactive centers in the catalytic process [18]. Furthermore, forming diatomic active sites has been suggested to be another effective strategy to enhance the stability. For instance, single-atom alloys and carbide supported SACs might be a good choice for the acid OER due to their high conductivity and good corrosion resistance in acid environments [24, 25]. These approaches would be effective for developing excellent catalysts for further industrial applications.

4) Most of the currently developed catalysts are “pre-catalysts”, which partially or completely transform into real catalytically active structures under different conditions of HER, OER, or working electrolytes [26]. Elucidating the real active species, electronic and geometric structure changes under *in situ* states for electrocatalysts in a particular reaction is essential to help researchers deeply understand their structure-activity relationship and lay a foundation for rational design high performance electrocatalysts. It is important to study the reaction intermediates and real-time monitor the dynamic behaviors of both the electronic environment and geometric structure of the active sites by advanced *in situ* or operando characterization techniques, including spectroscopic techniques (such as XAS, XPS, Raman, FT-IR, Mössbauer, nuclear resonant inelastic X-ray scattering, EIS and XRD) [27] as well as microscopic techniques (such as atomic force microscope (AFM) and TEM) [28]. Besides, theoretical methods, which can be applied in simulated, controlled, and reproducible conditions, are greatly anticipated to unravel the possible reaction pathway. Thus, with the advanced characterization

techniques and theoretical simulation and calculations, we can make great progress in understanding the fundamental properties of efficient electrocatalysts and realize the ultimate goal of manipulating individual atoms for function.

All in all, it is still highly challenging and urgent for the rational design of high-performance electrocatalysts. Substantial interest has been devoted to tuning the electronic structure, insight into the fundamentals of active sites and mechanisms, and fabricating integrated electrodes for practical applications. This renders the combination of single atoms and 3D self-supported substrates extremely promising for the rational design of ADCs with superior activity and selectivity. In this way, specific catalysts can be designed for the target reactions at the atomic scale to give full play to the maximum capacity of each atom to boost reaction kinetics, mass transfer, and achieve the green catalytic process of the atomic economy.

6.3 Reference

[1] L. Fu, X. Hu, Y. Li, G. Cheng, W. Luo, IrW nanobranches as an advanced electrocatalyst for pH-universal overall water splitting. Nanoscale 11 (2019) 8898-8905.

[2] J.R. Kish, M.B. Ives, J.R. Rodda, Corrosion Mechanism of Nickel in Hot, Concentrated H_2SO_4. J. Electrochem. Soc. 147 (2000) 3637.

[3] H. Yang, M. Driess, P.W. Menezes, Self-Supported Electrocatalysts for Practical Water Electrolysis. Adv. Energy Mater. 11 (2021) 2102074.

[4] B. Chakraborty, R. Beltrán-Suito, J.N. Hausmann, S. Garai, M. Driess, P.W. Menezes, Enabling Iron-Based Highly Effective Electrochemical Water-Splitting and Selective Oxygenation of Organic Substrates through In Situ Surface Modification of Intermetallic Iron Stannide Precatalyst. Adv. Energy Mater. 10 (2020) 2001377.

[5] N.T. Suen, S.F. Hung, Q. Quan, N. Zhang, Y.J. Xu, H.M. Chen, Electrocatalysis for the oxygen evolution reaction: recent development and future perspectives. Chem. Soc. Rev. 46 (2017) 337-365.

[6] C. Walter, P.W. Menezes, M. Driess, Perspective on intermetallics towards efficient electrocatalytic water-splitting. Chem. Sci. 12 (2021) 8603-8631.

[7] L. Lin, S. Piao, Y. Choi, L. Lyu, H. Hong, D. Kim, J. Lee, W. Zhang, Y. Piao, Nanostructured Transition Metal Nitrides as Emerging Electrocatalysts for Water Electrolysis: Status and Challenges. EnergyChem 4 (2022) 100072.

[8] Y. Li, Z. Dong, L. Jiao, Multifunctional Transition Metal-Based Phosphides in Energy-Related Electrocatalysis. Adv. Energy Mater. 10 (2020) 1902104.

[9] Z. Yu, J. Xu, Y. Li, B. Wei, N. Zhang, Y. Li, O. Bondarchuk, H. Miao, A. Araujo, Z. Wang, J.L. Faria, Y. Liu, L. Liu, Ultrafine oxygen-defective iridium oxide nanoclusters for efficient and durable water oxidation at high current densities in acidic media. J. Mater. Chem. A 8 (2020) 24743-24751.

[10] D. Schonvogel, J. Hülstede, P. Wagner, A. Dyck, C. Agert, M. Wark, Durability of Electrocatalysts for ORR: Pt on Nanocomposite of Reduced Graphene Oxide with FTO versus Pt/C. J. Electrochem. Soc. 165 (2018) F3373-F3382.

[11] J. Deng, P. Ren, D. Deng, L. Yu, F. Yang, X. Bao, Highly active and durable non-precious-metal catalysts encapsulated in carbon nanotubes for hydrogen evolution reaction. Energy Environ. Sci. 7 (2014) 1919-1923.

[12] S. Zhao, R. Jin, R. Jin, Opportunities and Challenges in CO_2 Reduction by Gold- and Silver-Based Electrocatalysts: From Bulk Metals to Nanoparticles and Atomically Precise Nanoclusters. ACS Energy Lett. 3 (2018) 452-462.

[13] Z. Xu, F.S. Xiao, S.K. Purnell, O. Alexeev, S. Kawi, S.E. Deutsch, B.C. Gates, Size-dependent catalytic activity of supported metal clusters. Nature 372 (1994) 346-348.

[14] K. Yamamoto, T. Imaoka, W.J. Chun, O. Enoki, H. Katoh, M. Takenaga, A. Sonoi, Size-specific catalytic activity of platinum clusters enhances oxygen reduction reactions. Nat. Chem. 1 (2009) 397-402.

[15] Y. Attia, M. Samer, Metal clusters: New era of hydrogen production. Renew. Sust. Energ. Rev. 79 (2017) 878-892.

[16] X. Mao, L. Wang, Y. Xu, P. Wang, Y. Li, J. Zhao, Computational high-throughput screening of alloy nanoclusters for electrocatalytic hydrogen evolution. npj Computational Materials 7 (2021) 46.

[17] H. Rong, S. Ji, J. Zhang, D. Wang, Y. Li, Synthetic strategies of supported atomic clusters for heterogeneous catalysis. Nat. Commun. 11 (2020) 5884.

[18] L. Liu, A. Corma, Metal Catalysts for Heterogeneous Catalysis: From Single Atoms to Nanoclusters and Nanoparticles. Chem. Rev. 118 (2018) 4981-5079.

[19] J. Zhang, H. Zhang, Y. Wu, C. Liu, Y. Huang, W. Zhou, B. Zhang, Single-atom catalysts for thermal- and electro-catalytic hydrogenation reactions. J. Mater. Chem. A 10 (2022) 5743-5757.

[20] X.F. Yang, A. Wang, B. Qiao, J. Li, J. Liu, T. Zhang, Single-Atom Catalysts: A New Frontier in Heterogeneous Catalysis. Acc. Chem. Res. 46 (2013) 1740-1748.

[21] F. Zhang, Y. Zhu, Q. Lin, L. Zhang, X. Zhang, H. Wang, Noble-metal single-atoms in thermocatalysis, electrocatalysis, and photocatalysis. Energy Environ. Sci. 14 (2021) 2954-3009.

[22] Z.W. Chen, L.X. Chen, C.C. Yang, Q. Jiang, Atomic (single, double, and triple atoms) catalysis: frontiers, opportunities, and challenges. J. Mater. Chem. A 7 (2019) 3492-3515.

[23] T. He, A.R.P. Santiago, Y. Kong, M.A. Ahsan, R. Luque, A. Du, H. Pan, Atomically Dispersed Heteronuclear Dual-Atom Catalysts: A New Rising Star in Atomic Catalysis. Small 18 (2022) 2106091.

[24] N. Han, K.R. Yang, Z. Lu, Y. Li, W. Xu, T. Gao, Z. Cai, Y. Zhang, V.S. Batista, W. Liu, X. Sun, Nitrogen-doped tungsten carbide nanoarray as an efficient bifunctional electrocatalyst for water splitting in acid. Nat. Commun. 9 (2018) 924.

[25] J. Mao, J. Yin, J. Pei, D. Wang, Y. Li, Single atom alloy: An emerging atomic site material for catalytic applications. Nano Today 34 (2020) 100917.

[26] W. Li, D. Xiong, X. Gao, L. Liu, The oxygen evolution reaction enabled by transition metal phosphide and chalcogenide pre-catalysts with dynamic changes. Chem. Commun. 55 (2019) 8744-8763.

[27] X. Li, H.Y. Wang, H. Yang, W. Cai, S. Liu, B. Liu, In Situ/Operando Characterization Techniques to Probe the Electrochemical Reactions for Energy Conversion. Small Methods 2 (2018) 1700395.

[28] S. Hwang, X. Chen, G. Zhou, D. Su, In Situ Transmission Electron Microscopy on Energy-Related Catalysis. Adv. Energy Mater. 10 (2020) 1902105.

Annex

List of publications

International peer-reviewed publications

[1] **Zhipeng Yu**, Chaowei Si, Alec P. LaGrow, Zhixin Tai, Wolfgang A. Caliebe, Akhil Tayal, Maria J. Sampaio, Juliana P.S. Sousa, Isilda Amorim, Ana Araujo, Lijian Meng, Joaquim L. Faria*, Junyuan Xu*, Bo Li*, Lifeng Liu*, Iridium–Iron Diatomic Active Sites for Efficient Bifunctional Oxygen Electrocatalysis, **ACS Catalysis,** *2022*, 12, 9397-9409.

[2] **Zhipeng Yu**, Yifan Li, Vlad Martin-Diaconescu, Laura Simonelli, Jonathan Ruiz Esquius, Isilda Amorim, Ana Araujo, Lijian Meng, Joaquim L. Faria, Lifeng Liu*, Highly efficient and stable saline water electrolysis enabled by self-supported nickel-iron phosphosulfide nanotubes with heterointerfaces and under-coordinated metal active sites, **Advanced Functional Materials,** *2022*, 32, 2206138.

[3] **Zhipeng Yu,** Chaowei Si, Francisco Javier Escobar-Bedia, Alec P. LaGrow, Junyuan Xu, Maria J. Sabater, Isilda Amorim, Ana Araujo, Juliana P.S. Sousa, Lijian Meng, Joaquim L. Faria, Patricia Concepcion, Bo Li*, Lifeng Liu*, Bifunctional atomically dispersed ruthenium electrocatalysts for efficient bipolar membrane water electrolysis, **Inorganic Chemistry Frontiers,** *2022*, 9, 4142-4150.

[4] **Zhipeng Yu**, Yifan Li, André Torres-Pinto, Alec P. LaGrow, Maria J. Sampaio, Oleksandr Bondarchuk, Isilda Amorim, Ana Araujo, Adrián M. T. Silva, Cláudia G. Silva, Joaquim L. Faria*, Lifeng Liu*, Single-atom Ir and Ru anchored on graphitic carbon nitride for efficient and stable electrocatalytic/photocatalytic hydrogen evolution, **Applied Catalysis B: Environmental,** *2022***,** 310, 121318.

[5] Zhixin Tai, Yajie Liu, **Zhipeng Yu**, Ziyu Lu, Oleksandr Bondarchuk, Zhijian Peng, Lifeng Liu*, Non-collapsing 3D solid-electrolyte interphase for high-rate rechargeable sodium metal batteries, **Nano Energy**, *2022*, 94, 106947.

[6] **Zhipeng Yu**, Junyuan Xu, Lijian Meng, Lifeng Liu*, Efficient hydrogen production by saline water electrolysis at high current densities without the interfering chlorine evolution, **Journal of Materials Chemistry A**, *2021*, 9, 22248-22253.

[7] Maria J. Sampaio*, **Zhipeng Yu**, Joana C. Lopes, Pedro B. Tavares, Cláudia G. Silva, Lifeng Liu, Joaquim L. Faria, Light-driven oxygen evolution from water oxidation: TiO_2 engineering in the performance of the immobilised photocatalysts, **Scientific Reports**, *2021*, 11, 21306.

[8] Ziyu Lu, Zhixin Tai, **Zhipeng Yu**, Alec P. LaGrow, Oleksandr Bondarchuk, Juliana P.S. Sousa, Lijian Meng, Zhijian Peng*, Lifeng Liu*, Lithium–copper alloy embedded in 3D porous copper foam with enhanced electrochemical performance toward lithium metal batteries, **Material Today Energy**, *2021*, 22, 100871.

[9] **Zhipeng Yu**, Junyuan Xu, Siquan Feng, Xiangen Song, Oleksandr Bondarchuk, Joaquim L. Faria, Yunjie Ding*, Lifeng Liu*, Rhodium single-atom catalysts with enhanced electrocatalytic hydrogen evolution performance, **New Journal of Chemistry**, *2021*, 45, 5770-5774.

[10] **Zhipeng Yu**, Xiankui Wei, Junyuan Xu, Yue Li, Ana Araujo, Joaquim L. Faria, Rafal E. Dunin-Borkowski, Lifeng Liu*, Multifunctional Noble Metal Phosphide Electrocatalysts for Organic Molecule Electro-Oxidation, **ACS Applied Energy Materials**, *2021*, 4, 1593-1600.

[11] **Zhipeng Yu**, Junyuan Xu, Isilda Amorim, Yue Li, Lifeng Liu*, Easy preparation of multifunctional ternary PdNiP/C catalysts toward enhanced small organic molecule electro-oxidation and hydrogen evolution reactions, **Journal of Energy Chemistry**, *2021*, 58, 256-263.

[12] Isilda Amorim, Junyuan Xu, Nan Zhang, **Zhipeng Yu**, Ana Araújo, Fátima Bento, Lifeng Liu*, Dual-phase CoP−$CoTe_2$ nanowires as an efficient bifunctional electrocatalyst for bipolar membrane-assisted acid-alkaline water splitting, **Chemical Engineering Journal**, *2021*, 420, 130454.

[13] Junyuan Xu, Junjie Li, Zan Lian, Ana Araujo, Yue Li, Bin Wei, **Zhipeng Yu**, Oleksandr Bondarchuk, Isilda Amorim, Vasiliki Tileli*, Bo Li*, Lifeng Liu*, Atomic-Step Enriched Ruthenium–Iridium Nanocrystals Anchored Homogeneously on MOF-Derived Support for Efficient and Stable Oxygen Evolution in Acidic and Neutral Media, **ACS Catalysis**, *2021*, 11, 3402–3413.

[14] **Zhipeng Yu**, Junyuan Xu, Yifan Li, Bin Wei, Nan Zhang, Yue Li, Oleksandr Bondarchuk, Hongwei Miao, Ana Araujo, Zhongchang Wang, Joaquim L. Faria, Yuanyue Liu*, Lifeng Liu*, Ultrafine oxygen-defective iridium oxide nanoclusters for efficient and durable water oxidation at high current densities in acidic media, **Journal of Materials Chemistry A**, *2020*, 8, 24743-24751.

[15] Yue Li, Bin Wei, **Zhipeng Yu**, Oleksandr Bondarchuk, Ana Araujo, Isilda Amorim, Nan Zhang, Junyuan Xu, Isabel C. Neves, Lifeng Liu*, Bifunctional Porous Cobalt Phosphide Foam for High-Current-Density Alkaline Water Electrolysis with 4000-h Long Stability, **ACS Sustainable Chemistry & Engineering**, *2020*, 8, 27, 10193–10200.

[16] Junyuan Xu, Isilda Amorim, Yue Li, Junjie Li, **Zhipeng Yu**, Bingsen Zhang, Ana Araujo, Nan Zhang, Lifeng Liu*, Stable overall water splitting in an asymmetric

acid/alkaline electrolyzer comprising a bipolar membrane sandwiched by bifunctional cobalt-nickel phosphide nanowire electrodes, **Carbon Energy**, *2020,* 2, 646– 655.

[17] Junyuan Xu, Zan Lian, Bin Wei, Yue Li, Oleksandr Bondarchuk, Nan Zhang, **Zhipeng Yu**, Ana Araujo, Isilda Amorim, Zhongchang Wang*, Bo Li*, Lifeng Liu*, Strong Electronic Coupling between Ultrafine Iridium–Ruthenium Nanoclusters and Conductive, Acid-Stable Tellurium Nanoparticle Support for Efficient and Durable Oxygen Evolution in Acidic and Neutral Media, **ACS Catalysis**, *2020*, 10, 6, 3571–3579.

Book chapters

[1] "Supported Metal Single – Atom Photocatalysis"
Bruno F. Machado, Lifeng Liu, **Zhipeng Yu**, Joaquim L. Faria
Chapter 14 in the book "Supported Metal Single Atom Catalysis" (Print ISBN: 9783527348442; Online ISBN: 9783527830169), Editor(s): Philippe Serp, Doan Pham Minh, WILEY-VCH GmbH. March 2022

Conference contributions

[1] Metal organic framework derived iridium-iron diatomic active sites for efficient bifunctional oxygen electrocatalysis. [**Oral presentation**]
Zhipeng Yu, Chaowei Si, Alec P. LaGrow, Zhixin Tai, Wolfgang A. Caliebe, Akhil Tayal, Maria J. Sampaio, Juliana P.S. Sousa, Isilda Amorim, Ana Araujo, Joaquim L. Faria, Junyuan Xu, Bo Li and Lifeng Liu
Symposium Q, 2022 Fall Meeting of the European Materials Research Society (E-MRS), Sep 19-22, 2022 Warsaw
https://www.european-mrs.com/meetings/2022-fall-meeting

[2] Efficient saline water electrolysis enabled by under-coordinated metal active sites and heterointerfaces over NiFeSP electrode. [**Poster presentation**]
Zhipeng Yu, Yifan Li, Vlad M. Diaconescu, Laura Simonelli, Jonathan R. Esquius, Isilda Amorim, Ana Araujo, Joaquim L. Faria and Lifeng Liu
Symposium Q, 2022 Fall Meeting of the European Materials Research Society (E-MRS), Sep 19-22, 2022 Warsaw
https://www.european-mrs.com/meetings/2022-fall-meeting

[3] Bipolar membrane enabled overall water electrolysis using bifunctional atomically dispersed ruthenium electrocatalysts. [**Oral presentation**]
Zhipeng Yu, Francisco Javier Escobar-Bedia, Maria J. Sabater, Isilda Amorim, Ana Araujo, Patricia Concepcion and Lifeng Liu
Symposium C, 2021 Fall Meeting of the European Materials Research Society (E-MRS), Sep 20-23, 2021

https://www.european-mrs.com/meetings/2021-fall-meeting

[4] Easy preparation of multifunctional ternary PdNiP/C catalysts toward enhanced small organic molecule electro-oxidation and hydrogen evolution reactions. [**Poster presentation**]

Zhipeng Yu, Junyuan Xu, Isilda Amorim, Yue Li and Lifeng Liu

Symposium C, 2021 Fall Meeting of the European Materials Research Society (E-MRS), Sep 20-23, 2021

https://www.european-mrs.com/meetings/2021-fall-meeting

[5] Atomically dispersed noble metal-based carbon nitride catalyst for highly efficient and stable electrocatalytic/photocatalytic hydrogen evolution reaction. [**Oral presentation**]

Zhipeng Yu, André Torres-Pinto, Maria J. Sampaio, Isilda Amorim, Ana Araujo, Cláudia G. Silva Joaquim L. Faria and Lifeng Liu

The 2nd edition of the NanoPT Online Conference (NanoPT2021), Sep 16-17, 2021

https://www.confstreaming.com/nanoPT2021

[6] Highly dispersed noble metal-based carbon nitride as efficient electrocatalytic/photocatalytic hydrogen evolution reaction catalysts. [**Oral presentation**]

Zhipeng Yu, André Torres-Pinto, Maria J. Sampaio, Isilda Amorim, Ana Araujo, Cláudia G. Silva, Lifeng Liu and Joaquim L. Faria

The XXVII National Meeting of the Portuguese Chemical Society, July 14-16, 2021, Braga

https://xxviienspq.events.chemistry.pt

[7] Ultrafine oxygen-defective iridium oxide nanoclusters for efficient and durable water oxidation at high current densities in acidic media. [**Oral presentation**]

Zhipeng Yu, Junyuan Xu, Yifan Li, Bin Wei, Yue Li, Oleksandr Bondarchuk, Ana Araujo, Zhongchang Wang, Joaquim L. Faria, Yuanyue Liu and Lifeng Liu

Symposium on Chemical and Biological Engineering, The 4th Doctoral Congress in Engineering, June 28-29, 2021

https://paginas.fe.up.pt/~dce/2021

[8] Multifunctional noble metal phosphide electrocatalysts for the organic molecule electro-oxidation. [**Oral presentation**]

Zhipeng Yu, Xiankui Wei, Junyuan Xu, Yue Li, Ana Araujo, Isilda Amorim, Joaquim L. Faria, Rafal E. Dunin-Borkowski and Lifeng Liu

Symposium I, The 239th ECS Meeting, May 30-June 3, 2021

https://www.electrochem.org/239

[9] Highly dispersed ruthenium-based multifunctional electrocatalyst for efficient overall water splitting with bipolar membrane assisted. [**Oral presentation**]

Zhipeng Yu, Francisco Javier Escobar-Bedia, Maria J. Sabater, Isilda Amorim, Ana Araujo, Patricia Concepcion and Lifeng Liu

Symposium L, The 239th ECS Meeting, May 30-June 3, 2021

https://www.electrochem.org/239

[10] Ultrafine oxygen vacancy-rich iridium oxide nanoclusters supported on high-surface-area, acid-stable titanium substrate for efficient and durable water oxidation at high current densities in acidic media. [**Oral presentation**]

Zhipeng Yu, Junyuan Xu, Yifan Li, Bin Wei, Nan Zhang, Yue Li, Hongwei Miao, Ana Araujo, Zhongchang Wang, Joaquim L. Faria, Yuanyue Liu and Lifeng Liu

Future Materials 2020, Materials Science & Nanotechnology Conference, Feb 26-28, 2020, Lisbon

https://materialsconference.yuktan.com/2020